Soils and Rocks publishes papers in English in the broad fields of Geotechnical Engineering, Engineering Geology, and Geoenvironmental Engineering. The Journal is published quarterly in March, June, September and December. The first issue was released in 1978, under the name *Solos e Rochas*, being originally published by the Graduate School of Engineering of the Federal University of Rio de Janeiro. In 1980, the Brazilian Association for Soil Mechanics and Geotechnical Engineering took over the editorial and publishing responsibilities of *Solos e Rochas*, increasing its reach. In 2007, the journal was renamed Soils and Rocks and acquired the status of an international journal, being published jointly by the Brazilian Association for Soil Mechanics and Geotechnical Engineering, by the Portuguese Geotechnical Society, and until 2010 by the Brazilian Association for Engineering Geology and the Environment.

Table of Contents

ARTICLES

A new seismic tomography system for geotechnical centrifuges

Khader Ibrahim Rammah[1#] (iD), Mostafa Ali Ismail[1] (iD), Jesse Costa[2] (iD),

Mario Vicente Riccio Filho[3] (iD)

Article

Abstract
Seismic tomography has been extensively used in geophysics for different purposes, including geological mapping, characterisation of inner earth structure and prospecting for oil and gas. In geophysics, seismic or electromagnetic waves are commonly used to provide tomographic information. In the geotechnical area, seismic tomography is emerging as a promising technique that can be used to determine the spatial variability of shear wave velocities and hence the small strain stiffness of geomaterials, especially when used in the centrifuge where in-situ stress conditions can be mimicked closely. This paper describes the development of a seismic tomography technique in the centrifuge. This technology can be used to image variations of soil stiffness under various mechanical, chemical and physical conditions. The paper describes the various components of the system, which includes arrays of small-size bender elements, hardware and software used to transmit, receive and acquire the shear wave signals during a centrifuge test. The paper illustrates the performance of the system at both 1g and in the centrifuge. Results of tomographic inversion performed on travel-time data obtained from these tests are discussed.

1. Introduction

Tomography is a well-known technique used in many branches of science to create images of projections ('tomograms') of hidden objects by inverting boundary measurements of chemical, electrical, thermal or mechanical parameters. The technique is extensively applied in inverting X-ray measurements (X-ray tomography) in medicine. In other fields of science, such as geophysics, oil and gas exploration, and geotechnical field testing, seismic or electromagnetic waves are used as a tomographic measurement. This type of tomography is known as 'seismic tomography' or ST. During the past few decades, the use of seismic tomography has become more common in earth sciences for the purpose of both compression and shear wave velocity imaging in the area of geophysics, geotechnics and oil and gas exploration (Woodward et al., 2008).

In seismic tomography, the technique commonly refers to the measurement of arrival times of either compression or shear waves that propagate through the subsurface medium. The arrival time of a propagating wave depends on the properties of the medium through which the wave propagates, such as the compression and shear moduli of the soil (Menke, 1984; Young et al., 1988).

In geotechnical engineering, seismic methods can be an excellent diagnostic tool for soil characterisation since wave propagation characteristics can be directly related to geotechnical parameters, such as the elastic moduli at small strains. The majority of geotechnical projects nowadays require the determination of the shear stiffness at small strains, G_0, which is an essential parameter for many geotechnical applications, including the evaluation of deformations around geotechnical structures and the prediction of dynamic/earthquake response (Pennington et al., 2001; Rammah et al., 2004).

Centrifuge testing has become a routine experimental method in both onshore and offshore geotechnical engineering. Therefore, it is crucial to characterise soil models in terms of G_0 during flight. This requires a system for propagating shear waves within the soil body and receivers to pick up the arrival of the shear waves. Several of these components can enable ST to be performed on centrifuge soil models.

A literature review has revealed that few attempts have been made to perform seismic measurements in a geotechnical centrifuge or even 1g models. An attempt was made by Ismail & Hourani (2003) for a simple 1g model in an acrylic cylinder filled with clay. A centrifuge system was described by Fu et al. (2004), where shear waves were generated through sand samples during centrifuge experiments. In their system, the shear waves were generated by a series

Rammah et al., Soil. Rocks, São Paulo, 2023 46(1):e2023000922

1

of three pairs (transmitter and receiver) of bender element transducers installed at different depths in the soil model. Earlier, Kita et al. (1992) measured the shear wave velocity of sand in a centrifuge model. Recently, a small-scale shear wave tomography device was built by Lee et al. (2005) for geotechnical application. They used mainly an array of bender elements as sources and receivers to scan a soil body in a box under $1g$ conditions.

The literature has shown that no attempt has been made to build a complete ST facility with high resolution for routine use in centrifuge modelling. Such a powerful facility can help better understand soil behaviour by providing a complete picture of the spatial variation of the shear wave velocity under general stress, chemical and/or physical conditions.

In the present research, a high-resolution ST system has been developed for the geotechnical centrifuge at the University of Western Australia (UWA). This system was used to image the variation of shear wave velocity (and hence soil stiffness) for different soil models in the centrifuge. A brief description of the development has already been published (Rammah et al., 2006). The present paper describes the system components in detail, emphasising its performance. Critical issues relating to the selection of transducers and their performance and the resolution of the resulting tomographic images are discussed. The paper presents some of the results of tomographic inversion of travel-time data obtained from $1g$ and centrifuge tests.

2. Design requirements for centrifuge ST system

Design criteria for tomographic studies can be found in the geophysics literature (Nolet, 1987; Santamarina & Fratta, 1998; Berryman, 1991). In addition, a study relevant to geotomography (seismic tomography applied in geotechnical engineering) addressing the design criteria was carried out by Fernandez & Santamarina (2002).

2.1 Fundamentals of a tomographic experiment

The most common configuration in a tomographic experiment is cross-hole tomography, shown in Figure 1a. The aim of a tomographic experiment is to image the medium between the two boreholes depicted and collect data relevant to the unknown parameters. For this purpose, the medium is discretised into a mesh of n pixels (or cells), as shown in Figure 1b and Figure 1c. The number of measurements m is equal to the number of rays between the sources and receivers (i.e., m is a function of the number of sources and receivers).

For a single ray path, the travel time along the ray AB in Figure 1c is given in Equation 1:

$$t = \int_A^B \left(\frac{1}{V}\right) dl \tag{1}$$

where A and B are the source (transmitter) and receiver positions, V is the wave velocity, and dl is an increment of length along the arc between the two (in this case, it is considered a straight line). Equation 1 can be rewritten in a summation form given in Equation 2:

$$t_i = \sum_{j-1}^n \left[\frac{L_{ij}}{V_j}\right] \tag{2}$$

where t_i is the travel time along the i-th ray (Figure 1c), L_{ij} is the travel distance or length travelled by the i-th ray in each j-th cell (pixel) at velocity V_j as presented in Figure 1d, and n is the number of cells the i-th ray intersects.

For all the rays (m rays), Equation 2 can be written in a matrix form as presented in Equation 3:

$$[T] = [L].[S] \tag{3}$$

where $[T]$ is the travel time vector (dimensions $m \times 1$), which is formed by all the measurements in the tomographic experiment, $[L]$ is the matrix of travel lengths (dimensions $m \times n$) obtained from the geometry of the model (i.e., the mesh shown in Figure 1, and $[S]$ is the slowness vector for all the pixels in the mesh (dimension $n \times 1$). In geophysics, it is common to address a medium with its slowness values. The slowness is the reciprocal of the velocity as expressed in Equation 4:

$$S = \frac{1}{V} \tag{4}$$

A tomographic experiment involves the determination of the slowness matrix, and hence velocity, by carrying out an inversion procedure for the linear system given in Equation 3.

The number of pixels, N_p, representing the unknown region between the two boreholes in Figure 1 depends on the number of transducers in the vertical dimension and the separation distance between the two boreholes L_b. This can be written in Equation 5:

$$N_p = \text{Integer}\left(\frac{H}{\Delta z} + 0.5\right).\text{Integer}\left(\frac{L_b}{\Delta z} + 0.5\right) \tag{5}$$

where Δz is the vertical separation distance between transducers, and H is the depth of the borehole. The above equation implies that the higher the number of transducers, the smaller the separation distance and the higher the number of pixels. Therefore, a higher resolution implies a smaller pixel size, which can be achieved by increasing the number of pixels.

As mentioned before, the tomographic inversion aims to determine the velocity (or slowness) in each pixel, and, therefore, the number of unknowns in the tomographic inversion process equals the number of cells. This is valid only in the case of an isotropic medium, where each cell is represented by invariant velocity. However, the number of

2

Rammah et al., Soil. Rocks, São Paulo, 2023 46(1):e2023000922
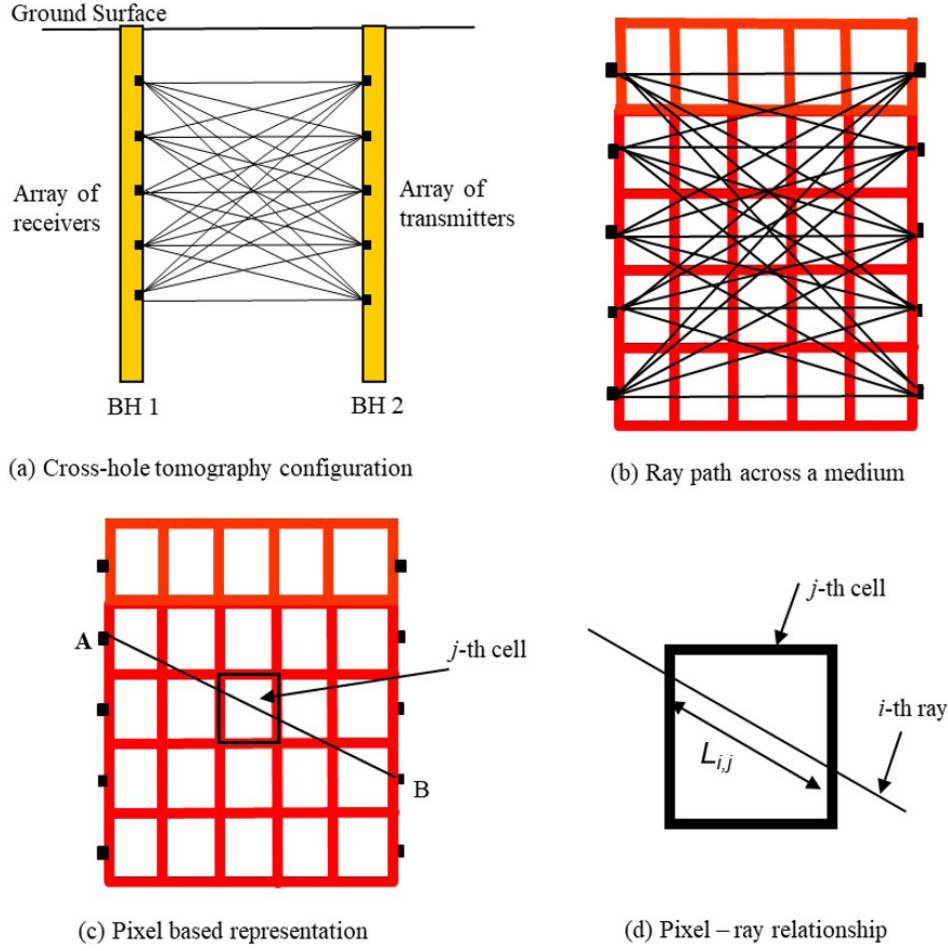
Figure 1. Model representation in cross-hole tomography.

unknowns will increase if anisotropy is considered. In elliptical anisotropy (where the wavefront travels in an elliptic shape), each cell is represented by two perpendicular components of unknown slowness.

The number of measurements, m, in cross-hole tomographic configuration is equal to the number of sources times the number of receivers, as expressed in Equation 6:

$$m = \left[\text{Integer} \left(\frac{H}{\Delta z} + 0.5 \right) \right]^2 \quad (6)$$

Ideally, a well-determined problem is obtained when the number of measurements equals the number of unknowns, and in this case, the solution would be exact. However, this is not always the case, as sometimes the number of measurements is higher than the number of unknowns, which yields an "over-determined problem". Ill-conditioned problems occur if the number of measurements is less than the number of unknowns. In most cases in cross-hole tomography, some pixels do not have enough information (i.e. insufficient number of rays crossing them), such as those pixels at the

top and bottom regions in Figure 1b. This normally results in a case called a "mixed-determined" problem.

A solution to overcome an ill-conditioned problem is to increase the number of measurements. This can be achieved by increasing the rays covering (or the spatial coverage) the unknown region (Berryman, 1991).

3. Determination of the resolution of a tomographic image

As indicated, better tomography resolution can be achieved by decreasing the vertical distance between the wave transducers Δz. However, as explained below, theoretical and practical restrictions may limit the minimum separation between successive transducers.

3.1 Wavelength

The wavelength λ defines the maximum resolution that can possibly be achieved by tomography. In general, it is not feasible to detect anomalies or variations that are smaller than one wavelength (Berryman, 1991). The wavelength is,

in turn, dependent on the velocity V of the scanned medium as well as the transmitted wave frequency f (it should be noted that frequency should be selected such that the wave can be felt clearly by the receivers before it attenuates due to the geometry and the material damping). Equation 7 links all these three quantities:

$$\lambda = \frac{V}{f} \tag{7}$$

3.2 Fresnel ellipse criterion

Fresnel ellipse provides a criterion for the optimal separation between transducers below which the resolution does not improve. Such optimisation reduces both cost and time. To avoid redundancy, the separation of the transducers should conform to the criterion of Fresnel's ellipse (according to Fresnel's principle, each ray has an elliptical zone). In order to avoid any redundant measurements, the transducer's separation Δz has to be chosen in a way to avoid any intersection between these ellipses and yet leaving no regions uncovered. The size of Fresnel's ellipse in Figure 2 is estimated in Equation 8:

$$(L_1 + L_2) \leq (L_b + \frac{\lambda}{2}) \tag{8}$$

Based on the above, the criterion is that the minimum interval between each two successive transducers is $\lambda / 2$.

3.3 Resolution of travel time

The vertical separation between transducers Δz must be chosen so that the difference in travel time between one source and any two consecutive receivers, t_1 and t_2 (Figure 3), can be detected within the resolution in travel time measurement ε_t (Lee, 2003; Lee et al., 2005). This is expressed by Equations 9 to 11 as follows:

$$t_1 = \frac{L_b}{V_{med}} \tag{9}$$

$$t_2 = \frac{\sqrt{L_b^2 + \Delta z^2}}{V_{med}} \approx \frac{L_b}{V_{med}} \left[1 + \left(\frac{\Delta z}{L_b} \right)^2 \right] \tag{10}$$

$$\Delta z \geq \sqrt{L_b . V_{med} . \varepsilon_t} \tag{11}$$

This criterion often imposes larger values of Δz than Fresnel's criterion. Therefore, it is very crucial to increase the resolution of travel time measurement (i.e. decreasing ε_t) in order to improve the tomographic resolution, ideally to a level where the Fresnel criterion governs.

4. Optimum vertical spacing and associated tomographic resolution

It is essential to check the highest achievable resolution in the tomographic experiment by checking the criteria explained in the previous section. To this end, the wavelength was considered for a medium with an average shear wave velocity of about 100-250 m/s, which is the range expected

Figure 2. Fresnel's ellipse criterion, after Fernandez & Santamarina (2002) and Santamarina & Fratta (1998): (a) intersection of two Fresnel's ellipses; (b) size of Fresnel's ellipse.
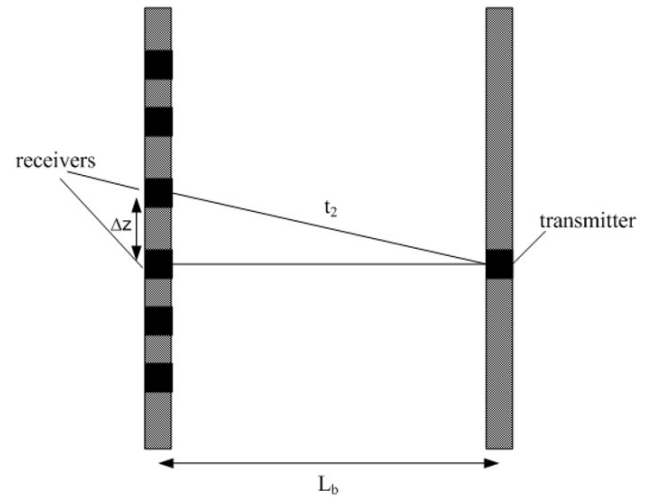
Figure 3. Resolution of travel time criterion.

4

Rammah et al., Soil. Rocks, São Paulo, 2023 46(1):e2023000922

for uncemented soils. This range of shear wave velocity was estimated using the power law relationship between shear wave velocity and the mean effective stress for silica sand at a range of stresses that will be imposed in a centrifuge model, given in Equation 12, where A is a factor depending on the soil properties:

$$V_s = A(\sigma')^m \tag{12}$$

The expected suitable frequency at this stress level will be about 10-20 kHz (from preliminary experimenting in the centrifuge). These values yield a wavelength of 0.5 – 2.5 cm. Checking against Fresnel's criterion, the separation between transducers Δz should not be less than $\lambda / 2$, which gives a Δz range of 0.25 – 1.25 cm. To check against the third criterion expressed in Equation 11, L_b was taken as 30 cm as the maximum value in a centrifuge model. The resolution of travel time measurement, ε_t, was taken as 2 µs, which depends on the data acquisition system. Inserting these values into Equation 11 gives $\Delta z \geq 1.22$ cm.

Theoretically, based on the above analysis, an average resolution of about 1 cm for any cell dimension can be achieved. This will give a tomographic image with a cell size of 1 cm^2 in a 2-dimensional model or 1 cm^3 for 3-D tomography. To achieve a resolution of 1 cm experimentally, the size of the transducers should be ≤ 1 cm. This study has made a breakthrough by reducing the spacing between the shear wave transducers to only 8 mm, as explained next.

5. Components of the ST system of the beam centrifuge at UWA

The ST system was developed for use with the beam centrifuge at UWA. The beam centrifuge is an Acutronic Model 661. It has a maximum payload of 400 kg at up to 100 g ($\approx$ 1000 m/s^2), decreasing to 200 kg at 200 g. The maximum radial distance between the cradle platform and the axis of rotation is 1.8 m. A full description of the beam centrifuge at UWA can be found in Fahey et al. (1990) and Randolph et al. (1991). The different components of the developed ST system are described in the following sections.

5.1 Bender element transducers

A basic description of the bender element can be found in many references (Dyvik & Madshus, 1985; Kuwano et al., 2000; Pennington et al., 2001; Lee & Santamarina, 2005; Leong et al., 2005). The most common piezoelectric ceramic used for bender elements is Lead Zirconate Titanate (PZT). There are different types of PZT: Shirley & Hampton (1978) used PZT4 bender elements; Brignoli et al. (1996) used PZT5A and PZT5HN bender elements, and Pennington et al. (2001) and Rammah et al. (2004) used PZT5B bender elements. In this study, the piezoceramic material type used for manufacturing

the bender elements is PZT5A supplied by Piezo Systems Inc. (PiezoSystemInc., 2005), USA. Two types of sheets were used: T220-A4-503X is X-poled for series connection, which was used for fabricating the receiver bender elements, and T220-A4-503Y is a Y-poled sheet with a parallel connection, which was used for the fabrication of the transmitter bender elements. The dimensions of these sheets are: width = 31.8 mm, length = 63.5 mm, and thickness = 0.51 mm.

5.2 Design and fabrication of a miniature bender element transducer

Initially, it was necessary to design one pair of prototype bender elements (one transducer and one receiver) that meets the requirements below:
- The benders must have a small size to meet the spacing requirement of the transducers and hence the desired resolution as discussed above.
- The benders must provide a range of frequencies that provides the wavelength necessary for the required resolution.
- The benders must be waterproof for use in moist conditions.
- Cross-talks must be eliminated by providing robust shielding.
- The bender elements must be sufficiently robust and reliable to withstand the relatively harsh environment of the centrifuge.

To achieve the above requirements, the following design criteria were addressed:

The diameter of the bender element socket was chosen to be 8 mm (outside diameter) to allow a spacing of 10 mm from centre to centre. Accordingly, the width of the bender element itself, b, had to be reduced to only 6 mm to fit the socket. The thickness of the bender element t, is 0.51 mm (for the PZT5A). These dimensions apply to both the transmitters and receivers.

The resonant frequency of a bender element in the air differs from the resonant frequency when it is embedded into the soil. Lee & Santamarina (2005) conducted both analytical and experimental studies to estimate the resonant frequency of bender elements in the air and the soil. The cantilever length (i.e. protrusion outside the socket) of a bender element, L_b, affects its resonant frequency in air and soil, its free deflection, the force generated by the transmitter, and the output voltage generated by the receiver. For the system presented here, a cantilever length, L_b, of 4 mm was chosen, which provides a theoretical resonant frequency of about 14.7 kHz. This resonant frequency lies within the range of frequencies required to achieve a resolution of 10 mm.

5.3 Fabrication of a miniature bender element

For the ST system with a resolution of 1 cm and model cross-section dimensions of 26 cm × 26 cm, the number of

transducers needed for a cross-hole tomography configuration is 52 (26 transmitters and 26 receivers). For a three-sided illumination tomography setup, the number of transducers will be 78; one array contains 26 transmitters and two arrays, each containing 26 receivers. Based on that, there was a need for a large number of bender element transducers to be manufactured. The most effective way was to manufacture all bender elements in an assembly-line fashion. To achieve this, a procedure was developed to allow 16 bender elements to be coated simultaneously using a mould which was designed and made in the workshop at UWA. Prior to coating, a number of strips of 6 mm x 15 mm piezoelectric elements were cut and then coated simultaneously. Then each strip was connected to a water-proof well-shielded co-axial cable after allowing the epoxy to harden. Each coated strip was placed in the centre of a stainless-steel cylindrical socket, 8 mm outer diameter and 20 mm long, with the bender element protruding 4 mm beyond the end of the socket. The sockets were filled under a vacuum with epoxy resin to ensure that the bender element behaves as a fixed-ended cantilever. Figure 4 shows a schematic diagram of the produced bender element.

5.4 Checking time delay in tip-to-tip contact

To illustrate the time delay caused by the electronic components and coating material, the transmitter and receiver were brought into tip-to-tip contact. Then both transmitted and received signals were recorded. A time delay of 12 μs was monitored when the bender elements were brought to tip-tip contact. In all cases, this time delay value was subtracted from the measured arrival time for the calculation of shear wave velocity.

5.5 Measuring the resonance frequency of bender elements

The resonance frequency of the bender elements was measured by bringing a transmitter and a receiver into tip-to-tip contact. Then a series of sine waves of a frequency of 1 kHz to 100 kHz were sent, and the receiver response was monitored by the oscilloscope. The peak-to-peak amplitude of the received signal was measured for each value of the input frequency input. The resonance frequency in the air is the value that produced the highest response from the receiver in terms of voltage. The obtained resonance frequency was ≈10 kHz.

6. Tomographic frame for holding transducers

The tomographic frame for a centrifuge seismic tomography had to be designed to:
- hold the bender element transducers while providing a small gap (2 mm) of isolating material between any two successive transducers;
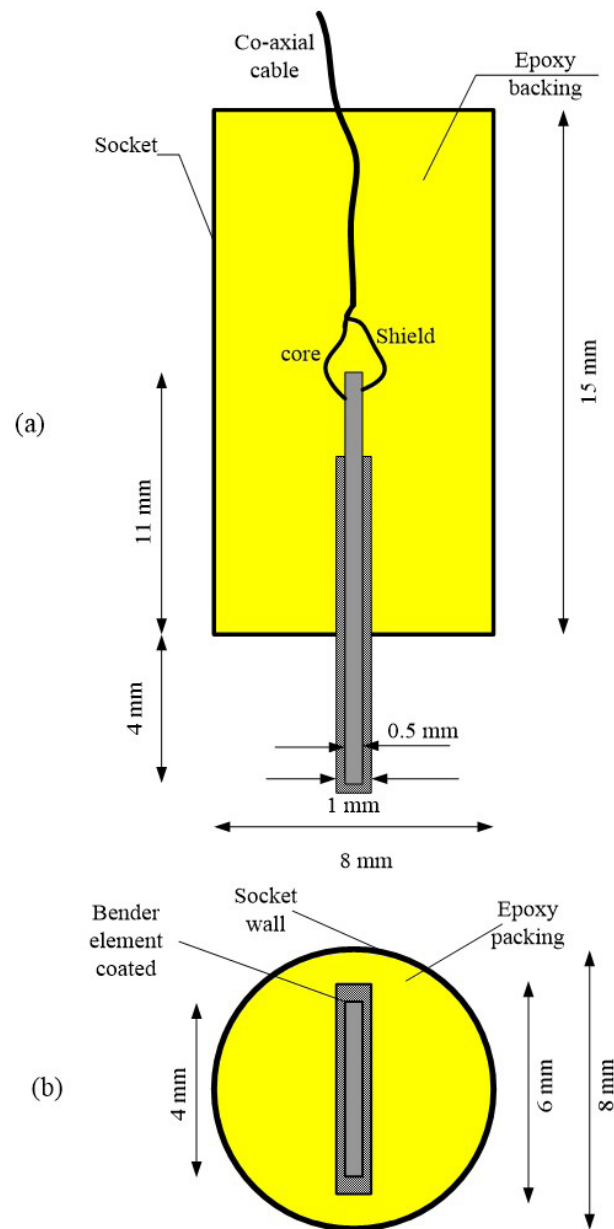
Figure 4. Bender element produced at UWA: (a) side elevation (b) front view of the bender element transducer.

- prevent the vibration that may be transmitted from any activated bender element through the frame body;
- provide proper electrical shielding for the bender element body to reduce the electrical noise and eliminate any possible cross-talk;
- prevent any reflections of compression waves due to the transverse directivity nature of the bender elements; some of these challenges have been discussed in (Lee et al., 2005) and (Lee, 2003).

Different configurations and materials were tried in designing a frame to meet the above requirements; eventually, relatively stiff rubber strips (300 mm long by 25 mm wide by

6

Rammah et al., Soil. Rocks, São Paulo, 2023 46(1):e2023000922

20 mm thick) were used as frames. Holes of 8 mm diameter and 10 mm centre-to-centre spacing were carefully drilled along the rubber strip, and the bender elements were pushed into these holes. Figure 5 shows part of the array.

To provide robust electrical shielding, all bender element casings were connected using a thin conductive wire, which eventually was connected to the centrifuge electrical earthing system. Three identical strips were prepared, each capable of accommodating up to 30 bender elements.

The reason for using separate holders (strips) was to avoid any possibility of cross-talk between transmitters and receivers through the holder and to have flexibility in setting the spacing between transmitters and receivers in the model. Figure 6 shows a schematic diagram of the arrangement of the frames within a centrifuge box.

The advantage of using three-sided illumination (i.e. bender arrangement) (Figure 6) is to improve the ray coverage and hence improve the quality of a tomographic image. If needed in the future, further improvement of ray coverage can be achieved by adding a similar array of either transmitters or receivers at the top of the soil model.

Figure 5. Array of bender elements mounted on a tomographic frame.

7. High voltage amplifiers and multiplexing system

The configuration of the tomographic model in Figure 6 consisted of 26 transmitters in the left-hand vertical array and 52 receivers (26 in the right-hand vertical array and 26 in the array at the bottom). A tomographic experiment requires scanning a medium by sending waves from all transmitters to all receivers. This implies that, during centrifuge testing, a system is required to provide the ability to switch through all transmitters and receivers whilst the centrifuge is spinning. To achieve this, a reliable and robust hardware system with the capability of accommodating such a large number of transducers was designed and built in the electronic workshop at UWA.

7.1. High voltage piezo driver

Four high-voltage amplifiers (HVA) boxes were manufactured. Each box has a capacity of 16 channels, giving a total capacity of 64 channels, which can be connected to 64 transmitters. Each channel on any specific HVA box can be addressed digitally by a Binary Coded Decimal (BCD) code written as a subroutine in the data acquisition software. Strong cases that withstand centrifugal forces were used to house the boards in flight.

7.2 Piezo receiver amplifiers

Six amplifier boxes, each with a capacity of 10 channels, were manufactured. Each channel can be addressed digitally using a second Binary Coded Decimal (BCD) code written in the data acquisition software. The amplification factor was set to ×100 for the received signal.

8. Data acquisition system for tomographic scanning

A National Instruments data acquisition card (NI PCI-6251 – M-series - 16 bit) with a 1.2 Mega sample per second sampling rate. The sampling rate is a key parameter for acquiring and receiving signals driven at a high frequency, such as the 20 kHz used in this development.

An efficient data acquisition software was written in *Labview 7.1* with the following features:
- The parameters of the transmitted signal can be specified in terms of amplitude, waveform, frequency, sampling rate and delay time between successive transmitted signals. In addition, the waveform can be chosen to be a sine wave or a step or pulse function.
- The desired bender element transmitter can be chosen by selecting its channel number (1 to 64). The required channel in the high-voltage amplifier is addressed digitally by the BCD.
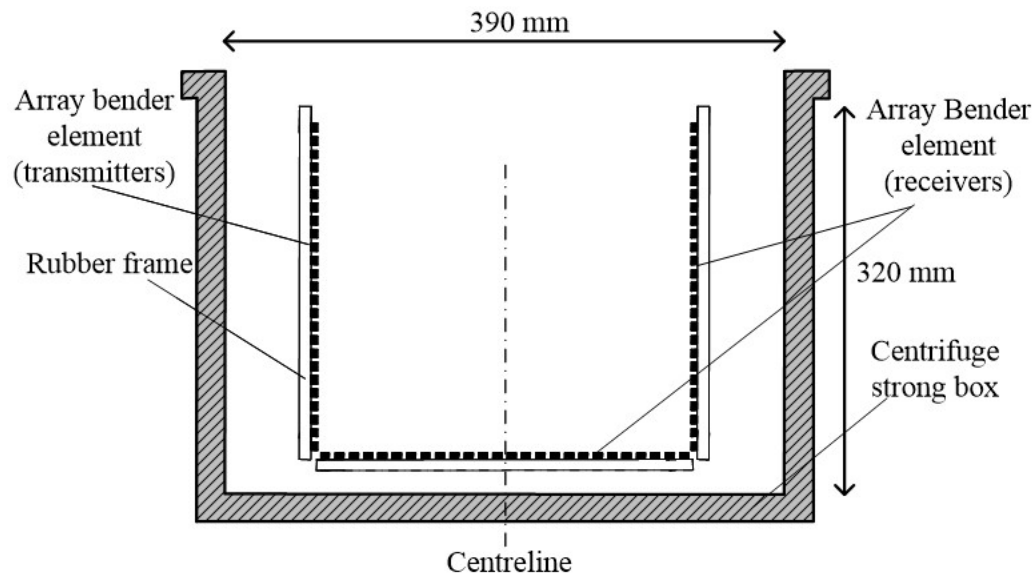
Figure 6. Tomographic model in centrifuge box (3-side illumination).

- The desired bender element receiver can be activated by selecting its channel number (1 to 60), also by the BCD.
- Both transmitted and received signals are displayed on the screen, with cursors to allow manual measurement of the travel time.
- Records of both transmitted and received signals are saved in both ASCII and binary formats.
- An option for stacking signals (averaging) is provided. This is crucial for increasing the signal-to-noise ratio, especially in the centrifuge, where considerable mechanical and electrical noise is expected.
- The software allows automatic scanning by specifying the initial and final channel numbers for transmitters and receivers. For example, in the model shown in Figure 6 with 26 transmitters and 52 receivers, if complete tomographic scanning is required, the program generates a signal from transmitter #1 to all 52 receivers, starting from # 1 up to #52. Then it repeats the same for transmitter #2 until it covers all possible combinations. This leads to a large number of signals (1352 signals in this particular case). All these records are stored on the hard drive of the computer.

9. Picking the arrival times of shear waves in a tomographic experiment

The number of measurements (signals) for the three-sided illumination is 1326; this can reach 2500 measurements if an additional array of transmitters is installed at the top of the centrifuge model. This large number requires both practical and efficient methods to pick the shear wave's first arrival. Therefore, it was decided to use **Promax 2D** software. This software enables both automatic and manual picking of arrival time, and it also has a complete library of signal processing routines, including different types of filtering.

9.1 Tomographic inversion

It should be noted that for the case where straight ray tomography is considered, the matrix of travel lengths L is independent of the slowness model S. In this case, L can simply be obtained from the model's geometry and locations of sources and receivers. However, in nonlinear tomography, L becomes an implicit function of S. Therefore, in this case, a ray-tracing technique should be applied to define the ray path through the slowness model.

In linear tomography, L and T are given, and the objective is to determine the slowness model S. The assumption here is that the ray paths are known *a priori*, which is justified by a linear approximation, which ignores the ray paths' dependence on the slowness distribution. Typically, the ray paths are assumed to be straight lines connecting sources and receivers.

In nonlinear tomography, the only given information is the vector of measured travel time T, along with data acquisition geometry (the coordinates of all sources and receivers). Therefore, the non-linear tomographic inversion aims to determine the slowness model S. The nonlinear inversion is an iterative process that starts with the computation of the initial S model. First, a forward ray-tracing process is performed on the initial S to obtain L, hence the computed travel time. The difference between the measured and computed travel time is then calculated. In the next iteration step, the S model is updated. The iteration process continues until the

8

Rammah et al., Soil. Rocks, São Paulo, 2023 46(1):e2023000922

difference between the measured and computed travel time vectors is sufficiently small.

In nonlinear problems, the dependence of the ray paths on the slowness distribution of the medium strongly influences the design of the inversion algorithm. Therefore, nonlinear inversion is required for problems with significant slowness variation across the medium. For such media, the ray paths normally show large curvature (i.e., nonlinear), which cannot be known before the inversion process begins.

Both linear and nonlinear tomographic inversions were applied to the travel-time data obtained from the different tests to recover the V_s models. The linear tomographic inversion assumes that the rays are straight. In a nonlinear inversion, the rays were traced using the eikonal method. In general, the tomographic inversion is highly dependent on the ray coverage. It has been shown that by increasing the ray coverage, the solution becomes more stable, the resulting images become better, and the error decreases (Woodward et al., 2008).

There is no unique solution in tomography because of the uneven ray coverage. Therefore, adding constraints or *a prior* information to the solution system is essential. This is usually achieved by implementing regularisation approaches. There are no unique guidelines for selecting the different regularisation factors. However, optimal values for these factors should be selected in order to meet two criteria: 1) the output model is physically meaningful; 2) the resulting model conforms as closely as possible to the measured travel time data by minimising the residuals in travel-time data.

The tomographic inversion results carried out on travel-time data from both 1*g* and centrifuge tests are presented in the following sections.

9.2 Tomographic experiment using the ST system on a homogeneous-isotropic wax block at 1*g*

Before performing centrifuge tests using the ST system, it was decided to carry out a seismic tomography test at 1*g* on a model with a known shear-wave velocity. The test aimed to calibrate and verify the performance of the ST system, including hardware, data acquisition software, and inversion codes. For this purpose, a wax block with dimensions of 269 × 280 × 200 mm was prepared. A cube of wax with an edge dimension of 269 mm was prepared by pouring molten wax into a mould and allowing it to harden. A dimension of 269 mm was chosen in order to avoid near-field effects. Moreover, increasing the travel distance was also desirable to reduce the impact of any error associated with determining the arrival time in the high-shear-wave-velocity wax. Therefore, the bender elements were embedded on two opposite ends of the wax block, such that the tip-to-tip travel distance was 260 mm.

In order to embed the two arrays of receivers and transmitters, a channel with a width of 1.5 mm and a depth of 4.5 mm was made on two opposite sides (the sides with the dimension of 280 × 200 mm) of the already hardened wax block. These dimensions were chosen to be slightly bigger than the dimensions of the bender elements, which are 4 × 1 mm. In order to ensure a good coupling between the bender elements and the wax block, the molten wax was poured into the channel, and one array was inserted immediately before the wax in the channel hardened. The same was repeated for installing the other array of bender elements.

Ideally, the wax block is supposed to be both homogeneous and isotropic; therefore, it was decided to use linear tomographic inversion as a first choice. The output tomogram resulting from inverting the travel-time data is shown in Figure 7. For the purpose of evaluating the inverted tomogram, a homogenous model with V_s = 960 m/s was considered to be the exact model. The resulting V_s tomogram of the wax block indicates a maximum relative difference of 14% compared to the "theoretical" wax model with V_s = 960 m/s. Therefore, the measured data set collected on the wax block was inverted using nonlinear tomography based on the eikonal method (Rammah, 2008).

In the case of a homogeneous model, both linear and nonlinear tomography gave similar results, i.e., either method can be used for the inversion. Therefore, any deviation from a homogenous model exhibited by the tomogram could be due to 1) that the wax block is not 100% homogenous, i.e., ideal homogeneity could not be achieved during the sample preparation and hardening; 2) certain error and randomness in picking the first arrival of shear waves could have yielded an error, i.e., miss picking the first arrival by a small value would yield a significant error, especially for such fast shear wave travel times (travel time ranges between 270 μs and 480 μs).
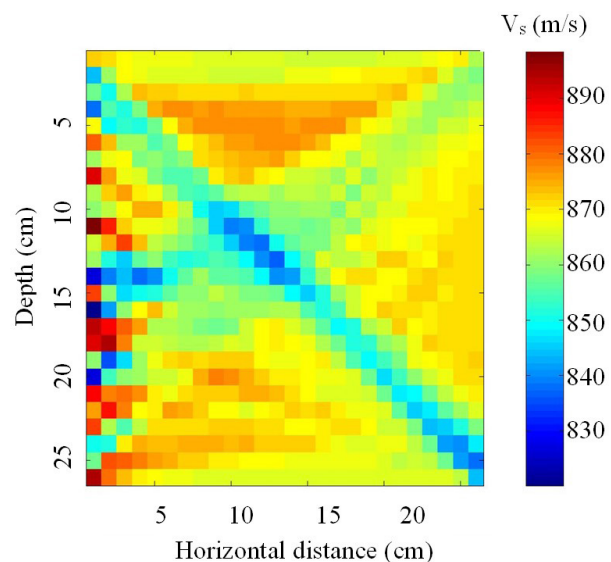
Figure 7. Output tomogram of shear wave velocity obtained from straight-ray tomographic inversion of travel-time data obtained on the wax block.

9.3 Tomographic experiments using the ST system in a centrifuge model

Four centrifuge tests were carried out on models with overburden stresses resulting from the self-weight stress of the silica sand used in the models. The seismic tomography centrifuge model was prepared by the dry pluviation method using a 'travelling sand curtain' hopper. After placing a 20 mm layer of fine silica sand in the base of the centrifuge box (to prevent possible crosstalk between the tomographic frame and the strongbox), the seismic tomography frames were installed in the desired position using temporary clamps attached to the box (Figure 8). The horizontal distance between the two vertical arrays of bender elements was 260 mm. The sand was rained from a constant height of 1.20 m, with a curtain travel speed of 120 mm/s. The drop height was adjusted every 10 mm to ensure the homogeneity of the sand. The resulting relative density (D_r) was 95%, the void ratio (e) was 0.50, and the dry unit weight (γ_d) was 17.8 kN/m³.

To confirm the absence of mechanical crosstalk either through the frames themselves or the centrifuge box, the sand hopper was stopped when the centrifuge box had been filled to mid-height. Then the clamps shown in Figure 8 were removed, and several shear wave measurements were taken between one of the buried transmitters and the unburied receivers.

No signal was detected by any of these receivers, confirming the absence of mechanical crosstalk. The sand-raining procedure was resumed until the two vertical arrays of bender elements were embedded into the soil. Finally, the two clamps were removed, and the box was mounted on the centrifuge platform.

Four centrifuge tests were carried out at 50, 100, 150 and 200g. In each test, a complete tomographic scan was performed. For the tests at 50 and 100g, the input signal consisted of a single 10 kHz sine wave, repeated 20 times, with the outputs stacked to obtain a single output signal. However, the frequency was increased to 15 kHz for the tests at 150 and 200g, repeated 30 times due to a higher noise level at these higher g-levels.

Figure 9 shows a typical shear wave signal from the centrifuge test at 200g. This signal is for transmitter and receiver pair located at a depth of 130 mm under the soil surface. This depth is equivalent to 26 m at the prototype scale, with an effective vertical stress of 463 kPa. The high signal-to-noise ratio in this (after stacking 30 signals) signal can be noted in Figure 9.

The first arrivals of the shear waves gathered in the above tests were picked using Promax. Figure 10a shows the horizon of the first arrival of the common-source signal for transmitter # 9. Next, the first arrivals of all 1352 signals were plotted in the form of a map, as shown in Figure 10b. Unlike the wax block model, where the rays were straight lines due to the homogeneity of the model, the seismic rays propagating through the silica sand model in the centrifuge are expected to curve due to the nonlinearity of the soil
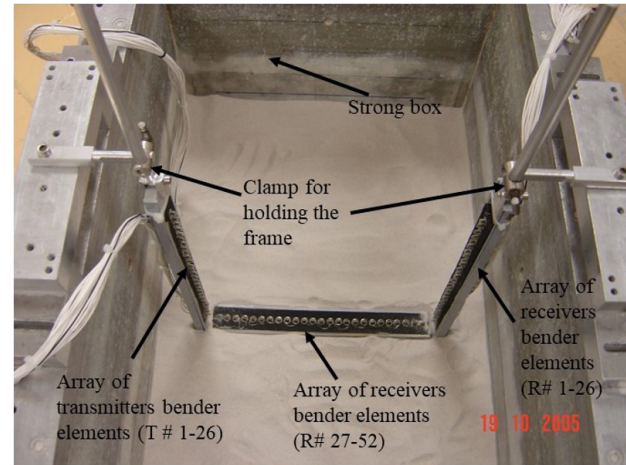
Figure 8. Tomographic model in centrifuge box prior to sand raining.
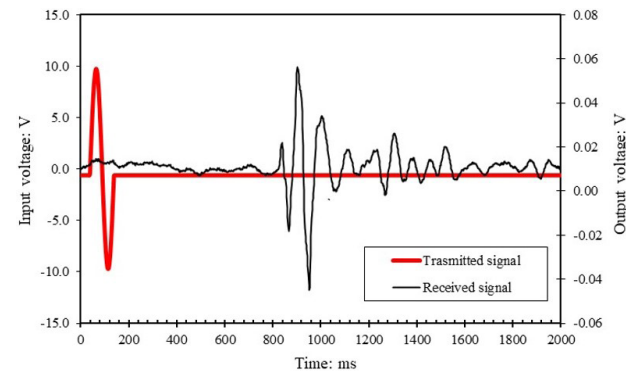
Figure 9. Improved shear wave measurement on silica sand at 200g at a depth of 13 cm: shear wave between transmitter # 13 and receiver # 13.

stiffness resulting from the nonlinearity of the variation of stresses over the depth of the sand layer. This was illustrated by carrying out forward modelling in which the seismic rays were traced through a model equivalent to the silica sand model tested at 100g. The relationship in Equation 12 was used to derive the V_s model. Figure 11a shows the model in the background and the family rays for source #2, which were traced using the eikonal method.

It can be seen that the rays are indeed curved, and the curvature is evident in the top part of the model. Therefore, it is clear that the imposition of a straight-ray assumption in the inversion process would not be the proper choice in this case. Thus, the travel-time data sets obtained from the silica sand models in the centrifuge were inverted using nonlinear tomography based on the eikonal method for tracing the rays. Figure 11b shows an interpolated output tomogram obtained by inverting the data from the test at 100g, which was acquired by applying a regularisation approach that adds smoothing in the horizontal direction. The regularisation coefficient for the horizontal smoothening was used to minimise the root-mean-squares of

10

Rammah et al., Soil. Rocks, São Paulo, 2023 46(1):e2023000922
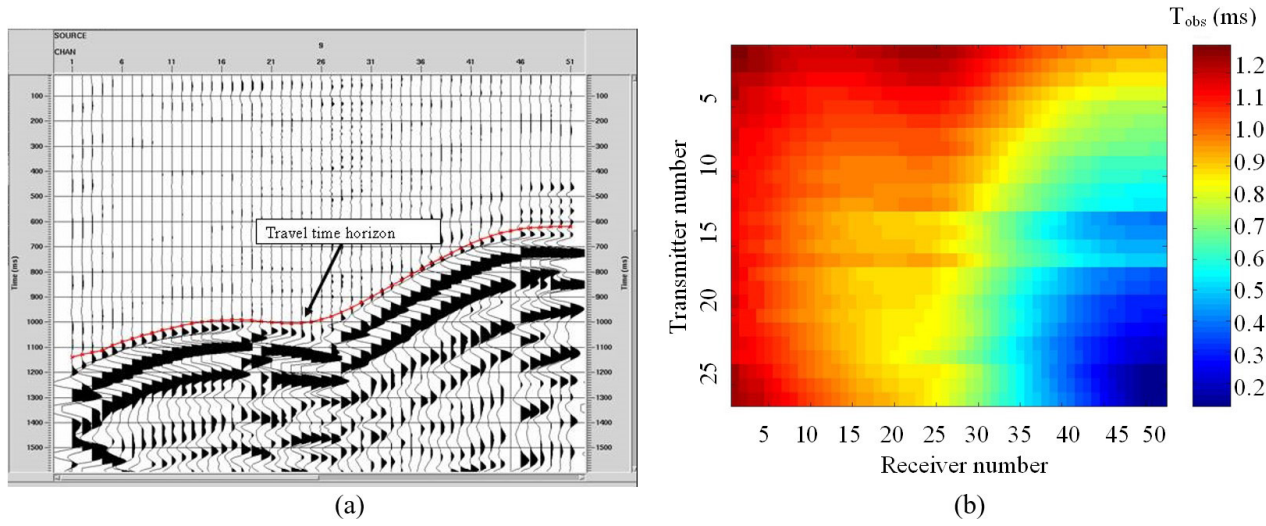
Figure 10. First arrivals of shear wave signals obtained from the centrifuge test on silica sand at 100g: (a) results from the Promax program for common source shots – transmitter # 9 shots; (b) map of observed first arrivals of shear waves.
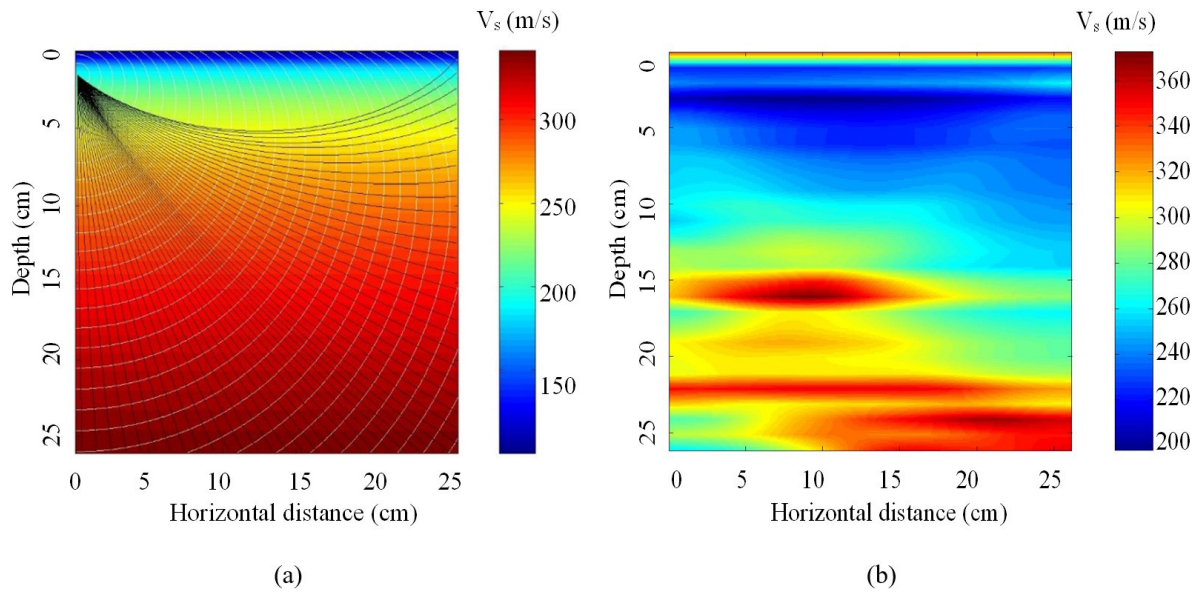
Figure 11. Nonlinear tomographic inversion of travel-time data obtained from the centrifuge test on silica sand at 100g: (a) forward modelling by tracing the rays using the eikonal method on an equivalent isotropic V_s model due to overburden stresses at $100g$ - family rays and wavefronts for source# 2; (b) interpolated output tomogram of V_s.

residuals of the travel-time data. As expected, the tomogram of Vs presented in Figure 11b indicates increasing values of V_s with depth. In addition, some lenses of higher values of V_s (anomalies) can be observed, such as those at an approximate depth of 15 cm, which might be attributed to a high density of sand.

10. Conclusions

This paper described the development of a high-resolution seismic tomography (ST) system for the beam centrifuge at UWA. The paper documents the different components of the system, including bender element transducers, tomographic frame, high-voltage piezo drivers and data acquisition software. Design criteria that affect the determination of the resolution of the tomographic image were discussed.

The ST system was calibrated at 1*g* using a block of wax with a known shear-wave velocity. A homogenous V_s model of the wax block was recovered properly by inverting the travel-time data using linear tomography based on the assumption of straight rays.

The ST system was used on a silica sand model subjected to self-weight stresses in the geotechnical centrifuge at

a 100g level. Tomographic inversion was carried out on the measured travel time data obtained from these tests. Forward modelling carried out on a theoretical V_s model resembling the silica sand model in the centrifuge showed that the seismic rays are curved due to the nonlinearity of the soil over the soil depth. Therefore, nonlinear inversion was performed on the travel-time data to recover the V_s models in the centrifuge. The resulting V_s obtained at 100g resembled the expected variation of V_s. The results of the inversion and the rays traced during the inversion process confirm the nonlinearity of the rays in the tested soil in the centrifuge.

The overall results obtained from applying the ST system at both 1g and the centrifuge demonstrated that the ST system is a promising tool for imaging V_s models involved in different geotechnical problems. However, studies carried out on both synthetic, 1g and 100g centrifuge models showed that, in most cases, there are some limitations with regard to the limited ray coverage and the dependency of the inversion on *a priori* information. Nevertheless, increasing the ray coverage from 3-sided to 4-sided by adding a fourth array at the surface can improve the ray coverage, particularly for the nonlinear soil model tested in the centrifuge.

Acknowledgements

Declaration of interest

The authors have no conflicts of interest to declare. All co-authors have observed and affirmed the contents of the paper, and there is no financial interest to report.

Authors' contributions

Khader Ibrahim Rammah: conceptualization, investigation, methodology, formal analysis, software, writing – original draft, writing – review & editing. Mostafa Ali Ismail: conceptualization. Jesse Costa: software. Mario Vicente Riccio Filho: writing – review & editing.

Data availability

Data generated and analyzed in the course of the current study are not publicly available due to data ownership, but a complete or limited dataset can be made available by the corresponding author upon reasonable request.

List of symbols and abbreviations

BCD	Binary Coded Decimal
e	void ratio
f	Wave frequency
G_0	small strain stiffness
H	height of a tomographic model
HVA	High-Voltage Amplifiers
L	array travel distances
$[L]$	matrix of travel lengths
L_b	distance between arrays of transmitters and receivers in a cross-hole tomography
m	number of measurements in a tomographic experiment
N_p	number of nodes in a tomographic mesh
PZT	Lead Zirconate Titanate (Piezoceramic)
S	slowness of seismic ray
$[S]$	slowness vector for all pixels in the mesh of the tomographic model
ST	Seismic Tomography
t	travel time of a seismic ray
$[T]$	vector of travel time in a tomographic model
V	phase velocity of a wave
V_s	Shear wave velocity
γ_d	dry unit weight
Δz	vertical separation distance between transducers in a tomographic model
ε_t	Resolution of travel time measurement
λ	wavelength

References

Berryman, J.G. (1991). *Lectures notes on nonlinear inversion and tomography*. University of California.

Brignoli, E.G.M., Gotti, M., & Stokoe, K.H.I. (1996). Measurement of shear waves in laboratory specimens by means of piezoelectric transducers. *Geotechnical Testing Journal*, 35(6), 1032-1040.

Dyvik, R., & Madshus, C. (1985). Lab measurements of Gmax using bender elements. In *Proceedings of the Conference on Advances in the Art of Testing Soils Under Cyclic Conditions* (pp. 186-196). Detroit, MI.

Fahey, M., Finnie, I., Hensley, P.J., Jewell, R.J., Randolph, M.F., Stewart, D.P., Stone, K.J.L., Toh, S.H., & Windsor, C.S. (1990). *Geotechnical centrifuge modelling at the University of Western Australia* (Report No: Geo:90092). The Department of Civil Engineering, The University of Western Australia.

Fernandez, A., & Santamarina, J.C. (2002). Design criteria of geotomographic field studies. *Geotechnical Testing Journal*, 26(4), 410-420.

Fu, L., Zeng, X., & Figueroa, L. (2004). Shear wave measurement in centrifuge using bender elements. *International Journal of Physical Modelling in Geotechnics*, 4(2), 01-11. https://doi.org/10.1680/ijpmg.2004.040201.

Ismail, M.A., & Hourani, Y. (2003). An innovative facility to measure shear-wave velocity in centrifuge and 1-g models, deformation Characteristics of Geomaterials. In *Proceedings of the 3th International Symposium ISLyon* (pp. 21-29). A.A. Balkema Publishers.

Kita, K., Shibata, T., Yashima, A., & Kobayashi, S. (1992). Measurement of shear wave velocities of sand in a centrifuge. *Soil and Foundation*, 32(2), 134-140. http://dx.doi.org/10.1520/GTJ20130189.

Kuwano, R., Connolly, T.M., & Jardine, R.J. (2000). An isotropic stiffness measurements in a stress-path triaxial cell. *ASTM Geotechnical Testing*, 23(2), 141-157. http://dx.doi.org/10.1520/GTJ11039J.

Lee, J.-S. (2003). *High resolution geophysical techniques for small-scale soil model testing* [Doctoral thesis, Georgia Institute of Technology]. Georgia Institute of Technology's repository. Retrieved in January 23, 2022, from http://hdl.handle.net/1853/5329

Lee, J.-S., & Santamarina, J.C. (2005). Bender elements: performance and signal interpretation. *Journal of Geotechnical and Geoenvironmental Engineering*, 131(9), 1063-1070. http://dx.doi.org/10.1061/(ASCE)1090-0241(2005)131:9(1063).

Lee, J.-S., Fernandez, A., & Santamarina, J.C. (2005). S-Wave velocity tomography: small-scale laboratory application. *Geotechnical Testing Journal*, 28(4), 336-344.

Leong, E.C., Yeo, S.H., & Rahardjo, H. (2005). Measuring shear wave velocity using bender elements. *Geotechnical Testing Journal*, 28(5), 329-342. http://dx.doi.org/10.1016/j.sandf.2015.02.009.

Menke, W. (1984). *Geophysical data analysis: discrete inverse theory*. Academic Press.

Nolet, G. (1987). *Seismic tomography with application in global seismology and exploration geophysics*. Springer.

Pennington, D.S., Nash, D.F.T., & Lings, M. (2001). Horizontally mounted bender element for measuring anisotropic shear moduli in triaxial clay specimens. *Geotechnical Testing Journal*, 24(2), 133-144. Retrieved in January 23, 2022, from https://www.astm.org/gtj11333j.html

PiezoSystemInc. (2005). *Piezoelectric Sheets & Plates*. Piezo. Retrieved in January 23, 2022, from http://www.piezo.com/

Rammah, K.I. (2008). *Development of a seismic tomography system for use on a geotechnical centrifuge* (Doctoral thesis, The University of Western Australia). The University of Western Australia's repository. Retrieved in January 23, 2022, from https://research-repository.uwa.edu.au/en/publications/development-of-a-seismic-tomography-system-for-use-on-a-geotechni

Rammah, K.I., Ismail, M.A., & Fahey, M. (2006). Development of a centrifuge seismic tomography system at UWA. In *Proceedings of the 6th International Conference on Physical Modelling in Geotechnics* (Vol. 1, pp. 229-234). Hong-Kong.

Rammah, K.I., Val, D.V., & Puzrin, A.M. (2004). Effects of ageing on small-strain stiffness of overconsolidated clays. *Geotechnique*, 54(5), 319-322. http://dx.doi.org/10.1680/geot.2004.54.5.319.

Randolph, M.F., Jewell, R.J., Stone, K.J.L., & Brown, T.A. (1991). Establishing a new centrifuge facility. In: *Proceedings of the International Conference Centrifuge 91* (pp. 3-9). Boulder.

Santamarina, J.C., & Fratta, D. (1998). *Introduction to discrete signals and inverse problems in civil engineering*. The American Society of Civil Engineers (ASCE).

Shirley, D.J., & Hampton, L.D. (1978). Shear-wave measurements in laboratory sediments. *The Journal of the Acoustical Society of America*, 63(2), 607-612. https://doi.org/10.1121/1.381760.

Woodward, M.J., Nichols, D., Zdraveva, O., Whitfield, P., & Johns, T. (2008). A decade of tomography. *Geophysics*, 73(5), VE5. http://dx.doi.org/10.1190/1.2969907.

Young, J.M., Sanchez-Salinero, I., Stokoe, K.H., & Roesset, J.M. (1988). In situ damping measurements by crosshole seismic method. In J.M. Joung. *Earthquake Engineering and Soil Dynamics II—Recent Advances in Ground-Motion Evaluation* (pp. 305-320). American Society of Civil Engineers.

Environmental and technical feasibility of a waste foundry sand applied to pavement granular layers

Manuella de Morais[1] , William Mateus Kubiaki Levandoski[1] ,

Joice Batista Reis[2] , Francisco Dalla Rosa[3] , Eduardo Pavan Korf[1#]

Article

Keywords
Environmental classification
Industrial byproducts
Sustainable materials
Resilient modulus
Granulometric stabilized subbases

Abstract

The foundry industry generates large amounts of residual byproducts, such as waste foundry sand (WFS). This high generation has motivated studies concerning the disposition of WFS, which in turn can be used for road subbases. Nevertheless, paving applications are still limited, especially regarding the behavior of WFS when added to a mixture of crushed materials. Hence, the objective of this study was to evaluate WFS reuse in mixtures with crushed materials, applied as granular layers of granulometric stabilized pavements. The crushed materials and WFS were characterized by size distribution, physical aspects, and different mixtures, and later submitted to mechanical testing. Initial tests were utilized to define mixtures (crushed material + WFS) that fulfilled the technical requirements for road subbases. California bearing ratio and resilient modulus tests indicated that WFS additions up to 12% for "A" grading improved the bearing capacity of the mixture; while in "E" grading, WFS additions up to 38% resulted in no expressive improvement in bearing characteristics. Thus, for both gradings, a structure with high density, strength, and low susceptibility to deformations can be used for road subbase construction without technical issues. Finally, the highest WFS content (38%) mixture was environmentally classified as a Class II A non-inert waste, indicating its environmental viability for road applications.

1. Introduction

Foundry industries are linked to a high solid waste generation. It is estimated that for each ton of foundry metal, 4 to 5 tons of waste foundry sand (WFS) are generated (Doğan-Sağlamtimur, 2018). WFS is a byproduct that originates from green sand, consisting of a mixture of sand, organic additives, bentonite, and water; being mostly utilized for mold manufacturing, in which liquid metal is poured to produce desired goods (Siddique & Singh, 2011; Matos et al., 2019).

Internal reuse strategies are applied to reduce WFS generation; these strategies consist in reintroducing WFS in the production process until the material is no longer able to perform the required technical functions. After that, the material is normally discarded. (Dayton et al., 2010; Bansal et al., 2019). WFS disposition is normally made on industrial waste landfills, following the indications of NBR 10004 (ABNT, 2004a); which classifies WFS as a Class II A waste (non-inert and with possible biodegradability, combustibility, or solubility in water). Therefore, the final disposition represents an additional cost to industries, in addition to the generation of environmental passives (Klinsky & Fabbri, 2009; Khan et al., 2021).

Several authors have studied alternative applications of WFS, aiming to develop technologies that may increase its value as a raw material for engineering practice. This range of applications includes civil construction; aggregates for asphalt mixtures, concrete, and ceramic goods; hydraulic barriers and reactive permeable barriers; and even subgrade fill (Abichou et al., 2002; Oliveira et al., 2011; Ganesh Prabhu et al., 2014; Dyer et al., 2018; Hossiney et al., 2018; Arulrajah et al., 2019).

Due to a high demand for aggregates, the road construction and the pavement maintenance industries have been standing out as possible WFS prospectors; especially considering that aggregates constitute about 70 – 80% of roads and pavements (Gökalp et al., 2018). In addition, more severe environmental laws have become obstacles for the exploitation of raw materials in natural deposits. Consequently, the acquisition cost of natural aggregates has highly increased. alongside the cost of transportation in general (Arulrajah et al., 2019). Thus, in addition to providing sustainability for waste recycling,

[1]Universidade Federal da Fronteira Sul, Laboratório de Geotecnia Ambiental, Programa de Pós-Graduação em Ciência e Tecnologia Ambiental, Erechim, RS, Brasil.
[2]Universidade Federal da Fronteira Sul, Laboratório de Geotecnia Ambiental, Erechim, RS, Brasil.
[3]Universidade de Passo Fundo, Programa de Pós-graduação em Engenharia Civil e Ambiental, Passo Fundo, RS, Brasil.
#Corresponding author. E-mail address: eduardo.korf@uffs.edu.br

Morais et al., Soil. Rocks, São Paulo, 2023 46(1):e2023001722

1

WFS reutilization allows a reduction in the exploitation of virgin materials (Yazoghli-Marzouk et al., 2014).

Extensive research (Guney et al., 2006; Klinsky & Fabbri, 2009; Yazoghli-Marzouk et al., 2014; Matos et al., 2019) has been dedicated to studying the stabilization of clayey soils with WFS (60 – 70%) and cement (5.0 – 5.5%), for application in flexible pavement subbases with low traffic. Nevertheless, there is still a research gap in investigations focused on verifying the WFS capacity of integrating mixtures with crushed materials, frequently used as paving materials — specifically for granular layers of granulometric stabilized pavements applications. Also, full adjustment to technical and environmental conditions has still not been explored, such as swelling due to bentonite presence or leaching and solubilization of toxic compounds from WFS, considering that most research focused only on the mechanical behavior (Basar & Aksoy, 2012; Palansooriya et al., 2020).

The understanding of the mechanical and environmental behavior of WFS and crushed materials mixtures ensures that WFS recycling alternatives in road subbases satisfy the performance criteria proposed by responsible departments, securing safety for both society and the environment. Along these lines, the objective of this research consists in studying the geotechnical and environmental behavior of WFS with crushed material mixtures applied to pavement subbases that were granulometrically stabilized.

2. Materials and methods

WFS is a green sand provided by a foundry industry located in southern Brazil. Materials designated as crushed stone A (CSA), crushed stone B (CSB), and crushed stone C (CSC) were collected in a crushing unit located in the same region, that utilizes such materials for the construction of urban pavements.

The crushed materials were from volcanic floods of the Serra Geral Formation situated in the Center-South region of Brazil and were composed mostly of basalt and andesite.

For all materials, sampling and reduction procedures by quartering were performed following NBR 16915 (ABNT, 2021a).

Table 1 shows the physical characterization of CSA, CSB, and CSC, as well as WFS. Considering that CSB exceeded 2% of the grains passing through the 4.75 mm sieve, the sample was divided between fine and coarse aggregates to adhere to the Brazilian standard (ABNT, 2021c).

CSC presented the largest powder content (7.98%), followed by WFS (3.57%), CSB (1.55%), and CSA (0.57%). The powder content of the natural aggregates was similar to the ones presented by Gómez-Soberón (2002) for natural aggregates of basaltic origin, although the different production processes can condition different contents of powder material, as reported by Deng & Tikalsky (2008) and Kleven et al. (2000).

Different particle size distributions were found for the four studied materials, as shown in Table 1, which are essential conditions for applying the granulometric stabilization method (DNIT, 2010a, b). In this procedure, small size grains fill the voids of the mixtures, increasing density and strength, while reducing permeability and deformability (Bernucci et al., 2008). All materials related to D10 were considered poorly graded. As for WFS, the values of Cu and Cc (2.06 and 0.92, respectively) were close to those presented by Arulrajah et al. (2017).

For WFS, the specific weight of grains presented values close to those observed by Kleven et al. (2000), which ranged from 2.52 to 2.73 g/cm³ for 14 different WFS. The water absorption was consistent with the findings of Deng & Tikalsky (2008), Gökalp et al. (2018), and Tugrul Tunc & Esat Alyamac (2019) for basaltic originated aggregates. Variations in the specific weight of grains and water absorption could be attributed to sand mineralogy variation, gradation range, grain shape, and powder content (Deng & Tikalsky, 2008).

Although WFS addition incorporated some clay minerals to the mixtures (e.g., bentonite), the Atterberg limits indicated a non-plastic behavior for the studied waste according to

Table 1. Table synthesis of physical parameters for the studied materials.

Properties	Fine aggregate			Coarse aggregate	
	WFS	CSC	CSB	CSB	CSA
Powder content (%) - NBR NM 46 (ABNT, 2003a)	3.57	7.98	1.55		0.57
Effective diameter D_{10} (mm)*	0.12	0.11	3.65		13.30
D_{30} (mm)*	0.17	0.86	6.50		15.90
D_{60} (mm)*	0.23	1.70	9.00		20.10
Uniformity coefficient (Cu)*	1.97	15.18	2.47		1.51
Curvature coefficient (Cc)*	1.1	3.89	1.29		0.95
Specific mass (g/cm³) - NBR 16916 (ABNT, 2021b) and NBR 16917 (ABNT, 2021c)	2.53	2.92	2.98	2.94	2.94
Water absorption (%)	1.86	3.58	3.52	1.81	1.81
Los Angeles abrasion value (%) - NBR NM 51 (ABNT, 2001)	-	-	10.64	16.06	12.26

*obtained from particle size distribution tests - NBR NM 248 (ABNT, 2003b).

NBR 7180 and NBR 6459 (ABNT, 2016; ABNT, 2017a), as also noted by Arulrajah et al. (2017) and Woodson (2011). Los Angeles abrasion values indicate that all mixtures follow the Brazilian roadway standard, DNIT 141-ES (DNIT, 2010b).

DNIT 141 - ES (DNIT, 2010b) standard criteria were utilized to select the grading conditions of the studied mixtures, using three crushed materials and WFS. The dry unit weight and optimum moisture content of the mixtures were determined in accordance with ASTM D1557 (ASTM, 2012), using the modified energy. This energy allows subbases with higher bearing capacity and resilient behavior. California bearing ratio (CBR) and swelling potential were determined following the procedures of NBR 9895 (ABNT, 2017b), for all mixtures at the optimum conditions of the compaction test. Specimens were considerable suitable for testing if the following criteria was met: ± 0.5% for optimum water content level, and ± 0.10 g/cm³ for maximum dry density.

Specimens of 100 mm in diameter and 200 mm in height, molded in optimum compaction conditions, were utilized for the resilient modulus tests. The test procedures were as indicated by DNIT 134 – ME (DNIT, 2018) and the AASHTO T 307 (AASHTO, 2003), executed using a cyclic triaxial device. Specimens were considered suitable for testing if the 1.0% water content tolerance was met. The mathematical model proposed by Papagiannakis & Masad (2012) was utilized to calculate the test parameters, considering nonlinear elastic behavior for granular soils (i.e., less than 50% of the grains pass through the 0.075 mm sieve).

The impact of WFS addition on the mixtures was quantified following a mechanical model 1 (Equation 1), as described by Papagiannakis & Masad (2012). This model establishes that the Resilient Modulus (RM) is a nonlinear function of confining pressure (σ_3), which is typically applied for granular materials. Since a lesser amount of fine particle size (smaller than 0.75 mm) is presented into the mixtures for all the samples, a combined mechanical model 2 (Equation 2) based on the deviator stress σ_d (Equation 3) and principal stress or bulk stress θ (Equation 4) was explored.

$$RM = k_1.\sigma_3^{k_2} \qquad (1)$$

$$RM = k_1.\theta^{k2}.\sigma_d^{k_3} \qquad (2)$$

where

$$\sigma_d = \left(\sigma_1 - \sigma_3\right) \qquad (3)$$

$$\theta = \left(\sigma_1 + \sigma_2 + \sigma_3\right) \qquad (4)$$

k_1, k_2, and k_3 represent the model's constants obtained from a nonlinear regression, while the root mean square error (*RMSE*), as observed in Equation 5, was used to achieve

the optimized model's constant. n represents the number of points used in the regression analysis, while RM_i and $RM_i \wedge$ define the observed and predicted Resilient Modulus, respectively. Also, R^2 was investigated once the optimal solution was found.

$$RMSE = \sqrt{\frac{1}{n}\sum_{i=1}^{n}\left(RM_i - RM_i \wedge\right)^2} \qquad (5)$$

To compare the structural performance between the WFS and the traditional granular materials, a mechanistic analysis was performed. The mechanistic evaluation was carried out in the proposed pavement structure, in which the sublayer was replaced by WFS. The simulations were performed throughout the elastic multilayer theory and using the AEMC software, version 2.4.2 (Franco, 2020).

The structural evaluation was carried out to identify the effects of different WSF grading over the fatigue life of the asphalt layer and the potential subgrade overloading. The performance models considered for asphalt and the subgrade layers are defined by the FHWA (1976) and Dormon & Metcalf (1965), which are described in Equations 6 and 7. Both models give an estimation of the repetition number of standard wheel axles available, considering the initial elastic tensile and vertical strains.

$$N_{AASHTO} = 1,902.10^{-6}.\left(\varepsilon_t\right)^{-3,512} \qquad (6)$$

$$N_{Dormon\,\&\,Metcalf\,(1965)} = 6,069.10^{-10}.\left(\varepsilon_v\right)^{-4,762} \qquad (7)$$

Where:
ε_t - Tensile strain at the asphalt bottom layer
ε_v - Vertical strain at subgrade top layer
N - Number of permissible standard wheel axle repetition

Furthermore, the solubilization and leaching of metals from WFS were evaluated through the environmental classification of the highest WFS content mixture, according to NBR 10004 (ABNT, 2004a).

3. Analysis and results

3.1. Design mixtures

The upper and lower limits ("A" and "E") were selected to fulfill the design requirements of DNIT (2010b), regarding the mixture of three crushed materials and WFS

Grading "A" mixtures were designed to contain three crushed materials and WFS. Three mixtures were stabilized, fixing the values of coarse aggregates at 30% and 20% for CSA and CSB, respectively, reducing the content of coarse aggregates to the minimum; WFS was added as a substitution

for CSC at contents of 0% (Mixture 1A), 6% (Mixture 2A), and 12% (Mixture 3A).

In the case of grading "E," only fine aggregates were added to the mixtures; WFS was added as a substitution for CSC, with 2% (Mixture 1E), 10% (Mixture 2E), 22% (Mixture 3E), and 38% (Mixture 4E).

These two ranges differ by the number "N", which is defined by the number of repetitions of a standard-axle of 82 kN during the project's lifetime, which would have the same effect as the expected traffic on the pavement structure (DNIT, 2006). Therefore, subbases made using "A" grading are intended for roads with high traffic volume (N > 5 × 106), while "E" grading ones are designed for roads with low and medium traffic volume (N < 5 × 106).

Figures 1 and 2 show the particle size distribution for grading "A" and "E". Mixture contents were established inside each range to study the influence of progressive WFS addition.

3.2. Compaction tests

Figures 3 and 4 present the Proctor curves for gradings "A" and "E" obtained through the Modified Proctor Compaction Test.

For both grading ranges, the increase in WFS content led to a reduction in dry density and an increase in moisture content. Furthermore, the maximum dry density, as well as the pattern obtained from the Proctor tests, indicated that mixtures present characteristics of sands with coarse, well-graded, and few clay particles. Mixtures of crushed material and 27% WFS, studied by Guney et al. (2006), resulted in values of dry density and water level content close to those observed in this study.

This behavior can be better seen in Figures 3 and 4, where the relationship between maximum dry density and optimum moisture content according to WFS content are identified. The reduction in the dry density parameter is associated
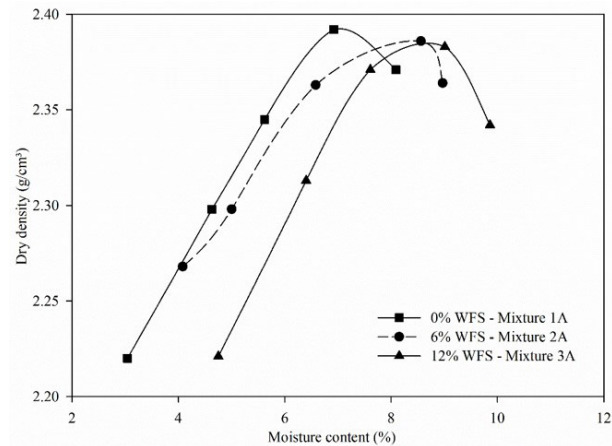
Figure 1. Particle size distribution for grade "A" mixtures.

Figure 3. Compaction curves for specimens tested with different WFS contents, referring to grading "A."

Figure 2. Particle size distribution for grade "E" mixtures.
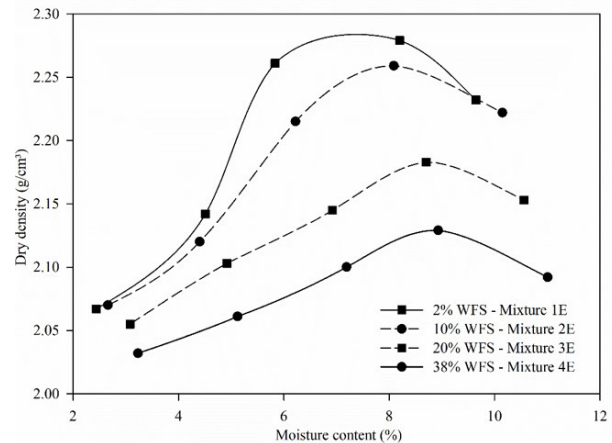
Figure 4. Compaction curves for specimens tested with different WFS contents, referring to grading "E".

with the specific unit weight of the materials, considering that WFS presents a lower density when compared to the other materials in the mixture. Pasetto & Baldo (2016), have also indicated that the specific unit weight of the materials directly affects the dry density parameter of the mixtures. Analyzing the mixtures with minimum and maximum WFS content, the dry density reduced 0.75% for grading "A" and 7.07% for grading "E". Considering that in both gradings the addition of WFS took place in substitution for CSC, the most significant reduction in the maximum dry unit weight was in grading "E"; due to the waste content being substantially higher.

Moisture content levels increased by 14.82% and 19.44% for gradings "A" and "E," respectively, considering mixtures with minimum and maximum WFS content. Mohammadinia et al. (2017) stated that the presence of materials with fine granulometry in the compaction process increases the mixture workability and consequently reduces the quantity of water needed for the process. In this context, WFS addition increased the fines content, contributing to the evidenced increase in the optimum water content level; implying that that higher volumes of water are required for compaction on site.

3.3. Swelling and California Bearing Ratio (CBR)

The results for swelling capacity and California Bearing Ratio (CBR) are presented in Table 2. The swelling was close to zero for all specimens, which was below the maximum limits set by Brazilian standards for the construction of road subbases.

The addition of WFS up to 38% presented no significant effect on the swelling of the mixtures. In fact, WFS can even reduce the swelling of soils, as observed by Klinsky & Fabbri (2009). Despite the presence of a small amount of bentonite in the mixture composition, the content of clayey material of WFS was about 1%.

CBR values for all mixtures with grading "A" and "E" were compacted under optimum conditions using modified energy, which resulted in high CBR values. Regarding grading "A", WFS addition increased CBR values by 1.5 times when compared to mixtures of lower (1A) and higher (3A) WFS content. This represented 267.50% in mixture 3A, which was the highest bearing capacity recorded for this grading. The increase in bearing capacity regarding WFS addition was due to the improvement of the granulometric mixture composition, which ensured better material stabilization. CBR values were much higher than those observed by

Arulrajah et al. (2019), with a CBR of 130% for crushed material, and by Guney et al. (2006) of 80% and 155% for mixtures of crushed rock.

For grading "E" the increase in WFS content led to a decrease in CBR values. This behavior can be associated with the lower strength parameters of WFS when compared to CSC (especially regarding mineralogical characteristics). Saha & Mandal (2017), studied mixtures of crushed rock, reclaimed asphalt pavement, and cement at levels of 75%, 25%, and 1%, observing similar CBR values. The largest recorded load capacity corresponded to "1E".

Considering that all studied contents satisfied the performance criteria established for each grading, the optimum WFS content was defined based on the largest waste reutilization. Thus, for the "A" and "E" gradings, the additional contents of 3A and 4E were considered optimum.

3.4. Resilient Modulus

A total of seven cyclic triaxial tests were carried out to identify the influence of WFS on the mechanical properties of each mixture. Three samples were tested using the grading "A" (Figure 5) and the four remaining samples were prepared following grading "E" (Figure 6)

Results indicate that WFS contributed to the improvement of the mechanical performance. This behavior may be associated with the granulometric stabilization resulting from fine WFS particles. Also, WFS addition improved the original granular interlocking due to the more efficient void filling, creating a more compact structure. Once particle
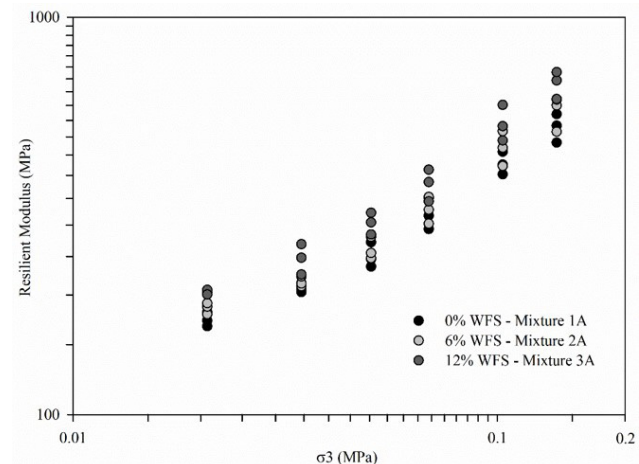
Figure 5. Resilient Modulus versus confining stress for grading "A".

Table 2. Variability of swelling and CBR for mixtures with different WFS contents, referring to gradings "A" and "E."

Mixture	Grading "E"				Grading "A"		
	1E	2E	3E	4E	1A	2A	3A
California Bearing Ratio (CBR) (%)	111.35	92.75	94.86	85.16	173.22	188.15	267.50
Swelling (%)	0.01	0.01	0.00	0.03	0.00	0.00	0.00

rearrangement occurred, higher particle contacts improved the mechanical properties, resulting in little susceptibility to deformation through the interlocking of the grains.

The regression parameters for both mechanistic models are summarized in Table 3. Considering that the first model accounts only for the effects of confining stress (Equation 1), the results indicate a satisfactory RMSE, as well as a determination coefficient (R^2) exceeding 0.94. Model 1 suggests that WFS can improve granular interlocking once it reaches higher values of k_1 and k_2. This increment is more impactful for "A" grading mixtures, in which the fine particles can fill the remaining voids, reaching higher density levels (as observed in Figures 3 and 4), and consequently, allowing the mixture to show a better response under higher confining stresses. The addition of WFS in "A" grading mixtures resulted in an increment of k_1 parameter of approximately 33%.

The regression results of the second model (Equation 2) were useful for comprehending the WFS effect on "A" grading mixtures. This model suggests that the regression
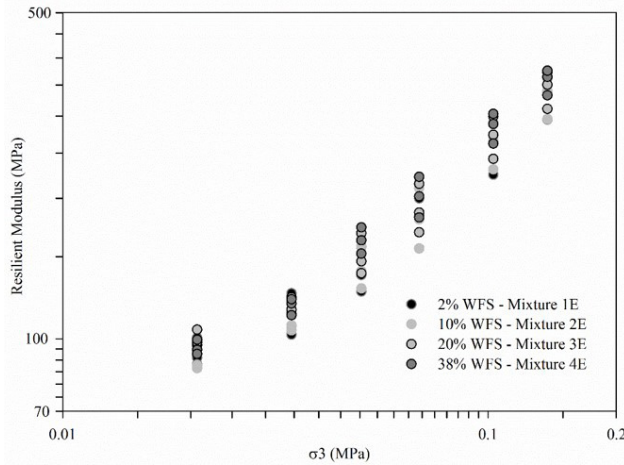
constant k_2, is less impacted than k_3, which indicates that the presence of WFS should account for both the confining and deviator stress.

Although "E" grading mixtures resulted in worse mechanical performance when compared to "A" grading, a similar pattern was detected between gradings. Even though a lesser amount of WFS was added to the raw material (mixture 1E), the analyzed data implied the increase of k_2 for both models, indicating once again that WFS improves the interlocking of particles.

Mohammadinia et al. (2017), studied mixtures of crushed materials and recycled asphalt pavement with different contents of fly ash, presenting resilient modulus results extremely similar to the ones shown in this research. In addition, k_1 values obtained for gradings "A" and "E" corresponded to a similar behavior of granite and basalt materials presented by Marmitt et al. (2010).

Geometric and mechanical properties of the materials can be found in Table 4. The conducted analysis was performed considering only the strain responses at the asphalt layer (Bottom layer tensile strain) and the top of the subgrade layer (Vertical strain). k_1 and k_2 parameters were considered as the average of grading "A" and "B"; with values of 2330 and 0.697 for "A" grading and 1496 and 0.759 for "E" grading. Both WFS gradings were considered appropriate as subbase layers. The standard double wheel axle with 82 kN (20,5 kN/wheel) was considered as the typical loading in the analysis and all structural responses were determined between two wheels.

Table 5 presents the results from the mechanistic analysis carried out with the AEMC elastic multilayer analysis. Subbase layers of WFS resulted in similar behavior to the one found on conventional asphalt bottom layers

Tensile strain results on the lower face of the pavement (fatigue criterion), indicated that the repetition number of the standard vehicle axis was 4.1 x 10⁶ for the WFS mixtures and 4.9 x 10⁶ for the conventional basalt gravel, following the

Figure 6. Resilient Modulus versus confining stress for grading "E."

Table 3. Regression parameters of both models for mixtures with gradings "A" and "E."

Grading	Mix.	$RM = k_1.\sigma_3^{k_2}$				$RM = k_1.\theta^{k2}.\sigma_d^{k_3}$				
		k_1	k_2	$RMSE$ (MPa)	R^2	k_1	k_2	k_3	$RMSE$ (MPa)	R^2
"A"	1A	1930	0.661	25	0.963	1815	1.002	-0.339	16	0.984
	2A	2291	0.703	33	0.948	2111	1.022	-0.318	22	0.977
	3A	2829	0.728	36	0.957	2610	1.074	-0.345	22	0.984
"E"	1E	1297	0.727	17	0.946	1373	1.086	-0.305	12	0.973
	2E	1556	0.785	20	0.947	1401	1.104	-0.318	10	0.987
	3E	1517	0.756	20	0.952	1389	1.097	-0.339	11	0.984
	4E	1617	0.766	14	0.977	1517	1.199	-0.433	9	0.991
Crushed basalt - A		953	0.446			N.A.	N.A.	N.A.	N.A.	N.A.

N.A. - Not Applicable A - Frederico Wesphallen (Marmitt et al., 2010).

Table 4. Geometric and mechanical properties of pavement materials used in the simulations.

Layer	Thickness (cm)	RM (MPa)	Poisson coefficient (v)	Reference
Asphalt	10	6300	0.27	Klinsky & Faria (2018)
Base	20	$RM = 953.\left(\sigma_3\right)^{0.446}$	0.35	This study
Subbase	20	WFS gradings A and E	0.35	Marmitt et al., (2010)
Subgrade	-	54	0.45	Santos (2019)

Table 5. Observed structural response for suggested structures.

Subbase layer	ε_t (Asphalt bottom layer)	ε_v (Subgrade top layer)	N_{AASHTO}	$N_{Dormon\,\&\,Metcalf}$ (1965)
Grading A	852	585	4.8×10^6	1.5×10^6
Grading E	903	920	4.1×10^6	1.7×10^5
Basalt crushed stone	844	541	4.9×10^6	2.2×10^6

Table 6. Results of the leaching and solubilization tests for mixture 4E.

Element	Leaching Tests NBR 10005 (ABNT, 2004b)		Solubilization Tests NBR 10006 (ABNT, 2004c)	
	Results	Limits (mg/L)	Results	Limits (mg/L)
As	ND*	1.0	ND*	0.01
Ba	ND*	70.0	ND*	0.7
Cd	ND*	0.5	ND*	0.005
Pb	ND*	1.0	ND*	0.01
Cr	ND*	5.0	ND*	0.05
F	ND*	150.0	0.7	1.5
Hg	ND*	01	ND*	0.001
Ag	ND*	5.0	ND*	0.05
Se	ND*	1.0	ND*	0.01
Al	-	-	ND*	0.2
Fe	-	-	2.4	0.3
Mn	-	-	0.05	0.1
Na	-	-	39.8	200.0
Zn	-	-	ND*	5.0
Cu	-	-	ND*	2.0

ND: not detected.

AASHTO model. Nevertheless, higher values of vertical strain on top of the subgrade were identified for the WFS structure when compared to the conventional one; this strain directly affects the admissible N value in the model analysis (Dormon & Metcalf, 1965). For the conducted analysis, this study admitted as a reference the lowest N value of each structure. For the same subbase thickness (20 cm), mixtures with "A" and "E" gradings resulted in a performance equivalent to 68% and 7% of the traditional materials. Although a reduction in performance was evidenced for WFS mixtures, this study suggests that such materials can meet the requirements of light to medium traffic conditions. Finally, it is important to highlight that further studies are necessary regarding permanent strain.

3.5. Leaching and solubilization of metals

On large industrial scales, the correct disposal of WFS can be very onerous, requiring large storage areas. Thus, the reutilization of this waste benefits not only industries, but also the environment, minimizing the use of natural resources and landfills areas (Penkaitis & Sígolo, 2012). Considering that all mixtures satisfied the specifications for granulometric stabilized subbases, an environmental classification by leaching and solubilization tests was carried out only on the highest WFS mixture (4E – 40% WFS). Table 6 presents the results of the leaching and solubilization tests for the mixture according to NBR 10004 (ABNT, 2004a).

The sample was classified as non-inert Class II A (ABNT, 2004a), for exceeding the solubilized iron concentration of the solubilization test; the raw waste presented similar results, considering that iron can be leached from both the molten metals of the molds and the additives of the foundry sand processing. In addition, WFS can also be classified as a nontoxic waste by NBR 10004 since none of the tested metals were detected on the leaching tests. A similar behavior

was also evidenced by Alves et al. (2014). Finally, Basar & Aksoy (2012) also corroborated this behavior while studying the addition of 40% WFS in concrete mixtures.

4. Conclusion

This study evaluated the physical, geomechanical, and environmental aspects of WFS and crushed aggregate mixtures applied to road subbases using granulometric stabilization as a building method.

Low fine contents of the four materials limited the selection of grading to two options, "A" and "E," with a maximum waste content of 12% and 38%, respectively. For both gradings, WFS satisfied the minimum requirements of granulometric stabilized subbase pavement layers. Nevertheless, it is recommended to utilize WFS exclusively for subbase layers, considering that conventional materials usually result in a better mechanical performance. Also, it is recommended to investigate permanent strain properties for pavement structural evaluation.

The mixtures presented no significant swelling and showed high California Bearing Ratios, reaching maximum values of 267.50% and 111.35% for contents of 12% and 2%, corresponding to gradings "A" and "E." Regarding grading "A," the progressive WFS increase improved the support characteristics of the mixture and the Resilient Modulus. Satisfactory values of the Resilient Modulus and the California Bearing Ratio were observed for mixtures with waste contents of 12% and 38% (gradings "A" and "E," respectively), ensuring a structure with high density, strength, and little susceptibility to strain.

The highest WFS mixture (38%) was classified as a non-inert Class II A waste, indicating an environmental feasibility of using crushed material mixtures with up to 38% WFS for building road subbases.

Acknowledgements

Declaration of interest

The authors have no conflicts of interest to declare. All co-authors have observed and affirmed the contents of the paper and there is no financial interest to report.

Authors' contributions

Manuella de Morais: writing – original draft, conceptualization, methodology. William Mateus Kubiaki Levandoski: methodology, writing – reviewing and editing. Joice Batista Reis: methodology, writing – reviewing and editing. Francisco Dalla Rosa: supervision, validation. Eduardo Pavan Korf: Supervision, validation, resources.

Data availability

The datasets used and/or analyzed during the current study are available from the corresponding author on reasonable request.

List of symbols

CBR	Swelling and California Bearing Ratio
C_c	Curvature coefficient
C_u	Uniformity coefficient
D_{10}	Effective diameter
D_{30}	Particle diameter equivalent to 60% of passing material extracted from particles size distribution curve
D_{60}	Particle diameter equivalent to 60% of passing material extracted from particles size distribution curve
DNIT	National Department of Transport Infrastructure of Brazil
k_1, k_2, and k_3	model's constants obtained from the nonlinear regression
N	number of permissible standard wheel axle repetition
n	the number of used points in the regression analysis
NBR	Brazilian standard from Brazilian Association of technical standards (ABNT)
ND	not detected
R^2	determination coefficient
RM	Resilient Modulus
RM_i	observed Resilient Modulus
RM_i ^	predicted Resilient Modulus
RMSE	Root Mean Square Error
WFS	waste foundry sand
ε_t	tensile strain at the asphalt bottom layer
ε_v	vertical strain at subgrade top layer
θ	principal stress or bulk stress
σ_3	confining pressure
σ_d	deviator stress

References

AASHTO T 307. (2003). *Determining the Resilient Modulus of Soils and Aggregate Materials*. Washington, DC, USA, pp. 41.

Abichou, T., Benson, C.H., & Edil, T.B. (2002). Foundry green sands as hydraulic barriers: field study. *Journal of Geotechnical and Geoenvironmental Engineering*,

128, 206-215. http://dx.doi.org/10.1061/(asce)1090-0241(2002)128:3(206).

ABNT NBR NM 51. (2001). *Small-size coarse aggregate – Test method for resistance to degradation by Los Angeles machine*. ABNT - Associação Brasileira de Normas Técnicas, Rio de Janeiro, RJ (in Portuguese).

ABNT NBR NM 46. (2003a). *Aggregates – Determination of material finer than 75 micrometer sieve by washing*. ABNT - Associação Brasileira de Normas Técnicas, Rio de Janeiro, RJ (in Portuguese).

ABNT NBR NM 248. (2003b). *Aggregates – Sieve analysis of fine and coarse aggregates*. ABNT - Associação Brasileira de Normas Técnicas, Rio de Janeiro, RJ (in Portuguese).

ABNT NBR 10004. (2004a). *Solid waste - Classification*. ABNT - Associação Brasileira de Normas Técnicas, Rio de Janeiro, RJ (in Portuguese).

ABNT NBR 10005. (2004b). *Procedure for obtention leaching extract of solid wastes*. ABNT - Associação Brasileira de Normas Técnicas, Rio de Janeiro, RJ (in Portuguese).

ABNT NBR 10006. (2004c). *Procedure for obtention solubilized extract of solid wastes*. ABNT - Associação Brasileira de Normas Técnicas, Rio de Janeiro, RJ (in Portuguese).

ABNT NBR 7180. (2016). *Soil – Plasticity limit determination*. ABNT - Associação Brasileira de Normas Técnicas, Rio de Janeiro, RJ (in Portuguese).

ABNT NBR 6459. (2017a). *Soil – Liquid limit determination*. ABNT - Associação Brasileira de Normas Técnicas, Rio de Janeiro, RJ (in Portuguese).

ABNT NBR 9895. (2017b). *Soil – California bearing ratio (CBR) – Testing method.* ABNT - Associação Brasileira de Normas Técnicas, Rio de Janeiro, RJ (in Portuguese).

ABNT NBR 16915. (2021a). *Aggregates - Sampling*. ABNT - Associação Brasileira de Normas Técnicas, Rio de Janeiro, RJ (in Portuguese).

ABNT NBR 16916. (2021b). *Fine aggregate – Determination of density and water absorption*. ABNT - Associação Brasileira de Normas Técnicas, Rio de Janeiro, RJ (in Portuguese).

ABNT NBR 16917. (2021c). *Coarse aggregate – Determination of density and water absorption.* ABNT - Associação Brasileira de Normas Técnicas, Rio de Janeiro, RJ (in Portuguese).

Alves, B.S.Q., Dungan, R.S., Carnin, R.L.P., Galvez, R., & de Carvalho Pinto, C.R.S. (2014). Metals in waste foundry sands and an evaluation of their leaching and transport to groundwater. *Water, Air, and Soil Pollution*, 225(5), http://dx.doi.org/10.1007/s11270-014-1963-4.

Arulrajah, A., Yaghoubi, E., Imteaz, M., & Horpibulsuk, S. (2017). Recycled waste foundry sand as a sustainable subgrade fill and pipe-bedding construction material: *engineering and environmental evaluation. Sustainable Cities and Society*, 28, 343-349. http://dx.doi.org/10.1016/j.scs.2016.10.009.

Arulrajah, A., Mohammadinia, A., Maghool, F., & Horpibulsuk, S. (2019). Tyre derived aggregates and waste rock blends:

resilient moduli characteristics. *Construction & Building Materials*, 201, 207-217. http://dx.doi.org/10.1016/j.conbuildmat.2018.12.189.

ASTM D1557. (2012). *Standard test methods for laboratory compaction characteristics of soil using modified effort (56,000 ft-lbf/ft3 (2,700 kN-m/m3))*. ASTM International, West Conshohocken, PA.

Bansal, P., Verma, A., Mehta, C., & Sangal, V.K. (2019). Potential use of waste foundry sand in dual process (photocatalysis and photo-Fenton) for the effective removal of phenazone from water: slurry and fixed-bed approach. *Journal of Environmental Management*, 233, 793-801. http://dx.doi.org/10.1016/j.jenvman.2018.10.005.

Basar, H.M., & Aksoy, N.D. (2012). The effect of waste foundry sand (WFS) as partial replacement of sand on the mechanical, leaching and micro-structural characteristics of ready-mixed concrete. *Construction & Building Materials*, 35, 508-515. http://dx.doi.org/10.1016/j.conbuildmat.2012.04.078.

Bernucci, L., Ceratti, J.A.P., Soares, J.B., & Motta, L. (2008). P*avimentação Asfáltica - Formação básica para engenheiros.* Petrobras – ABEDA.

Dayton, E.A., Whitacre, S.D., Dungan, R.S., & Basta, N.T. (2010). Characterization of physical and chemical properties of spent foundry sands pertinent to beneficial use in manufactured soils. *Plant and Soil*, 329, 27-33. http://dx.doi.org/10.1007/s11104-009-0120-0.

Deng, A., & Tikalsky, P.J. (2008). Geotechnical and leaching properties of flowable fill incorporating waste foundry sand. *Waste Management (New York, N.Y.)*, 28, 2161-2170. http://dx.doi.org/10.1016/j.wasman.2007.09.018.

DNIT. (2006). *Manual de Estudos de Tráfego*. IPR, Rio de Janeiro, RJ.

DNIT 139 – ES. (2010a). *Pavimentação – Sub-base estabilizada granulometricamente - Especificação de serviço.* IPR, Rio de Janeiro, RJ (in Portuguese).

DNIT 141 – ES. (2010b). *Pavimentação – Base estabilizada granulometricamente - Especificação de serviço.* IPR, Rio de Janeiro, RJ (in Portuguese).

DNIT 134 – ME. (2018). *Pavimentação - Solos - Determinação do módulo de resiliência – Método de ensaio.* IPR, Rio de Janeiro, RJ (in Portuguese).

Doğan-Sağlamtimur, N. (2018). Waste foundry sand usage for building material production: a first geopolymer record in material reuse. *Advances in Civil Engineering*, 2018, 1-10. http://dx.doi.org/10.1155/2018/1927135.

Dormon, G.M., & Metcalf, C.T. (1965). Design curves for flexible pavements based on layered system theory. *Highway Research Record*, 71, 1-16.

Dyer, P.P.O.L., de Lima, M.G., Klinsky, L.M.G., Silva, S.A., & Coppio, G.J.L. (2018). Environmental characterization of Foundry Waste Sand (WFS) in hot mix asphalt (HMA) mixtures. *Construction & Building Materials*, 171, 474-484. http://dx.doi.org/10.1016/j.conbuildmat.2018.03.151.

Ferderal Highway Administration – FHWA. (1976). *Sensitivity Analysis of FHWA Structural Model VESYS II*. Final Report. FHWA, Washington, DC. 266 p.

Franco, F.A.C.P. (2020). *Software AEMC. Análise Elástica de Múltiplas Camadas*. Retrieved in September 10, 2022, from https://www.gov.br/dnit/pt-br/assuntos/planejamento-e-pesquisa/ipr/medina

Ganesh Prabhu, G., Hyun, J.H., & Kim, Y.Y. (2014). Effects of foundry sand as a fine aggregate in concrete production. *Construction & Building Materials*, 70, 514-521. http://dx.doi.org/10.1016/j.conbuildmat.2014.07.070.

Gökalp, İ., Uz, V.E., Saltan, M., & Tutumluer, E. (2018). Technical and environmental evaluation of metallurgical slags as aggregate for sustainable pavement layer applications. *Transportation Geotechnics*, 14, 61-69. http://dx.doi.org/10.1016/j.trgeo.2017.10.003.

Gómez-Soberón, J. M. (2002). Porosity of recycled concrete with substitution of recycled concrete aggregate. *Cement and Concrete Research*, 32(8), 1301-1311. http://dx.doi.org/10.1016/s0008-8846(02)00795-0.

Guney, Y., Aydilek, A.H., & Demirkan, M.M. (2006). Geoenvironmental behavior of foundry sand amended mixtures for highway subbases. *Waste Management (New York, N.Y.)*, 26(9), 932-945. http://dx.doi.org/10.1016/j.wasman.2005.06.007.

Hossiney, N., Das, P., Mohan, M.K., & George, J. (2018). In-plant production of bricks containing waste foundry sand: a study with Belgaum foundry industry. *Case Studies in Construction Materials.*, 9, e00170. http://dx.doi.org/10.1016/j.cscm.2018.e00170.

Khan, M.M., Mahajani, S.M., Jadhav, G.N., Vishwakarma, R., Malgaonkar, V., & Mandre, S. (2021). Mechanical and thermal methods for reclamation of waste foundry sand. *Journal of Environmental Management*, 111628, http://dx.doi.org/10.1016/j.jenvman.2020.111628.

Kleven, J., Edil, T., & Benson, C. (2000). Evaluation of excess foundry system sands for use as subbase material. *Transportation Research Record: Journal of the Transportation Research Board*, 1714(1), 40-48. http://dx.doi.org/10.3141/1714-06.

Klinsky, L.M.G., & Fabbri, G.T.P. (2009). Reaproveitamento da areia de fundição como material de base e sub-base de pavimentos flexíveis. *Revista Transportes*, 1, 36-45. http://dx.doi.org/10.14295/transportes.v17i2.358.

Klinsky, L.M.G., & Faria, V.C. (2018). *Determinação do módulo de resiliência, módulo dinâmico e flow number de misturas asfálticas com diversos ligantes asfálticos e faixas granulométricas*. Relatório Número: CCR-ND-MOD- RF-MAR/2018. Agência Nacional de Transportes Terrestres (ANTT), Brasília, DF. 241 p.

Marmitt, H.M., Casagrande, M.D.T., & Ceratti, J. (2010). Caracterização de propriedades resilientes de três britas graduadas utilizadas em pavimentos no sul do Brasil. *Teoria e Prática na Engenharia Civil (Online)*, 15, 63-69.

Matos, P.R., Marcon, M.F., Schankoski, R.A., & Prudêncio Junior, L.R. (2019). Novel applications of waste foundry sand in conventional and dry-mix concretes. *Journal of Environmental Management*, 244, 294-303. http://dx.doi.org/10.1016/j.jenvman.2019.04.048.

Mohammadinia, A., Arulrajah, A., Horpibulsuk, S., & Chinkulkijniwat, A. (2017). Effect of fly ash on properties of crushed brick and reclaimed asphalt in pavement base/subbase applications. *Journal of Hazardous Materials*, 321, 547-556. http://dx.doi.org/10.1016/j.jhazmat.2016.09.039.

Oliveira, P.E.F., Oliveira, L.D., Ardisson, J.D., & Lago, R.M. (2011). Potential of modified iron-rich foundry waste for environmental applications: fenton reaction and Cr(VI) reduction. *Journal of Hazardous Materials*, 194, 393-398. http://dx.doi.org/10.1016/j.jhazmat.2011.08.002.

Palansooriya, K.N., Shaheen, S.M., Chen, S.S., Tsang, D.C.W., Hashimoto, Y., Hou, D., Bolan, N.S., Rinklebe, J., & Ok, Y.S. (2020). Soil amendments for immobilization of potentially toxic elements in contaminated soils: a critical review. *Environment International*, 134, 105046. http://dx.doi.org/10.1016/j.envint.2019.105046.

Papagiannakis, A.T., & Masad, E.A. (2012). *Pavement design and materials*. John Wiley & Sons, Inc. https://doi.org/10.1002/9780470259924.

Pasetto, M., & Baldo, N. (2016). Recycling of waste aggregate in cement bound mixtures for road pavement bases and sub-bases. *Construction & Building Materials*, 108, 112-118. http://dx.doi.org/10.1016/j.conbuildmat.2016.01.023.

Penkaitis, G., & Sígolo, J.B. (2012). Waste foundry sand. Environmental implication and characterization. *Geologia USP. Série Científica*, 12(3), 57-70. http://dx.doi.org/10.5327/Z1519-874X2012000300004.

Saha, D.C., & Mandal, J.N. (2017). Laboratory Investigations on Reclaimed Asphalt Pavement (RAP) for using it as Base Course of Flexible Pavement. *Procedia Engineering*, 189, 434-439. http://dx.doi.org/10.1016/j.proeng.2017.05.069.

Santos, T.A., Specht, L.P., Pinheiro, R.J.B., Ceratti, J.A.E., & Brito, L.A.T. (2019). Avaliação da resistência e da deformação resiliente de quatro solos de subleitos rodoviários no estado do Rio Grande do Sul. *Revista Transportes*, 27(1), http://dx.doi.org/10.14295/transportes.v27i1.1531.

Siddique, R., & Singh, G. (2011). Utilization of waste foundry sand (WFS) in concrete manufacturing. *Resources, Conservation and Recycling*, 55(11), 885-892. http://dx.doi.org/10.1016/j.resconrec.2011.05.001.

Tugrul Tunc, E., & Esat Alyamac, K. (2019). A preliminary estimation method of Los Angeles abrasion value of concrete aggregates. *Construction & Building Materials*, 222, 437-446. http://dx.doi.org/10.1016/j.conbuildmat.2019.06.176.

Woodson, D.R. (2011). *Concrete portable handbook*. Elsevier.

Yazoghli-Marzouk, O., Vulcano-greullet, N., Cantegrit, L., Friteyre, L., & Jullien, A. (2014). Recycling foundry sand in road construction–field assessment. *Construction & Building Materials*, 61, 69-78. http://dx.doi.org/10.1016/j.conbuildmat.2014.02.055.

Compressive and tensile strength of aeolian sand stabilized with porcelain polishing waste and hydrated lime

José Daniel Jales Silva[1#] (ID), Olavo Francisco dos Santos Júnior[2] (ID),

William de Paiva[3] (ID)

Article

Abstract

The improvement of sandy soils by incorporating new stabilizing agents in a physical and/or chemical process has become the subject of many studies in recent decades. In addition, the use of industrial wastes in this process can bring significant benefits to the environment and savings in natural resources. This work aims to evaluate the implications of incorporating porcelain polishing waste (PPW) and hydrated lime on the mechanical properties of an aeolian dune sand from the city of Natal/RN. Tests of unconfined compressive strength and split tensile strength were performed on compacted soil specimens with different contents of PPW (10%, 20% and 30%), hydrated lime (3%, 5% and 7%) and relative densities (25%, 50% and 75%). To evaluate the effects of each factor, the Response Surface Methodology with Central Composite Design was used. The results have shown that all three factors have a positive effect on the response variables. The highest strengths were obtained in regions combining high values of relative density and PPW content and an optimum lime content was found. An inversely proportional correlation and good fit to the experimental data was obtained between the strength values and the porosity/binder index (η / B_{iv}). The strength gains were attributed to densification of the soil structure and cementation of the particles by the compounds formed in the reaction between lime and PPW. The results also showed an increase in the strength with curing time, indicating a pozzolanic activity of the mixtures.

1. Introduction

Aeolian soils cover large areas in the coastal environment and in regions with arid and semi-arid climates. Urban sprawl and the need for raw materials in the construction industry have led to the use of this type of soil as a foundation layer for buildings and roads or as fill material in embankments and retaining structures (Elipe & López-Querol, 2014). In natural state they have low bearing capacity and a structure susceptible to collapse when wetted (Mohamedzein et al., 2019). Moreover, when saturated and in loose state, are subject to liquefaction under static or cyclic loading, which can cause great damage to materials and human life (Bucci et al., 2018; Bao et al., 2019; Souza Júnior et al., 2020).

The engineering properties of sandy soils, of aeolian origin or formed by other mechanisms, can be significantly improved by a variety of techniques that include densification, reinforcement, drainage or by introducing other materials in a physical, chemical or biological process (Venda Oliveira et al.,

2015; Abbasi & Mahdieh, 2018; Venda Oliveira & Rosa, 2020). In the case of chemical stabilization, soil improvement can be achieved by including traditional cementing agents such as Portland cement or newer alternatives such as colloidal silica, bentonite, biopolymers and geopolymers obtained from industrial wastes (Khajeh et al., 2020; Vranna & Tika, 2021; Venda Oliveira & Cabral, 2021; Sharma et al., 2021).

The geotechnical behavior of cemented soils has been studied for decades (Saxena & Lastrico, 1978; Clough et al., 1981; Schnaid et al., 2001; Rios et al., 2014; Vranna & Tika, 2020; Moon et al., 2020). Cementation changes the soil microstructure and hydration products are concentrated at contact points or may also fill part of the voids. In more granular soils the formation of strong bonds at the contact points between the particles increases the strength and stiffness of the structure, with the degree of cementation being directly proportional to the density and number of contacts and inversely proportional to the pore size (Baldovino et al., 2020a). Vranna & Tika (2020) found that even small amounts

#Corresponding author. E-mail address: josedanieljales@gmail.com
[1]Universidade Federal de Campina Grande, Unidade Acadêmica de Engenharia Civil, Campina Grande, PB, Brasil.
[2]Universidade Federal do Rio Grande do Norte, Departamento de Engenharia Civil, Natal, RN, Brasil.
[3]Universidade Estadual da Paraíba, Departamento de Engenharia Sanitária e Ambiental, Campina Grande, PB, Brasil.

of cement can optimize the compressive and tensile strength as well as liquefaction resistance of sandy soils by forming bonds between the particles.

On the other hand, alternative materials to Portland cement are being proposed due to the high costs and large environmental impacts associated with the production of this compound (Sharma & Sivapullaiah, 2016; Andrew, 2018). The use of domestic or industrial waste, previously destined for landfills only for containment purposes, helps in the creation of more sustainable and less costly processes and in the conservation of natural resources (Jayanthi & Singh, 2016; Latifi et al., 2018).

Fly ash (Åhnberg, 2006; Mahvash et al., 2018; Simatupang et al., 2020), glass powder (Consoli et al., 2021), nanomaterials (Correia et al., 2021) and biomass waste, especially rice husk ash (Consoli et al., 2019a), have already been effectively used for soil stabilization in mixtures with cement, lime, or by means of the geopolymerization technique, allowing gains in strength, stiffness, and durability. The analysis and prediction of the strength of chemically stabilized soils depends on several factors and has become essential for the use of these materials in engineering applications (Horpibulsuk et al., 2003; Zhang et al., 2013; Correia et al., 2019, 2020).

In the case of pozzolan and lime mixtures, the compressive and tensile strength of the samples can be correlated with the porosity (η) and the volumetric binder content (B_{iv}) using the parameter (η / B_{iv}), which is the ratio between the volume of binder and the total volume of the sample (Consoli et al., 2018). Several authors have verified the effectiveness of using these parameters for normalizing compressive and tensile strength data (Baldovino et al., 2020b; Consoli et al., 2020a, 2021).

During the manufacturing of porcelain tiles, one of the stages is the polishing of the pieces, responsible for improving the finishing of the product. During this process, which occurs in the presence of water, the residue, generated as a result of the detachment of particles from the tile and the abrasive material, is discarded and is called porcelain polishing waste (PPW). It is estimated that about 100 g of PPW is generated for each m^2 of porcelain tile manufactured (Jacoby & Pelisser, 2015).

This waste, usually discarded in landfills, has a high daily production, requires large storage areas in the industries and can be a source of soil and groundwater contamination, or even be carried by winds affecting the local vegetation (Breitenbach, 2013). Brazil, for example, considered the third largest producer of ceramic pieces in the world, produced 871.9 million m^2 of ceramic tile in 2018 (Anfacer, 2019), and generates about 60,000 tons of PPW per year (De Matos et al., 2018a).

The composition of PPW includes elements present in the ceramic and may also have elements of the abrasive material used in polishing the pieces. Thus, its chemical analysis results in large quantities of silica and alumina.

Magnesium and other fluxing oxides found in porcelain tiles can also be present (Medeiros et al., 2021). Specific tests such as electrical conductivity and calcium hydroxide consumption (Medeiros et al., 2021) or the analysis of cementitious materials with PPW incorporation using mechanical strength tests and thermogravimetry (Jacoby & Pelisser, 2015; De Matos et al., 2018b) confirmed the existence of pozzolanic activity of this material. The incorporation of the residue resulted in an optimization of the hydration reactions of the compounds, allowing gains in strength and durability, and thus constituting a potential candidate for use in soil improvement in mixtures with lime and cement.

However, while several studies have already evaluated the use of this material in the production of cements (Andreola et al., 2010; Jacoby & Pelisser, 2015; De Matos et al., 2020), mortars (Jacoby & Pelisser, 2015; Sánchez de Rojas et al., 2018; Li et al., 2019, 2020) and concretes (De Matos et al., 2018a, b; Medeiros et al., 2021), no research was found evaluating its use in soil improvement processes, thus constituting the main gap that this work aims to address.

In this context, this research aims to use mechanical tests to study the incorporation of porcelain polishing waste and hydrated lime to improve a sandy aeolian soil from a coastal dune located in the city of Natal/RN. Fontoura et al. (2021) investigated the influence of cement content and molding moisture on the mechanical behavior of this soil and obtained an increase in unconfined compressive strength with increasing cement content.

2. Materials and methods

2.1 Materials

In this research, dune sand, hydrated lime and a residue from the porcelain tile polishing process were the three materials used. The soil is a quartz sand from sedimentary deposits that form dunes in the coastal region of Natal in Rio Grande do Norte. Figure 1 shows the grain size distribution curve of the sand, while Table 1 presents its physical properties. The material has angular to sub-angular grains and a uniform grading composed of 96.23% particles in the sand fraction (0.06 - 2.00 mm), approximately 70% medium sand, and fines content below 5%, being classified as a poorly graded sand (SP) by the Unified Soil Classification System.

Porcelain polishing waste was obtained from an industry that produces ceramic tiles in the state of Paraíba, Brazil. This waste is generated in the porcelain tile polishing operation with an abrasive material and in the presence of large amounts of water. The material used in this research was the solids resulting from the dewatering of the effluent in a filter press and which is stored in large piles outdoors. Around 200 kg of material was collected in different piles stored at a maximum time of one week, providing greater homogeneity given the variations in the production line.

2

Silva et al., Soil. Rocks, São Paulo, 2023 46(1):e2023002322

Table 1. Physical properties of dune sand.

Properties	Symbol	Value
Specific gravity (-)	G_s	2.66
Mean diameter (mm)	d_{50}	0.265
Effective diameter (mm)	d_{10}	0.151
Coefficient of uniformity (-)	C_u	1.94
Coefficient of curvature (-)	C_c	0.98
Maximum void ratio (-)	e_{max}	0.84
Minimum void ratio (-)	e_{min}	0.60
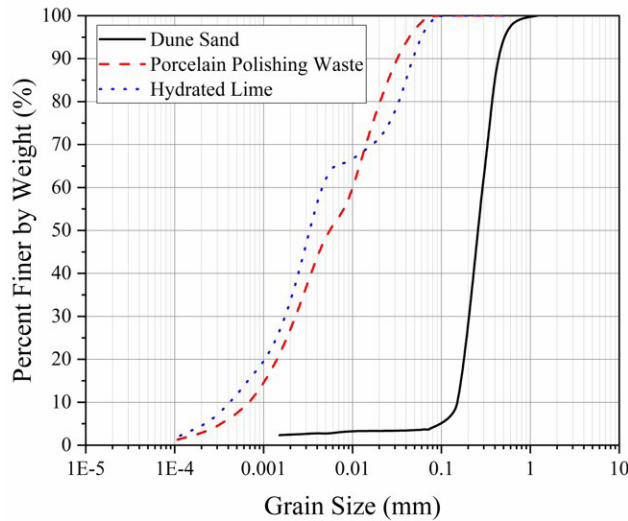
Figure 1. Grain size distribution curves of the materials used in this research.

The collected material was initially homogenized and dried at a temperature of approximately 100 °C for 24 h. The dry material was manually crushed, passed through a sieve with 0.42 mm mesh and then subjected to characterization tests. Figure 1 shows the particle size distribution of PPW that was obtained by laser diffraction granulometer.

The material is composed of 26.93% of particles with dimensions equivalent to clays (< 0.002 mm), 71.61% in the range of silts (0.002 - 0.06 mm) and only 1.46% of particles in the range of fine sands (0.06 - 0.2 mm). In addition, it has 99.74% of fine particles with size below 75 μm, an average diameter (d_{50}) of 0.0055 mm and an effective diameter (d_{10}) of 0.00068 mm. It presented liquid limit, plastic limit and plasticity index equal to 31%, 27% and 4%, respectively, being classified as a low plastic material. The specific gravity obtained was 2.55. Regarding the chemical composition, PPW presented as main components silica (67.48%) and aluminum (17.91%) that plus iron amount to 86.4%, allowing the material to be classified as a class N pozzolan by ABNT NBR 12653 (ABNT, 2014). The compounds calcium, sodium, magnesium and potassium were also present in smaller amounts.

The main crystalline phases identified were quartz, albite, mullite and silicon carbide, with the first three probably derived from the porcelain paste and the last one from the abrasive material used. The morphology of PPW particles is composed of rough and angular particles of irregular shapes. The consumption of 394 mg of calcium oxide per gram of PPW measured by the Modified Chapelle method was higher than the 330 mg/g limit proposed by Raverdy (Hoppe Filho et al., 2017) confirming the pozzolanic activity of this material. CH-I high purity hydrated lime was used as a source of reactive calcium, this material has a specific gravity of 2.30.

2.2 Methods

The variables controlled for the produced samples were relative density (RD), lime content (L) and PPW content (P). To define the levels of each variable and optimize the experimental program the Response Surface Methodology with Central Composite Rotatable Design (CCRD) was used. This technique allows an optimization in the combinations between the various analyzed factors, reducing the necessary amount of samples to be produced (Atkinson & Donev, 1992). The number of experiments is defined based on Equation 1, where k is the number of factors and CP the number of central points.

$$n = 2^k + CP + 2 \times k \tag{1}$$

Thus, for 3 factors or independent variables, 15 experiments are obtained, being 8 factorial points (FP), 6 axial points (AP) and 1 central point (CP). All experiments were performed in triplicate. For this research, the PPW content was defined as a replacement for sand and the lime content was defined as an addition to the sand plus PPW mixture.

In order to evaluate the influence of low to high contents of PPW incorporation, 10%, 20%, and 30% were chosen as levels for this variable. In the case of lime, the Initial Lime Consumption method proposed by Rogers et al. (1997) was applied to determine the minimum amount of hydrated lime necessary to reach a pH sufficient to induce pozzolanic reactions in the mixture. The results showed that for the maximum PPW content incorporated the minimum lime content is 3%. Thus, considering the work of other researchers in the area of pozzolan-lime mixtures (Abbasi & Mahdieh, 2018; Consoli et al., 2019b, 2021), contents of 3%, 5% and 7% were adopted. As for the relative density, the aim was to evaluate mixtures in the loose, medium dense and dense states, adopting values of 25%, 50% and 75%, respectively.

The independent variables and the proposed levels with real and coded values for the CCRD are shown in Table 2, while the design matrix of the experiments is shown in Table 3. For each composition, maximum and minimum void ratios tests were performed, whose results are shown in Table 4. The specific gravity of each mixture (G_s) is a

function of the contents (S, L, P) and densities (ρ_S, ρ_L, ρ_P) of each material and the equation for its calculation is derived below (Equations 2 and 3), where M_S, M_L and M_P and V_S, V_L and V_P are the mass and volume of sand, lime and PPW particles, respectively. M_d is the total dry mass of the mixture and ρ_w the density of water.

$$G_s = \frac{M_{solids}}{(V_{solids})\rho_w} = \frac{M_S + M_L + M_P}{(V_S + V_L + V_P)\rho_w} = \frac{\dfrac{M_d}{1+L}(S+L+P)}{\dfrac{M_d}{1+L}\left(\dfrac{S}{\rho_S}+\dfrac{L}{\rho_L}+\dfrac{P}{\rho_P}\right)\rho_w} \quad (2)$$

$$G_s = \frac{S+L+P}{\left(\dfrac{S}{\rho_S}+\dfrac{L}{\rho_L}+\dfrac{P}{\rho_P}\right)\rho_w} \quad (3)$$

The experimental data were fitted to a second order polynomial equation Y (quadratic model), similar to Equation 4. Where, $X_{(1,2,3)}$ are the independent variables and β_0, $\beta_{(1,2,3)}$, $\beta_{(11,22,33)}$ and $\beta_{(12,13,23)}$ are the regression coefficients for, respectively, the intercept, linear and quadratic behavior and interaction between the factors.

$$Y = \beta_0 + \beta_1 X_1 + \beta_2 X_2 + \beta_3 X_3 + \beta_{11}X_1^2 + \beta_{22}X_2^2 + \beta_{33}X_3^2 + \beta_{12}X_1X_2 + \beta_{13}X_1X_3 + \beta_{23}X_2X_3 \quad (4)$$

In order to validate the statistical models obtained, additional tests in triplicate for unconfined compressive strength and tensile strength were performed under two new conditions (40% RD, 4% lime, 25% PPW and 60% RD, 6% lime, 15% PPW) on samples at 28 days of curing and the results were compared with the predicted values.

Table 2. Independent variables and levels used in the CCRD.

Factors	Levels				
	-1.68	-1	0	+1	+1.68
Relative density (%)	7.96	25	50	75	92.04
Lime content (%)	1.64	3	5	7	8.36
PPW content (%)	3.18	10	20	30	36.82

Table 3. CCRD matrix for compressive and tensile strength tests.

Mixtures	Real value (Coded value)		
	Relative density	Lime content	PPW content
FP-1	25% (-1)	3% (-1)	10% (-1)
FP-2	25% (-1)	3% (-1)	30% (+1)
FP-3	25% (-1)	7% (+1)	10% (-1)
FP-4	25% (-1)	7% (+1)	30% (+1)
FP-5	75% (+1)	3% (-1)	10% (-1)
FP-6	75% (+1)	3% (-1)	30% (+1)
FP-7	75% (+1)	7% (+1)	10% (-1)
FP-8	75% (+1)	7% (+1)	30% (+1)
AP-1	7.96% (-1.68)	5% (0)	20% (0)
AP-2	92.04% (+1.68)	5% (0)	20% (0)
AP-3	50% (0)	1.64% (-1.68)	20% (0)
AP-4	50% (0)	8.36% (+1.68)	20% (0)
AP-5	50% (0)	5% (0)	3.18% (-1.68)
AP-6	50% (0)	5% (0)	36.82% (+1.68)
CP	50% (0)	5% (0)	20% (0)

Table 4. Physical properties of each composition.

Contents		Properties				
Lime	PPW	$\gamma_{d_{max}}$ (kN/m³)	$\gamma_{d_{min}}$ (kN/m³)	e_{max}	e_{min}	G_s
3%	10%	17.0	14.4	0.84	0.55	2.64
3%	30%	17.1	12.7	1.06	0.53	2.62
7%	10%	16.6	14.0	0.88	0.58	2.62
7%	30%	16.0	12.1	1.15	0.62	2.60
1.64%	20%	16.8	13.7	0.91	0.56	2.63
8.36%	20%	16.4	12.7	1.05	0.59	2.61
5%	3.18%	16.7	14.3	0.84	0.58	2.64
5%	36.82%	15.5	11.6	1.24	0.68	2.60
50%	20%	16.6	13.2	0.99	0.58	2.62

2.2.1 Molding and curing of the specimens

For all tests, cylindrical specimens with dimensions of 50 mm in diameter and 100 mm in height were used. Initially, the PPW and the sand in dry condition were mixed manually until a homogeneous appearance was obtained. Then hydrated lime was added and a new homogenization was carried out. Distilled water was added to the final material. The void ratio (e) (Equation 5) and total dry mass (M_d), whose calculation is derived in Equations 6 and 7, were used to obtain the dry mass of each material used in the mixture (Equations 8 to 10). Where ρ_d is the dry density of the mixtures and V_{total} the total volume of the sample.

$$e = e_{max} - RD \times \left(e_{max} - e_{min}\right) \tag{5}$$

$$\rho_d = \frac{M_d}{V_{total}} = \frac{M_S + M_L + M_P}{V_{solids}\left(1+e\right)} = \tag{}$$

$$\frac{\dfrac{M_d}{1+L}\left(S+L+P\right)}{\dfrac{M_d}{1+L}\left(\dfrac{S}{\rho_S}+\dfrac{L}{\rho_L}+\dfrac{P}{\rho_P}\right)} \times \frac{1}{\left(1+e\right)} \tag{6}$$

$$M_d = \frac{\left(S+L+P\right)}{\left(\dfrac{S}{\rho_S}+\dfrac{L}{\rho_L}+\dfrac{P}{\rho_P}\right)} \times \frac{V_{total}}{\left(1+e\right)} \tag{7}$$

$$M_S = \frac{M_d}{1+L} \times S \tag{8}$$

$$M_L = \frac{M_d}{1+L} \times L \tag{9}$$

$$M_P = \frac{M_d}{1+L} \times P \tag{10}$$

Since the moisture required by each material is different, the mass of water (   ) was calculated based on Equation 11 by adding 5% in relation to the mass of sand (M_S) with a water/binder ratio of 0.32. The binder was taken as the sum of the mass between the PPW (M_P) and hydrated lime (M_L) and this content was chosen based on previous tests in order to have good workability when molding.

$$M_w = 0.05 \times M_S + 0.32 \times \left(M_L + M_P\right) \tag{11}$$

The mixtures were statically compacted using a mechanical loading machine in a tripartite cylindrical mold in four layers of equal mass and height. The compaction energy used in each layer was that sufficient to achieve the desired height and, consequently, the target dry unit weight and relative density. The top of each layer was scarified to improve the adhesion between them. A maximum time of 20 minutes was adopted for the mixing and compaction processes in order

to minimize its influence on particle cementation. Three samples were taken to verify the moisture content.

At the end of molding, the specimens were removed from the mold and then weighed to verify their wet weight with 0.01 g precision. Due to the fragility of the samples, dimensions were measured only on some specimens to obtain an average volume used to calculate the relative density. The maximum tolerances adopted for sample acceptance were ± 0.5% for moisture and ± 2% for relative density.

Then the specimens were placed in a humid chamber for curing at a temperature of 23 °C ± 3 °C and humidity above 95%. The standard curing time was 28 days, however, for the FP-8 mixture, samples were also analyzed at 7 and 91 days of curing to observe the development of cementation reactions over time.

2.2.2 Compressive strength tests

At 27 days of curing, the specimens were immersed for 24 h in a container of water to minimize the effects of suction. They were then removed from the tank and superficially dried with an absorbent cloth. The tests were performed on a hydraulic press with a maximum capacity of 100 kN and a load cell with a capacity of 10 kN and resolution of 0.01 kN. The test followed the prescriptions of ABNT NBR 5739 (ABNT, 2018), similar to ASTM C39 (ASTM, 2021), and was initiated immediately after surface drying at a rate of 1.00 mm/min with the maximum load being obtained for each specimen.

The compressive strength is defined as the ratio between the maximum load and the cross-sectional area of the specimen. As an acceptance criterion for the mechanical tests, it was adopted that the individual strengths of the three specimens could not deviate by more than 10% from the average strength.

2.2.3 Split tensile strength tests

To obtain the tensile strength of the specimens, split tensile tests, also known as the indirect tensile test or Brazilian Test, were performed. The same machine was used as for the axial compression tests. The procedure followed the prescriptions of ABNT NBR 7222 (ABNT, 2011), similar to ASTM C496 (ASTM, 2017). The specimen, prepared as in the previous test, was placed between two rectangular pieces of wood with dimensions calculated according to the dimensions of the specimen and diametrically opposite to each other. A compression load was then applied generating a diametrical rupture. The tensile strength (q_t) was obtained from Equation 12, which relates the maximum applied force (F), the diameter (D) and height (H) of the specimen.

$$q_t = \frac{2F}{\pi DH} \tag{12}$$

For analysis of the results obtained for the response variables, including generation and fitting of the model, obtaining the response surfaces and analysis of data variance, the Statistica 12.0 software was used.

3. Results and discussion

3.1 Statistical analysis

A total of 114 specimens were prepared for the experimental program. Table 5 shows all values of unconfined compressive strength (q_u) and split tensile strength (q_t) calculated as the average of the strength of three specimens as well as the respective standard deviation for 28 days curing time. The q_u values obtained ranged from 57.39 kPa to 1561.43 kPa, and the q_t values from 7.13 kPa to 162.48 kPa. This indicates that the variables involved in the design have an influence on the mechanical strength of the soil samples. Similar ranges were obtained by Abbasi & Mahdieh (2018), Consoli et al. (2018, 2019b, 2021) in mixtures of soil, pozzolan and lime cured at 28 days.

The data analysis using CCRD allowed the identification of significant factors and their respective coefficients to build the regression model. Since the actual values of relative density vary around the planned values (± 2%) due to factors inherent to the molding process and to allow the calculation of the pure error and lack of fit parameters, the planned values were considered for all specimens.

In the case of compressive strength, ignoring the effects of insignificant terms (p-value > 0.05), it was possible to obtain an adjusted regression model with coefficient of determination R^2 value of 0.980, i.e., which explains 98.0% of the variability of the process (only 2.0% of the total variability cannot be explained) that is given in Equation 13.

In addition, the adjusted R^2 of 0.976 was very close to the R^2 actual value, indicating a good fit of the second-order polynomial equation to the experimental data. The result of the analysis of variance (ANOVA) with the fitted model is shown in Table 6. The sum of squares (*SS*), degrees of freedom (*df*), mean square (*MS*) and p-value are shown. The lack of fit test was used to evaluate the model fit by comparing the pure error with the residual error. The result showed a significant lack of fit, however, the other evaluations such as the coefficient of determination and an analysis of the distribution of residuals showed that the model is able to predict with quality the values of the response variable.

$$q_u = -3.936(RD) - 0.036(RD^2) + 339.488(L) - 27.457(L^2) + 22.052(P) - 0.637(P^2) + 0.865(RD)(P) - 943.208 \qquad (13)$$

For the tensile strength only the quadratic term of the PPW content proved to be insignificant and was ignored in the final regression equation. Thus, it was possible to obtain a model with R^2 also equal to 0.980 and adjusted R^2 of 0.976, given in Equation 14. The result of the analysis of variance with the fitted model is shown in Table 7.

$$q_t = -1.551(RD) + 0.005(RD^2) + 24.507(L) - 2.464(L^2) + 0.559(P) + 0.079(RD)(L) + 0.068(RD)(P) + 0.085(L)(P) - 31.841 \qquad (14)$$

3.1.1 Model validation

The results of the additional tests for unconfined compressive strength and tensile strength to validate the

Table 5. Compressive and tensile strength results for each mixture.

Mixtures	q_u (kPa)	Standard deviation (kPa)	q_t (kPa)	Standard deviation (kPa)	q_t/q_u
FP-1	99.30	3.25	8.75	0.32	0.09
FP-2	495.15	16.89	72.65	3.70	0.15
FP-3	288.61	13.43	23.30	0.93	0.08
FP-4	719.66	62.30	74.01	5.11	0.10
FP-5	128.70	9.53	13.73	0.88	0.11
FP-6	1408.08	17.79	125.38	6.09	0.09
FP-7	284.13	8.05	24.05	1.72	0.08
FP-8	1561.43	33.07	162.48	4.96	0.10
AP-1	325.15	22.45	54.52	4.72	0.17
AP-2	1241.88	107.04	113.18	1.57	0.09
AP-3	224.77	6.25	20.83	1.85	0.09
AP-4	849.45	67.47	72.68	5.18	0.09
AP-5	57.39	1.47	7.13	0.13	0.12
AP-6	1277.55	71.74	145.19	5.91	0.11
CP	825.45	66.00	67.64	4.07	0.08

statistical models obtained are presented in this section. The levels of each factor as well as the results found (average values) and percentage error relative to the value predicted by the model are presented in Table 8.

It can be seen that there is a good agreement between the predicted and observed values. All the tests showed a percentage error lower than 10%, indicating that the obtained models can be used to predict with good accuracy the compressive and tensile strengths of this dune sand stabilized with PPW and lime.

3.2 Unconfined compressive strength and split tensile strength results

The interaction model of the three independent variables evaluated in the research with the response was obtained to assess the effect of each one on the compressive strength (q_u) and tensile strength (q_t) of mixtures. With the model it was possible to generate the response surfaces for the variables studied as well as contour plots allowing the combined influence of the variables on soil strength to be verified. The contour plot provides a two-dimensional representation while the response surface adds a new axis for easy visualization. These graphs allows the evaluation of how each independent variable affects the response at different levels while keeping another independent variable constant. Figure 2 illustrates the response surfaces and contour plots for compressive strength relating it with two independent variables while the third independent variable is held fixed at the center value. The results for tensile strength can be seen in Figure 3.

It can be observed that q_u and q_t of the samples present a parabolic increase with the increase in the PPW content for any relative density, however, this increase is more significant and linear at higher values of relative density. These results are in agreement with other works that have evaluated the incorporation of pozzolanic materials and lime for the improvement of soils (Abbasi & Mahdieh, 2018; Consoli et al., 2018, 2021).

In these cases, the strength gain is especially attributed to the cementation of the grains as a result of the pozzolanic reactions between pozzolan and lime, which is amplified with higher silica and aluminum reserves present in the residue. Increases in strength with increasing content of incorporation of pozzolanic wastes were reported by other authors in similar research (Silvani et al., 2019; Simatupang et al., 2020). Lime carbonation can also generate compounds that helps in particle cementation. Furthermore, an increase in relative density promotes gains for q_u and q_t, especially at high PPW levels. This can be attributed to the reduction in void ratio that increases the number of contacts between the particles and optimizes the load transfer allowing the soil to withstand higher stresses (Vranna & Tika, 2020).

With a reduction in PPW content the effect of relative density is also reduced. At low PPW contents, this material tends to be concentrated in the voids between the larger sand particles that dominate the soil strength mechanism even for denser samples. However, with an increase in the PPW content, the cementation generated can act on the contact between the sand grains and an increase in density amplifies the number of contacts, thus allowing greater impacts on the strength (Chang & Woods, 1992; German, 2014; Vranna & Tika, 2020; Moon et al., 2020; Consoli et al., 2021). The incorporation of smaller particles causes, for the same mass, the number of particles to increase, thus increasing

Table 6. ANOVA for compressive strength quadratic model.

Source	SS	df	MS	p-value
RD	2423320	1	2423320	0.000000
RD^2	9366	1	9366	0.044625
L	690686	1	690686	0.000000
L^2	219029	1	219029	0.000000
P	6490356	1	6490356	0.000000
P^2	73773	1	73773	0.000002
$RD \times P$	1122071	1	1122071	0.000000
Lack of Fit	164859	7	23551	0.000001
Pure Error	63960	30	2132	
Total	11241543	44		

Table 7. ANOVA for tensile strength quadratic model.

Source	SS	df	MS	p-value
RD	13246.0	1	13246.02	0.000000
RD^2	314.6	1	314.61	0.000053
L	4977.8	1	4977.83	0.000000
L^2	2874.4	1	2874.38	0.000000
P	78262.9	1	78262.94	0.000000
$RD \times L$	372.5	1	372.54	0.000016
$RD \times P$	6881.7	1	6881.74	0.000000
$L \times P$	69.4	1	69.38	0.034724
Lack of Fit	1745.6	6	290.93	0.000000
Pure Error	425.4	30	14.18	
Total	110574.6	44		

Table 8. Predicted and observed values for the validation of the statistical models.

Mixtures	Relative density	Lime content	PPW content	q_u (kPa)			q_t (kPa)		
				Predicted	Observed	Error	Predicted	Observed	Error
1	60%	6%	15%	704.07	677.52	-3.77%	57.59	53.88	-6.44%
2	40%	4%	25%	777.69	849.86	9.28%	75.89	79.16	4.31%

Figure 2. CCRD response surfaces and contour plots for compressive strength.
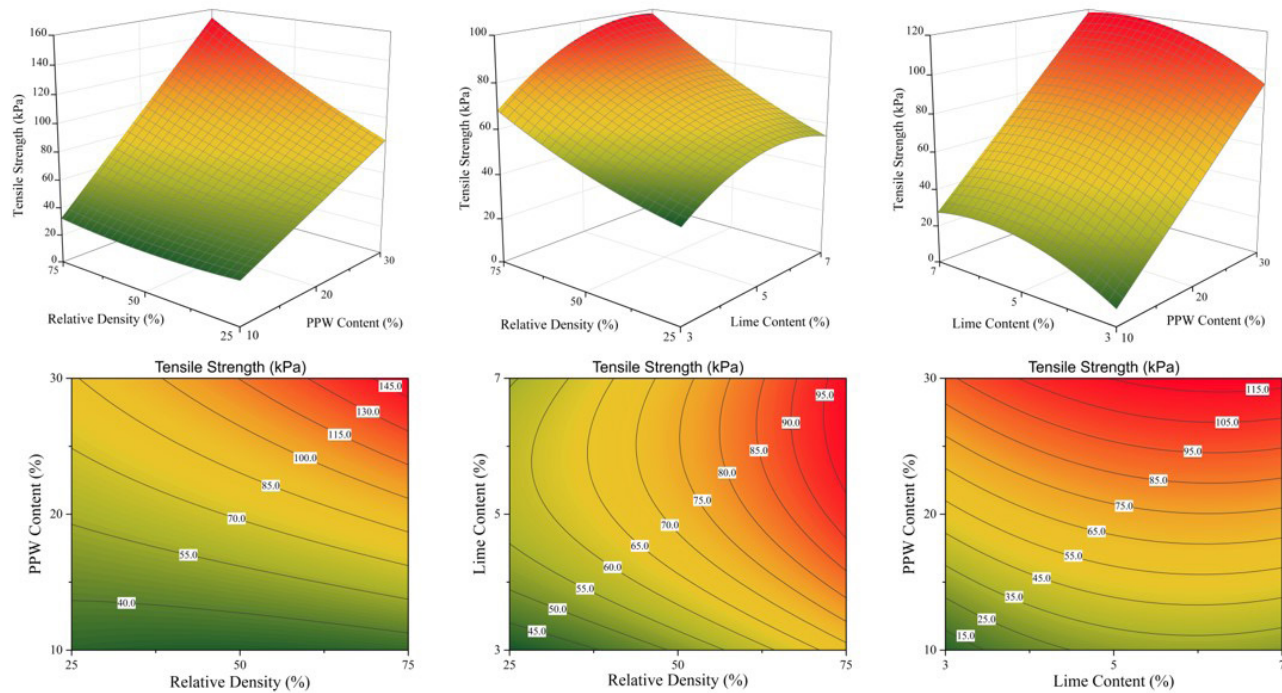
Figure 3. CCRD response surfaces and contour plots for tensile strength.

the number of contacts (Wiącek & Molenda, 2014). Another aspect is that for low saturation levels, hydration products tend to precipitate in regions where the meniscus are formed and that occur in greater numbers with an increase in the number of contacts (Ribeiro et al., 2016). The highest strengths were

found in the region combining high values of PPW content and relative density, indicating that the interaction between them is more important than their isolated effects.

The effect of the lime content on both strengths is given by a parabolic curve with the concavity downward,

8

Silva et al., Soil. Rocks, São Paulo, 2023 46(1):e2023002322

indicating that there is an optimum lime content, this behavior is maintained for any relative density. While there is a significant improvement in strength between the samples with 3% and 5% lime, this improvement reduces considerably between 5% and 7% content. A mathematical analysis of the parabolic function returns an optimum lime content near 6%. Similar behavior was obtained by Abbasi & Mahdieh (2018). The dissolution of calcium hydroxide raises the pH of the mixture and allows the amorphous silica and alumina present in the pozzolanic material to combine with calcium to form hydrated compounds, in particular calcium silicate hydrate (Walker & Pavía, 2011; Sharma & Sivapullaiah, 2016). An increase in the lime content allows an optimization in the maintenance of this pH besides making more calcium ions available in the solution for the reactions to occur, however the low speed of the pozzolanic reaction and the reaching of an equilibrium pH can limit the strength gains.

An increase in relative density, as in the previous case, has a positive effect on the values of q_u and q_t for any lime content, meanwhile, the combined effect of relative density and lime content is less significant than the combined effect of relative density and PPW content. This can be attributed to the small difference between the lime contents studied, which has little impact on the amount of fines and hence on the granulometric characteristics of the mixtures.

As for the interaction between lime and PPW content the optimum region occurs at high values of PPW incorporation and lime contents between 5% and 7%. An increase in the amount of incorporated PPW requires greater amounts of calcium available for pozzolanic reactions, thus, mixtures with a high content of PPW and low amount of lime can limit strength gains by lack of calcium. In this case, part of the incorporated waste is dissolved and helps in the formation of the cementing compounds while other particles act only with a physical filling effect in the pores created by the larger sand particles (Moon et al., 2020).

It can be inferred that the optimization points for the response variables taking into account all three factors simultaneously have not yet been reached. The data indicate that these points are located at higher values of relative density and PPW content than those studied in this research. In other words, higher compressive and tensile strengths can be obtained for compacted samples with lime content between 5 and 7%, relative densities higher than 75%, and PPW contents above 30% simultaneously.

Figure 4 shows the variation of q_u and q_t with the volumetric binder content (B_{iv}) for each relative density and lime content. Data predicted by Equations 13 and 14 were used. It can be noted that there is a tendency for the strength to increase with the increase of B_{iv}, with the slope of the curve being more pronounced for denser mixtures. Moreover, with the increase in relative density the behavior becomes more linear. An increase in the volume of binder incorporated enhances the cementation reactions, which is optimized by increasing the relative density, as discussed above. An important aspect is that the curves referring to the
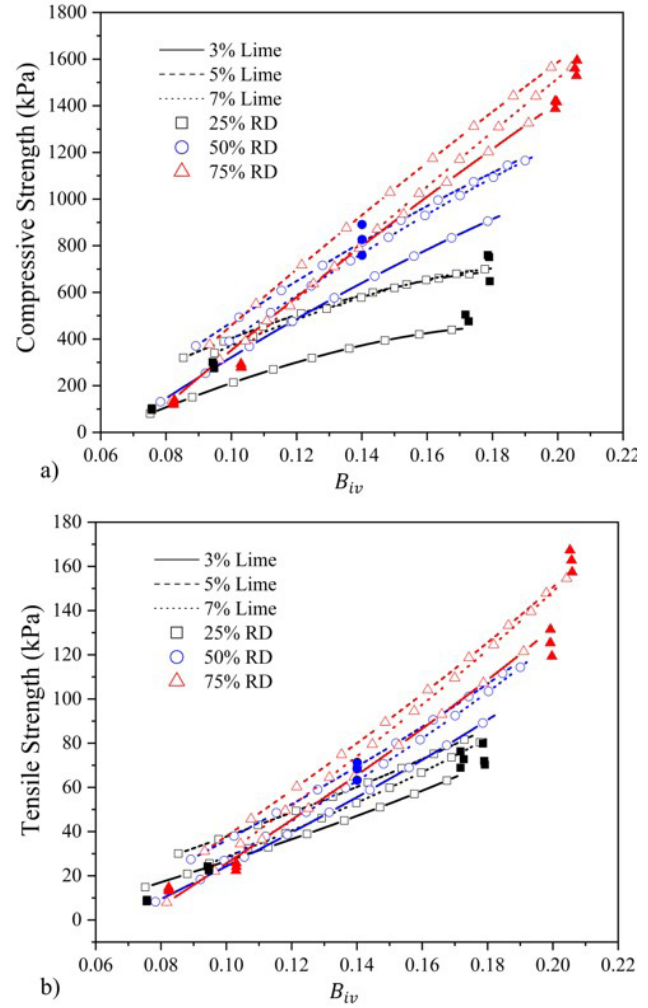
Figure 4. (a) Compressive and (b) Tensile strengths versus volumetric binder content.

7% lime content are located below those referring to the 5% content, i.e., for the same parameter B_{iv}, mixtures with 5% lime present higher strengths. Besides a better mechanical performance, this also indicates a better environmental performance of these mixtures since they require a smaller amount of lime and use larger volumes of waste.

Figure 5 illustrates the correlation of q_u and q_t with the parameter (η / B_{iv}). According to Consoli et al. (2016) the strength of soils treated with cementitious materials can be predicted by an equation such as Equation 15, where A is a scalar and B and β adjustment exponents. The values of B and β depend on the type of binder and the characteristics (particle size distribution and mineralogy) of the soil (Rios et al., 2013). The scalar A, according to Diambra et al. (2017), is related to the sand and binder matrix and is affected by the exponent B.

$$q_u = A \left[\frac{\eta}{\left(B_{iv} \right)^\beta} \right]^{-B} \tag{15}$$

In this paper a coefficient of determination R^2 of 0.89 was obtained for the fitting curve. An exponent equal to 1.00 was applied to B_{iv}. Exponents smaller than 1.00 indicate that sample porosity has a greater effect on the mechanical strength of cemented soil. Values close to 1.00 indicate that the two parameters have similar effects and are most commonly used for the case of sandy soils (Baldovino et al., 2020a). Similar value was reported by Fontoura et al. (2021) who used the same soil as in this research. Mola-Abasi & Shooshpasha (2016) and Consoli et al. (2011, 2013, 2020b) obtained the same exponent for sands from other locations. However, the value of B equal to 2.30 differs from that reported in the other studies. According to Baldovino et al. (2020a) these parameters also depend on the compaction conditions, most often related to the optimum point obtained in the Proctor test.

In general, a reduction in $\eta \quad B_{iv}$ leads to an increase in q_u and q_t with an exponential trend. Thus, a reduction in porosity combined with an increase in the amount of binder in the paste has a positive effect on the strength. Similar behavior was found by Baldovino et al. (2020b), Consoli et al. (2021) and Fontoura et al. (2021).

Another important aspect is that different mixture combinations can be obtained taking into account the same strength value. From Figure 5 it can be seen that the same strength can be obtained for different combinations of relative density, PPW content, and lime content. This indicates that although the parameter η / B_{iv} allows a good correlation of the data with the strength, a correct design of pozzolan-lime mixtures can only be made knowing the behavior of the strength in relation to the combinations between all the variables.

To be able to correlate the equations of the fit curves between q_t and q_u graphs, the q_t data was fitted to an equation with the same exponent B found for q_u (i.e., 2.30). It is worth mentioning that since it was the same soil, binder and preparation mode, these values were already close.

The ratio between q_t and q_u is shown in Equation 16. The value of 0.10 is a common value for the case of cemented materials (Khajeh et al., 2020; Consoli et al., 2020b). As shown in Table 5, the ratio between q_t and q_u for each mixture is also around 0.10.

$$\xi = \frac{q_t}{q_u} = \frac{802.7\left(\dfrac{\eta}{B_{iv}}\right)^{-2.30}}{8020.6\left(\dfrac{\eta}{B_{iv}}\right)^{-2.30}} = 0.10 \qquad (16)$$

3.3 Effect of curing time on strength

Figure 6 shows q_u and q_t values of the FP-8 mixture (75% RD, 7% lime and 30% PPW) for 7, 28, and 91 days of curing. It is evident the strength improvement with the
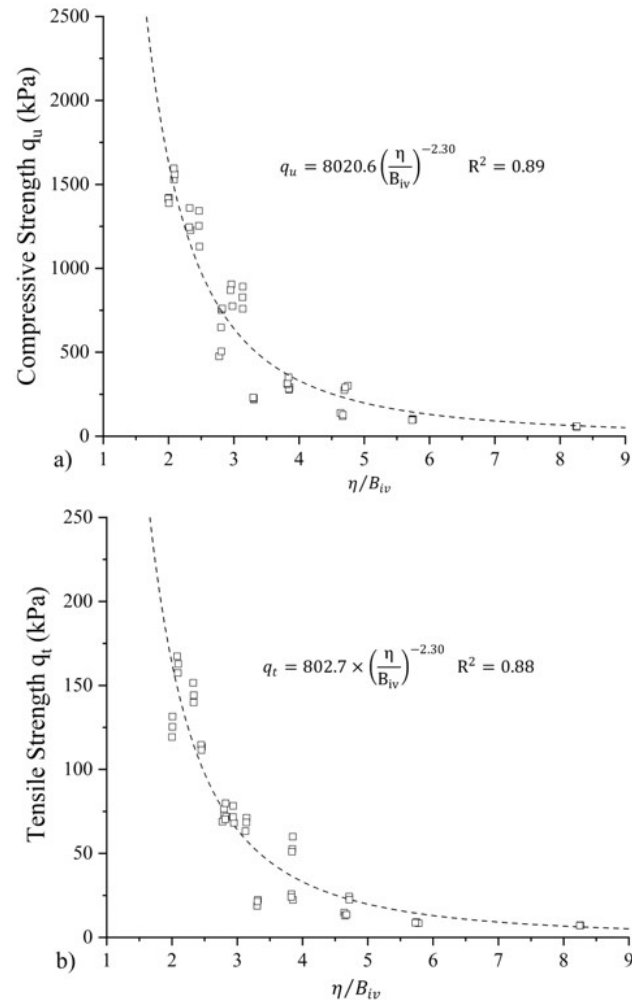
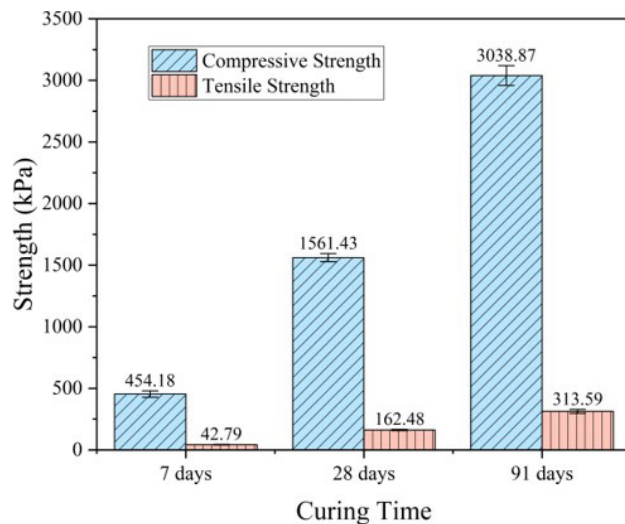**Figure 5.** (a) Compressive and (b) Tensile strengths versus porosity/binder index.

Figure 6. Variation of compressive and tensile strength with curing time.

increase of curing time. Values of q_u at 28 days and 91 days were, respectively, 243.7% and 569.1% higher than those found for 7 days. For q_t these increases were 279.7% and 632.9%. In addition, the ratio q_t / q_u is almost 0.1 for any of the curing times studied.

The increase in curing time allows the pozzolanic reactions, of low velocity, to occur, providing improvement in the bonding between the particles and increment in the mechanical performance of the soil (Consoli et al., 2001; Jha et al., 2009; Amadi & Osu, 2018; Khajeh et al., 2020). Increased strength with curing time was also obtained by Abbasi & Mahdieh (2018) which evaluated the incorporation of a natural pozzolan and lime for the improvement of a sandy soil. Simatupang et al. (2020) also reported the increase of strength with curing time for sands stabilized with fly ash.

4. Conclusion

In this research, the influence of porcelain polishing waste and hydrated lime on the mechanical properties of an aeolian dune sand was investigated by unconfined compressive strength and split tensile strength tests. For this purpose, the variables relative density, lime content and PPW content were combined using a Surface Response Methodology with Central Composite Rotatable Design.

The PPW and lime contents as well as the relative density have a positive effect on q_u and q_t of the mixtures. The highest strength values were found for the region that combines high values of PPW content and relative density, being the optimum region above the one covered in this study. The influence of the lime content showed a parabolic behavior with the optimum content around 6%.

The improvement in the mechanical performance of the samples can be attributed to grain bonding due to cementation reactions. Pozzolanic reactions between lime and PPW and carbonation of lime are the most probable. At high PPW contents, the cementing compounds tend to be formed in the contact between the particles and an increment in the relative density and number of fines increases the number of contacts allowing higher strength gains.

It was possible to establish a good correlation of q_u and q_t data with the parameter η / B_{iv} and the strength is inversely proportional to this parameter. An exponent β equal to 1.00 was obtained indicating that porosity and volumetric binder content has similar effects. Finally, increases in q_u and q_t were obtained with increasing time of curing, demonstrating the dependence of cementation reactions to this factor in mixtures of soil, pozzolan and lime.

Acknowledgements

Declaration of interest

The authors have no conflicts of interest to declare.

Authors' contributions

José Daniel Jales Silva: conceptualization, data curation, methodology, formal analysis, investigation, writing – original draft, writing – review & editing. Olavo Francisco dos Santos Júnior: conceptualization, data curation, project administration, supervision, funding acquisition, writing – review & editing. William de Paiva: conceptualization, supervision, formal analysis, writing – review & editing.

Data availability

The datasets generated analyzed in the course of the current study are available from the corresponding author upon request.

List of symbols

A	Scalar for the relation between strength and η / B_{iv}
ANOVA	Analysis of variance
AP	Axial point
B	Second exponent of adjustment for the relation between strength and η / B_{iv}
B_{iv}	Volumetric binder content
C_{iv}	Volumetric cement content
C_c	Coefficient of curvature
C_u	Coefficient of uniformity
CCRD	Central composite rotatable design
CP	Central point
d_{50}	Mean diameter
d_{10}	Effective diameter
df	Degrees of freedom
D	Diameter of the sample
e	Void ratio
e_{max}	Maximum void ratio
e_{min}	Minimum void ratio
F	Maximum applied diametrical force
FP	Factorial point
G_s	Specific gravity
H	Height of the sample
k	Number of factors
L	Lime content
M_d	Total dry mass of the mixture
M_{solids}	Mass of solids
M_S	Mass of sand particles
M_L	Mass of lime particles

M_P	Mass of PPW particles
M_w	Mass of water
MS	Mean square
n	Number of experiments
P	PPW content
PPW	Porcelain polishing waste
q_u	Unconfined compressive strength
q_t	Split tensile strength
R^2	Coefficient of determination
RD	Relative density
S	Sand content
SP	Poorly graded sand
SS	Sum of squares
V_{total}	Total volume of the sample
V_{solids}	Volume of solids
V_S	Volume of sand particles
V_L	Volume of lime particles
V_P	Volume of PPW particles
$X_{(1,2,3)}$	Independent variables of polynomial equation
Y	Second order polynomial equation
β	First exponent of adjustment for the relation between strength and η / B_{iv}
β_0	Regression coefficient for intercept
$\beta_{(1,2,3)}$	Regression coefficients for linear behavior
$\beta_{(11,22,33)}$	Regression coefficients for quadratic behavior
$\beta_{(12,13,23)}$	Regression coefficients for interaction between factors
$\gamma_{d_{max}}$	Maximum dry unit weight
$\gamma_{d_{min}}$	Minimum dry unit weight
η	Porosity
η / B_{iv}	Porosity/binder index
ξ	Ratio between tensile strength and compressive strength
ρ_d	Dry density of the mixture
ρ_S	Density of sand particles
ρ_L	Density of lime particles
ρ_P	Density of PPW particles
ρ_w	Density of water

References

Abbasi, N., & Mahdieh, M. (2018). Improvement of geotechnical properties of silty sand soils using natural pozzolan and lime. *International Journal of Geo-Engineering*, 9(1), 1-12. http://dx.doi.org/10.1186/s40703-018-0072-4.

ABNT NBR 12653. (2014). *Pozzolanic materials - Requirements*. ABNT - Associação Brasileira de Normas Técnicas, Rio de Janeiro, RJ (in Portuguese).

ABNT NBR 5739. (2018). *Concrete - Compression test of cylindrical specimens*. ABNT - Associação Brasileira de Normas Técnicas, Rio de Janeiro, RJ (in Portuguese).

ABNT NBR 7222. (2011). *Concrete and mortar - Determination of the tension strength by diametrical compression of cylindrical test specimens*. ABNT - Associação Brasileira de Normas Técnicas, Rio de Janeiro, RJ (in Portuguese).

Åhnberg, H. (2006). *Strength of stabilised soil – a laboratory study on clays and organic soils stabilised with different types of binder* [Doctoral thesis, Lund University]. Lund University.

Amadi, A.A., & Osu, A.S. (2018). Effect of curing time on strength development in black cotton soil–Quarry fines composite stabilized with cement kiln dust (CKD). *Journal of King Saud University-Engineering Sciences*, 30(4), 305-312. http://dx.doi.org/10.1016/j.jksues.2016.04.001.

Andreola, F., Barbieri, L., Lancellotti, I., Bignozzi, M.C., & Sandrolini, F. (2010). New blended cement from polishing and glazing ceramic sludge. *International Journal of Applied Ceramic Technology*, 7(4), 546-555. http://dx.doi.org/10.1111/j.1744-7402.2009.02368.x.

Andrew, R.M. (2018). Global CO_2 emissions from cement production. *Earth System Science Data*, 10(1), 195-217. http://dx.doi.org/10.5194/essd-10-195-2018.

Anfacer, National Association of Ceramic Coating Manufacturers, Sanitary and Congeneral Suitcases. (2019). *Porfólio Anfacer 2019*. Retrieved in September 11, 2021, from https://www.anfacer.org.br/setor-ceramico/numeros-do-setor.

ASTM C39-21. (2021). *Standard Test Method for Compressive Strength of Cylindrical Concrete Specimens*. ASTM International, West Conshohocken, PA. https://doi.org/10.1520/C0039_C0039M-21.

ASTM C496-17. (2017). *Standard Test Method for Splitting Tensile Strength of Cylindrical Concrete Specimens*. ASTM International, West Conshohocken, PA. https://doi.org/10.1520/C0496_C0496M-11.

Atkinson, A.C., & Donev, A.N. (1992). *Optimum experimental designs*. Oxford University Press.

Baldovino, J.J.A., Izzo, R.L.S., da Silva, É.R., & Rose, J.L. (2020b). Sustainable use of recycled-glass powder in soil stabilization. *Journal of Materials in Civil Engineering*, 32(5), 04020080. http://dx.doi.org/10.1061/(ASCE)MT.1943-5533.0003081.

Baldovino, J.J.A., Izzo, R.L.S., Pereira, M.D., Rocha, E.V.G., Rose, J.L., & Bordignon, V.R. (2020a). Equations controlling tensile and compressive strength ratio of sedimentary soil–cement mixtures under optimal compaction conditions. *Journal of Materials in Civil Engineering*, 32(1), 04019320. http://dx.doi.org/10.1061/(ASCE)MT.1943-5533.0002973.

Bao, X., Jin, Z., Cui, H., Chen, X., & Xie, X. (2019). Soil liquefaction mitigation in geotechnical engineering: an overview of recently developed methods. *Soil Dynamics and Earthquake Engineering*, 120, 273-291. http://dx.doi.org/10.1016/j.soildyn.2019.01.020.

Breitenbach, S.B. (2013). *Desenvolvimento de argamassa para restauração utilizando resíduo do polimento do porcelanato* [Master's dissertation, Universidade Federal

do Rio Grande do Norte]. Universidade Federal do Rio Grande do Norte (in Portuguese).

Bucci, M.G., Almond, P.C., Villamor, P., Tuttle, M.P., Stringer, M., Smith, C.M.S., Ries, W., Bourgeois, J., Loame, R., Howarth, J., & Watson, M. (2018). Controls on patterns of liquefaction in a coastal dune environment, Christchurch, New Zealand. *Sedimentary Geology*, 377, 17-33. http://dx.doi.org/10.1016/j.sedgeo.2018.09.005.

Chang, T.S., & Woods, R.D. (1992). Effect of particle contact bond on shear modulus. *Journal of Geotechnical Engineering*, 118(8), 1216-1233. http://dx.doi.org/10.1061/(ASCE)0733-9410(1992)118:8(1216).

Clough, G.W., Sitar, N., Bachus, R.C., & Shafii Rad, N. (1981). Cemented sands under static loading. *Journal of Geotechnical Engineering*, 107(6), 799-817. http://dx.doi.org/10.1016/0148-9062(81)90544-1.

Consoli, N.C., Bittar Marin, E.J., Quiñónez Samaniego, R.A., Heineck, K.S., & Johann, A.D.R. (2019b). Use of sustainable binders in soil stabilization. *Journal of Materials in Civil Engineering*, 31(2), 06018023. http://dx.doi.org/10.1061/(ASCE)MT.1943-5533.0002571.

Consoli, N.C., Carretta, M.S., Festugato, L., Leon, H.B., Tomasi, L.F., & Heineck, K.S. (2021). Ground waste glass–carbide lime as a sustainable binder stabilising three different silica sands. *Geotechnique*, 71(6), 480-493. http://dx.doi.org/10.1680/jgeot.18.P.099.

Consoli, N.C., Cruz, R.C., & Floss, M.F. (2011). Variables controlling strength of artificially cemented sand: influence of curing time. *Journal of Materials in Civil Engineering*, 23(5), 692-696. http://dx.doi.org/10.1061/(ASCE)MT.1943-5533.0000205.

Consoli, N.C., da Silva, A., Barcelos, A.M., Festugato, L., & Favretto, F. (2020b). Porosity/cement index controlling flexural tensile strength of artificially cemented soils in Brazil. *Geotechnical and Geological Engineering*, 38(1), 713-722. http://dx.doi.org/10.1007/s10706-019-01059-w.

Consoli, N.C., Ferreira, P.M.V., Tang, C.S., Marques, S.F.V., Festugato, L., & Corte, M.B. (2016). A unique relationship determining strength of silty/clayey soils–Portland cement mixes. *Soil and Foundation*, 56(6), 1082-1088. http://dx.doi.org/10.1016/j.sandf.2016.11.011.

Consoli, N.C., Festugato, L., da Rocha, C.G., & Cruz, R.C. (2013). Key parameters for strength control of rammed sand–cement mixtures: influence of types of portland cement. *Construction & Building Materials*, 49, 591-597. http://dx.doi.org/10.1016/j.conbuildmat.2013.08.062.

Consoli, N.C., Festugato, L., Scheuermann Filho, H.C., Miguel, G.D., Tebechrani Neto, A., & Andreghetto, D. (2020a). Durability assessment of soil-pozzolan-lime blends through ultrasonic-pulse velocity test. *Journal of Materials in Civil Engineering*, 32(8), 04020223. http://dx.doi.org/10.1061/(ASCE)MT.1943-5533.0003298.

Consoli, N.C., Leon, H.B., Carretta, M.S., Daronco, J.V.L., & Lourenço, D.E. (2019a). The effects of curing time and temperature on stiffness, strength and durability of sand-environment friendly binder blends. *Soil and Foundation*, 59(5), 1428-1439. http://dx.doi.org/10.1016/j.sandf.2019.06.007.

Consoli, N.C., Prietto, P.D.M., Carraro, J.A.H., & Heineck, K.S. (2001). Behavior of compacted soil-fly ash-carbide lime mixtures. *Journal of Geotechnical and Geoenvironmental Engineering*, 127(9), 774-782. http://dx.doi.org/10.1061/(ASCE)1090-0241(2001)127:9(774).

Consoli, N.C., Winter, D., Leon, H.B., & Scheuermann Filho, H.C. (2018). Durability, strength, and stiffness of green stabilized sand. *Journal of Geotechnical and Geoenvironmental Engineering*, 144(9), 04018057. http://dx.doi.org/10.1061/(ASCE)GT.1943-5606.0001928.

Correia, A.A.S., Casaleiro, P.D.F., Figueiredo, D.T.R., Moura, M.S.M.R., & Rasteiro, M.G. (2021). Key-parameters in chemical stabilization of soils with multiwall carbon nanotubes. *Applied Sciences (Basel, Switzerland)*, 11(18), 8754. http://dx.doi.org/10.3390/app11188754.

Correia, A.A.S., Lopes, L., & Reis, M.S. (2020). Advanced predictive modelling applied to the chemical stabilisation of soft soils. *Proc. of the Institution of Civil Engineers –. Geotechnical Engineering*, (In Press) http://dx.doi.org/10.1680/jgeen.19.00295.

Correia, A.A.S., Venda Oliveira, P.J., & Lemos, L.J.L. (2019). Strength assessment of chemically stabilised soft soils. *Proc. of the Institution of Civil Engineers –. Geotechnical Engineering*, 172(3), 218-227. http://dx.doi.org/10.1680/jgeen.17.00011.

De Matos, P.R., de Oliveira, A.L., Pelisser, F., & Prudêncio Junior, L.R. (2018a). Rheological behavior of Portland cement pastes and self-compacting concretes containing porcelain polishing residue. *Construction & Building Materials*, 175, 508-518. http://dx.doi.org/10.1016/j.conbuildmat.2018.04.212.

De Matos, P.R., Jiao, D., Roberti, F., Pelisser, F., & Gleize, P.J. (2020). Rheological and hydration behaviour of cement pastes containing porcelain polishing residue and different water-reducing admixtures. *Construction & Building Materials*, 262, 120850. http://dx.doi.org/10.1016/j.conbuildmat.2020.120850.

De Matos, P.R., Prudencio Junior, L.R., de Oliveira, A.L., Pelisser, F., & Gleize, P.J.P. (2018b). Use of porcelain polishing residue as a supplementary tabilizeds material in self-compacting concrete. *Construction & Building Materials*, 193, 623-630. http://dx.doi.org/10.1016/j.conbuildmat.2018.10.228.

Diambra, A., Ibraim, E., Peccin, A., Consoli, N.C., & Festugato, L. (2017). Theoretical derivation of artificially cemented granular soil strength. *Journal of Geotechnical and Geoenvironmental Engineering*, 143(5), 04017003. http://dx.doi.org/10.1061/(ASCE)GT.1943-5606.0001646.

Elipe, M.G.M., & López-Querol, S. (2014). Aeolian sands: Characterization, options of improvement and possible employment in construction–The State-of-the-art.

Construction & Building Materials, 73, 728-739. http://dx.doi.org/10.1016/j.conbuildmat.2014.10.008.

Fontoura, T.B., Santos Junior, O.F., Severo, R.N.F., Coutinho, R.Q., & Souza Junior, P.L. (2021). Unconfined compression strength of an artificially cemented aeolian dune sand of Natal/Brazil. *Soils and Rocks*, 44(1), e2021049920. http://dx.doi.org/10.28927/SR.2021.049920.

German, R.M. (2014). Coordination number changes during powder densification. *Powder Technology*, 253, 368-376. http://dx.doi.org/10.1016/j.powtec.2013.12.006.

Hoppe Filho, J., Gobbi, A., Pereira, E., Quarcioni, V.A., & Medeiros, M.H.F. (2017). Pozzolanic activity of mineral additions to Portland cement (Part I): pozzolanic activity index with lime (PAI), X-ray diffraction (XRD), thermogravimetry (TG/DTG) and modified Chapelle. *Matéria (Rio de Janeiro)*, 22(3), e11872. https://doi.org/10.1590/S1517-707620170003.0206

Horpibulsuk, S., Miura, N., & Nagaraj, T.S. (2003). Assessment of strength development in cement-admixed high water content clays with Abrams' law as a basis. *Geotechnique*, 53(4), 439-444. http://dx.doi.org/10.1680/geot.2003.53.4.439.

Jacoby, P.C., & Pelisser, F. (2015). Pozzolanic effect of porcelain polishing residue in Portland cement. *Journal of Cleaner Production*, 100, 84-88. http://dx.doi.org/10.1016/j.jclepro.2015.03.096.

Jayanthi, P.N., & Singh, D.N. (2016). Utilization of sustainable materials for soil stabilization: state-of-the-art. *Advances in Civil Engineering Materials*, 5(1), 46-79. http://dx.doi.org/10.1520/ACEM20150013.

Jha, J.N., Gill, K.S., & Choudhary, A.K. (2009). Effect of high fraction class F flyash on lime stabilization of soil. *International Journal of Geotechnics and Environment*, 1(2), 105-128.

Khajeh, A., Chenari, R.J., & Payan, M. (2020). A simple review of cemented non-conventional materials: soil composites. *Geotechnical and Geological Engineering*, 38(2), 1019-1040. http://dx.doi.org/10.1007/s10706-019-01090-x.

Latifi, N., Vahedifard, F., Ghazanfari, E., & Rashid, A.S.A. (2018). Sustainable usage of calcium carbide residue for stabilization of clays. *Journal of Materials in Civil Engineering*, 30(6), 04018099. http://dx.doi.org/10.1061/(ASCE)MT.1943-5533.0002313.

Li, L.G., Zhuo, Z.Y., Zhu, J., & Kwan, A.K.H. (2020). Adding ceramic polishing waste as paste substitute to improve sulphate and shrinkage resistances of mortar. *Powder Technology*, 362, 149-156. http://dx.doi.org/10.1016/j.powtec.2019.11.117.

Li, L.G., Zhuo, Z.Y., Zhu, J., Chen, J.J., & Kwan, A.K.H. (2019). Reutilizing ceramic polishing waste as powder filler in mortar to reduce cement content by 33% and increase strength by 85%. *Powder Technology*, 355, 119-126. http://dx.doi.org/10.1016/j.powtec.2019.07.043.

Mahvash, S., López-Querol, S., & Bahadori-Jahromi, A. (2018). Effect of fly ash on the bearing capacity of tabilized fine sand. *Proc. of the Institution of Civil Engineers -. Ground Improvement*, 171(2), 82-95. http://dx.doi.org/10.1680/jgrim.17.00036.

Medeiros, A.G., Gurgel, M.T., da Silva, W.G., de Oliveira, M.P., Ferreira, R.L., & de Lima, F.J. (2021). Evaluation of the mechanical and durability properties of eco-efficient concretes produced with porcelain polishing and scheelite wastes. *Construction & Building Materials*, 296, 123719. http://dx.doi.org/10.1016/j.conbuildmat.2021.123719.

Mohamedzein, Y., Al-Hashmi, A., Al-Abri, A., & Al-Shereiqi, A. (2019). Polymers for stabilisation of Wahiba dune sands, Oman. *Proc. of the Institution of Civil Engineers -. Ground Improvement*, 172(2), 76-84. http://dx.doi.org/10.1680/jgrim.17.00063.

Mola-Abasi, H., & Shooshpasha, I. (2016). Influence of zeolite and cement additions on mechanical behavior of sandy soil. *Journal of Rock Mechanics and Geotechnical Engineering*, 8(5), 746-752. http://dx.doi.org/10.1016/j.jrmge.2016.01.008.

Moon, S.W., Vinoth, G., Subramanian, S., Kim, J., & Ku, T. (2020). Effect of fine particles on strength and stiffness of cement treated sand. *Granular Matter*, 22(1), 1-13. http://dx.doi.org/10.1007/s10035-019-0975-6.

Ribeiro, D., Néri, R., & Cardoso, R. (2016). Influence of water content in the UCS of soil-cement mixtures for different cement dosages. *Procedia Engineering*, 143, 59-66. http://dx.doi.org/10.1016/j.proeng.2016.06.008.

Rios, S., Fonseca, A.V., & Baudet, B.A. (2014). On the shearing behaviour of an artificially cemented soil. *Acta Geotechnica*, 9(2), 215-226. http://dx.doi.org/10.1007/s11440-013-0242-7.

Rios, S., Fonseca, A.V., Consoli, N.C., Floss, M., & Cristelo, N. (2013). Influence of grain size and mineralogy on the porosity/cement ratio. *Géotechnique Letters*, 3(3), 130-136. http://dx.doi.org/10.1680/geolett.13.00003.

Rogers, C.D.F., Glendinning, S., & Roff, T.E.J. (1997). Lime modification of clay soils for construction expediency. *Proc. of the Institution of Civil Engineers - Geotechnical Engineering*, 125(4), 242-249. http://dx.doi.org/10.1680/igeng.1997.29660.

Sánchez de Rojas, M.I., Frías, M., Sabador, E., Asensio, E., Rivera, J., & Medina, C. (2018). Use of ceramic industry milling and glazing waste as an active addition in cement. *Journal of the American Ceramic Society*, 101(5), 2028-2037. http://dx.doi.org/10.1111/jace.15355.

Saxena, S.K., & Lastrico, R.M. (1978). Static properties of lightly cemented sand. *Journal of the Geotechnical Engineering Division*, 104(12), 1449-1465. http://dx.doi.org/10.1061/AJGEB6.0000728.

Schnaid, F., Prietto, P.D.M., & Consoli, N.C. (2001). Characterization of cemented sand in triaxial compression. *Journal of Geotechnical and Geoenvironmental Engineering*,

127(10), 857-868. http://dx.doi.org/10.1061/(ASCE)1090-0241(2001)127:10(857).

Sharma, A.K., & Sivapullaiah, P.V. (2016). Strength development in fly ash and slag mixtures with lime. *Proc. of the Institution of Civil Engineers -. Ground Improvement*, 169(3), 194-205. http://dx.doi.org/10.1680/jgrim.14.00024.

Sharma, M., Satyam, N., & Reddy, K.R. (2021). State of the art review of emerging and biogeotechnical methods for liquefaction mitigation in sands. *Journal of Hazardous, Toxic and Radioactive Waste*, 25(1), 03120002. http://dx.doi.org/10.1061/(ASCE)HZ.2153-5515.0000557.

Silvani, C., Benetti, M., & Consoli, N.C. (2019). Maximum tensile strength of sand-coal fly ash-lime blends for varying curing period and temperature. *Soils and Rocks*, 42(1), 83-89. http://dx.doi.org/10.28927/SR.421083.

Simatupang, M., Mangalla, L.K., Edwin, R.S., Putra, A.A., Azikin, M.T., Aswad, N.H., & Mustika, W. (2020). The mechanical properties of fly-ash-stabilized sands. *Geosciences*, 10(4), 132. http://dx.doi.org/10.3390/geosciences10040132.

Souza Júnior, P.L., Santos Junior, O.F., Fontoura, T.B., & Freitas Neto, O. (2020). Drained and undrained behavior of an aeolian sand from Natal, Brazil. *Soils and Rocks*, 43(2), 263-270. http://dx.doi.org/10.28927/SR.432263.

Venda Oliveira, P.J., & Cabral, D.J.R. (2021). Behaviour of a silty sand stabilized with xanthan gum under unconfined and confined conditions. *Proceedings of the Institution of Civil Engineers - Ground Improvement* (In press) http://dx.doi.org/10.1680/jgrim.20.00065.

Venda Oliveira, P.J., & Rosa, J.A.O. (2020). Confined and unconfined behavior of a silty sand improved by the enzymatic biocementation method. *Transportation Geotechnics*, 24, 100400. http://dx.doi.org/10.1016/j.trgeo.2020.100400.

Venda Oliveira, P.J., Costa, M.S., Costa, J.N.P., & Nobre, M.F. (2015). Comparison of the ability of two bacteria to improve the behaviour of a sandy soil. *Journal of Materials in Civil Engineering*, 27(1), 06014025. http://dx.doi.org/10.1061/(ASCE)MT.1943-5533.0001138.

Vranna, A., & Tika, T. (2020). Undrained monotonic and cyclic response of weakly cemented sand. *Journal of Geotechnical and Geoenvironmental Engineering*, 146(5), 04020018. http://dx.doi.org/10.1061/(ASCE)GT.1943-5606.0002246.

Vranna, A., & Tika, T. (2021). Laboratory improvement of liquefiable sand by colloidal silica and weak cementation. *Proceedings of the Institution of Civil Engineers - Ground Improvement*, 174(4), 240-251.

Walker, R., & Pavía, S. (2011). Physical properties and reactivity of pozzolans, and their influence on the properties of lime–pozzolan pastes. *Materials and Structures*, 44(6), 1139-1150. http://dx.doi.org/10.1617/s11527-010-9689-2.

Wiącek, J., & Molenda, M. (2014). Effect of particle size distribution on micro-and macromechanical response of granular packings under compression. *International Journal of Solids and Structures*, 51(25-26), 4189-4195. http://dx.doi.org/10.1016/j.ijsolstr.2014.06.029.

Zhang, R.J., Santoso, A.M., Tan, T.S., & Phoon, K.K. (2013). Strength of high water-content marine clay stabilized by low amount of cement. *Journal of Geotechnical and Geoenvironmental Engineering*, 139(12), 2170-2181. http://dx.doi.org/10.1061/(ASCE)GT.1943-5606.0000951.

Assessment of bauxite residue stabilized with lime and graphene oxide as a geomaterial for road applications

Ajay Jatoliya[1] (ID), Subhojit Saha[1] (ID), Bheem Pratap[2] (ID), Somenath Mondal[2] (ID), Bendadi Hanumantha Rao[1#] (ID)

Article

Abstract

Negative traits of bauxite residue (*BR*) include low shear strength, inconsistent compaction characteristics and dispersion, render it unsuited geomaterial for engineering applications. The present study aims at stabilizing *BR* with the combination of lime (*L*) and graphene oxide (*GO*) in suitable proportions and investigating their impact on improvement in engineering properties (viz., density, unconfined compressive strength (*UCS*), dispersion, and durability). Lime of 2-10% and *GO* of 0.05-0.1% dosages (% weight of *BR*) are selected for experimentation purpose. Results demonstrate that *L* and *GO* together, not the individual additive, is effective to stabilize *BR*. A substantial improvement in *UCS* from 710 kPa of raw *BR* to 3890 kPa after treating with 10% *L* and 0.1% *GO* with 60 days curing period has been observed. 6% *L* and 0.05% *GO* for strength only in the short-term, and 10% *L* and 0.05% *GO* in durability aspect in the long-term are found as optimum dosages. Drastic decline in turbidity from 453 to 83 NTU establishes that *L* (6%) and *GO* (0.05%) addition completely alleviates dispersion behavior in *BR*. Though *GO* addition is trivial, its effect on strength and durability enhancement of *BR* is significant. Cementitious gel formations and bonding mechanism leading to particle aggregations are evidenced as the reason behind the improvement in strength and durability of *BR*. To verify the applicability of amended *BR*, the obtained findings are compared vis-à-vis with standards, which illustrated that the amended *BR* could be an excellent resource material in road construction, especially in base or sub-base courses.

1. Introduction

Primary problems in the use of bauxite residue (*BR*) as a construction material are lower shear strength, collapse potential, and dispersion (Mishra et al., 2020b). Past research has established that the strength of *BR* is very low owing to the presence of an excessive quantity of monovalent sodium (Na^+) ions, which hinder particle flocculation (Reddy et al., 2021a, b; Reddy & Rao, 2018; Zhang & Tao, 2008). The dispersion behavior of *BR* makes it vulnerable to severe erosion (Reddy et al., 2016a, 2018, 2021b; Singh et al., 2020). Thus, addressing the strength and dispersion becomes key problems when *BR* is to be considered as a construction material. Alongside, *pH* above 10 and the possible leaching of toxic elements under severe alkaline circumstances are a few more deterrents for the low volume usage of *BR* (Singh et al., 2020; Zhang et al., 2018, 2020a).

On the other hand, road construction requires a substantial quantity of resource materials, which are acquired from naturally available resources. In view of the excessive exploitation of nature and natural resources, the conversion of waste materials into usable geomaterials by appropriately stabilizing them with additives seems promising. *BR* is one of the potential materials that could be devised as an alternative to naturally depleting materials. Dual problems of low strength and dispersion of *BR* can be alleviated by amending with suitable additive(s) such that the modified residue meets the requirement when it is to be employed for constructing embankments, rural roads, making of bricks and paving blocks, and developing *BR* based geopolymer products (Reddy et al., 2016b; Zhang et al., 2020b; Zhao et al., 2019, 2020). Zhang et al. (2016) have developed a composite material using *BR* and slag with improved strength characteristics. Jha et al. (2020) have investigated the possibility of using *BR* to stabilize expansive soils to be used in clay lining system. Kumar & Kumar (2013) have conducted research

#Corresponding author. E-mail address: bhrao@iitbbs.ac.in
[1]Indian Institute of Technology Bhubaneswar, School of Infrastructure, Bhubaneswar, Odisha, India.
[2]National Institute of Technology Jamshedpur, Department of Civil Engineering, Jharkhand, India.

on the utilization of *BR* in conjunction with other industrial by-products such as fly ash to produce paving blocks. On a pilot project scale, Kehagia (2008) has used *BR* for the development of a soil subgrade and road embankment.

Lime is documented as a highly effective additive for treating a range of geomaterials in the field of soil stabilization (Mishra et al., 2020a). Its treatment impacts consistency, compaction, strength, swelling, and dispersion characteristics of various types of problematic soils such as black cotton soil and organic soil (Ajayi, 2012). This can be linked to the versatility and heterogeneity as well as the variety of mineralogical properties of lime (Farhan et al., 2020). A typical comparison of the effect of lime with cement indicates that the improvement of shear strength in lime stabilized soil lasts for more than two years, whereas the latter additive effect continued only for six months (Al-Rawas et al., 2005). In this context, lime could be a potential additive to stabilize the *BR*. Based on the systematic review of literature, another important knowledge gap that the authors identified is poor understanding of the effect of curing time on lime stabilization. In the knowledge of authors, there are a few literatures available that discusses the influence of lime on *BR*. Table 1 elucidates the studies as regards to treatment of *BR* with calcium rich waste materials or lime.

Nano-sized elements, such as graphene oxide, have recently become popular as cementitious composites to improve the mechanical properties of soils. The use of graphene oxide (*GO*) in civil engineering applications has recently seen a significant upsurge in light of its merit as an additive to cementitious material. The review of literature reveals that majority of *GO* applications are remain confined to cement and concrete, either to improve strength (Gong et al., 2015; Liu et al., 2019), freeze-thaw resistance (Mohammed et al., 2016); porosity (Mohammed et al., 2015); workability (Indukuri et al., 2020) or durability (Priya et al., 2021). *GO* has also successfully been introduced as part of a hybrid additive to improve the performance of construction materials (Gao et al., 2019; Pateriya et al., 2021). Liu et al. (2018) used *GO* in hot mix asphalt binder for three types of warm mix additives and reported an increase in viscosity, deformation resistance, and elasticity at high temperatures

in the *GO*-modified mixes. A greater degree of interfacial adhesion between *GO* and cement mix might explain the significant strength increment of the resultant mix.

It appears from the literature that a few efforts are devoted to explore the usability of *GO* in soil and waste material stabilization. Zhu et al. (2010) have noticed that liquid limit, plastic limit, and plasticity index of the cement-treated soil samples declines as *GO* concentration increases. The addition of *GO* to cement-treated soil resulting in an increment of unconfined compressive strength and shear strength has been reported by Naseri et al. (2016). Strength improvement, reduced compressibility and hydraulic conductivity are all factors in the development of the treated soil (Kai et al., 2019; Pateriya et al., 2019; Zhu et al., 2010).

The review of literature pertinent to *BR* suggests that it can be stabilized using lime, cement, and other pozzolanic additives with variable success rates. The majority of studies emphasize that it is necessary to stabilize the *BR* with more than one type of additive, bearing in mind multiple problems as aforementioned. There are no studies to the knowledge of authors that employ lime and graphene oxide, in tandem, to improve the geotechnical properties of *BR*. The present research focuses on evaluating the performance of *L* and *GO* in different proportions together to stabilize the *BR*. The efficacy is assessed in terms of compaction parameters and strength. In addition to the mechanical studies, durability properties of stabilized *BR* are evaluated. The results outlined in the paper have practical implications in terms of encouraging the use of *BR* in road construction as a base/subbase material, backfill material in geotechnical structures, and geomaterial in construction sector.

2. Materials and testing methodology

Bauxite Residue used in the present study was collected from the waste disposal pond of Vedanta Aluminium Limited, located at Lanjigarh in Kalahandi, Odisha, India. The samples collected were in wet and disturbed state and were collected from 1 m depth at the pond to ensure homogeneous sample collection. Soon after the collection, the wet samples were oven dried and pulverized with wooden mallet to prepared

Table 1. Description and contribution of studies pertinent to treatment of *BR* with calcium rich waste materials.

Reference	Brief description of study	Major contributions/observations
Anastasiou et al. (2014)	Mechanical strength of bricks made from calcareous fly ash and red mud mix.	Increment in percentage of fly ash led to increment in mechanical strength of brick block in 28 days.
Kumar & Prasad (2019)	Effect of water content, ratio of water to lime, dry density and ratio of porosity to lime on the *UCS* of lime stabilized *BR*	Increment in *UCS* with an increase in lime content.
Aswathy et al. (2019)	Compaction behaviour, *UCS*, *CBR* value of soil stabilized with red mud and lime	Introduction of lime to *BR* stabilized clay soil improved *CBR*, *MDD*, and *UCS* values.
Mishra et al. (2019)	Comparison between the effect of lime only treatment and lime with organic acids treatment on compaction characteristics, *UCS* and *pH* of *BR*.	Characteristics of treated *BR* improved when the treatment was performed with both lime alone and lime and organic acid together.

the samples for subsequent laboratory testing programmes. Laboratory tests for establishing geotechnical properties including, specific gravity (*G*), gradational characteristics, consistency limits, compaction characteristics, alkalinity (*pH*), and classification were performed following ASTM codes. Table 2 presents the results of the aforementioned tests on *BR* samples.

To examine the effect of lime (*L*) and graphene oxide (*GO*) treatment on the strength parameters of the *BR*, commercial-grade *L* and *GO* were purchased from the Golchha enterprises, Jamshedpur. The dosage selected for lime were 0, 2, 4, 6, 8, and 10% and that of *GO* is 0, 0.05, and 0.1% (by basis of % dry weight of *BR*). The choice of dosage of lime is based on study by Satayanarayana et al. (2012), who have showed a steady increment in *UCS* up to 10% of lime dosage. Similalry, the above dosage of *GO* is decided such that the resultant produce is cost effective. Table 3 shows sample combinations along with designations for which laboratory experiments were performed.

Initially, standard Proctor compaction tests were performed for the aforementioned combinations as per ASTM (2007d) standard. Unconfined compressive strength (*UCS*) tests were carried out on stabilized samples as per the ASTM (2007a). A series of samples for the combinations shown in Table 2 were prepared by compacting to maximum dry unit weight (γ_{dmax}) at optimum moisture content (w_{opt}). The prepared samples were placed in the polybags to prevent moisture loss and cured for 7, 21, 45, and 60 days. Another identical set of samples was prepared for durability testing purposes. Each stabilized sample for durability test was initially cured for 7 days at an ambient condition and thereafter, it was immersed in water for 4 hours. After continuous 4 hours of immersion in water, *UCS* of the sample was measured. As there are no specified guidelines available to determine the durability of stabilized waste materials, values specified in the IRC: SP 89 (IRC, 2018) were referred to.

Additionally, dispersion tests (crumb tests) on the stabilized samples were conducted, as per ASTM (2019). For testing purposes, cylindrical samples were prepared with a length-to-diameter ratio of two, similar to that needed for *UCS* test according to ASTM (2007c). The samples were visually observed and photographed for any disintegration effect. The disintegrated particles from the sample affect the turbidity of the water. Hence, the turbidity of the water was measured using a Hach 2100N turbidity meter. Finally, *pH* of all the stabilized samples was measured according to ASTM (2007b).

To verify the inter-particle bonding and cementation effects of stabilized *BR* with *L* and *GO*, Scanning Electron Microscope (*SEM*) analysis was performed. It is to be noted that the *SEM* analysis was conducted on those stabilized samples, which were already subjected to *UCS*. Thus, curing periods remain common across samples used for *SEM* and *UCS*. A small portion of the stabilized soil was separated from the middle of soil core and was coated with a thin layer of gold for two minutes using Hitachi E-1010 Ion Sputter at a vacuum of 6 Pa before the analysis. The gold coating facilities to reveal the best morphological characteristic of the sample, simultaneously avoiding charging problems during testing.

To establish mineralogical compositions of the stabilized samples, X-Ray Diffraction (*XRD*) analysis was performed. For this purpose, sample grabbed from the stabilized soil core that was already subjected to *UCS* test was used. It was then oven dried at 105 °C for 24 hours, ground to powder form and sieved through 75 μm sieve. 4 g of this powder sample was scanned for 2θ ranging from 5 ° to 70 ° (Bragg angle) with a step increment of 0.01 ° and a time of 0.5 s/step size using a copper X-ray tube (Cu-Ka) at current and voltage of 30 mA and 40 kV.

Table 2. Physical properties of bauxite residue used for the study.

Sl. No.	Property	Value
1.	*G*	3.09
2.	Atterberg's limit (%)	
	Liquid limit (w_L)	40
	Plastic limit (w_P)	29
	Plasticity index (*PI*)	11
3.	% Fraction	
	Sand	18
	Silt	56
	Clay	26
4.	Compaction characteristics	
	γ_{dmax} (kN/m³)	16.6
	w_{opt} (%)	28
5.	*pH*	12.5
6.	USCS classification	ML*

*Inorganic silts of slight plasticity.

Table 3. Mix proportions with designation of *BR* samples adopted in the study.

Sl. No.	Mix proportion	Mix designation
1.	Raw *BR*+0% Lime+ 0% *GO*	RBR
2.	*BR* + 2% Lime + 0% *GO*	R1
3.	*BR* + 4% Lime + 0% *GO*	R2
4.	*BR* + 6% Lime + 0% *GO*	R3
5.	*BR* + 8% Lime + 0% *GO*	R4
6.	*BR* + 10% Lime + 0% *GO*	R5
7.	*BR* + 2% Lime + 0.05% *GO*	R6
8.	*BR* + 4% Lime + 0.05% *GO*	R7
9.	*BR* + 6% Lime + 0.05% *GO*	R8
10.	*BR* + 8% Lime + 0.05% *GO*	R9
11.	*BR* + 10% Lime + 0.05% *GO*	R10
12.	*BR* + 2% Lime + 0.1% *GO*	R11
13.	*BR* + 4% Lime + 0.1% *GO*	R12
14.	*BR* + 6% Lime + 0.1% *GO*	R13
15.	*BR* + 8% Lime + 0.1% *GO*	R14
16.	*BR* + 10% Lime + 0.1% *GO*	R15

Jatoliya et al., Soil. Rocks, São Paulo, 2023 46(1):e2023003722

3

3. Results and discussion

3.1 Effect of *L* and *GO* on compaction properties

Dry unit weight (γ_d) versus moisture content (*w %*) relationships are developed for raw *BR* as well as *BR* treated with varying proportions of *L* is shown in Figure 1. It is seen from the figure that γ_{dmax} decreased and w_{opt} increased with an increase in lime content, except corresponding to 2%. Generally, lime imbibes water for hydration. As the lime content increases, water requirement for its hydration increases. It is however can be noted that the reaction of lime with water is exothermic in nature. As a result, some part of water generally gets evaporated during the reaction process. These statements can be linked to an increase in w_{opt} with an increase in lime content.

Figure 2 represents the variation of γ_{dmax} and w_{opt} with a change in dosage of lime. It is evident from Figure 2 that there is a continuous decrease in γ_{dmax} and an increase in w_{opt} with increment of lime dosage. The maximum and minimum values of γ_{dmax} and w_{opt} are measured as 16.9 and 15.1 kN/m³ at 26.1 and 32.2% respectively. When lime content is increased from 2 to 10%, γ_{dmax} decreased from 16.9 to 15.1 kN/m³ whereas w_{opt} increased from 26.1 to 32.2%. Though lime content of 2% has yielded the highest values of γ_{dmax} and w_{opt}, trend lines of these parameters merged at a lime dosage of 6%. Thus, 6% of lime dosage is used for experimentation to understand the effect of *L* and *GO* hybrid additive in *BR*. It is also obvious that γ_{dmax} value of 16.3 kN/m³ meets the density requirement as prescribed by IRC 89 (IRC, 2010) for various civil engineering applications. The results in Figure 2 corroborate well with earlier studies by Mishra et al. (2019) and Ajayi (2012), who have stabilized the bauxite residue and soil using lime and noticed a decline in γ_{dmax} with simultaneous increase in w_{opt}.

Similarly, Figure 3 depicts compaction curves established on *BR* for *GO* content of 0, 0.05, and 0.1% against a fixed *L* dosage of 6%. It is seen that γ_{dmax} increased and w_{opt} decreased with an increase in *GO* content. The reason behind the increment of density and decrement of moisture content can be explained by Lambs' theory. According to which, at low water content, attractive forces between the particles are stronger than repulsive forces. Hence, soils compacted at moisture content less than optimum moisture content have a flocculated structure (Zhu et al., 2010).

An increment of moisture content increases the repulsive forces. The soil compacted at moisture content more than w_{opt} usually has a dispersed structure. It can be observed an improved compaction characteristic of *BR* samples when different percentages of *GO* (0, 0.05, and 0.1%) are incorporated but by keeping constant amount of lime (6%). The γ_{dmax} value increased from 16.3 to 17.5 kN/m³ and w_{opt} decreased from 30 to 27%. These observations excellently confirm the study by Naseri et al. (2016), who
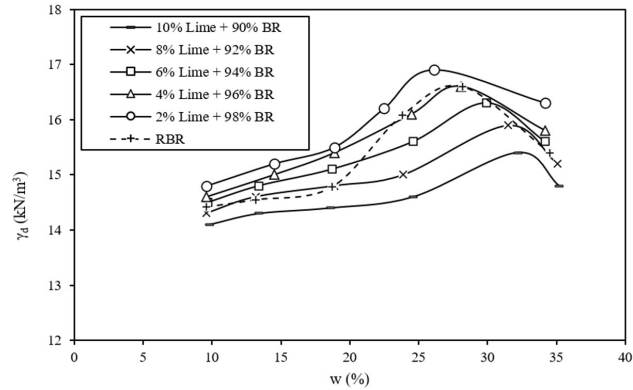
Figure 1. Relationship between dry unit weight and moisture content of untreated and lime treated bauxite residue samples.
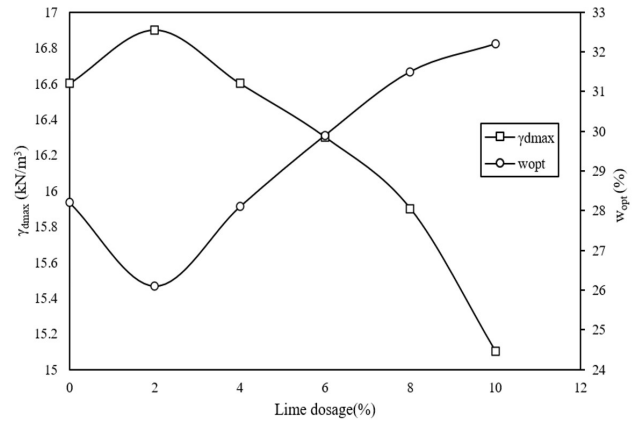
Figure 2. Variation of γ_{dmax} and w_{opt} with lime dosage.
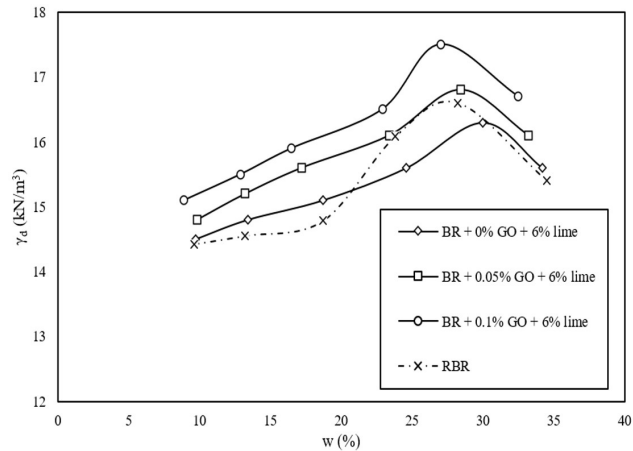
Figure 3. Compaction curves for *BR* amended with graphene oxide at lime dosage of 6%.

have illustrated an increase in *GO* quantity in the soil sample increases γ_{dmax}, while lowering w_{opt}. The increment of γ_{dmax} is not only consistent but also meets IRC SP: 20-2002 (IRC , 2002) recommendations for road construction applications, as it prescribes a minimum value of 16.19 kN/m³.

The increase in dry unit weight can be attributed to interaction between *GO* and cementitious compounds formed by the reaction of lime with *BR*. As *GO* acts as nuclei sites for hydration products, its presence plays an important role in the formation of thicker crystals with denser growth, which have a capability to intertwine *BR* particles (Zhu et al., 2010). The decrement in w_{opt} can be attributed to interface bonding between *GO* and cementitious products, as well as decrement of pores in samples. Corroborating the same, Naseri et al. (2016) have reported similar results of increment in γ_{dmax} and decrement in w_{opt} when *GO* sheets are added to soil/cement matrix. Confirming the above delineations, Lima et al (2017) have demonstrated a similarity in the hydration reaction occurring due to the admix of *BR* to calcium hydroxide to that of reaction between cement and water. On similar lines, Gordon et al. (1996) have highlighted the possible production of cementitious compounds including C-S-H gels when lime is added to *BR*. However, the quantity may comparatively low as reactive silica content in *BR* is relatively low and strength improvement of the matrix may also be due to formation of calcium aluminates (CA, possibly C_5A_3) as well through the leftover alumina in *BR*. Mishra et al. (2019) have performed the *XRD* analysis on lime treated BR and illustrated the generation of cementitious compounds in presence of water. The results of *XRD* analysis performed in the present study, which will be discussed in the later section, also confirm the generation of various cementitious materials when lime and *GO* are added to *BR*.

It is a proven fact that *BR* contains high alkaline content and predominance of iron oxide, which is unusually greater than in normal soils. Thus, the impact of these variables on compaction parameters must be thoroughly understood, as there are no earlier studies that focused on such impacts of these variables on compaction properties. In the present study, compaction curves, as presented in Figure 1, clearly show that treated *BR* is sensitive to the moisture content. This implies that *BR* requires more compaction energy to achieve desirable outcomes.

Validation of the compaction characteristics in Figures 1 and 3 with the literature shows that these trends are quite similar to other wastes (Reddy & Rao, 2018), except for non-ferrous slags, which exhibits extremely high $\gamma_{dmax}$ at little w_{opt}. The findings in Figures 1 and 3 suggest that admix of *L* and *GO* together apparently overwhelms the extreme alkalinity and high iron content effects. It is also evident from the curves that the effect of *GO* is more vivid than *L* as regards to compaction properties of *BR*.

Understandably, the effect of *GO* on compaction characteristics of *BR* is quite opposite to that treatment with lime only. When used latter additive alone there is a continual decrement of density and increment of moisture content, which will not fetch any advantage. The *GO* content in the present study is limited to 0.1% bearing in mind the cost of this material. Demonstrably, the compaction results when compared vis-à-vis with different code recommendations portray that the combination of *L* and *GO* is doable to stabilize the highly alkaline bauxite residue.

3.2 Dispersion behavior

The performance of the *L* and *GO* combination on dispersion, is checked by crumb tests that are carried out on samples prepared by varying *GO* dosages (0, 0.05, and 0.1%) and lime of 0-10%. Corresponding to 0% *L* plus *GO*, the sample is considered a control test. Images of *BR* samples immersed in water after treating with *L* and *GO* are presented in Figure 4.
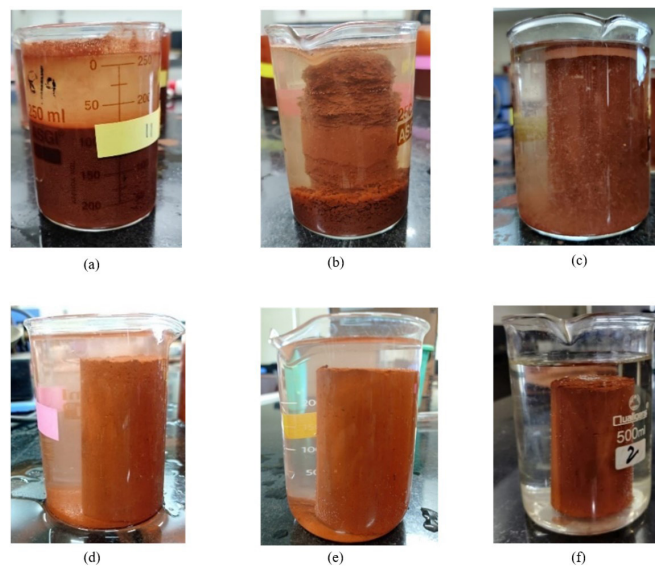

(a) (b) (c)

(d) (e) (f)

Figure 4. Pictures of *L* and *GO* amended *BR* samples after subjecting to crumb tests: (a) raw BR, (b) *L*=2% and *GO*=0.05%, (c) *L*=4% and *GO*=0.05%, (d) *L*=6% and *GO*=0.05%, (e) *L*=8% and *GO*=0.05%, and (f) *L*=10% and *GO*=0.05%.

As is evident from the results illustrated in Figure 4, the untreated sample (Figure 4a) is heavily dispersed, resulting in dark and cloudy water inside the beaker. Whereas samples treated with increasing dosage of L and GO showed recession in dispersion behavior (Figure 4b and Figure 4f). The density of suspended particles decreased in which samples treated with L and GO are immersed, as the solution in these beakers became clearer. Stable samples with less disintegration of particles can also be seen with an increase in dosage of L and GO. Further to ascertain the dispersion behavior, change in turbidity of the solution is measured, as shown in Figure 5.

The turbidity value of untreated BR is measured as high as 453 NTU (Nephelometric turbidity unit). A continual decrement in turbidity for higher dosage of L and GO indicates the ability of these additives in mitigating the dispersion behavior of BR samples. However, there are no specific guidelines in the literature that link turbidity to dispersion activity. Therefore, no proposition is made about the optimum dosage of L and GO combination. Incidentally, L of 6% and GO of 0.05%, and L of 10% and GO of 0.1% have yielded significantly lower values of turbidity of 88 and 14 NTU.

Dispersion is a phenomenon that occurs in soil when it has a sizeable amount of exchangeable sodium ions (Li et al., 2021; Mishra et al., 2020a). Dispersion behavior in the BR appears to be exacerbated by the deficiency of clay particles and the existence of substantial sodium ions concentration. Compared to the presence of monovalent excess Na^+ ions in the BR, concentrations of these divalent cations are exceedingly limited, resulting in the dispersive character (Reddy et al., 2019). As evident from Figure 4, dispersion activity in BR is decreased. This may be linked to the predominance of Ca^{2+} ions with the addition of lime. Divalent cations (Ca^{2+} and Mg^{2+}) might have mitigated the dispersion by lowering the flocculation state. As the dosage of GO is increased, as it includes many hydroxyl groups that are formed by hydrogen bonding between the network of hydrogels and free water, there is a decrement in turbidity value. GO can also form a cross-linkage with calcium. The vast network of hydrogels, hydrogen bonding, and gel formed by cross-linking of GO with calcium all work together to improve particle binding and thereby, decline dispersion behavior in BR (Kai et al., 2019).

3.3 Effect of L and GO on UCS

UCS measured on BR samples stabilized with varying proportions of L and GO (refer to Table 2 for designation of mixes) for short (7 & 21 days) and long-term (45 & 60 days) curing periods are presented in Figure 6 in the form of bar chart.

A remarkable improvement in UCS of treated samples can be noticed, highlighting the performance as well as the effectiveness of L and GO together for stabilizing highly alkaline wastes like BR. The variation of UCS is also fairly distinct between L and GO. It can be seen that as curing period increases so does UCS value. It is observed that the
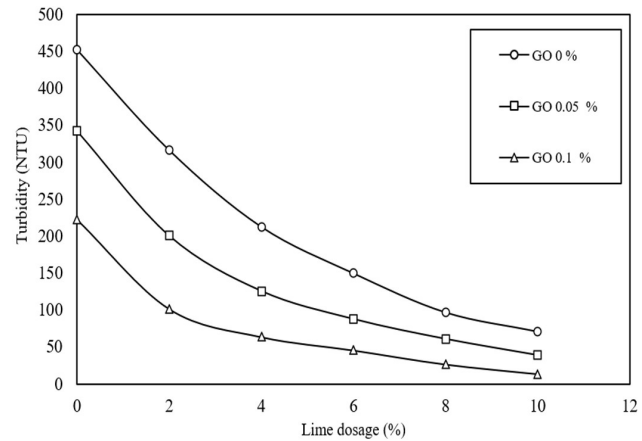
Figure 5. Turbidity test results of BR after treating with varying percentages of L and GO.
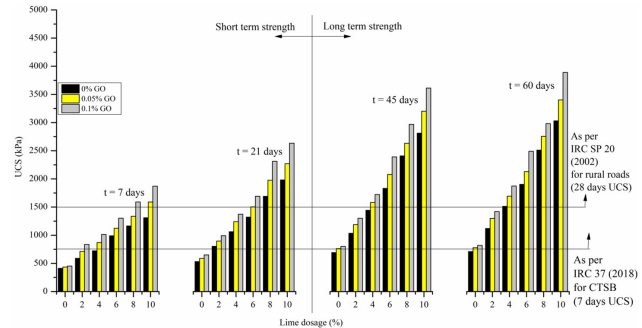
Figure 6. Measured compressive strength of BR samples amended with varying percentages of L and GO at different curing periods.

strength attained by untreated BR on 7th, 21st, 45th, and 60th day of curing is 412, 532, 692, and 710 kPa. Where as, those BR samples treated with 10% L and 0.1% GO attained a maximum strength of 1871, 2635, 3612, and 3890 kPa on the 7th, 21st, 45th, and 60th day of curing. The improvement in UCS is 4.54, 4.95, 5.22, and 5.47 times the strength of untreated BR sample. The considerable increment in strength is a strong indication that the amended BR complies with the code provisions for a specific engineering application. Bearing this in mind, an attempt is made to find out the field applications of stabilized BR in various civil engineering applications, as discussed herein.

As such, Indian Road Congress (IRC) SP:20 (2002) recommends a minimum UCS value of 1500 kPa of the chemically stabilized waste after 28 days of curing to be used in sub-base or base course of rural roads. Similarly, the required minimum UCS value according to IS-37 (2018) at 7 days for cement-treated sub-base ($CTSB$) is 750 kPa. Evidently, many combinations of mixes meet the above requirement of minimum UCS as per the IRC codes. Incidentally, the strength attained in the long-term default conforms to or even exceeds the strength requirement of sub-base and base

6

Jatoliya et al., Soil. Rocks, São Paulo, 2023 46(1):e2023003722

course of rural roads and chemically treated sub-base course for pavements. However, the base course of flexible pavement requires to have a minimum of 4500 kPa of *UCS* value in 7 days. *L* of 10% and *GO* of 0.1% have produced *UCS* of 3890 kPa after 60 days, which is nearer to the required value of 4500 kPa, though it is unable to accomplish the desired strength. Higher dosage of *L* and *GO* might enhance the strength beyond 4500 kPa. However, such combination might increase the overall cost of the construction. Thus, in terms of cost economics, it is prudent to choose the lower percentage of *L* and *GO* combination. Understandably, combinations of *L* of 6% and *GO* of 0.05% in the short-term (*UCS* value of 1504 kPa after 21 days) and *L* of 4% and *GO* of 0.05% (*UCS* value after 60 days is 1581 kPa) in the long-term produced a minimum strength of 1500 kPa, which renders suitability of the samples as resource materials for sub-base and base course of rural roads.

3.4 Durability properties

The durability test is conducted to identify the stability of the material under diverse environmental conditions. Figure 7 presents the durability test results for different mix combinations. It is observed that mixed proportions of R1, R2, and R3 have either collapsed or are unable to retain their shape in water. Hence, *UCS* tests are not conducted on these samples. Samples treated with 8 and 10% *L* maintain their shape and size and produced adequate results after 4 hours of immersion.

From Table 4 and Figure 7, it is evident that samples R4 to R10 displayed a significant decrease in strength, as is true that the ratio of *UCS* of immersed samples to non-immersed samples is calculated as < 80%. As per IRC: SP:

89 Part-1 (2010), if the strength ratio is < 80% such samples are unfit to be recommended for road construction purposes. It can be witnessed that mixes from R10 to R15 exhibited the strength that is greater than 80% of the strength of samples that are not plunged in water. Such combinations satisfy the a fore mentioned criteria and thus, they may be considered as regards to the durability. Further from the durability viewpoint, it can be stated that *L* of 10% and *GO* of 0.05% can be considered optimum dosage, as it fulfills the minimum strength requirement.

Figures 6 and 7 establish that when only the lime content and combination of *L* and *GO* in *BR* is increased, *UCS* improvement is striking. Clearly, the increase in mechanical strength is obvious before and after dipping in water, where the before state indicates strength in the short-term and the after state indicates durability in the long-term. As the silica content
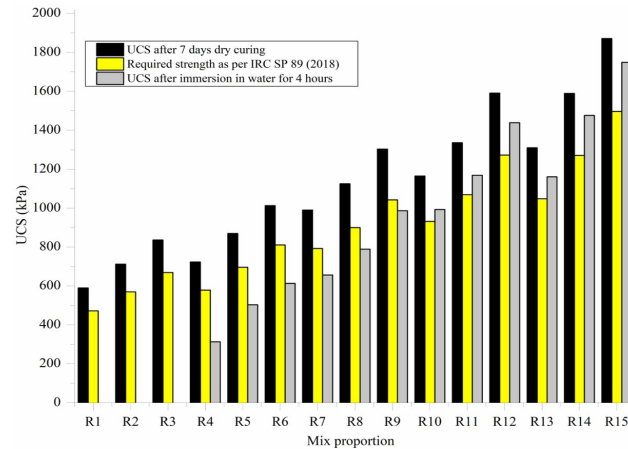
Figure 7. Comparison of *UCS* measured before and after immersion of treated *BR* samples in water.

Table 4. The value of *UCS* measured from mechanical and durability tests.

Mix proportion	*UCS* (kPa) at 7 days without immersion in water	*UCS* (kPa) after 7 days of curing followed by immersion in water for 4 hours	Immersed *UCS* as a percentage of *UCS* without immersion (%)
R1	590	Failed	-
R2	712	Failed	-
R3	836	Failed	-
R4	723	313	43.29
R5	870	503	57.82
R6	1013	613	60.51
R7	990	656	66.26
R8	1125	789	70.13
R9	1303	987	75.75
R10	1165	993	85.24
R11	1336	1169	87.50
R12	1591	1439	90.45
R13	1310	1161	88.63
R14	1589	1476	92.89
R15	1871	1749	93.48

in BR is reportedly low, amount of generated cementitious products can understandably low when admixed lime alone. Hence, the increment in *UCS* is also lower when only *L* is added to *BR*, as evident from Figure 6. Results from study by Satayanarayana et al. (2012) shows a steady increase in *UCS* of lime treated *BR* and it postulates that this increase is due to the interaction between silica and alumina of *BR* and lime mix. Intriguingly, the introduction of *GO* to the matrix seemingly generated additional strength in the treated *BR* samples. At this juncture, the addition of *GO* together with *L* largely might have aided to attain higher strength of the desired level, as can be witnessed that strength of *L* + *GO* combination samples are pointedly higher vis-à-vis with those samples treated only with *L*. Generation of cementitious products due to reaction of *L* and *BR* (Gordon et al., 1996) and subsequent reaction of the cementitious and hydration products with *GO* is postulated to be contributing to the higher strength of the *BR* modified with the combination of *L* and *GO*. It is even interesting to note that a very modest addition of *GO* has greatly contributed to strength and durability enhancement, as is true from Figures 6 and 7.

3.5 *pH* of lime and graphene oxide stabilized *BR* samples

Table 5 shows the value of *pH* measured on *BR* samples stabilized with *GO* and *L* at various combinations and curing periods. The *pH* of raw *BR* is measured as 12.5. A glance at the results illustrates that the addition of *L* and *GO* has led to only a trivial reduction in *pH* of treated samples (the lowest observed *pH* is 11.8) against 12.5 of RBR, even after curing period of 60 days. A minute change in *pH* emphasizes that there are no obvious impacts, in terms of environmental, on the stabilized *BR*.

Table 5. The value of *pH* measured of amended *BR* samples at different curing periods.

Mix designation	pH after different curing periods				
	0 day	7 days	21 days	45 days	60 days
RBR	12.5	12.45	12.3	12.4	12.4
R1	12.43	12.40	12.34	12.30	12.25
R2	12.38	12.35	12.20	12.22	12.18
R3	12.30	12.24	12.18	12.12	12.08
R4	12.26	12.16	12.10	12.01	11.90
R5	12.25	12.10	12.02	12.00	11.88
R6	12.5	12.40	12.33	12.22	12.16
R7	12.45	12.39	12.20	12.18	12.11
R8	12.36	12.28	12.11	12.02	11.92
R9	12.30	12.22	12.16	12.13	12.00
R10	12.25	12.04	12.12	11.96	11.88
R11	12.47	12.32	12.23	12.05	11.91
R12	12.39	12.30	12.22	12.18	12.01
R13	12.30	12.12	12.05	11.90	11.88
R14	12.25	12.11	12.01	11.94	11.85
R15	12.20	12.01	11.90	11.85	11.80

The primary reason for the small change in *pH* can be linked to the fact that both *L* and *RBR* have *pH* values in the same range which is nearly 12-12.5. Hence, the addition of lime does not affect the *pH* of treated samples. The quantity of *GO* available in treated samples is also minimal. This may be a reason why there is an insignificant change in the *pH* of treated samples.

3.6 Mineralogical and morphological analysis

An attempt further is made to understand and confirm the improvement in strength, durability, and dispersion by confirming the mineralogical compositions of *BR* treated with *L* alone and that with *L* and *GO* by *XRD* analysis. Mix designated as R3 (*BR* + 6% *L*) and R8 (BR + 6% *L* + 0.05% *GO*) are considered for the analysis, as these are found to be the optimum dosage from the perspective of strength, compaction and dispersion. Figure 8 shows the X-Ray diffractogram patterns after identifying the dominant minerals and cementitious compounds.

Major mineralogical compositions identified in *BR* are Hematite (ICSD #01-089-8103), Boehmite (ICSD #01-083-2384), Sodalite (ICSD #01-089-9099), Calcite (ICSD #01-072-1652), Cancrinite (ICSD #01-089-8047) (Mishra et al., 2019, Castaldi et al., 2008). Incidentally, all these mineral compositions are identified in R3 and R8 samples. Additionally, cementitious and hydration products namely, Portlandite (ICSD #00-044-1481), Calcium silicate hydroxide hydrate (*CSHH*) (ICSD #00-026-0307), Di-calcium silicate (C_2S) (ICSD #00-031-0302), Tricalcium aluminate (ICSD #00-038-1429), and calcium aluminate silicate hydrate (*CASH*) (ICSD #01-085-1567) are also found. Apart from these, a peak belonging to iron aluminate silicate (ICSD #01-082-1546) is also identified in both the samples. Presence of these cementitious and hydration products well affirm the increment in *UCS* of lime and *BR* mix at 7 and 28 days (Figure 6) besides the chemical reaction between calcium present in the lime and silica present in the BR (Kai et al., 2019). These inferences further prove the hypothesis that the mixture of *BR* and calcium hydroxide is similar to that of reaction between cement and water (Lima et al., 2017; Satayanarayana et al., 2012). However, a marginal difference in peaks is seen between R3 and R8 demonstrating that mineralogical compositions of both the matrix are nearly same. Although intensity of di-calcium silicate is visibly higher in case of R8, which reinforces the idea that due to addition of *GO* to the matrix, it helps in accumulation of cementitious and hydration products as the nanomaterial additive acts as nuclei for the cementitious products.

As per the Kai et al. (2019), the mechanism behind strength improvement when *GO* along with cement is admixed to unstabilized material, is a reaction of calcium silicate hydrate (C–S–H) and Ca(OH)$_2$ which are products formed after the hydration of cement, with carboxylic acid groups on *GO* particles. It is stated that the contact produces

8

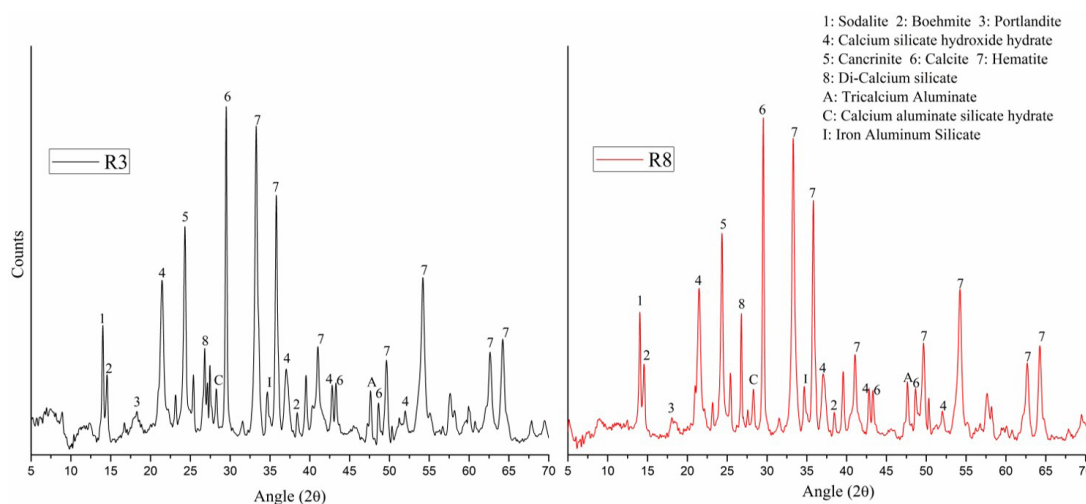Jatoliya et al., Soil. Rocks, São Paulo, 2023 46(1):e2023003722

Figure 8. X-ray diffractogram patterns of *BR* samples stabilized with *L* alone (R3) and *L + GO* (R8).

a strong covalent connection at *GO*-composite interface, which improves load-transfer efficiency from the cement matrix to the *GO* and consequently improves the composite's mechanical characteristics. Whereas in the study by Wan & Zhang (2020), it is elaborated that the chemical reaction occurs at the interface between *GO* and cementitious gels leads to an increase in Young's modulus as well as concentration of gel formations under alkaline environment. Contrary to C-S-H as reported by Kai et al. (2019), *CSHH* and *CASH* are found in the *L* and *GO* treated samples in the present study (Figure 8). Thus, it can be inferred that the reaction of *CSHH*, *CASH* along with Ca(OH)$_2$ with carboxylic acid groups on *GO* might be occurring in the *L* and *GO* treated samples. Further, the study by Pateriya et al. (2019) demonstrates that *GO* is a nanomaterial additive and it plays an important role in filling the pores within the matrix by providing nucleation sites. The prevalence of strong covalent bonding, increased Young's modulus and the activity of pore filling might have led to imparting additional strength to the matrix through creation of dense compact structure and further improvement in the durability properties, as reported in Figures 6 and 7.

Addition of *L* and *GO* also introduces refinement in morphology of treated *BR* samples. For this purpose, morphological features of treated *BR* samples have been established by *SEM* analysis. Figure 9 depicts *SEM* images captured on *RBR* and that amended with *L* of 6% only and *L* of 6% with *GO* of 0.05%. These mix proportions are chosen based on the conclusions derived from the foregoing results and discussion. Visual observations reveal a higher degree of particle agglomerations of *L* stabilized BR (Figure 9b) as compared with RBR (Figure 9a). Generation of *CSHH* and other cementitious products in the treated *BR* microstructure can be postulated as the reason for agglomerations in the matrix when lime is added to *BR*. Generally, the generated crystals are clustered to create bundles that result in pore filling and crystal overlapping. Since the *BR* and *L* promote

the pozzolanic reaction, the mineral structure of *L* stabilized *BR* has changed to the agglomerated columnar mixture, as is evident from Figure 9b. These phenomena well justify the improvement in strength in the short-term period (Figure 6) and durability in the long-term (Figure 7) simultaneously descending dispersion behavior (Figure 5).

Figure 9c shows the densified aggregation of cementitious products after adding *GO* to the mixture and they adhere each other tightly. When *GO* is introduced in the matrix, it fills the pores and acts as a nuclei to the cementitious products, resulting the mixture continue to develop, gradually becoming thicker and form the circular shape, and eventually agglomerate to cover the pores (Kai et al., 2019). They may also cross-link with calcium present in lime, allowing the substance to convert into the gel. The combination of the vast network of cementitious products such as Portlandite, Tricalcium aluminate, Dicalcium silicate, Calcium aluminum silicate hydrate, and Calcium silicate hydroxide hydrate along with *GO* resulted in an improvement in particle binding, bonding and aggregation. These processes well rationalize the strength and durability improvement in the long-term period (Figures 6 and 7).

Bonding of the particles can exist in several ways in the resultant matrix of *L* and *GO* stabilized *BR*. To delineate the same, a conceptual schematic has been drawn, as shown in Figure 10. Boehmite [ALO(OH)] can replace the carbon in the COOH group to form bonding between *BR* particles and *GO*. Hydrogen bonds can develop through hydroxyl ions in water with *GO* sheets, as is shown in Figure 10. These hydrogen bonds can also exist through the bonding of *GO* and water present in tricalcium aluminate (3CaO·Al$_2$O$_3$·6H$_2$O) (refer to Figure 8) generated due to the reaction between *BR* and lime in presence of water. Generally, water decomposes into hydroxyl ions (OH$^-$) and hydrogen ions (H$^+$) when a mixture of water, *BR*, *L*, and *GO* is admixed, by virtue of their chemical nature. The decomposed hydroxyl ions from
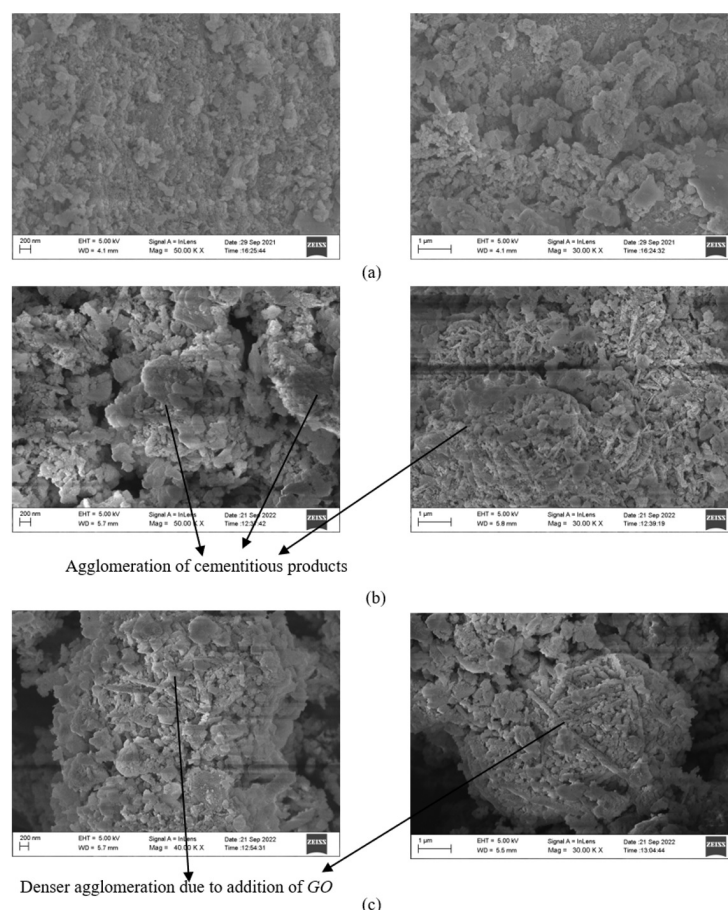
Figure 9. Morphological changes captured by SEM of *L* and *GO* amended bauxite residue samples, (a) raw *BR*, (b) *BR* treated with 6% *L*, and (c) *BR* treated with 6% *L* and 0.05% *GO*.
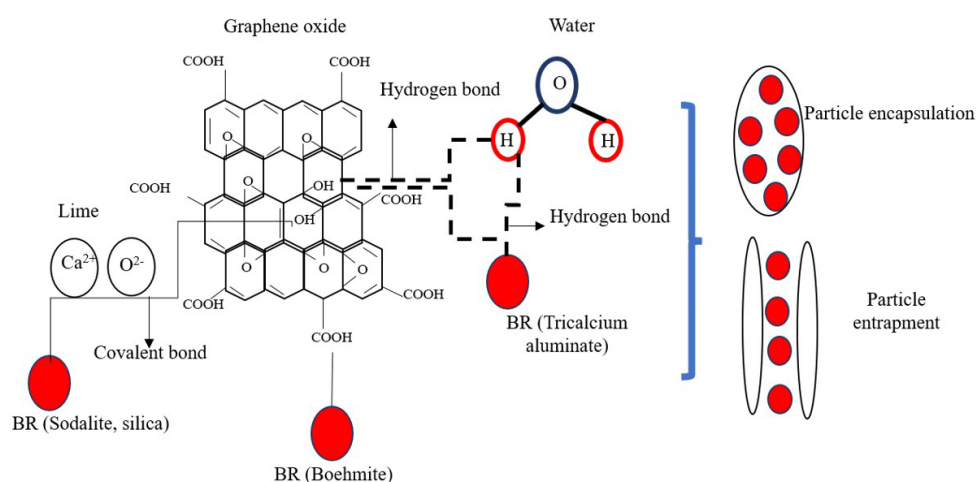
Figure 10. Conceptual diagram showing *BR*, *GO*, and *L* interaction.

water as well as from broken edges of *GO* sheets can combine with calcium oxide to generate Portlandite [Ca(OH)$_2$] (refer to Figure 8). This leads to a constant generation of OH$^-$ in the matrix. Further sodalite (3Na$_2$O·3Al$_2$O$_3$·6SiO$_2$·Na$_2$SO$_4$) in *BR*

will continue to react with Ca(OH)$_2$ to create *CSHH* in the presence of opulent hydroxides. Aluminum oxide and free sodium ions present in the *BR* can also react with hydroxyl ions to produce aluminum hydroxide [Al(OH)$_3$] and sodium

hydroxide (NaOH). These compounds encapsulate the *BR* particles within the gel substance or entrap the particles by adherence. Figure 10 illustrates the encapsulation and entrapment mechanism of *BR* particles and the consequent aggregation process, as visualized from SEM images depicted Figure 9. Such consequences excellently corroborate the strength and durability increment with the addition of *L* and *GO* together, as reported in Figures 6 and 7, and mitigation of dispersion as illustrated in Figure 5.

4. Conclusions

This study presents a novel viewpoint on the effective amendment of the extremely alkaline *BR* and demonstrates that the lime and graphene oxide combination are necessary and could be considered as potential stabilizer combination. The various results show that lime and *GO* can significantly improve the strength and durability characteristics concurrently declining the dispersion behavior of bauxite residue. It is important to note that though the addition of *GO* is trivial, it yet contributed for successful conversion of *BR* into usable geomaterial. The study finds that 6% *L* + 0.05% *GO* in strength, compaction and dispersion perspective and 10% *L* + 0.05%*GO* in durability perspective are found as optimum dosages. The strength attainment of 3031 kPa with 10% *L* alone and 1500 kPa with 6% *L* + 0.05% *GO* surpass the acceptability criteria of IRC SP: 20-2002 and IRC 37:2018, indicating that the stabilized *BR* could be a rich resource material for constructing base and sub-base layers of rural roads and subbase of flexible pavements. The crumb test results reveal that the addition of small amount of *L* and *GO* greatly helped in stability i.e. retention of shape and prevention of collapse or dispersion, of *BR* samples. The morphological analysis visibly displayed encapsulation and entrapment of particles by gel structures and inter-particle binding and bonding in the treated *BR* samples. Overall, the study complements the utilization of bauxite residue as a road construction material. Nevertheless, the strength properties of bauxite residue with amendments under extreme climatic conditions (such as drought and freeze-thaw) including leaching characteristics are also worth exploring in the future studies.

Declaration of interest

The authors have no conflicts of interest to declare. All co-authors have observed and affirmed the contents of the paper and there is no financial interest to report.

Authors' contributions

Ajay Jatoliya: conceptualization, investigation, methodology, data curation. Subhojit Saha: conceptualization, investigation, data curation, formal analysis, validation, writing – original draft. Bheem Pratap: data curation, formal analysis, validation, writing – original draft. Somenath Mondal: conceptualization, supervision, writing – review & editing. Bendadi Hanumantha Rao: conceptualization, supervision, writing – review & editing.

Data availability

The datasets generated analyzed in the course of the current study are available from the corresponding author upon request.

List of symbols

BR	Bauxite residue
CASH	Calcium Aluminate Silicate Hydrate
CSHH	Calcium Silicate Hydroxide Hydrate
G	Specific Gravity
GO	Graphene Oxide
L	Lime
NTU	Nephelometric turbidity unit
pH	Potential of Hydrogen
PI	Plasticity index
UCS	Unconfined compressive strength
w_L	Liquid limit
w_{opt}	Optimum moisture content
w_p	Plastic limit
XRD	X-ray Diffraction
γ_{dmax}	Maximum dry density
ML	low plasticity silt

References

Ajayi, E.S. (2012). Effect of lime variation on the moisture content and dry density of lateritic soil in Ilorin, Nigeria. *International Journal of Forest, Soil and Erosion*, 2(4), 159-162.

Al-Rawas, A. A., Hago, A. W., & Al-Sarmi, H. (2005). Effect of lime, cement and Sarooj (artificial pozzolan) on the swelling potential of an expansive soil from Oman. *Building and Environment*, 40(5), 681-687.

Anastasiou, E.K., Papayianni, I., Konopissi, S., & Papachristoforou, M. (2014). Fly ash-red mud mixtures for masonry block production. In *1st Concrete Innovation Conference*, Oslo, Norway.

ASTM D1633. (2007a). *Standard test methods for compressive strength of molded soil-cement cylinders* (pp. 1-15). ASTM International, West Conshohocken, PA.

ASTM D4972. (2007b). Standard test methods for pH of soils. In ASTM International (Ed.), *Annual Book of ASTM Standards* (Vol. 1, No. 10, pp. 10-12). ASTM International, West Conshohocken, PA.

ASTM D2166-87. (2007c). *Standard test method for unconfined compressive strength of cohesive soil.* ASTM International, West Conshohocken, PA.

ASTM D698-07. (2007d). *Standard test methods for laboratory compaction characteristics of soil using standard effort.* ASTM International, West Conshohocken, PA.

ASTM D6572-13e2. (2019). *Standard test methods for determination of dispersion characteristics of clayey soils by the crumb test.* ASTM International, West Conshohocken, PA.

Aswathy, M., Salini, U., & Gayathri, V. G. (2019). Utility of lime and red mud in clay soil stabilization. In V. Stalin & M. Muttharam (Eds.), *Geotechnical characterisation and geoenvironmental engineering* (pp. 19-26). Cham: Springer.

Castaldi, P., Silvetti, M., Santona, L., Enzo, S., & Melis, P. (2008). XRD, FTIR, and thermal analysis of bauxite ore-processing waste (red mud) exchanged with heavy metals. *Clays and Clay Minerals*, 56(4), 461-469.

Farhan, K.Z., Johari, M.A.M., & Demirboğa, R. (2020). Assessment of important parameters involved in the synthesis of geopolymer composites: a review. *Construction & Building Materials*, 264, 120276.

Gao, Y., Jing, H.W., Chen, S.J., Du, M.R., Chen, W.Q., & Duan, W.H. (2019). Influence of ultrasonication on the dispersion and enhancing effect of graphene oxide-carbon nanotube hybrid nanoreinforcement in cementitious composite. *Composites. Part B, Engineering*, 164, 45-53.

Gong, K., Pan, Z., Korayem, A.H., Qiu, L., Li, D., Collins, F., Wang, C.M., & Duan, W.H. (2015). Reinforcing effects of graphene oxide on Portland cement paste. *Journal of Materials in Civil Engineering*, 27(2), A4014010. http://dx.doi.org/10.1061/(ASCE)MT.1943-5533.0001125.

Gordon, J.N., Pinnock, W.R., & Moore, M.M. (1996). A preliminary investigation of strength development in Jamaican red mud composites. *Cement and Concrete Composites*, 18(6), 371-379.

Indukuri, C.S.R., Nerella, R., & Madduru, S.R.C. (2020). Workability, microstructure, strength properties and durability properties of graphene oxide reinforced cement paste. *Australian Journal of Civil Engineering*, 18(1), 73-81.

IRC SP 20. (2002). Indian Road Congress for Rural Roads. In *Indian Road Congress* (pp. 1-2), India.

IRC SP 89. (2010). IRC SP 89 part 1: guidelines for soil and granular material stabilization using cement, lime and fly ash. In *Indian Road Congress* (Vol. 53, No. 9, pp. 1689-1699), India.

IRC SP 89. (2018). Guidelines for the design of stabilized pavements (part 2). In *Indian Road Congress*. India.

Jha, A. K., Kumar, D., & Sivapullaiah, P. V. (2020). Influence of fly ash on geotechnical behavior of red mud: a micro-mechanistic study. *Geotechnical and Geological Engineering*, 38, 6157-6176.

Kai, M.F., Zhang, L.W., & Liew, K.M. (2019). Graphene and graphene oxide in calcium silicate hydrates: chemical reactions, mechanical behavior, and interfacial sliding. *Carbon*, 146, 181-193.

Kehagia, F. (2008). An innovative geotechnical application of bauxite residue. *Electronic Journal of Geotechnical Engineering*, 13, 1-9.

Kumar, A., & Kumar, S. (2013). Development of paving blocks from synergistic use of red mud and fly ash using geopolymerization. *Construction & Building Materials*, 38, 865-871.

Kumar, S., & Prasad, A. (2019). Parameters controlling strength of red mud-lime mix. *European Journal of Environmental and Civil Engineering*, 23(6), 743-757.

Li, S., Zhang, J., Li, Z., Gao, Y., & Liu, C. (2021). Feasibility study of red mud-blast furnace slag based geopolymeric grouting material: effect of superplasticizers. *Construction & Building Materials*, 267, 120910.

Lima, M.S.S., Thives, L.P., Haritonovs, V., & Bajars, K. (2017). Red mud application in construction industry: review of benefits and possibilities. *IOP Conference Series: Materials Science and Engineering*, 251(1), 012-033.

Liu, J., Li, Q., & Xu, S. (2019). Reinforcing mechanism of graphene and graphene oxide sheets on cement-based materials. *Journal of Materials in Civil Engineering*, 31(4), 04019014.

Liu, K., Zhang, K., Wu, J., Muhunthan, B., & Shi, X. (2018). Evaluation of mechanical performance and modification mechanism of asphalt modified with graphene oxide and warm mix additives. *Journal of Cleaner Production*, 193, 87-96.

Mishra, M.C., Babu, K.S., Reddy, N.G., Dey, P.P., & Rao, B.H. (2019). Performance of lime stabilization on extremely alkaline red mud waste under acidic environment. *Journal of Hazardous, Toxic and Radioactive Waste*, 23(4), 04019012.

Mishra, M.C., Gangadhara Reddy, N., Hanumantha Rao, B., & Kumar Das, S. (2020a). A Study on evaluating the usefulness and applicability of additives for neutralizing extremely alkaline red mud waste. In K.R. Reddy, A.K. Agnihotri, Y. Yukselen-Aksoy, B.K. Dubey & A. Bansal (Eds.), *Sustainable environmental geotechnics* (Lecture Notes in Civil Engineering, No. 89, pp. 139-149). Cham: Springer.

Mishra, M.C., Reddy, N.G., & Rao, B.H. (2020b). Potential of citric acid for treatment of extremely alkaline bauxite residue: effect on geotechnical and geoenvironmental properties. *Journal of Hazardous, Toxic and Radioactive Waste*, 24(4), 04020047.

Mohammed, A., Sanjayan, J.G., Duan, W.H., & Nazari, A. (2015). Incorporating graphene oxide in cement composites: a study of transport properties. *Construction & Building Materials*, 84, 341-347.

Mohammed, A., Sanjayan, J.G., Duan, W.H., & Nazari, A. (2016). Graphene oxide impact on hardened cement expressed in enhanced freeze-thaw resistance. *Journal of Materials in Civil Engineering*, 28(9), 04016072.

Naseri, F., Irani, M., & Dehkhodarajabi, M. (2016). Science Direct Effect of graphene oxide nanosheets on the

geotechnical properties of cemented silty soil. *Archives of Civil and Mechanical Engineering. Politechnika Wrocławska*, 16(4), 695-701.

Pateriya, A.S., Dharavath, K., & Robert, D.J. (2021). Enhancing the strength characteristics of No-fine concrete using wastes and nano materials. *Construction & Building Materials*, 276, 122222.

Pateriya, A., Kishan, D., & Kushwaha, S.S. (2019). Evolution of the geotechnical properties of fly ash stabilized silty soil activated by Graphene Oxide (GO). *International Journal of Recent Technology and Engineering*, 8(2), 4732-4737.

Priya, S.T., Mehra, A., Jain, S., & Kakria, K. (2021). Effect of graphene oxide on high-strength concrete induced with rice husk ash: mechanical and durability performance. *Innovative Infrastructure Solutions*, 6(1), 1-16.

Reddy, M.S., Dinakar, P., & Rao, B.H. (2016a). A review of the influence of source material's oxide composition on the compressive strength of geopolymer concrete. *Microporous and Mesoporous Materials*, 234, 12-23.

Reddy, N.G., & Rao, B.H. (2018). Compaction and consolidation behaviour of untreated and treated waste of Indian red mud. *Geotechnical Research*, 5(2), 106-121.

Reddy, N.G., Chandra, S., & Rao, B.H. (2016b). Assessment of industrial wastes as a road construction material: a review assessment of industrial wastes as a road construction material: a review. In *Proceedings of 1st International Conference on Recent Innovations in Engineering and Technology (ICREIAT-2016)* (pp. 22-23), Bhalki.

Reddy, N.G., Rao, B.H., & Reddy, K.R. (2018). Biopolymer amendment for mitigating dispersive characteristics of red mud waste. *Géotechnique Letters*, 8(3), 201-207. http://dx.doi.org/10.1680/jgele.18.00033.

Reddy, N.G., Rao, B.H., & Reddy, K.R. (2019). Chemical analysis procedures for determining the dispersion behaviour of red mud. *Lecture Notes in Civil Engineering*, 32, 19-26.

Reddy NG, Nongmaithem RS, Basu D, Rao BH. Application of biopolymers for improving the strength characteristics of red mud waste. Environmental Geotechnics. 2021a;9(6):340-59.

Reddy, P.S., Reddy, N.G., Serjun, V.Z., Mohanty, B., Das, S.K., Reddy, K.R., & Rao, B.H. (2021b). Properties and assessment of applications of red mud (bauxite residue): current status and research needs. *Waste and Biomass Valorization*, 12(3), 1185-1217.

Satayanarayana, P. V. V., Naidu, P. G., Adiseshu, S., & Rao, CH. V. (2012). Characterization of lime stabilized red mud mix for feasibility in road construction. *International Journal of Engineering Research and Development*, 3(7), 20-26.

Singh, S., Aswath, M.U., & Ranganath, R.V. (2020). Performance assessment of bricks and prisms: red mud-based geopolymer composite. *Journal of Building Engineering*, 32, 101462.

Wan, H., & Zhang, Y. (2020). Interfacial bonding between graphene oxide and calcium silicate hydrate gel of ultra-high-performance concrete. *Materials and Structures*, 53(2), 34.

Zhang, J., Liu, S., Yao, Z., Wu, S., Jiang, H., Liang, M., & Qiao, Y. (2018). Environmental aspects and pavement properties of red mud waste as the replacement of mineral filler in asphalt mixture. *Construction & Building Materials*, 180, 605-613.

Zhang, J., Li, P., Liang, M., Jiang, H., Yao, Z., Zhang, X., & Yu, S. (2020a). Utilization of red mud as an alternative mineral filler in asphalt mastics to replace natural limestone powder. *Construction & Building Materials*, 237, 117821.

Zhang, J., Yao, Z., Wang, K., Wang, F., Jiang, H., Liang, M., Wei, J., & Airey, G. (2020b). Sustainable utilization of bauxite residue (Red Mud) as a road material in pavements: a critical review. *Construction & Building Materials*, 270, 121419.

Zhang, M., Zhao, M., Zhang, G., Mann, D., Lumsden, K., & Tao, M. (2016). Durability of red mud-fly ash based geopolymer and leaching behavior of heavy metals in sulfuric acid solutions and deionized water. *Construction & Building Materials*, 124, 373-382.

Zhang, Z., & Tao, M. (2008). Durability of cement stabilized low plasticity soils. *Journal of Geotechnical and Geoenvironmental Engineering*, 134(2), 203-213.

Zhao, M., Zhang, G., Htet, K.W., Kwon, M., Liu, C., Xu, Y., & Tao, M. (2019). Freeze-thaw durability of red mud slurry-class F fly ash-based geopolymer: effect of curing conditions. *Construction & Building Materials*, 215, 381-390.

Zhao, Y., Liang, N.X., Chen, H., & Li, Y. (2020). Preparation and properties of sintering red mud unburned road brick using orthogonal experiments. *Construction & Building Materials*, 238, 117739.

Zhu, B.Y., Murali, S., Cai, W., Li, X., Suk, J.W., Potts, J.R., & Ruoff, R.S. (2010). Graphene and graphene oxide: synthesis, properties, and applications. *Advanced Materials*, 22(35), 3906-3924.

Jatoliya et al., Soil. Rocks, São Paulo, 2023 46(1):e2023003722

13

Durability and mechanical long-term performance of reclaimed asphalt pavement stabilized by alkali-activation

Alessandro Graeff Goldoni[1] (iD), Deise Trevizan Pelissaro[1] (iD), Eriky Silveira[1] (iD), Pedro Domingos Marques Prietto[1] (iD), Francisco Dalla Rosa[1#] (iD)

Article

Abstract

The application of alkali-activated industrial by-products for the stabilization of reclaimed asphalt pavement (RAP), can become a sustainable solution to reduce the carbon footprint of road construction and maintenance activities. Furthermore, this approach can also reduce the increasing depletion of natural resources. Thus, the durability and long-term mechanical performance of RAP stabilized with alkali-activated fly ash were assessed in this study. The alkaline activator was a solution composed of sodium hydroxide and sodium silicate. To this extent, unconfined compressive strength (UCS) and durability tests were conducted in this research. The proposed alkali-activated binder significantly increased the UCS of RAP mixtures, with long-term (365 days) results reaching values up to 32 MPa; fulfilling the strength requirements for cement-stabilized soil mixtures and even stable inorganic binder materials for road base and sub-base layers of pavements. These results indicate that when stabilized with an alkali-activated fly ash binder, RAP presents several applications for road engineering; even when subjected to seasonal variations in humidity and temperature, as shown by the durability tests.

1. Introduction

The increase in traffic load has been a constant concern on the performance of existing roadways. In Brazil, maintenance operations are mainly focused on resurfacing the older asphalt layer; however, to preserve a satisfactory Level of Service (LOS), the other structural layers of the pavement should also be considered for maintenance. Among the different solutions available to improve the structural response, reclaimed asphalt pavement (RAP) materials are becoming a viable option to increase the mechanical performance of pavements.

The increase in the extraction of raw materials for roadway applications has been the focus of different studies, especially regarding its impact on mechanical consequences and environmental and economic aspects. Traditional techniques, such as granular materials stabilized with Portland cement (PC), increase the bearing capacity of pavements. Furthermore, alternative types of cement have shown comparable mechanical and economical performances to OPC, while resulting in better environmental behavior. It is estimated that 7% to 8% of total the global CO_2 generation results from PC production (Celik et al., 2015; Luukkonen et al., 2018). The growing PC demand on infrastructure construction or maintenance operations has represented a critical issue for Global Warming

Potential (GWP) since these operations usually consume reasonable volumes of raw materials.

Different sustainable techniques have been proposed to improve the bearing capacity of granular materials with PC, such as biopolymers (Rezende et al., 2021; Porter et al., 2018), lime-ash blends (Haas & Ritter, 2019; Shen et al., 2007) and geosynthetic reinforcements (Consoli et al., 2009; Gowthaman et al., 2018; Wu et al., 2015). On the other hand, alkali-activated binders have represented an alternative to the chemical stabilization of granular materials. Alkali-activated mixtures are normally composed of two components: precursors (e.g. slags, amorphous silica, or silicates) and activators (e.g. solid sodium or potassium hydroxide). It is important to highlight that different industrial waste can be applied as precursor materials. In this sense, an important industrial waste is coal fly ash (FA) derived from the burning of coal in thermoelectric plants. More than 750 Mt of this waste are generated annually worldwide, but the average reuse in this global perspective is only about 25% (Blissett & Rowson, 2012).

Several studies have demonstrated the benefits of alkali-activated materials in RAP mixtures (Adhikari et al., 2020; Avirneni et al., 2016; Horpibulsuk et al., 2017; Hoy et al., 2018, 2016a, c; Singh & Middendorf, 2020). Most research has been focused on the strength behavior of the mixtures

Goldoni et al., Soil. Rocks, São Paulo, 2023 46(1):e2023007422

1

while trying to set a relationship between field and laboratory performance. These alkali-activated mixtures are known for obtaining quick hardening when compared to PC, which in turn may be suitable for roadway structure reconstruction. In addition, alkali-activation could be seen as a competitive alternative to PC, considering that this technique is less energy intensive and, consequently, represents a more sustainable roadway life cycle.

On the other hand, the durability performance of alkali-activated mixtures is an important issue, considering that maintenance operations in granular layers are not usually a technical solution to improve roadway performance. Previous studies (Solanki & Zaman, 2014) have utilized the wetting/drying durability tests to evaluate the long-term performance of cemented layers. In general, the wetting-drying cycles increased the unconfined compressive strength (UCS), not representing the proper deterioration mechanism of the cemented layer; this increase in UCS is related to the water availability and temperature increase during testing, which accelerates the cementitious reactions. An alternative to this problem would be the frost/defrost durability test, however, this test is more appropriate for cold-weather places (e.g. Europe and North America). Tropical countries, such as Brazil, normally experience hot and wet weather conditions, resulting in more complex analysis of the weathering effects on long-term performance.

With that in mind, this research analyzed RAP mixtures stabilized with alkali-activated FA in different proportions, aiming to test their efficiency as a base material for flexible pavements. To this extent, wetting-drying durability tests were carried out on the stabilized RAP mixtures, with a new method for evaluating the weathering effects. In addition, cement fixation and strength of the mixtures were also evaluated in long-term periods (up to 365 days). This study aims to help in the promotion of innovative and sustainable materials such as RAP stabilized with alkali-activated FA in pavement construction without premature failures.

2. Materials and methods

RAP was collected in a Brazilian roadway (BR-285, kilometers 275-276) in southern Brazil. The virgin aggregates were acquired from a deposit in the city of Passo Fundo, also southern Brazil; these aggregates are normally composed of basaltic rocks. In addition, tropical weather is observed in this region, with an annual average temperature of 16 °C (INPE, 2021). The RAP utilized in this research is the result of a milling operation, that was later transported and conditioned into specific piles. Considering that the milling process usually results in large pieces of RAP, all the mixtures were sieved down to 25 mm. Other three virgin aggregates: gravel 3/8" (20mm grain size), gravel 3/8" (12.5mm grain size), and stone powder (4.0mm grain size) were used in the mixture composition. The grain size distribution of the materials is shown in Figure 1a. The bitumen content of the RAP was
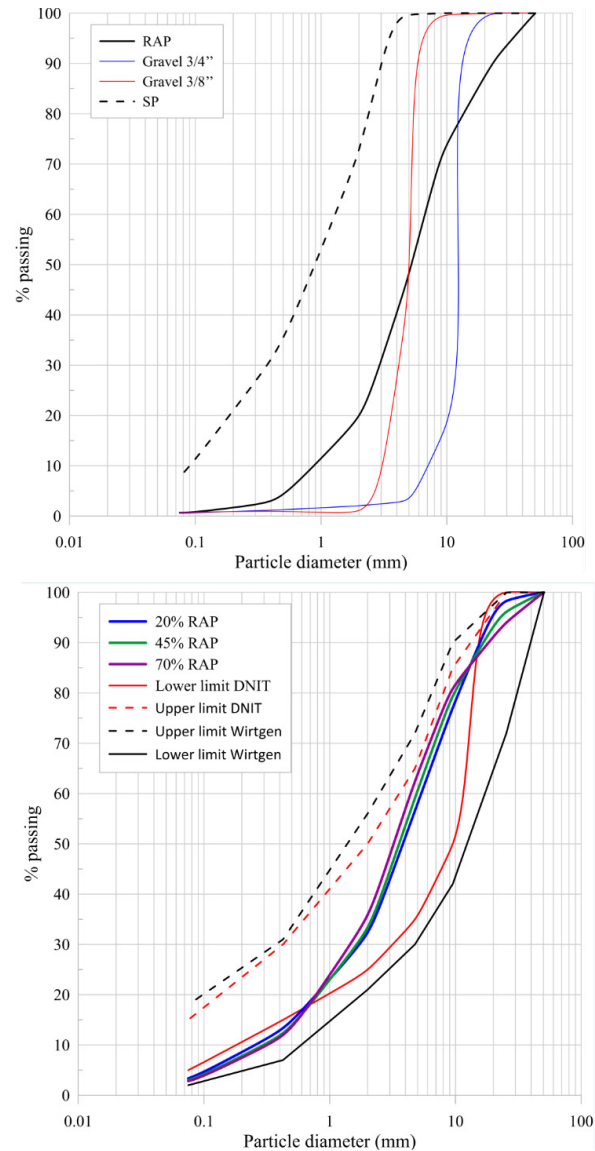
Figure 1. Grain size distribution of (a) granular materials and (b) mixtures.

determined in accordance with ASTM D2172 (ASTM, 2011), resulting in a value of 5.5%, while the specific gravity was 2.7 g/cm³.

Two types of cement were explored in this research: high early-strength Portland cement (control group) (ASTM, 2012a) and alkali-activated cement. The first cement was chosen based on its capacity of developing most of its strength on the first days of curing.

As for the second cement, its composition was based on an alkali-activated solution obtained from the precursor and activator mixture. Two precursors were applied in this research, commercial metakaolin and FA, with FA being a byproduct of a thermoelectric power plant located in Charqueadas, southern Brazil (260 km from the local of this study). Two main minerals (diffraction intensity) of quartz

and mullite were detected by XRD pattern in the region of 15 °- 50 ° 2θ for FA, as shown in Figure 2. Alkali-activate materials produced from sodium hydroxide regularly exhibit lower mechanical strength compared to mixtures produced with silicate-based activators (Provis et al., 2005). With that in mind, two compounds were used as activators to establish proper conditions for the precursor activation. The activation process was carried out using a solution combination of sodium hydroxide (NaOH) and sodium silicate. Due to its lower cost and reasonable efficiency, NaOH has also been used in different research. The 99% purity NaOH was dissolved into water and then added the precursors until a 10M concentration was reached.

2.1 Dosage parameters, molding, and curing procedures

RAP percentage in Full Depth Recycling (FDR) is considered an important issue in structural conception of pavements, considering that it establishes the necessary binder amount to reach a satisfactory mechanical performance. To obtain a proper grain size distribution, virgin aggregates were added to complement the fine grain size portion (Figure 1). This procedure was needed, once RAP was collected directly from the milling process, which results in larger particles, not representing the grain size of material after the reclamation process. Figure 1b shows the maximum and minimum limits of grain size distribution. These limits are compatible with the "C" granular distribution interval as specified in the Brazilian standard (DNIT, 2010). Table 1 shows the percentages of each material used to compose the grain size distribution curves that fit the DNIT curve "C" and Figure 1b shows the grain size distribution curves resulting from these compositions. The adopted mixture intervals have been considered satisfactory to the ones suggested by the Wirtgen company (Wirtgen GmbH, 2012).

As for the mixtures composition, the objective was always to utilize the highest amount of RAP possible. Thus,
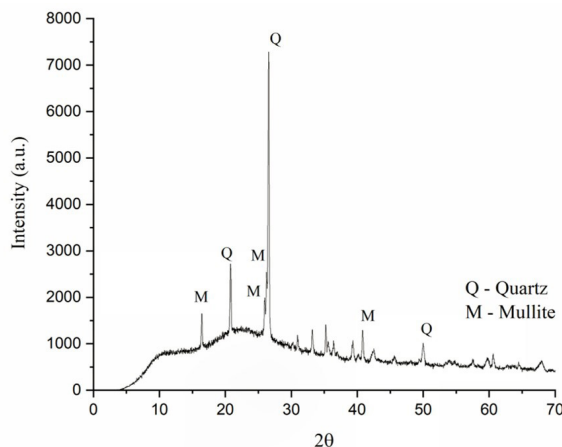
mixtures with 20, 45, and 70% of RAP stabilized with contents of 2%, 4%, and 6% cement were studied. The 45% RAP content was considered satisfactory and this value was later set for the stabilization analysis. The alkali-activated binder was utilized in amounts of 10%, 20%, and 30% (S/L ratio of 0.5). In addition, $NaOH:Na_2SiO_3$ ratios of 70:30, 80:20, and 90:10 were also studied for the alkali-activated cement. These mixtures were submitted to UCS testing to verify the requirements/guidelines for base layers of flexible pavements (DNIT, 2013). The weathering of the specimens was studied by the wetting-drying cycles of the durability test. It is important to highlight that the performance of the mixtures can also decline over time due to specimen deterioration. Thus, UCS tests were carried out in the durability specimens, to estimate the strength loss after the weathering cycles. A detailed flowchart of the experimental program is shown in Figure 3.

As for the molding procedures, specimens of 100mm in diameter and 200mm in height were utilized. A tolerance of 0.1 g/cm^3 and 1% were adopted for specific mass and moisture content, respectively. After molding, OPC specimens were immediately placed in a temperature and moisture content controlled chamber. On the other hand, alkali-activated specimens required a different treatment; specimens were oven-cured at 50°C for 24 hours after the molding process. After this process, specimens were also placed in a temperature and moisture content controlled chamber.

As previously mentioned, the curing process of all samples was carried out in a temperature and moisture content controlled chamber ($\omega = 90 \pm 2\%$ and T = 23 ± 2 °C). The curing period for UCS testing was set as seven days for all specimens.

2.2 Compaction test

The Proctor compaction test (modified energy) was performed to define the optimal moisture content ($w_{optimal}$) and the maximum dry unit weight (γ_d) of all mixtures. A typical behavior for granular compacted materials was obtained from the compaction tests; however, a clear maximum γ_d was not identified for all mixtures. For the molding procedures, a dry unit weight of 19.5 kN/m^3 and a moisture content of 7.5% were utilized for all combinations, representing the minimum water content to obtain the highest γ_d. It is noted that for the alkali-activated mixtures, the compaction test was conducted

Figure 2. Mineralogical composition of FA.

Table 1. Proportions of granular materials.

Reclaimed asphalt pavement content (%)	Stone powder content (%)	Gravel 3/4 " content (%)	Gravel 3/8 " content (%)
20	38	21	21
45	33	10	12
70	30	0	0

Figure 3. Flowchart of the experimental program.

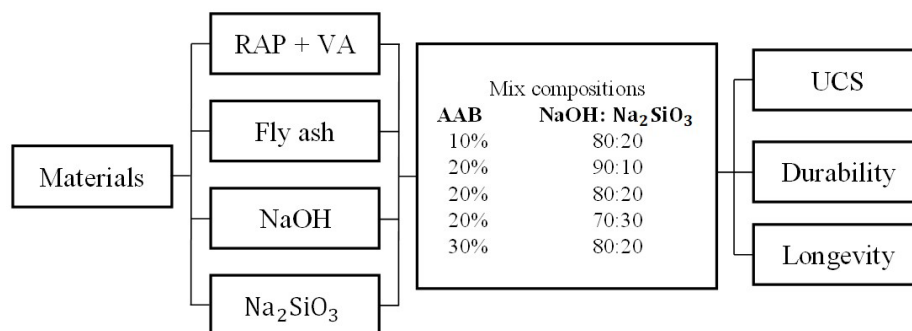without adding the activating solution, considering that the cementitious process occurs quickly; also, an adjustment in water content was necessary to obtain the optimum moisture for compaction, which resulted in an equal discounting of the water volume of the activator solution. Therefore, the solution was prepared 24 hours before the final mixture with the raw materials.

2.3 Unconfined compressive strength (UCS)

UCS tests were carried out following the procedures of ASTM D2166 (ASTM, 2016). The cylindrical mold mass was checked before and after molding to obtain the mass of the wet specimen. After that, specimens were placed in hermetic bags for 24 hours; then, specimens were demolded and placed in a temperature and moisture content ($\omega = 90 \pm 2\%$ and T = 23 $\pm$ 2 °C) controlled chamber for curing during 7 days. A hydraulic loading press with a 0.45 MPa/s shear speed was utilized. Neoprene disks were used at the ends of the specimens to improve the contact area during testing.

2.4 Durability testing and long-term performance

The durability and long-term performance test followed the guidelines of ASTM D 559 (ASTM, 2012b). The specimens were immersed in water for 5 h at room temperature. Then, specimens were oven-dried at 70 °C for 42 h. This exposure for 47 h to both wet and dry scenarios constitute a single cycle. After wetting and drying, specimens were weighed after two firm strokes all around the surface with a wire brush. Contrary to the standard procedure, the number of cycles of this research was increased to 16, providing an evaluation of the specimens' deterioration at long-term.

The long-term performance of stabilized RAP as base course material in pavements is questionable, since several reactions between the stabilizer and the amorphous asphalt content are not clearly understood. Concerning the potential effects of the different binder combinations over long curing periods, a long-term behavior investigation was also conducted. To this extent, specimens cured for 365 days

were submitted to 2, 4, 8, and 16 wet/dry cycles and then tested regarding their UCS.

3. Results

3.1 Unconfined compression strength of PC-stabilized RAP

The influence of RAP and cement content on the unconfined compressive strength is shown in Figure 4. Results indicate that the increase in PC content increases the mechanical strength, especially for the lowest RAP content. This behavior was also observed in other studies (Consoli et al., 2007; Diambra et al., 2017; Festugato et al., 2018; Mohammadinia et al., 2016; Suebsuk & Suksan, 2014; Taha et al., 2002).

RAP content presents no significant influence on the mechanical behavior of the mixtures. This preliminary result attests to the possibility of using high levels of RAP for cemented bases. However, a great variability was evidenced for 6% cement content specimens. This behavior can be attributed to the greater amount of water needed for higher cement content specimens, impairing the molding process. In addition, despite being statistically equal, the average values of UCS for the 70% RAP specimens presented a worse mechanical behavior; which can be attributed to the grain size composition of the mixture. For 70% RAP specimens, only stone powder was added to the mixture, with no other granular materials; thus, less packing of the particles was evidenced, resulting in a reduction of strength. With that in mind, the other mechanical parameters of this study were evaluated only for the 45% RAP content specimens.

3.2 Unconfined compression strength of alkali-activated stabilized RAP mixtures

Figure 5 presents the UCS results for the alkali-activated binder (AAB) stabilized RAP blends. The increase in AAB content led to an increase in UCS for all mixtures; increasing AAB content reduces porosity, enhancing strength development.

The porosity reduction induces a larger contact area between particles, intensifying the interlocking and mobilizing the friction between particles. Furthermore, the increase in AAB content is linked to the increase in cementitious reactions, also contributing to the development of strength (Pereira dos Santos et al., 2022). Similar results were found for RAP stabilized with alkali-activated ligands (Hoy et al., 2016b, d; Mohammadinia et al., 2016).

In addition, only mixtures with 30% AAB and NaOH:Na$_2$SiO$_3$ ratio of 70:30 and 80:20 showed a minimum
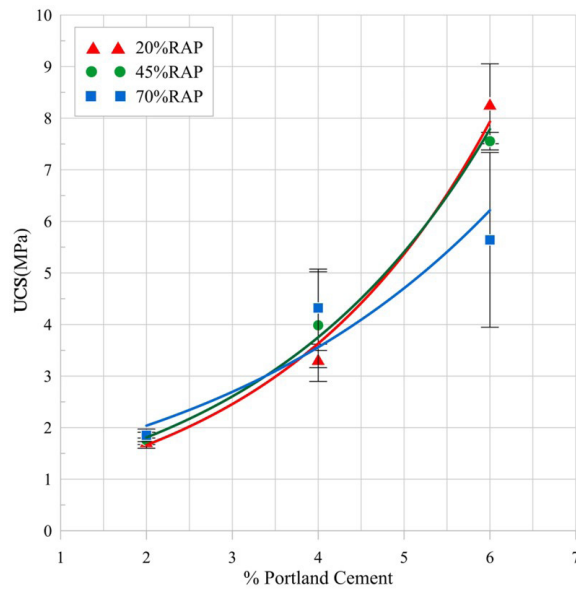
Figure 4. Unconfined compressive strength of PC-stabilized RAP.
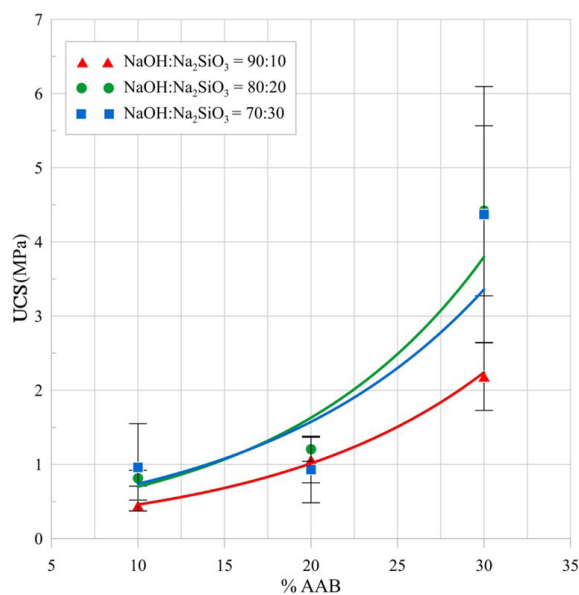
strength of 2.1 MPa at 7 days (minimum requirement of the National Department of Infrastructure and Transport in Brazil (ABNT, 2012a) for utilization as road construction material).

3.3 Durability and long-term performance

Figure 6 presents the accumulated loss of mass (ALM) results of the alkali-activated mixtures. In general, it is noted that the ALM is more significant in the first cycle, considering that more unbounded grains can be found on the surface of the specimen. Furthermore, most of the ALM occurred at the interface between the RAP and the binder, where the RAP particles are coated by bitumen. This can be attributed to the poor cementation/bonding between the asphalt coating and the binder (fly ash) (Avirneni et al., 2016). The sample with the lowest AAB content (10%AAB – NaOH:Na$_2$SiO$_3$ ratio = 80:20) presented a contradictory behavior, resulting in a significant loss of mass in the last 6 cycles, possibly due to the low amount of binder that was not able to involve most of the aggregates.

The increase in silicate content reduced the ALM for the studied mixtures; this behavior can be associated with the greater amount of material that reacted with the NaOH solution and fly ash. Thus, the increase in silicate content resulted in more durable specimens, corroborating the behavior found in the other mechanical tests and indicating that durability is directly linked to strength. Such behavior may also be associated with a greater mobilization of friction due to the reduction of porosity associated with the increase of cementitious reactions (Pereira dos Santos et al., 2022). Similar behavior was also found for soils stabilized with Portland cement (Consoli & Tomasi, 2018); stabilized dispersive
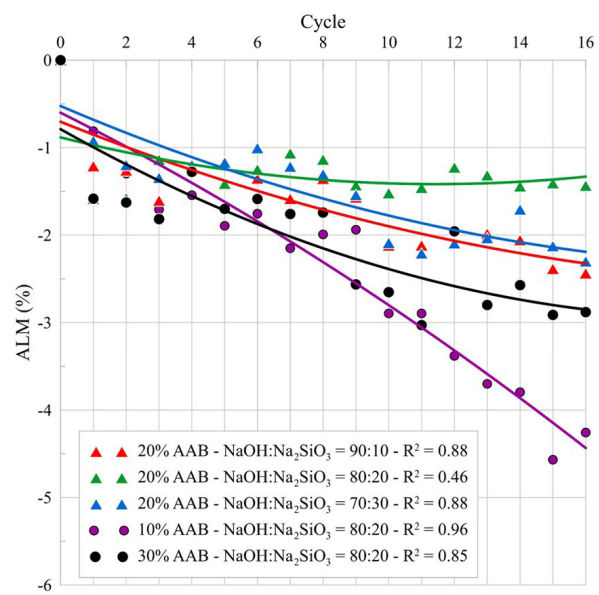

Figure 5. Unconfined Compression Strength of alkali-activated FA binder stabilized RAP.

Figure 6. Accumulated loss of mass after wet-dry cycles for alkali-activated FA binder stabilized RAP.

soils (Consoli et al., 2016); soils stabilized with ash and lime (Consoli et al., 2020, 2018b); stabilized reclaimed asphalt pavement (Consoli et al., 2021, 2018a) and gold tailings stabilized with Portland cement (Consoli et al., 2018c), in which lower porosities showed greater durability.

Regarding the AAB content, the highest ALM values were observed for 10% and 30% AAB specimens, indicating the existence of an optimal content that provides a matrix with greater durability, when subjected to weathering conditions.

According to the Portland Cement Association (PCA, 1956), the maximum ALM after 12 wet-dry cycles for granular soils cured at room temperature for 7 days is 14%. In this study, all mixtures met this requirement, indicating the feasibility of the proposed treatments to improve durability. However, specimens with higher levels of sodium silicate had better performance. Thus, mixtures with 20% AAB and 20% sodium silicate (20% AAB – NaOH:Na$_2$SiO$_3$ ratio = 80:20) are potentially better in terms of performance under field conditions. However, the other mixtures are also considered feasible, as the mass loss is within the limits of PCA.

The long-term strength (365 days) of the mixtures after the wetting-drying cycles was also evaluated and the results are shown in Figure 7. Although there are no standard specifications for the compressive strength after the wetting/drying cycles, this long term assessment is important especially when alternative/waste materials are used in high amounts.

The mixture with the highest ALM resulted in a reduction of strength over the cycles, while the other maintained or even increased strength over time. Even after the weathering cycles, all specimens still met the minimum regulatory strength requirements of 2.1 MPa (ABNT, 2012b). For specimens that increased in strength over time, the wetting-drying cycles played the role of thermal curing and not of material

degradation mechanisms as observed in previous studies (Miraki et al., 2022; Nazari et al., 2011).

Despite the slow reaction process, characteristic of activated alkali materials, an average increase of about 3 times was observed when compared with the strength obtained at 7 days (Figure 5). The tendency of increasing strength for long-term periods was also observed in similar works using secondary materials (e.g., RAP and fly ash); however, authors concluded that from the 56-days mark, the rate of improvement in strength was negligible (Avirneni et al., 2016).

Furthermore, it can be concluded that the AAB content influenced the results, and the 30% content showed the best strength performance after the wetting-drying cycles. In addition, based on the performance of the mixtures submitted to the 16 cycles of wetting/drying, more than 16 years of project life in the field can be estimated, since each cycle can be considered a year of seasonal variation in humidity and temperature (Avirneni et al., 2016).

4. Conclusions

This study investigated the durability and long-term mechanical performance of RAP stabilized by an alkali-activated fly ash-based binder, activated by a combination of sodium hydroxide and sodium silicate. A group 84 samples were utilized to investigate the strength and durability performance of cemented materials.

Fly ash was successfully activated for the 30% AAB mixtures at activator ratios (NaOH:Na$_2$SiO$_3$) of 70:30 and 80:20, increasing strength and fulfilling design requirements for granular materials. This indicates a great potential of alkali-activated materials for ground improvement applications. In addition, the durability investigation indicated that all blends satisfactorily attended the Portland Cement Association ALM specifications.

Even though the specimens were submitted to weathering cycles, all mixtures demonstrated UCS higher than the standard requirements for paving applications. Nevertheless, the durability test methodology was not useful to evaluate the degradation of the mixtures, since strength increased over the cycles. This evidence suggests that the weathering cycles played a role in curing due to the process of drying into the thermal chamber.

The long-term study has shown no significant reduction in strength over time, which indicates that the binder remained in the RAP mixtures. Thus, alkali-activated materials may be an alternative for traditional Portland cement. However, futures studies considering experimental segments are required for the road structural performance.
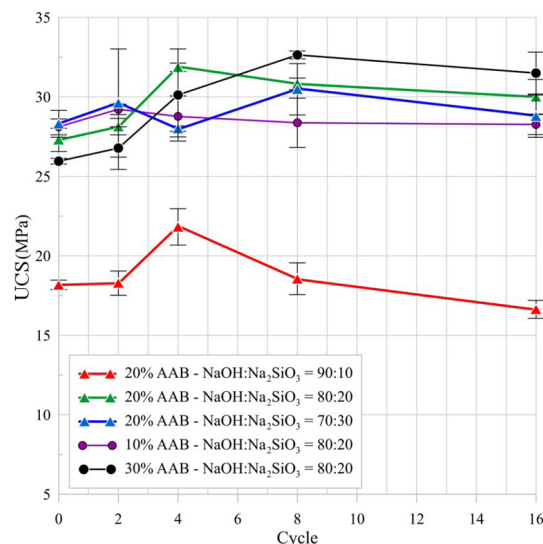
Acknowledgements

Figure 7. Long-term UCS after wet and dry cycling for alkali-activated FA binder stabilized RAP.

Declaration of interest

The authors whose names are listed in this manuscript certify that they have NO affiliations with or involvement in any organization or entity with any financial interest (such as honoraria; educational grants; participation in speakers' bureaus; membership, employment, consultancies, stock ownership, or other equity interest; and expert testimony or patent-licensing arrangements), or non-financial interest (such as personal or professional relationships, affiliations, knowledge or beliefs) in the subject matter or materials discussed in this manuscript.

Authors' contributions

Alessandro Graeff Goldoni: conceptualization, data curation, investigation, methodology, visualization, writing – original draft, funding acquisition. Deise Trevizan Pelissaro: conceptualization, data curation, methodology, supervision, validation, writing – original draft. Eriky Silveira: data curation, investigation, methodology. Pedro Domingos Marques Prietto: writing – reviewing; Francisco Dalla Rosa: formal analysis, funding acquisition, investigation, methodology, project administration, resources, software.

Data Availability

Some or all data, models, or code that support the findings of this study are available from the corresponding author upon reasonable request.

List of symbols

AAB   Alkali-Activated Binder
ALM   Accumulated Loss of Mass
FA   Fly Ash
FDR   Full Depth Recycling
LOS   Level of Service
PC   Portland Cement
RAP   Reclaimed Asphalt Pavement
UCS   Unconfined Compression Strength
VA   Virgin Aggregate
$w_{optimal}$ Optimal Moisture Content
XRD   X-ray Diffraction
γ_d Dry unit weight

References

ABNT NBR 12253. (2012a). *Solo-cimento - Dosagem para Emprego como Camada de Pavimento*. ABNT - Associação Brasileira de Normas Técnicas, Rio de Janeiro, RJ.

ABNT NBR 12253. (2012b). *Solo-cimento - Dosagem para Emprego como Camada de Pavimento*. ABNT - Associação Brasileira de Normas Técnicas, Rio de Janeiro, RJ.

Adhikari, S., Khattak, M.J., & Adhikari, B. (2020). Mechanical characteristics of Soil-RAP-Geopolymer mixtures for road base and subbase layers. *The International Journal of Pavement Engineering*, 21, 483-496. http://dx.doi.org/10.1080/10298436.2018.1492131.

ASTM D2172/D2172M-11. (2011). *Standard Test Methods for Quantitative Extraction of Bitumen from Bituminous Paving Mixtures. American Society for Testing and Materials*. ASTM International, West Conshohocken, PA. https://doi.org/10.1520/D2172-11.2.

ASTM C150/C150M–12. (2012a). *Standard Specification for Portland Cement*. ASTM International, West Conshohocken, PA. https://doi.org/10.1520/C0150-07.

ASTM D559-03. (2012b). *Standard Test Methods for Wetting and Drying Compacted Soil-Cement Mixtures*. ASTM International, West Conshohocken, PA.

ASTM D2166/D2166M. (2016). *Standard Test Method for Unconfined Compressive Strength of Cohesive Soil*. ASTM International, West Conshohocken, PA. https://doi.org/10.1520/D2166.

Avirneni, D., Peddinti, P.R.T., & Saride, S. (2016). Durability and long term performance of geopolymer stabilized reclaimed asphalt pavement base courses. *Construction & Building Materials*, 121, 198-209. http://dx.doi.org/10.1016/j.conbuildmat.2016.05.162.

Blissett, R.S., & Rowson, N.A. (2012). A review of the multi-component utilisation of coal fly ash. *Fuel*, 97, 1-23. http://dx.doi.org/10.1016/j.fuel.2012.03.024.

Celik, K., Meral, C., Petek Gursel, A., Mehta, P.K., Horvath, A., & Monteiro, P.J.M. (2015). Mechanical properties, durability, and life-cycle assessment of self-consolidating concrete mixtures made with blended portland cements containing fly ash and limestone powder. *Cement and Concrete Composites*, 56, 59-72. http://dx.doi.org/10.1016/j.cemconcomp.2014.11.003.

Consoli, N.C., Foppa, D., Festugato, L., & Heineck, K.S. (2007). Key parameters for strength control of artificially cemented soils. *Journal of Geotechnical and Geoenvironmental Engineering*, 133, 197-205. http://dx.doi.org/10.1061/(ASCE)1090-0241(2007)133:2(197).

Consoli, N.C., Vendruscolo, M.A., Fonini, A., & Rosa, F.D. (2009). Fiber reinforcement effects on sand considering a wide cementation range. *Geotextiles and Geomembranes*, 27, 196-203. http://dx.doi.org/10.1016/j.geotexmem.2008.11.005.

Consoli, N.C., Samaniego, R.A.Q., & Villalba, N.M.K. (2016). Durability, strength, and stiffness of dispersive clay–lime blends. *Journal of Materials in Civil Engineering*, 28(11), 04016124. http://dx.doi.org/10.1061/(ASCE)MT.1943-5533.0001632.

Consoli, N.C., & Tomasi, L.F. (2018). The impact of dry unit weight and cement content on the durability of sand-cement blends. *Proceedings of the Institution of Civil Engineers: Ground Improvement*, 171, 96-102. http://dx.doi.org/10.1680/jgrim.17.00034.

Consoli, N.C., Giese, D.N., Leon, H.B., Mocelin, D.M., Wetzel, R., & Marques, S.F.V. (2018a). Sodium chloride as a catalyser for crushed reclaimed asphalt pavement – Fly ash – Carbide lime blends. *Transportation Geotechnics*, 15, 13-19. http://dx.doi.org/10.1016/j.trgeo.2018.02.001.

Consoli, N.C., Samaniego, R.A.Q., González, L.E., & Bittar, E.J. (2018b). Impact of severe climate conditions on loss of mass, strength, and stiffness of compacted fine-grained soils–portland cement blends. *Journal of Materials in Civil Engineering*, 30(8), 04018174. http://dx.doi.org/10.1061/(ASCE)MT.1943-5533.0002392.

Consoli, N.C., da Silva, A.P., Nierwinski, H.P., & Sosnoski, J. (2018c). Durability, strength, and stiffness of compacted gold tailings – cement mixes. *Canadian Geotechnical Journal*, 55, 486-494. http://dx.doi.org/10.1139/cgj-2016-0391.

Consoli, N.C., Festugato, L., Scheuermann Filho, H.C., Miguel, G.D., Tebechrani Neto, A., & Andreghetto, D. (2020). Durability assessment of soil-pozzolan-lime blends through ultrasonic-pulse velocity test. *Journal of Materials in Civil Engineering*, 32(8), 04020223. http://dx.doi.org/10.1061/(ASCE)MT.1943-5533.0003298.

Consoli, N.C., Tebechrani Neto, A., Correa, B.R.S., Quiñónez Samaniego, R.A., & Cristelo, N. (2021). Durability evaluation of reclaimed asphalt pavement, ground glass and carbide lime blends based on unconfined compression tests. *Transportation Geotechnics*, 27, 100461. http://dx.doi.org/10.1016/j.trgeo.2020.100461.

Diambra, A., Ibraim, E., Peccin da Silva, A., Consoli, N.C., & Festugato, L. (2017). Theoretical derivation of artificially cemented granular soil strength. *Journal of Geotechnical and Geoenvironmental Engineering*, 143(5), 1-25. http://dx.doi.org/10.1061/(ASCE)GT.1943-5606.0001646.

DNIT. (2010). *Pavimentação – Base estabilizada granulometricamente – ES DNIT 141/2010*. DNIT - Departamento Nacional de Infraestrutura de Transportes, Rio de Janeiro, RJ.

DNIT. (2013). *Pavimentação – Reciclagem profunda de pavimentos "in situ" com adição de cimento Portland – Especificação de Serviço - ES-167*. DNIT - Departamento Nacional de Infraestrutura de Transportes, Rio de Janeiro, RJ.

Festugato, L., Peccin da Silva, A., Diambra, A., Consoli, N.C., & Ibraim, E. (2018). Modelling tensile/compressive strength ratio of fibre reinforced cemented soils. *Geotextiles and Geomembranes*, 46, 155-165. http://dx.doi.org/10.1016/j.geotexmem.2017.11.003.

Gowthaman, S., Nakashima, K., & Kawasaki, S. (2018). A state-of-the-art review on soil reinforcement technology using natural plant fiber materials: past findings, present trends and future directions. *Materials (Basel)*, 11(4), 553. http://dx.doi.org/10.3390/ma11040553.

Haas, S., & Ritter, H.-J. (2019). Soil improvement with quicklime – long-time behaviour and carbonation. *Road Materials and Pavement Design*, 20, 1941-1951. http://dx.doi.org/10.1080/14680629.2018.1474793.

Horpibulsuk, S., Hoy, M., Witchayaphong, P., Rachan, R., & Arulrajah, A. (2017). Recycled asphalt pavement fly ash geopolymer as a sustainable stabilized pavement material. *IOP Conference Series. Materials Science and Engineering*, 273, 012005. http://dx.doi.org/10.1088/1757-899x/273/1/012005.

Hoy, M., Horpibulsuk, S., & Arulrajah, A. (2016a). Strength development of Recycled Asphalt Pavement - Fly ash geopolymer as a road construction material. *Construction & Building Materials*, 117, 209-219. http://dx.doi.org/10.1016/j.conbuildmat.2016.04.136.

Hoy, M., Horpibulsuk, S., & Arulrajah, A. (2016b). Strength development of Recycled Asphalt Pavement - Fly ash geopolymer as a road construction material. *Construction & Building Materials*, 117, 209-219. http://dx.doi.org/10.1016/j.conbuildmat.2016.04.136.

Hoy, M., Horpibulsuk, S., Rachan, R., Chinkulkijniwat, A., & Arulrajah, A. (2016c). Recycled asphalt pavement – fly ash geopolymers as a sustainable pavement base material: strength and toxic leaching investigations. *The Science of the Total Environment*, 573, 19-26. http://dx.doi.org/10.1016/j.scitotenv.2016.08.078.

Hoy, M., Horpibulsuk, S., Rachan, R., Chinkulkijniwat, A., & Arulrajah, A. (2016d). Recycled asphalt pavement – fly ash geopolymers as a sustainable pavement base material: strength and toxic leaching investigations. *The Science of the Total Environment*, 573, 19-26. http://dx.doi.org/10.1016/j.scitotenv.2016.08.078.

Hoy, M., Horpibulsuk, S., Arulrajah, A., & Mohajerani, A. (2018). Strength and microstructural study of recycled asphalt pavement: slag geopolymer as a pavement base material. *Journal of Materials in Civil Engineering*, 30, 1-11. http://dx.doi.org/10.1061/(ASCE)MT.1943-5533.0002393.

Instituto Nacional de Pesquisas Espaciais – INPE. (2021). Retrieved in July 2, 2022, from http://www.inpe.br/

Luukkonen, T., Abdollahnejad, Z., Yliniemi, J., Kinnunen, P., & Illikainen, M. (2018). One-part alkali-activated materials: a review. *Cement and Concrete Research*, 103, 21-34. http://dx.doi.org/10.1016/j.cemconres.2017.10.001.

Miraki, H., Shariatmadari, N., Ghadir, P., Jahandari, S., Tao, Z., & Siddique, R. (2022). Clayey soil stabilization using alkali-activated volcanic ash and slag. *Journal of Rock Mechanics and Geotechnical Engineering*, 14(2), 576-591. http://dx.doi.org/10.1016/j.jrmge.2021.08.012.

Mohammadinia, A., Arulrajah, A., Sanjayan, J., Disfani, M.M., Bo, M.W., & Darmawan, S. (2016). Strength development and microfabric structure of construction and demolition aggregates stabilized with fly ash–based geopolymers. *Journal of Materials in Civil Engineering*, 28, 04016141. http://dx.doi.org/10.1061/(asce)mt.1943-5533.0001652.

Nazari, A., Bagheri, A., & Riahi, S. (2011). Properties of geopolymer with seeded fly ash and rice husk bark ash.

Materials Science and Engineering A, 528, 7395-7401. http://dx.doi.org/10.1016/j.msea.2011.06.027.

Pereira dos Santos, C., Bruschi, G.J., Mattos, J.R.G., & Consoli, N.C. (2022). Stabilization of gold mining tailings with alkali-activated carbide lime and sugarcane bagasse ash. *Transportation Geotechnics*, 32, 100704. http://dx.doi.org/10.1016/j.trgeo.2021.100704.

Porter, H., Dhami, N.K., & Mukherjee, A. (2018). Sustainable road bases with microbial precipitation. *Proceedings of Institution of Civil Engineers: Construction Materials*, 171, 95-108. http://dx.doi.org/10.1680/jcoma.16.00075.

Portland Cement Association – PCA. (1956). *Soil-cement laboratory handbook*. Portland Cement Association.

Provis, J.L., Duxson, P., van Deventer, J.S.J., & Lukey, G.C. (2005). The role of mathematical modelling and gel chemistry in advancing geopolymer technology. *Chemical Engineering Research & Design*, 83, 853-860. http://dx.doi.org/10.1205/cherd.04329.

Rezende, I.M., Prietto, P.D.M., Thomé, A., & Dalla Rosa, F. (2021). Mechanical behavior of microbially induced calcite precipitation cemented sand. *Geotechnical and Geological Engineering*, 4, 1997-2008. http://dx.doi.org/10.1007/s10706-021-02006-4.

Shen, W., Zhou, M., & Zhao, Q. (2007). Study on lime-fly ash-phosphogypsum binder. *Construction & Building Materials*, 21, 1480-1485. http://dx.doi.org/10.1016/j.conbuildmat.2006.07.010.

Singh, N.B., & Middendorf, B. (2020). Geopolymers as an alternative to Portland cement: an overview. *Construction & Building Materials*, 237, 117455. http://dx.doi.org/10.1016/j.conbuildmat.2019.117455.

Solanki, P., & Zaman, M. (2014). Effect of wet-dry cycling on the mechanical properties of stabilized subgrade soils. In *Geo-Congress 2014 Technical Papers : Geo-Characterization and Modeling for Sustainability* (pp. 3625-3634). ASCE. http://dx.doi.org/10.1061/9780784413272.351.

Suebsuk, J., & Suksan, A. (2014). Strength assessment of cement treated soil-reclaimed asphalt pavement (RAP) mixture. *International Journal of GEOMATE*, 6, 878-884. Retrieved in July 2, 2022, from https://geomatejournal.com/geomate/article/view/2931

Taha, R., Al-Harthy, A., Al-Shamsi, K., & Al-Zubeidi, M. (2002). Cement stabilization of reclaimed asphalt pavement aggregate for road bases and subbases. *Journal of Materials in Civil Engineering*, 14, 239-245. http://dx.doi.org/10.1061/(asce)0899-1561(2002)14:3(239).

Wirtgen GmbH. (2012). *Wirtgen cold recycling technology*. Wirtgen GmbH.

Wu, H., Huang, B., Shu, X., & Zhao, S. (2015). Evaluation of geogrid reinforcement effects on unbound granular pavement base courses using loaded wheel tester. *Geotextiles and Geomembranes*, 43, 462-469. http://dx.doi.org/10.1016/j.geotexmem.2015.04.014.

Numerical simulations of displacement piles in a tropical soil

Bismarck Chaussê Oliveira[1#] 🆔, Maurício Martines Sales[1] 🆔,

Renato Resende Angelim[1] 🆔, Luiz Carlos Galvani Junior[2] 🆔

Article

Abstract
The behavior of pile foundations under axial loading is directly influenced by the effects that its installation process induces in the surrounding soil. Consequently, the consideration of these effects is essential for the correct numerical modeling of these geotechnical structures. In the present study, numerical simulations of driven cast-in-situ piles under axial loading have been carried out using finite element analysis. Three 3.5 m long piles with diameters ranging from 114.3 to 219.1 mm were analyzed. The pile installation effects have been considered indirectly by employing two distinct approaches, both based on the concepts of cylindrical cavity expansion. The behavior of the tropical soil profile is described with the Hardening Soil constitutive model. The load-displacement response and load distribution along the pile obtained with the numerical simulations have been analyzed and compared with in-situ load tests results. In the failure conditions, both approaches accurately predicted the bearing capacity of the piles, with an average error of only 2% compared to the measured values. The results in terms of load distribution over depth were also satisfactory. The difference between measured and numerical ultimate base resistance values ranged from 0% to 30%. The good agreement between the numerical and experimental results indicates that the proposed numerical approaches have been effective in simulating the piles installation process and reinforces the importance of considering the installation effects in the numerical modeling of these geotechnical structures. Both approaches can also be used to predict the bearing capacity of displacement piles.

1. Introduction

Pile foundations can be classified according to different criteria. Considering the induced changes in the density and stress state of the surrounding soil during the installation process, it is possible to categorize pile foundations into three groups: non-displacement piles, partial displacement piles, and full-displacement piles. Non-displacement piles installation usually results in a reduction in the density and stress state of the surrounding soil, while installation technologies of partial and full-displacement piles tend to increase such values proportionally to the magnitude of the induced displacement. Particularities in observed behavior depend on factors such as type of pile, installation technology, and soil type. These installation effects directly influence the mechanical response of the piles when subjected to external loads.

Driven cast-in-situ (DCIS) piles are a type of deep foundation classified as full-displacement piles due to their installation technology, but they have some similar aspects to non-displacement piles, such as in-situ casting of concrete and the resulting rough shaft interface (Flynn & McCabe, 2016).

Over the past few decades, numerical methods have been increasingly employed in the solution of engineering problems. When it comes to pile performance, the accuracy of numerical analyses is dependent on the pile modeling steps being representative of the pile installation technology and the soil constitutive model parameters being properly calibrated. While in the analysis of non-displacement piles installation effects can often be ignored without major losses in simulation accuracy (Wehnert & Vermeer, 2004), in the analysis of full-displacement piles, the consideration of these effects is essential.

Given the nature of the problem, numerical methods with formulations capable of analyzing large deformations problems are the most suitable for modeling full-displacement piles. Several researches have been done on this subject, using the discrete element method (Li et al., 2021; Lobo-Guerrero & Vallejo, 2005), the material point method (Lorenzo et al., 2018; Phuong et al., 2016; Tehrani et al., 2016) the arbitrary Lagrangian-Eulerian method (Rooz & Hamidi, 2019; Yang et al., 2020) and the coupled Eulerian-Lagrangian method (Heins & Grabe, 2017; Pucker & Grabe, 2012; Qiu et al., 2011).

#Corresponding author. E-mail address: bismarckchausse@gmail.com.
[1]Universidade Federal de Goiás, Escola de Engenharia Civil e Ambiental, Goiânia, GO, Brasil.
[2]SETE Engenharia, Goiânia, GO, Brasil.

The standard finite element method (FEM), which uses Lagrangian formulation, has limitations in simulating large deformation problems due to distortions of the finite element mesh, which result in inaccurate or diverging solutions (Engin et al., 2015). Even when using remeshing after each calculation step (updated Lagrangian formulation), direct simulation of full-displacement pile installation processes can result in numerical problems due to the remapping of the state variables (Engin, 2013), and it is necessary to resort to modeling strategies that allow considering the installation of these geotechnical structures in an idealized way.

Several studies use varied numerical approaches to incorporate the installation effects of full-displacement piles indirectly via standard FEM (Broere & van Tol, 2006; Engin et al., 2015; Said et al., 2009) and using the updated mesh option (Krasinski, 2014; Rezania et al., 2017; Schmüdderich et al., 2020). However, there are still few works on this subject evaluating DCIS piles, especially those installed in heterogeneous tropical soil profiles.

This paper proposes adaptations to two different numerical approaches based on the concepts of cylindrical cavity expansion to simulate the installation of DCIS piles installed in a tropical soil profile. The approaches emphasize incorporating changes in the density and stress state of the soil surrounding the pile caused by the installation processes. The analyses are conducted in Plaxis 2D® finite element software (Brinkgreve et al., 2021) and the updated mesh option is used in some steps. The suitability of the approaches is attested by the agreement between numerical and experimental results, the latter obtained from in-situ static load tests.

2. Pile testing program

2.1 Geotechnical characterization of the tropical soil profile of the experimental field

The piles analyzed in this paper were installed in the Experimental Field of the School of Civil and Environmental Engineering of the Federal University of Goiás, located in Goiânia, a city in the state of Goiás, in the Center-West region of Brazil. The climatic conditions of the region favor the pedogenetic evolution and an intense chemical weathering that originate lateritic soils, whose mineralogical constitution is mainly composed of quartz, kaolinite, and iron/aluminum oxides and hydroxides. Among the main characteristics of these soils are high porosity, high permeability, high strength when compacted, and the presence of clay particle aggregates (Camapum de Carvalho & Gitirana Junior, 2021; Freitas et al., 2020).

According to the geotechnical characterization performed by Nascimento (2019) and Machado et al. (2020) (Figure 1), using MCT classification (Nogami & Villibor, 1995), the soil profile of the experimental field is composed of lateritic clayey sand (LA'-LG'), apparently transported, up to a depth of 4 m. The layer between 4 and 7 m depth seems to be a transition horizon, with a higher content of gravel in the middle of the layer. From 7 m depth on, the soil is no longer lateritic, and its clay content decreases, suggesting the beginning of the residual (saprolite) horizon. The values determined of specific gravity (G_s), unit weight of moist soil (γ), and void ratio (e) are typical of tropical soils. The percentages of the clay fraction in the grain size distributions with and without
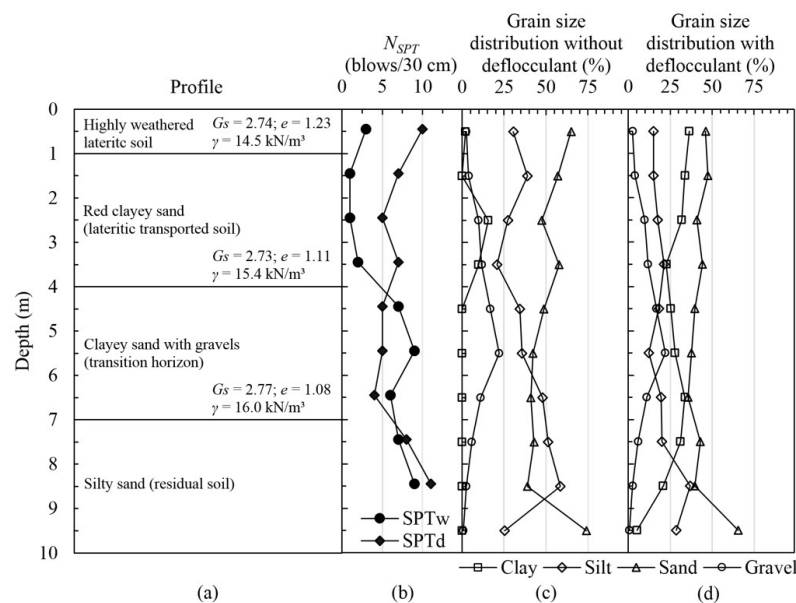
Figure 1. Characteristics of the soil profile of the experimental field: (a) stratigraphy and index properties; (b) SPT test results; (c) grain size distribution without deflocculant and (d) with deflocculant. Modified after Nascimento (2019) and Machado et al. (2020).

deflocculant (sodium hexametaphosphate, for the fraction passing through a no. 10 sieve or 75 µm) showed that in some layers the clay particles are 100% aggregated.

Standard penetration tests (SPT) were performed in the experimental field in the wet season (Machado et al., 2018) and also in the dry season (Rezende & Rocha, 2020) of the local rainfall regime (Figure 1b). In the lateritic soil layer, an increase in N_{SPT} was recorded from 1–3 blows in the wet season (SPT$_w$) to 5–10 blows in the dry season (SPT$_d$), evidencing the influence of matric suction on soil strength. The water table was not identified during all the tests, carried out until 10 m depth.

In the experimental field, Ménard-type (or pre-bored) pressuremeter tests (PMT), were also performed at depths of 0.5, 1.5, 2.5, 3.5, 4.5, and 5.5 (Bernardes et al., 2022). Figure 2 shows the pressuremeter curves of two PMT soundings with 6 tests performed on each, both carried out in the dry season. The corrected measured pressure is plotted on the vertical axis and the relative increase in cavity radius (ε_r) on the horizontal axis. Due to inconsistent results, PMT-2 performed at the 4.5 m depth (Figure 2b) was excluded from the graph. Data from these tests were used to estimate some parameters of the constitutive model, as will be discussed in Section 3.2.

2.2 Test piles

The static load tests analyzed in this paper were conducted on three DCIS piles (C4, C6, and C8). As illustrated in Figure 3a, these piles are installed by driving or, as in the present case, by jacking a closed-ended steel tube into the ground. The tube is extracted after reaching the required penetration depth. Then the rebar cage is lowered, and the cavity is filled with concrete. Both the installation and the load tests were performed during the dry season of the local rainfall regime.

The piles C4, C6, and C8 are respectively 114.3 mm, 165.1 mm, and 219.1 mm in diameter, and all three piles are 3.5 m in length. A 0.5 m deep shallow excavation was made at the locations of the piles, due to a large amount of organic soil in this layer. Thus, the piles were installed between 0.5–4.0 m deep concerning the natural profile

Figure 2. Pressuremeter curves of (a) PMT-1 and (b) PMT-2. Modified after Bernardes et al. (2022).

Figure 3. Schematic sketch of: (a) DCIS piles constructive sequence; (b) DCIS piles installed in the experimental field.

Oliveira et al., Soil. Rocks, São Paulo, 2023 46(1):e2023004522

3

(Figure 3b). The piles C6 and C8 were instrumented with strain gauges positioned 100 mm from the top and bottom of the pile (Figure 3b).

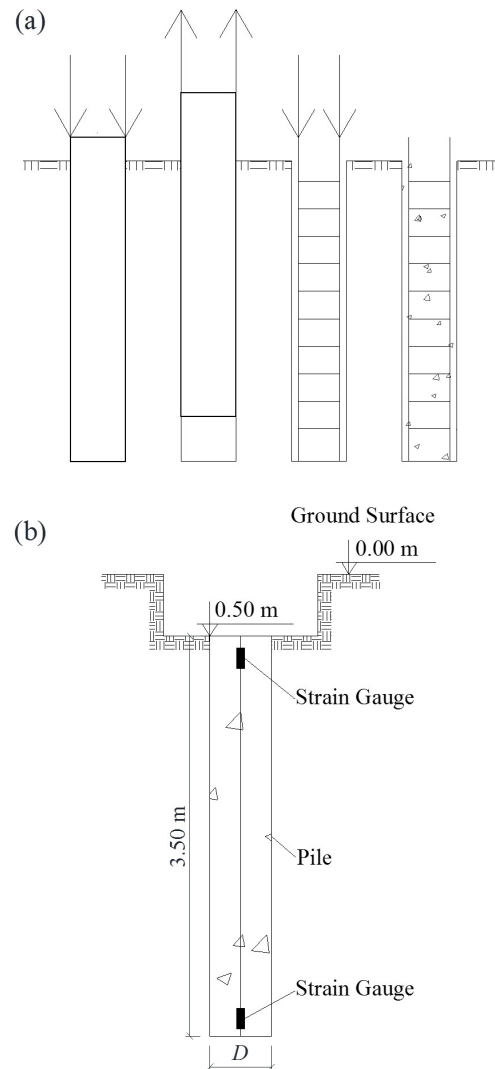As can be seen in Figure 4, the piles and in-situ tests were located close to each other. Therefore, it was considered that the stratigraphy and soil parameters do not vary significantly in the location of each pile and that the average index values obtained from the same type of test (e.g., PMT) are representative of the entire area.

3. Numerical modeling

3.1 Description of the model

The numerical analyses conducted in this paper were carried out in Plaxis 2D® finite element software, with axisymmetric geometry. The horizontal and vertical boundaries limits of the domain were set as 3 and 4 times the pile length, respectively. The model domain is discretized by 15-node triangular elements. A denser mesh was used within the pile structure and in a zone of $6D$ horizontally from the pile shaft and $3D$ below the pile tip, being D the pile diameter (Figure 5). Both the domain boundaries and the mesh density were determined by sensitivity analyses.

The groundwater table was not considered, since it was not identified in in-situ tests up to 10 m, so the numerical analyses were conducted under drained conditions. The geostatic stresses are determined using the K_0-procedure, in which the vertical stresses are generated in equilibrium with the self-weight of the soil and the horizontal stresses are calculated from the specified value of the coefficient of earth pressure at rest, K_0.

For proper modeling of pile-soil interaction, interface elements were placed between the pile and soil. In Plaxis 2D®,

the interface behavior is described by an elastoplastic model with the Mohr-Coulomb failure criterion. The interface shear strength is related to the soil shear strength by the strength reduction factor, R_{inter}, which can reduce the interface cohesion and friction angle ($R_{inter} < 1$) or keep it equal to that of the surrounding soil ($R_{inter} = 1$).

3.2 Estimation of the constitutive model parameters

Soil behavior is described by the elastoplastic Hardening Soil (HS) constitutive model (Schanz et al., 1999). Among the basic features of the HS model that motivated its adoption are the stress dependency of stiffness and the use of different stiffness modulus for virgin loading and unloading/reloading conditions. By its characteristics, the HS model has proven superior to an elastic perfectly-plastic model in modeling piles in finite element analysis (Broere & van Tol, 2006; Wehnert & Vermeer, 2004).

Conventionally, the parameters of the HS model are calibrated via triaxial and oedometer tests. In practice, the feasibility of these tests is often limited due to difficulties related to soil sampling or the complexity and cost of testing, especially for geotechnical problems involving the characterization of thick soil layers. Thus, laboratory tests are often replaced by field tests, such as PMT and SPT, whose results can be used to estimate the model parameters
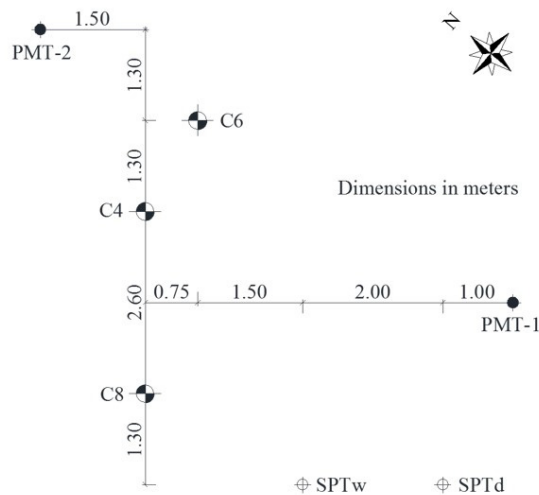

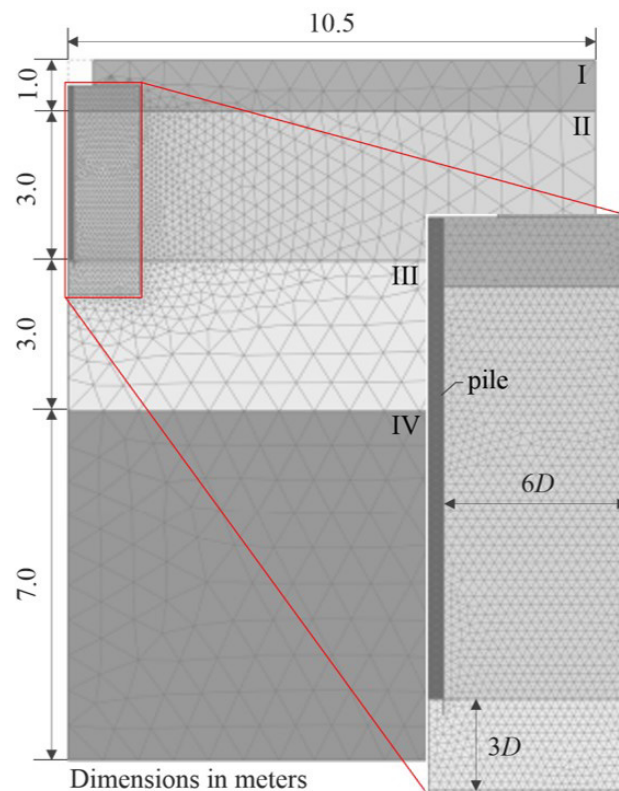**Figure 4.** The relative position of the DCIS piles and in-situ tests located in the experimental field (dimensions in meters).

Figure 5. Finite element mesh discretization (dimensions in meters).

4

Oliveira et al., Soil. Rocks, São Paulo, 2023 46(1):e2023004522

through numerical techniques or empirical correlations, but the latter must be used with care. In the present work, the input parameters of the HS model were estimated using different methods: interpretation of field tests using both numerical techniques and empirical correlations; default values suggested by Plaxis 2D®; reference values found in the literature.

The HS model has eleven input parameters, which can be divided between strength, stiffness, and advanced parameters. The first group includes the cohesion (c), the friction angle (ϕ), and the angle of dilatancy (ψ). The stiffness parameters are the reference stiffness modulus related to primary deviatoric loading (E_{50}^{ref}), primary compression (E_{oed}^{ref}) and unloading/reloading (E_{ur}^{ref}), and the stiffness power law exponent, m, which defines the stiffness dependence on the stress level.

The advanced parameters of the HS model are the reference confining pressure (p^{REF}), the Poisson's ratio for unloading/reloading (υ_{ur}), the failure ratio (R_f), and the coefficient of earth pressure at rest for normal consolidation (K_0^{NC}), for which default values suggested by Plaxis 2D® were used.

The angle of dilatancy is set equal to zero for all soil layers. This assumption agrees with what has been observed for tropical soil profiles from the Center-West region of Brazil such as the soil profile of the experimental field (Bernardes et al., 2022; Rebolledo et al., 2019).

The parameters c, ϕ, and E_{50}^{ref} of the first three layers were determined through the methodology for numerical simulation of pressuremeter tests proposed by Goulart (2021). The method allows estimating Young's modulus, apparent cohesion, and friction angle of the soil through a curve-fitting approach. As an approximation, the parameter E_{50}^{ref} was set equal to the stiffness modulus obtained through this technique. It should be noted that despite considering drained conditions in the numerical analyses, apparent cohesion was used instead of effective cohesion to indirectly incorporate the effect of matric suction.

As mentioned in Section 2.1, the pressuremeter tests were performed up to 5.5 m depth, so no data were available for estimating the parameters c, ϕ, and E_{50}^{ref} of the fourth layer (7–14 m depth) using the methodology of Goulart (2021). Due to the length of the piles (3.5 m), the variation of parameters in this layer has little influence on the results.

Therefore, it was decided to estimate the modulus E_{50}^{ref} of this layer through an empirical correlation with the N_{SPT} value of SPT$_d$ (Figure 1a). As an approximation, this parameter was considered equal to the modulus obtained by the relation $E = \alpha\beta N_{SPT}$, proposed by Teixeira & Godoy (1998), where α and β are soil-dependent coefficients, which for silty sands are equal to 0.7 and 3.0, respectively. The other parameters were considered equal to those of the third layer (4–7 m depth), which are discussed below.

The other stiffness parameters (E_{oed}^{ref}, E_{ur}^{ref}, and m) were estimated based on simplifications considered valid for medium to dense silty sands (Schmüdderich et al., 2020) and tropical sandy soils of the Center-West region of Brazil (Bernardes et al., 2022; Rebolledo et al., 2019). For all soil layers, the modulus E_{oed}^{ref} and E_{ur}^{ref} were obtained by the relations $E_{oed}^{ref}/E_{50}^{ref} = 1$ and $E_{ur}^{ref}/E_{50}^{ref} = 3$, respectively, and the exponent m is set equal to 0.5.

In addition to the HS model parameters, the unit weight of moist soil (γ), the coefficient of earth pressure at rest (K_0), and the overconsolidation ratio (OCR) are also input parameters. The parameters γ and K_0 were determined by Machado (2020) to a depth of 5.5 m. The former through laboratory tests and the latter through PMT results. The OCR was estimated using Equation 1 (Mayne & Kulhawy, 1982; Schmidt, 1966). Again, the parameters of the fourth layer were considered equal to those of the third layer. A summary of the model parameters for each layer is provided in Table 1.

$$K_0 = K_0^{NC} OCR^{\sin\phi} \tag{1}$$

The behavior of the concrete piles is assumed linear elastic, with a unit weight of 24 kN/m³, a Poisson's ratio of 0.2, and Young's modulus equal to 21 GPa.

3.3 Approaches for numerical simulation of full-displacement piles

The numerical approaches proposed in this paper for simulating the installation and axial loading of DCIS piles are the result of modifications made to pre-existing methods. As will be discussed in the next sections, the original approaches were initially calibrated for

Table 1. Parameters of the constitutive model.

Layer	Depth	γ	c	ϕ	E_{50}^{ref}	E_{oed}^{ref}	E_{ur}^{ref}	K_0^{NC}	K_0	OCR
	(m)	(kN/m³)	(kPa)	(°)	(kPa)	(kPa)	(kPa)	-	-	-
1	0 - 1	14.5	58	30	17053	17053	51158	0.51	2.34	22.2
2	1 - 4	15.4	24	30	7537	7537	22610	0.50	0.68	1.9
3	4 - 7	16.0	50	31	11755	11755	35266	0.49	0.50	1.0
4	7 - 14	16.0	50	31	19950	19950	59850	0.49	0.50	1.0

Constant model parameters: $\psi = 0$; $\upsilon_{ur} = 0.2$; $R_f = 0.9$; $p^{ref} = 100\ kPa$; $K_0^{NC} = 1-\text{sen}(\phi)$. Columns 3 and 10: data from (Machado, 2020). Columns 4 to 6: data from (Goulart, 2021).

the analysis of screw displacement piles (i.e., SDP or "Omega" piles). Thus, these methods have been modified to better incorporate the installation effects of DCIS piles. The calculation steps of each method employed in this work (original and modified) are shown in Figure 6. The original methods are discussed in Sections 3.3.1 and 3.3.2, while the proposed approaches are presented in detail in Sections 3.3.3 and 3.3.4.

3.3.1 Cavity Expansion (CE) method

This method was initially proposed by Krasinski (2014) and later employed by Schmüdderich et al. (2020) for the finite element simulation of SDP. Its basic principle consists in simulating the radial displacements induced in the soil by the displacement auger through the expansion process of a cylindrical cavity. The calculation steps are illustrated in Figure 6a.
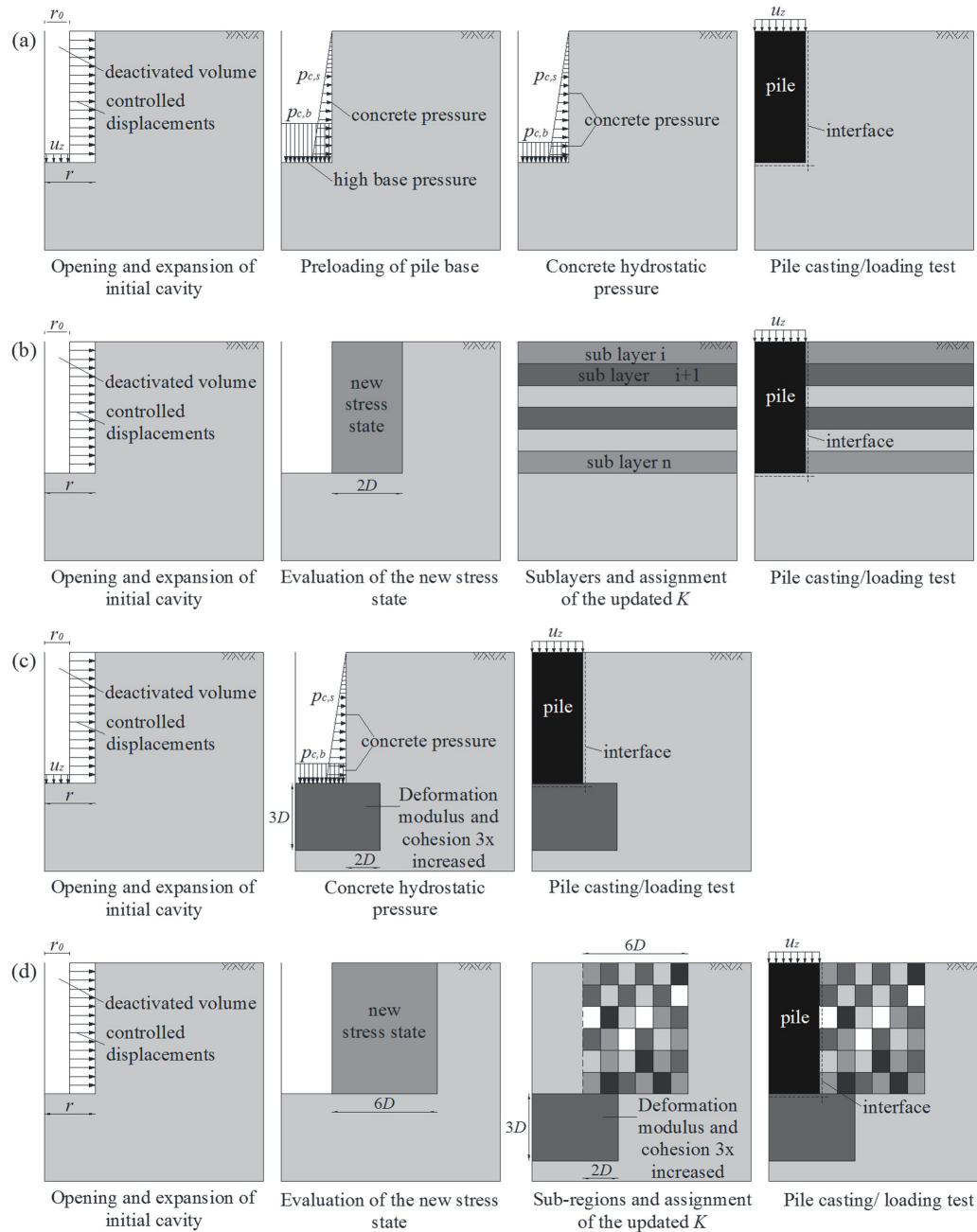

Figure 6. Calculation steps of the original Cavity Expansion (a) and Cavity Expansion with Sub-Layering (b) methods (modified after Schmüdderich et al., 2020) and of the proposed Cavity Expansion with Base iImprovement (c) and Cavity Expansion with Sub-Regions (d) methods.

After the generation of geostatic stresses by the K_0-procedure, an initial cavity is created by deactivating a soil volume with a radius r_0, equal to $r/2$ (r = pile radius). The adoption of an adequate value of r_0 is important in this step. The smaller the r_0, the greater the expanded soil volume, which approximates the actual pile installation process, in which the displaced soil volume is equal to the pile volume (situation equivalent to $r_0 = 0$). However, very small r_0 values can lead to numerical problems due to mesh distortions. Krasinski (2014) determines the value of r_0 through trials. In the present work, the r_0 value was reevaluated for the case study, and the most appropriate value remained equal to $r/2$.

Simultaneously with the creation of the initial cavity, a displacement boundary condition of $\Delta = r - r_0$ is applied to the cavity wall, resulting in a final cavity of radius r. Moreover, to avoid stress concentrations and mesh distortions around the top and bottom of the pile, Krasinski (2014) gradually decreases the displacements to zero by forming a triangular distribution of 0.5 m height on both ends of the cavity. However, it was found that this procedure impairs the final geometry of the head and base of the pile, as well as the continuity of the interface elements in the pile shaft. Figure 7 shows a zoomed view of the pile base region illustrating this effect. Therefore, in the present work, a uniform distribution was applied, and to suppress any unwanted mesh distortions at the bottom of the cavity, very small vertical displacements (of the order of 0.1 mm) were also applied at the bottom of the initial cavity in the expansion phase. These vertical displacements were determined through trials, aiming to obtain a value that was sufficient to prevent mesh deformations and that did not interfere with the results.

The concreting phase is simulated next by applying a horizontal pressure p_{cs} to the cavity wall and a vertical pressure p_{cb} to the cavity base. The magnitude of p_{cs} was set equal to the hydrostatic pressure of the fresh concrete. Since it was not possible to incorporate the stresses induced by the penetration of the SDP displacement auger around the bottom of the cavity in the expansion phase, a value of p_{cb} considerably higher than the hydrostatic concrete pressure was first applied. Then, in the next step, the base pressure was reduced to the hydrostatic pressure of the concrete. In this way, a preconsolidation effect under the pile tip is obtained.

Krasinski (2014) calibrates the highest p_{cb} value through trials to obtain the field-measured pile base resistance. In this work, it was not possible to reach a p_{cb} value that was sufficient to obtain a base resistance consistent with the experimental results without generating excessive deformation of the soil below the cavity bottom. Thus, the value adopted by Krasinski (2014) of p_{cb} = 1800 kN/m² was used in the analyses.

To model the pile, concrete properties are assigned to the soil volume that had initially been deactivated. Simultaneously, the interface elements are activated. Finally, a static load test is simulated by applying prescribed displacements at the top of the pile.

Furthermore, Krasinski (2014) assumes a zone around the pile shaft with reduced stiffness parameters. This assumption was not made in this work since, as will be discussed later, the pile load capacity obtained without reductions in the interface strength (R_{inter} = 1) was already lower than that verified experimentally. It should be noted that all calculation steps use the updated mesh option available in Plaxis 2D®.

3.3.2 Cavity Expansion with Sub-Layering (CE-SL) method

Introduced by Schmüdderich et al. (2020) for finite element analysis of SDP, the original approach (Figure 6b) simulates the pile installation process and the subsequent load test in two separate numerical models so that installation effects are considered indirectly in a model that has not undergone finite element mesh deformation. In the first model, the radial displacements induced in the ground by the displacement auger are simulated as the expansion of a cylindrical cavity, as in the CE approach. The post-expansion radial stresses within a zone of $2D$ (D = pile diameter) around the pile shaft are used to calculate an updated coefficient of lateral earth pressure profile, K.

The value of r_0 used by Schmüdderich et al. (2020) is calculated based on the geometry of the SDP displacement auger, so the same logic does not apply to DCIS piles. Therefore, a value of r_0 equal to $r/2$ was adopted for this method as well. Furthermore, the original approach also gradually decreases the horizontal displacements applied in the expansion phase near the top and bottom of the cavity, which is not adopted in the present work for the reasons already exposed in the CE approach.

In a second model, the soil adjacent to the pile shaft is divided into 1 m thick sub-layers and for each is assigned an
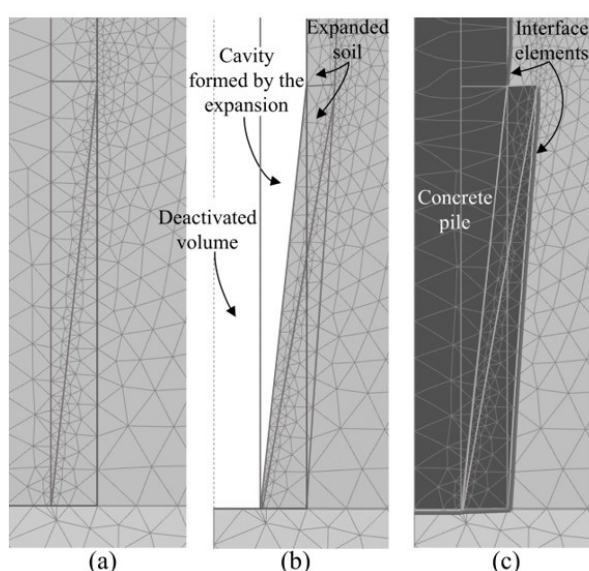

Figure 7. Final geometry of the pile base when the displacement distribution is triangular at the cavity ends: (a) initial phase; (b) after expansion; (c) after pile casting.

average *K* value obtained from the previous model. Then, the pile is installed wished-in-place by assigning the concrete properties to the soil volume representing it, and the interface elements are activated. As will be discussed later, in this approach, it was necessary to reduce the interface strength by 40% (R_{inter} = 0.60). Finally, a load test was simulated as discussed in the previous section.

3.3.3 Cavity Expansion with Base Improvement (CE-BI) method

The first approach proposed in this paper is the result of modifications made to the CE method. In the new approach (Figure 6c), the cavity expansion phase remains the same as in the original approach. After expansion, the phase in which hydrostatic concrete pressures are applied to the base and the cavity wall follows. The phase of pre-consolidation of the base is suppressed. Instead, to obtain the densification effect in this region, a zone is created below the pile tip in which the stiffness modulus (E_{50}^{ref}, E_{oed}^{ref}, and E_{ur}^{ref}) and soil cohesion are increased 3 times. Experimental results from model piles indicate that the main strains occurring below the pile tip are within a zone extending vertically from 2 to 4*D* and radially from 1 to 3*D* from the pile axis (Liu et al., 2020; White & Bolton, 2004). Thus, a zone extending 3*D* below the pile tip and 2.5*D* in the side direction from the pile axis was adopted. Furthermore, this zone comprises the main vertical stresses developed due to pile loading. As shown in Figure 8, the isobar corresponding to 5% of the mean vertical pressure acting at the pile tip (σ_b) is within this zone.

The magnitude of the parameters increase was determined by trial and error to obtain base resistances consistent with

Figure 8. Pressure bulb due to pile loading for pile C8.

experimentally measured values of pile C6. The shearing that occurs in the cavity wall due to the jacking and subsequent extraction of the closed-ended steel tube is not considered in the analyses. The last two phases (pile casting and load test) remain unchanged.

The interface shear strength was considered equal to that of the surrounding soil (R_{inter} = 1). Despite the absence of laboratory tests to determine the interface friction angle (δ), the evidence found in the literature indicates that the assumption made is close to reality. Experimental studies suggest that the interface friction angle between sandy soils and rough surfaces (such as that of the shaft of cast-in-situ piles) is close to the soil friction angle so that under external loads, shearing tends to occur within the soil mass adjacent to the pile shaft and not at the pile-soil interface (Flynn & McCabe, 2016; Frost et al., 2002; Martinez & Frost, 2017).

Moreover, the phenomenon of friction fatigue on displacement piles depends on several factors, such as soil type, surface roughness, and pile installation technology (Randolph et al., 1994; White & Lehane, 2004). Dynamic installation techniques that induce cyclic shearing at the pile shaft, such as pile driving, cause greater degradation of the shaft friction than a monotonic or jacked installation (White & Lehane, 2004). Materials with smooth surfaces (such as steel) also cause less degradation than those with rough surfaces (Tovar-Valencia et al., 2018). Considering that the installation process of the DCIS piles analyzed in the present work involves the jacking of closed-ended steel tubes, the authors of the current study considered it reasonable to expect less severe friction fatigue in this case.

3.3.4 Cavity Expansion with Sub-Regions (CE-SR) method

The CE-SR method (Figure 6d) is the result of modifications made to the CE-SL method. The first modification was the introduction of a zone below the pile base with improved soil stiffness and strength parameters. The amount of parameter increase and the size of the zone is the same as in the CE-BI approach.

The other modifications are related to the way that changes in radial stresses in the soil adjacent to the pile shaft are considered. The stress reading was expanded to 6*D* horizontally from the pile shaft. The soil adjacent to the pile shaft was divided into 0.5 m thick sub-layers, which was motivated by the shorter length of the piles under analysis (3.5 m) compared to the 9.5 m length of the pile analyzed by Schmüdderich et al. (2020). Furthermore, the region to which the updated *K* profile is assigned was limited radially in 6*D* from the pile shaft, with vertical divisions every 1*D*. Each sub-region thus obtained was assigned an average *K* value calculated according to the radial stresses evaluated in the same region.

The extent of this zone was determined after weighing the zone of influence of radial stresses (σ_r) induced by
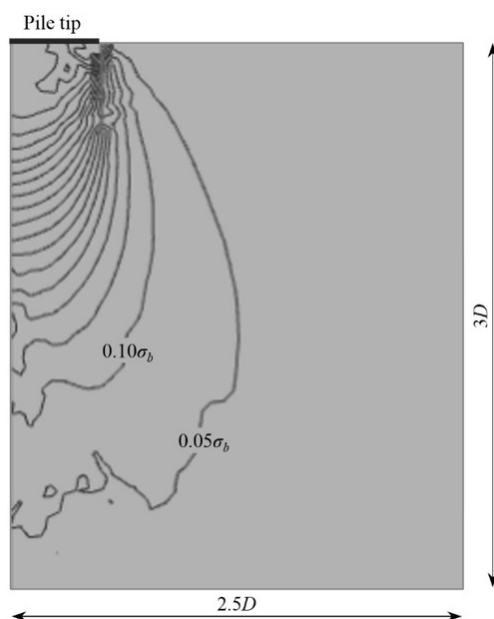
the cavity expansion and the applicability of the method. Figure 9 shows curves of the radial stresses of the soil adjacent to the C6 pile shaft before and after the cavity expansion phase for two depth levels (1.5 and 3.5 m). It can be seen that from a radial distance of the order of 6D, the increment in radial stresses induced by the expansion is low and tends to constancy for greater distances.

The last two calculation steps (pile casting and load test) remain unchanged. However, in the modified approach, the interface shear strength was not reduced (R_{inter} = 1), for the reasons previously discussed for the CE-BI approach.
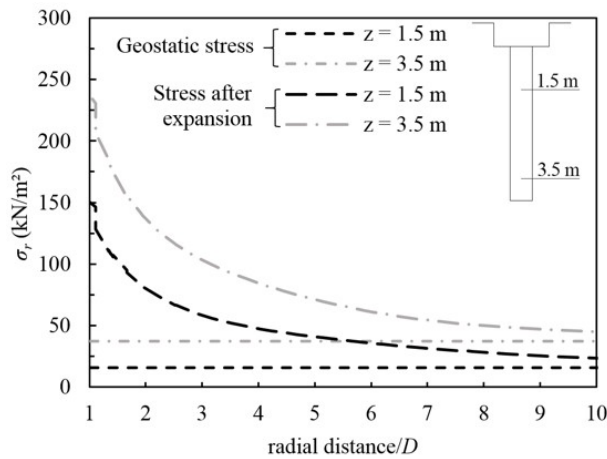
Figure 9. Radial stresses pre and post cavity expansion for pile C6.

4. Analysis and results

4.1 Original CE and CE-SL methods

The load-settlement curves measured in the field and obtained with the numerical approaches are presented in Figure 10. The bearing capacity of piles C4, C6, and C8 obtained with the CE approach was approximately 17% lower than the values verified in the field (Figure 10a). On the other hand, with the CE-SL approach, it was necessary to reduce the interface shear strength to 60% of the mobilized shear strength in the surrounding soil (R_{inter} = 0.60) to obtain failure values close to those measured experimentally (Figure 10b). The load-settlement behavior for settlements < 5 mm was similar with both methods for all piles.

Figure 11 shows the mobilization of the average shear stress at the pile shaft and of the pile base pressure with the evolution of the pile head settlements (w), which were normalized by the pile diameter. Both the results computed with the numerical approaches and those measured in the field are presented. The numerical results for pile C4 are also shown, although no experimental data were available for comparison due to the lack of instrumentation on this pile.

For settlements greater than 0.02D, both numerical approaches predict greater shaft friction mobilization than verified in the field. At failure conditions, while the CE method (Figure 11a) predicts a reasonable shaft friction mobilization relative to field-measured values, the CE-SL method (Figure 11b) considerably overestimates these values. Concerning the pile base pressure, both methods resulted in
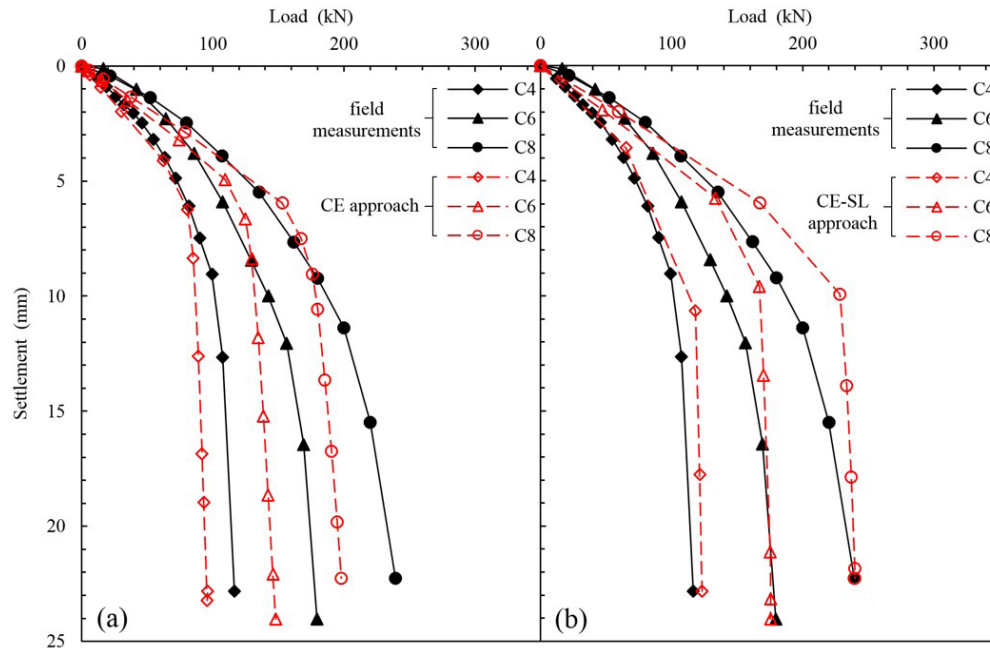
Figure 10. Comparison of load-settlement curves for (a) CE approach and (b) CE-SL approach.

Figure 11. Average shear stress at the pile shaft for (a) CE approach and (b) CE-SL approach and pile base pressure for (c) CE approach and (d) CE-SL approach.

similar behavior, underestimating the base resistance of the piles. This underestimation was the main reason for the error in the estimation of the bearing capacity of the piles with the CE method. Furthermore, the base pressure mobilization computed from the numerical models was quite similar among the piles, regardless of pile diameter, with a slightly lower mobilization for pile C8.

These results are attributed to the fact that both approaches were originally developed for the analysis of SDP, whose installation technology differs from the DCIS piles. In the case of driven or jacked piles, the stress state of the soil below the pile base is greatly influenced by the installation, while in the case of SDP the soil adjacent to the pile shaft is more affected (Krasinski, 2014). Moreover, Flynn & McCabe (2016) reported that the shaft friction mobilization mechanisms of DCIS piles installed in sandy soils are closer to those of bored piles, due to the rough shaft surface resulting from in-situ concreting and the absence of residual stresses related to the driving process, since in the case of DCIS piles, the installation tube is extracted before concreting.

4.2 Proposed CE-BI and CE-SR methods

Figure 12 shows the load-settlement curves measured in the field and obtained with the proposed numerical approaches. Despite the differences between the methods, both resulted in quite similar behavior. In terms of bearing capacity, the numerical results were very reliable when compared to those measured experimentally, with errors ranging from 1% to 3% for both approaches. It can be seen from the load-settlement curves for piles C4 to C8, that for settlements between about 2% and 6% of the pile diameter, both numerical models result in a stiffer stress-strain behavior than the one observed in the field, especially the CE-SR method.

Modifications made to the CE-SL approach in the way of incorporating the installation effects around the pile shaft improved the prediction of shear stress mobilization (Figure 13b), although both numerical approaches still slightly overestimate the shaft resistance of the piles. In addition, the numerical models predict a shear stress mobilization proportional to the pile diameter, with a trend more evident for the CE-BI method (Figure 13a).

Figure 12. Comparison of load-settlement curves for (a) CE-BI approach and (b) CE-SR approach.
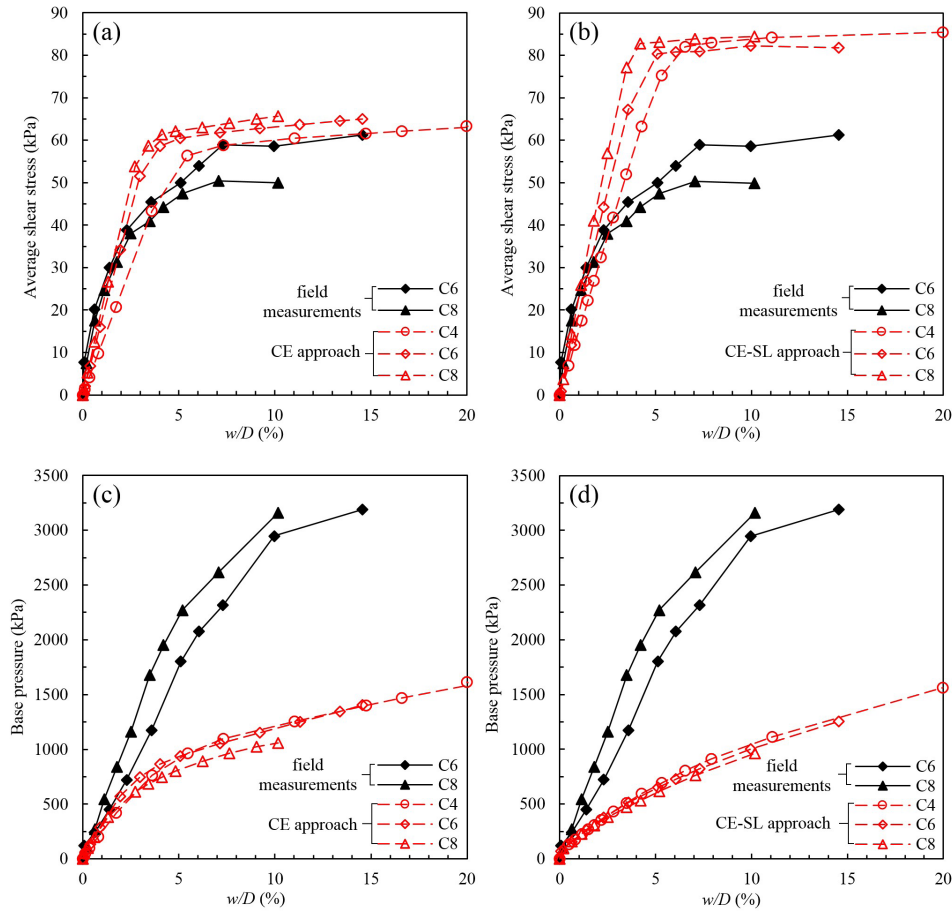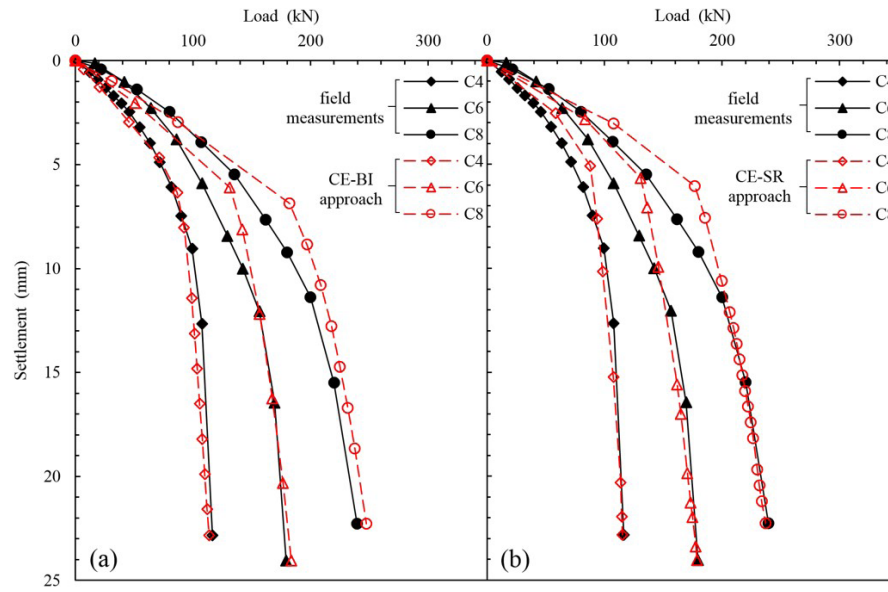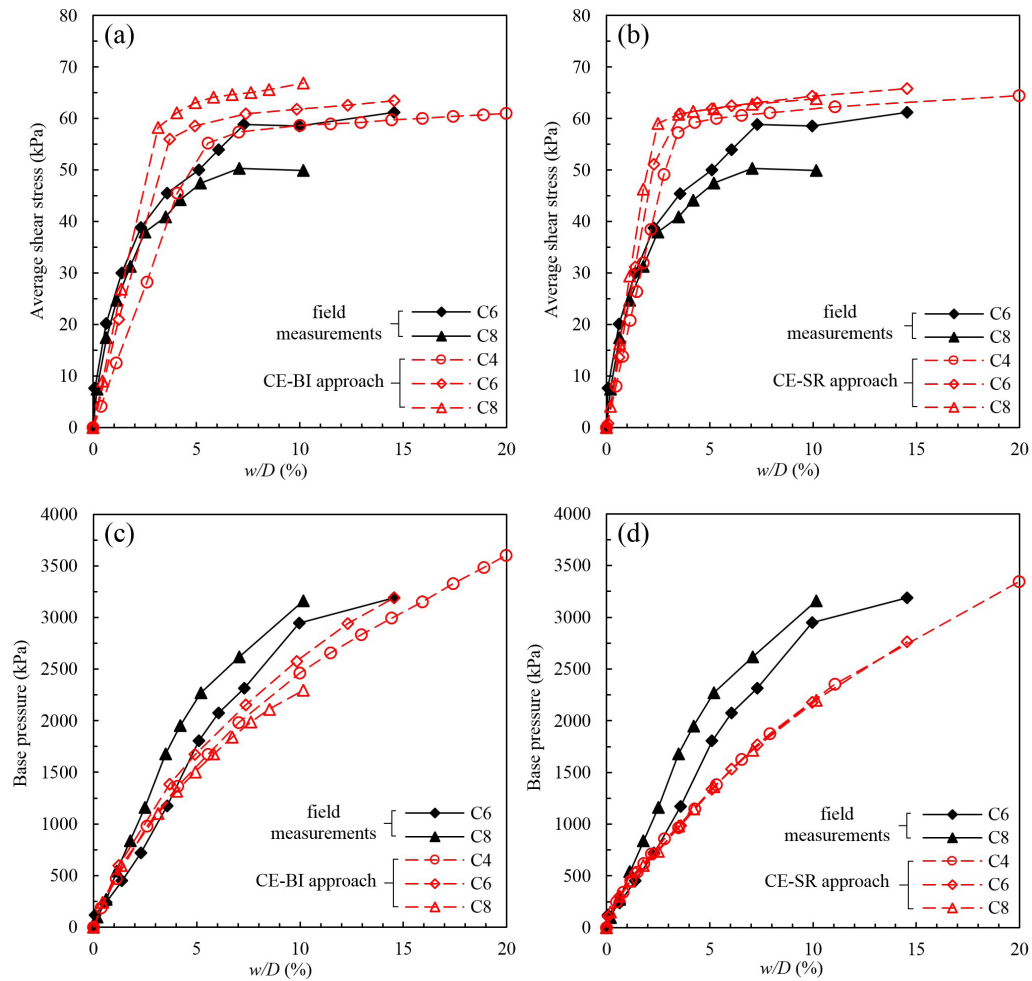

Figure 13. Average shear stress at the pile shaft for (a) CE-BI approach and (b) CE-SR approach and pile base pressure for (c) CE-BI approach and (d) CE-SR approach.

The increase of the stiffness parameters and the soil cohesion below the piles tips allowed a better mobilization of the base pressure, with the CE-BI method predicting slightly higher values. At failure conditions, the base resistance obtained with the CE-BI method (Figure 13c) was quite accurate for pile C6, while in the case of pile C8 there was an underestimation of 27%. With the CE-SR method (Figure 13d), the errors in estimating the ultimate base resistance of piles C6 and C8 were 13% and 30%, respectively. These results highlight the importance of considering soil densification below the pile base in numerical modeling of DCIS piles.

5. Conclusions

This paper proposed two numerical approaches for finite element analysis of DCIS piles that allow incorporating the installation effects in an idealized manner. The approaches, named CE-BI and CE-SR methods, are the result of improvements made to preexisting methods. The modified approaches introduce a densified zone under the pile tip and improve the way of incorporating the installation-induced changes in radial stresses of the surrounding soil. The results obtained allow the following conclusions:

- Both proposed numerical approaches were able to satisfactorily reproduce axial load tests conducted on DCIS piles, being sensitive to pile diameter variation. The numerical bearing capacity predictions showed an average error of 2% compared to the measured values. In the failure conditions, the models accurately obtained the pile shaft and base resistances. The average error between measured and numerical values was 18% for both shaft and base resistances. In the case of base resistance, this is due to an overestimation, while in the case of shaft resistance it is due to an underestimation of the values. In terms of relative pile-soil stiffness, there was a slightly overestimated response for intermediate loading stages.

- Despite the methodological differences between the approaches, both result in a behavior that is quite similar to each other. In terms of applicability, the CE-BI method has the advantage of being modeled in a single numerical model. However, due to distortions of the finite element mesh in the cavity expansion and pile casting phases, the method may present some numerical instabilities that do not occur in the CE-SR method, since the latter separates the cited stages into two different models. Under these circumstances, the CE-SR method is superior to the CE-BI method.

- To apply the methods for predicting the behavior of displacement piles under axial compression loads, the limiting factor is the need for data that can be used to calibrate the characteristics of the pile-soil interface and to determine the magnitude of the increase in soil strength and stiffness parameters in the improved

zone below the pile base. An instrumented load test, such as those used in this paper, is an adequate tool for this purpose.

Declaration of interest

The authors have no conflicts of interest to declare.

Authors' contributions

Bismarck Chaussê Oliveira: conceptualization, data curation, formal analysis, methodology, validation, visualization, writing – original draft. Maurício Martines Sales: conceptualization, methodology, supervision, validation, riting – review & editing. Renato Resende Angelim: investigation, writing – review & editing. Luiz Carlos Galvani Junior: investigation, writing – review and editing.

Data availability

All data produced or examined in the course of the current study are included in this article.

List of symbols

c	Soil cohesion
D	Pile diameter
e	Void ratio of soil
E	Young's modulus
E_{50}^{ref}	Reference stiffness modulus for primary deviatoric loading
E_{oed}^{ref}	Reference stiffness modulus for primary compression
E_{ur}^{ref}	Reference stiffness modulus for unloading/reloading
G_s	Specific gravity of soil
K	Coefficient of lateral earth pressure
K_0	Coefficient of earth pressure at rest
K_0^{NC}	Coefficient of earth pressure at rest for normal consolidation
m	Stiffness power law exponent
N_{SPT}	SPT N-value
OCR	Overconsolidation ratio
$p_{c,s}$	Horizontal pressure at cavity wall
$p_{c,b}$	Vertical pressure at cavity bottom
p^{REF}	Reference confining pressure
r	Pile radius
r_0	Initial cavity radius

12

Oliveira et al., Soil. Rocks, São Paulo, 2023 46(1):e2023004522

R_f	Failure ratio
R_{inter}	Interface strength reduction factor
w	Pile head settlement
α	Teixeira & Godoy (1998) first soil-dependent coefficient
β	Teixeira & Godoy (1998) second soil-dependent coefficient
γ	Unit weight of moist soil
δ	Interface friction angle
ε_r	Relative increase in cavity radius measured in the pressuremeter tests
σ_b	Mean vertical pressure at the pile base
σ_r	Radial stress
υ_{ur}	Poisson's ratio for unloading/reloading
ϕ	Friction angle of soil
ψ	Angle of dilatancy of soil

References

Bernardes, H.C., Sales, M.M., Machado, R.R., Cruz Junior, A.J., Cunha, R.P., Angelim, R.R., & Rebolledo, J.F.R. (2022). Coupling hardening soil model and Ménard pressuremeter tests to predict pile behavior. *European Journal of Environmental and Civil Engineering*, 26(11), 5221-5240. http://dx.doi.org/10.1080/19648189.2021.1886180.

Brinkgreve, R. B. J., Kumarswamy, S., Swolfs, W. M., Fonseca, F., Monoj, N. R., Zampich, L., & Zalamea, N. (2021). *Plaxis connect edition: general information manual*. Plaxis bv.

Broere, W., & van Tol, A.F. (2006). Modelling the bearing capacity of displacement piles in sand. *Proceedings of the Institution of Civil Engineers - Geotechnical Engineering*, 159(3), 195-206. http://dx.doi.org/10.1680/geng.2006.159.3.195.

Camapum de Carvalho, J., & Gitirana Junior, G.F.N. (2021). Unsaturated soils in the context of tropical soils. *Soils and Rocks*, 44(3), 1-25. http://dx.doi.org/10.28927/SR.2021.068121.

Engin, H.K. (2013). *Modelling pile installation effects - a numerical approach* [Doctoral thesis]. Delft University of Technology. https://doi.org/10.4233/uuid:3e8cc9e2-b70c-403a-b800-f68d65e6ea85.

Engin, H.K., Brinkgreve, R.B.J., & van Tol, A.F. (2015). Simplified numerical modelling of pile penetration – the press-replace technique. *International Journal for Numerical and Analytical Methods in Geomechanics*, 39(15), 1713-1734. http://dx.doi.org/10.1002/nag.2376.

Flynn, K.N., & McCabe, B.A. (2016). Shaft resistance of driven cast-in-situ piles in sand. *Canadian Geotechnical Journal*, 53(1), 49-59. http://dx.doi.org/10.1139/cgj-2015-0032.

Freitas, J.B., Rezende, L.R., & Gitirana Junior, G.F.N. (2020). Prediction of the resilient modulus of two tropical subgrade soils considering unsaturated conditions. *Engineering Geology*, 270, 105580. http://dx.doi.org/10.1016/j.enggeo.2020.105580.

Frost, J.D., DeJong, J.T., & Recalde, M. (2002). Shear failure behavior of granular-continuum interfaces. *Engineering Fracture Mechanics*, 69(17), 2029-2048. http://dx.doi.org/10.1016/S0013-7944(02)00075-9.

Goulart, R.L. (2021). *Análise numérica de ensaios pressiométricos do campo experimental da EECA* [Unpublished master's dissertation]. Federal University of Goiás (in Portuguese).

Heins, E., & Grabe, J. (2017). Class-A-prediction of lateral pile deformation with respect to vibratory and impact pile driving. *Computers and Geotechnics*, 86, 108-119. http://dx.doi.org/10.1016/j.compgeo.2017.01.007.

Krasinski, A. (2014). Numerical simulation of screw displacement pile interaction with non-cohesive soil. *Archives of Civil and Mechanical Engineering*, 14(1), 122-133. http://dx.doi.org/10.1016/j.acme.2013.05.010.

Li, Y., Liu, C., & Song, J. (2021). The pile end mechanism of jacked pile in layered soils. *Indian Geotechnical Journal*, 51, 1087-1098. http://dx.doi.org/10.1007/s40098-021-00510-1.

Liu, C., Tang, X., Wei, H., Wang, P., & Zhao, H. (2020). Model tests of jacked-pile penetration into sand using transparent soil and incremental particle image velocimetry. *KSCE Journal of Civil Engineering*, 24(4), 1128-1145. http://dx.doi.org/10.1007/s12205-020-1643-4.

Lobo-Guerrero, S., & Vallejo, L.E. (2005). DEM analysis of crushing around driven piles in granular materials. *Geotechnique*, 55(8), 617-623. http://dx.doi.org/10.1680/geot.2005.55.8.617.

Lorenzo, R., Cunha, R.P., Cordão Neto, M.P., & Nairn, J.A. (2018). Numerical simulation of installation of jacked piles in sand using material point method. *Canadian Geotechnical Journal*, 55(1), 131-146. http://dx.doi.org/10.1139/cgj-2016-0455.

Machado, R.R. (2020). *Ensaios pressiométricos para estimativa de parâmetros de resistência e deformabilidade do solo do campo experimental da EECA/UFG* [Unpublished master's dissertation]. Federal University of Goiás (in Portuguese).

Machado, R.R., do Nascimento, B.B., Rodrigues, J.L. da M., Angelim, R.R., Sales, M.M., Lima Junior, J.C., Merighi, V.A., & Fonseca, A.L.E. (2018). Medição de energia em ensaio SPT realizado no campo experimental da EECA/UFG. In *19° Congresso Brasileiro de Mecânica dos Solos e Engenharia Geotécnica* (Vol. 3). Salvador: ABMS, CBMR, ISRM & SPG. (in Portuguese)

Machado, R.R., Galvani Junior, L.C., Angelim, R.R., & Sales, M.M. (2020). Utilização de ensaios pressiométricos Ménard para avaliação de um perfil de solo tropical. *Tecnia – Revista de Educação, Ciência e Tecnologia do IFG*, 5(2), 219-243. (in Portuguese)

Martinez, A., & Frost, J.D. (2017). The influence of surface roughness form on the strength of sand-structure interfaces.

Géotechnique Letters, 7(1), 104-111. http://dx.doi.org/10.1680/jgele.16.00169.

Mayne, P.W., & Kulhawy, F.H. (1982). K_0-OCR relationships in soil. *Journal of the Geotechnical Engineering Division*, 108(6), 851-872. http://dx.doi.org/10.1061/AJGEB6.0001306.

Nascimento, B.B. (2019). *Provas de carga estáticas em estacas metálicas tubulares de ponta aberta em um solo tropical* [Unpublished master's dissertation]. Federal University of Goiás (in Portuguese).

Nogami, J.S., & Villibor, D.F. (1995). *Pavimentação de baixo custo com solos lateríticos*. Vilibor. (in Portuguese).

Phuong, N.T.V., van Tol, A.F., Elkadi, A.S.K., & Rohe, A. (2016). Numerical investigation of pile installation effects in sand using material point method. *Computers and Geotechnics*, 73, 58-71. http://dx.doi.org/10.1016/j.compgeo.2015.11.012.

Pucker, T., & Grabe, J. (2012). Numerical simulation of the installation process of full displacement piles. *Computers and Geotechnics*, 45, 93-106. http://dx.doi.org/10.1016/j.compgeo.2012.05.006.

Qiu, G., Henke, S., & Grabe, J. (2011). Application of a Coupled Eulerian-Lagrangian approach on geomechanical problems involving large deformations. *Computers and Geotechnics*, 38(1), 30-39. http://dx.doi.org/10.1016/j.compgeo.2010.09.002.

Randolph, M.F., Dolwin, J., & Beck, R. (1994). Design of driven piles in sand. *Geotechnique*, 44(3), 427-448. http://dx.doi.org/10.1680/geot.1994.44.3.427.

Rebolledo, J.F.R., León, R.F.P., & Camapum de Carvalho, J. (2019). Obtaining the mechanical parameters for the Hardening Soil model of tropical soils in the city of Brasília. *Soils and Rocks*, 42(1), 61-74. http://dx.doi.org/10.28927/sr.421061.

Rezania, M., Nezhad, M.M., Zanganeh, H., Castro, J., & Sivasithamparam, N. (2017). Modeling pile setup in natural clay deposit considering soil anisotropy, structure, and creep effects: case study. *International Journal of Geomechanics*, 17(3), 04016075. http://dx.doi.org/10.1061/(asce)gm.1943-5622.0000774.

Rezende, B.L.M., & Rocha, L.B. (2020). *Influência da energia nos resultados do ensaio SPT* [Unpublished undergraduate final project]. Federal University of Goiás. (in Portuguese).

Rooz, A.F.H., & Hamidi, A. (2019). A numerical model for continuous impact pile driving using ALE adaptive mesh method. *Soil Dynamics and Earthquake Engineering*, 118, 134-143. http://dx.doi.org/10.1016/j.soildyn.2018.12.014.

Said, I., De Gennaro, V., & Frank, R. (2009). Axisymmetric finite element analysis of pile loading tests. *Computers and Geotechnics*, 36(1-2), 6-19. http://dx.doi.org/10.1016/j.compgeo.2008.02.011.

Schanz, T., Vermeer, P.A., & Bonnier, P.G. (1999). The hardening soil model: formulation and verification. In *International Symposium Beyond 2000 in Computational Geotechnics* (pp. 281-296). Amsterdam: Routledge.

Schmidt, B. (1966). Discussion on: earth pressure at rest related to stress history. *Canadian Geotechnical Journal*, 3(4), 239-242. http://dx.doi.org/10.1139/t66-028.

Schmüdderich, C., Shahrabi, M.M., Taiebat, M., & Lavasan, A.A. (2020). Strategies for numerical simulation of cast-in-place piles under axial loading. *Computers and Geotechnics*, 125, 103656. http://dx.doi.org/10.1016/j.compgeo.2020.103656.

Tehrani, F.S., Nguyen, P., Brinkgreve, R.B.J., & van Tol, A.F. (2016). Comparison of press-replace method and material point method for analysis of jacked piles. *Computers and Geotechnics*, 78, 38-53. http://dx.doi.org/10.1016/j.compgeo.2016.04.017.

Teixeira, A.H., & Godoy, N.S. (1998). Análise, projeto e execução de fundações rasas. In Hachich, W., Falconi, F.F., Saes, J.L., Frota, R.G.Q., Carvalho, C.S., & Niyama, S. (Eds.), *Fundações: teoria e prática* (pp. 227-264). Pini. (in Portuguese).

Tovar-Valencia, R.D., Galvis-Castro, A., Salgado, R., & Prezzi, M. (2018). Effect of surface roughness on the shaft resistance of displacement model piles in sand. *Journal of Geotechnical and Geoenvironmental Engineering*, 144(3), 04017120. http://dx.doi.org/10.1061/(asce)gt.1943-5606.0001828.

Wehnert, M., & Vermeer, P.A. (2004). Numerical analyses of load tests on bored piles. In *9th International Symposium on Numerical Models in Geomechanics* (pp. 505-511). Ottawa: CRC Press.

White, D.J., & Bolton, M.D. (2004). Displacement and strain paths during plane-strain model pile installation in sand. *Geotechnique*, 54(6), 375-397. http://dx.doi.org/10.1680/geot.54.6.375.45427.

White, D.J., & Lehane, B.M. (2004). Friction fatigue on displacement piles in sand. *Geotechnique*, 54(10), 645-658. http://dx.doi.org/10.1680/geot.2004.54.10.645.

Yang, Z.X., Gao, Y.Y., Jardine, R.J., Guo, W.B., & Wang, D. (2020). Large deformation finite-element simulation of displacement-pile installation experiments in sand. *Journal of Geotechnical and Geoenvironmental Engineering*, 146(6), 04020044.

14

Oliveira et al., Soil. Rocks, São Paulo, 2023 46(1):e2023004522

Study of the hydro-mechanical behavior of a stabilized soil with water treatment plant sludge for application in sanitary landfills

Elisangela Aparecida Mazzutti[1#] (ID), Rodrigo André Klamt[2] (ID),

Vítor Pereira Faro[1] (ID)

Article

Abstract
The improper disposal of water treatment plant sludge (WTPS) into the environment can cause irreparable damage. One way to minimize this negative impact is to mix the sludge with the soil, applying the materials in engineering works. In this research, the objective was the use of WTPS for soil stabilization purposes, verifying the improvement of the characteristics and properties of a stabilized clay soil with different sludge percentages for application in waterproofing layers of bottom and final coverage of landfills. Formulations were prepared with additions of 0, 15, 30 and 50% of WTPS. Characterization, compaction, permeability and simple compression resistance tests were carried out. All mixtures met the Brazilian requirements for use in landfill layers, but the mixture composed of 70% soil + 30% WTPS was defined as the best for application in bottom layers and final coverage for the following reasons: it meets the coefficient of permeability and has the highest simple compression resistance of all blends. Furthermore, it is noteworthy that the use of the mixtures, especially 50% soil + 50% WTPS, in daily (intermediate) layers would be an environmentally beneficial alternative that would contribute to the circular economy and to achieving sustainable development goals 11, 12 and 15 by 2030. These applications would bring advantages in the destination of WTPS and reduced consumption of natural resources (soil).

1. Introduction

Water coming from underground or surface springs is extremely important to supply the population. However, fresh water needs to be treated so that it can be consumed by humans, passing through Water Treatment Stations (WTS) and through various physical, biological and chemical processes.

At the beginning of the water treatment, chemical products are added in order to separate the existing impurities, and in this separation the particles are dispersed in a liquid medium, where, later, they agglomerate and form flakes, which sediment by the action of gravity. The residue that accumulates in the sedimentation process is called Water Treatment Plant Sludge (WTPS), being obtained from the washing of the decanters. Initially, after removing the sludge from the decanters, it has a liquid consistency and large volume, requiring adequate treatment and disposal (Montalvan, 2016; Guimarães & Urashima, 2013).

The sludge consists of solid residues of organic and inorganic nature, therefore, depending on the characteristics, the residues of the WTPs increase the degree of pollution and contamination of the water bodies, contributing to the loss of the quality of life of the populations existing downstream of the sludge releases (Roque et al., 2022).

The WTPS was initially deposited in water bodies, without any adequate treatment, providing negative aspects to water quality and causing silting of rivers. However, this practice was abolished by CONAMA (Brazilian National Environmental Council) resolution n° 357 (Brasil, 2005), which classifies this material as a pollutant of these bodies, requiring adequate disposal. In addition, the Brazilian Standard ABNT NBR 10004 (ABNT, 2004) brings WTPS as a solid waste, so it cannot be disposed of in bodies of water. However, according to a study carried out by Achon & Cordeiro (2015), in the Water Treatment Stations of São Paulo, only 9% of them sent the sludge to Waste Treatment

*Corresponding author. E-mail address: elisamazzutti@hotmail.com
[1] Universidade Federal do Paraná, Departamento de Engenharia Civil, Curitiba, PR, Brasil.
[2] Universidade Federal de Santa Maria, Departamento de Engenharia Civil, Santa Maria, RS, Brasil.

Units and had the same dewatered in industrial landfills, 86% of the WTS disposed of the untreated sludge in bodies of water and 5% sent it to one of the available Sewage Treatment Stations.

The final destination of WTPS is a very important and complex activity, as the capacity of treatment plants and landfills is usually extrapolated. Therefore, there is a need for alternatives to the final destination of the waste, which is the responsibility of the producers of the tailings. In this way, some environmental agencies have demanded details of the final disposal in the WTPs licensing process, representing an advance in environmental management in the country (Montalvan, 2016).

The great production of WTPS and the environmental concern of the final destination of this residue has instigated researchers to seek appropriate forms of management, one of them being the use in civil construction. Due to the high consumption of aggregates by this branch, materials from the deposits are increasingly scarce, requiring the use of materials that often do not meet the specifications of use (Santos et al., 2018).

In Brazil, the construction of sanitary landfill covers depends on the exploitation of clay deposits, extracted from the place of execution itself or from the deposit closest to the landfill. In several situations, due to the large volume of transport, or even the distance from the deposits, the cost of transporting these soils is higher than the extraction itself, when considering the frequent increases in fuel prices, not showing economic viability to use nobler soils in landfills. In addition, the soils available in the locality often do not achieve an efficient waterproofing for landfill layers, resulting in the need to use less noble soils, stabilizing them with binders and residues that improve their properties (Knierim, 2020).

The use of sludge is one of the ways out for the use of the residue, which has already been used in some research at the national level that justify this trend: the dosage of lime and sludge from the WTP for use as a supplementary material to Portland cement by Ferreira et al. (2022); as raw material for precast concrete floors by Castro (2014); use as ceramic material for the manufacture of tiles by Cremades et al. (2018); as a material incorporated into the asphalt binder by Martinez (2014); in road paving for its incorporation into the base layer and sub-base of road pavement by Medaoud et al. (2022). The cited works resume the importance of a study of this residue so that it can be used as a raw material or final product, contributing even more to a sustainable organizational growth.

This research aimed to use sludge for soil stabilization purposes, verifying the improvement of the characteristics and properties of clayey soil stabilized with different percentages of WTPS for application in sanitary landfills.

2. Materials and methods

This chapter describes the procedures during the experimental phase of the research. This was developed in 3 stages: in the first stage, we sought to develop a bibliographic review on the subject, in order to deepen our knowledge on the subject and to better understand the behaviors found by other researchers in relation to WTPS and soil + WTPS mixtures.

Subsequently, in the second phase, soil and WTPS characterization tests were developed, in addition to the development of Compaction, Permeability and Simple Compressive Strength tests of all mixtures, in order to know the characteristics and properties of soil and soil + WTPS.

In the third and final phase, the results found were analyzed and compared to those found in the literature under study, in order to give greater veracity to them and also to verify the possibility of using soil and mixtures within the standards established as mandatory by the Brazilian Standard ABNT NBR 13896 (ABNT, 1997), which defines criteria for non-hazardous waste landfills, by the United States Environmental Protection Agency (USEPA, 1998, 2003), by German Standard (1993) and also desirable requirements found in the study literature for bottom layers and final cover of landfills, thus increasing the spectrum of analysis for the implementation of the technique in other countries.

The research was developed with the joint work of bibliographic research and laboratory tests, mainly in the Materials and Civil Construction Laboratory (MCCL) and in the Soil Laboratory of the Integrated Regional University of Alto Uruguai and Missões - Frederico Westphalen Campus (URI -FW).

2.1 Materials

2.1.1 Soil

The soil used in the research was obtained from a deposit in the city of Frederico Westphalen (FW), State of Rio Grande do Sul (RS), Brazil. The deposit is located in Volta Grande, on the banks of BR-386 highway, km 38, with coordinates of latitude 27°24'9.35" South and longitude 53°24'28.93" West, being this soil used in the works carried out by the city government.

The soil of the place has a clayey characteristic, due to the previous tactile-visual analysis and the characteristics of the soils found in the North and Northwest of the State of Rio Grande do Sul.

2.1.2 Water Treatment Plant Sludge

The WTPS used in the research was collected at the water treatment plant, located in the north of the state of Rio Grande do Sul, at CORSAN/FW (Riograndense sanitation company). The station collects water by pumping from the Pardo River dam, located in the interior of the same city, and takes it through pipes to the treatment site, located at the highest point within the urban environment.

The station works with full cycle treatment. Basically, the treatment consists of the following phases: coagulation/

flocculation, decantation, filtration, chlorination and fluoridation. It is known that in WTPs of this classification the largest amount of sludge (in terms of mass) is generated in the decanters. At the WTP where the sludge was collected, there are two decanters with a capacity of 800 m³ each, however the company did not inform the amount of sludge generated there.

2.2 Description of processes

2.2.1 Soil collection and preparation

The soil was collected in accordance with the specifications of the Brazilian Standard ABNT NBR 9604 (ABNT, 2016c). Previously, before excavation, a surface cleaning of the land was carried out, removing any trace of vegetation present, as specified in the regulations. The soil was collected at a depth of 2 m and packed in clean bags for transport and laboratory storage. In the laboratory, the sample was broken up for use in the tests.

2.2.2 Soil characterization

For the characterization of the soil, the granulometric analysis test was carried out according to Brazilian Standard ABNT NBR 7181 (ABNT, 2018). The determination of the Liquid Limit of the soil was carried out according to ABNT NBR 6459 (ABNT, 2017) and the Plasticity Limit was carried out in accordance with ABNT NBR 7180 (ABNT, 2016b). The density of soil particles was determined by the ABNT NBR 6458 (ABNT, 2016a).

In addition to the tests already mentioned, to complement the characterization, a chemical analysis test was carried out for the soil. It should be noted that for all the above-mentioned soil characterization tests, tests were carried out on 3 samples, in order to obtain greater reliability in the results.

2.2.3 Collection and preparation of WTPS

At the time of collection, WTPS had a gravimetric moisture content of about 2385%, which characterized it as a thixotropic material, that is, it is in the form of a gel, with a gravimetric moisture value - ratio of water mass per mass of particles solid – which exceeds 900%. Thus, it would be necessary to perform drying in drainage beds to improve workability. However, it was not possible to perform this drainage due to lack of adequate equipment. Thus, the sludge was obtained directly from the conditioning tanks and placed in plastic drums for storage in the laboratory.

In the laboratory, the sludge was dried in an oven at a temperature of 60 °C. This temperature was defined in order to avoid the possibility of burning the organic matter present in the material.

The dry sludge sample was obtained when the moisture reached a value below 15%, which was evidenced after the seventh day in the oven. The material was characterized at that time as granular, the size of a pebble with about 99.4% retained in the sieve with an opening of 0.075 mm.

2.2.4 Characterization of WTPS

For the sludge, in order to know its properties, the chemical analysis test was performed. In the same way as for the characterization of the soil, for the characterization of the WTPS, tests were carried out on 3 samples, giving greater credibility to the results.

2.2.5 Dosage and mixing

As the WTPS and the soil were previously dried, they were mixed and homogenized and then water was added to the mixture. The mixtures to be studied are presented in Table 1, which were defined from the researched literature.

The mixture 5 was used only in the characterization tests to know the properties of WTPS. Furthermore, in order to characterize the mixtures highlighted in Table 1, granulometry tests, Atterberg limits test, soil particles density analysis and chemical analysis were performed.

2.2.6 Compaction test

In this study, the use of intermediate energy prevailed, since this energy is commonly used in sanitary landfill compaction. The test procedure followed the methodology described in the Brazilian Standard ABNT NBR 7182 (ABNT, 2020) with 3 samples for each mixture.

2.2.7 Simple compression strength test

The preparation of the specimens was carried out in cylindrical molds measuring 10 cm in diameter and 20 cm in height, at the optimum moisture and maximum specific weight for each mixture, determined from the Proctor compaction test, at the intermediate energy.

The molding took place dynamically, using a manual compactor. Three specimens were molded for each dosage in order to obtain the average of the Simple Compressive Strength (SCS). After molding, the specimens were packed in plastic film and proceeded to cure, in a temperature-controlled environment, for 7 and 28 days. The test followed the precepts of the Brazilian Standard ABNT NBR 12025 (ABNT, 2012).

Table 1. Mixtures.

Nomenclature	Soil (%)	WTPS (%)
M1	100	0
M2	85	15
M3	70	30
M4	50	50
M5	0	100

2.2.8 Permeability test

The permeability test of soil and soil + WTPS mixtures was carried out with variable load, due to the possible low permeability of the mixtures. For this, the Brazilian Standard ABNT NBR 14545 was used (ABNT, 2000). For each mixture, tests were carried out on 3 specimens, molded in cylindrical molds of 10 cm in diameter by 20 cm in height. Soon after molding, the specimens were prepared for the start of the test.

2.2.9 Data analysis

After obtaining the results of the characterization, hydrous and mechanical tests, the data was compiled. Subsequently, these were compared to other studies and standards and the possibility of use in bottom layers and final cover of sanitary landfills was verified.

3. Analysis and results

3.1 Mixture characterization tests

Initially, the physical characterization of the mixtures under study was performed. The granulometric analysis consists of coarse sieving together with the sedimentation test with and without a deflocculant agent, for subsequent performance of the fine sieving. With these results, together with the unit weight of soil particles and Atterberg limits, it is possible to classify the materials according to the Transportation Research Board (TRB) and Unified Soil Classification System (USCS) systems, thus being able to predict the behavior of the same. In the Table 2 is possible to visualize the results of the physical characteristics of the mixtures, the Atterberg limits and the respective classifications according to the USCS and TRB.

Regarding the granulometry test (sieving + sedimentation), more specifically for mixtures without deflocculant, from Table 2, it is possible to observe that:

- With the addition of sludge in the mixtures, there was a tendency to increase the percentage of gravel and decrease the percentage of coarse sand, which stabilized from M2. Furthermore, mixtures 1, 2, 3 and 4 had more than 50% of their fractions composed of fine material (silt and clay); and mixture 5 showed a predominance of stony, with more than 80% of material in this fraction;

- Changes in granulometric characteristics of soil + WTPS mixtures are evident when compared to natural soil. The average sand percentage was doubled from M1 to M2, M3 and M4, and for M2, M3 and M4 the value found was the same for all. Another important perception is that, with the increase in the percentages of soil replacement by sludge, there was a tendency to decrease in the percentages of fine sand and silt, in addition to a small tendency to increase in the clay fraction;

- Also, in relation to the amount of sand, the soil presented an average of 27% (being this material with the highest sandy fraction), the mixture 85%

Table 2. Characterization of mixtures.

Parameters		M1 (100% Soil)	M2 (85% Soil + 15% WTPS)	M3 (70% Soil + 30% WTPS)	M4 (50% Soil + 50% WTPS)	M5 (100% WTPS)
Physical characteristics from the no deflocculant test	Gravel (%)	3	8	14	29	81
	Coarse Sand (%)	5	4	3	3	4
	Medium Sand (%)	1	2	2	2	2
	Fine Sand (%)	21	19	17	13	5
	Silt (%)	53	49	45	31	6
	Clay (%)	17	18	19	22	2
	γ_s (g/cm^3)	3.009	2.945	2.694	2.590	2.559
Physical characteristics from the deflocculant test	Gravel (%)	2	10	14	29	44
	Coarse Sand (%)	1	1	1	1	2
	Medium Sand (%)	1	2	2	2	1
	Fine Sand (%)	6	7	7	8	4
	Silt (%)	33	33	33	27	37
	Clay (%)	57	47	43	33	12
Atterberg Limits	LL (%)	55	56	58	58	NP
	PL (%)	35	35	37	37	NP
	PI (%)	20	21	21	21	NP
Classification without deflocculant	USCS Classification	MH	MH	MH	MH	GP-GM
	TRB Classification	A-7-5	A-7-5	A-7-5	A-7-5	A-2-7
Classification with deflocculant	USCS Classification	CH	CH	CH	CH	GP-GM
	TRB Classification	A-7-5	A-7-5	A-7-5	A-7-5	A-4

γ_s: unit weight of soil particles; LL: liquid limit; PL: plasticity limit; PI: plasticity index; NP: not plastic.

4

Mazzutti et al., Soil. Rocks, São Paulo, 2023 46(1):e2023011222

Soil + 15% WTPS presented 25%, the mixture of 70% Soil + 30% WTPS presented 22% and in the 50% Soil + 50% WTPS there was only 18%, that is, there was a tendency to decrease the amount of sand with the increase of WTPS in the mixture. Finally, the mixture of 100% WTPS had 11% of sand in its composition;

- The non-linearity of growth or decrease in the variations in the percentages of the soil + WTPS mixtures can be attributed mainly to the variability of the sludge granulometry, which is affected depending on the place of water collection, the time of year and what happens around the sludge collection place;

- Analyzing all samples using the Unified Soil Classification System (USCS), mixtures 1, 2, 3 and 4 were classified as medium to high plasticity silt (MH); mixture 5 was classified as poorly graded silty gravel (GP-GM);

- Evaluating the materials by the TRB classification system, it fits mixtures 1, 2, 3 and 4 as A-7-5, typical classification of silty clay materials with moderate plasticity index in relation to the liquid limit, being subject to high changes volume and may be excessively elastic. WTPS was classified as A-2-7 (high plasticity silty stony soil).

For the granulometry test with defloculant, in Table 2, it is possible to observe that:

- With the increase of sludge in the mixtures there was a tendency of growth in the percentage of clay, if compared to the natural soil. Furthermore, the percentage of 33% of silt was maintained for mixtures 1, 2 and 3, and for mixture 4 it decreased to 27%. Furthermore, mixtures 1, 2, 3 had more than 70% of their fractions composed of fine materials and M4 more than 50%. M5, on the other hand, showed a predominance of silty stony;

- There was a tendency to increase the percentages of fine sand and gravel. The percentage of coarse sand remained the same for mixtures 1, 2, 3 and 4. In addition, coarse sand remained the same for M1, M2, M3 and M4;

- Analyzing the materials by the TRB classification system, it fits mixtures 1, 2, 3 and 4 as A-7-5. The WTPS was classified as A-4 (low compressibility silty soil). In the Unified Soil Classification System, mixtures 1, 2, 3 and 4 were classified as high compressibility clays (CH). Mixture 5, which is composed only of WTPS, was classified as GP-GM.

In general, comparing the mixtures tested without defloculant and with defloculant, it is noted that the classes of gravel and medium sand remained similar. In relation to the fractions of coarse sand, fine sand and silt, there was a decrease in these percentages and, consequently, an increase in the clay fraction, showing the efficiency of the defloculant.

Regarding the unit weight of soil particles, Pinto (2006) points out that this parameter is around 2.7 g/cm^3 for clayey soils. In the case of sandy soils this value may be lower, around 2.65 g/cm^3. In lateritic clays, the unit weight of soil particles can reach values of up to 3 g/cm^3. Therefore, by Table 2, the average value of 3.009 g/cm^3 for unit weight of soil particles, found in Mixture 1, is a plausible value for lateritic clayey soils, therefore, being consistent with the local soil.

The increase in sludge in the mixtures caused the unit weight to decrease, with values of 2.945 g/cm^3, 2.694 g/cm^3, 2.590 g/cm^3 and 2.559 g/cm^3 for mixtures 2, 3, 4 and 5, respectively. This decrease with the addition of sludge occurred because the sludge has a lower unit weight than the soil under study. This situation was also verified in the study by Knierim (2020), which in mixtures 100% soil, 85% soil + 15% WTPS, 70% soil + 30% WTPS and 50% soil + 50% WTPS, a reduction of 2.702 g/cm^3 of the 100% soil mixture to 2.297 g/cm^3 of the 50% soil + 50% WTPS mixture.

The Plasticity Index determines the plasticity of the soil and the amount of water that must be added to the mixture to change it from the plastic to the liquid state. Observing the Atterberg limit tests, according to Table 2, the PI value in Mixture 1 was 20%, considered of high plasticity (20% ≤ PI ≤ 40%). For Mixtures 2, 3 and 4, although with a small variation in the LL and PL values, the Plasticity Index was 21%, also considered to be of high plasticity. This high plasticity can be credited to the greater presence of clay in the samples. Also, from Table 2, it can be seen that there is a small variation in the values of LL and PL with the increase of WTPS. Although 50% of the soil was replaced by WTPS, there was practically no change in the parameters.

Comparing the results found in this chapter with those of Montalvan (2016) and Delgado (2016), it can be seen that both authors found higher proportions of fine materials in the sludge, while in this study more granular materials were found in the sludge. It was also found that Delgado (2016) found WTPS Atterberg limits to be non-plastic. Finally, it is noted that in the study by Montalvan (2016) there was a lack of linearity in the increases or decreases of the fractions in the mixtures according to the increment of sludge.

As previously mentioned, the WTPS have great variation in characteristics, which depend on the water potability system used in each station and on the water collection site, so the differences at this stage of the study are justified.

3.2 Chemical analysis tests

The chemical analysis test was performed for the four mixtures under study and also for a sample of 100% WTPS (M5), and the results are shown in Table 3 for Mixtures 1, 2, 3, 4 and 5.

From the correlation with values of Cation Exchange Capacity - CEC - it is possible to know the clay mineral present in the structure of the material under study, which helps in the perception of the behavior of the material.

According to the results achieved in the chemical analysis (Table 3) of Mixture 1, soil saturation by bases of 38% was verified, a characteristic value of dystrophic soils, with low fertility (Vasconcellos, 1986). The aluminum saturation is less than 50%, which means that the amount of aluminum present in the soil is not toxic to the plants present in the place. The CEC value was exactly 10 cmolc/L, which according to the usual values of Ronquim (2010) indicates that there is presence of kaolinite in the soil and, possibly, there is also illite, which is a clay mineral with a tendency to have medium expandability. In relation to the values of OM and pH of the soil, they indicate little presence of organic matter and that the acidity of the soil is high (Vasconcellos, 1986).

Based on the results of the Mixture 85% Soil + 15% WTPS, according to Table 3, they showed that the mixture under analysis presents a saturation of the material by bases of 52.1%, which characterizes the material as being eutrophic (with high fertility). The aluminum saturation is 1.8%, which means that M2 is not toxic to plants. Still, the mixture presented 10.2 cmolc/kg of CEC, which characterizes a material constituted by kaolinite and illite. Moreover, the mixture showed little presence of organic matter (OM) and low pH, indicating a material of high acidity.

From Table 3, it is noted that the material present in M3, due to aluminum saturation, is not toxic, as it has zero saturation. Analyzing the base saturation (63%) the mixture can be characterized as eutrophic, with high fertility. In the CEC value, the value of 10.6 cmol/L was obtained, which means that there is presence of kaolinite and illite in the mixture. The mixture also showed low values of OM (1.7%) and pH (5.2) indicating little presence of organic matter and that the acidity of the material is medium.

According to the results achieved in the chemical analysis of Mixture 4 (Table 3), there was a saturation of the material by bases of 73.5%, a characteristic value of eutrophic soils, with high fertility. Again, the aluminum saturation is null, which means that the mixture is not toxic to the plants present in the place. The CEC value was exactly 11.7 cmolc/L, which means that kaolinite is present in addition to illite. In relation to the values of OM and pH of the material, they indicate little presence of organic matter and a low acidity.

The results of Table 3, for Mixture 100% WTPS, showed that the mixture under analysis presents a saturation of the mixture by bases of 81.8%, which characterizes the material as being eutrophic (with high fertility). The aluminum saturation is zero, which means that M5 is not toxic to plants. Still, the material presented 13.8 cmolc/kg of CEC, which characterizes a mixture constituted by illite and kaolinite. In relation to OM, the mixture showed little presence of organic matter and pH indicating a material with very low acidity. The result of the chemical analysis also indicates that Mixture 5 has a low amount of clay compared to the other mixtures, about 22%.

Analyzing the results found for the sludge with those of Montalvan (2016) and Knierim (2020) there are some results close to those of this study, but for the most part they differ, once again confirming the heterogeneity of the sludge in each WTP.

3.3 Compaction tests

With the compaction curves, the optimal moisture content and maximum dry density (MDD) were obtained, and the Table 4 illustrates the optimal compaction parameters of mixtures 1, 2, 3 and 4.

Table 3. Chemical analysis of the mixtures under study (LASTV, 2020a, b, c, d, e).

Mixtures	Clay (%)	pH/ H_2O	SMP Index	P (mg/L)	K (mg/L)	OM (%)	Al (cmolc/L)	Ca (cmolc/L)
M1 (100% Soil)	79	4.7	5.7	2.1	36.5	0.9	0.6	2.8
M2 (85% Soil + 15% WTPS)	65	4.9	5.9	3.2	49.5	1.4	0.1	4
M3 (70% Soil + 30% WTPS)	51	5.2	6.1	4.8	61	1.7	0	5.1
M4 (50% Soil + 50% WTPS)	40	5.7	6.3	7.1	80	2.4	0	6.7
M5 (100% WTPS)	22	6.2	6.5	7.1	107.5	3.5	0	9
	Mg (cmolc/L)	CEC (cmolc/L)	H + L (cmolc/L)	% Sat. of CEC		Relations		
				Bases	Al	Ca/Mg	Ca/K	Mg/K
M1 (100% Soil)	0.9	10	6.2	38	13.7	3.1	30	9.6
M2 (85% Soil + 15% WTPS)	1.2	10.2	4.9	52.1	1.8	3.3	31.6	9.5
M3 (70% Soil + 30% WTPS)	1.4	10.6	3.9	63	0	3.6	32.7	9
M4 (50% Soil + 50% WTPS)	1.7	11.7	3.1	73.5	0	3.9	32.7	8.3
M5 (100% WTPS)	2	13.8	2.5	81.8	0	4.5	32.7	7.3

Analyzing the Table 4, In general, there was an increase in optimal moisture content and decreased the MDD in the mixes. This can be explained because the sludge is lighter than the soil, causing the MDD to decrease in mixtures 2, 3 and 4. Still, it was identified that with the increase of WTPS there is a tendency that there is an increase of the optimal moisture content, since it has a higher natural moisture content, as well as a greater power of absorption of water compared to the soil.

From the results presented in Table 4, it was possible to observe that with the addition of 15% of WTP sludge to the soil there was a small decrease in MDD, this reduction being about 2.7% in relation to the soil. With the addition of 30% and 50% of sludge, the decrease was 3.16% and 6.11%, respectively, in relation to M1. It was also identified an increase in optimal moisture of about 7.7% and 15.62%, in the proper order of M2 and M4 in relation to the soil. That is, in the maximum dry apparent specific weight there was a tendency to decrease and in the optimal moisture content there was a tendency to increase, with an exception in this last criterion in M3 which was slightly lower than M2, but even so they were close values.

The results obtained in this research are in line with the results found by Delgado (2016). In his study, the author analyzed a clayey soil + 5% WTPS, presenting a behavior similar to that of this study: after the addition of 5% of sludge, there was a decrease of about 8% in the maximum dry apparent specific weight and an increase in the moisture content of about 32.4%, when compared to values obtained only from clayey soil. The same author also studied the percentages of 5%, 10% and 15% of sludge mixed with stone dust, even though they were not equivalent soils, the author also found a decrease in MDASW with increasing sludge in the mixtures. For the mixtures of 5% and 10%, he found equal optimum moisture content values and for the mixture of 15%, a higher moisture content than that found for the other two samples. This small variation of the optimum moisture content for M2 and M3 of the present research and the non-variation for 5% and 10% of the research by Delgado (2016) are justified by the heterogeneity of the WTPS.

According to Lucena (2012), the decrease in the maximum dry density and the increase in water absorption caused after the addition of sludge in the mixture is due to the mineralogical composition of the particles, because the sludge has a considerable surface area, its high void and for its porosity.

3.4 Simple compression strength tests

The unconfined compressive strength (UCS) tests followed the instructions described in the methodology, and the results are presented in Table 5. The soil presented an average UCS of 0.255 MPa for both 7 and 28 days of curing, which is consistent with the UCS of clayey soils. The replacement of soil by WTPS, in all mixtures, showed an increase in UCS compared to soil, and the best performance was presented by the mixture of 70% Soil + 30% WTPS, with UCS of 0.619 MPa, with an increase of 142.75% of average resistance superior to the soil. It is noteworthy that Knierim (2020) also found in her studies the same mixture presenting the highest resistance when compared to soil.

Mixture 2 presented 34.51% and 36.47% of average UCS above the soil for the ages of 7 and 28 days, respectively. M3 showed an average resistance of 56.47% above the soil for the 7 days. Finally, the mixture 50% Soil + 50% WTPS showed average strengths of 42.75% and 102.75% for 7 and 28 days, respectively.

It is noticeable, through Table 5, that with the increase in the curing time, there was also an increase in resistance for M2, M3 and M4. It is believed that this occurred due to the presence of some chemical material present in the WTPS.

Soil replacements by WTPS made it possible to increase SCS in the samples up to 30% replacement, while at 50% there was a decrease in relation to M3. This situation possibly occurred due to the different behavior of the WTPS, which tends to increase the friction between the particles and, consequently, increase the compressive strength of the samples. This fact is in line with the study by Knierim (2020), where the author found that the addition of WTP sludge in the mixtures tended to increase SCS compared to soil. And, in the highest proportion of WTPS, there was a small reduction in the parameter, but still remaining superior to the natural soil, as also occurred in this work.

3.5 Permeability tests

The permeability tests followed the instructions presented in the methodology, in order to determine the permeability coefficient of soil and soil + WTPS mixtures, for samples compacted at intermediate energy. The permeability coefficient values are presented in Table 6.

It is observed that the soil under study presented an average permeability coefficient (k) of 1.66E^{-8} m/s, which

Table 4. Chemical analysis of the mixtures under study.

Mixtures	Mixture 1	Mixture 2	Mixture 3	Mixture 4
Maximum dry density (g/cm³)	1.521	1.480	1.473	1.428
Optimum moisture content (%)	28.3	30.48	29.98	32.72

according to Terzaghi & Peck (1967) represent soils with very low permeability (k from 1E^{-7} to 1E^{-9} m/s).

In the mixture 85% Soil + 15% WTPS, when substituting 15% of the soil for WTPS, there was a reduction in the permeability coefficient value of the mixture when compared to the soil. The average permeability coefficient was 1.71E^{-9} m/s; the mixture 70% Soil + 30% WTPS showed an average permeability coefficient of 2.44E^{-9} m/s; the mixture 50% Soil + 50% WTPS presented an average coefficient of 2.03E^{-9} m/s. All results found, for all mixtures, are characteristic of materials with very low permeability.

Although the WTPS presents a different behavior, it is believed that, in this case, the inclusion of the material in the soil caused a better intermeshing of the particles, reducing the permeability coefficient value and making the mixtures more impermeable compared to the natural soil. This occurred, possibly, because even with the decrease of the clay percentage, the silt percentage remained practically stable with the increase of sludge in the tests with defloculant and this silt filled the lack of clay material, reducing the void index.

Knierim (2020) found permeability values that did not follow a linearity, where for 85% Soil + 15% WTPS the coefficient decreased in relation to the soil and increased for the other mixtures. These results are in agreement with the present research, and the difference in the results between the two studies was generated by the different granulometry of the sludge in each study.

3.6 Analysis of the technical viability of using the mixtures in bottom layers and final cover of sanitary landfills

In this item, we sought to analyze the application of the materials under study in bottom layers and in the final cover

Table 5. Average unconfined compressive strength test results for the mixtures.

Mixture	Time of curing	UCS (MPa)
M1 (100% Soil)	7 days	0.255
	28 days	0.255
M2 (85% Soil + 15% WTPS)	7 days	0.343
	28 days	0.348
M3 (70% Soil + 30% WTPS)	7 days	0.399
	28 days	0.619
M4 (50% Soil + 50% WTPS)	7 days	0.364
	28 days	0.517

Table 6. Permeability coefficient of the mixtures under study.

Mixture	k (m/s)
M1 (100% Soil)	1.66E^{-8}
M2 (85% Soil + 15% WTPS)	1.71E^{-9}
M3 (70% Soil + 30% WTPS)	2.44E^{-9}
M4 (50% Soil + 50% WTPS)	2.03E^{-9}

of sanitary landfills. For this, it was made a compilation of mandatory requirements, standards, and desirable, found in research. Requirements specified with "NBR" are from Brazilian Standards, from "USEPA" are from the United States Environmental Protection Agency and with "German" are from German standards. Then, due to the imposed conditions, a checklist was carried out to verify the possibility of application of each of the materials. To facilitate this analysis, the requirements were compiled in Table 7.

Regarding Table 7, the following analyzes can be made:
- Regarding the final covering layer, all mixtures complied with the permeability coefficient requirements of NBR and USEPA, however, none of the mixtures met the criteria of the German standard. In addition, all other requirements for percentage passing through sieve #200, liquid limit, plasticity index and USCS classifications were met.
- Regarding the bottom layer, all mixtures complied with the permeability coefficient requirements of the Brazilian standard, however, M1 did not respect the same requirement of the US standard and no mixture met the criterion of the German standard. In addition, all other requirements for percentage passing through sieve #200, liquid limit, plasticity index and USCS classifications were met.

Still, together with the results discussed, as well as the others obtained in the research, the following considerations can be made:
- The chemical analyzes carried out in this research showed that all materials tend to have kaolinite in their composition, causing no material to be prevented from being applied in layers of sanitary landfills due to possible expansion problems;
- The simple compressive strength of soil + WTPS mixtures showed improvement compared to soil. The best performance in this regard occurred in the mixture 70% Soil + 30% WTPS and, together with the requirements presented in Table 7, it is the most favorable for application in bottom layers and final cover of sanitary landfills;

It is important to highlight that, analyzing only the requirements of the Brazilian standard, the soil and all mixtures meet the minimum requirements of the same, therefore, being subject to use in the bottom layer and final cover of sanitary landfills. In this specific analysis, the material with the best performance is the mixture 70% Soil + 30% WTPS, for the following reasons: it meets the permeability coefficient and presents the highest resistance to simple compression among all mixtures.

It is also indicated the use of the materials under study as intermediate layers (daily), since there are no requirements and recommendations for these. Authors cited in the theoretical framework indicate the use of organic compounds, WTPS and Sewage Treatment Sludge for these layers, therefore, the use of mixtures (mainly the mixture 50% Soil + 50% WTPS)

8

Mazzutti et al., Soil. Rocks, São Paulo, 2023 46(1):e2023011222

Table 7. Verification of the mixtures under study for use in layers of sanitary landfills.

Parameter		Condition for application	Requirements		Material / Application Verification			
			M	D	M1	M2	M3	M4
Final cover layer	k (NBR) [m/s]	$\leq 5\times10^{-7}$	X		YES	YES	YES	YES
	k (USEPA) [m/s]	$\leq 10^{-7}$	X		YES	YES	YES	YES
	k (German) [m/s]	$\leq 5\times10^{-10}$	X		NO	NO	NO	NO
	SP#200 (USEPA) [%]	≥ 30	X		YES	YES	YES	YES
	SP#200 [%]	≥ 40		X	YES	YES	YES	YES
	LL (USEPA) [%]	≥ 30	X		YES	YES	YES	YES
	LL [%]	≥ 30		X	YES	YES	YES	YES
	PI [%]	10 a 50		X	YES	YES	YES	YES
	USCS	CL/CH/SC/OH		X	YES	YES	YES	YES
Background layer	k (NBR) [m/s]	$\leq 10^{-8}$		X	YES	YES	YES	YES
	k (USEPA) [m/s]	$\leq 10^{-9}$	X		NO	YES	YES	YES
	k (German) [m/s]	$\leq 10^{-10}$	X		NO	NO	NO	NO
	SP#200 [%]	≥ 30		X	YES	YES	YES	YES
	LL [%]	≥ 30		X	YES	YES	YES	YES
	PI [%]	≥ 15		X	YES	YES	YES	YES
	USCS	CL/CH/SC/OH		X	YES	YES	YES	YES

k: permeability; SP: sieve pass; LL: liquid limit; PI: plasticity index; M: mandatory; D: desirable.

would be beneficial, due to the reduction the exploitation of natural resources (soil) and the reduction of environmental liabilities with the use of WTPS.

4. Conclusion

The classic results of Soil Mechanics characterized the soil as a clayey material. Still, in the WTPS additions to the soil, it was noticeable, with the increase of substitution, a reduction in the fractions of silt and sand, and an increase in clay and gravel. The inclusion of WTPS, in terms of consistency, made the mixtures even more plastic. The real specific weight of the soil grains is within the lateritic clayey soil standard, and as the percentage of WTPS in the soil increased, there was a reduction in the parameter, due to the low real specific weight of the sludge grains.

In specific to the chemical analysis of the soil and mixtures, it is highlighted that all presented kaolinite and illite, non-expandable and partially expandable clay minerals, respectively, so that no material was prevented from being applied in layers of sanitary landfills due to the low possibility of expansion problems.

In relation to the results obtained in the compaction test of the materials under study, it could be seen that the greater the addition of WTPS to the soil, the greater the decrease in the value of the maximum dry density. In addition, there was an increase in the optimal moisture content found with increasing sludge content in the soil. This situation can be credited to the low real specific weight of the grains of the mixtures.

The permeability test showed an increase in the impermeability of the mixtures, being beneficial in terms of application in engineering works. The permeability coefficient of the soil and mixtures was in the order of $1E^{-9}$, characterizing the materials as having high impermeability.

Regarding the mechanical tests, from the unconfined compressive strength tests, it was possible to conclude that there was an increase in resistance with the increase of sludge in the mixtures, and the mixture that presented the highest SCS was 70% soil + 30% WTPS at 28 days, with a resistance 142.75% superior to the soil.

In general terms, following ABNT NBR 13896 (ABNT, 1997), which defines the criteria for non-hazardous waste landfills, the mixture composed of 70% Soil + 30% WTPS was defined as the best for application in base layers and covering of landfills for meeting the permeability coefficient and presenting the highest Simple Compression Strength among all mixtures. However, the other mixtures (85% Soil + 15% WTPS and 50% Soil + 50% WTPS) could also be used, contributing to a circular economy and to Environmental, Social and Governance (ESG), a term used to refer to the what companies and entities are doing to be socially responsible, environmentally sustainable and managed correctly.

In addition, it is noteworthy that the use of mixtures, especially 50% Soil + 50% WTPS, in daily (intermediate) layers would be a sustainable alternative that cooperates to achieve Sustainable Development Goals 11, 12 and 15 of the United Nations United until 2030. The co-disposal of sludge is presented as a gain for the management of this waste, mainly for small WTPs, since, once its potential is observed, the stations can use this technique, minimizing the volume of waste that could be sent to the sanitary landfill, as well as avoiding the implementation of more costly technologies.

It is also noteworthy that the sludge showed excellent characteristics for other applications in specific quantities in geotechnics such as base layers, sub-base, subgrade reinforcement and landfills in general. There is the possibility of quantifying the sludge from the WTP, for tokenization (process by which an asset gains a digital representation) and generation of recycling credits in the Bitcoin Market, contributing to a better destination of this residue and to the generation of revenue for the Water Treatment Station. In addition, mixtures with sludge accelerate the decomposition of waste and increase the production of methane in landfills (Granato, 2010), thus, projects that perform the clean burning of methane can increase the tons burned, generating even more carbon credits and electricity, clean and renewable during firing, consequently also producing higher revenue.

These applications would bring advantages in the destination of WTPS and reduction of consumption of natural resources (soil). In this way, the benefits and importance of an adequate disposal of sludge in geotechnics are evident, in order to avoid environmental liabilities generated by this residue, in addition to acting in an innovative, technological and sustainable way, minimizing the use of natural resources with economically efficient solutions, profitable and environmentally advantageous in engineering works.

Acknowledgements

Declaration of interest

The authors have no conflicts of interest to declare. All co-authors have observed and affirmed the contents of the paper and there is no financial interest to report.

Authors' contributions

Elisangela Aparecida Mazzutti: data curation, formal analysis, investigation, visualization, writing – original draft. Rodrigo André Klamt: conceptualization, data curation, funding acquisition, resources, methodology, supervision, validation, writing – original draft. Vítor Pereira Faro: methodology, project administration, supervision, validation, writing – review & editing.

Data availability

All data produced or examined in the course of the current study are included in this article.

List of symbols

k	Permeability
A-4	Low compressibility silty material
A-7-5	Silty clay material with moderate Plasticity Index
CEC	Cation Exchange Capacity
FW	Frederico Westphalen
LL	Liquidity Limit
MH	Medium to High Plasticity Silt
ML	Low Compressibility Silt
NP	Not Plastic
OH	Medium to high plasticity organic clay
PH	Hydrogen potential
PI	Plasticity Limit
PL	Plasticity Index
RS	Rio Grande do Sul
SC	Clayey Sand
SP	Sieve Pass;
TRB	Transportation Research Board
UCS	Unconfined compressive strength
USCS	Unified Soil Classification System
USEPA	United States Environmental Protection Agency
WTPS	Water Treatment Plant Sludge
WTS	Water Treatment Stations
γ_s	Unit weight of soil particles;

References

ABNT NBR 13896. (1997). *Aterro de resíduos não perigosos – Critérios para projeto, implantação e operação*. ABNT – Associação Brasileira de Normas Técnicas, Rio de Janeiro, RJ (in Portuguese).

ABNT NBR 14545. (2000). *Solo – Determinação do coeficiente de permeabilidade de solos argilosos a carga variável*. ABNT – Associação Brasileira de Normas Técnicas, Rio de Janeiro, RJ (in Portuguese).

ABNT NBR 10004. (2004). *Resíduos sólidos – classificação*. ABNT – Associação Brasileira de Normas Técnicas, Rio de Janeiro, RJ (in Portuguese).

ABNT NBR 12025. (2012). *Solo-cimento - Ensaio de compressão simples de corpos de prova cilíndricos - Método de ensaio*. ABNT – Associação Brasileira de Normas Técnicas, Rio de Janeiro, RJ (in Portuguese).

ABNT NBR 6458. (2016a). *Grãos de pedregulho retidos na peneira de abertura 4,8 mm - Determinação da massa específica, da massa específica aparente e da absorção de água*. ABNT – Associação Brasileira de Normas Técnicas, Rio de Janeiro, RJ (in Portuguese).

ABNT NBR 7180. (2016b). *Solo – Determinação do Limite de Plasticidade*. ABNT – Associação Brasileira de Normas Técnicas, Rio de Janeiro, RJ (in Portuguese).

ABNT NBR 9604. (2016c). *Abertura de Poço e Trincheira de Inspeção em Solo, com Retirada de Amostras Deformadas e Indeformadas*. ABNT – Associação Brasileira de Normas Técnicas, Rio de Janeiro, RJ (in Portuguese).

ABNT NBR 6459. (2017). *Solo – Determinação do Limite de Liquidez*. ABNT – Associação Brasileira de Normas Técnicas, Rio de Janeiro, RJ (in Portuguese).

ABNT NBR 7181. (2018). *Solo – Análise Granulométrica*. ABNT – Associação Brasileira de Normas Técnicas, Rio de Janeiro, RJ (in Portuguese).

ABNT NBR 7182. (2020). *Solo – Ensaio de Compactação*. ABNT – Associação Brasileira de Normas Técnicas, Rio de Janeiro, RJ (in Portuguese).

Achon, C.L., & Cordeiro, J.S. (2015). Destinação e disposição final de lodo gerado em ETA - Lei 12.305/2010. In *Anais do XIX Exposição de Experiências Municipais em Saneamento*. Poços de Caldas, Brazil (in Portuguese).

Brasil. Conselho Nacional do Meio Ambiente – CONAMA. (2005). Resolução CONAMA n° 357, de 17 de março de 2005. Dispõe sobre a classificação dos corpos de água e diretrizes ambientais para o seu enquadramento, bem como estabelece as condições e padrões de lançamento de efluentes, e dá outras providências. *Diário Oficial [da] República Federativa do Brasil*.

Castro, C.E. (2014). *Uso de lodo de estação de tratamento de água (LETA) para fabricação de pavimentos pré-moldados de concreto* [Master's dissertation]. Federal University of Itajubá (in Portuguese).

Cremades, L.V., Cusidó, J.A., & Arteaga, F. (2018). Recycling of sludge from drinking water treatment as ceramic material for the manufacture of tiles. *Journal of Cleaner Production*, 201, 1071-1080. http://dx.doi.org/10.1016/j.jclepro.2018.08.094.

Delgado, J.V.C. (2016). *Avaliação da aplicação do lodo da ETA Guandu na pavimentação como disposição final ambientalmente adequada* [Master's dissertation]. Federal University of Rio de Janeiro (in Portuguese).

Ferreira, G., Barbosa, K.T., Quadro, M.S., Trindade, G.H., Beltrame, R, Morselli, L.B.G.A., & Andreazza, R. (2022). Use of sludge from a water treatment plant processed as a supplementary material to Portland cement. *Engenharia Sanitária e Ambiental*, 27(4), 653-661. https://doi.org/10.1590/S1413-415220210035.

German Standard. (1993). *TA siedlungsabfall: technishe anleitung zur verwertung, behandlung und sonstigen entsorgung von siedlungsabfällen. Dritte Allgemeine Verwaltungsvorschrift zum Abfallgesetz: BAnz*. Bundesanzeiger, Berlin. NR. 99ª. 65 seiten. vom 1993. (in German).

Granato, T.C. (2010). Biosolids land application by the metropolitan water reclamation district of greater Chica-go: an overview of the program, its benefits, and environmental impacts. In *Anais do Simpósio Interamericano de Biossólidos*. Campinas, Brazil (in Portuguese).

Guimarães, M.G.A., & Urashima, D.C. (2013). Dewatering sludge in geotextile closed systems: brazilian experiences. *Soils and Rocks*, 36(3), 251-263. http://dx.doi.org/10.28927/SR.363251.

Knierim, L.D.S. (2020). *Study of the mechanical and hydric behavior of the use of water treatment station sludge in mixtures with lateritic clay soil* [Master's dissertation]. Federal University of Santa Maria (in Portuguese).

LASTV. (2020a). *Laudo n° 8255418: análise química básica do solo de Frederico Westphalen/RS (Mistura 1). Laboratório de Análise de Solos e Tecidos Vegetais*, Universidade Regional Integrada do Alto Uruguai e das Missões (URI), Frederico Westphalen, Brazil (in Portuguese).

LASTV. (2020b). *Laudo n° 8255419: análise química básica da amostra 85% Solo + 15% LETA (Mistura 2). Laboratório de Análise de Solos e Tecidos Vegetais*. Universidade Regional Integrada do Alto Uruguai e das Missões (URI), Frederico Westphalen, Brazil (in Portuguese).

LASTV. (2020c). *Laudo n° 8255420: análise química básica da amostra 70% Solo + 30% LETA (Mistura 3). Laboratório de Análise de Solos e Tecidos Vegetais*. Universidade Regional Integrada do Alto Uruguai e das Missões (URI), Frederico Westphalen, Brazil (in Portuguese).

LASTV. (2020d). *Laudo n° 8255421: análise química básica da amostra 50% Solo + 50% LETA (Mistura 4). Laboratório de Análise de Solos e Tecidos Vegetais*. Universidade Regional Integrada do Alto Uruguai e das Missões (URI), Frederico Westphalen, Brazil (in Portuguese).

LASTV. (2020e). *Laudo n° 8255422: análise química básica do resíduo da Estação de Tratamento de Água de Frederico Westphalen/RS (Mistura 5)*. Laboratório de Análise de Solos e Tecidos Vegetais, Universidade Regional Integrada do Alto Uruguai e das Missões (URI), Frederico Westphalen, Brazil (in Portuguese).

Lucena, L.C. (2012). *Study of the use of soil and sludge mixture from water and sewage treatment stations for application in base and subbase in paving* [Doctoral thesis]. Federal University of Pernambuco (in Portuguese).

Martinez, J.G. (2014). *Performance evaluation of bituminous mixtures with addition of sludge water and sewage sludge* [Master's dissertation]. University of Brasília repository (in Portuguese). https://repositorio.unb.br/handle/10482/16690

Medaoud, S., Mokrani, L., Mezhoud, S., & Ziane, S. (2022). Characterization of stabilised sewage sludge for reuse in road pavement. *Sciendo*, 32(1), 201-207. https://doi.org/10.2478/ceer-2022-0012.

Montalvan, E.L.T. (2016). *Research on the geotechnical behavior of mixtures of sandy soil with sludge from Cubatão water treatment plant* [Master's dissertation]. Polytechnic School, University of São Paulo (in Portuguese). https://doi.org/10.11606/D.3.2016.tde-02122016-091816.

Pinto, C.S. (2006). *Curso básico de mecânica dos solos*. 3. ed. Oficina de Textos (in Portuguese).

Ronquim, C.C. (2010). *Conceitos de fertilidade do solo e manejo adequado para as regiões tropicais*. Embrapa Monitoramento por Satélite (in Portuguese).

Roque, A., Montalvan, E.L.T., & Boscov, M.E.G. (2022). Reuse of water treatment plant sludge mixed with lateritic

soil in geotechnical works. *Environmental Challenges*, 7, 100465. http://dx.doi.org/10.1016/j.envc.2022.100465.

Santos, G.Z.B.D., Melo Filho, J.D.A., & Manzato, L. (2018). Prospects of technological applications of sludge from water treatment process of the Negro and Solimões rivers. *Revista Matéria*, 23(3), 1-14. https://doi.org/10.1590/S1517-707620180003.0501.

Terzaghi, K., & Peck, R.B. (1967). *Soil mechanics in engineering practice* (2nd ed.). John Willey & Sons.

United States Environmental Protection Agency – USEPA. (1998). *Guidance for Design and Installation of Final Covers. 40 CFR 258.2*. USEPA.

United States Environmental Protection Agency – USEPA. (2003). *Evapotranspiration Landfill Cover Systems Fact Sheet. Solid Waste and Emergency Response. EPA 542-F-03-015. Agency (5102G)*. USEPA.

Vasconcellos, C.A. (1986). *Análise de solo: entendimento e interpretação. Apostila do Curso de Uso e Manejo da Irrigação*. EMBRAPA. (in Portuguese).

The cavity's effect on the bearing capacity of a shallow footing in reinforced slope sand

Bendaas Azeddine[1#] (iD), Merdas Abdelghani[1] (iD)

Article

Keywords
Reinforced
Bearing capacity
Sand slope
PVC pipe

Abstract

This paper presents an experimental and numerical study for the effect of the cavity on the behaviour of a strip footing positioned on a reinforced sand slope. This study used a new type of geosynthetics called fiber carbon and fiber glass. These components have the potential to isolate the soil inside the geosynthetic and prevent shears stress mobilization. The investigation aimed to determine the effect of cavity depth (h) and the number of reinforcing layers (N) on the bearing capacity and settlement characteristics of footing, empirically for investigating the effect of cavity on the bearing capacity, some parameters were assumed constant in all tests, for example, relative density, a distance of the footing from the slope edge, and length between layers of reinforcement. The variable parameters are the distance between footings and centre of cavity and the number of reinforcing layers. The results show that the settlement behaviour of footing adjacent to a soil slope is significantly affected by h and N. It is observed that qu, which represents the ultimate bearing capacity, improves with an increase in N. The influence of the cavity appeared insignificant when it was positioned at a depth equal to twice the width of footing.

1. Introduction

Bearing capacity and settlement are important factors in the construction of many types of geotechnical structures, particularly in hilly areas where it is necessary that foundations of those structures to be constructed on sloping grounds. Examples of such projects include buildings, electrical transmission towers, and bridges.

When a footing is constructed near a slope, the bearing capacity is relatively reduced compared to the footing on level ground. Having a strong grasp of the response of footing built close to slopes, particularly slope with a cavity, is crucial to the stability of structures, which can be expressed in terms of factor of safety.

Cavities are associated with tunnels, rail ways and canals, water, sewage, gas pipes, and power lines. All these cavities are affecting the ground stability. Knowing the location of the cavity and the characteristics of the materials formed in the cavities is an essential factor in ensuring the soils stability and choosing good reinforcement (Culshaw & Waltham, 1987).

Under such conditions, solutions such as improving the geometry of sloping surfaces, injections, or use of soil reinforcement are required to improve the bearing capacity of foundations and reinforce the slope with geosynthetic layers (Afshar & Ghazavi, 2014). Soil reinforcement is considered a suitable method for improving the bearing capacity of footing that can widen the road and repair collapsed slopes (Al-Jazaairry & Toma-Sabbagh, 2017; Leshchinsky, 1997).

The literature has shown that the performance of the surface footing can be influenced by other parameters such as the geometrical slope parameters (footing shape, slope angle and height, void size, and void shape), slope soil properties (total unit weight, cohesiveness, and angle of shearing resistance), the type of geosynthetic reinforcement used and the arrangement of the geosynthetic reinforcement layers, depth of top layer, the number and vertical spacing of layers. According to the majority of researchers, placing geosynthetic reinforcing layers at the proper places inside slopes may substantially enhance the bearing capacity and reduce settlements of footings located on the crest of hills. Dahoua et al. (2018) proposed a mathematical approach for estimating the stability of geotextile reinforcements. According to the void size and position, the experimental observation of Kiyosumi et al. (2011) demonstrated three sorts of failure modes for a single void. Upper-bound calculations were presented to interpret the observed changes in bearing capacity.

Kolay et al. (2013) studied a footing placed on double-layer soil to find the load-settlement for reinforced and

Azeddine & Abdelghani, Soil. Rocks, São Paulo, 2023 46(1):e2023003622

1

unreinforced soils and noticed that the increment of load-bearing capacity is dependent on the number of reinforcement layers. Zahri et al. (2016) proposed a multi-step method for analysing slope stability in open pit mines.

An investigation of the influence of a cavity on geogrid reinforced soil was carried out by Kapoor et al. (2019). The presence of cavities at specific depths was investigated and an analysis was performed to determine the load-bearing capacity and settlement of a footing on a geogrid-reinforced surface. The Plaxis-2D (v8) finite element package with the Mohr-Coulomb model was used to assess the elastic failure and determine the effect of many factors, such as the number of geogrid layers utilized, the spacing between each successive layer, the position of the cavity and its size, as well as the depth of the footing.

Results of recent research conducted by Zhou et al. (2018) demonstrate that the undrained bearing capacity with voids responds to soil features, and that the failure mechanism is related to numerous soil parameters, the location of single voids, and the straight distance between two voids.

According to Zhao et al. (2018), the stability analysis of asymmetrical cavities is conducted using the upper limit technique. The findings suggest that the local shear failure type is the eldest in the soil around the cavity. The stability is augmented with an increase in the friction angle and reduced with an increase in the horizontal distance and descriptor diameter values.

Xiao et al. (2018) used finite element limit analysis to examine the undrained bearing capacity of strip footing over voids in two-layered clays, and to provide charts and formulas to calculate the undrained bearing capacity factor Ns. The cited authors also examined what effect the various soil properties, including the undrained shear stress ratio, top layer thickness, void size, and spacing of voids have on the Ns factor.

On the other hand, Mansouri et al. (2021) investigated the bearing capacity-settlement of footing on a slope with void and the effect of several factors, such as top vertical distance of void from the base of footing, horizontal space connecting the void-footing center, and load eccentricity where the subterranean void, as well as the critical depth between the soil and the top layer of the void, were found to have an impact on the stability of strip footing.

Baah-Frempong & Shukla (2020) presented the findings of laboratory model testing and numerical analysis for strip footing stability buried in a geotextile-reinforced sand slope and study. The influence of footing embedding depth (D), number of geotextile layers N on bearing capacity and settling properties of the embedded footing was investigated. Results indicate that D and N substantially influence the load-settlement behavior of the embedded footing. It is observed that bearing capacity ratio (BCRu) improves with an increase in N and reduces when D and B increase being D = B (B is the base width), while the highest BCRu was obtained when D/B = 0.

Satvati et al. (2020) developed a novel type of three-dimensional geosynthetic that outperformed geogrid in terms of decreasing soil permeability. They used a laboratory modelling method to examine the effects of different factors on the bearing capacity of footings on soil slopes. The results showed that cylindrical reinforcement has a more significant effect than planar reinforcement in terms of increasing bearing capacity and decreasing settlement under the same circumstances as certain parameters.

Saadi et al. (2020) conducted an experimental investigation on the effect of interference on the bearing capacity of two adjacent foundations in cavitated soil. The results revealed that cavities and dual footing interference affecting the bearing capacity as well as the efficiency factor when the cavity effect is eliminated by increasing the distance between the footing and the cavity. In this study, the cavity's effect on the behavior of geosynthetic reinforced footing on soil slope was investigated to evaluate some important parameters of reinforced soil, because of the lack in the literature of similar studies in this field, a set of laboratory tests to assess the effects mentioned main parameters on the reinforced slopes were performed. The conclusions of this study can be applied to future designs by geotechnical engineers to achieve a better estimation of the bearing capacity of footing on soil slopes. Also, a new type of geosynthetics was used in this study such as carbon and glass fiber reinforced polymer to reinforce the soil slope, so the effects of using this type of geosynthetics to determine the bearing capacity of the shallow footings were evaluated.
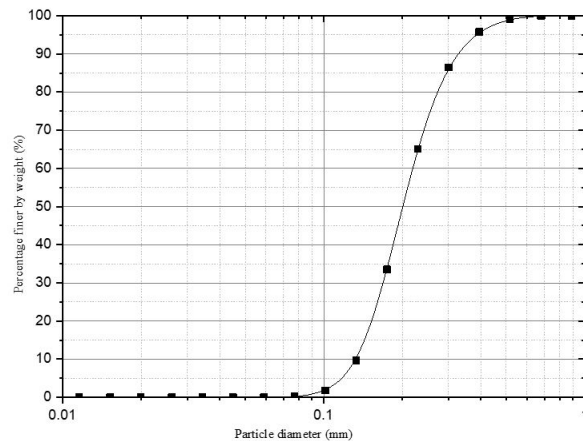
2. Experimental study

2.1 Materials

2.1.1 Soil properties

The soil used in this study is sand. Laboratory tests were performed according to test methods described in ASTM Standards to determine the geotechnical properties next; grain distribution tests were performed according to ASTM D422-63 (ASTM, 2007), the values detected of D_{10}, D_{30}, D_{60}, was performed according to ASTM D854-14 (ASTM, 2014), the mean value of specific gravity $G_s = 2.65$ was determined by pycnometer test. According to ASTM D4253-00 (ASTM, 2000), the maximum and the minimum unit weight of the sand was measured and the corresponding values of the minimum and the maximum void ratio were calculated, the relative density of sand bed as $D_r = 60\%$ resulting in a unit weight of 15.75 kN/m³, direct shear tests were performed according to ASTM D3080-90 (ASTM, 1990) to determine the shear strength parameters (c and φ). Table 1 groups the characteristics of sand and their average values. The particle-size distribution of soil is shown in Figure 1. According to the unified soil classification system (USCS), the soil is classified as poorly graded sand (SP).

Table 1. Properties of sandy soil.

Parameters	value
Specific gravity	2.65
Maximum dry unit weight, $\gamma_{d\,max}$ (kN/m³)	16.3
Minimum dry unit weight, $\gamma_{d\,min}$ (kN/m³)	15
Maximum void ratio	0.67
Minimum void ratio	0.50
Relative density, D_r (%)	60
Peak friction angle, φ (°)	38
Cohesion, c (kPa)	1
Uniformity coefficient, C_u	1.83
Coefficient of curvature, C_c	1.08
Effective particle size, D_{10} (mm)	0.185
D_{30} (mm)	0.26
D_{60} (mm)	0.34

Table 2. Summary of geosynthetics parameters.

Parameters	Fiber glass	Fiber carbon
Color	White	Black
Form	Sheet	Sheet
Thickness (mm)	0.16	0.20
Tensile modulus of elasticity (GPa)	72	231
Elongation (%)	4.9	1.9

Table 3. Properties of the PVC used.

Parameters	Value
Unit weight (kN/m³)	13.5 - 14.5
Tensile strength (MPa)	45
Elongation %	80
Elastic modulus (MPa)	3000

Figure 1. Particle-size distribution of soil.

Figure 2. Fiber glass and carbon fiber elements used in this study.

2.1.2 Geosynthetic properties

Modern geosynthetics such as fiber glass and carbon fiber were used to verify the results of this analysis as seen in Figure 2. The test results for measuring the reinforcing layer tensile strength are presented in Table 2.

2.1.3 Cavity properties

In order to actually simulate a cavity, we are using PVC, the thickness of PVC is 2 mm, and the exterior diameter is 110 mm, in the design of the test model. The parameters of the PVC tube are shown in Table 3.

2.2 Test tank and model footing

The experiment conducted in a test tank with dimensions of 1000 mm × 490 mm in plan and 600 mm in height, two sides of the tank were constructed with rigid steel plates to prevent lateral movement and offer plain strain condition within the soil mass during the test, the back face of the tank was made with a 10 mm-thick transparent glass for

monitoring the slope failure mechanism or cavity collapse during the test. A steel strip footing of 100 mm × 480 mm in plan and a thickness of 10 mm used for the study. The base length was thus almost equivalent to the tank width for the simple strain state to be retained throughout the test.

2.3 Loading method

We used MTS universal testing system that combines high-performance loading frame technology, ease of use of MTS test suite (TW) software compatible precision sensors, and practical and ergonomic manual terminals. This system includes a load cell capable of applying up to 50 kN on the footing. We apply load at the centroid of the footing to avoid the loading eccentricity effect. The loading speed of this unit can be adjusted to a maximum of 1 mm/min. Since lower-speed loading more accurately simulate static loading conditions, all laboratory experiments are conducted at a speed of 1 mm/min (Figure 3).

2.4 Model preparation method

The sand slope form, sand layers, reinforcement levels and cavity depths are initially marked inside the glass installed

in the tank and the method described in Yoo (2001), Lee & Manjunath (2000), and Sawwaf (2007) is followed for the slope preparation where sand was poured into the tank into 50 mm thick sand layers and manually compacted till achieving the target relative density Dr = 60%. After reaching the cavity height marked h = 150 mm, a circular PVC with a diameter of 110 mm was positioned at the desired height, as shown in Figure 4b. Subsequently, the sand compaction continued until reaching the position of the reinforcement layers in this case. Two types of reinforcement (glass and carbon fiber) were used, with reinforcement layers all along placed at their desired levels (Figure 4a), where the compaction of sand layers is performed after placing each layer of reinforcement as presented in Figure 5. The figure shows, that B represents the footing width, a is the distance of the first layer of reinforcement and the base of the footing (u). The space between two layers of reinforcement, h, illustrates the vertical distance between the cavity and footing, N is the number of reinforcement layers, b is the footing distance from the edge of the slope, and D is the diameter of the cavity. After the slope was established, the surface of the slope was leveled well so that the footing could be placed on a level surface for the stress distribution under the footing and avoid eccentric loading, as shown in Figure 5c. It should be mentioned that the dimensions selected in this analysis of the soil slope are consistent with those used in

previous laboratory study (Ueno et al., 1998). Table 4 lists the experiments conducted in this analysis by holding a range of parameters constant and examining other variable parameters effect on load capacity and settlement.

3. Numerical study

A series of three-dimensional finite-element analyses (FEA) was performed using the software Plaxis 3D to simulate the experimental program. A plane strain model was used to carry out the FEA. The geometry and characteristics of the model used in the finite element analysis are the same as those employed in the laboratory test. A prescribed footing load was used to simulate the rigid footing settlement. The behaviour of sand was simulated using the non-linear Mohr-Coulomb criterion available in Plaxis 3D. The Mohr-Coulomb model has five input parameters: Young's modulus (E), Poisson ratio (ν), friction angle (φ), cohesion (c), and angle of dilatancy (ψ). The modulus of subgrade reaction of the sand bed (ks) can be estimated from the load–settlement curve using the following equation.

$$k_s = \frac{q_{1.25}}{1.25\times10^{-3}}\left[\frac{kN}{m^3}\right] \quad (1)$$

Where q1.25 is the uniform pressure applied to the footing at 1.25 mm of settlement. Was used to find the E values obtained from Equation 2 (Selvadurai, 2013; Shukla & Chandra, 1996). The value of E is dependent on the sand relative density, number of reinforcement layers, and cavity location. Therefore, a unique value of E was utilised in each case studied in the
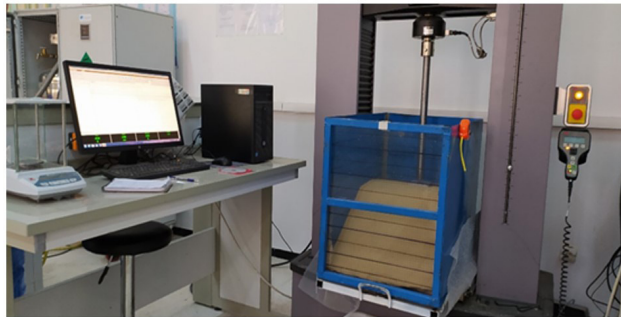
Table 4. Tests performed in this study.

Series	Constant			Variable
1-fiber glass	βslope = 35° b/B = 1 h/B = 1.5			N = 1; 2; 3
2-fiber carbon	S/B = 0.25 u/B = 0.25 Dr = 60%			N = 1; 2; 3

Figure 3. A view of the laboratory model footing load test set-up.
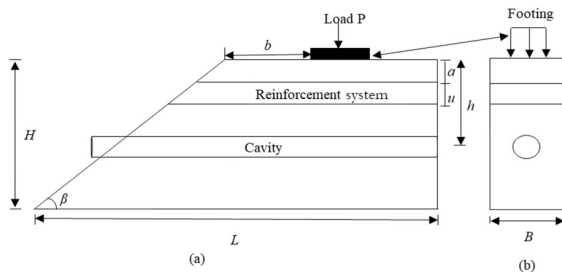

Figure 4. Schematic diagram of a shallow footing near slope: (a) side view and (b) cross-section along the footing.

Figure 5. (a) A carbon fiber layer being installed within the slope; (b) rear view; (c) top view.

4

Azeddine & Abdelghani, Soil. Rocks, São Paulo, 2023 46(1):e2023003622

numerical simulation. Some Plaxis 3D simulations were conducted and compared to their experimental counterparts to determine an appropriate value for the thickness of the sand bed (H). It was confirmed that a reasonable value of E could be obtained when H was approximately three times the footing width (B) (Kazi et al., 2015; Lovisa et al., 2010). The soil Poisson's ratio (ν) was assumed to be 0.25 for all cases. The angle of dilatancy (ψ) was obtained from the friction angle (φ) using the Equation 3 (Bolton, 1986).

$$E = k_s H (1 + v)(1 - 2v) \qquad (2)$$

$$\psi = \varphi - 30° \qquad (3)$$

The interaction between the reinforcement layers and the surrounding soil was simulated by interface elements located between the reinforcement layers, and soil. The interface elements are the strength reduction factor Rinter, which was assumed to be 2/3 (Kazi et al., 2015). The foundation was modeled as a plate with a high flexural rigidity (EI) and normal stiffness (EA). The reinforcement fibers were drawn using software (AutoCAD) and then imported to the model as modified geogrid elements as available in the software Plaxis 3D. This option allows the users to define the only required parameter, the elastic normal stiffness (EA), which was determined from the laboratory test conducted on a specimen of the reinforcement layer. The cavity is represented in the study as a circle with a diameter of D = 1B and a wall thickness of 1 mm, to exactly simulate the experimental model. The cavity model system is considered a plane strain condition with 15-node elements. Mohr-Coulomb plasticity model was specified to solid element which symbolizes soil around the PVC pipe. Fifteen nodded plane strain triangular elements were used to model the backfill (Rajkumar & Ilamparuthi, 2008), with a restricted horizontal displacement and free vertical displacement. The other parameters used for the numerical analysis are well defined in the Plaxis 3D guide. The numerically simulated model is as shown in Figure 6.

The initial stress within the slope was determined by gravity loading, this method was utilized because the slope is not a horizontal surface. In Plaxis 3D the load–settlement analysis of a footing can be done, by either the prescribed footing load method (load controlled) or prescribed displacement method (displacement controlled). A prescribed displacement was applied to the footing in increments accompanied by iterative analysis until the failure occurred.

The study consists of two stages, the first one deals a prescribed displacement applied to the footing with increments until the failure occurred without reinforcement. To reduce the effect of surface load on the cavity and improve its performance, the fiber reinforcements were used in the second stage. Table 5 summarizes the material properties used in the analysis.

4. Results and discussion

4.1 Experimental results

Findings from the results of small-scale laboratory model tests performed to evaluate the ultimate bearing capacity of a footing with a width B = 100 mm placed at a constant edge distance ratio b/B = 1 on sand slope with a variable cavity depth ratio h/b = 0.5B, 1B, 1.5B in a single (N =1) double (N = 2) and triple (N = 3) layers of carbon and glass fiber reinforcement for a sand slope having an angle of inclination β = 35° to the horizontal and a relative density Dr = 60%. In all the experiments carried out, the reinforcing layers were stretched from the slope face to the rear of the test tank. The first (top) layer was installed at a constant depth ratio of u/B = 0, 25 below the footing base. A consistent vertical spacing ratio s/B = 0.25 was maintained between the subsequent layers and the initial layer during installation.

The load-settlement curves of the footing can be used to determine the ultimate bearing capacity of the footing. The highest possible value of q is defined through the peak in the applied pressure-settlement curve. It is possible to accurately define the peak value of q (of peak) by referring to the applied pressure-settlement curve, based on the procedure suggested by Vesić (1973) and Terzaghi et al. (1996). According to this approach, qu is the point on the load-settlement curve at which the curve becomes steep and straight.
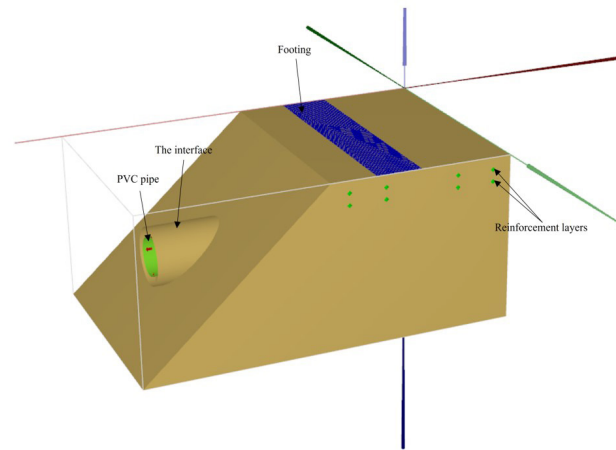

Figure 6. Plot of geometry model with boundary conditions.

Table 5. Parameters used in the numerical analysis.

Parameter for soil	Parameter of fiber	Parameter of footing
E = 3000-4500 (kN/m³)	Glass fiber	EA = 640000 (kN/m)
φ = 38 °	EA = 400 (kN/m)	EI = 85 (kN/m²)
ψ = 8°	Carbon fiber	Thickness = 0.01 m
γ_d = 15.75 kN/m³	EA = 600 (kN/m)	
ν = 0.25		
c = 1 kPa		
Rinter= 2/3		

The laboratory test results are presented as load (q)-settlement (s) curves where s is the settlement of the footing corresponding to a particular q and B the footing width. It is observed that as the footing's applied pressure q increases, the settlement (s) also increases until the footing fails. It is also observed that in the case of unreinforced soil, the effect of the cavity on the bearing capacity of the footing is estimated based on the optimum cavity depth in different values of 3B, 2.5B, 2B, and 1.5B. The ultimate bearing capacity values obtained are 4.55 kN, 3.38 kN, 2.86 kN, and 2.37 kN respectively, with Figure 7 illustrating the maximum effect of the cavity on the bearing capacity of the footing in depth 1.5B. As a result, 1.5B is used to calculate the cavity effect in different reinforcement layer numbers, N = 1, N = 2, N = 3.

Figure 8 shows the influence of number of reinforcement layers N of glass fiber for a cavity depth h/B =1.5. The figure shows that increasing the number of reinforcement layers improves the load-bearing capacity q from 13% to 88%, and 88% to 258%, for N = 0 (unreinforced), N = 1, N = 2, and N = 3, respectively.

In Figure 9 is observed that qu increases with N. The footing bearing capacity significantly improves from 46% to 143%, and 143% to 424% for reinforced with carbon fiber single layer, double layer, triple-layer respectively.

Figure 10 shows a comparison between the different types of reinforcements used in this study. It is observed that carbon fibers have a greater improvement to the load bearing capacity of the footing in comparison with glass fiber, this difference is significantly apparent when using multiple reinforcement layers.

4.2 Numerical results and comparison

In finite element modeling, a finer mesh typically results in a more accurate solution. However, as mesh is made finer, the computation time increases. Mesh convergence study is thus performed to obtain a satisfactory tradeoff between the accuracy and computing resources. Figure 11 shows mesh convergence analysis carried out on model unreinforced slope. It can be observed that as mesh gets finer, the results converge. But there is no significant difference between the medium and the fine mesh. The medium mesh was selected for the present study because it takes a shorter duration to complete the modelling than the fine and very fine meshes. Figure 12 show the deformed mesh for a typical analysis. Displacements and stress concentration in a typical model are presented in Figures 13-14.

Figures 15-16 show a comparison of the load settlement curves of the experimental and the FEA results for all specimens. These results indicate that the FEA model was able to accurately predict the behavior of the reinforced soil. Furthermore, the use of both carbon and glass fibers resulted in a significant increase in the load-bearing capacity of the footing. It is clearly noticed that the numerical values closely follow the experimental values. Some variations are well expected because of the in-built limitations of the Plaxis to simulate the behaviour of unreinforced and reinforced soils.
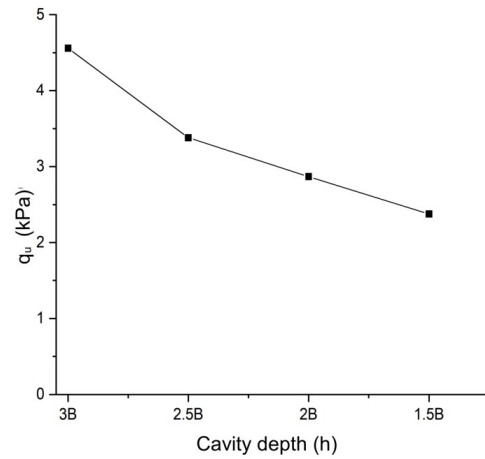

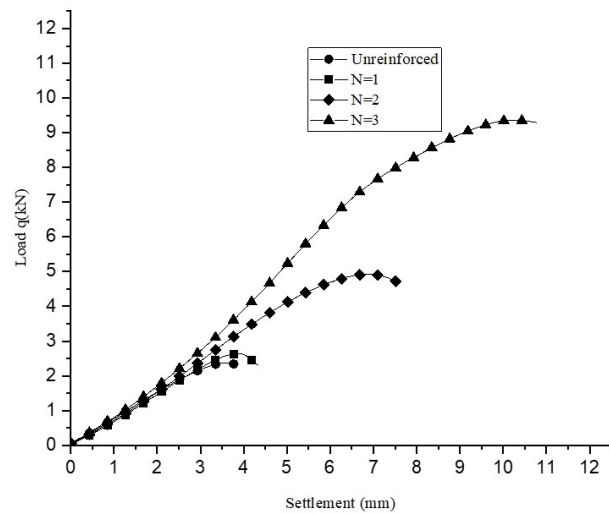**Figure 7.** Variation of ultimate bearing capacity qu with cavity depth ratio.

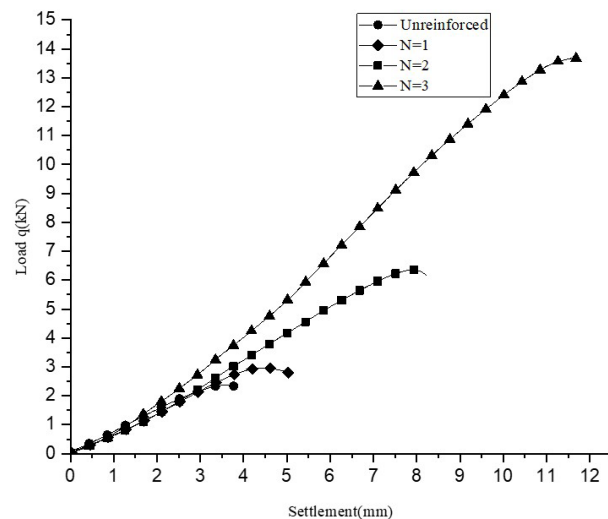**Figure 8.** Effect the number of reinforcing layers N for glass fiber on load-bearing pressure (q) and settlement.

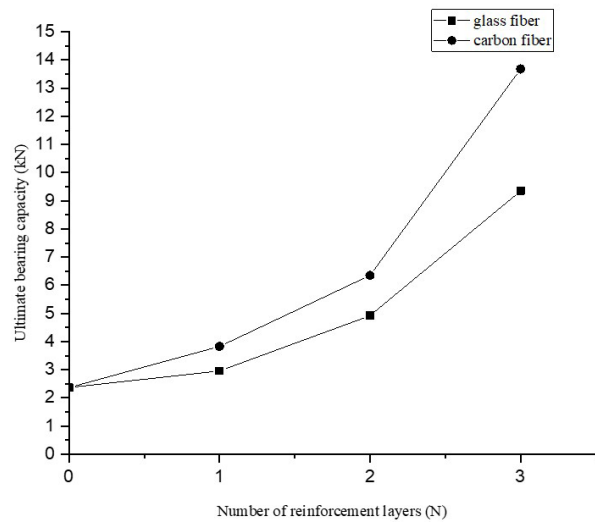**Figure 9.** Effect the number of reinforcing layers N for carbon fiber on load-bearing pressure (q) and settlement.

Figure 10. Comparison of ultimate bearing capacity with number of reinforcement layers N from carbon and glass fiber.
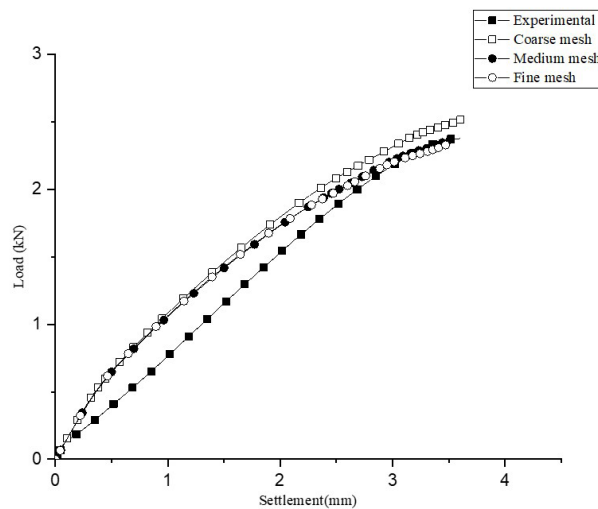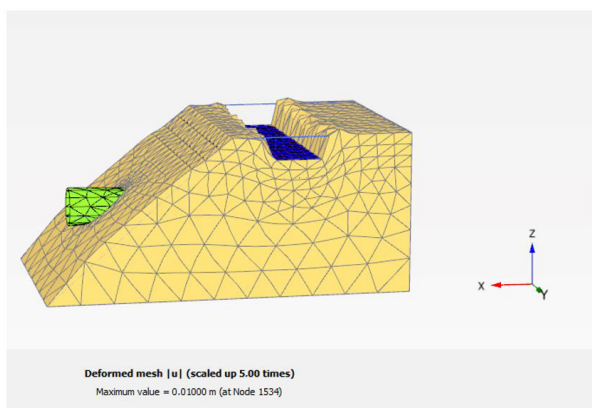

Figure 11. Mesh convergence study.

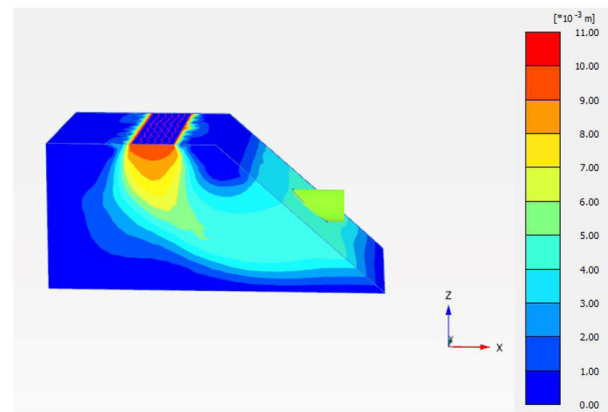**Figure 12.** Deformation of mesh of a typical finite-element model with reinforcement.

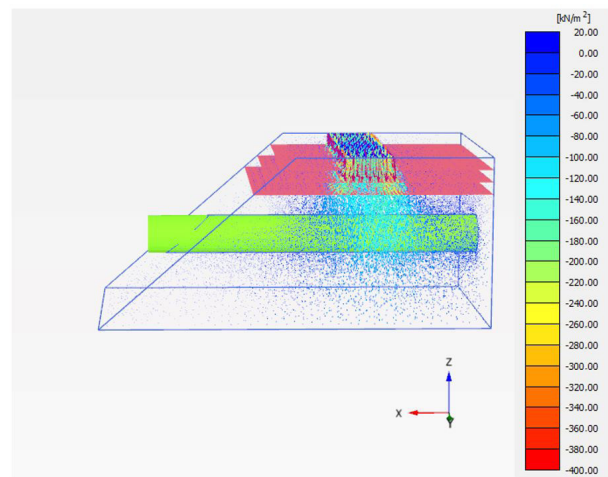**Figure 13.** Typical displacement shading contours (in meters).

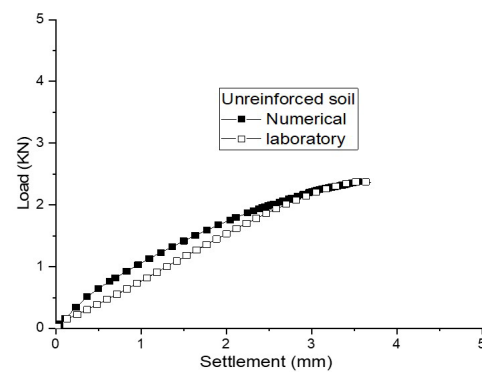

Figure 14. Stress concentration (in kPa).

Figure 15. Comparison of load-settlement curves in unreinforced soil case.

Figure 17 compares the ultimate bearing capacities obtained from the numerical simulations to those established from the laboratory model tests for different reinforcement types used in this study. It is observed that the ultimate bearing capacities are in good agreement.
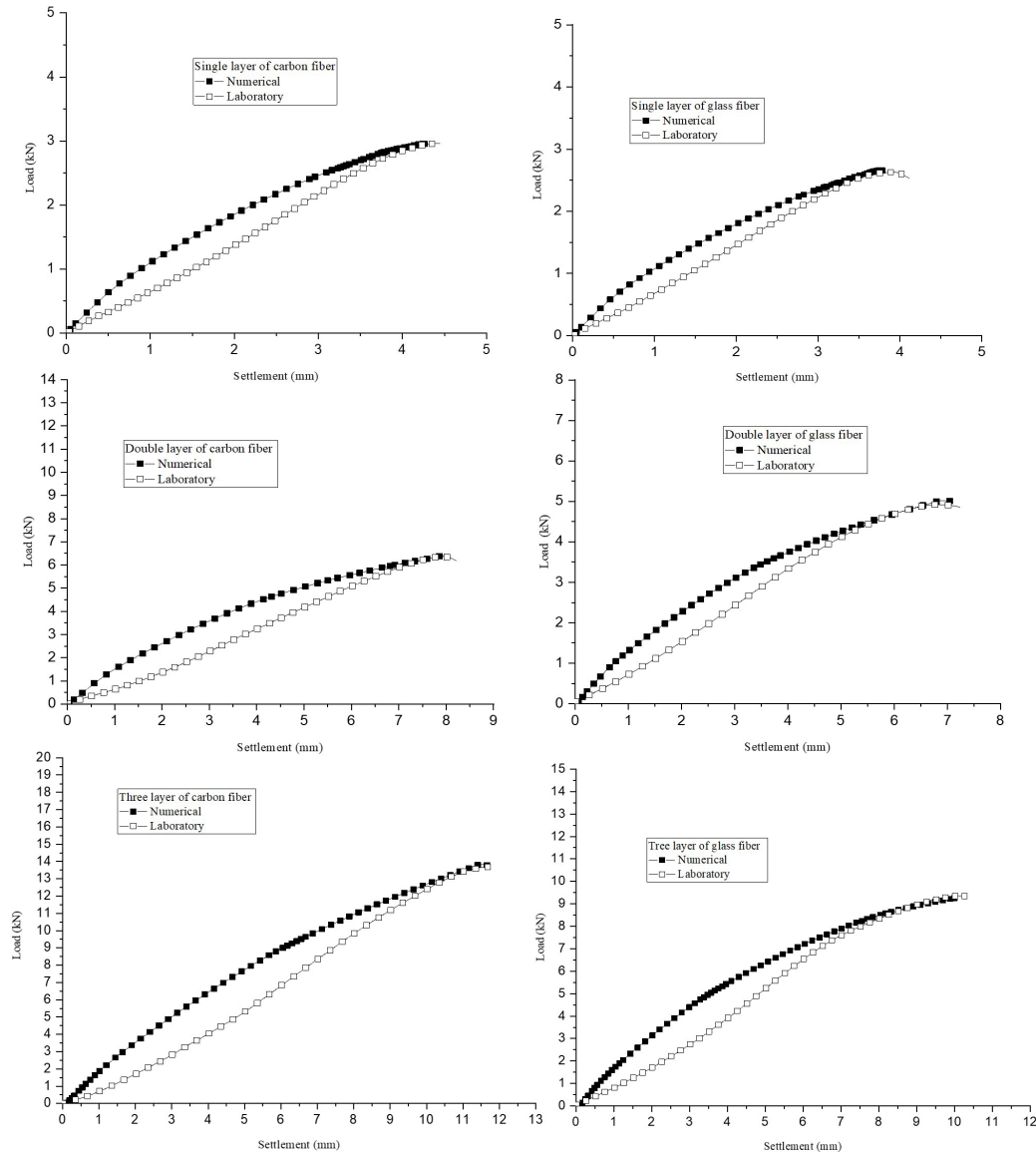
Figure 16. Comparison of load-settlement curves in reinforced soil cases.
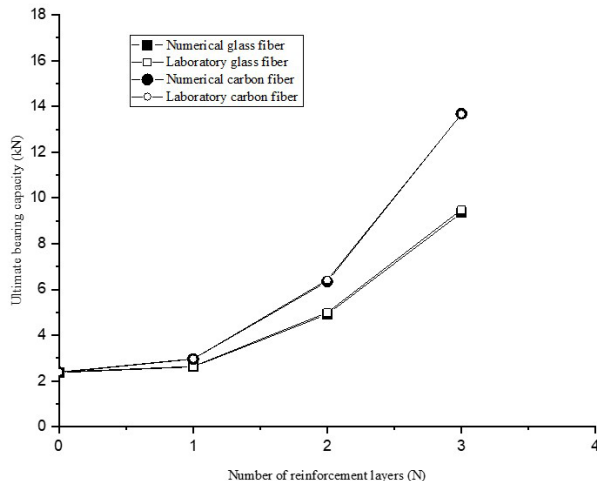

Figure 17. Comparison of the ultimate bearing capacity qu from experimental and numerical studies.

5. Conclusions

For the purpose of evaluating the effect of the cavity on the bearing capacity and settlement of a footing in sand slope reinforced with a multilayer carbon and glass fibers, a series of laboratory model experiments were carried out. In this study, specifically, to show the relationship between the cavity depth ratio h/B, the number of reinforcing layers N and type of reinforcement on the bearing capacity and settlement characteristics of the footing. The following are the most important conclusions that can be drawn from the findings:

- The cavity depth D, below the slope crest, significantly affects the bearing capacity and settlement characteristics of the footing, the risk of collapse increases when the distance between the cavity and the base is small. Where the bearing capacity of the footing is

directly proportional to the cavity depth. The greater the depth from 1.5b to 2b, 2b to 2.5b, and 2.5b to 3b the greater the bearing capacity from 20% to 42% and from 42% to 91%.

- Using glass and carbon fibers as a reinforcement significantly increases the load bearing capacity of the footing.
- The footing ultimate bearing capacity (q_u) increases with the increase in the number of reinforcing layers (N), by 46%, 143% and 424% for N = 1, N = 2 and N = 3, respectively.
- The use of carbon fibers in reinforcement resulted in significantly higher bearing capacity by up to 46% compared to the glass fibers.
- The results obtained from the finite element analysis using the software Plaxis follow the experimental results closely, at the lower settlement values in all cases, but for higher relative density cases, the results are almost identical.
- The numerical results of the ultimate bearing capacity (qu) of the footing are identical with their experimental counterpart.

Declaration of interest

The authors have no conflicts of interest to disclose.

Authors' contributions

Bendaas Azeddine: methodology, investigation, data curation, writing. Merdas Abdelghani: supervision, validation.

Data availability

The datasets generated and analyzed in the course of the current study are available from the corresponding author upon reasonable request.

List of symbols

a	depth of reinforcement from base of footing
b	edge distance of footing from slope crest
c	cohesion
C_c	coefficient of curvature
C_u	uniformity coefficient
h	embedded depth of cavity
qu	ultimate bearing capacity of footing
u	vertical spacing between reinforcement layers
B	width of footing
D_r	relative density of sand
D_{10}	particle diameter corresponding to 10% finer by weight
D_{30}	particle diameter corresponding to 30% finer by weight

D_{60}	particle diameter corresponding to 60% finer by weight
E	Young's modulus
EA	normal stiffness
EI	flexural rigidity
H	slope height
Ks	modulus of subgrade reaction
N	number of reinforcement layers
Rinter	strength reduction factor
β	slope angle
$\gamma_{d\,max}$	maximum dry unit weight
$\gamma_{d\,min}$	minimum dry unit weight
γ_d	dry unit weight
φ	angle of internal friction
ν	Poisson's ratio
ψ	angle of dilatancy

References

Afshar, J.N., & Ghazavi, M. (2014). A simple analytical method for calculation of bearing capacity of stone-column. International Journal of Civil Engineering, 12(1), 15-25.

Al-Jazaairry, A.A., & Toma-Sabbagh, T.M. (2017). Effect of cavities on the behaviour of strip footing subjected to inclined load. International Journal of Civil, Environmental, Structural, Construction and Architectural Engineering, 11(3), 292-298.

ASTM D3080-90. (1990). Standard Test Method for Direct Shear Test of Soils Under Consolidated Drained Conditions. ASTM International, West Conshohocken, PA.

ASTM D422-62. (2007). Standard Test Method for Particle-Size Analysis of Soils. ASTM International, West Conshohocken, PA. https://doi.org/10.1520/D0422-63R07E02.

ASTM D4253-00. (2000). Standard Test Methods for Maximum Index Density and Unit Weight of Soils Using a Vibratory Table. ASTM International, West Conshohocken, PA.

ASTM D854-14. (2014). Standard Test Methods for Specific Gravity of Soil Solids by Water Pycnometer. ASTM International, West Conshohocken, PA. https://doi.org/10.1520/D0854-14.

Baah-Frempong, E., & Shukla, S.K. (2020). Behaviour of a strip footing embedded in a sand slope reinforced with multilayer geotextile. Indian Geotechnical Journal, 50(4), 560-576. http://dx.doi.org/10.1007/s40098-019-00393-3.

Bolton, M.D. (1986). The strength and dilatancy of sands. Geotechnique, 36(1), 65-78. http://dx.doi.org/10.1680/geot.1986.36.1.65.

Culshaw, M.G., & Waltham, A.C. (1987). Natural and artificial cavities as ground engineering hazards. Quarterly Journal of Engineering Geology and Hydrogeology, 20(2), 139-150. http://dx.doi.org/10.1144/GSL.QJEG.1987.020.02.04.

Dahoua, L., Usychenko, O., Savenko, V.Y., & Hadji, R. (2018). Mathematical approach for estimating the stability of geotextile-reinforced embankments during an

earthquake. Mining Science, 25, 207-217. http://dx.doi.org/10.5277/msc182501.

Kapoor, A., Walia, B.S., & Singh, C. (November 2-3, 2019). Effect of cavity on bearing capacity of shallow foundation in reinforced soil. In H. Singh, P. Garg, & I. Kaur (Eds.), Proceedings of the 1st International Conference on Sustainable Waste Management through Design (pp. 313-322). Cham, Switzerland: Springer. https://doi.org/10.1007/978-3-030-02707-0_37.

Kazi, M., Shukla, S.K., & Habibi, D. (2015). An improved method to increase the load-bearing capacity of strip footing resting on geotextile-reinforced sand bed. Indian Geotechnical Journal, 45(1), 98-109. http://dx.doi.org/10.1007/s40098-014-0111-9.

Kiyosumi, M., Kusakabe, O., & Ohuchi, M. (2011). Model tests and analyses of bearing capacity of strip footing on stiff ground with voids. Journal of Geotechnical and Geoenvironmental Engineering, 137(4), 363-375. http://dx.doi.org/10.1061/(ASCE)GT.1943-5606.0000440.

Kolay, P., Kumar, S.K.P., & Tiwari, D. (2013). Improvement of bearing capacity of shallow foundation by using geogrid reinforced double layered soil. Journal of Construction Engineering, 2013, 293809.

Lee, K.M., & Manjunath, V.R. (2000). Experimental and numerical studies of geosynthetic-reinforced sand slopes loaded with a footing. Canadian Geotechnical Journal, 37(4), 828-842. http://dx.doi.org/10.1139/t00-016.

Leshchinsky, D. (1997). Design procedure for geosynthetic reinforced steep slopes. Washington DC: US Army Corps Engineers. Retrieved in November 4, 2022, from https://apps.dtic.mil/sti/citations/ADA321646.

Lovisa, J., Shukla, S., & Sivakugan, N. (2010). Behaviour of prestressed geotextile-reinforced sand bed supporting a loaded circular footing. Geotextiles and Geomembranes, 28(1), 23-32. http://dx.doi.org/10.1016/j.geotexmem.2009.09.002.

Mansouri, T., Boufarh, R., & Saadi, D. (2021). Effects of underground circular void on strip footing laid on the edge of a cohesionless slope under eccentric loads. Soils and Rocks, 44(1), 1-10. http://dx.doi.org/10.28927/SR.2021.055920.

Rajkumar, R., & Ilamparuthi, D.K. (2008). Experimental study on the behaviour of buried flexible plastic pipe. The Electronic Journal of Geotechnical Engineering, 13, 1-10.

Saadi, D., Abbeche, K., & Boufarh, R. (2020). Model experiments to assess effect of cavities on bearing capacity of two interfering superficial foundations resting on granular soil. Studia Geotechnica et Mechanica, 42(3), 222-231. http://dx.doi.org/10.2478/sgem-2019-0046.

Satvati, S., Alimohammadi, H., Rowshanzamir, M., & Hejazi, S.M. (2020). Bearing capacity of shallow footings reinforced with braid and geogrid adjacent to soil slope. International Journal of Geosynthetics and Ground Engineering, 6(4), 1-12. http://dx.doi.org/10.1007/s40891-020-00226-x.

Sawwaf, M.A. (2007). Behavior of strip footing on geogrid-reinforced sand over a soft clay slope. Geotextiles and Geomembranes, 25(1), 50-60. http://dx.doi.org/10.1016/j.geotexmem.2006.06.001.

Selvadurai, A.P.S. (2013). Elastic analysis of soil-foundation interaction. Amsterdam: Elsevier.

Shukla, S.K., & Chandra, S. (1996). A study on a new mechanical model for foundations and its elastic settlement response. International Journal for Numerical and Analytical Methods in Geomechanics, 20(8), 595-604. http://dx.doi.org/10.1002/(SICI)1096-9853(199608)20:8<595:AID-NAG835>3.0.CO;2-9.

Terzaghi, K., Peck, R.B., & Mesri, G. (1996). Soil mechanics in engineering practice. Hoboken: John Wiley & Sons.

Ueno, K., Miura, K., & Maeda, Y. (1998). Prediction of ultimate bearing capacity of surface footings with regard to size effects. Soil and Foundation, 38(3), 165-178. http://dx.doi.org/10.3208/sandf.38.3_165.

Vesić, A.S. (1973). Analysis of ultimate loads of shallow foundations. Journal of the Soil Mechanics and Foundations Division, 99, 45-73. http://dx.doi.org/10.1061/JSFEAQ.0001846.

Xiao, Y., Zhao, M., & Zhao, H. (2018). Undrained stability of strip footing above voids in two-layered clays by finite element limit analysis. Computers and Geotechnics, 97, 124-133. http://dx.doi.org/10.1016/j.compgeo.2018.01.005.

Yoo, C. (2001). Laboratory investigation of bearing capacity behavior of strip footing on geogrid-reinforced sand slope. Geotextiles and Geomembranes, 19(5), 279-298. http://dx.doi.org/10.1016/S0266-1144(01)00009-7.

Zahri, F., Boukelloul, M.L., Hadji, R., & Talhi, K. (2016). Slope stability analysis in open pit mines of Jebel Gustar career, NE Algeria–a multi-steps approach. Mining Science, 23, 137-146.

Zhao, L., Huang, S., Zhang, R., & Zuo, S. (2018). Stability analysis of irregular cavities using upper bound finite element limit analysis method. Computers and Geotechnics, 103, 1-12. http://dx.doi.org/10.1016/j.compgeo.2018.06.018.

Zhou, H., Zheng, G., He, X., Xu, X., Zhang, T., & Yang, X. (2018). Bearing capacity of strip footings on c–φ soils with square voids. Acta Geotechnica, 13(3), 747-755. http://dx.doi.org/10.1007/s11440-018-0630-0.

Shear strength analysis of interfaces between granular soils and concrete cured under stress

André Luis Meier[1#] (iD), Vitor Pereira Faro[1] (iD), Edgar Odebrecht[2] (iD)

Article

Abstract
The goal of this study was to improve the understanding of the soil-structure interaction mechanisms at the interface of bored concrete piles cast in sandy soils. In addition, this study aimed to quantify the interface shear strength and identify the factors that influence the response. Roughness measurements and direct shear tests were performed at the interface between two samples of sand (medium and coarse) and concrete cured under stress. The influence of the mean grain diameter, relative density, water content, concrete curing time and normal stress on the interface shear strength were statistically analyzed. The results showed a consistent behavior with the technical literature, but with higher values, which can be attributed to the concrete curing time, a factor not studied by other authors.

1. Introduction

During the execution of bored concrete piles, small displacements can occur along the shaft, which generate shear stresses between pile and soil, called residual stresses (Fellenius & Altaee, 1995). The practical consequence of this phenomenon is inaccurate static load test results, which may result in a higher shaft resistance than the real value and a lower tip resistance (Fellenius, 2020).

Salgado (2008) states that for piles without displacement, the values of the interface friction angle (δ) can be expressed in terms of the critical state friction angle (ϕ'_{cs}) obtained through direct shear tests. Some authors (Lehane et al., 1993; Randolph et al., 1994; Salgado, 2008) found δ values between $0.8\phi'_{cs}$ and ϕ'_{cs} for this type of pile. The explanation for this variation comes from the conditions of pile execution: when well executed, concrete surface roughness tends to be greater than the average diameter of the grains, causing shear to occur in the soil near the pile and not at the interface, which results in a value of δ equal to ϕ'_{cs}. However, in executions with lower quality, the roughness can be reduced, which causes failure to occur at the soil–pile interface, indicating values of δ equal to or smaller than $0.8\phi'_{cs}$.

Ring and direct shear tests are commonly used to estimate the pile axial load capacity through the interface friction angle; nonetheless, the compatibility between laboratory and field conditions needs to be ensured through soil characteristics, surface structures and confinement conditions (Reddy et al., 2000). According to Nardelli et al. (2019), there is a consensus

in the technical literature that the interface shear response is mainly influenced by the following conditions: grain characteristics, confining conditions, soil properties, water content, structure surface characteristics and temperature.

The first prominent factor is the roughness on the pile surface. The average roughness (R_a) is one of the most accepted parameters for quantifying surface roughness and is defined as the arithmetic average of the absolute values of the profile height deviations measured from the average line. Another parameter also widely used is maximum roughness (R_{max}), which corresponds to the difference between the highest peak and the lowest valley on a surface (ASME, 2009).

To better evaluate the effects of roughness at a sand-steel interface, Uesugi & Kishida (1986a, b) defined the normalized roughness (R_n) as the ratio of maximum surface roughness to mean grain diameter. In addition, the authors found a bilinear relationship between the normalized roughness and the friction coefficient: first, there is an increase in the friction coefficient with the rise in roughness until the critical point, from which the value becomes constant.

For a sand-concrete interface, Uesugi et al. (1990) observed that the critical point of normalized roughness occurred around the value of 0.1, resulting in a friction coefficient greater than 0.95. Furthermore, based on the normalized roughness value, Paikowsky et al. (1995) defined three categories of surface texture: smooth, for $R_n < 0.02$; intermediate, for $0.02 < R_n < 0.5$; and rough for $R_n > 0.5$.

Regarding the grain characteristics, in soils with subrounded and smooth particles, there is a lower interlock,

#Corresponding author. E-mail address: de.luis.meier@gmail.com
[1]Universidade Federal do Paraná, Postgraduate Program in Civil Engineering, Curitiba, PR, Brasil.
[2]Universidade do Estado de Santa Catarina, Department of Civil Engineering, Joinville, SC, Brasil.

which allows for rotations during shear. On the other hand, for angular grains, the interlock is higher, increasing the shear strength (Brumund & Leonards, 1973; DeJong & Westgate, 2009).

In interface shear tests, the confining conditions refer to the normal stress applied to the equipment set, which aims to simulate the field characteristics of horizontal stresses. Increasing the normal stress causes an increase in the interface strength due to the decrease in interface dilatancy, which provides a rearrangement of particles within a smaller thickness of the shear zone (Jardine et al., 1993; Dietz & Lings, 2006; Gómez et al., 2008; DeJong & Westgate, 2009; Tiwari & Al-Adhadh, 2014; Tehrani et al., 2016).

Among the soil properties, the main factors affecting the shear strength are the relative density and the mean grain diameter (Uesugi & Kishida, 1986b; Jardine et al., 1993; Dietz & Lings, 2006). At sand-steel interfaces, Uesugi & Kishida (1986b) observed that with the increase in mean grain diameter, the friction coefficient decreased, but with the increase in relative density, the peak value of the friction coefficient increased.

Evaluating the relative density effect in shear stress in rough surfaces, Fakharian & Evgin (1996) observed a hardening behavior in loose sands and a softening behavior in compact sands. For smooth surfaces, a hardening behavior was observed independent of the initial relative density. DeJong & Westgate (2009) noted that dense samples initially presented a contraction and, with the advance of deformations, began to dilate in a zone near the interface.

The loose soils, on the other hand, dilated along the interface shear zone, experiencing, nonetheless, a volume contraction above this region. However, for the postpeak interface shear strength, several authors concluded that it is independent of the initial relative density because the soil had achieved the critical state at the interface (Uesugi & Kishida, 1986b; Jardine et al., 1993; Lehane et al., 1993; Fakharian & Evgin, 1996; Reddy et al., 2000; Dietz & Lings, 2006).

The soil water content, in turn, can be studied in three cases: dry, saturated and unsaturated. Gómez et al. (2008) and Tiwari & Al-Adhadh (2014) observed that the behavior of stress–displacement responses was similar for dry and saturated samples, but dry soil presented higher interface shear strength. Unsaturated soils were investigated by Miller & Hamid (2006) and later by Hamid & Miller (2009), who proposed the use of the shear strength equations, as they noted that the interface strength increases with matric suction, and the linear predictions provide a reasonable model for low suction values, while the nonlinear shear envelope for higher values.

Finally, according to Borges et al. (2020), the concrete curing under stress, as is the case for bored piles, causes an increase in stresses due to thermal expansion, which are relieved, in part, with the thermal shrinkage generated by the drop in temperature. This effect, nonetheless, is more noticeable in large-diameter piles ($D \geq 1$ m) (Pennington, 1995).

At the moment, however, there are no studies in the literature that indicate the effect of concrete curing on the interface shear strength. Therefore, this study aims to improve the understanding of the interaction mechanisms between the soil and concrete surfaces through the influence of the following factors on the behavior of the interface shear strength: mean grain diameter, relative density, water content, normal stress and concrete curing time.

2. Experimental methodology

2.1 Equipment and materials

In the present research, two main pieces of equipment were used: a profilometer and a direct shear apparatus. A Mahr PCV profilometer, shown in Figure 1, was used to measure surface roughness, with a test speed of 0.2 mm/s, which allowed for a shorter scanning time without damaging the sample surface. These measurements provided the primary profile (P-profile), so it was necessary to filter the curve to obtain the roughness profile.

The box of the direct shear equipment, shown in Figure 2, had plan dimensions of 100 mm × 100 mm. The data acquisition, with a frequency of 1.25 Hz, was performed automatically: the displacement measurements were obtained by resistive electronic rulers, while the horizontal force was computed through an S-type load cell.

Two sands were used in this study, named medium and coarse. The soil samples came from the region of Joinville, in the north of the state of Santa Catarina, Brazil, collected by dredging and processing of sand from the Cubatão River. Table 1 shows the properties of the medium sand
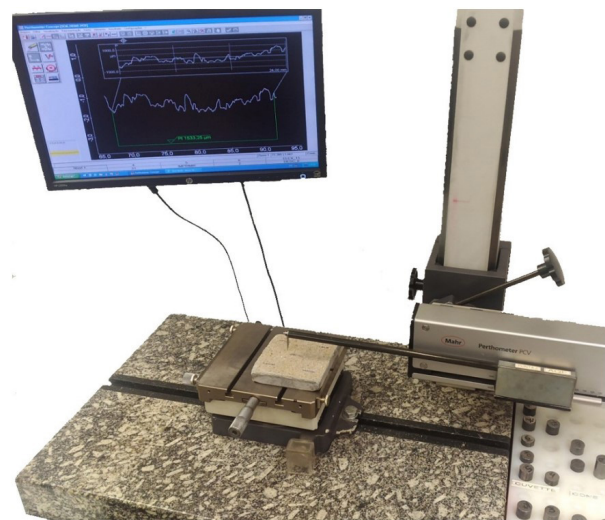

Figure 1. Mahr PCV profilometer.

(D_{50} = 0.60 mm) and coarse sand (D_{50} = 1.10 mm) used in the experimental program. According to the USCS, both soils were classified as poorly graded sand (SP). The grains of both samples were classified as subangular using the criteria prescribed by ASTM D2488 (ASTM, 2017).

The concrete mix used was proposed by Nienov (2016), referring to the piles used in the Araquari Test Site, located near the study area. The materials used were cement CP IV RS, sand (D_{50} = 0.72 mm), gravel (D_{50} = 6.20 mm), water and a superplasticizer admixture. The mixture proportions of the concrete are shown in Table 2. After 28 days, the concrete showed an average uniaxial compressive strength of 35.9 MPa, according to the procedures of ABNT NBR 5739 (ABNT, 2018).

Table 1. Soil characterization.

Description	Medium	Coarse
D_{50} (mm)	0.60	1.10
CU	3.43	5.00
CC	1.06	1.00
G (g/cm³)	2.660	2.649
e_{min} [a]	0.62	0.62
e_{max} [b]	0.79	0.72
Aspect ratio [c]	1.370	1.392
Form factor [d]	0.766	0.761

[a]ABNT NBR 12051 (ABNT, 1991); [b]ABNT NBR 12004 (ABNT, 1990); [c]Aspect ratio = length/width; [d]Form factor = 4π·area/perimeter².

Table 2. Mixture proportion for the concrete (Nienov, 2016).

Feature or component	Quantity
$f_{ck, min}$ (MPa)	20
$f_{ck, mix}$ (MPa)	35.9
Slump test (cm)	23 +/- 2
Water (kg)	216
Cement CP IV (kg)	415
Sand (kg)	800
Gravel (kg)	870
Superplasticizer (L)	3.0

2.2 Experimental program

The experimental program was divided into two groups: the roughness measurement of concrete specimens cured under stress and the direct shear tests at the sand-concrete interface and of pure sand. First, the independent variables of the study were defined as the mean grain diameter, the relative density of sand, the soil water content, the normal stress and the concrete curing time. However, it should be noted that the concrete curing time was only analyzed in the interface direct shear tests.

The levels of variation of the independent variables were chosen for the following reasons:

- The mean grain diameter the sands should have different granulometries and similarity of the medium sand with the Brazilian normal sand, which is the standardized sand for performing Portland cement compressive strength tests, according to ABNT NBR 7214 (ABNT, 2015);
- The relative density was aimed to include the various levels of density of soils;
- For the water content, a variation of 3% was adopted, equivalent to a 10% change in the saturation of the sand, based on the void ratio;
- For the concrete curing time, a 24 h period was adopted as the maximum feasible time, with the times of 6 h and 18 h being adopted within this interval;
- Finally, for the normal stress, a stress of 180 kPa was obtained as the upper limit of the equipment, and a stress of 100 kPa was considered the center of the set of tests due to its correspondence with the horizontal stresses at approximately 10 m depth in a bored pile.

For the first group of tests, the average roughness (R_a), the maximum roughness (R_{max}) and the normalized roughness (R_n) were the selected responses. The analysis was performed separately for the variables using two statistical methods: crossed and 2k factorial (3rd order). Through the
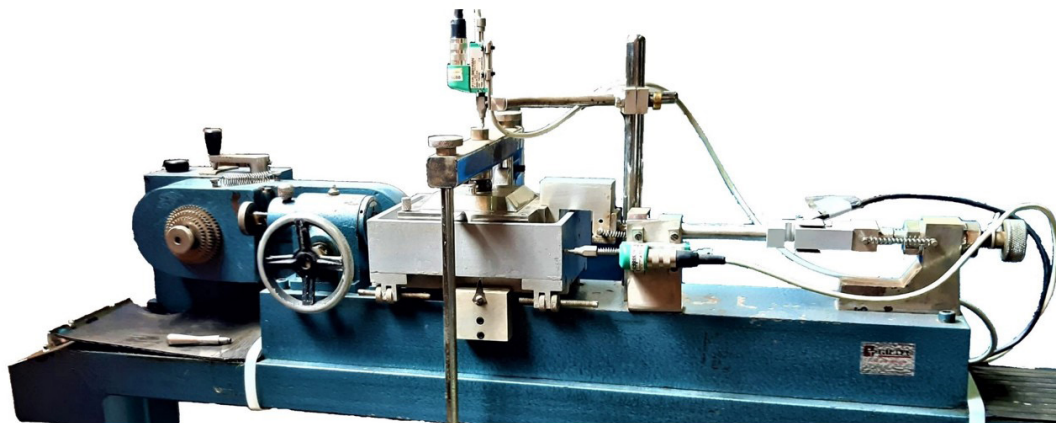

Figure 2. Direct shear apparatus.

crossed factorial method, the influence of grain diameter and normal stress was evaluated; therefore, the relative density was standardized at 70%, and the water content was standardized at 9%. With the 2k factorial method, the aim was to evaluate the effect of grain diameter, relative density and water content on different specimens pressed with the same normal stress of 100 kPa. Sixteen specimens were tested, ten for the cross-factorial stage and eight for the 2k factorial stage.

For the direct shear tests, the response variables were defined as the maximum friction coefficient, called the peak, and the lowest value after the maximum, called the postpeak. The experimental stage used for this group was the crossed factorial method, which allowed obtaining the shear strength parameters through linear regression for different relative densities, water contents, curing times and mean grain diameters. Forty-eight direct shear tests were performed in the sand-concrete interface, and twenty-four tests were performed in pure sand.

2.3 Procedures for interface testing

Figure 3 shows the flowchart for interface testing. After the concrete preparation, it was poured by gravity into the mold (Figure 4A). The surface was then smoothed so that the only roughness came from the impression of the sand on

Figure 3. Flowchart for interface testing.

the specimen. Finally, the mold was deposited in the bottom box of the direct shear equipment (Figure 4B).

The soil samples were first dried in an oven at 105 °C, and the mass of sand was separated for the addition of water until the desired water content was reached for each test. The sand was then compacted inside a ring with a filter (Figure 4C) with the aid of a wooden socket. The compaction control was performed by measuring the mass and water content of the sand inside the mold.

The sample was then extracted from the mold and placed in the upper box of the direct shear equipment (Figure 4D). The total duration of the preparation of each test was approximately 40 minutes. After placing the set in the equipment, the normal stress corresponding to the test was applied. The stabilization period of the vertical displacements was equivalent to the curing time of the concrete, varying, therefore, for each test.

For the roughness measurement tests, this stabilization period was 24 hours, and at the end of this stage, the sample was removed from the equipment, and the sand was cleared away (Figure 4E). Due to the high surface area of the sample, it was chosen to perform 5 roughness readings of 25 mm length per concrete slab cured under stress in the profilometer. The profiles were distributed in different positions on the surface to map the center and sides of each sample. Then, surface metrology software was used to apply a Gaussian filter, with a 2.5 mm cutoff, which generated the roughness profiles and, consequently, the surface roughness parameters.

For the direct shear tests, a shear stress was applied after the stabilization period. After the end of the curing period, a gap was added between the two boxes to avoid breakage of the grains during shear. The total sample displacement was 12 mm, with a shear rate of approximately 0.14 mm/min, resulting in a time to failure of 90 min, higher than the minimum recommended by ASTM D3080 (ASTM, 2011) for the material, but which allowed the next sample to be prepared for testing. At the end of the test, the sheared sample was removed from the equipment (Figure 4F), and its final water content was determined.

3. Analysis and results

The results of this paper were divided into two groups: the surface roughness of concrete specimens cured under stress and the shear strength of the sand-concrete interface and pure sand.

3.1 Surface roughness

The roughness profiles resulting from the measurements in the profilometer are shown in Figure 5, in which it can be seen that the sand with a larger mean grain diameter generates deeper and more frequent peaks and valleys on the concrete surface.

In the crossed factorial analysis, Figure 6a shows the variation in the roughness parameters versus the mean grain
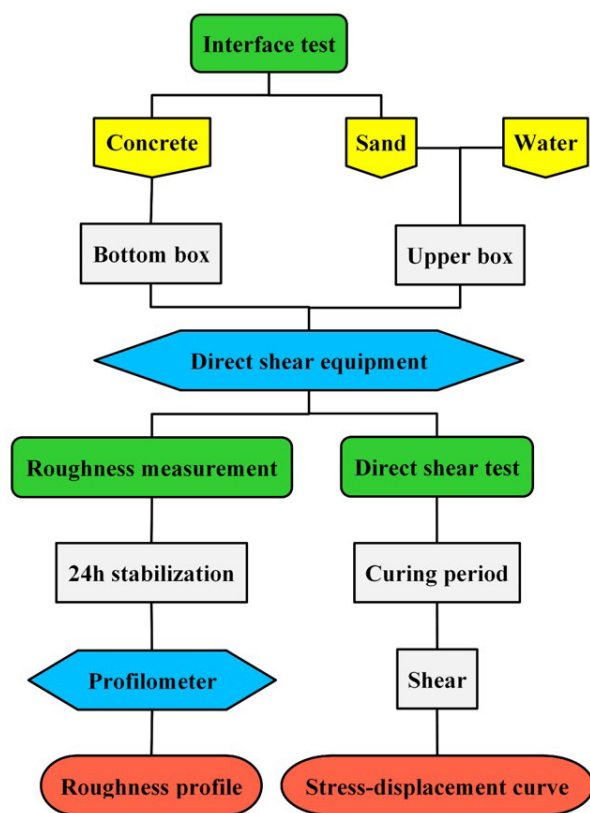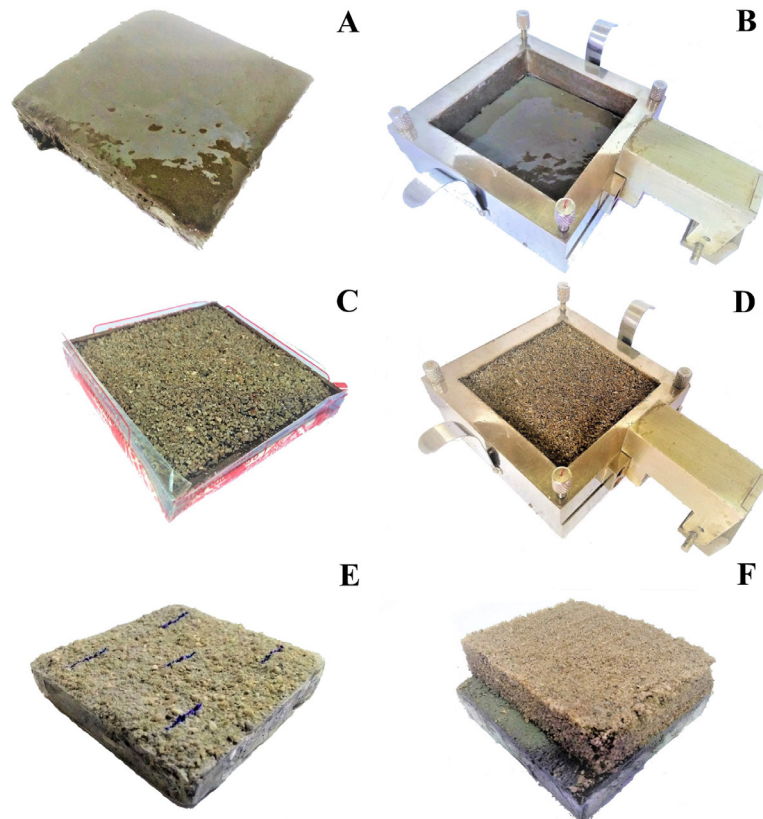
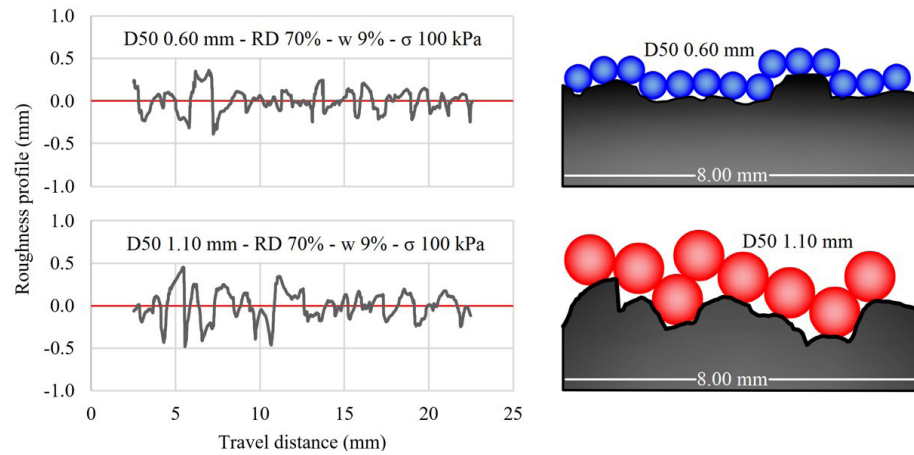**Figure 4.** Steps of the interface tests.

Figure 5. Typical roughness profiles.

diameter, in which a small increase in the average roughness (R_a) and a significant increase in the maximum roughness (R_{max}) were observed with increasing grain size. However, the normalized roughness (R_n) decreased as it was inversely proportional to the grain size. For the effect of normal stress, presented in Figure 6b, only small variations of the results around the average were observed, which indicates that, at this stress level, the variable is not a significant parameter for surface roughness.

Figure 7a shows the 2k factorial analysis for the mean grain diameter, in which the behavior observed for the responses was the same as the crossed factorial analysis, which indicates consistency in the results. It is observed, however, that there is a greater number of outliers. In the
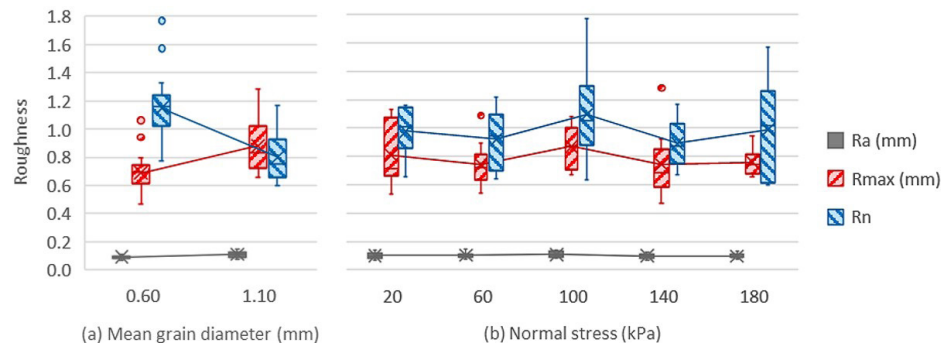
Figure 6. Crossed factorial method: influence of the independent variables on the surface roughness parameters.
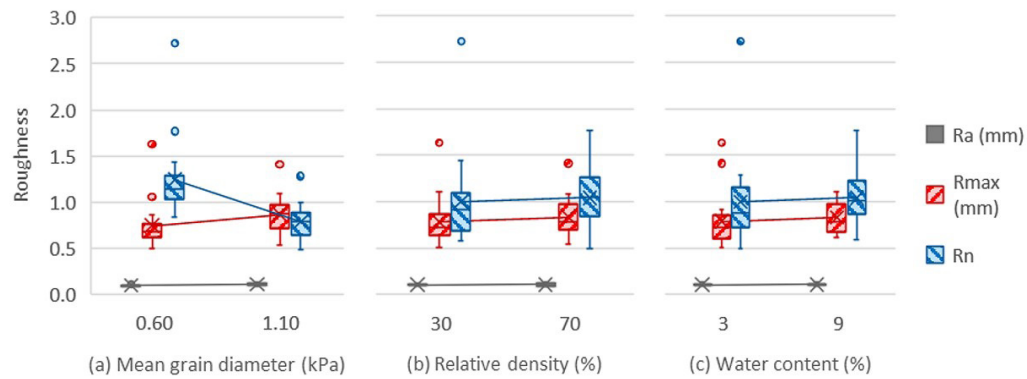

Figure 7. 2k factorial method: influence of the independent variables on the surface roughness parameters.

relative density evaluation (Figure 7b), no variations in the responses were observed, which indicates its noninfluence on the roughness values. A behavior analogous to this is seen in the graph concerning water content (Figure 7c), in which the effect on the test results is also not significant.

Finally, it was concluded that it is possible to assign an average value of the roughness parameters as a function of the mean diameter of the sand grains, without taking into account the variation in the levels of the other independent variables in the present study (normal stress, water content and relative density). Thus, the average values of the parameters for the medium sand ($D_{50} = 0.60$ mm) are $R_a = 0.092$ mm, $R_{max} = 0.690$ mm and $R_n = 1.149$, while those for the coarse sand ($D_{50} = 1.10$ mm) are $R_a = 0.111$ mm, $R_{max} = 0.881$ mm and $R_n = 0.801$. Using the criteria defined by Paikowsky et al. (1995), all surfaces were classified as rough, having a value of $R_n > 0.5$.

3.2 Shear strength

The results of the direct shear tests are presented in Figure 8. From the stress–displacement response, a softening behavior can be noted due to the relative density of 70% of the soil. Moreover, the last graphs generated through the test are the vertical displacement versus horizontal displacement, through which it is possible to visualize the initial behavior of contraction, followed by expansion for both cases, agreeing with the definition of softening of the stress–displacement response.

The effect of the mean grain diameter on the friction coefficient is presented in Figure 9a. The general behavior of the friction coefficient is its rise with increasing grain size ($r \approx 0.3$). It is observed, however, that for the postpeak interface shear stress, this factor has practically no influence ($r = 0.03$), with a nearly horizontal straight line.

A similar behavior was observed in the tests of Nardelli et al. (2019) at sand-concrete interfaces, in which a small increase in (δ/ϕ) values for the peak and postpeak cases occurred with increasing mean grain diameter and decreasing normalized roughness. For the magnitude of the response range of variation, the same influence on the peak shear stress is noticed, whether at the interface or in the sand. This similarity, nonetheless, is not observed in the postpeak tests, whose cause may be related to the dispersion of the sand tests.

The effects of the relative density on the friction coefficient are presented in Figure 9b. First, the shear strength behavior with increasing relative density increases for the interface and sand peak situations, stabilizes at the postpeak interface and decreases for the postpeak sand. The expected behavior,
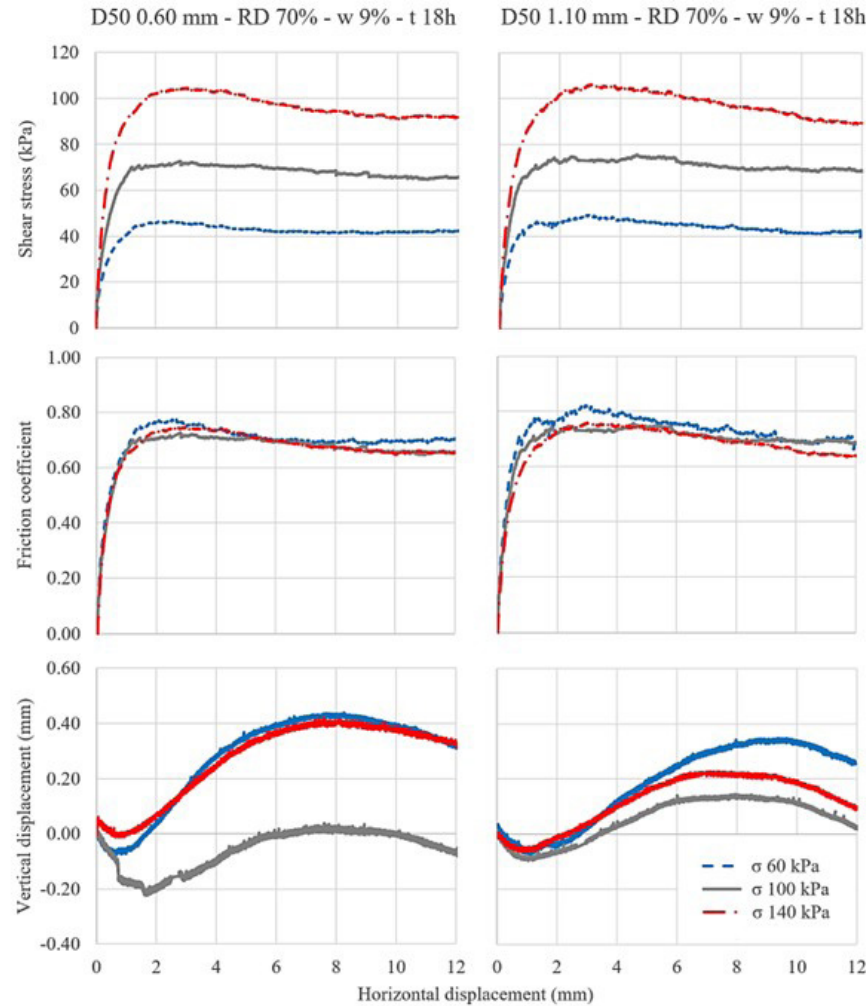
6

Meier et al., Soil. Rocks, São Paulo, 2023 46(1):e2023004022

Figure 8. Typical direct shear test results.

according to Uesugi & Kishida (1986b), was that of shear stress rise with increasing relative density for the peak case and no influence in the postpeak. Therefore, it can be stated that there was partial agreement in this case due to the postpeak graph in sand, which despite presenting a decreasing behavior, has an outlier above the upper limit, which indicates the possibility of higher values for the average value.

In the comparison between the interface and sand tests for peak and postpeak stresses, a higher friction coefficient is obtained for the interface case, except for the tests in the postpeak condition with 30% relative density, in which the averages are statistically equal. Finally, regarding the dispersion, there is a similarity in all cases, except for the postpeak tests in sand, for the 70% relative density, in which there is the presence of an outlier, indicating the possibility of greater dispersion of the results, as seen in the graph of the 30% relative density.

The results for the water content evaluation are presented in Figure 9c. The general behavior of the friction coefficient

is its decrease with increasing water content, which is expected according to Tiwari & Al-Adhadh (2014), being present in most cases, with the exception of the sand tests to obtain the peak stress. This variation may have been caused by the soil being partially saturated, which would require a more robust statistical evaluation to precisely define the behavior observed.

Regarding the comparison between the peak and postpeak interface and the sand test, a similar behavior was obtained to the relative density case, with higher average values attributed to the interface analyses. This similarity is also observed in the dispersion of the results, which present narrow size intervals.

The subsequent analysis was the effect of the concrete curing time, as shown in Figure 9d. For this analysis, only the interface test results are considered, as they presented different behaviors for the peak and postpeak cases. A slightly higher peak friction coefficient is perceived with increasing curing time, while for postpeak, a lower value occurs. It is
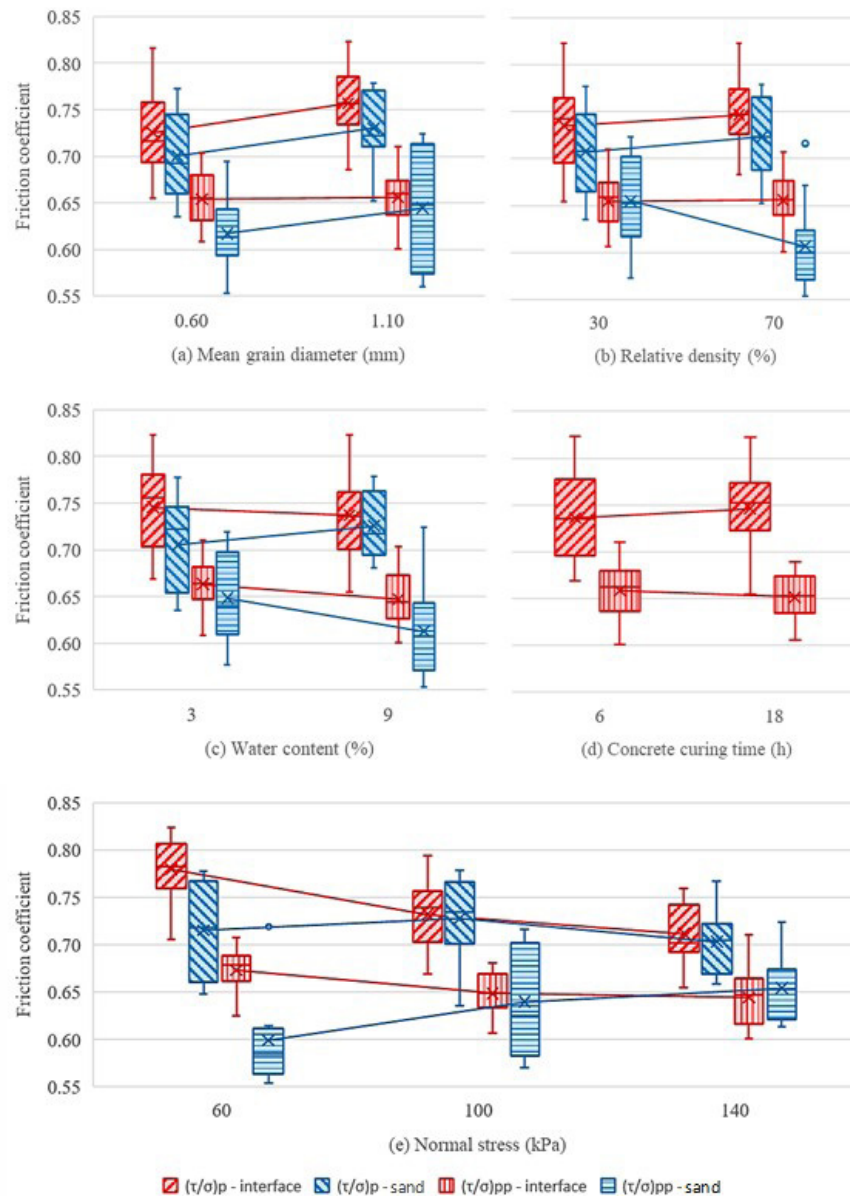
Figure 9. Crossed factorial method: influence of the independent variables on the friction coefficient.

worth mentioning, however, the small numerical difference between the averages for each curing time. Regarding the dispersion of the results, it is observed that the postpeak tests have a smaller variation than the peak tests.

As shown in Figure 9e, the normal stress was studied at 3 actual levels, which allowed a better understanding of the shear strength behavior. First, it is observed that the friction coefficient decreased for the interface tests and increased for the sand tests with increasing normal stress.

Comparing the interface and sand tests for the peak and postpeak stresses, a higher friction coefficient is obtained for the interface case; however, the difference between the averages decreases with increasing normal stress. Finally, regarding the dispersion, a higher accuracy is noticed for the interface tests in relation to the sand tests, which still present an outlier for the case of the postpeak tests in sand for the normal stress of 60 kPa.

The interface and sand shear strength parameters were also obtained and are presented in Table 3. The Mohr–Coulomb envelope was used for the normal stress levels of 60, 100 and 140 kPa. The values of adhesion (c_a), interface friction angle (δ), soil friction angle (ϕ) and the ratio between interface and soil friction angles (δ/ϕ) were calculated for the peak, indicated by the p-index, and for the postpeak situation, with the pp-index.

From the analysis of the friction angle ratios, it can be noticed, in general, that the postpeak results are higher than the peak ones due to the nonconsideration of adhesion.

8

Meier et al., Soil. Rocks, São Paulo, 2023 46(1):e2023004022

Table 3. Shear strength parameters.

D_{50} (mm)	RD (%)	w (%)	t (h)	c_{ap} (kPa)	δ_p	ϕ_p	$(\delta/\phi)_p$	δ_{pp}	ϕ_{pp}	$(\delta/\phi)_{pp}$
0.6	30	3	6	7.78	31.44	33.03	0.95	33.33	32.69	1.02
0.6	30	9	6	8.64	32.31	35.52	0.91	32.16	33.33	0.96
0.6	70	3	6	6.95	32.73	34.69	0.94	33.02	31.64	1.04
0.6	70	9	6	12.68	31.16	35.25	0.88	32.31	30.75	1.05
0.6	30	3	18	6.27	32.92	33.03	1.00	33.18	32.69	1.02
0.6	30	9	18	5.66	31.64	35.52	0.89	32.07	33.33	0.96
0.6	70	3	18	5.41	34.73	34.69	1.00	34.08	31.64	1.08
0.6	70	9	18	1.95	35.97	35.25	1.02	33.06	30.75	1.08
1.1	30	3	6	7.25	35.42	36.23	0.98	34.87	34.55	1.01
1.1	30	9	6	8.50	32.58	36.47	0.89	33.06	34.12	0.97
1.1	70	3	6	9.56	32.30	36.08	0.90	33.48	34.01	0.98
1.1	70	9	6	6.48	33.06	36.16	0.91	31.85	30.88	1.03
1.1	30	3	18	6.02	35.24	36.23	0.97	33.11	34.55	0.96
1.1	30	9	18	8.07	33.54	36.47	0.92	31.79	34.12	0.93
1.1	70	3	18	7.04	34.34	36.08	0.95	32.88	34.01	0.97
1.1	70	9	18	6.04	35.38	36.16	0.98	33.08	30.88	1.07

The adhesion value was chosen to be considered in the peak strength because of the sand grains imprinted on the concrete surface during curing, requiring the breakage of this bond for the displacements to advance. For the postpeak situation, however, there is no physical meaning for the existence of an adhesion parcel; therefore, the average value found was disregarded, and the linear regression line was forced to pass through the origin.

Furthermore, it is noted that the interface friction angle values were very similar, or even higher, than the sand friction angles. This is because the failure studied occurred on a sand–sand surface, as visually observed in the samples after failure, in which high roughness allows a large interlock of the grains and the filling of the surface valleys.

4. Conclusions

The experimental work and the statistical analyses performed throughout this research allowed outlining several considerations on the shear strength of sand-concrete interfaces:

- In the concrete specimens cured under stress, failure occurred at a sand–sand interface due to the high surface roughness, which had valleys filled with sand grains.
- The mean grain diameter was the only relevant factor for the roughness parameters among the variation levels of the independent variables. The relationship between the roughness value and grain size increases for R_a and R_{max} but decreases for R_n.
- The influence of the controllable factors on the friction coefficient was evaluated for the peak and

postpeak cases. For the mean grain diameter, the general behavior of the friction coefficient was its rise with increasing particle size, but with low influence on the postpeak interface shear stress. For the relative density, an increasing relation was observed for the interface and sand peak situations but was constant for the interface postpeak case and decreased for the sand postpeak. The variation in the friction coefficient in relation to the water content was also analyzed, which decreased with increasing water content, except for the sand peak case. Regarding the effect of normal stress, a decreasing behavior of the coefficient was observed for the interface tests, and an increase was observed for the sand tests. Finally, a slight increase in the peak friction coefficient is observed due to the effect of the concrete curing time, while for the postpeak, there is a decrease; however, for both cases, the numerical difference is small.

- The results of this study obtained higher values of shear strength parameters than other authors. It is inferred that the cause of this difference is the concrete curing time, a variable not addressed in other studies.

Acknowledgements

Declaration of interest

The authors have no conflicts of interest to declare. All coauthors have observed and affirmed the contents of the paper, and there is no financial interest to report.

Authors' contributions

André Luis Meier: Conceptualization, Data curation, Formal analysis, Investigation, Methodology, Visualization, Writing – original draft. Vitor Pereira Faro: Conceptualization, Resources, Supervision, Writing – review & editing. Edgar Odebrecht: Conceptualization, Resources, Supervision, Writing – review & editing.

Data availability

The datasets generated during and/or analyzed during the current study are available from the corresponding author on reasonable request.

List of symbols

c_a	Interface adhesion
c_{ap}	Peak interface adhesion
e_{max}	Maximum void ratio
e_{min}	Minimum void ratio
f_{ck}	Characteristic compressive strength
$f_{ck, min}$	Minimum characteristic compressive strength
$f_{ck, mix}$	Characteristic compressive strength of the mixture
r	Correlation coefficient
t	Concrete curing time
w	Water content
CC	Curvature coefficient
CU	Uniformity coefficient
D	Pile diameter
D_{50}	Mean particle diameter
G	Soil particles density
RD	Relative density
R_a	Average roughness
R_{max}	Maximum roughness
R_n	Normalized roughness
δ	Interface friction angle
δ_p	Peak interface friction angle
δ_{pp}	Post peak interface friction angle
δ/ϕ	Interface-soil friction angle ratio
$(\delta/\phi)_p$	Peak interface-soil friction angle ratio
$(\delta/\phi)_{pp}$	Post peak interface-soil friction angle ratio
σ	Normal stress
τ	Shear stress
ϕ	Soil friction angle
ϕ'_c	Critical state friction angle
ϕ_p	Peak soil friction angle
ϕ_{pp}	Post peak soil friction angle

References

ABNT NBR 12004. (1990). *Soil: determination of the maximum index void ratio of cohesionless soils.* ABNT - Associação Brasileira de Normas Técnicas, Rio de Janeiro, RJ (in Portuguese).

ABNT NBR 12051. (1991). *Soil - determination of minimum index void ratio of cohesionless soils - method of test.* ABNT - Associação Brasileira de Normas Técnicas, Rio de Janeiro, RJ (in Portuguese).

ABNT NBR 7214. (2015). *Standard sand for cement tests – specification.* ABNT - Associação Brasileira de Normas Técnicas, Rio de Janeiro, RJ (in Portuguese).

ABNT NBR 5739. (2018). *Concrete - compression test of cylindrical specimens.* ABNT - Associação Brasileira de Normas Técnicas, Rio de Janeiro, RJ (in Portuguese).

ASME B46.1. (2009). *Surface texture: surface roughness, waviness, and lay.* ASME – American Society of Mechanical Engineers, New York.

ASTM D3080. (2011). *Standard test method for direct shear test of soils under consolidated drained conditions.* ASTM International, West Conshohocken, PA. http://dx.doi.org/10.1520/D3080-04.

ASTM D2488. (2017). *Standard practice for description and identification of soils (visual-manual procedures).* ASTM International, West Conshohocken, PA. http://dx.doi.org/10.1520/D2488-17E01.

Borges, A.B., Linn, R.V., Schnaid, F., & Maghous, S. (2020). A simplified numerical approach to the evaluation of residual shaft friction induced by concrete curing in drilled shafts on granular soils. *Revista IBRACON de Estruturas e Materiais*, 13(5), e13505. http://dx.doi.org/10.1590/s1983-41952020000500005.

Brumund, W.F., & Leonards, G.A. (1973). Experimental study of static and dynamic friction between soil and typical construction materials. *Journal of Testing and Evaluation*, 1(2), 162-165. http://dx.doi.org/10.1520/JTE10893J.

DeJong, J.T., & Westgate, Z.J. (2009). Role of initial state, material properties, and confinement condition on local and global soil-structure interface behavior. *Journal of Geotechnical and Geoenvironmental Engineering*, 135(11), 1646-1660. http://dx.doi.org/10.1061/(ASCE)1090-0241(2009)135:11(1646).

Dietz, M.S., & Lings, M.L. (2006). Postpeak strength of interfaces in a stress-dilatancy framework. *Journal of Geotechnical and Geoenvironmental Engineering*, 132(11), 1474-1484. http://dx.doi.org/10.1061/(ASCE)1090-0241(2006)132:11(1474).

Fakharian, K., & Evgin, E. (1996). An automated apparatus for three-dimensional monotonic and cyclic testing of interfaces. *Geotechnical Testing Journal*, 19(1), 22-31. http://dx.doi.org/10.1520/GTJ11404J.

Fellenius, B.H. (2020). *Basics of foundation design.* Retrieved in April 19, 2022, from www.fellenius.net

Fellenius, B.H., & Altaee, A.A. (1995). Critical depth: how it came into being and why it does not exist. *Proceedings of the Institution of Civil Engineers - Geotechnical Engineering*, 113(2), 107-111. http://dx.doi.org/10.1680/igeng.1995.27590.

Gómez, J.E., Filz, G.M., Ebeling, R.M., & Dove, J.E. (2008). Sand-to-concrete interface response to complex load paths in a large displacement shear box. *Geotechnical Testing Journal*, 31(4), 358-369. http://dx.doi.org/10.1520/GTJ100220.

Hamid, T.B., & Miller, G.A. (2009). Shear strength of unsaturated soil interfaces. *Canadian Geotechnical Journal*, 46(5), 595-606. http://dx.doi.org/10.1139/T09-002.

Jardine, R.J., Lehane, B.M., & Everton, S.J. (1993). Friction coefficients for piles in sands and silts. In D.A. Ardus, D. Clare, A. Hill, R. Hobbs, R.J. Jardine & J.M. Squire (Eds.), *Offshore site investigation and foundation behavior* (Advances in Underwater Technology, Ocean Science and Offshore Engineering, Vol. 28, pp. 661-677). London: Springer. http://dx.doi.org/10.1007/978-94-017-2473-9_31.

Lehane, B.M., Jardine, R.J., Bond, A.J., & Frank, R. (1993). Mechanisms of shaft friction in sand from instrumented pile tests. *Journal of Geotechnical Engineering*, 119(1), 19-35. http://dx.doi.org/10.1061/(ASCE)0733-9410(1993)119:1(19).

Miller, G.A., & Hamid, T.B. (2006). Interface direct shear testing of unsaturated soil. *Geotechnical Testing Journal*, 30(3), 13301. http://dx.doi.org/10.1520/GTJ13301.

Nardelli, A., Cacciari, P.P., & Futai, M.M. (2019). Sand-concrete interface response: the role of surface texture and confinement conditions. *Soil and Foundation*, 59(6), 1675-1694. http://dx.doi.org/10.1016/j.sandf.2019.05.013.

Nienov, F.A. (2016). *Bored pile performance of large diameter in sandy soil under vertical load* [Doctoral thesis, Federal University of Rio Grande do Sul]. Federal University of Rio Grande do Sul's repository (in Portuguese). Retrieved in April 19, 2022, from http://hdl.handle.net/10183/150506

Paikowsky, S.G., Player, C.M., & Connors, P.J. (1995). A dual interface apparatus for testing unrestricted friction of soil along solid surfaces. *Geotechnical Testing Journal*, 18(2), 168-193. http://dx.doi.org/10.1520/GTJ10320J.

Pennington, D.S. (1995). Cracked? Exploring postconstruction evidence in the interpretation of trial pile data. *Geotechnical Engineering*, 113(3), 132-143. http://dx.doi.org/10.1680/igeng.1995.27809.

Randolph, M.F., Dolwin, J., & Beck, R. (1994). Design of driven piles in sand. *Geotechnique*, 44(3), 427-448. http://dx.doi.org/10.1680/geot.1994.44.3.427.

Reddy, E.S., Chapman, D.N., & Sastry, V.V.R.N. (2000). Direct shear interface test for shaft capacity of piles in sand. *Geotechnical Testing Journal*, 23(2), 199-205. http://dx.doi.org/10.1520/GTJ11044J.

Salgado, R. (2008). *The engineering of foundations*. Boston: McGraw-Hill.

Tehrani, F.S., Han, F., Salgado, R., Prezzi, M., Tovar, R.D., & Castro, A.G. (2016). Effect of surface roughness on the shaft resistance of nondisplacement piles embedded in sand. *Geotechnique*, 66(5), 386-400. http://dx.doi.org/10.1680/jgeot.15.P.007.

Tiwari, B., & Al-Adhadh, A.R. (2014). Influence of relative density on static soil-structure frictional resistance of dry and saturated sand. *Geotechnical and Geological Engineering*, 32(2), 411-427. http://dx.doi.org/10.1007/s10706-013-9723-6.

Uesugi, M., & Kishida, H. (1986a). Influential factors of friction between steel and dry sands. *Soil and Foundation*, 26(2), 33-46. http://dx.doi.org/10.3208/sandf1972.26.2_33.

Uesugi, M., & Kishida, H. (1986b). Frictional resistance at yield between dry sand and mild steel. *Soil and Foundation*, 26(4), 139-149. http://dx.doi.org/10.3208/sandf1972.26.4_139.

Uesugi, M., Kishida, H., & Uchikawa, Y. (1990). Friction between dry sand concrete under monotonic and repeated loading. *Soil and Foundation*, 30(1), 115-128. http://dx.doi.org/10.3208/sandf1972.30.115.

Proposition of correlations for the dynamic parameters of carbonate sands

Felipe Oscar Pinto Barroso[1#] (ID), Alfran Sampaio Moura[1] (ID)

Article

Keywords
Carbonate sands
Soil dynamic parameters
Shear strain modulus
Damping ratio
Multiple linear regression

Abstract
The offshore industry has been challenged with the necessity to build structures with foundations on carbonate soils, found in extensive areas of the tropical and intertropical zones of the planet. As a better understanding of the behavior of these soils becomes more and more indispensable, this paper presents equations to predict the dynamic behavior of carbonate sands, in which two expressions (G/G_{max} *versus* γ and D *versus* γ) were obtained via multiple linear regression using data from resonant column tests carried out on carbonate sands from Cabo Rojo, Puerto Rico (Cataño & Pando, 2010). The proposed equations agreed well with experimental data. The error for the expressions G/G_{max} *versus* γ was less than 10%, while the expressions D *versus* γ trended to underestimate the values for the loose condition ($D_r = 24\%$), presenting an effective confining stress of 50kPa. Furthermore, the proposed equations were compared with predictions exhibited by Javdanian & Jafarian (2018) of G/G_{max} *versus* γ and D *versus* γ for carbonate sands, also yielding fairly concordant results.

1. Introduction

Carbonate soils are found in extensive areas of the tropical and intertropical zones of the Earth, forming deep layers of limestone sediments (Hyodo et al., 1996). The offshore oil and gas industry has often faced the need to build and install structures with foundations laid on this type of soil, creating the demand to develop research in order to better understand the behavior of carbonate soils, as well as its divergences in relation to soils originated from quartz (King & Lodge, 1988 *apud* Sharma & Ismail, 2006).

Carbonate sands have a more ductile and contractive behavior. When compared to quartz sands and tested under similar conditions, they tend to reduce their volume during shearing. A better way to understand their behavior is through laboratory and field tests.

This study aimed at developing correlations to predict the dynamic parameters of carbonate sands – maximum shear modulus (G_{max}) and damping ratio (D) – using multiple linear regression, comparing the predictions obtained through the proposed equations for G/G_{max} *versus* γ (shear strain) and D *versus* γ with experimental data from other studies.

2. Soil dynamic parameters

Soil dynamic parameters are highly dependent on the imposed level of strain. The shear modulus (G), for example, can be 10 times smaller when going from a shear strain of 0.001% to 1% (Barros & Hachich, 1998). The ranges of shear strain values vary according to the engineering problems, varying between $10^{-4}\%$ (foundation of precise equipment) and $10^{-1}\%$ (offshore problems).

Soil dynamic parameters can be determined through laboratory and field tests. However, in order to get the proper values, it is necessary to consider the strain levels involved in the situation and then conduct the tests in the same strain magnitude. According to Barros & Hachich (1998), examples of laboratory tests that can be used to obtain the soil dynamic parameters are: resonant column, bender elements, cyclic simple shear, cyclic triaxial and cyclic torsion.

Usual field tests to obtain dynamic properties are based on seismic methods. They cause shear strains of less than 0.001% and provide parameters related to reduced strains, such as the maximum shear modulus. According to Barros & Hachich (1998), examples of field tests commonly used to determine soil dynamic properties are: crosshole, downhole, uphole, seismic piezocone and pressiometric test.

Ponte & Moura (2017) assessed methods that considered small and large strains to obtain soil dynamic parameters. The cited authors concluded that the G_{max} obtained through large strain methods (such as the Standard Penetration Test, *SPT*) was on average three times smaller than that estimated by small strain ones (such as the downhole test). Since G_{max} is associated with small shear strains, the study showed how crucial it is to use the appropriate scale when estimating soil parameters. Analyzing how G varies with shear strain, it is

#Corresponding author. E-mail address: fp.oscarbarroso@gmail.com
[1]Universidade Federal do Ceará, Departamento de Engenharia Hidráulica e Ambiental, Fortaleza, CE, Brasil.

possible to qualitatively evaluate the decrease in shear strain modulus with the increase of γ. Barros & Hachich (1998) observed that it is common practice to determine G from the curve G/G_{max} versus γ, which is obtained using laboratory data, whereas G_{max} is determined through field testing.

3. Carbonate soils

Carbonate soils are the result of the natural sedimentation of particles, comprising biological, mechanical, physical, and chemical processes (Salem et al., 2013). They are characterized by remarkable intraparticle voids (cavities within the soil mass) and irregular shapes of their particles (such as curved plates and hollow tubes), originated from fragments of seashells and skeletal remains of small marine microorganisms. Moura & Freitas (2021) showed that the presence of structures with calcium carbonate, whose degradation can give rise to sands of carbonate origin, is quite recurrent around the world but especially common on the Northeastern coast of Brazil. According to Salem et al. (2013), samples of this type of soil subjected to X-ray diffraction revealed the mineralogical constitution of its particles, highly rich in calcium. As shown in Table 1, carbonate sands from Dabaa (Northern coast of Egypt) have 55.4% of CaO content, due to the environment where these soils are formed.

Table 1. Mineralogical composition of a carbonate sand (Salem et al., 2013).

Mineral	Percentage (%)
SiO_2	0.28
TiO_2	0.02
Al_2O_3	0.12
Fe_2O_3	0.02
MnO	< 0.01
MgO	0.2
CaO	55.4
Na_2O	< 0.01
K_2O	0.02
P_2O_5	0.06
SO_3	0.12
Cl	< 0.01
Ignition loss	43.53

The void ratio (e) of sands normally varies between 0.20 and 0.50 when they are more compact and between 0.8 and 1.2 when loose (Kullhawy & Mayne, 1990). Cataño (2006) carried out 13 tests on carbonate sands, changing their compactness state and determining e. The authors concluded that e for carbonate sands was higher than for typical sands, varying between 0.5 and 1.6 for the most compact states and between 1.1 and 2 for loose condition.

The specific gravity (G_s) is a property of the solid particles of a soil and is strongly linked to its mineralogy. Salem et al. (2013) stated that quartz sands have a G_s of 2.65, whereas carbonate sands usually have higher values, such as calcite (2.75) and aragonite (2.95). Table 2 presents the physical indexes of carbonate sands from different locations cited in the literature.

4. Dynamic parameters for carbonate sands and related research

Jafarian & Javdanian (2019) carried out dynamic and cyclic tests on carbonate sands of the Persian Gulf (Iran), verifying the influence of relative density (D_r) and confining stress (σ_c) on soil dynamic parameters. Their tests were performed at confining stress of 40, 200, and 400 kPa, and relative densities of 50% and 80%.

In their study, resonant column tests were used to obtain soil dynamic parameters for shear strains between 10^{-4}% and 10^{-2}% and cyclic triaxial tests for shear strains of 10^{-2}% to 1%. The maximum shear modulus was obtained for small strains ($\sim 10^{-4}$%) through the resonant column test.

From there, Jafarian & Javdanian (2019) analyzed in a graph the effects of varying relative density and confining stress on the normalized shear modulus (G/G_{max} curve) and on the damping ratio, for compact state ($D_r = 80$%) and loose state ($D_r = 50$%). They concluded that the dynamic properties G_{max} and D are minimally influenced by the relative density D_r. Also, if the effective confining stress increases, the maximum shear modulus increases and the damping ratio decreases.

In a study on carbonate sands from Nansha (Southern China), Kuang et al. (2020) verified the influence of grain-size distribution on the friction angle through triaxial tests, concluding that for carbonate sands friction angle increases as particle size decreases.

Table 2. Physical indexes of carbonate sands (Salem et al., 2013).

Origin	G_s	D_{10} (mm)	C_u	e_{min}	e_{max}
North Coast (Puerto Rico)	2.79	0.15	2.4	0.75	1.04
Cabo Rojo (Puerto Rico)	2.86	0.2	1.05	1.34	1.71
Playa Santa (Puerto Rico)	2.75	0.16	2.75	0.8	1.22
Dogs Bay (Ireland)	2.75	0.24	2.06	0.98	1.83
Ewa Plains (United States)	2.72	0.2	5.05	0.66	1.3

2

Barroso & Moura, Soil. Rocks, São Paulo, 2023 46(1):e2023001422

The literature presents several proposals to predict soil dynamic parameters, for example: Hardin & Drnevich (1972), Ishibashi & Zhang (1993), Ishihara (1996), Rollins et al. (1998), Darendeli (2001), and Oztoprak & Bolton (2013).

The hyperbolic model proposed by Ishihara (1996) has been widely used to describe the nonlinear stress-strain behavior of a wide variety of soils (Kondner & Zelasko, 1963; Duncan & Chang, 1970) and used in the Theory of Plasticity to implement laws for material hardening (Vermeer, 1978). It is a model recognized as the cornerstone for several other studies and models developed on the dynamic response of sands.

Equation 1 shows the hyperbolic model expression for G/G_{max} and Equation 2, for damping ratio, both expressed in terms of the shear strain. In Equation 1 and Equation 2, γ_r is the reference shear strain when $G/G_{max} = 0.5$.

$$\frac{G}{G_{max}} = \frac{1}{1 + \gamma / \gamma_r} \tag{1}$$

$$D = \frac{4}{\pi} \bullet \left[1 + \frac{1}{\gamma / \gamma_r} \right] \bullet \left[1 - \frac{\ln\left(1 + \gamma / \gamma_r\right)}{\gamma / \gamma_r} \right] - \frac{2}{\pi} \tag{2}$$

On the other hand, Ishibashi & Zhang (1993) evaluated experimental data regarding the dynamic shear modulus and damping ratio for several types of soils, including sands and clays of high plasticity. The equations developed for G/G_{max} and D are expressed in terms of shear strain, confining effective stress, and plasticity index (*PI*). In this model, Equations 3-5 can be used to determine G/G_{max}, and Equation 6 to determine the damping ratio of non-cohesive soils (as the carbonate sands).

$$\frac{G}{G_{max}} = k\left(\gamma\right) \bullet \sigma_0'^{\left[m(\gamma) - m_0 \right]} \tag{3}$$

$$k\left(\gamma\right) = 0,5 \bullet \left[1 + \tanh\left\{ \ln\left(\frac{0.00012}{\gamma} \right)^{0.492} \right\} \right] \tag{4}$$

$$m\left(\gamma\right) - m_0 = 0.272 \bullet \left[1 - \tanh\left\{ \ln\left(\frac{0.000556}{\gamma} \right)^{0.4} \right\} \right] \tag{5}$$

$$D = 0.333 \bullet \left\{ 0.586 \bullet \left(\frac{G}{G_{máx}} \right)^2 - 1.547 \bullet \left(\frac{G}{G_{máx}} \right) + 1 \right\} \tag{6}$$

5. Method

In order to develop the equations, the study site was chosen and the characterization of the soil was performed.

In this study, two equations are presented to predict the dynamic behavior of carbonate sands: (1) G/G_{max} versus γ; and (2) D versus γ. The expressions were obtained using multiple linear regression and data from resonant column tests carried out in a carbonate sand from Cataño & Pando (2010).

5.1 Study site

The soil assessed in this study was a carbonate sand from Cabo Rojo, southwest of Puerto Rico, which was tested by Cataño & Pando (2010). They performed characterization and dynamic tests, including resonant column tests, and obtained the physical properties and the dynamic parameters (maximum shear modulus and damping ratio), as well as the curves G/G_{max} versus γ and D versus γ.

The studied carbonate sand was poorly graded, with fine to medium grain size, comprising grains between 0.2 mm and 2 mm and without any fines. Table 3 presents its physical properties, with higher G_s and e than the usual values for quartz sands, which implied lower maximum and minimum specific weights.

For more works related to the dynamic behavior of carbonate sands, the following works are cited: Giretti et al. (2018), Liu et al. (2020) and Zhou et al. (2020).

6. Proposals of correlations for shear modulus and damping

6.1 Relations *G versus* γ and *D versus* γ

In order to determine the correlations, the authors used the data presented in Cataño & Pando (2010), which obtained G/G_{max} versus γ curves through resonant column tests performed in the carbonate sands of Cabo Rojo.

The correlations were based on two different relative densities: loose (relative compactness between 21% and 26%) and compact (relative compactness of 91%). The tests were carried out considering two effective confining stress levels (50 and 300 kPa).

6.2 Development of proposed equations

The development of the equations G/G_{max} versus γ and D versus γ sought to establish mathematical relationships between G/G_{max} and D and the shear strain, as a function of

Table 3. Physical properties of the carbonate sand used in this study (Cataño & Pando, 2010).

G_s	e_{max}	e_{min}	% CaCO$_3$
2.86	1.71	1.34	92.8%

explanatory variables. Very few models present expressions as a function of more than one explanatory variable (in addition to γ) and one of them is the hyperbolic model proposed by Ishihara (1996), which considers solely the relative shear strain (γ / γ_r).

In order to develop the equations here proposed, a generic expression (Equation 7) was used to represent the multiple linear regression, i.e., the linear relationship between a dependent variable (y) and two or more independent variables ($x_1, x_2, ..., x_k$). In Equation 7, a_0 is the intercept y (or the value of y) when all the independent variables are zero, while a_1, a_2 and a_k are the coefficients of the independent variables.

$$y = a_0 + a_1 \bullet x_1 + a_2 \bullet x_2 + \ldots + a_k \bullet x_k \qquad (7)$$

Since multiple linear regressions involve calculations of complex nature, impractical to be performed manually (Triola, 2008), an electronic spreadsheet was used to process them. The independent variables used in this study were relative density D_r (the compactness state in which the carbonate sand was found), effective confining stress σ'_0 (the stress state to which the material was subjected), and shear strain, which has a great influence on the dynamic response.

Initially, equations correlating G/G_{max} and D with the independent variables were proposed (Equations 8-9).

$$\frac{G}{G_{max}} = a_0 \bullet D_r^{a_1} \bullet \sigma_0'^{a_2} \bullet \left(\frac{1}{1+\gamma} \right)^{a_3} \qquad (8)$$

$$D = a_0' \bullet D_r^{a_1'} \bullet \sigma_0'^{a_2'} \bullet \gamma^{a_3'} \qquad (9)$$

Using values obtained from the curves G/G_{max} versus γ and D versus γ in Cataño & Pando (2010) for the independent variables, the coefficients $a_0, a_1, a_2, a_3, a'_0, a'_1, a'_2$, and a'_3 were determined through multiple linear regression. And since the variables D_r, σ'_0, and γ are nonlinearly related to G/G_{max} and D, a logarithmic transformation was used to proceed with the multiple linear regression (Equations 10-11).

$$\ln\left(\frac{G}{G_{max}} \right) = \ln a_0 + a_1 \bullet \ln D_r + a_2 \bullet \ln \sigma_0' + a_3 \bullet \ln\left(\frac{1}{1+\gamma} \right) \qquad (10)$$

$$\ln\left(D \right) = \ln a_0' + a_1' \bullet \ln D_r + a_2' \bullet \ln \sigma_0' + a_3' \bullet \ln \gamma \qquad (11)$$

Important to mention that points 1 to 4 in Table 4 (see below) were obtained from Cataño & Pando (2010) and spared to later validate the proposed equations (the validation dataset, *not* used in the development step).

6.3 Proposal for the equation G/G_{max} versus γ and validation

The coefficients of Equation 8 were determined using multiple linear regression in an electronic spreadsheet. Results are shown in Table 5. The obtained expression for G/G_{max} versus γ is shown in Equation 12 and its coefficient of determination (R^2) was 0.87.

$$\frac{G}{G_{max}} = 0.42886 \bullet D_r^{-0.048698} \bullet \sigma_0'^{0.20891} \bullet \left(\frac{1}{1+\gamma} \right)^{13.2937} \qquad (12)$$

As previously mentioned, in order to validate Equation 12, some experimental values (points 1 to 4 in Table 4) presented by Cataño & Pando (2010) were considered as a reference and not used in the development of the equations. The comparison between the experimental values and the predicted G/G_{max} (obtained with the proposed equation) is presented in Table 6 and Figure Figure 1.

The results of the proposed expressions (Equation 12) agreed fairly well (error < 10%) with the experimental values presented in Cataño & Pando (2010) for the carbonate sands evaluated in this study, both for soft and compact states.

Figure 2 shows the curves G/G_{max} versus γ obtained by applying the expression proposed in this study to estimate G/G_{max} versus γ (i.e., Equation 12). By analyzing Figure 2, it can be observed that, for $\sigma'_c = 50$ kPa, the equation underestimated G/G_{max} for lower shear strains but had a good convergence for higher values. For $\sigma'_c = 100$ kPa, the same trends were also found.
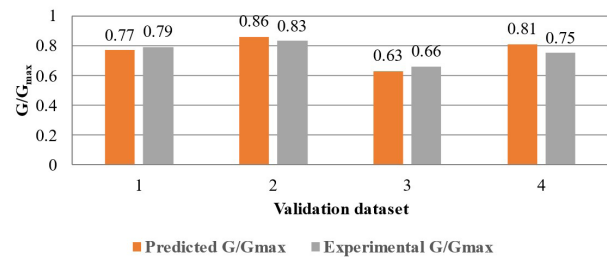

Figure 1. Comparison between predicted and experimental values for G/G_{max}.

Table 4. Test results used in the validation step of the proposed equations [adapted from Cataño & Pando (2010)].

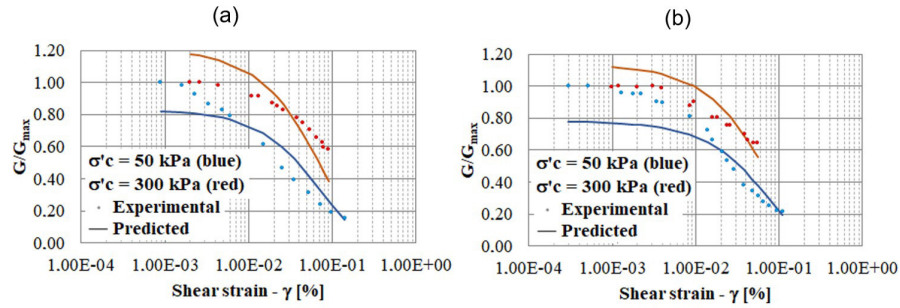| Point	D_r (%)	σ'_c (kPa)	γ (%)	G (MPa)	D (%)
1	21 - 26	50	6×10^{-3}	34.23	3.17
2	21 - 26	300	2.6×10^{-2}	110.2	1.89
3	91	50	1.6×10^{-2}	47.37	3.62
4	91	300	2.6×10^{-2}	119.91	3.16

(a)

(b)

Figure 2. Comparison between the prediction for G/G_{max} and experimental values considering (a) $D_r = 24\%$ and (b) $D_r = 91\%$.

Table 5. Coefficients obtained for equation G/G_{max} *versus* γ.

a_0	a_1	a_2	a_3
0.42886	-0.048698	0.20891	13.2937

Table 6. Validation of the proposed equation G/G_{max} *versus* γ.

Point	Predicted G/G_{max}	Experimental G/G_{max}	$\Delta[\%]$
1	0.77	0.79	-2.53
2	0.86	0.83	+3.61
3	0.63	0.66	-4.55
4	0.81	0.75	+8

Table 7. Coefficients obtained for equation D *versus* γ.

a_0	a_1	a_2	a_3
103.61	0.076315	-0.40996	0.50658

Table 8. Validation of the proposed equation D *versus* γ.

Point	Predicted D	Experimental D	$\Delta[\%]$
1	1.99	3.17	-37.22
2	2.01	1.89	+6.35
3	3.62	3.62	0
4	2.22	3.16	-29.75

6.4 Proposal for the equation *D versus* γ and validation

Similarly, the coefficients of Equation 9 were determined using multiple linear regression in an electronic spreadsheet. Results are shown in Table 7. The obtained expression for D *versus* γ is shown in Equation 13 and its R^2 was 0.92.

$$D = 103.61 \cdot D_r^{0.076315} \cdot \sigma_0'^{-0.40996} \cdot \gamma^{0.50658} \qquad (13)$$

Similarly, when validating Equation 13, some experimental values (points 1 to 4 in Table 4) from Cataño & Pando (2010) were also taken as a reference and not
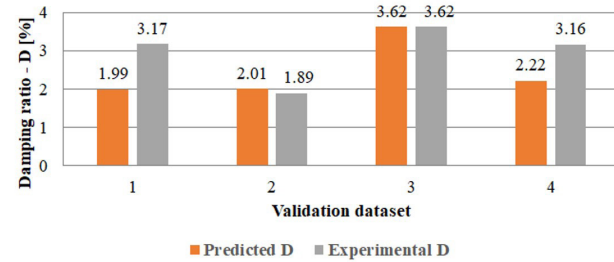
Figure 3. Comparison between predicted and experimental values for D.

used in the development step. The comparison between the predicted and the experimental values for D is shown in Table 8 and Figure 3.

Based on Table 8 and Figure 3, one can observe that there were differences between predicted and experimental values of D of up to 37.22%. On the other hand, two of the four predictions presented very small to negligible differences.

Figure 4 shows the new curves D *versus* γ obtained by applying the expression proposed in this study to estimate D *versus* γ (i.e., Equation 13). Based on the graphs, the proposed equation provided satisfactory concordant predictions when compared with experimental values. However, the expression showed a trend to underestimate predictions for loose sands ($D_r = 24\%$) and effective confining stress of 50 kPa.

6.5 Comparison between predictions of the proposed equations and experimental values from Javdanian & Jafarian (2018)

Javdanian & Jafarian (2018) tested a carbonate sand from the Island of Hormuz, a seismic region of the Persian Gulf, in Iran. They studied the dynamic behavior of that sand through resonant column and cyclic triaxial tests, considering effective confining stress of 200, 400, and 800 kPa, and obtaining the curves G/G_{max} *versus* γ and D *versus* γ. The physical indexes of the referred carbonate sand are $G_s = 2.73$, $\gamma_{max} = 18.1$ kN/m³ and $\gamma_{min} = 16.1$ kN/m³.

Predictions of the proposed equations on the dynamic parameters for the carbonate sand from the Island of Hormuz were evaluated and then compared with the experimental
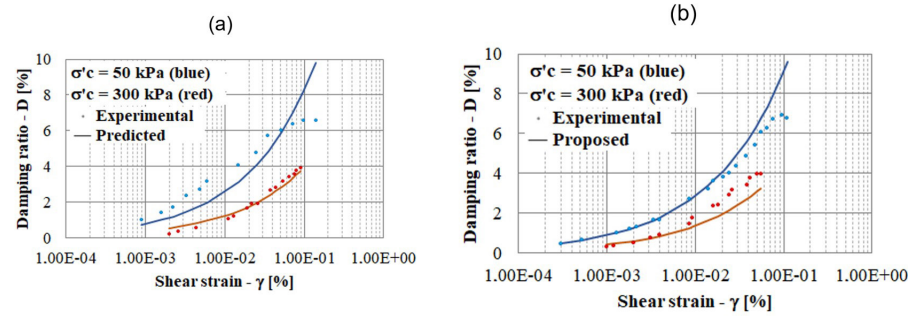
Figure 4. Comparison between the prediction for *D* and experimental values considering $D_r = 24\%$ (a) and $D_r = 91\%$ (b).
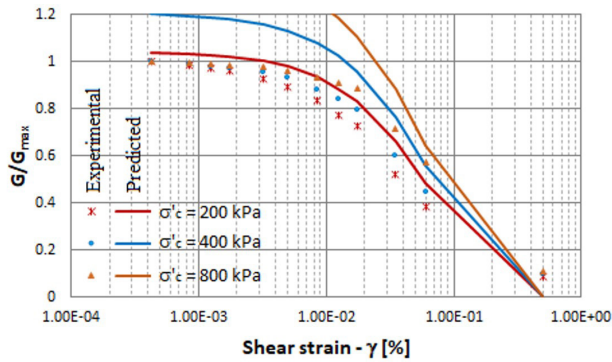

Figure 5. Comparison between predictions for G/G_{max} using proposed equations and experimental data for the carbonate sand from Javdanian & Jafarian (2018).
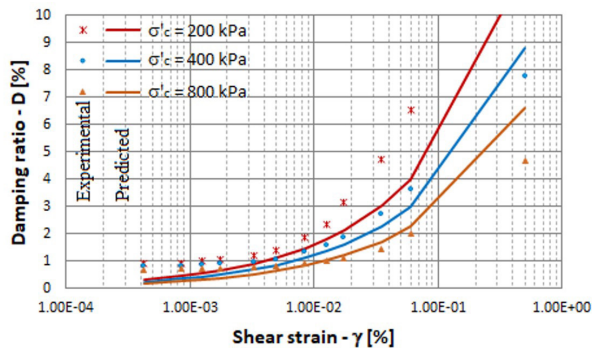

Figure 6. Comparison between predictions and experimental values for *D versus* γ of the carbonate sand from Javdanian & Jafarian (2018).

data presented in the study by Javdanian & Jafarian (2018). Figures 5-6 show the predicted and experimental curves for G/G_{max} *versus* γ and *D versus* γ of the aforementioned carbonate sand, in which solid lines represent the predictions obtained with the proposed expressions and the markers correspond to laboratory data.

From Figure 5, it can be observed that, in general, predicted values for G/G_{max} were a little overestimated when compared with experimental data (Δ of up to 32%), especially

for smaller shear strains (12%). This can be explained by the fact that the expression here presented (Equation 6) was developed based on experimental data obtained from tests carried out at low confining stress (50 to 300 kPa). Thus, for scenarios of higher confining stress, as in this case, less convergent results can be accepted.

Figure 6 shows that the predicted values for the damping ratio were in fair agreement with the experimental data from Javdanian & Jafarian (2018), even for effective confining stress higher than the range used to develop Equation 9, proposed in this study.

7. Conclusions

The carbonate sand from Cabo Rojo (Puerto Rico) evaluated in Cataño & Pando (2010) presented different physical indexes when compared to common quartz sands. Both G_s and void ratio were higher than typical values for quartz sands, which implied lower maximum and minimum specific weights.

In this study, multiple linear regression was used to determine equations to predict the curves G/G_{max} *versus* γ and *D versus* γ for carbonate sands, reaching coefficients of determination (R^2) of 0.87 and 0.92, respectively.

The predictions regarding the relationship G/G_{max} *versus* γ showed good agreement with the experimental values obtained by Cataño & Pando (2010), with an average error of less than 10% (in relation to reference/experimental values). For *D versus* γ, the proposed equation also presented concordant results, with a slight trend to underestimation but mainly for the loose condition ($D_r = 24\%$) of the sands and lower effective confining stress (50 kPa).

Predictions on the dynamic parameters using the equations proposed in this study were also compared with the experimental results of a carbonate sand from Iran (Javdanian & Jafarian, 2018). The predictions for the damping ratio agreed with the experimental data regardless of the effective confining stress, a fact not observed for the curve G/G_{max} *versus* γ, which presented good results only for the confining stress of 200 kPa. The highest variation obtained for G/G_{max} was 32% for higher confining stresses and less than 12% for lower confining stresses.

6

Barroso & Moura, Soil. Rocks, São Paulo, 2023 46(1):e2023001422

Acknowledgements

Declaration of interest

The authors have no conflicts of interest to declare. All co-authors have observed and affirmed the contents of the paper and there is no financial interest to report.

Authors' contributions

Felipe Oscar Pinto Barroso: conceptualization, funding acquisition, investigation, data curation, methodology, software, visualization, writing – original draft. Alfran Sampaio Moura: conceptualization, formal analysis, funding acquisition, data curation, supervision, validation, writing – review & editing.

Data availability

Data analyzed in the course of the current study are available in the GeoFlorida 2010 repository, https://doi. org/10.1061/41095(365)83.

List of symbols

a_0, a_1, a_2, a_3: coefficients of the multiple linear regression
e: void ratio
e_{max}: maximum void ratio
e_{min}: minimum void ratio
v_R: Rayleigh wave velocity
v_s: shear wave velocity
C_u: coefficient of uniformity
D: damping ratio
D_r: relative density
D_{10}: soil effective diameter
G: shear modulus
G_{max}: maximum shear modulus
G_s: specific gravity
R^2: coefficient of determination
SPT: standard penetration test
γ: shear strain
γ_r: reference shear strain when $G/G_{max} = 0.5$
γ_{max}: maximum specific weight
γ_{min}: minimum specific weight
σ'_c or σ'_0: confining effective stress
Δ: percentage variation

References

Barros, J.M.C., & Hachich, W. (1998). Fundações sujeitas a esforços dinâmicos. In W.C. Hachich & F.F. Falconi (Eds.), *Fundações: teoria e prática* (pp. 409-442). Pini.

Cataño, A.J. (2006). *Stress strain behavior and dynamic properties of Cabo Rojo calcareous sands* [Master's dissertation, University of Puerto Rico]. University of Puerto Rico's repository. Retrieved in December 22, 2022, from https://scholar.uprm.edu/handle/20.500.11801/1782?show=full

Cataño, A.J., & Pando, M.A. (2010). Static and dynamic properties of a calcareous sand from Southwest Puerto Rico. In D.O. Fratta, A.J. Puppala & B. Muhunthan (Eds.), *GeoFlorida 2010: Advances in Analysis, Modeling & Design* (pp. 842-851). Reston, United States of America: American Society of Civil Engineers. https://doi.org/10.1061/41095(365)83.

Darendeli, B.M. (2001). *Development of a new family of normalized modulus reduction and material damping curves* [Doctoral thesis, The University of Texas at Austin]. The University of Texas at Austin's repository. Retrieved in December 22, 2022, from http://hdl.handle.net/2152/10396

Duncan, J.M., & Chang, C.Y. (1970). Nonlinear analysis of stress and strain in soils. *Journal of the Soil Mechanics and Foundations Division*, *96*(5), 1629-1653. http://dx.doi.org/10.1061/JSFEAQ.0001458.

Giretti, D., Fioravante, V., Been, K., & Dickenson, S. (2018). Mechanical properties of a carbonate sand from a dredged hydraulic fill. *Geotechnique*, *68*(5), 410-420. http://dx.doi.org/10.1680/jgeot.16.P.304.

Hardin, B.O., & Drnevich, V.P. (1972). Shear modulus and damping in soils: design equations and curves. *Journal of the Soil Mechanics and Foundations Division*, *98*(7), 667-692. http://dx.doi.org/10.1061/JSFEAQ.0001760.

Hyodo, M., Aramaki, N., Itoh, M., & Hyde, A.F.L. (1996). Cyclic strength and deformation of crushable carbonate sand. *Soil Dynamics and Earthquake Engineering*, *15*(5), 331-336. http://dx.doi.org/10.1016/0267-7261(96)00003-6.

Ishibashi, I., & Zhang, X. (1993). Unified dynamic shear moduli and damping ratios of sand and clay. *Soil and Foundation*, *33*(1), 182-191. http://dx.doi.org/10.3208/sandf1972.33.182.

Ishihara, K. (1996). *Soil behaviour in earthquake geotechnics*. Oxford University Press.

Jafarian, Y., & Javdanian, H. (2019). Dynamic properties of calcareous sand from the Persian Gulf in comparison with siliceous sands database. *International Journal of Civil Engineering*, *18*, 245-249. http://dx.doi.org/10.1007/s40999-019-00402-9.

Javdanian, H., & Jafarian, Y. (2018). Dynamic shear stiffness and damping ratio of marine calcareous and siliceous sands. *Geo-Marine Letters*, *38*, 315-322. http://dx.doi.org/10.1007/s00367-018-0535-9.

Kondner, R.L., & Zelasko, J.S. (1963). A hyperbolic stress-strain formulation of sands. In Associação Brasileira de Mecânica dos Solos (Ed.), *Proceedings of the Second Panamerican Conference on Soil Mechanics and Foundation Engineering* (pp. 289-324). São Paulo, Brazil: Associação Brasileira de Mecânica dos Solos.

Kuang, D., Long, Z., Wang, J., Zhou, X., & Yu, P. (2020). Experimental study on particle size effect on mechanical behaviour of dense calcareous sand. *Soils and Rocks*, *43*(9), 567-574. http://dx.doi.org/10.28927/SR.434567.

Kullhawy, F.H., & Mayne, P.H. (1990). *Manual on estimating soil properties for foundation design*. Cornell University.

Liu, X., Li, S., & Sun, L. (2020). The study of dynamic properties of carbonate sand through a laboratory database. *Bulletin of Engineering Geology and the Environment*, *79*, 3843-3855. http://dx.doi.org/10.1007/s10064-020-01785-z.

Moura, R.L., & Freitas, M.O. (2021). *Rodolitos: os desconhecidos recifes "rolling stones"*. Retrieved in January 12, 2023, from https://oeco.org.br/analises/rodolitos-os-desconhecidos-recifes-rolling-stones/

Oztoprak, S., & Bolton, M.D. (2013). Stiffness of sands through a laboratory test database. *Geotechnique*, *63*(1), 54-70. http://dx.doi.org/10.1680/geot.10.P.078.

Ponte, G.F., & Moura, A.S. (2017). Avaliação do comportamento dinâmico das fundações superficiais de aerogeradores a partir de ensaios de pequena e grande deformações. *Revista Eletrônica de Engenharia Civil*, *13*(1), 95-105. http://dx.doi.org/10.5216/reec.v13i1.40950.

Rollins, K.M., Evans, M.D., Diehl, N.B., & Daily III, W.D. (1998). Shear modulus and damping relationships for gravels. *Journal of Geotechnical and Geoenvironmental Engineering*, *124*(5), 398-405. http://dx.doi.org/10.1061/(ASCE)1090-0241(1998)124:5(396).

Salem, M., Elmamlouk, H., & Agaiby, S. (2013). Static and cyclic behavior of North Coast calcareous sand in Egypt. *Soil Dynamics and Earthquake Engineering*, *55*, 83-91. http://dx.doi.org/10.1016/j.soildyn.2013.09.001.

Sharma, S.S., & Ismail, M.A. (2006). Monotonic and cyclic behavior of two calcareous soils of different origins. *Journal of Geotechnical and Geoenvironmental Engineering*, *132*(12), 1581-1591. http://dx.doi.org/10.1061/(ASCE)1090-0241(2006)132:12(1581).

Triola, M.F. (2008). *Introdução à estatística*. LTC.

Vermeer, P.A. (1978). A double hardening model for sand. *Geotechnique*, *28*(4), 413-433. http://dx.doi.org/10.1680/geot.1978.28.4.413.

Zhou, X.Z., Chen, Y.M., Liu, H.L., & Zhang, X.L. (2020). Experimental study on the cyclic behavior of loose calcareous sand under linear stress paths. *Marine Georesources and Geotechnology*, *38*(3), 277-290. http://dx.doi.org/10.1080/1064119X.2019.1567631.

Overconsolidated flysch-type clays. Engineering considerations for the Strait of Gibraltar tunnel project

Francisco Javier Manzano[1#] (ID), Francisco Lamas[2] (ID), José Miguel Azañón[3] (ID)

Article

Keywords
Flysch clay
Gibraltar Strait tunnel
Cam clay model
Triaxial testing
Hardening Soil model
Soil modelling

Abstract

The stress-strain behaviour of 85 overconsolidated clay samples from Campo de Gibraltar Flysch Through Domain (Algeciras Unit, South Spain) is presented and discussed. The samples were identified and classified following ASTM standards while their chemical and mineralogical composition were determined by chemical and X-ray techniques. Several samples were tested under triaxial as well as oedometric conditions. Given the results, a detailed comparison was made between different theoretical constitutive models and real testing data, using the finite-elements method. The comparison indicated a good fit between experimental data and those found with finite-elements modelling when the Hardening Soil constitutive model was used. This model showed a better fit than did the Modified Cam-Clay model (historically used for modelling clayey soils), although the latter fit proved better for lower strain values (<5%) than higher ones. These results clarify this intermediate material (hard soils – weak rocks) behaviour and will help in Strait of Gibraltar tunnel project design, as these materials are widely involved in this tunnel design.

1. Introduction

Joining Africa and Europe by a tunnel under the Strait of Gibraltar is a longstanding idea from the 19th century, first appearing as a project in documents related to Charles Villedeuil in 1869 (Velasco, 2016). Since then, various plans had been proposed until 1995, when the latest proposal was finally submitted. This project consists of a single railway tunnel running from Punta Paloma (Spain) to Punta Malabata (Morocco), which would be completed by a second tunnel in a subsequent stage (Figure 1).

This huge engineering project would involve a complex geological scheme associated with flysch-type deposits (Manzano et al., 2020).

The Campo de Gibraltar Flysch Trough Domain represents part of the Gibraltar Arc System, which is in turn formed by Betic System, the Rift, and the Alboran Basin. Formed during Alpine orogenesis in the Betic Cordillera, it is widely represented in southern Spain and northern Morocco. Lithologically, it has mainly deep marine facies with multicoloured clays (often marls) and carbonatic siliciclastic sandstones, typical of flysch-type deposits (Balanyá et al., 2004).

The term "flysch", introduced by Studer (1827), has historically been used by Alpine geologists to define "sedimentary deposits consisting in varying alternation of clastic sediments associated with orogenesis" (Marinos & Hoek, 2001). These deposits are formed by a rhythmic alternation of fine-grained materials and sandstone layers. Geotechnically, these formations are characterised by their diversity, clay-mineral content, and several sheared discontinuities.

Despite the existence of wide outcrops of flysch worldwide and the complexity of studying their behaviour, relatively little research has been conducted in this field, despite the fact that these formations pose several critical engineering problems for public works (Palomba et al., 2013; Dounias et al., 1996). Over-consolidated clays related to flysch deposits are widely recognized to be involved in several engineering problems. Slope instabilities associated with such deposits are well known throughout the world (Mikoš et al., 2009; Arbanas et al., 2008; Azañón et al., 2010; Pánek et al., 2009, etc). Landslides constitute the main hazard related to flysch deposits though not the only one. Coastal cliff retreats (Moon & Healy, 1994), or the complexities of tunnel support (Jovičić et al, 2009; Aydin et al., 2004) are some of the problems caused by these deposits. All of these hazards together require fuller knowledge of this special soft rock- hard soil deposits.

In particular, the study of the behaviour of Campo de Gibraltar Flysch clays (Betic Cordillera, southern Spain) has led engineering geologists to propose an approach for

#Corresponding author. E-mail address: franciscojavier.manzano@uca.es
[1]Universidad de Cádiz, Escuela Politécnica Superior, Departamento de Ingeniería Civil e Industrial, Algeciras, Cádiz, España.
[2]Universidad de Granada, Escuela Técnica Superior de Ingeniería de Caminos Canales y Puertos, Departamento de Ingeniería Civil, Granada, España.
[3]Universidad de Granada, Facultad de Ciencias, Departamento de Geodinámica, Granada, España.

Manzano et al., Soil. Rocks, São Paulo, 2023 46(1):e2023002222

1

analysing such complex soils, which show intermediate behaviour between hard soils and soft rocks. This soil presents serious difficulties for taking good-quality samples (Arbanas et al., 2008). For example, soil samples often become disturbed and must be tested in a short period of time (Roje-Bonacci, 1998).

The present paper highlights a case study in southern Spain with the aim of improving knowledge of Flysch soil characteristics by presenting the results of several intensive soil investigations in different locations within Campo de Gibraltar Flysch Trough Domain. A full set of mechanical and chemical testing is presented and discussed. These tests allowed us to understand this soil behavior and suppose a better knowledge of such complex and uninvestigated soils. This has major implications for future engineering projects,

including tunnel under the Strait of Gibraltar as its design will strongly be affected by geotechnical characteristics of these soils.

2. Sampling, laboratory testing methods, and results

2.1 Sampling and samples

Map of Figure 2 shows the locations of the samples used in this study. A total of 85 samples were tested, all taken as undisturbed as possible according to ASTM D1587 (ASTM, 2000). When undisturbed sampling was not feasible or samples
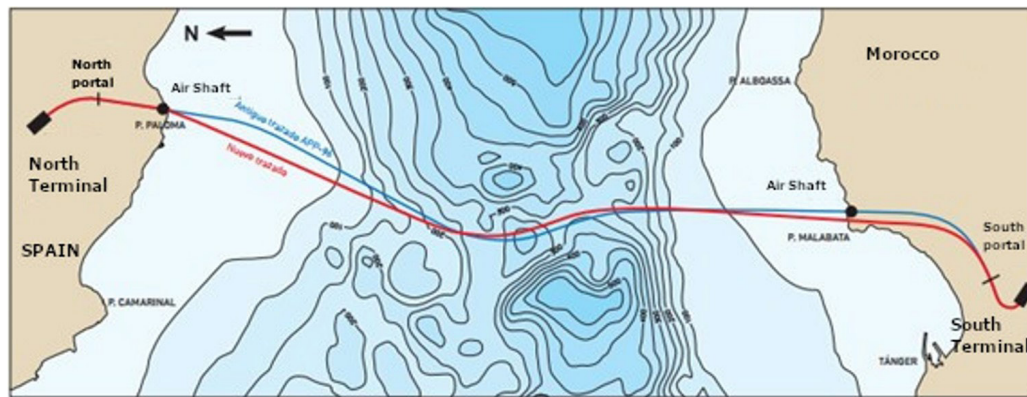
Figure 1. Tunnel layout proposal. Red line shows new proposal whereas blue one shows previous one.
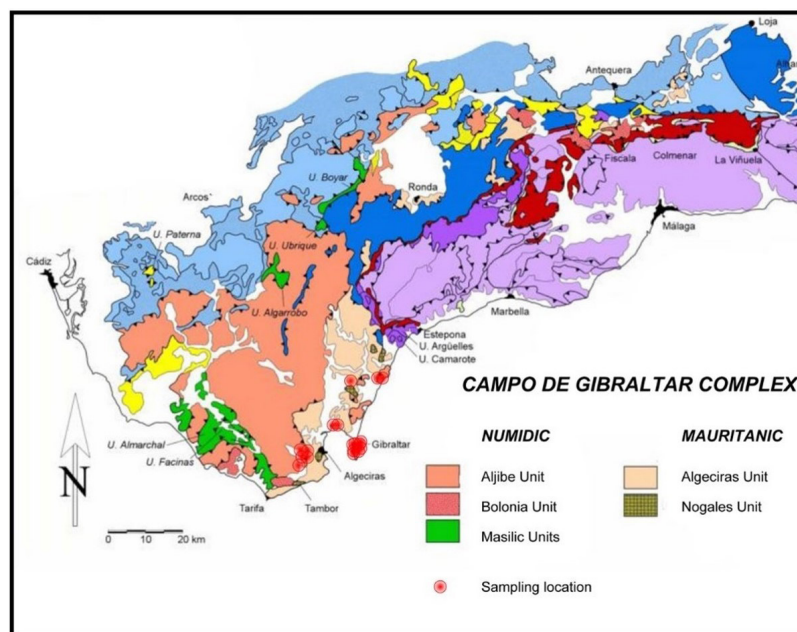
Figure 2. Geological plan of the study area showing sampling locations.

Table 1. Samples depth.

Sample	Depth	Sample	Depth	Sample	Depth
TES-01-12	4.60 - 5.00	TES 34-12	8.60 - 9.00	TES 26-13	19.00-19.60
TES-02-12	10.30 - 10.60	TES 35-12	7.15 - 7.96	TES 27-13	16.00-17.00
TES-03-12	11.60 - 12.00	TES 36-12	5.60 - 5.90	TES 28-13	4.80 - 5.20
TES-04-12	14.25 - 14.65	TES 01-13	12.20 - 12.45	TES 29-13	8.80 - 9.20
TES-08-12	10.60 - 11.00	TES 02-13	3.00 - 3.60	TES 30-13	12.20 - 12.50
TES-10-12	8.40 - 8.65	TES 03-13 (SR)	6.10 - 6.70	TES 31-13	7.00 - 7.33
TES-11-12	12.60 - 12.85	TES 03-13 (M)	6.70 - 7.30	TES 32-13	5.30 - 5.90
TES-12-12	16.10 - 16.30	TES 04-13	8.90 - 9.30	TES 33-13	19.00 - 19.40
TES 13-12	5.10 - 5.40	TES 05-13	14.20 - 14.5	TES 34-13	7.80 - 8.15
TES 14-12	3.60 - 3.90	TES 06-13	15.35 - 15.70	TES 37-13	10.00 - 10.30
TES 15-12	9.85 - 10.10	TES 07-13	8.70 - 9.00	TES 35-13	10.50 - 11.00
TES 16-12	8.50 - 8.80	TES 08-13	10.10 - 10.60	TES 36-13	11.25 - 11.80
TES 17-12	7.30 - 7.70	TES 09-13	14.25 - 14.55	TES 01-14	7.35 - 7.8
TES 18-12	13.75 - 14.00	TES 11-13	1.20 - 1.80	TES 02-14	10.8 - 11.23
TES 19-12	7.70 - 8.30	TES 12-13	5.0 - 5.6	TES 03-14	6.1 - 6.5
TES 20-12	14.10 - 14-35	TES 13-13	7.5 - 8.1	TES 04-14	8.10 - 8.70
TES 21-12	14.10 - 14-35	TES 14-13	10.80 - 11.12	TES 05-14	16.75 - 17.10
TES 22-12	15.00 - 15.40	TES 15-13	3.0 - 3.3	TES 06-14	10.95 - 11.90
TES 23-12	4.75 - 5.00	TES 16-13	8.3 - 8.6	TES 07-14	18.20 - 18.57
TES 24-12	6.55-6.75	TES 17-13	3.35 - 3.9	TES 08-14	22.90 - 23.27
TES 25-12	19.6 - 20.00	TES 18-13	4.1 - 4.4	TES 09-14	4.00 - 4.45
TES 26-12	14.7 - 15.10	TES 19-13	16.9 - 17.5	TES 10-14	6.20 - 6.60
TES 27-12	28.00 - 28.40	TES 20-13	16.13 - 16.60	TES 11-14	1.98 - 2.50
TES 28-12	16.10-16.35	TES 21-13	18.90 - 19.34	TES 12-14	9.20 - 9.50
TES 29-12	9.00 - 10.00	TES 22-13	18.40-18.84	TES 13-14	4.60 - 5.00
TES 30-12	10.00 - 11-00	TES 23-13	15.20-15.60	TES 15-14	2.85 - 3.60
TES 31-12	6.50-7.50	TES 24-13	17.00-17.60	TES 18-14	7.00 - 7.37
TES 32-12	4.50 - 5.50	TES 25-13	17.48-17.80	TES 19-14	9.20 - 9.60
TES 33-12	9.00 - 10.00				

were of poor quality, a triple barrel was used to obtain good quality cores that could be tested in the laboratory. Samples were obtained at different depths in each location (Table 1)

All samples were taken in soils belonging to Algeciras Unit which is the upper unit within Mauritanic facies of Campo de Gibraltar flysh domain. This unit is aged from upper cretacic to Neogene and it is characterized by a rhythmic alternance of sandstones and overconsolidated hard clays. These clayey levels were sampled for further laboratory testing.

2.2 Sample description: phase relationships, particle size, and composition

All the samples were taken for laboratory testing. Geotechnical characterization followed ASTM standards (Table 2) for different parameters and variables.

Table 3 presents data concerning the natural moisture, percentage of particle sizes below 0.08 mm, and Atterberg consistency parameters: liquid limit (LL), plastic limit (PL), and plasticity index (PI).

Table 2. Standards used for soil testing.

Test	ASTM Standard
Sieving Analysis	D 6913
Atterberg Limits	D 4318
Moisture	D 4959
Density	D 7263
Soil classification	D 2487
Triaxial tests	D 4767, D 7181, D2850
Oedometric test	D 2435
Organic matter content	D 2974
SO4 content	C 1580
CO3 content	D 4373
Soluble salts content	D 4542

Most of the samples could be classified as inorganic low-plasticity clays of the CL type, in accordance with the Unified Soil-Classification System (Figure 3). Only three samples were classified as high-plasticity clays (CH), three as CL-ML soils, and five as a low-plasticity mud (ML).

Table 3. Classification tests results.

	w	*Fc*	*LL*	*PL*	*PI*	*γ′*	*γ_d*
Maximum	34.00	100.00	70.80	37.90	41.80	2.34	2.10
Mean	15.73	69.92	38.19	21.13	17.54	2.05	1.78
Minimum	5.50	28.30	20.00	6.70	6.60	1.74	1.45
Standard Dev.	5.34	19.39	8.83	4.63	7.07	0.14	0.16

w = Moisture Content, %; FC = %<0,08; LL = Liquid Limit; PL = Plastic Limit; PI = Plasticity Index; γ′ = Apparent Density; γ_d = Dry Density.
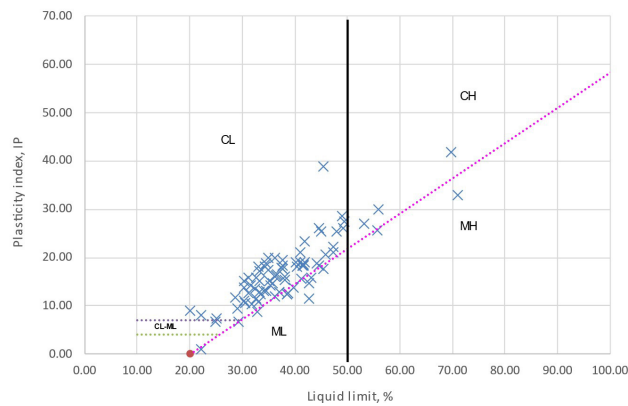
Figure 3. Plasticity chart showing test results.
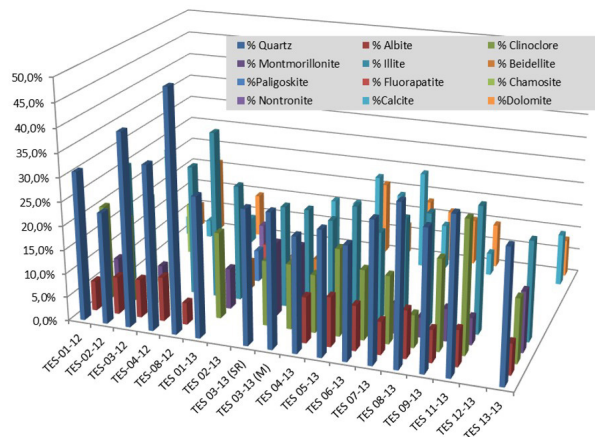
Figure 4. Mineralogical composition of the samples analysed.

For a mineralogical characterization of the clay samples, X-ray diffraction analyses were made on 16 samples. A powder aggregate prepared by milling was placed in the XR equipment, using a test with a speed of 2º/min and a wavelength of 1.5405 nanometres. The results were interpreted using XPowder software (Martín-Ramos, 2004). Figure 4 shows the mineralogical distribution of samples analysed, indicating that the main component was invariably quartz, with a high percentage of illite. Calcite and dolomite were also major constituents while albite, montmorillonite, and clinoclore also

registered significant percentages. The minor constituents of these clays were beidellite, paligoskite, fluorapatite, chamosite, and nontronite.

The chemical composition was established both by analytical methods following the usual standards (Table 2) and by X-ray fluorescence. The latter is also an analytical technique based on measuring intensities that can later be translated into component concentrations. In this method, a continuous spectrum of characteristic radiation is sent from the equipment to the sample, producing primary fluorescent radiation which produces an X-ray emission that can be analysed. A Brunker spectrometer (model S4 Pioneer) was used, equipped with a Rh tube (60 kV; 150 mA) having a detection limit from 0.1 to 10 ppm.

With the analytical methods applied, the percentages of sulphates, total carbonates, soluble salts and organic matter were calculated whereas X-ray fluorescence showed a screening of chemical elements (expressed as oxide percentages) in the samples. Table 4 presents the results of both analyses. These results are consistent with the mineralogy of the samples where quartz was the main mineral phase.

As a complement to the chemical and mineralogical tests, five undisturbed samples were analyzed using SEM (Carl Zeiss Scanning Electron Microscope, model ULTRA 55). Those samples were dried at 50ºC to avoid losing the inner water content. Then, samples were prepared using gold powder to improve their electrical conductivity to ensure the clearest possible images. Due to the low electrical conductivity of the samples, 2 keV of acceleration potential of the electron beam was used with a working distance of 2-4 mm. A secondary electron detector was used to determine the crystalline structure of minerals and their texture.

Figure 5 (a, b, c, d and e) indicate images showing the soil texture and the mineralogical assemblages of those undisturbed samples. As reflected in the figure, almost no organic clastic pieces can be found (only three microfossils were found in all the images), compatible with low to medium carbonate content in these samples. The phyllosilicates showed a medium to open texture, which could explain the medium to high swelling behaviour found in these samples. Also, in Figure 5c and 5d, the grains have a laminar, non-rounded shape for phyllosilicates and a rounded shape for quartz grains. No marked differences were detected between the samples analyzed.

4

Manzano et al., Soil. Rocks, São Paulo, 2023 46(1):e2023002222

2.3 Oedometric and triaxial tests

52 Oedometer tests were performed to establish consolidation coefficients. These results (Table 5) are reported in terms of lambda (λ) and kappa (κ), following methodology described in Cam Clay models methodology (Schofield, 1993).

Given the low permeability of the soil samples tested and their behavior as cohesive undrained soils, undrained triaxial CU tests with pore pressure measurement were considered the best approach to the in situ stress–strain behavior. A total of 57 triaxial tests (9 drained and 48 undrained) were conducted on undisturbed samples. All tests (stress controlled) were carried out using usual chamber pressures of 650, 750 and 900 kPa and back pressure of 600 kPa. All samples were fully saturated as a first stage of the testing.

Table 5 lists the values of cohesion and friction angle determined in the triaxial tests (minimum, maximum and mean values).

3. Results discussion

3.1 Soil nature, phase relationship, particle size and composition.

The samples analysed were mainly low-plasticity clays of the group CL in the Unified Soil Classification System

Table 4. Results of the chemical composition analysis.

| | X-ray diffraction results | | | | | | | | | | Analytical results | | | |
	SiO2	Al2O3	Fe2O3	MnO	MgO	CaO	Na2O	K2O	TiO2	P2O5	Soluble salts	Sulphates	Organic Matter	Carbonates
TES-01-12	51.67	21.61	6.37	0.03	2.37	1.50	0.26	3.17	0.96	0.10	0.00	0.00	1.11	4.47
TES-02-12	50.39	20.21	6.80	0.37	3.26	2.84	0.66	3.46	0.82	0.16	0.00	0.00	0.80	8.06
TES-03-12	46.68	17.52	6.82	0.15	3.74	8.95	0.84	3.30	0.77	0.28	0.00	0.00	0.66	2.10
TES-04-12	51.06	19.51	8.05	0.25	3.11	2.36	0.71	3.65	0.83	0.17	0.00	0.01	0.37	3.89
TES-08-12	56.38	19.08	7.46	0.11	2.41	1.61	0.93	3.39	0.84	0.82	0.00	0.00	0.21	1.52
TES 01-13	50.97	20.18	7.09	0.04	1.74	1.94	0.45	2.30	0.94	0.18	0.00	0.00	0.00	5.99
TES 02-13	51.87	20.51	7.40	0.03	1.69	1.44	0.50	2.27	0.97	0.19	0.00	0.32	0.33	2.20
TES 03-13 (SR)	0.48	16.40	7.14	0.07	2.06	6.74	0.47	1.91	0.92	0.39				
TES 04-13	45.43	16.93	6.40	0.08	3.71	9.17	0.91	3.18	0.76	0.12	0.00	0.00	0.45	16.44
TES 05-13	0.44	15.56	7.28	0.12	3.46	10.73	0.78	3.09	0.75	0.12				
TES 06-13	0.42	15.73	6.76	0.10	3.20	11.26	0.64	3.16	0.78	0.12	0.00	0.00	0.00	7.81
TES 07-13	44.33	18.51	6.62	0.06	3.00	7.99	0.47	2.86	0.97	0.10	0.00	0.00	0.21	7.82
TES 08-13	42.00	15.65	6.13	0.12	3.62	12.79	0.80	2.95	0.73	0.11	0.00	0.00	0.00	1.52
TES 09-13	49.90	18.89	8.60	0.30	3.01	2.53	0.66	3.86	0.89	0.16				
TES 11-13	50.86	21.52	8.71	0.03	1.81	0.83	0.58	2.45	1.19	0.18	0.00	0.00	0.66	9.30
TES 13-13	44.00	19.12	6.04	0.05	2.52	8.74	0.54	2.33	0.94	0.11	0.00	0.00	0.70	15.81
TES 20-13											0.32	0.00	0.25	0.16
TES 21-13											0.20	0.00	0.28	0.16
TES 22-13											0.32	0.00	0.29	0.24
TES 23-13											0.23	0.00	0.23	0.23
TES 24-13											0.54	0.00	0.41	4.30
TES 25-13											0.04	0.00	0.32	3.00
TES 26-13											0.46	0.00	0.61	9.80
TES 27-13											0.44	0.00	0.32	1.80
Minimum	0.42	15.56	6.04	0.03	1.69	0.83	0.26	1.91	0.73	0.10	0.00	0.00	0.00	0.16
Mean	39.80	18.56	7.10	0.12	2.79	5.71	0.64	2.96	0.88	0.21	0.12	0.02	0.39	5.08
Maximum	56.38	21.61	8.71	0.37	3.74	12.79	0.93	3.86	1.19	0.82	0.54	0.32	1.11	16.44
Standard Dev.	19.86	2.04	0.80	0.10	0.71	4.20	0.19	0.56	0.12	0.18	0.19	0.07	0.28	4.82

Table 5. Oedometric and Triaxial test results. Note minimum value of friction angle was obtained in a anomalous testing result (TES-23-12).

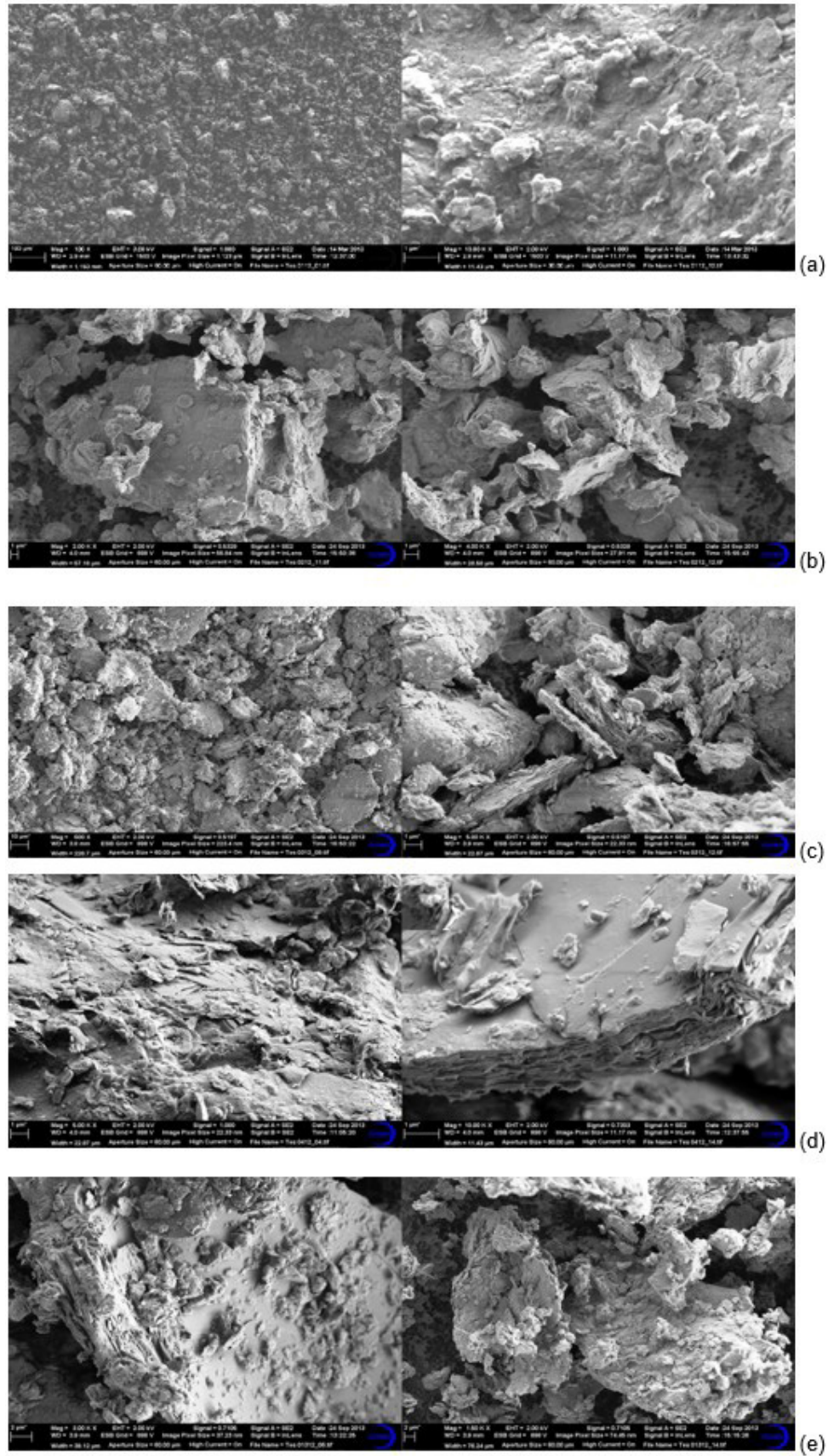|	c' (kPa)	φ' (º)	λ	κ	e_i
Maximum	150.00	49.60	0.130	0.041	0.760
Mean	36.24	26.75	0.050	0.013	0.492
Minimum	0.00	6.84	0.007	0.000	0.107
Standard Dev.	35.03	8.30	0.023	0.009	0.156

Figure 5. SEM image of samples: (a) TES 001/12; (b) TES 002/12; (c) TES 003/12; (d) TES 004/12; (e) TES 005/12.

6

Manzano et al., Soil. Rocks, São Paulo, 2023 46(1):e2023002222

for Engineering Purposes (ASTM, 2011). Only 11 samples were not classified as CL (3 samples classified as CH, 3 as CL-ML, and 5 as ML).

The samples proved highly homogeneous in terms of particle-size distribution and had no significant gravel content but a high content in particles smaller than 0.08 mm (mean value = 69.92%; standard deviation = 19.39). Regarding the clay-silt differentiation, the 23 sedimentation-analysis tests undertaken indicated a substantial percentage of silt in the fraction smaller than 0.08 mm (in some cases even higher than the clay percentage), indicating low activity in those samples (Figure 6) according to the Skempton activity criteria (Skempton, 1953).

Table 4 shows the chemical composition established by X-ray diffraction and analytical methods. The carbonate content (which could influence the geotechnical behavior of these soils), was found to range from 0.16 to 34.72 with a mean value of 10.29 (standard deviation = 9.87). The highest percentages corresponded to aluminum and silica (the majority component being quartz).

Regarding the mineralogical composition, as expected, clay minerals were not main component. In all cases the main component was quartz, followed by a substantial percentage of illite. Calcite and dolomite were also major constituents, with albite, montmorillonite, and clinoclore in significant percentages. This mineralogical composition, with almost no skeletal grains in its composition, accounts for the medium to low carbonate content (mean value under15%) even when those soils were formed in an environment where the carbonate content could be expected to be higher. Also, illite and montmorillonite in the samples explain the swelling behaviour, which was medium to high in some of the samples and well known in these soils (Azañón et al., 2010).

3.2 Stress-strain relationships

3.2.1 Oedometric and triaxial behaviour

For an understanding and characterisation of soil behaviour under uniaxial oedometric compression, 52 oedometric tests were undertaken. In all cases, the oedometric coefficients were reduced following Critical State methodology (Schofield, 1993) in terms of lambda and kappa. Table 5 shows the results, which establish a low compressibility in noval loading, with a mean lambda value of 0.050 (standard deviation = 0.023). The kappa mean value was 0.013 (standard deviation = 0.009) and the initial void ratio had a mean value of 0.492 with a standard deviation of 0.156.

The results reflected a stiff soil with low compressibility indexes and an initial void ratio notably lower than expected.

Some additional facts should be highlighted regarding behaviour under triaxial compression. All tests showed a homogeneous behaviour under triaxial compression. Firstly, almost all the samples showed a progressive hardening under

strain, this being more notable for higher chamber pressures but also recognizable at low pressures (Figure 7, 8 & 9). Secondly, in relation to the pore pressure, in almost all cases, the pore pressure increased until a peak value was reached in the test, at which point values started to decrease until failure (Figure 10). This demonstrates an important aspect of the behavior of the soil: the pore pressure led to suction in many cases whereas vertical effective pressure continued to augment. Also noticeable is the behavior in a p-q diagram, showing a clear linear trend (Figure 7) with a high R^2 value (R^2=0.96).

4. Soil modelling

Once all the tests were analyzed and soil parameters estimated, comparisons were made among the experimental
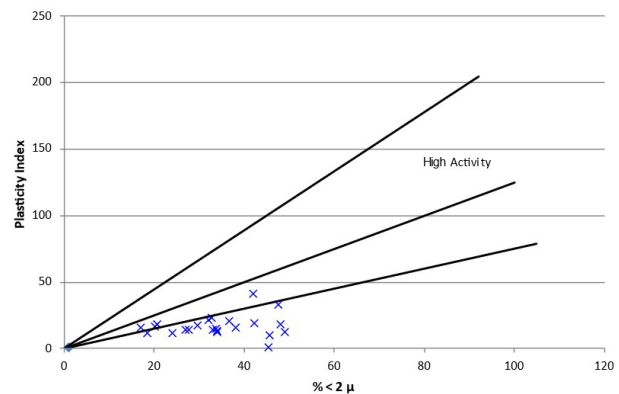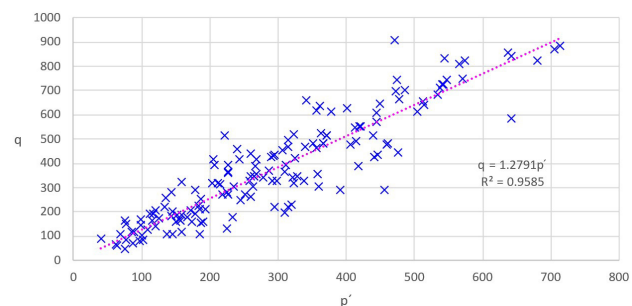

Figure 6. Activity chart.

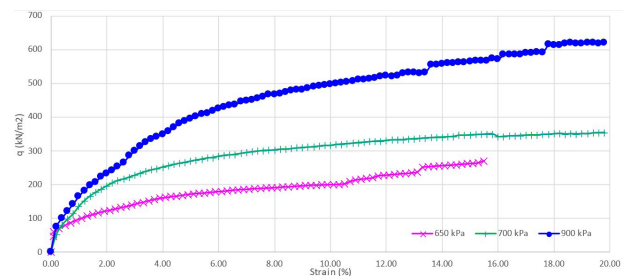**Figure 7.** Failure data (q/pe vs p/pe).

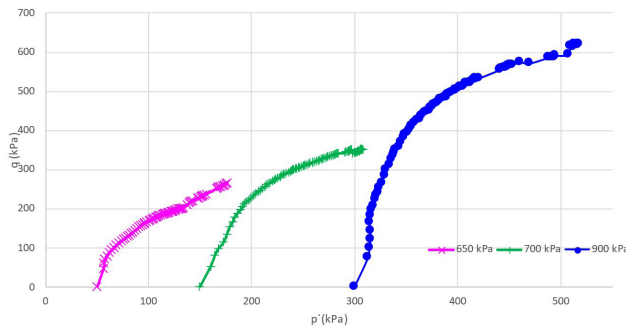**Figure 8.** q vs. strain obtained for different chamber pressures. Graph shows mean value of all tests.

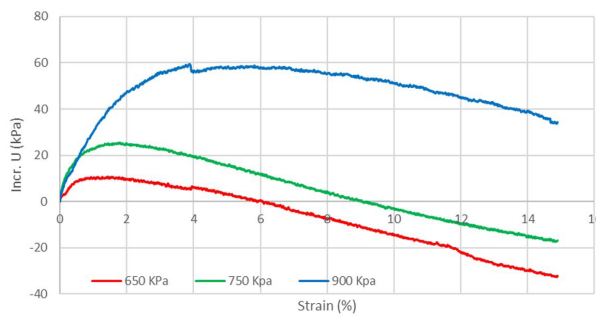**Figure 9.** p´-q diagram (mean values) for different chamber pressures.

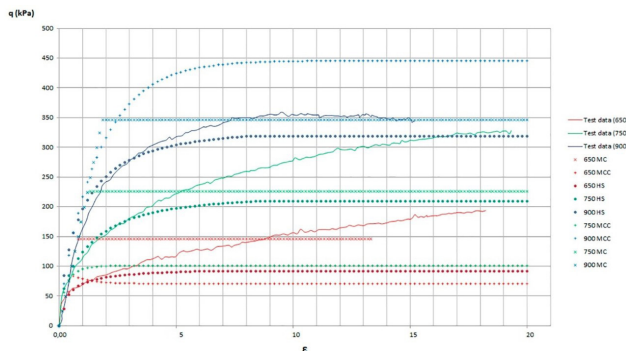**Figure 10.** Mean values of pore pressure increments during testing.

Figure 11. Triaxial testing and finite-elements model comparison.

data and theoretical models. The comparisons were undertaken by modelling the triaxial test using the soil-testing tool of Plaxis 2D software. This tool enables virtual soil modelling under the same conditions used for real laboratory testing and then allows the results to be compared. Each soil test was modelled using Mohr-Coulomb. Modified Cam-Clay. and Hardening Soil models (Plaxis, 2014). Mohr-Coulomb was selected for being the most widely used model in initial approaches to engineering problems whereas Modified Cam-Clay was selected for being broadly applied for clay modelling. On the other hand, the Hardening Soil constitutive model was selected in order to check its feasibility for accurate modelling the behaviour of this soil. Parameters used for soil modelling correspond to mean values shown in Table 5.

The results for each constitutive model vs. real test data were plotted in terms of deviatoric stress and strain, and the findings were analyzed to establish whether these constitutive models were consistent with real soil behavior. The Hardening Soil model best fit real lab testing, with a better fit for chamber pressures of 650 and 750 kPa (Figure 11). In any case, the correlation was good for strain values under 5 in all cases. For strain values from 5% to 15%, the model fit the test results except for chamber pressure equal to 900 kPa.

5. Conclusions

A full set of laboratory testing was conducted on 83 clay samples taken in the Campo de Gibraltar Flysch Trough Domain related to the material that will be found during Gibraltar Strait Tunnel. These tests showed these clays to be of low plasticity with quartz consistently as the main component, followed by a high percentage of illite (albite, montmorillonite, and clinoclore also registering notable percentages). Oedometric testing revealed these clays to be a stiff soil with low compressibility indexes and a low initial void ratio (mean lambda value of 0.050 with a standard deviation = 0.023; mean kappa value = 0.013 with standard deviation of 0.009 and initial mean void ratio of 0.492 with a standard deviation of 0.156). With respect to behavior under triaxial compression tests, the cohesion found indicates high variability between 0 and 150 kPa (mean value = 36.24 kPa; standard deviation = 35.03) whereas the friction angle showed a more homogeneous value (mean value = 26.75º; standard deviation = 6.84). The samples tested showed a progressive hardening with strain and also indicated that the pore pressure led to suction in many cases, whilst vertical effective pressure was still increasing.

A good fit of the laboratory testing results with finite-element modelling when the Hardening Soil constitutive model was used was clearly established. This constitutive model fits real results better than does the Modified Cam-Clay model, although it has been used for typical clays (Roscoe & Burland, 1968; Burland, 1990; Wood, 1990). The Theoretical Hardening soil model fit the laboratory testing values better at low strain values (<5%), this constituting a crucial issue to be taken into account when model data are analyzed in engineering practice.

Acknowledgements

Declaration of interest

The authors have no conflicts of interest to declare. All co-authors have observed and affirmed the contents of the paper and there is no financial interest to report.

Authors´ contributions

Francisco Javier Manzano: conceptualization, investigation, software, writing original draft preparation, reviewing and editing. Francisco Lamas: conceptualization, methodology, validation, data curation. José Miguel Azañón: supervision.

Data availability

The datasets generated analyzed in the course of the current study are available from the 267 corresponding author upon request.

List of symbols

$c´$	Effective cohesion.
e_i	Initial void ratio.
$p´$	Mean effective stress.
q	Deviatoric stress.
q/p_e	Normalized mean effective stress.
q/p_e	Normalized deviatoric stress.
w	Moisture content (%).
ºC	Degrees centigrade.
FC	Fines content (particles lower than 0.08 mm).
HS	Hardening Soil constitutive model.
LL	Liquid Limit.
MC	Mohr Coulomb constitutive model.
MCC	Modified Cam Clay constitutive model.
PL	Plastic limit.
PI	Plasticity index.
SEM	Scanning electronic microscope.
$\gamma´$	Apparent Density.
γ_d	Dry Density.
ε	Strain.
κ	Kappa parameter (Wood, 1990).
λ	Lambda parameter (Wood, 1990).
$\varphi´$	Effective friction angle.

References

Arbanas, Ž., Grošić, M., & Briški, G. (2008). Behaviour of Engineered Slopes in Flysch Rock Mass. In *Proceedings of the 1st Southern Hemisphere International Rock Mechanics Symposium (SHIRMS)* (pp. 403-504). Australia: Australian Centre for Geomechanics. https://doi.org/10.36487/ACG_repo/808_07

ASTM D1587. (2000). *Standard Practice for Thin-Walled Tube Sampling of Soils for Geotechnical Purposes*. ASTM International, West Conshohocken, PA.

ASTM D2487. (2011). *Standard Practice for Classification of Soils for Engineering Purpouses (Unified Soil Classification System)*. ASTM International, West Conshohocken, PA.

Aydin, A., Ozbek, A., & Cobanoglu, I. (2004). Tunnelling in difficult ground: a case study from Dranaz tunnel, Sinop, Turkey. *Engineering Geology*, 74(3-4), 293-301. http://dx.doi.org/10.1016/j.enggeo.2004.04.003.

Azañón, J.M.A., Antonio, A., Yesares, J., Tsige, M., Mateos, R.M., Nieto, F., Delgado, J., López-Chicano, M., Martín, W., & Rodríguez-Fernández, J. (2010). Regional-scale high-plasticity clay-bearing formation as controlling factor on landslides in Southeast Spain. *Geomorphology*, 120(1-2), 26-37. http://dx.doi.org/10.1016/j.geomorph.2009.09.012.

Balanyá, J.C., Crespo-Blanc, A., Esteras, M., Luján, M., Martín Algarra, A., & Martín-Martín, M. (2004) Complejo del campo de Gibraltar. In J.A. Vera (Ed.), *Geología de España* (pp. 384-395). Instituto Geológico y Minero de España.

Burland, J.B. (1990). On the compressibility and shear strength of natural clays. *Geotechnique*, 40(3), 329-378. http://dx.doi.org/10.1680/geot.1990.40.3.329.

Dounias, G.P.P., Marinos, P., & Vaugham, P. (1996). Landslide reactivation in flysch colluvial at the Evinos dam site. In *Proceedings of the 7th International Symposium on Landslides* (pp. 201-206). Trondheim: Balkema.

Jovičić, V., Šušteršič, J., & Vukelič, Ž. (2009). The application of fibre reinforced shotcrete as primary support for a tunnel in flysch. *Tunnelling and Underground Space Technology*, 24(6), 723-730. http://dx.doi.org/10.1016/j.tust.2009.05.003.

Manzano, F.J., Lamas, F., & Azañón, J.M. (2020). Geotechnics as a conditioning factor in large infrastructures. The link Europe–Africa. *Ciudad y Territorio Estudios Territoriales*, 52(206), 739-752. http://dx.doi.org/10.37230/CyTET.2020.206.02.

Marinos, P., & Hoek, E. (2001). Estimating the geotechnical properties of heterogeneous rock masses such as flysch. *Bulletin of Engineering Geology and the Environment*, 60(2), 85-92. http://dx.doi.org/10.1007/s100640000090.

Martín-Ramos, J.D. (2004). *X-Powder, a software package for powder X-ray diffraction analysis*. Retrieved in February 20, 2022, from http://www.xpowder.com.

Mikoš, M., Petkovšek, A., & Majes, B. (2009). Mechanisms of landslides in over-consolidated clays and flysch. *Activity scale and targeted region: national. Landslides*, 6(4), 367-371.

Moon, V.G., & Healy, T. (1994). Mechanisms of coastal cliff retreat and hazard zone delineation in soft flysch deposits. *Journal of Coastal Research*, 10 (3), 1994, pp 663–680. *International Journal of Rock Mechanics and Mining Sciences & Geomechanics Abstracts*, 31(6), 267-268. http://dx.doi.org/10.1016/0148-9062(94)90051-5.

Palomba, M.R.G., Amadini, F., Carrieri, G., & Jain, A.R. (2013). Chenani-Nashri Tunnel, the longest road tunnel in India: a challenging case for design-optimization during construction. In *World Tunnel Congress 2013.*

Underground - the way to the future! (pp. 964-971). Geneva: Taylor & Francis Group.

Pánek, T., Hradecký, J., Minár, J., Hungr, O., & Dušek, R. (2009). Late Holocene catastrophic slope collapse affected by deep-seated gravitational deformation in flysch: ropice Mountain, Czech Republic. *Geomorphology*, 103(3), 414-429. http://dx.doi.org/10.1016/j.geomorph.2008.07.012.

Plaxis. (2014). *Material Models Manual*. Retrieved in February 20, 2022, from https://communities.bentley. com/cfs-file/__key/communityserver-wikis-components-files/00-00-00-05-58/0118.PLAXIS3DCE_2D00_V20.02_2D00_3_2D00_Material_2D00_Models.pdf.

Roje-Bonacci, T. (1998). Parameter changes after weathering of soft rock in flysch: the geotechnics of hard soils - soft rocks. In *Proceedings of the second international symopsium on hard soils-soft rocks* (pp. 799-804). Napoles: Ed. A. Evangelista.

Roscoe, K., & Burland, J.B. (1968). On the generalised stress strain behaviour on wet clay. In J. Heyman & F. Leckie (Eds.), *Engineering plasticity* (pp. 535-609). Cambridge University Press.

Schofield, A.N. (1993). Original cam-clay. In *International Conference on Soft Soil Engineering*. Guangzhou. Retrieved in February 20, 2022, from http://www-civ.eng.cam.ac.uk/geotech_new/publications/TR/TR259.pdf.

Skempton, A.W. (1953). The colloidal activity of clays. In *Proceedings of the 3 th International Conference of Soil Mechanics and Foundation Engineering* (pp. 57-60). Switzerland: ICOSOMEF.

Studer, B. (1827). Geognostische Bemerkungen uber einige Theile der nordlichen Alpenkette. *Zeitschr. fur Mineralogie*, 1, 1-52.

Velasco, C. (2016). *Historia documental de los proyectos de enlace fijo del Estrecho de Gibraltar*. SECEGSA.

Wood, D.M. (1990). *Soil behaviour and critical state soil mechanics.* Cambridge University Press. https://doi.org/10.1017/CBO9781139878272

10

Manzano et al., Soil. Rocks, São Paulo, 2023 46(1):e2023002222

Numerical analysis of laterally loaded barrette foundation

Djamila Behloul[1] ⓘD, Sid Ali Rafa[2] ⓘD, Belkacem Moussai[1#] ⓘD

Article

Abstract
The effect of soil constitutive models, nonlinearity of the barrette material, loading direction as well as the cross-sectional shape and second moment of inertia on the response the barrette foundation under lateral loading is investigated in this research. The numerical analyses were conducted on a well-documented barrette load test using Plaxis 3D. The investigation results revealed that the response of the barrette is significantly affected by the direction of the applied load and nonlinear behavior of the soil and barrette materials. For rectangular, square, and circular piles with different cross-section areas and same second moment of inertia, the square and circular piles exhibit similar behavior but different from that of the rectangular pile. However, when these piles have the same cross-section area and different second moments of inertia, the behavior of rectangular pile is close to that of square pile when the load is applied along the *x* direction and is close to that of circular pile shape when the load is applied along the y direction.

1. Introduction

The use of foundations with rectangular shape is more advantageous than circular shape, when they have to be designed to resist lateral loads and bending moments in a preferred direction (Ramaswamy & Pertusier, 1986). Wakil & Nazir (2013) performed numerical analyses on barrettes tested in laboratory and indicated that the response of barrettes to lateral loadings depends on the direction of loading and the loading along the major axis resulted in the greatest lateral load capacity. Similar results were reported by Zhang (2003) on lateral barrette load test using FLPIER software.

Most of the published numerical analyses studying the pile behaviour under lateral loading employed the simple elastic model to describe the pile material behaviour [Basu & Salgado (2007), Broms (1964), Choi et al. (2013), Comodromos et al. (2009), Matlock (1970), Poulos (1971), Poulos et al. (2019), etc]. However, the use of this model may lead to an overestimation of the pile lateral capacity, in particular the piles subjected to high rates of loading (Conte et al., 2013).

Choi et al. (2013) reported that rectangular, square and circular cross-sections have similar behaviour under lateral loading when they have the same second moment of inertia, with the assumption that the soil and pile material are to behave as elastic medium.

Poulos et al. (2019) reported that the barrette behaviour can be modelled using equivalent circular pile. An equivalent pile foundation with the same circumference and second moment of inertia as the barrette (in the direction of loading) showed a very similar load-deflection curve.

Siriwan et al. (2020) indicated that the nonlinear concrete model (Schädlich & Schweiger, 2014) captures the deep cement mixing wall failure mechanisms reasonably well compared to Mohr-Coulomb model. Furthermore, the Mohr-Coulomb model overestimates the stability of this type of wall.

This study investigates the effect of some factors such as nonlinearity of the barrette material, barrette cross-sectional shape, second moment of inertia, barrette slenderness, direction of load as well as the soil constitutive models (elastic model, Mohr-Coulomb model and Hardening Soil model) on the behavior of a barrette subjected to horizontal loads using the barrette load test published by Conte et al. (2013) and the software Plaxis 3D.

2. Concrete model

The model takes into account creep, shrinkage, strain hardening (tension and compression), strain softening (tension and compression) as well as strength and stiffness depending on time. Also, it takes into account the non-linearity of the material behavior (Schädlich & Schweiger, 2014). This model was implemented in Plaxis software and was primary used

Behloul et al., Soil. Rocks, São Paulo, 2023 46(1):e2023002122
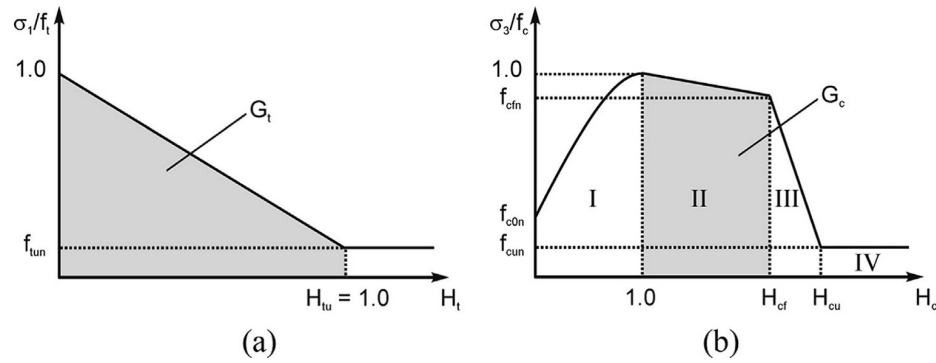
1

Figure 1. Normalized stress-strain curve in [adapted from Schädlich & Schweiger (2014)]: (a) tension; (b) compression.

to model the shotcrete behavior for tunnels, but it can also be used for other cement-based materials.

The stress-strain curve shown in (Figure 1) includes quadratic strain hardening (I), linear strain softening (II), linear strain softening (III), and constant residual strength (IV). A normalized hardening/softening parameter $H_c = \varepsilon_3^P / \varepsilon_{cp}^P$ is used, with ε_3^P = minor principal plastic strain and ε_{cp}^P = plastic peak strain in uniaxial compression. The input parameters of this model are shown in Table 1.

3. Numerical analysis

Figure 2 shows the barrette load test (Conte et al., 2013) used in the numerical analysis. The barrette cross section is 2.8 m x 1.2 m and its length is 11 m. The barrette cap has a cross-section of 1.5 m x 3.1 m and a thickness of 1.5 m. The barrette embedded in a sandy soil was modelled using nonlinear model for concrete and elastic model for steel reinforcement (Tables 1-2). The Mohr-Coulomb (MC) approach (Brinkgreve et al., 2012) was used to model the soil behaviour.

The subsoil is composed of dense sand with interbedded thin layers of gravel and silty sand. The standard penetration test values vary from 30 to 60. For depths less than 5 m, the cone penetration test values (q_c) vary from 5 to 15 MPa and below this depth, q_c varies from 15 to 30 MPa. Table 3 shows the soil parameters after their calibration by matching the experimental results from the barrette load test with those predicted by the numerical approach on a trial and error basis. Figure 3 shows the model of the barrette load test using Plaxis 3D. The barrette head was subjected to incremental horizontal loads up to 4.6 MPa.

4. Results and discussions

The measured and computed load – deflection curves of the barrette loaded along the major axis is shown in Figure 4a. The results indicated that the computed results using nonlinear model of the barrette concrete is in good
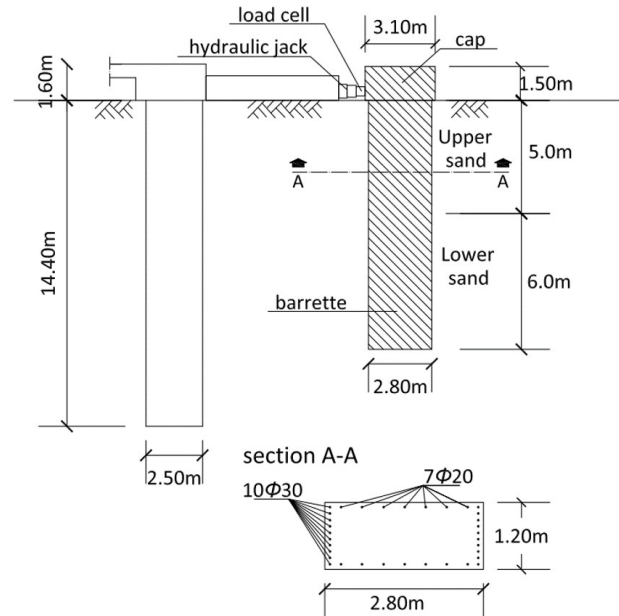
Figure 2. Barrette load test layout (Conte et al., 2013).

Table 1. Input parameters of the nonlinear concrete model.

Parameter	Description	Value
γ (kN/m³)	Unit weight of concrete	25
E_{28} (MPa)	Young's modulus	33600
ν	Poisson's ratio	0.2
$f_{c,28}$ (MPa)	Uniaxial compressive strength	33.2
$f_{t,28}$ (MPa)	Uniaxial tensile strength	3.1
f_{c0n}	Normalized initially mobilised strength	0.1
f_{cfn}	Normalized failure strength (compression)	0.85
f_{cun}	Normalized residual strength (compression)	0.1
ε_{cp}^P	Uniaxial plastic failure strain	-1.20 x10⁻³
$G_{c,28}$ (kN/m³)	Compressive fracture energy	70
$G_{t,28}$ (kN/m³)	Tensile fracture energy	6.9
ϕ^{MAX}	Maximum friction angle	37

agreement with the barrette load test results. However, the barrette deflections are significantly reduced when the linear model is used.

Figure 4b shows the relationship between the cracking expansion (grey color) and the applied lateral load. When the nonlinear model is used, the tensile strain increases linearly with the applied load until a value of 2.1 MN (initiation of cracking) after which it becomes nonlinear and cracking expands with the increase of load level (Figure 4c).

4.1 Effect of soil constitutive model

The linear elastic, Mohr Coulomb and hardening soil models were used to evaluate their effect on the barrette behaviour. The soil characteristics used in the numerical analysis are given in Table 3.

The results (Figure 5) indicated that the elastic model produces significantly lower deflections than those obtained using Mohr-Coulomb and hardening soil models (HS). As the lateral load increases, the difference in deflections between the three models increases.

The magnitude of the deflection predicted by HS model is slightly lower than that of MC model, especially for higher applied loads. This is because the HS model accounts for stress dependency of the stiffness modulus.

When Mohr Coulomb and hardening soil models are used, the deflection at a load of 4.6 MN is about 6 times greater than that when the linear elastic model is used. This indicates that the linear elastic model significantly underestimates the deflection of the barrette foundation.
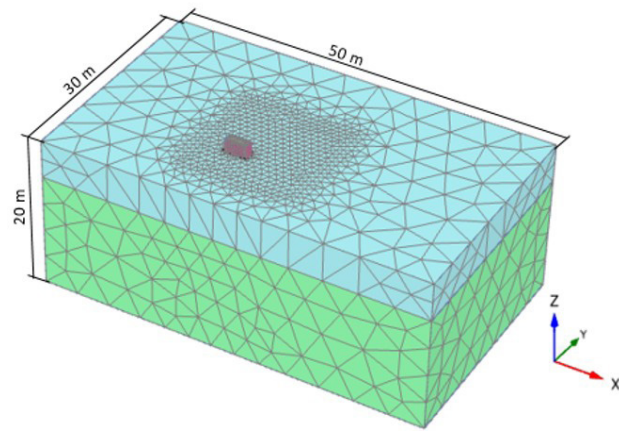
Figure 3. Finite element mesh.

Table 2. Properties of the barrette reinforcement steel.

E_s (MPa)	ν_s	F_y (MPa)
210000	0.3	430

Table 3. Soil parameters.

	Upper sand layer			Lower sand layer		
	Elastic model	Mohr-Coulomb Model	Hardening Soil model	Elastic model	Mohr-Coulomb Model	Hardening Soil model
γ_{unsat} [kN/m³]	18	18	18	20	20	20
γ_{sat} [kN/m³]	20	20	20	22	22	22
ν	0.3	0.3	0.3	0.3	0.3	0.3
φ	-	33	33	-	38	38
ψ	-	3	3	-	8	8
E [MN/m²]	70	70	-	100	100	-
E_{50}^{REF} [MN/m²]	-	-	70	-	-	100
E_{oed}^{REF} [MN/m²]	-	-	70	-	-	100
E_{ur}^{REF} [MN/m²]	-	-	210	-	-	300
ν_{ur}	-	-	0.2	-	-	0.2
m	-	-	0.5	-	-	0.5
R_f	-	-	0.9	-	-	0.9
R_{inter}	0.67	0.67	0.67	0.67	0.67	0.67

(a)

(b)

(c)
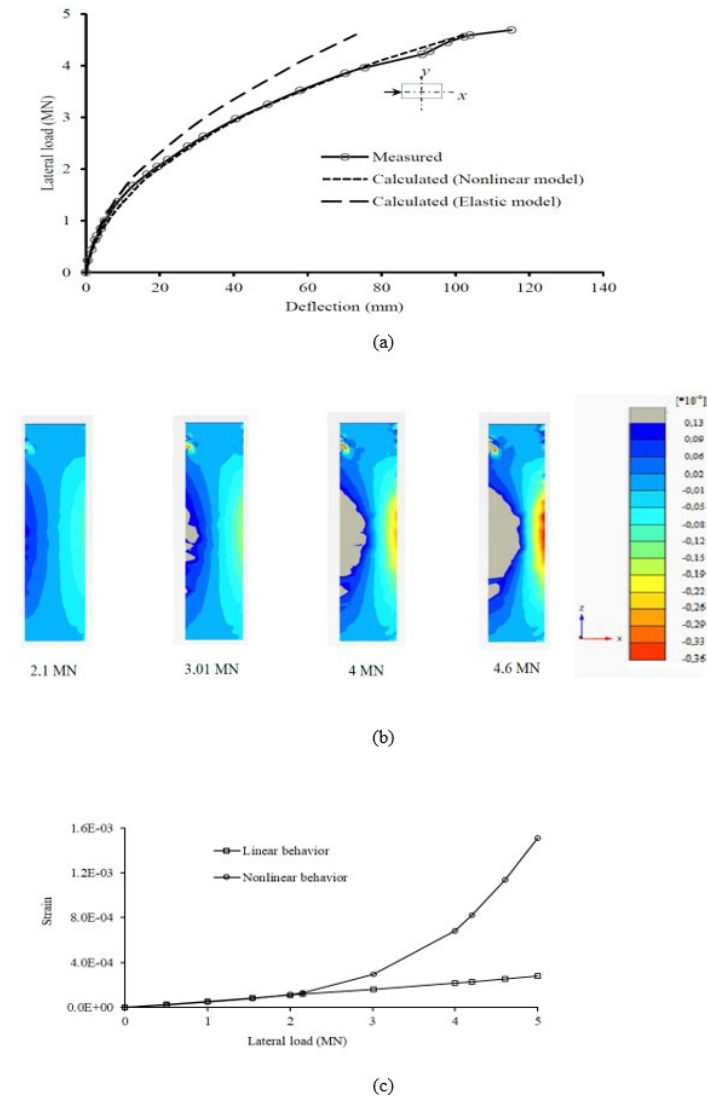
Figure 4. Results of numerical analyses: (a) measured and predicted load - deflection curves; (b) expansion of cracking (grey color) with increasing load level; and (c) evolution of tensile strain with lateral load level.

4.2 Effect of load direction

Figure 6a shows the deflection of the barrette head when it is loaded along x and y directions. The results revealed that the deflection of the barrette head is greater along y direction than that along x direction which may be due to the difference in the barrette moment of inertia about x and y axes. This result agrees well with those obtained by Zhang (2003) and Wakil & Nazir (2013).

Furthermore, the barrette rotates around its base when the loading is along x direction and around a point located above the base when the loading is along y direction (Figure 6b-6c).

4.3 Effect of the cross-sectional shape of the foundation

The investigation of the effect of the cross-sectional shape on the barrette behavior was conducted on square
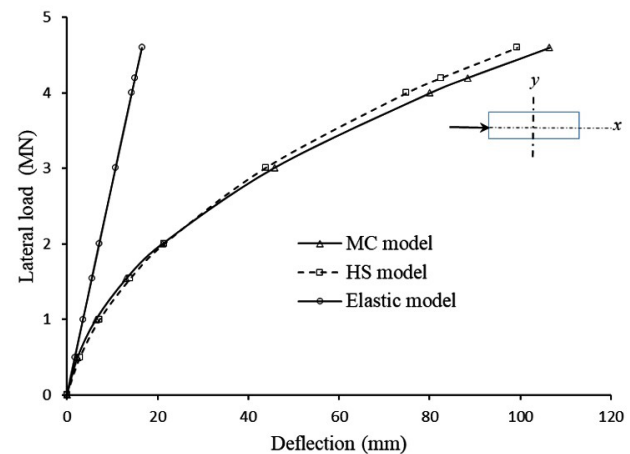
Figure 5. Applied load versus barrette head displacement using Elastic, MC and HS models.
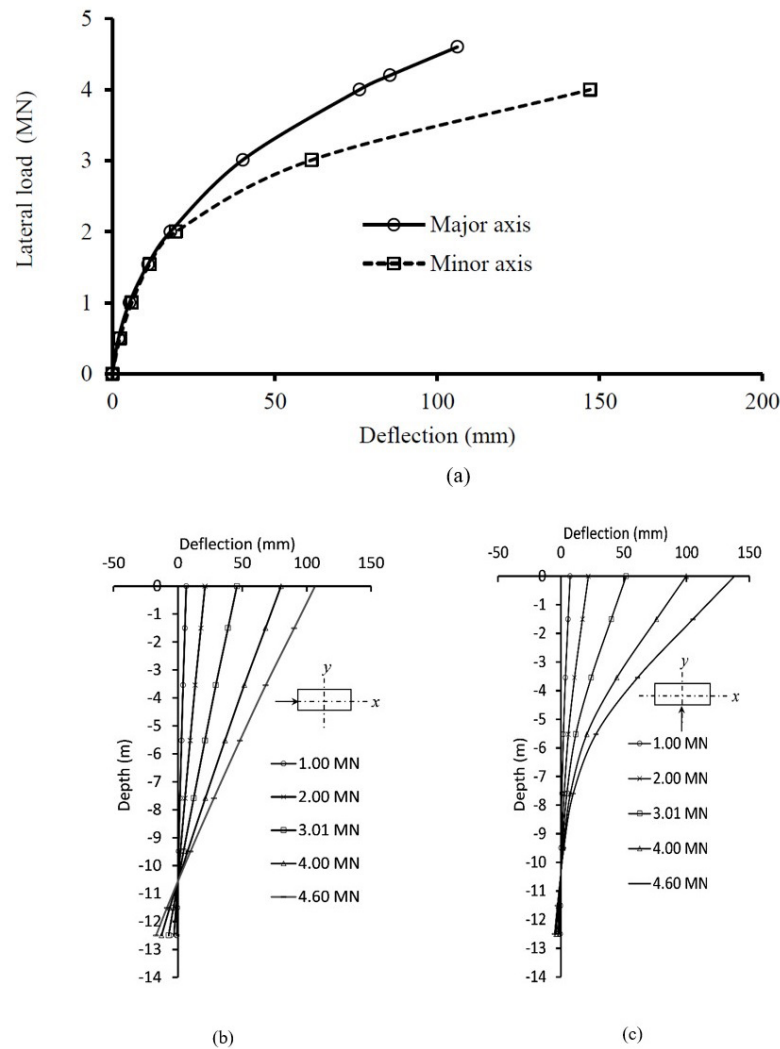
Figure 6. Effects of load direction: (a) applied load versus barrette head deflection along X and Y axes; (b) barrette deflection versus depth along X axis; and (c) along Y axis.

(1.83 x 1.83 m) and circular (2.06 m in diameter) cross-sections having the same cross section area as the reference barrette foundation (i.e. 1.2 x 2.8 m).

The results indicated that (Figure 7), when the applied load is on the major direction (X axis), the rectangular and square shapes showed more resistance than the circular shape. The rectangular and square shapes showed similar behavior until an applied load of about 3 MPa, beyond this load the difference between the two cross-sectional shapes increases as the applied load increases. At the maximum applied load (i.e. 4.6 MPa), the lateral deflection of the rectangular shape is 9% and 33.5% less than that of the square and circular shapes respectively.

However, when the applied load is on the minor direction (Y axis), the rectangular shape resistance is close to that of circular shape and is lower than that of the square shape.
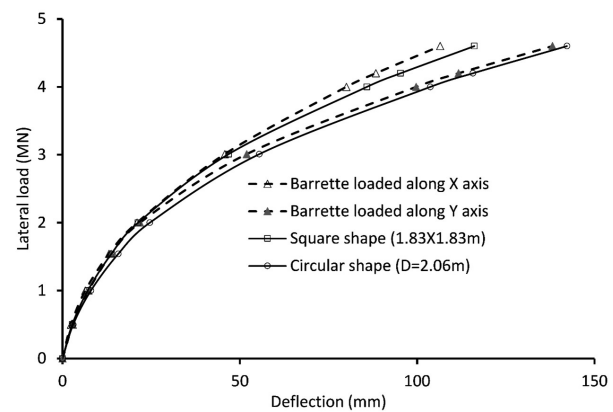
Figure 7. Applied load versus deflection for different cross-sectional shapes of the deep foundation.

4.4 Effect of the second moment of inertia

The analyses were carried -out on square (2.26 m x 2.26 m) and circular (2.54 m in diameter) cross-section

(a)

(b)

(c)
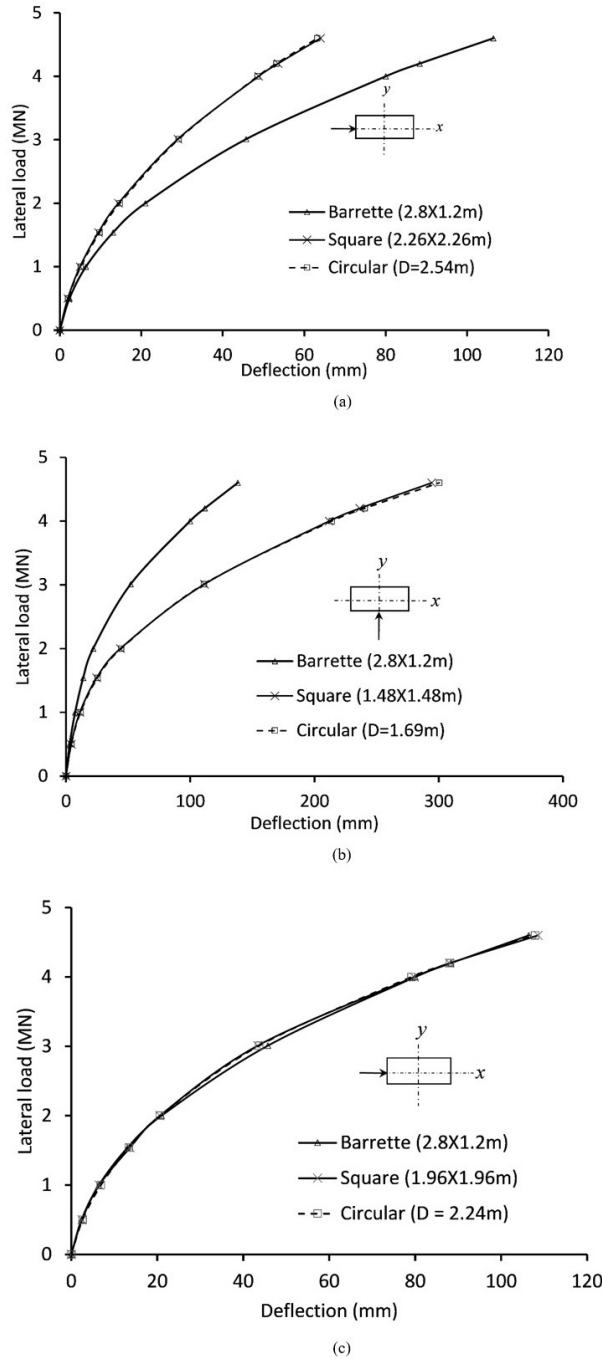
Figure 8. Lateral deflection of square and circular piles, and barrette with different cross-sections and having the same second moment of inertia (a) along X axis and (b) along Y axis, and (c) cross-sections of square and circular piles having the same deflection as the barrette foundation along X axis.

shapes having the same second moment of inertia as the barrette foundation loaded along the major axis. The results indicated that the square and circular shapes have similar lateral deflections and are more resistant than the rectangular shape (Figure 8a).

However, when the rectangular barrette foundation is loaded along the minor axis, the square (1.48 m x 1.48 m) and circular (1.69 m in diameter) cross-section shapes having the same second moment of inertia as the rectangular shape, showed similar lateral deflections and less resistance than the rectangular shape (Figure 8b).

Figure 8c shows that the square (1.96 m x 1.96 m) and circular (2.24 m in diameter) shapes are equivalent to the barrette foundation (2.8 x 1.2 m) loaded along the major axis (that is their deflections under lateral loads are similar).

However, the cross- sectional area of the square and circular foundations is more than that of the barrette foundation and therefore, it is more advantageous to use barrette foundation than other pile shapes.

4.5 Effect of the barrette slenderness

In order to investigate the effect of the barrette slenderness, the barrette cross – section width (B) is kept constant and the barrette depth (H) is increased. The analyses were performed with different barrette slenderness (H/B = 5, 10, 15, 20 and 25).

The results show (Figure 9) that the barrette head deflection decreases as the barrette slenderness increases. This effect becomes negligible when the barrette slenderness reaches 15. Furthermore, the barrette rotates around its base when the slenderness is less than 15 and around a point located above the base when the slenderness is more than 15 (Figure 10).
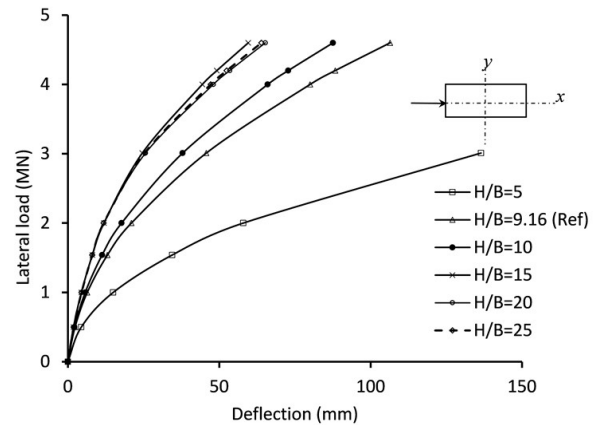
Figure 9. Lateral load versus deflection for different barrette slenderness.

6

Behloul et al., Soil. Rocks, São Paulo, 2023 46(1):e2023002122
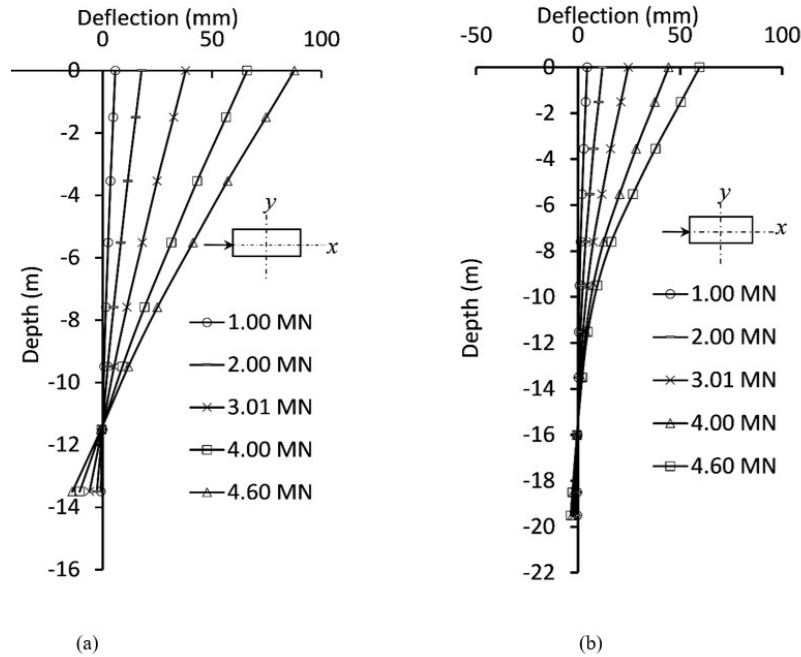
Figure 10. Barrette deflection versus depth for slenderness of (a) 10 and (b) 15.

5. Conclusions

The comparison between measured and predicted load-horizontal displacement curves reveals that the computed results using nonlinear model of the barrette concrete is in good agreement with the barrette load test results. However, the modelling of the barrette material using linear model leads to an underestimation of the barrette horizontal displacements compared to the non-linear model. The horizontal displacement of the barrette head obtained using non-linear model is about 42% more than that obtained using linear model at an applied load of 4.6 MPa.

The resistance of the barrette foundation to lateral loading depends on the direction of the applied load. Its resistance along the major axis is greater than that along the minor axis. Thus, it is more advantageous to use a barrette with rectangular shape loaded on the major direction rather than square or circular shape, especially for high lateral loads.

For foundations with different cross-section shapes and having the same second moment of inertia, their resistance to lateral deflection seems to increase as the width of the foundation in the direction of loading increases.

Declaration of interest

The authors have no conflicts of interest to declare. All co-authors have observed and affirmed the contents of the paper and there is no financial interest to report.

Authors' contributions

Djamila Behloul: conceptualization, methodology, data curation, writing - original draft preparation. Sid Ali Rafa: supervision, methodology, resources, validation. Belkacem Moussai: supervision, validation.

Data availability

The data that support the findings of this study are published by the authors Conte et al. (2013) at https://doi:10.1016/j.compgeo.2012.10.013 and Schädlich & Schweiger (2014) at https://doi.org/10.1201/b17017-20.

List of symbols

$f_{c,28}$:	uniaxial compressive strength
$f_{t,28}$:	uniaxial tensile strength
f_{c0}':	normalized initially mobilised strength
f_{cfn}':	normalized failure strength (compression)
f_{cun}':	normalized residual strength (compression)
m:	amount of stress dependency
q_c:	cone penetration resistance
E:	Young's modulus of soil
E_{28}:	Young's modulus of concrete
E_{50}^{REF}:	reference stiffness modulus for primary loading
E_{oed}^{REF}:	reference stiffness modulus for oedometer stress-strain conditions

E_s: Young's modulus of steel

E_{ur}^{REF}:   reference stiffness modulus for unloading and reloading

F_y: yield strength of steel

$G_{c,28}$:   compressive fracture energy

$G_{t,28}$:   tensile fracture energy

R_f: failure ratio

R_{inter}:   interaction factor

γ: unit weight

γ_{sat}:   saturated unit weight

γ_{unsat}:   unsaturated unit weight

ε_{cp}^{P}:   uniaxial plastic failure strain

v: Poisson's ratio

ϕ: friction angle of soil

ϕ^{MAX}:   maximum friction angle of concrete

Ψ: dilatancy angle

v_{ur}:   Poisson's ratio for unloading and reloading

References

Basu, D., & Salgado, R. (2007). Elastic analysis of laterally loaded pile in multilayered soil. *Geomechanics and Geoengineering*, *2*(3), 183-196. http://dx.doi.org/10.1080/17486020701401007.

Brinkgreve, R.B.J., Engin, E., & Swolfs, W.M. (2012). *Plaxis 3D user's manual*. Bentley.

Broms, B.B. (1964). Lateral resistance of piles in cohesionless soils. *Journal of the Soil Mechanics and Foundations Division*, *90*(3), 123-156.

Choi, Y.S., Basu, D., Salgado, R., & Prezzi, M. (2013). Response of laterally loaded rectangular and circular piles in soils with properties varying with depth. *Journal of Geotechnical and Geoenvironmental Engineering*, *140*(4), 04013049.

Comodromos, E.M., Papadopoulou, M.C., & Rentzeperis, I.K. (2009). Effect of cracking on the response of pile test under horizontal loading. *Journal of Geotechnical and Geoenvironmental Engineering*, *135*(9), 1275-1284. http://dx.doi.org/10.1061/(ASCE)GT.1943-5606.0000069.

Conte, E., Troncone, A., & Vena, M. (2013). Nonlinear three-dimensional analysis of reinforced concrete piles subjected to horizontal loading. *Computers and Geotechnics*, *49*, 123-133.

Matlock, H. (1970). Correlations for design of laterally loaded piles in soft clay. In Offshore Technology Conference (Org.), *Proceedings of the 2nd Offshore Technology Conference* (pp. 577-594). Richardson, United States of America: OnePetro. https://doi.org/10.4043/1204-MS.

Poulos, H.G. (1971). Behaviour of laterally loaded piles: I – single piles. *Journal of the Soil Mechanics and Foundations Division*, *97*(5), 711-731.

Poulos, H.G., Chow, H.S.W., & Small, J.C. (2019). The use of equivalent circular piles to model the behaviour of rectangular barrette foundations. *Geotechnical Engineering*, *50*(3), 106-109.

Ramaswamy, S.D., & Pertusier, E.M. (1986). Construction of barrettes for high-rise foundations. *Journal of Construction Engineering and Management*, *112*(4), 455-462.

Schädlich, B., & Schweiger, H.F. (2014). A new constitutive model for shotcrete. In MA Hicks, RBJ Brinkgreve & A Rohe (Eds.), *Numerical Methods in Geotechnical Engineering: Proceedings of the 8th European Conference on Numerical Methods in Geotechnical Engineering* (pp. 103-108). Boca Raton, United States of America: CRC Press. https://doi.org/10.1201/b17017-20.

Siriwan, W., Pornkasem, J., & Schweiger, H.F. (2020). Numerical and experimental investigation of failure of a DCM-wall considering softening behavior. *Computers and Geotechnics*, *119*, 103380. http://dx.doi.org/10.1016/j.compgeo.2019.103380.

Wakil, A.Z., & Nazir, A.K. (2013). Behavior of laterally loaded small scale barrettes in sand. *Ain Shams Engineering Journal*, *4*(3), 343-350.

Zhang, L.M. (2003). Behavior of laterally loaded large-section barrettes. *Journal of Geotechnical and Geoenvironmental Engineering*, *129*(7), 639-648.

Large-scale direct shear testing in coir fibers reinforced sand

Leila Maria Coelho de Carvalho[1] (ID), Fernando Feitosa Monteiro[2#] (ID),

Michéle Dal Toé Casagrande[1] (ID)

Article

Keywords
Coir fibers
Shear strength
Reinforced soils
Large scale direct shear test

Abstract
The need to develop and commercialize materials incorporating vegetable fibers has risen over the last 20 years to decrease environmental impact and achieve sustainability. In geotechnical engineering, soil reinforcement with plant-based fibers has gained a lot of interest, especially in temporary earthworks. Soil reinforcement with plant-based fibers is a low-cost, environmentally friendly method with excellent reproducibility and accessibility. In this context, growing appeals for using plant-based fibers such as sisal, coir, curauá, and kenaf for manufacturing new geomaterials have been verified. This paper aims to evaluate the mechanical behavior of soil-fiber composites by insertion of natural coir fibers into a sandy soil matrix with different fiber lengths and contents, where the fibers were randomly distributed in the soil mass. Large-scale direct shear test evaluated the strength-displacement behavior in samples with dimensions of 300 x 300 mm and 200 mm in height. The tests were carried out using fibers with 25 and 50 mm lengths, in 0.50 and 0.75% of fiber contents (in relation to the dry weight of the soil), in a relative density of 50% and 10% moisture content. The overall analysis of the results showed that the coir fibers addition in the well-graded sand increased the shear strength parameters and the ductility, compared with the unreinforced sand.

1. Introduction

Brazil is the world's fourth-largest producer of the coconut fruit. However, the industry only processes a small part of coconut wastes, which has resulted in a variety of environmental challenges. Coconut shells account for between 80% and 85% of the weight of the fruit and around 70% of the waste produced on Brazilian beaches, posing a severe environmental challenge, particularly in tropical nations. Nevertheless, coconut fiber applications are limited to evapotranspiration coverage (Sotomayor & Casagrande, 2018). In Brazil, most coconut output is deposited in landfills, occupying a reasonable amount of space. Coconut shell biodegradation takes approximately eight years, and its landfilling also produces methane (CH_4), which contributes to the climate impact if not recovered for electricity generation (Carijó et al., 2002; Themelis & Ulloa, 2007).

Vegetal fibers are increasingly being used to reinforce soil masses, notably in applications involving the stability of earth slopes, ground improvement for shallow foundations, as well as steep cover systems for landfills (Sadek et al., 2010). Furthermore, fiber-reinforced soils (FRSs) are being utilized for recycling and reusing shredded and fibrous inorganic wastes in engineering applications, as viable backfills,

and as enhanced pavement materials. Empirical evidence from laboratory research on composite FRS specimens or independent testing of soil and fiber specimens is often used to design geotechnical systems utilizing FRSs (Zornberg, 2002; Casagrande et al., 2003; Diambra et al., 2007; Consoli et al., 2007b; Sotomayor & Casagrande, 2018; Louzada et al., 2019; Correia & Rocha, 2021; Silveira & Casagrande, 2021; Silveira et al., 2022).

Research conducted on fiber-reinforced soils has shown that main parameters regarding shear strength are soil particle size and shape, soil relative density, fiber orientation, and fiber content and length (Maher & Gray, 1990; Al-Refeai, 1991; Michalowski & Cermak, 2003; Yetimoglu & Salbas, 2003; Sadek et al., 2010; Hejazi et al., 2012; Li & Zornberg, 2013; Ferreira et al., 2017; Ferreira et al., 2021). Moreover, research has shown that fibers randomly dispersed in the soil matrix have the benefit of intercepting the potential failure zone and improving the soil stress-strain behavior by mobilizing fiber tensile strength, increasing the sand-fiber composite ductility (Zornberg, 2002; Consoli et al., 2012; Li & Zornberg, 2013; Shukla, 2017).

Many researchers have shown interest in investigating coir fiber as concrete reinforcement (Majid et al., 2011; Ramli et al., 2013; Gupta & Kumar, 2019; Syed et al., 2020).

[#]Corresponding author. E-mail address: fernando.monteiro@unichristus.edu.br
[1]Universidade de Brasília, Departamento de Engenharia Civil e Ambiental, Brasília, DF, Brasil.
[2]Unichristus, Fortaleza, CE, Brasil.

Carvalho et al., Soil. Rocks, São Paulo, 2023 46(1):e2023002822

1

Moreover, few studies have focused on soil reinforcement with coir fiber (Menezes et al., 2020; Kaushik & Singh, 2021), and the use of large shearing equipment, which can reduce scale effects of standard soil direct shear tests.

This research aims to evaluate the mechanical behavior of soil reinforced with randomly distributed coir fibers, as well as fiber length and content effect on soil shear strength parameters. The findings apply to the use of fiber-reinforced composites in geotechnical engineering, as well as the selection of parameters in associated numerical analyses.

2. Materials and methods

2.1 Test materials

The composite matrix is formed by a sand soil (Figure 1A) with a specific gravity (Gs) of 2.68, a uniformity and curvature coefficient (C_u and C_c) of 2.40 and 1.06, respectively. As well as an average diameter (D_{50}) of 0.39 mm (Figure 2), and minimum and maximum void ratios of 0.58 and 0.89, respectively. The USCS classifies this material as SW, corresponding to a well-graded sand.

The use of specific fiber lengths and contents was required to accomplish the testing program's objectives, which included investigating the influence of fiber content relative to soil granulometry on the strength enhancement caused by fiber inclusion. The fibers utilized in this research were obtained using a customized tool to cut the fibers to the desired lengths to control fiber geometry.

A collaboration between the municipal company of urban cleaning and the department of public services conservation of Rio de Janeiro gathered coir fibers provided for this research. Before being employed, the fibers were cut to the necessary length (25 and 50 mm) and subjected to a beneficiation process to remove any residues attached to their surface (grease and natural resins). The fibers were washed in boiling water and air-dried throughout this procedure. Figure 1B depicts the coir fibers after all preparation procedures. The fiber average dimensions were 25 and 50 mm in length, and 0.50 and 0.75% contents were utilized according to soil dry weight. Prior research suggests that a 0.50% fiber content can be adopted as an upper limit considering workability and homogeneity (Consoli et al., 2003; Consoli et al., 2009b; Consoli et al.,

2007b; Anagnostopoulos et al., 2013). However, limited research has examined this upper limit for coir content influence.

2.2 Laboratory testing program

A comprehensive direct shear testing program was planned and conducted to explore the characteristics known to affect the composite shear strength of fiber-reinforced sands. Five series of drained large direct shear tests were conducted using a well-graded sand with varying fiber lengths and contents. Large direct shear testing was used because of the relative simplicity of sample preparation and testing procedure. This testing procedure was selected despite the inherent test restrictions, such as the kinematic constraints imposed on the sample, the nonuniform shear zone thickness, and the non-uniform stress distribution. A 300 x 300 x 220 mm shear box was utilized in all experiments to minimize the restrictions' influence and obtain reliable and representative samples (Figure 3). The tests were conducted by ASTM (2011) at a constant displacement rate of 0.508 mm/min. Using a load cell and LVDTs, the shearing load and vertical displacement were recorded as functions of the horizontal displacement. Total horizontal displacements of at least 35 mm were recorded.

The direct shear system consists of two hydraulic circuits equipped with two hydraulic jacks, and two 100 kN load cells and three LVDTs. Figure 3 also depicts the reaction system composed of a 1000 kN workload steel gantry. The hydraulic systems are employed to apply both shear, and normal loads, which also function with the support of a gear set arranged according to the test required velocity. The equipment's operation is driven utilizing hydraulic hose connections, thus allowing a constant and pre-established load transfer. Load cells and displacement sensors (Figure 4) are connected to a data acquisition system (*Spider 8*), with a 1 Hz acquisition frequency and Catman v 2.0® software.

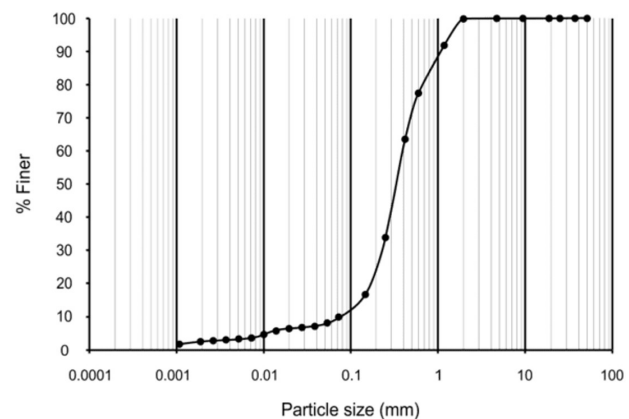
Figure 1. (a) Sand soil; (b) 50 mm length coir fiber.

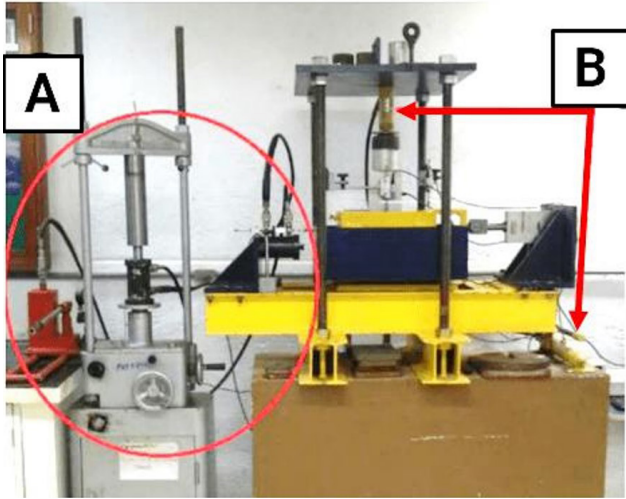**Figure 2.** The grain-size distribution curve of unreinforced sand soil.

Figure 3. Large direct shear test setup (a) hydraulic system which applies shearing loads; (b) hydraulic system which applies normal loads.
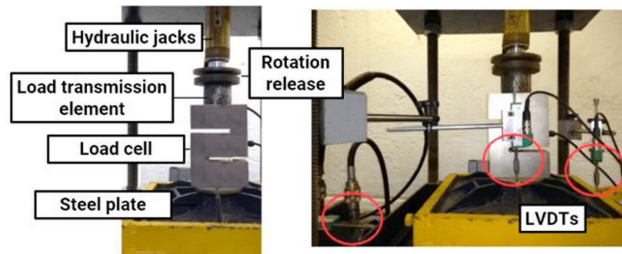

Figure 4. Large direct shear test setup: load cells and LVDTs.

Figure 5. Specimen molding procedure.
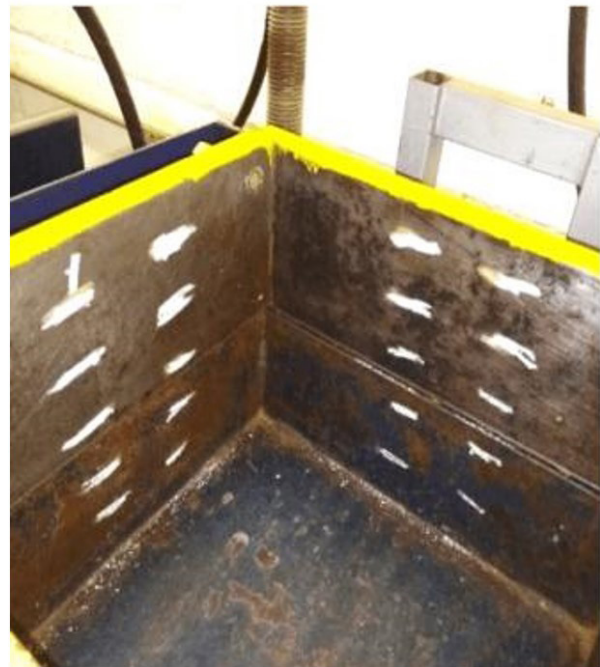
Figure 6. Inner view of the direct shear box during sample preparation.

2.3 Specimen preparation and testing

The molding parameters used for the non-reinforced sandy soil and the soil-fiber composite were identical, with a relative density of 50% and an initial moisture content of 10% in proportion to the soil dry weight. The soil-fiber mixes were made using fibers randomly dispersed in lengths of 25 and 50 mm, with fiber contents of 0.50 and 0.75% of the soil dry weight. To avoid segregation of the fibers and the sand, both the compacted sand and the fiber-reinforced specimens were first manually homogenized with the appropriate amounts of dry sand, vegetable fibers (if used), and water. The homogeneity of the components was visually verified after the mixture of all parts was prepared. All specimens were prepared by static compaction onto the direct shear box in a square mold 300 mm in length and 200 mm in height (Figure 5). The sample in the direct shear box was divided into five layers with 40 mm in size (Figure 6). The final height of each layer was controlled to ensure the 50% soil relative density.

Therefore, the specimen preparation method detailed above was adopted for molding soil samples at 50% relative density and 10% moisture content. The choice of relative density as the reference parameter was made since: (1) it allows better visualization of soil-fiber interaction effect (Consoli et al., 2007b; Consoli et al., 2007a; Consoli et al., 2009a) and (2) as the composite relative density increases, fiber mobilization within the soil mass occurs rapidly, due to a better interlock between the fibers and the soil matrix.

A summary of the testing program and sample notation is shown in Table 1. The fiber content of the well-graded sand ranged from 0 to 0.75%, about soil dry weight. Additionally, a minimum of three specimens were studied at normal stress levels of 25, 50, and 100 kPa for each set of parameters, for a total of nearly 15 large direct shear tests. These normal stresses were chosen to represent usual stress ranges in relevant geotechnical engineering applications.

3. Analysis and results

Shear stress and vertical displacement versus horizontal displacement plots for soil specimens evaluated at typical stress values of 25, 50, and 100 kPa are included in the experimental findings. These plots were examined to determine the effect of fibers on stress-displacement behavior, shear strength and friction angle increase, and volume change. Table 2 summarizes the relevant test parameters and calculated internal friction angles for unreinforced and fiber-reinforced samples.

Plots depicting the variation in shear stress and vertical displacement with horizontal displacement for unreinforced and fiber-reinforced soil samples with fiber lengths of 25 and 50 mm, as well as 0.50 and 0.75% fiber contents, are presented in Figures 7-8. Curves in Figure 7 correspond to soil samples reinforced with 25 mm length fibers with a fiber content of 0.50 and 0.75%, whereas curves in Figure 8 correspond to soil samples reinforced with 50 mm length fibers with a fiber content of 0.50 and 0.75%. The results presented in Figures 7-8 indicate increases in strength for 25 and 50 mm long fibers, particularly the first. Except for an increase in the slope of the stress-displacement curve at small displacements, the general form of the stress-displacement curves of fiber-reinforced specimens was like that of unreinforced samples. However, as normal stresses increased, fiber-reinforced specimens curves showed a shear stress growth at a horizontal displacement range between 10 to 40 mm, indicating a typical hardening behavior as observed by Silveira & Casagrande (2021).

Figures 7-8 indicate that fiber reinforcement inhibits dilatancy, particularly at high normal stresses. This result endorses prior research findings from direct shear testing (Gray & Ohashi, 1983) and triaxial tests (Michalowski & Zhao, 1996; Michalowski & Cermak, 2003). On the other hand, other researchers (Sadek et al., 2010; Hazirbaba, 2017) have shown that the presence of fibers consistently increases the tendency for dilation in fiber-reinforced, particularly

for longer fibers, which was the case to some extent for fiber-reinforced samples with 50 mm fiber lengths. The main distinction between published results and results reported in this paper is the soil relative density, which was taken as 50% in the current study but was always greater than 50% in the studies mentioned above, as well as the shear box size (scale effect), which may have contributed to the observed discrepancies since direct shear test results are known to be sensitive to the size of the soil specimen.

The maximum shear stress was attained for practically all unreinforced samples with a horizontal displacement of approximately 15 mm. Further than this value, the shear stress became nearly constant, which is evident that soil samples were prepared in a loose to medium dense state (DR ≈ 50%). On the contrary, reinforced specimens indicated increasing shear stress as normal stress, and horizontal displacement also rose. The mobilization of the fiber unit tensile stress
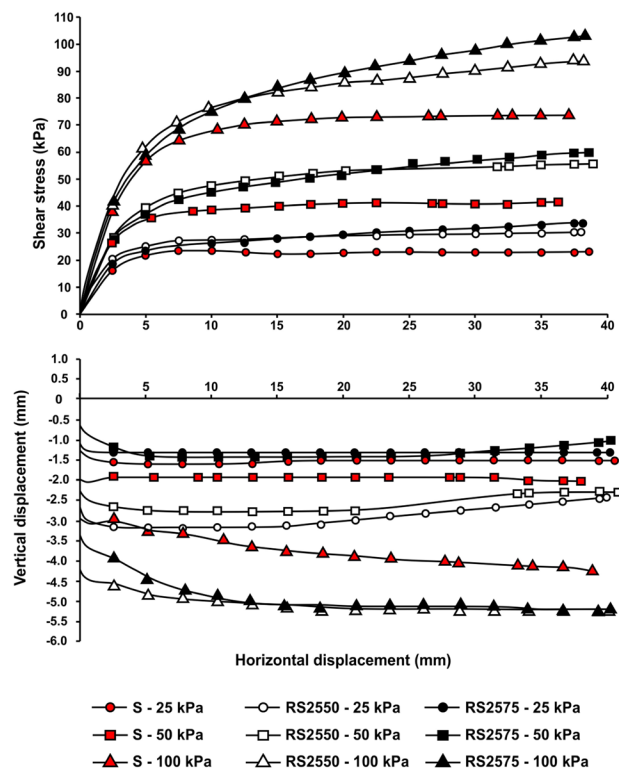

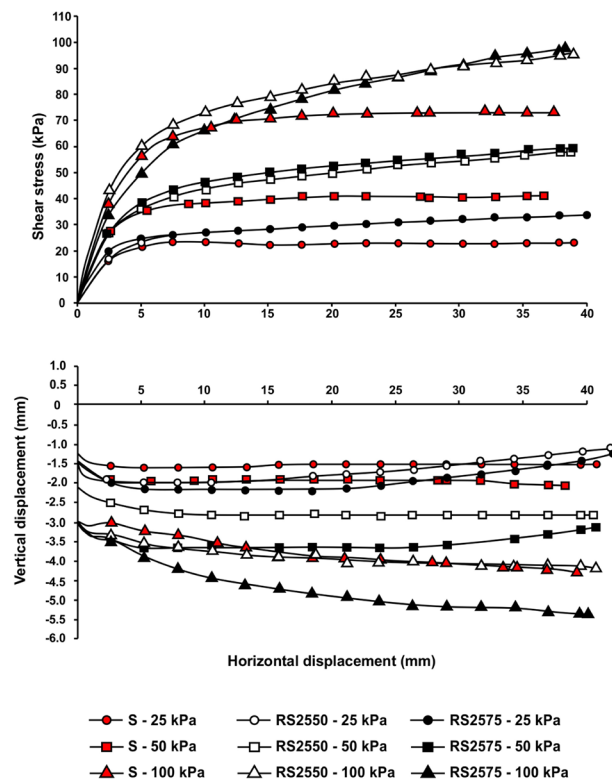**Figure 7.** Variation of shear stress and vertical displacement with horizontal displacement for fiber-reinforced sand with 25 mm fiber lengths.

Table 1. Laboratory testing program.

Sample	Fiber length (mm)	Fiber content (%)
S	—	—
RS2550	25	0.50
RS2575	25	0.75
RS5050	50	0.50
RS5075	50	0.75

Table 2. Laboratory testing program.

Sample	Fiber length (mm)	Fiber content (%)	Internal friction angle (°)	Improvement in shear strength parameters (%)
S	—	—	34.0	—
RS2550	25	0.50	40.0	18
RS2575	25	0.75	42.0	24
RS5050	50	0.50	39.0	15
RS5075	50	0.75	40.0	18

produced by a set of effects (interface bonding, friction, and interlocking) when the composite is under load can be attributed to the shear stress rise for fiber-reinforced specimen curves (Gowthaman et al., 2018). It is worth noting that the fiber strengthening effect requires some amount of deformation to initiate, as observed by Lawton et al. (1993) while performing triaxial tests on fiber-reinforced soil specimens. For the case without an obvious peak point, the failure criteria proposed by Campos & Carrillo (1995), based on the slope of the stress–displacement curve was adopted. In these cases, shear failure was assumed when the stress–displacement curve indicated a constant slope (d ≈ 35 mm for all reinforced specimens).

A considerable soil stiffness improvement due to fiber inclusion occurs in the initial test stage at small displacements of about 5 mm for all reinforced samples. Beyond this value, the stress-displacement curves evidence increases in shear stress of the sand-fiber composite compared to unreinforced specimens (Figures 7-8). The inclusion of fibers changes the failure mechanisms observed for non-reinforced sand. Soil hardening behavior (a constant rise in strength with increasing horizontal displacement) was observed for all normal stresses regarding the soil reinforced with coir fibers. When comparing the results of the fiber lengths and contents, it becomes evident that the samples reinforced with 25 mm length and 0.75% fiber content presented higher shear strength for all normal stresses.

The increase in the maximum shear stress as a function of the fiber content is illustrated in Figures 7-8 for sands reinforced with 25 and 50 mm length fibers. An increase in fiber content from 0.50 to 0.75% results in about a 12% improvement in shear strength for a fiber length of 25 mm and about a 4% improvement for a fiber length of 50 mm. This result is relevant because it indicates that more extensive improvements in shear strength can be obtained with relatively small fiber content variation.

Stress-displacement curves for reinforced-sand specimens with 25 mm fiber lengths show a consistent rise in maximum shear stress as fiber content increases. Unlike reinforced-sand samples with 50 mm fiber lengths and fiber contents of 0.50 and 0.75%. This suggests that the relative dimensions of the reinforced sand grains and the diameters of the reinforcing fibers significantly impact the level of improvement brought about by fiber inclusion in sands. When the fiber concentration is around 0.75%, the reinforcing effect in reinforced-sand specimens with 25 mm fiber lengths is more pronounced, whereas the relative increase in reinforcing effect in reinforced-sand samples with 50 mm fiber lengths is slightly smaller for similar fiber content.

Vertical displacement versus horizontal displacement curves were recorded to verify the sample volume change as the large direct shear test progresses. The vertical displacement curves indicate that unreinforced and fiber-reinforced sand specimen's behavior was similar to typical loose sand samples. The sample vertical displacement decreases as the shear stress increases to a maximum value. After that, a constant vertical displacement value is observed. A similar trend was verified for all samples at 25, 50, and 100 kPa normal stresses. However, for samples reinforced with 25 mm length fibers, the addition of fibers decreased the contraction behavior, indicating that the fibers merged the sandy soil grains, inhibiting particle movement. While fiber inclusion for samples reinforced with 50 mm length fibers had no significant effect on the sample volume change.

The friction between the soil and the reinforcement appears to control the soil-fiber composite strength, and it does not appear to be dependent on the ultimate strength properties of the coir fibers. Direct shear test results are compiled in Table 3 and the shear strength envelopes for unreinforced and reinforced sand specimens are depicted in Figure 9. The friction angle value is also affected by the confining stresses under which the samples are tested, implying that the general envelope is nonlinear. However, given the restricted range of effective normal stresses applied in this research and the simplicity by which the effects of fiber reinforcement can be quantified, a linear envelope determined using linear regression would be a reasonable estimate of the soil stress state at failure. This line's extrapolation towards zero effective normal stress yields a cohesion intercept.

As an uncemented particle system, sand soils should lack genuine cohesion under effective stresses. However, the inter-particle contacts (interlocking) created by the

Figure 8. Variation of shear stress and vertical displacement with horizontal displacement for fiber-reinforced sand with 50 mm fiber lengths.

Table 3. Shear strength parameters for all test series.

Sample	Fiber length (mm)	Fiber content (%)	Internal friction angle (°)	Improvement in shear strength parameters (%)	Cohesion intercept (kPa)
S	—	—	34.0	—	6
RS2550	25	0.50	40.0	18	11
RS2575	25	0.75	42.0	24	11
RS5050	50	0.50	39.0	15	14
RS5075	50	0.75	40.0	18	14
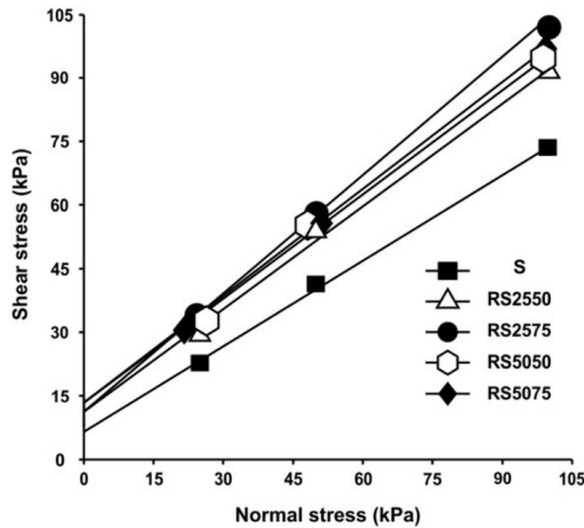
Figure 9. Unreinforced and fiber-reinforced sand samples shear strength envelopes.

tamping fabrication approach appear to be relevant, which might explain the presence of an apparent cohesion that rises marginally with fiber addition (Ibraim & Fourmont, 2006). Although more research is needed to determine the cause of this apparent cohesion, the failure envelopes in this study are defined in terms of the soil friction angle and cohesion intercept. Table 3 presents a maximum improvement in shear strength of 24% percent for the highest fiber content (0.75%). The increased maximum shear stress causes the composite's friction angle to increase from 34 ° for unreinforced sand to 42 ° for sand reinforced with 0.75% fiber content.

4. Conclusions

In this research, the shear strength behavior of a well-graded sand reinforced with coir fibers of different content and lengths was studied using a series of large-scale direct shear tests. The unreinforced and fiber-reinforced sand samples were compacted at 50% relative density and a moisture content of 10%. The following conclusions can be made based on the undertaken experimental study:

- The fiber-reinforced sand samples with coir fibers showed a significant increase in shear stress as the normal stress increased. This increase is attributed to the fiber's anchoring action (interface bonding,

friction, and interlocking) in the soil mass under load. The addition of fibers alters the failure mechanism observed in unreinforced sand. Furthermore, the modification of the failure mechanism may be seen as a plausible explanation for the soil hardening behavior observed in all stress-displacement curves of fiber-reinforced samples.

- The addition of coir fibers with lengths of 25 and 50 mm and fiber contents varying from 0.50 to 0.75% percent to a well-graded sand produced at a relative density of 50% improved the sand-fiber composite's shear strength and ductility. For sand reinforced with 0.75% fiber content and 25 mm fiber length, the most significant improvement in shear strength was nearly 32%.

- At low normal loads (25 kPa), the shear strength presents a slight increase for all reinforced specimens. However, for higher normal stresses, the shear strength increase with all fiber contents and lengths are more evident, particularly for 25 mm fiber lengths.

- Shorter (25 mm length) coir fibers resulted in a more significant improvement in the shear strength of fiber-reinforced sands, according to the limited experiments in this research. The results reported by Michalowski & Cermak (2003) on the relative dimensions impact of the reinforced sand grains and the reinforcing fiber diameters in determining the level of improvement provided by fiber inclusion might be one explanation for this finding.

- More broadly, the findings concerning the dilatancy of fiber-reinforced composites are consistent with previous studies that revealed a tendency for fibers to restrict sand dilatancy. According to the results of the experiments conducted in this study, the vertical displacements recorded during shearing for reinforced specimens with 25 mm fiber lengths were reduced with the addition of fibers. However, vertical displacements increased with fibers in reinforced specimens with 50 mm fiber lengths for both 0.50 and 0.75% fiber content. The increase in recorded vertical displacement during shear represents a greater tendency for dilatation of a narrow band of soil impacted by the presence of fibers, as also noted by Sadek et al. (2010).

The current research's broad implication is that the inclusion of coir fibers as soil reinforcement has a substantial potential for application in landfills on soft soils, slopes, and shallow foundations, giving this material a better end in the technical scope while also attending to economic, social, and environmental aspects.

Acknowledgements

Declaration of interest

The authors have no conflicts of interest to declare. All co-authors have observed and affirmed the paper's contents, and there is no financial interest to report.

Authors' contributions

Leila Maria Coelho de Carvalho: investigation, data curation, visualization, writing – original draft, formal analysis. Fernando Feitosa Monteiro: investigation, writing – review & editing. Michéle Dal Toé Casagrande: conceptualization, methodology, supervision, funding acquisition.

Data availability

All data produced or examined in the course of the current study are included in this article.

List of symbols

d	Horizontal displacement
C_c	Curvature coefficient
C_u	Uniformity coefficient
D_{50}	Average diameter
DR	Relative density
FRS	Fiber reinforced soil
G_s	Specific gravity
$LVDT$	Linear variable differential transformer
$USCS$	Unified soil classification system

References

Al-Refeai, T.O. (1991). Behavior of granular soils reinforced with discrete randomly oriented inclusions. *Geotextiles and Geomembranes*, *10*(4), 319-333. http://dx.doi.org/10.1016/0266-1144(91)90009-L.

Anagnostopoulos, C.A., Papaliangas, T.T., Konstantinidis, D., & Patronis, C. (2013). Shear strength of sands reinforced with polypropylene fibers. *Geotechnical and Geological Engineering*, *31*(2), 401-423. http://dx.doi.org/10.1007/s10706-012-9593-3.

ASTM D3080-11. (2011). *Standard test method for direct shear test of soils under consolidated drained conditions*. ASTM International, West Conshohocken, PA.

Campos, T., & Carrillo, C. (September 6-8, 1995). Direct shear testing on an unsaturated soil from Rio de Janeiro. In E.E. Alonso & P. Delage (Eds.), *Proceedings of the First International Conference on Unsaturated Soils* (Vol. 1, pp. 31-38). Paris, France: Balkema.

Carijó, O.A., Liz, R.D.S., & Makishima, N. (2002). Fibra de casca de coco verde como substrato agrícola. *Horticultura Brasileira*, *20*(4), 533-535. In Portuguese.

Casagrande, M.D.T., Consoli, N.C., Prietto, P.D.M., & Thome, A. (2003). Plate load test on fiber-reinforced soil. *Journal of Geotechnical and Geoenvironmental Engineering, 129*(10), 951-955. http://dx.doi.org/10.1061/(ASCE)1090-0241(2003)129:10(951).

Consoli, N.C., Casagrande, M.D.T., Thome, A., Rosa, F.D., & Fahey, M. (2009a). Effect of relative density on plate tests on fibre-reinforced sand. *Geotechnique*, *59*(5), 471-476. http://dx.doi.org/10.1680/geot.2007.00063.

Consoli, N.C., Coop, M.R., & Casagrande, M.D.T. (2007a). Performance of a fibre-reinforced sand at large shear strains. *Geotechnique*, *57*(9), 751-756. http://dx.doi.org/10.1680/geot.2007.57.9.751.

Consoli, N.C., Heineck, K.S., Casagrande, M.D.T., & Coop, M.R. (2007b). Shear strength behavior of fiber-reinforced sand considering triaxial tests under distinct stress paths. *Journal of Geotechnical and Geoenvironmental Engineering*, *133*(11), 1466-1469. http://dx.doi.org/10.1061/(ASCE)1090-0241(2007)133:11(1466).

Consoli, N.C., Thomé, A., Girardello, V., & Ruver, C.A. (2012). Uplift behavior of plates embedded in fiber-reinforced cement stabilized backfill. *Geotextiles and Geomembranes*, *35*, 107-111. http://dx.doi.org/10.1016/j.geotexmem.2012.09.002.

Consoli, N.C., Vendruscolo, M.A., & Prietto, P.D.M. (2003). Behavior of plate load tests on soil layers improved with cement and fiber. *Journal of Geotechnical and Geoenvironmental Engineering*, *129*(1), 96-101. http://dx.doi.org/10.1061/(ASCE)1090-0241(2003)129:1(96).

Consoli, N.C., Vendruscolo, M.A., Fonini, A., & Rosa, F.D. (2009b). Fiber reinforcement effects on sand considering a wide cementation range. *Geotextiles and Geomembranes*, *27*(3), 196-203. http://dx.doi.org/10.1016/j.geotexmem.2008.11.005.

Correia, N.S., & Rocha, S.A. (2021). Reinforcing effect of recycled polypropylene fibers on a clayey lateritic soil in different compaction degrees. *Soils and Rocks*, *44*(2), 1-9. http://dx.doi.org/10.28927/SR.2021.061520.

Diambra, A., Russell, A.R., Ibraim, E., & Wood, D.M. (2007). Determination of fiber orientation distribution in reinforced sands. *Geotechnique*, *57*(7), 623-628. http://dx.doi.org/10.1680/geot.2007.57.7.623.

Ferreira, J.W.S., Senez, P.C., & Casagrande, M.D.T. (2021). Pet fiber-reinforced sand performance under triaxial and plate load tests. *Case Studies in Construction Materials*, *15*, e00741. http://dx.doi.org/10.1016/j.cscm.2021.e00741.

Ferreira, S., Silva, F., Lima, P., & Toledo Filho, R. (2017). Effect of hornification on the structure, tensile behavior and fiber matrix bond of sisal, jute and curauá fiber cement based composite systems. *Construction & Building Materials*, *139*, 551-561. http://dx.doi.org/10.1016/j.conbuildmat.2016.10.004.

Gowthaman, S., Nakashima, K., & Kawasaki, S. (2018). A state-of-the-art review on soil reinforcement technology using natural plant fiber materials: past findings. *Present Trends and Future Directions*, *11*(4), 553-576. http://dx.doi.org/10.3390/ma11040553.

Gray, D.H., & Ohashi, H. (1983). Mechanics of fiber reinforcement in sand. *Journal of Geotechnical Engineering*, *109*(3), 335-353. http://dx.doi.org/10.1061/(ASCE)0733-9410(1983)109:3(335).

Gupta, M., & Kumar, M. (2019). Effect of nano-silica and coir fiber on compressive strength and abrasion resistance of Concrete. *Construction & Building Materials*, *226*, 44-50. http://dx.doi.org/10.1016/j.conbuildmat.2019.07.232.

Hazirbaba, K. (2017). Large-scale direct shear and CBR performance of geofibre-reinforced sand. *Road Materials and Pavement Design*, *19*(6), 1350-1371. http://dx.doi.org/10.1080/14680629.2017.1310667.

Hejazi, S.M., Sheikhzadeh, M., Abtahi, S.M., & Zadhoush, A. (2012). A simple review of soil reinforcement by using natural and synthetic fibers. *Construction & Building Materials*, *30*, 100-116. http://dx.doi.org/10.1016/j.conbuildmat.2011.11.045.

Ibraim, E., & Fourmont, S. (2006). Behavior of sand reinforced with fibres. In H.I. Ling, L. Callisto, D. Leshchinsky & J. Koseki (Eds.), *Soil stress-strain behavior: measurement, modeling and analysis* (pp. 807-818). Springer. https://doi.org/10.1007/978-1-4020-6146-2_60.

Kaushik, S.D., & Singh, S.K. (2021). Use of coir fiber and analysis of geotechnical properties of soil. *Materials Today: Proceedings*, *47*(14), 4418-4422. http://dx.doi.org/10.1016/j.matpr.2021.05.255.

Lawton, E.C., Khire, M.V., & Fox, N.S. (1993). Reinforcement of soils by multioriented geosynthetic inclusion. *Journal of Geotechnical Engineering*, *119*(2), 257-275. http://dx.doi.org/10.1061/(ASCE)0733-9410(1993)119:2(257).

Li, C., & Zornberg, J.G. (2013). Mobilization of reinforcement forces in fiber-reinforced soil. *Journal of Geotechnical and Geoenvironmental Engineering*, *139*(1), 107-115. http://dx.doi.org/10.1061/(ASCE)GT.1943-5606.0000745.

Louzada, N.S.L., Malko, J.A.C., & Casagrande, M.D.T. (2019). Behavior of clayey soil reinforced with polyethylene terephthalate. *Journal of Materials in Civil Engineering*, *31*(10), 04019218. https://doi.org/10.1061/(ASCE)MT.1943-5533.0002863.

Maher, M.H., & Gray, D.H. (1990). Static response of sands reinforced with randomly distributed fibers. *Journal of Geotechnical Engineering*, *116*(11), 1661-1677. http://dx.doi.org/10.1061/(ASCE)0733-9410(1990)116:11(1661).

Majid, A., Liu, A., Hou, S., & Nawawi, C. (2011). Mechanical and dynamic properties of coconut fibre reinforced concrete. *Construction & Building Materials*, *30*, 814-825. http://dx.doi.org/10.1016/j.conbuildmat.2011.12.068.

Menezes, L.C.P., Sousa, D.B., Fucale, S., & Ferreira, S.R.M. (2020). Analysis of the physical-mechanical behavior of clayey sand soil improved with coir fiber. *Soils and Rocks*, *42*(1), 31-42. http://dx.doi.org/10.28927/SR.421031.

Michalowski, R., & Cermak, J. (2003). Triaxial compression of sand reinforced with fibers. *Journal of Geotechnical and Geoenvironmental Engineering*, *129*(2), 125-136. http://dx.doi.org/10.1061/(ASCE)1090-0241(2003)129:2(125).

Michalowski, R.L., & Zhao, A. (1996). Failure of fiber-reinforced granular soils. *Journal of Geotechnical Engineering*, *122*(3), 226-234. http://dx.doi.org/10.1061/(ASCE)0733-9410(1996)122:3(226).

Ramli, M., Kwan, W.H., & Abas, N.F. (2013). Strength and durability of coconut-fiber-reinforced concrete in aggressive environments. *Construction & Building Materials*, *38*, 554-566. http://dx.doi.org/10.1016/j.conbuildmat.2012.09.002.

Sadek, S., Najjar, S.S., & Freiha, F. (2010). Shear strength of fiber-reinforced sands. *Journal of Geotechnical and Geoenvironmental Engineering*, *136*(3), 490-499. http://dx.doi.org/10.1061/(ASCE)GT.1943-5606.0000235.

Shukla, S.K. (2017). *Fundamentals of fibre-reinforced soil engineering*. Springer.

Silveira, M.V., & Casagrande, M.D.T. (2021). Effects of degradation of vegetal fibers on the mechanical behavior of reinforced sand. *Geotechnical and Geological Engineering*, *39*, 3875-3887. http://dx.doi.org/10.1007/s10706-021-01733-y.

Silveira, M.V., Ferreira, J.W.S., & Casagrande, M.D.T. (2022). Effect of surface treatment on natural aging and mechanical behavior of sisal fibers reinforced sand composite. *Journal of Materials in Civil Engineering*, *34*(6), 06022001. http://dx.doi.org/10.1061/(ASCE)MT.1943-5533.0004237.

Sotomayor, J.M.G., & Casagrande, M.D.T. (2018). The performance of a sand reinforced with coconut fibers through plate load tests on a true scale physical model. *Soils and Rocks*, *41*(3), 361-368. http://dx.doi.org/10.28927/SR.413361.

Syed, H., Nerella, R., & Madduru, S.R.C. (2020). Role of coconut coir fiber in concrete. *Materials Today: Proceedings*, *27*(2), 1104-1110. http://dx.doi.org/10.1016/j.matpr.2020.01.477.

Themelis, J.N., & Ulloa, P.A. (2007). Methane generation in landfills. *Renewable Energy*, *32*(7), 1243-1257. http://dx.doi.org/10.1016/j.renene.2006.04.020.

Yetimoglu, T., & Salbas, O. (2003). A study on shear strength of sands reinforced with randomly distributed discrete fibers. *Geotextiles and Geomembranes*, *21*(2), 103-110. http://dx.doi.org/10.1016/S0266-1144(03)00003-7.

Zornberg, J.G. (2002). Discrete framework for limit equilibrium analysis of fiber-reinforced soil. *Geotechnique*, *52*(8), 593-604. http://dx.doi.org/10.1680/geot.2002.52.8.593.

TECHNICAL NOTES

Maximum shear modulus estimative from SPT for some Brazilian tropical soils

Breno Padovezi Rocha[1#] (iD), Bruno Canoza da Silva[2] (iD),

Heraldo Luiz Giacheti[3] (iD)

Technical Note

Abstract

Maximum shear modulus (G_0) has been used in various geotechnical jobs (e.g., seismic site assessment, machine vibration and pile driven). Laboratory and in situ determination of G_0 is not a current practice in Brazil. G_0 can be estimated from empirical correlations based on in situ tests like Standard Penetration Test (SPT) and Cone Penetration Test (CPT) in the preliminary design phase. Several empirical correlations to estimate G_0 from SPT N value have been developed and are available in the literature. However, most of these correlations were established based on experience with well-behaved soils formed in temperate and glacial zones, which may not always be used for tropical soils. This paper assessed and discussed the applicability of some correlations for G_0 estimative from SPT data in lateritic and saprolitic soils. The classical correlations for sedimentary soils underestimated G_0 of tropical soils. After updating the database, the tropical soils correlations reasonably estimated G_0 for the lateritic ones, which was not the case for the saprolitic soils. It was observed that differentiating the soils only as lateritic or saprolitic was not adequate for a good G_0 estimate for the saprolitic sandy soils. It was found that only the lateritic soils correlation can be used with caution as a preliminary attempt to estimate G_0 from SPT N value in soils with similar characteristics to the ones presented in this paper.

1. Introduction

The maximum shear modulus (G_0) is an input parameter in soil dynamic and static analyses (Bang & Kim, 2007; Brandenberg et al., 2010; Décourt, 2018; Poulos, 2021). Another G_0 application is on the estimative of G-γ decay curves (Amoroso et al., 2014; Lehane & Fahey, 2004). Moreover, G_0 can be correlated with the SPT N value, cone resistance (q_c) or constrained modulus obtained by Flat Dilatometer (M_{DMT}) in order to assist soil classification, state parameter estimative, identification of microstructure (age and/or bonding structure) and collapsible soils (Robertson, 2016; Rocha et al., 2022; Schnaid et al., 2020, 2004).

The G_0 can be determined by in situ and laboratory tests. The available laboratory tests are the resonant column (ASTM, 1995; Hoyos et al., 2015; Werden et al., 2013) and the bender elements (Leong et al., 2005) tests. The main in situ tests to determine G_0 are the crosshole (ASTM, 2007), the downhole (ASTM, 2008), the seismic cone (SCPT) (Robertson et al., 1986) and seismic dilatometer (SDMT) (Marchetti et al., 2008). However, these tests are not always

available or cannot be supported in the preliminary site investigation program.

The SPT has been commonly used for site characterization because of its simplicity, robustness, speed, and cost-effectiveness (Akca, 2003; Anderson et al., 2007; Schnaid, 2008). For this reason, several researchers have studied and proposed correlations between SPT N value and G_0 mainly for well-behaved clays and sands (reconstituted and isotropically consolidated clay and the reconstituted sands) (Anbazhagan et al., 2012; Imai & Tonouchi, 1982; Leroueil & Hight, 2002; Seed et al., 1983).

Brazil is a large country where tropical soils occur. A typical tropical soil profile includes the lateritic (upper horizon) and the saprolitic (lower horizon) soils. The lateritic soil undergoes a pedogenetic evolution called laterization, which results in a highly porous horizon with minerals that are more stable (e.g., quartz and kaolinite) and with an enrichment of the soil with iron and aluminum and its associated oxides (Mio, 2005; Vargas, 1985). In addition, foundation engineering practice has shown that lateritic soils are stiffer than non-lateritic soils for the working load (Décourt,

#Corresponding author. E-mail address: breno.rocha@ifsp.edu.br
[1] Instituto Federal de Educação, Ciência e Tecnologia de São Paulo, Campus Avançado Ilha Solteira, Ilha Solteira, SP, Brasil.
[2] Universidade de São Paulo, Escola de Engenharia de São Carlos, Departamento de Geotecnia, São Carlos, SP, Brasil.
[3] Universidade Estadual Paulista "Júlio de Mesquita Filho", Faculdade de Engenharia, Departamento de Engenharia Civil e Ambiental, Bauru, SP, Brasil.

Rocha et al., Soil. Rocks, São Paulo, 2023 46(1):e2023005222

1

2018). Saprolitic horizon is residual and retains the macro fabric or the chemical bond of the parent rock (Brand, 1985; Mio & Giacheti, 2007; Lumb, 1965; Rahardjo et al., 2020).

Tropical soils have a unusual behavior compared to sedimentary soils (Gidigasu, 1976; Vargas, 1985). They are characterized by cohesive-frictional nature, unsaturated condition, bonding and structure, and anisotropy. This behavior cannot be accurately represented by means of models and correlations developed by well-behaved soils (Berisavljević & Berisavljević, 2019; Robertson, 2016; Schnaid et al., 2004).

Giacheti (1991) and Barros & Pinto (1997) observed that the estimated G_0 value by using empirical correlations obtained from well-behaved soils (Table 1) significantly underestimates measured G_0 for lateritic soils. The discrepancy can be associated to the cemented structure from the lateritic soils (Figure 1a). Barros & Pinto (1997) also observed that the investigated saprolitic soils presented G_0 values which were higher than calculated values for low SPT N values. The opposite was observed for high SPT N values (Figure 1b). The authors also concluded that lateritic and saprolitic soils present different behavior: the higher the SPT N value, the greater the differences in G_0 for these soils, as shown in Figure 1c. Hence, Barros & Pinto (1997) suggested correlations for estimating G_0 from SPT N value for lateritic and saprolitic soils for foundation engineering projects in Brazilian tropical soils (Décourt, 2018). These authors used the MCT Classification System (Mini, Compacted, Tropical) proposed by Nogami & Villibor (1981) to classify the soils with respect to their lateritic behavior. Table 1 shows the empirical correlations obtained from well-behaved soils and lateritic and saprolitic soils.

It is important to point out that the correlations proposed by Barros & Pinto (1997) were defined from the available G_0 and SPT N values derived from crosshole and SPT tests at that time: 46 data points for lateritic soils and 26 data points for saprolitic soils. A total of 16 pairs of G_0 and SPT N values were determined on sandy soils and 30 pairs of points on clayey soils for the lateritic soil. For the saprolitic soils, 24 pairs of G_0 and SPT N values were determined for clayey soils and only 2 pairs of points for sandy soils. It is important to mention that the use of only two points of saprolitic sandy soils might not represent the behavior of saprolitic sandy soils, a fact observed and discussed later in this paper. Note that some SPT N values higher than 60 blows per 30 cm
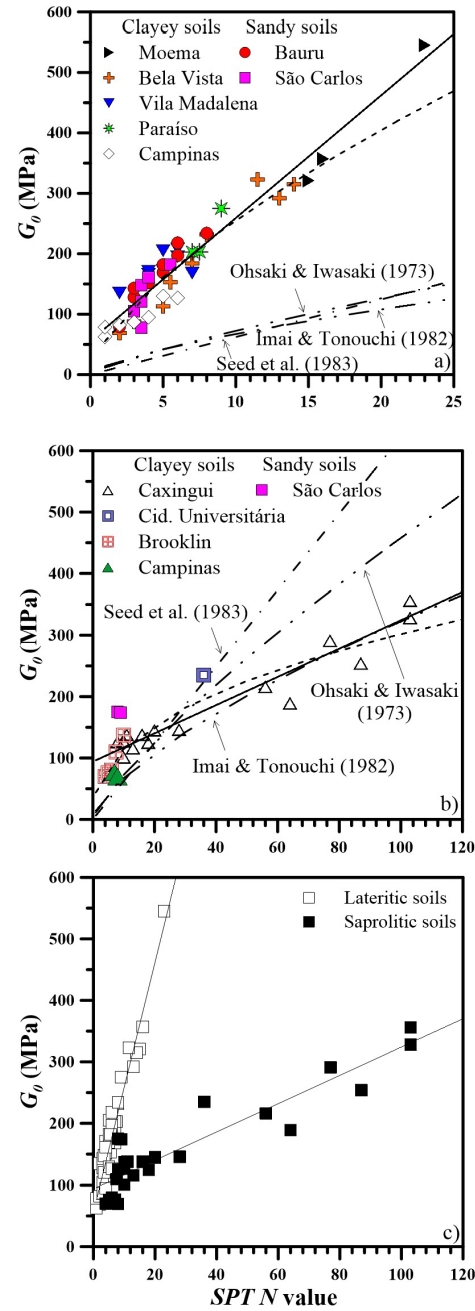

Figure 1. Experimental data for a) lateritic, b) saprolitic, and c) the comparison between lateritic and saprolitic soils [adapted from Barros & Pinto (1997)].

Table 1. Main correlations to estimate G_0 from SPT N value.

Type	Reference	Correlation	Type of soil
	Ohsaki & Iwasaki (1973)	$G_0 = 11.5N^{0.8}$	All soil types
Well-behaved soils	Imai & Tonouchi (1982)	$G_0\ 14.07N^{0.68}$	All soil types
	Seed et al. (1983)	$G_0 = 6.22N$	Sands
Lateritic soils	Barros & Pinto (1997)	$G_0 = 55.2N^{0.66}$	All types of lateritic soils
		$G_0 = 56 + 20.3N$	
Saprolitic soils	Barros & Pinto (1997)	$G_0 = 43.8N^{0.42}$	All types of saprolitic soils
		$G_0 = 94 + 2.3N$	

were defined by extrapolation in the proposed correlations for saprolitic soils.

This paper re-examines and discusses the correlations for estimating G_0 from SPT N value for some Brazilian tropical soils, considering not only the classification as lateritic or saprolitic soils, and points out the need to identify unusual soil behavior. The updated database incorporates additional G_0 and SPT N values (for clayey and sandy soils) by seismic cone (SCPT), downhole (DH), seismic SPT, and seismic dilatometer (SDMT) tests to those presented by Barros & Pinto (1997). It emphasizes the importance of performing G_0 measurements using appropriate techniques to check for unusual soil behavior and the need to adjust site-specific correlations.

2. Brazilian tropical soils correlations

Most of the correlations available in the literature between G_0 and SPT N value are defined as follows:

$$G_0 = A \cdot N^B \tag{1}$$

Where the constants A and B are obtained by statistical regression of a data set, although linear correlation ($G_0 = A + B.N$) is also used. Some authors recommend correcting the SPT N for energy efficiency, rod length, borehole diameter, and fine content (Andrus et al., 2004; Cetin et al., 2004; Hasancebi & Ulusay, 2007). Moreover, the SPT N value and G_0 can be corrected for overburden stress since both SPT N value and G_0 are affected by it, however, it is found that an uncorrected SPT N value and G_0 gives the best fit with a high regression coefficient when compared to G_0 and corrected SPT N values (Anbazhagan & Sitharam, 2010). Some key references cite the importance of associating behavior indices (i.e. I_c or SBT) in the correlations to estimate G_0 from a penetration test such as SPT and CPT (Jefferies & Davies, 1993; Jefferies & Been, 2006; Robertson, 1990, 2009), however, as previously presented, the vast majority of correlations between G_0 and SPT N value does not consider behavior indices (Anbazhagan & Sitharam, 2010; Hara et al., 1974; Ohsaki & Iwasaki, 1973).

2.1 In situ tests and database

A larger number of SPT and seismic tests (crosshole, downhole, seismic cone, seismic SPT and seismic dilatometer) performed in Bauru, São Carlos, and Campinas is now available (Table 2). There are 132 data points (G_0 versus SPT N values) for the lateritic soil and 82 for the saprolitic soil from Bauru. In São Carlos, there are 64 data points for the lateritic soil and 86 for the saprolitic soil. There are 38 data points for the lateritic soil and 62 data points for the saprolitic soil from Campinas. The thickness of the lateritic soil horizon for Bauru, São Carlos and Campinas is respectively 13, 6 and 7 m and it was defined based on the MCT Classification System (Nogami & Villibor, 1981). The average values of G_0 and SPT N along depth were calculated to assess the correlations

Table 2. Main soil characteristics and the references for all data.

Site	Reference	Geological information	Tropical soil classification	Soil type	*USCS*
Bauru	Giacheti & Mio (2008)[ℵ] Rocha (2018)[ℵ] Vitali et al. (2012)[ℵ]	Colluvium and Residual (Sandstone)	Lateritic and Saprolitic	Clayey sand	SM-SC
São Carlos	Giacheti & Mio (2008)[ℵ] Rocha (2013)[ℵ] Vitali et al. (2012)[ℵ]	Cenozoic Sediment and Residual (Sandstone)	Lateritic and Saprolitic	Clayey sand	SC
Campinas	Giacheti & Mio (2008)[ℵ] Rocha (2013)[ℵ] Vitali et al. (2012)[ℵ]	Colluvium and Residual (Sandstone)	Lateritic and Saprolitic	Silty clay	CL-ML
Moema	Barros & Pinto (1997)	Red clays São Paulo Sedimentary Basin	Lateritic	Sandy clay	CL
Bela Vista	Barros & Pinto (1997)	Red clays São Paulo Sedimentary Basin	Lateritic	Sandy clay	CL
Vila Madalena	Barros & Pinto (1997)	Red clays São Paulo Sedimentary Basin	Lateritic	Sandy clay	CL
Paraíso	Barros & Pinto (1997)	Red clays São Paulo Sedimentary Basin	Lateritic	Sandy clay	CL
Caxangui	Barros & Pinto (1997)	Residual (Gneiss)	Saprolitic	Sandy silt	SM
Cidade Universitária	Barros & Pinto (1997)	Residual (Migmatite)	Saprolitic	Silty sand	N.A.*
Brooklin	Barros & Pinto (1997)	Residual (Migmatite)	Saprolitic	N.A.*	N.A.*

*Information not available. [ℵ]New data.

considering representative data for each site, without having a disproportional increase of data between soils of different sites. It is important to mention that saprolitic soils from Bauru and São Carlos (clayey sand) and from Campinas (silty clay) with different grain sizes were included in the correlations: clayey sand from Bauru e São Carlos and silty clay from Campinas were not used in the correlations proposed by Barros & Pinto (1997).

2.2 Estimating G_0 from SPT N values

The data points (G_0 versus SPT N value) for the lateritic and the saprolitic soils for all sites as well as the regression lines are respectively shown in Figure 2 and Figure 3. The SPT N values were not corrected for energy efficiency. So, correlations were stablished assuming SPT N values for a 72% efficiency according to Brazilian SPT practice (Décourt, 2018; Décourt et al., 1989).

It is important to mention that correlations were also tested between SPT N and measured G_0 as well as for the values corrected for estimated energy and overburden stress. However, it was found that an uncorrected value of SPT N and G_0 gives the best fit with a higher regression coefficient when compared to corrected SPT N and G_0 values, as discussed by Anbazhagan & Sitharam (2010).

In addition, SPT N values higher than 60 were not considered for the correlations because they have no physical meaning, since they represent a condition beyond rupture (Aoki & Cintra, 2000). The potential and linear regression equations for the lateritic (Equations 2 and 3 – Figure 2) soils are given as follow:

$$G_0 = 57.3\,N^{0.66} \quad (R^2 = 0.801) \tag{2}$$

$$G_0 = 64.4 + 19.7N \quad (R^2 = 0.884) \tag{3}$$

The fitting equations obtained with a larger number of data are in accordance with the findings from Barros & Pinto (1997) for the lateritic soils (Figure 2). It is noteworthy that the well-behaved soils correlations (Table 1) significantly underestimated G_0 for the lateritic soils, as already presented and discussed by Barros & Pinto (1997). On the other hand, it was not possible to define the fitting equations for saprolitic soils since the values for the sandy soils are very different from those found for the clayey soils (Figure 3).

In order to verify the distinct behavior of sandy and clayey saprolitic soils (Figure 3), all lateritic and saprolitic data (previous and the new ones) are plotted in Figure 4, similarly to what was presented in Figure 1c. It can be seen in Figure 4 that lateritic and saprolitic soils present different behavior. It can also be observed in this figure that the data
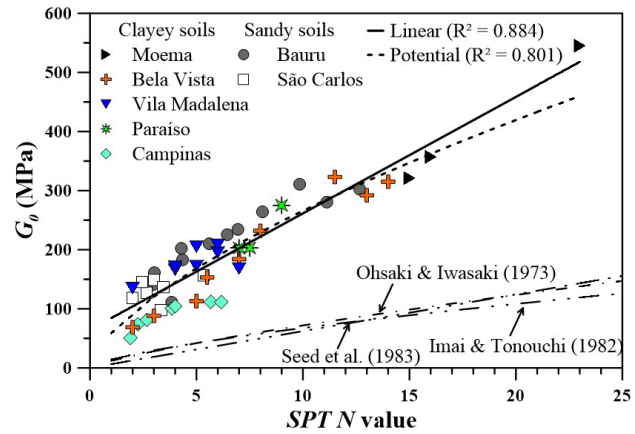
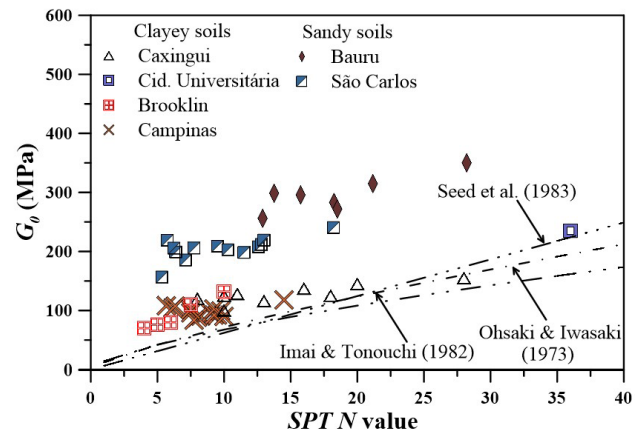**Figure 2.** G_0 versus SPT N value and updated correlations for the lateritic soils.

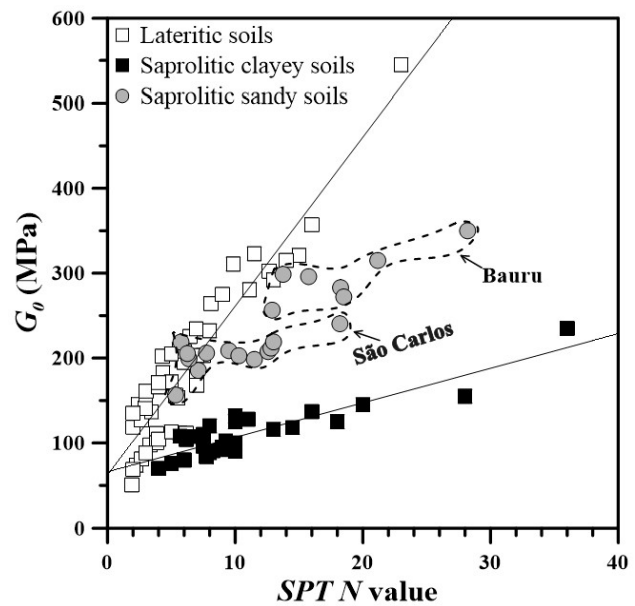**Figure 3.** G_0 versus SPT N value for the saprolitic soils.

Figure 4. Comparison between G_0 and SPT N values from lateritic and saprolitic soils.

4

Rocha et al., Soil. Rocks, São Paulo, 2023 46(1):e2023005222

for the saprolitic sandy soils from Bauru and São Carlos are closer to that of the lateritic soils. This behavior can be related to another soil characteristic, such as grain size distribution and unusual behavior associated to cementation and/or bonding structure (Robertson, 2016; Schnaid et al., 2004).

The unusual behavior was evaluated using the chart (Figure 5) proposed by Schnaid et al. (2004) for the lateritic and saprolitic soils presented in Table 2. It correlates the G_0/N_{60} ratio versus $(N_1)_{60}$, where $(N_1)_{60}$ is calculated by Equation 4. This chart allows to assess the presence of microstructure (cementation and/or bonding structure).

$$(N_1)_{60} = N_{60} \left(\frac{p_a}{\sigma'_{vo}} \right)^{0.5} \qquad (4)$$

where p_a is the atmospheric pressure, σ'_{vo} is the vertical effective stress and N_{60} is the SPT N value to a reference value of 60% of the potential energy of the SPT hammer calculated from Equation 5:

$$N_{60} = SPT\ N\ value\ \frac{72\%}{60\%} \qquad (5)$$
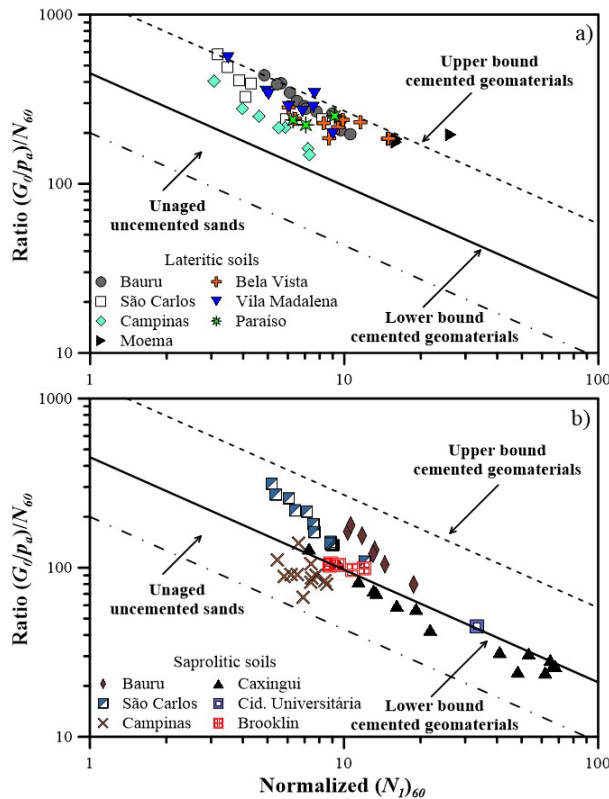
Figure 5. G_0/N_{60} versus $(N_1)_{60}$ chart and the boundaries for cemented and uncemented soils and the data for a) lateritic soils and b) saprolitic soils [adapted from Schnaid et al. (2004)].

It can be seen in Figure 5a that all lateritic soils data points are above the lower limit for cemented sands, indicating the presence of typical cementation from lateritic soils. It is the reason for the limitations of classical sedimentary soils correlations for estimating G_0 in soils with microstructure, such as the lateritic ones (Figure 2). For the saprolitic soils (Figure 5b), all clayey soils are below the lower limit for cemented soils while the sandy saprolitic soils (São Carlos and Bauru sites) are above the lower limit for cemented sands indicating they also have microstructure. This can be the reason for distinct behavior between sandy and clayey saprolitic soils, so it is not possible to define just one correlation for the saprolitic soils.

The correlations for G_0 estimation via SPT N value proposed by Barros & Pinto (1997) agree with the equations presented in this paper after expanding the database of lateritic soils from São Paulo state. It is important to emphasize that these correlations should be used with caution in a preliminary phase of the project and verified before their use. On the other hand, the equations proposed for saprolitic soils presented by Barros & Pinto (1997) did not adequately represent the behavior of the sandy saprolitic soils from Bauru and São Carlos and should not be applied. At the moment it is not possible to suggest correlations to estimate G_0 from SPT N values for saprolitic sandy soils due to the limited number of data and sites.

It is highly recommended to check whether the soil has microstructure before selecting a correlation, i.e., whether the soil has microstructure (cementation and aging), by using charts equivalent to that one proposed by Schnaid et al. (2004) with seismic CPT data and that one proposed by Cruz et al. (2012) with the seismic DMT data. The correlations developed for temperate and glacial zones cannot be used after the unusual soil behavior has been identified. In such cases correlations must be site specific.

3. Conclusion

The applicability of classical correlations for G_0 estimative from SPT data in lateritic and saprolitic soils was assessed. It was observed that lateritic soils behave differently from saprolitic soils and G_0 cannot be predicted by classical temperate and glacial zones soils correlations.

The equations proposed by Barros & Pinto (1997) for lateritic soils are consistent with those presented in this paper from a larger database. The equations for saprolitic soils proposed by these authors, however, should not be used for estimate G_0 for investigated saprolitic sandy soils. It can be related to the presence of microstructure (cementation and aging) in the saprolitic sandy soils. It is not possible to propose a correlation for estimating G_0 for saprolitic sandy soils due to the limited amount of data for this soil type. Furthermore, just identifying the soil as saprolitic does not guarantee an adequate estimate of G_0, since the soil type (sandy or clayey) and the presence of microstructure

(cementing and aging) must be considered. A laboratory or in situ test is recommended to identify possible unusual soil behavior before using correlations.

Acknowledgements

Declaration of interest

The authors declare that they have no conflict of interest.

Authors' contributions

Breno Padovezi Rocha: conceptualization, data curation, methodology, validation, writing – original draft, writing – review & editing. Bruno Canoza da Silva: conceptualization, methodology, validation. Heraldo Luiz Giacheti: formal analysis, supervision, writing – review, funding acquisition, project administration, resources.

Data availability

The datasets generated analyzed in the course of the current study are available from the corresponding author upon request.

List of symbols

p_a	atmospheric pressure (equal to 100 kPa)
q_c	cone tip resistance
A	constant determined by statistical regression
B	constant determined by statistical regression
CL	clays of low plasticity
CPT	cone penetration tests
DH	downhole
G	shear modulus
G_0	maximum shear modulus
I_c	normalized SBTn index
I_{SBT}	non-normalized SBT index
MCT	mini, compacted, tropical classification system
M_{DMT}	constrained modulus obtained by Flat Dilatometer
ML	silts of low plasticity
N_{60}	corrected N value for 60% energy delivery
$(N_1)_{60}$	normalized N_{60}
SC	clayey sands
$SCPT$	seismic cone penetration tests
$SDMT$	seismic dilatometer tests
SM	silty sands
SPT	standard penetration tests
$USCS$	unified soils classification system

V_s	shear wave velocity
γ	shear strain
ρ	total mass densities
σ'_{v0}	effective vertical stress

References

Akca, N. (2003). Correlation of SPT-CPT data from the United Arab Emirates. *Engineering Geology*, *67*(3-4), 219-231. http://dx.doi.org/10.1016/S0013-7952(02)00181-3.

Amoroso, S., Monaco, P., Lehane, B.M., & Marchetti, D. (2014). Examination of the potential of the seismic dilatometer (SDMT) to estimate in situ stiffness decay curves in various soil types. *Soils and Rocks*, *37*(3), 177-194.

Anbazhagan, P., & Sitharam, T. (2010). Relationship between low strain shear modulus and standard penetration test N values. *Geotechnical Testing Journal*, *33*(2), 150-164. http://dx.doi.org/10.1520/GTJ102278.

Anbazhagan, P., Parihar, A., & Rashmi, H.N. (2012). Review of correlations between SPT N and shear modulus: a new correlation applicable to any region. *Soil Dynamics and Earthquake Engineering*, *36*, 52-69. http://dx.doi.org/10.1016/j.soildyn.2012.01.005.

Anderson, J.B., Townsend, F.C., & Rahelison, L. (2007). Load testing and settlement prediction of shallow foundation. *Journal of Geotechnical and Geoenvironmental Engineering*, *133*(12), 1494-1502. http://dx.doi.org/10.1061/(asce)1090-0241(2007)133:12(1494).

Andrus, R.D., Stokoe, K.H., & Juang, C.H. (2004). Guide for shear-wave-based liquefaction potential evaluation. *Earthquake Spectra*, *20*(2), 285-308. http://dx.doi.org/10.1193/1.1715106.

Aoki, N., & Cintra, J.C.A. (September 11-13, 2000). The application of energy conservation Hamilton's principle to the determination of energy efficiency in SPT tests. In S. Niyama & J. Beim (Eds.), *6th International Conference on the Application of Stress-Wave Theory to Piles* (pp. 457-460). Rotterdam, Netherlands: Balkema.

ASTM D4015. (1995). *Standard test methods for modulus and damping of soils by the resonant-column – 92 (reapproved)*. ASTM International, West Conshohocken, PA. https://doi.org/10.1520/D4015-15E01.

ASTM D4428. (2007). *Standard test methods for crosshole seismic testing (ASTM 4488)*. ASTM International, West Conshohocken, PA.

ASTM D7400. (2008). *Standard test methods for downhole seismic testing*. ASTM International, West Conshohocken, PA. https://doi.org/10.1520/D4015-15E01.

Bang, E.-S., & Kim, D.-S. (2007). Evaluation of shear wave velocity profile using SPT based uphole method. *Soil Dynamics and Earthquake Engineering*, *27*(8), 741-758. http://dx.doi.org/10.1016/j.soildyn.2006.12.004.

Barros, J.M.C., & Pinto, C.S. (September 6-12, 1997). Estimation of maximum shear modulus of Brazilian tropical soils

from standard penetration test. In International Society for Soil Mechanics and Geotechnical Engineering (Org.), *Proceedings of the XIV International Conference on Soil Mechanics and Foundation Engineering* (pp. 29-30). London: United Kingdom: International Society for Soil Mechanics and Geotechnical Engineering.

Berisavljević, D., & Berisavljević, Z. (2019). Determination of the presence of microstructure in a soil using a seismic dilatometer. *Bulletin of Engineering Geology and the Environment*, *78*(3), 1709-1725. http://dx.doi.org/10.1007/s10064-018-1234-5.

Brand, E.W. (February 11-14, 1985). Geotechnical engineering in tropical residual soils. In Brazilian Society for Soil Mechanics (Org.), *Proceedings of the First International Conference Geomechanics in Tropical Lateritic and Saprolitic Soils* (pp. 23-91). São Paulo: Brazil: Brazilian Society for Soil Mechanics.

Brandenberg, S.J., Bellana, N., & Shantz, T. (2010). Shear wave velocity as function of standard penetration test resistance and vertical effective stress at California bridge sites. *Soil Dynamics and Earthquake Engineering*, *30*(10), 1026-1035. http://dx.doi.org/10.1016/j.soildyn.2010.04.014.

Cetin, K.O., Seed, R.B., Kiureghian, A., Tokimatsu, K., Harder, L.F., Kayen, R.E., & Moss, R.E.S. (2004). Standard penetration test-based probabilistic and deterministic assessment of seismic soil liquefaction potential. *Journal of Geotechnical and Geoenvironmental Engineering*, *130*(12), 1314-1340. http://dx.doi.org/10.1061/(ASCE)1090-0241(2004)130:12(1314).

Cruz, N., Rodrigues, C., & Fonseca, A.V. (September 18-21, 2012). Detecting the presence of cementation structures in soils, based in DMT interpreted charts. In R.Q. Coutinho & P.W. Mayne (Eds.), *Proceedings of the 4th International Conference on Site Characterization* (Vol. 2, pp. 1723-1728). London: United Kingdom: Taylor & Francis Group.

Décourt, L. (2018). Design of shallow foundations on soils and rocks on basis of settlement considerations. *Innovations in geotechnical engineering* (pp. 342-357). American Society of Civil Engineers, https://doi.org/10.1061/9780784481639.023.

Décourt, L., Belicanta, A., & Quaresma Filho, A.R. (August 13-18, 1989). Brazilian experience on SPT. In Publication Committee of XII ICSMFE (Ed.), *Proceedings of the XII International Conference on Soil Mechanics and Foundation Engineering* (pp. 49-54). London, United Kingdom: Taylor & Francis.

Giacheti, H.L. (1991). *Experimental study about dynamic soil parameters of some tropical soils of São Paulo State* [Doctoral thesis]. Universidade de São Paulo (in Portuguese).

Giacheti, H.L., & Mio, G. (April 1-4, 2008). Seismic cone tests in tropical soils and the Go / q c ratio. In A.-B. Huang & P.W. Mayne (Eds.), *Proceedings of the 3rd International Conference on Site Characterization* (pp. 1289-1296). London, United Kingdom: CRC Press.

Gidigasu, M.D. (1976). Pedogenic processes of tropical weathering and laterization. In M.D. Gidigasu (Ed.), *Developments in geotechnical engineering* (Vol. 9, pp. 35-70). Amsterdam: Elsevier. https://doi.org/10.1016/B978-0-444-41283-6.50010-1.

Hara, A., Ohta, T., Niwa, M., Tanaka, S., & Banno, T. (1974). Shear modulus and shear strength of cohesive soils. *Soil and Foundation*, *14*(3), 1-12. http://dx.doi.org/10.3208/sandf1972.14.3_1.

Hasancebi, N., & Ulusay, R. (2007). Empirical correlations between shear wave velocity and penetration resistance for ground shaking assessments. *Bulletin of Engineering Geology and the Environment*, *66*(2), 203-213. http://dx.doi.org/10.1007/s10064-006-0063-0.

Hoyos, L.R., Suescún-Florez, E.A., & Puppala, A.J. (2015). Stiffness of intermediate unsaturated soil from simultaneous suction-controlled resonant column and bender element testing. *Engineering Geology*, *188*, 10-28. http://dx.doi.org/10.1016/j.enggeo.2015.01.014.

Imai, T., & Tonouchi, K. (May 24-27, 1982). Correlation of N-value with S-wave velocity and shear modulus. In A. Verruijt, F.L. Beringen & E.H. Leeuw (Eds.), *Proceedings of the Second European Symposium on Penetration Testing* (pp. 67-72). London, United Kingdom: Taylor & Francis.

Jefferies, M., & Davies, M. (1993). Use of CPTu to estimate equivalent SPT N60. *Geotechnical Testing Journal*, *16*(4), 458-468. http://dx.doi.org/10.1520/GTJ10286J.

Jefferies, M.G., & Been, K. (2006). *Soil liquefaction – a critical state approach*. Taylor & Francis.

Lehane, B., & Fahey, M. (September 19-22, 2004). Using SCPT and DMT data for settlement prediction in sand. In A.V. Fonseca & P.W. Mayne (Eds.), *Proceedings of the Second International Conference on Site Characterization* (pp. 1673-1679). Rotterdam, Netherlands: Millpress.

Leong, E., Yeo, S., & Rahardjo, H. (2005). Measuring shear wave velocity using bender elements. *Geotechnical Testing Journal*, *28*(5), 12196. http://dx.doi.org/10.1520/GTJ12196.

Leroueil, S., & Hight, D.W. (December 2-4, 2002). Behaviour and properties of natural soils and soft rocks. In D.W. Hight, S. Leroueil, K.K. Phoon & T.S. Tan (Eds.), *Characterisation and Engineering Properties of Natural Soils* (pp. 29-253). Lisse, Netherlands: Swets and Zeitlinger.

Lumb, P. (1965). The residual soils of Hong Kong. *Geotechnique*, *15*(2), 180-194. http://dx.doi.org/10.1680/geot.1965.15.2.180.

Marchetti, S., Monaco, P., Totani, G., & Marchetti, D. (March 9-12, 2008). In situ tests by seismic dilatometer (SDMT). In J.H. Schmertmann, J.E. Laier, D.K. Crapps & M.H. Hussein (Eds.), *Symposium Honoring Dr. John H. Schmertmann for His Contributions to Civil Engineering at Research to Practice in Geotechnical Engineering Congress 2008* (pp. 292-311). Reston, United States of

America: American Society of Civil Engineers. https://doi.org/10.1061/40962(325)7.

Mio, G. (2005). *Geological conditioning aspects for piezocone test interpretation for stratigraphical identification in geotechnical and geo-environmental site investigation* [Doctoral thesis]. Universidade de São Paulo. https://doi.org/10.11606/T.18.2005.tde-27042006-170324.

Mio, G., & Giacheti, H.L. (2007). The use of piezocone tests for high-resolution stratigraphy of quaternary sediment sequences in the Brazilian coast. *Anais da Academia Brasileira de Ciências*, *79*(1), 153-170. http://dx.doi.org/10.1590/S0001-37652007000100017.

Nogami, J.S., & Villibor, D.F. (September 21-23, 1981). Uma nova classificação de solos para finalidades rodoviárias. In Associação Brasileira de Mecânica dos Solos (Org.), *Simpósio Brasileiro de Solos Tropicais em Engenharia* (pp. 30-41). Rio de Janeiro, Brazil: COPPE/UFRJ (in Portuguese).

Ohsaki, Y., & Iwasaki, R. (1973). On dynamic shear moduli and Poisson's ratios of soil deposits. *Soil and Foundation*, *13*(4), 61-73. http://dx.doi.org/10.3208/sandf1972.13.4_61.

Poulos, H.G. (2021). Use of shear wave velocity for foundation design. *Geotechnical and Geological Engineering*, *40*, 1921-1938. http://dx.doi.org/10.1007/s10706-021-02000-w.

Rahardjo, H., Toll, D.G., & Leong, E.C. (2020). *Unsaturated soils for Asia*. CRC Press. https://doi.org/10.1201/9781003078616.

Robertson, P.K. (1990). Soil classification using the cone penetration test. *Canadian Geotechnical Journal*, *27*(1), 151-158. http://dx.doi.org/10.1139/t90-014.

Robertson, P.K. (2009). Interpretation of cone penetration tests: a unified approach. *Canadian Geotechnical Journal*, *46*(11), 1337-1355. http://dx.doi.org/10.1139/T09-065.

Robertson, P.K. (2016). Cone penetration test (CPT)-based soil behaviour type (SBT) classification system: an update. *Canadian Geotechnical Journal*, *53*(12), 1910-1927. http://dx.doi.org/10.1139/cgj-2016-0044.

Robertson, P.K., Campanella, R.G., Gillespie, D., & Rice, A. (1986). Seismic CPT to measure in situ shear wave velocity. *Journal of Geotechnical Engineering*, *112*(8), 791-803. http://dx.doi.org/10.1061/(ASCE)0733-9410(1986)112:8(791).

Rocha, B.P. (2013). *Emprego do ensaio SPT sísmico na investigação de solos tropicais* [Master's dissertation]. Universidade de São Paulo (in Portuguese). https://doi.org/10.11606/D.18.2013.tde-28112013-100232.

Rocha, B.P. (2018). *Geotechnical characterization of unsaturated tropical soils by in situ tests* [Doctoral thesis]. Universidade de São Paulo. https://doi.org/10.11606/T.18.2018.tde-03122018-103909.

Rocha, B.P., Rodrigues, A.L.C., Rodrigues, R.A., & Giacheti, H.L. (2022). Using a seismic dilatometer to identify collapsible soils. *International Journal of Civil Engineering*, *20*(7), 857-867. http://dx.doi.org/10.1007/s40999-021-00687-9.

Schnaid, F. (2008). *In situ testing in geomechanics: the main tests*. CRC Press. https://doi.org/10.1201/9781482266054.

Schnaid, F., Lehane, B.M., & Fahey, M. (September 19-22, 2004). In situ test characterisation of unusual soils. In A.V. Fonseca & P.W. Mayne (Eds.), *Proceedings of the Second International Conference on Site Characterization* (Vol. 1, pp. 49-74). Rotterdam, Netherlands: Millpress.

Schnaid, F., Nierwinski, H.P., & Odebrecht, E. (2020). Classification and state-parameter assessment of granular soils using the seismic cone. *Journal of Geotechnical and Geoenvironmental Engineering*, *146*(8), 06020009. http://dx.doi.org/10.1061/(asce)gt.1943-5606.0002306.

Seed, H.B., Idriss, I.M., & Arango, I. (1983). Evaluation of liquefaction potential using field performance data. *Journal of Geotechnical Engineering*, *109*(3), 458-482. http://dx.doi.org/10.1061/(ASCE)0733-9410(1983)109:3(458).

Vargas, M. (February 11-14, 1985). The concept of tropical soils. In Associação Brasileira de Mecânica dos Solos & International Society of Soil Mechanics and Foundation Engineering (Orgs.), *First International Conference on Geomechanics in Tropical Lateritic and Saprolitic Soils* (pp. 101-134). São Paulo, Brazil: Associação Brasileira de Mecânica dos Solos.

Vitali, O.P.M., Pedrini, R.A.A., Oliveira, L.P.R., & Giacheti, H.L. (2012). Developing a system for down-hole seismic testing together with the CPTU. *Soils and Rocks*, *35*(1), 75-87.

Werden, S.K., Drnevich, V.P., Hall, J.R., Hankour, C., Conlee, C.T., & Marr, W.A. (2013). New approach to resonant column testing. *Geotechnical Testing Journal*, *36*(2), 20120122. http://dx.doi.org/10.1520/GTJ20120122.

Closed-form consolidation solutions for known loading functions

Raphael Felipe Carneiro[1#] iD, Karl Igor Martins Guerra[1] iD, Celso Romanel[1] iD,

Denise Maria Soares Gerscovich[2] iD, Bernadete Ragoni Danziger[2] iD

Technical Note

Abstract

In engineering practice, loading varies with time. However, the classical one-dimensional theory of consolidation assumes the stress increase is instantaneously applied. Many approaches to the problem of time-dependent loading have been proposed over the years, from approximate methods to full developments of differential equations. The paper presents a simple method for finding a closed-form consolidation solution for time-dependent loading without the need for differential equations. Two sets of general equations were derived for both excess pore pressure and average degree of consolidation. Equations were solved for linear, parabolic, sinusoidal, and exponential load functions. Stepped and cyclic loads were also addressed and a numerical solution was developed to verify the obtained result. The method proved to be easy to apply and provides solutions with great simplicity. A case study of non-instantaneous loading on soft clay was also analyzed, and settlement prediction showed good results when compared to readings of the settlement plates.

1. Introduction

Terzaghi & Fröhlich (1936) consolidation theory provides an equation for the excess pore pressure u_z at any depth z and time t, generated by a uniform load q_c. The solution follows:

$$u_z(z,T) = q_c \sum_{m=0}^{\infty} \frac{2}{M} \sin \frac{Mz}{H_d} e^{-M^2 T} \qquad (1)$$

Where

$$M = (2m+1)\frac{\pi}{2} \qquad (2)$$

For $m = 1, 2, 3\ldots$
And the Time Factor T is defined as:

$$T = \frac{c_v t}{H_d^2} \qquad (3)$$

The depth-dependent degree of consolidation U_z is given by:

$$U_z(z,T) = 1 - \sum_{m=0}^{\infty} \frac{2}{M} \sin \frac{Mz}{H_d} e^{-M^2 T} \qquad (4)$$

For practical problems, the particular interest is the average degree of consolidation U, given by:

$$U(T) = 1 - \sum_{m=0}^{\infty} \frac{2}{M^2} e^{-M^2 T} \qquad (5)$$

The classical theory uses several simplifying assumptions; among them, the load is instantaneously applied. In practice, however, the increment of total vertical stress often varies with time.

Several empirical and theoretical methods have been proposed to address non-instantaneous load conditions for 1D analyses (Terzaghi & Fröhlich, 1939; Terzaghi, 1943; Schiffman, 1958; Schiffman & Stein, 1970; Zhu & Yin, 1998; Jimenez et al., 2009; Liu & Ma, 2011; Qin et al., 2010; Razouki et al., 2013; Verruijt, 2014; Liu & Griffiths, 2015; Gerscovich et al., 2018).

The ramp loading (Olson, 1977) is the simplest way to address non-instantaneous loading. But some projects impose complex loading sequences. Soil foundations of silos, tanks, highway embankments, etc. undergo cyclic loading. Construction sequences with variable speeds can be represented by non-linear loads.

Hanna et al. (2013) used the concept of discretization of the applied load into infinitesimal increments to easily achieve Olson (1977) solution during construction. Carneiro et al. (2021) demonstrated that Hanna et al. (2013) method is

Carneiro et al., Soil. Rocks, São Paulo, 2023 46(1):e2023077721

1

capable to provide Olson (1977) solution for periods after construction as well. Conte & Troncone (2006) proposed a calculation procedure for a general time-dependent loading, making use of the Fourier series.

This paper presents an extension of and an alternative to the methodologies developed by Conte & Troncone (2006), Hanna et al. (2013), and Carneiro et al. (2021). The solution is a closed-form consolidation equation for different loading functions.

2. Proposed method

In this study, all the simplifying assumptions of the classical theory (Terzaghi & Fröhlich, 1936) are valid. The only exception is the applied vertical load, which is no longer constant but varies up to a Time Factor T_c. All equations for excess pore pressure and degrees of consolidation that refer to non-instantaneous loading are represented below with an apostrophe.

Let the total vertical stress increase $\Delta\sigma(T)$ be a function of T:

$$\Delta\sigma(T) = q(T) \text{ if } T \leq T_c$$
$$\Delta\sigma(T) = q(T_c) = q_c \text{ if } T > T_c \tag{6}$$

For the purpose of this development, it is assumed that $\Delta\sigma(0) = q(0) = 0$.
Now let $f(T)$ be the derivative of $q(T)$, that is:

$$dq = f(T)dT \tag{7}$$

During an infinitesimal dimensionless period dT, the total stress increase $dq = f(T)dT$ is instantaneously applied. Therefore, the initial increase of pore water pressure du_z is also $f(T)dT$. For ramp loads, for example, the load increment $(f(T) = q_c/T_c)$ is constant.

As shown in Figure 1, for a Time Factor $T_a \leq T_c$ before the end of construction, the infinitesimal loads were applied at an infinite number of times, from $T = 0$ to $T = T_a$. The infinitesimal excess pore pressures dissipate and contribute with dU'_z to compute the degree of consolidation U'_z at the given Time Factor T_a. This infinitesimal increasing of the degree of consolidation dU'_z at T_a is given by the ratio of the dissipated amount of excess pore pressure within the Time Factor interval up to T_a, and the total load.

$$dU'_z(z, T_a) = \frac{dq - du_z(z, T_a - T)}{q_c} = \frac{U_z(z, T_a - T)f(T)dT}{q_c} \tag{8}$$

Where U_z is given by classical theory (Equation 4).
Considering all time intervals up to T_a, the degree of consolidation U'_z takes into account all infinitesimal loads applied, that is:
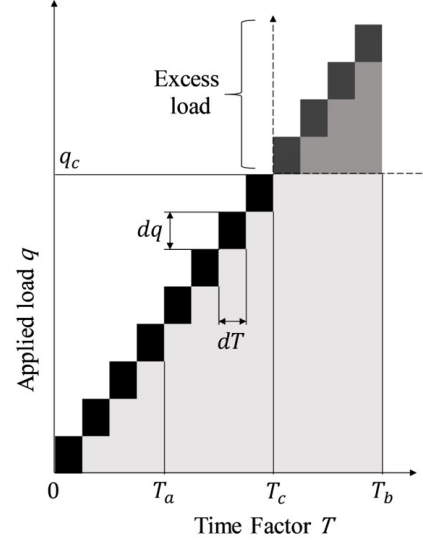
Figure 1. Total stress increase applied into infinitesimal increments [adapted from Hanna et al. (2013), and Carneiro et al. (2021)].

$$U'_z(z, T_a) = \frac{\int_0^{T_a} U_z(z, T_a - T)f(T)dT}{q_c} \tag{9}$$

Equation 9 holds for any $T_a \leq T_c$. This equation is characterized as a convolution of the functions of U_z and f. Solution can be obtained via Laplace transform $\mathcal{L}$:

$$\mathcal{L}\{U'_z\} = \frac{1}{q_c}\mathcal{L}\{U_z\}\mathcal{L}\{f\} \tag{10}$$

Laplace transform of U_z is given by:

$$\mathcal{L}\{U_z\} = \frac{1}{s} - \sum_{m=0}^{\infty}\left(\frac{2}{M}\right)\left(\sin\frac{Mz}{H_d}\right)\frac{1}{s+M^2} \tag{11}$$

Where s is the Laplace parameter.
Denoting $\mathcal{L}\{f\} = F(s)$, Equation 10 can now be rewritten as:

$$\mathcal{L}\{U'_z\} = \frac{1}{q_c}\left[\frac{F(s)}{s} - \sum_{m=0}^{\infty}\left(\frac{2}{M}\right)\left(\sin\frac{Mz}{H_d}\right)\frac{F(s)}{s+M^2}\right] \tag{12}$$

Applying the inverse Laplace transform, one has:

$$U'_z(T) = \frac{q(T)}{q_c} - \frac{1}{q_c}\sum_{m=0}^{\infty}\left(\frac{2}{M}\right)\left(\sin\frac{Mz}{H_d}\right)\mathcal{L}^{-1}\left\{\frac{F(s)}{s+M^2}\right\}\bigg|_0^T \tag{13}$$

After the end of construction, for a Time Factor $T_b \geq T_c$ shown in Figure 1, solution uses the principle of superposition. The degree of consolidation at a Time Factor T_b is calculated by subtracting the exceeding loading, calculated as if the

time-dependent loading has not finished, from the actual final value q_c.

Thus, the degree of consolidation is calculated by:

$$U'_z\left(T_b\right) = U'_{z1}\left(T_b\right) - U'_{z2}\left(T_b\right) \tag{14}$$

The expression of U'_{z1} is given by Equation 13 for $T = T_b$. For U'_{z2}, the origin is now at T_c, thus $T = T_b - T_c$. So, Equation 9 must be rewritten as follows:

$$U'_{z2}\left(T_b\right) = \frac{\int_0^{T_b-T_c} U_z\left(T_b - T_c - T\right) f\left(T + T_c\right) dT}{q_c} \tag{15}$$

Denoting the shifted function $f(T + T_c) = g(T)$, Equation 15 is the convolution of U_z and g. Applying the Laplace transform:

$$\mathcal{L}\{U'_{z2}\} = \frac{1}{q_c}\left[\frac{G(s)}{s} - \sum_{m=0}^{\infty}\left(\frac{2}{M}\right)\left(\sin\frac{Mz}{H_d}\right)\frac{G(s)}{s+M^2}\right] \tag{16}$$

Where $G(s) = \mathcal{L}\{g\}$. Applying the inverse Laplace transform, the solution is:

$$U'_{z2}\left(T_b\right) = \frac{q(T_b)}{q_c} - 1 - \frac{1}{q_c}\sum_{m=0}^{\infty}\left(\frac{2}{M}\right)\left(\sin\frac{Mz}{H_d}\right)\mathcal{L}^{-1}\left\{\frac{G(s)}{s+M^2}\right\}\Big|_0^{T_b-T_c} \tag{17}$$

Finally, Equation 14 can be expressed as:

$$U'_z(T) = 1 - \frac{1}{q_c}\sum_{m=0}^{\infty}\left(\frac{2}{M}\right)\left(\sin\frac{Mz}{H_d}\right)\left[\mathcal{L}^{-1}\left\{\frac{F(s)}{s+M^2}\right\}\Big|_0^T - \mathcal{L}^{-1}\left\{\frac{G(s)}{s+M^2}\right\}\Big|_0^{T-T_c}\right] \tag{18}$$

Equations 13 and 18 provide the degree of consolidation for periods before and after the end of construction, respectively. For any loading function $q(T)$, its derivative $f(T)$ and the function $g(T) = f(T + T_c)$ are known. Once $F(s)$ and $G(s)$ are determined, solution is obtained. Equations 13 and 18 are coincident for $T = T_c$.

From Equations 13 and 18, the excess pore pressure can be found:

$$u'_z(T) = \sum_{m=0}^{\infty}\left(\frac{2}{M}\right)\left(\sin\frac{Mz}{H_d}\right)\mathcal{L}^{-1}\left\{\frac{F(s)}{s+M^2}\right\}\Big|_0^T \quad \text{if } T \le T_c$$

$$u'_z(T) = \sum_{m=0}^{\infty}\left(\frac{2}{M}\right)\left(\sin\frac{Mz}{H_d}\right)\left[\mathcal{L}^{-1}\left\{\frac{F(s)}{s+M^2}\right\}\Big|_0^T - \mathcal{L}^{-1}\left\{\frac{G(s)}{s+M^2}\right\}\Big|_0^{T-T_c}\right] \quad \text{if } T > T_c \tag{19}$$

The average degree of consolidation U' provides the sum of the vertical compressions throughout the depth, and it is calculated by:

$$U'(T) = \frac{\int_0^{2H_d} U'_z\left(z,T\right)dz}{\int_0^{2H_d}dz} \tag{20}$$

Which gives:

$$U'(T) = \frac{q(T)}{q_c} - \frac{1}{q_c}\sum_{m=0}^{\infty}\left(\frac{2}{M^2}\right)\mathcal{L}^{-1}\left\{\frac{F(s)}{s+M^2}\right\}\Big|_0^T \quad \text{if } T \le T_c$$

$$U'(T) = 1 - \frac{1}{q_c}\sum_{m=0}^{\infty}\left(\frac{2}{M^2}\right)\left[\mathcal{L}^{-1}\left\{\frac{F(s)}{s+M^2}\right\}\Big|_0^T - \mathcal{L}^{-1}\left\{\frac{G(s)}{s+M^2}\right\}\Big|_0^{T-T_c}\right] \quad \text{if } T > T_c \tag{21}$$

While the loading in Figure 1 was represented as linear for simplification, the mathematical development allows to find general equations to compute the excess pore pressure (Equation 18) and the average degree of consolidation (Equation 21) for any loading function.

3. Applications

This section presents several applications of the equations. Calculations are detailed in Appendix 1.

Since the development was based on the simplifying assumptions of the classical theory, the solutions herein presented are limited to uniform initial excess pore pressure. The drainage conditions can be single or double.

3.1 Single ramp load

The consolidation theory for an increasing linear loading was primarily solved by Terzaghi & Fröhlich (1939), and later by Olson (1977). The function $q(T)$ is given by $q(T) = \frac{q_c}{T_c}T$, and, therefore, $f(T) = \frac{q_c}{T_c}$ is a constant. The solution of Equations 19 and 21 give the excess pore pressure and the average degree of consolidation before and after construction. It worth mentioning that the solutions coincide with Olson (1977).

$$u'_z\left(T \le T_c\right) = \frac{q_c}{T_c}\sum_{m=0}^{\infty}\left(\frac{2}{M^3}\right)\left(\sin\frac{Mz}{H_d}\right)\left[1 - e^{-M^2T}\right]$$

$$U'\left(T \le T_c\right) = \frac{T}{T_c} - \frac{1}{T_c}\sum_{m=0}^{\infty}\left(\frac{2}{M^4}\right)\left[1 - e^{-M^2T}\right]$$

$$u'_z\left(T > T_c\right) = \frac{q_c}{T_c}\sum_{m=0}^{\infty}\left(\frac{2}{M^3}\right)\left(\sin\frac{Mz}{H_d}\right)\left[e^{-M^2(T-T_c)} - e^{-M^2T}\right]$$

$$U'\left(T > T_c\right) = 1 - \frac{1}{T_c}\sum_{m=0}^{\infty}\left(\frac{2}{M^4}\right)\left[e^{-M^2(T-T_c)} - e^{-M^2T}\right] \tag{22}$$

3.2 Multiple ramp load

Embankments are typical examples of multiple ramp load constructions. The loading rate and the time interval between load sequences vary. The final load is achieved after n ramp loads intercalated with $n - 1$ pause periods. The end of construction corresponds to the n-th pause period. As illustrated in Figure 2, each ramp load may have a different inclination α_i, with i varing from 1 to n.

Assuming that the Time Factor at the beginning of a ramp load is defined as T_{2i-2}, and T_{2i-1} is the corresponding value at its end (or at the beginning of a pause period), the derivative $f(T)$ of the loading function $q(T)$ can be expressed as:

$$f(T) = \sum_{i=1}^{n} \alpha_i \mathcal{H}(T - T_{2i-2}) - \alpha_i \mathcal{H}(T - T_{2i-1}) \qquad (23)$$

Where the Heaviside function $\mathcal{H}(\ )$ yields zero or one, depending on the argument be negative or positive.

For simplification, it is beneficial to consider that the n-th pause period is still part of the construction, and the end of construction occurs at $T_c = T_{2n} \to \infty$. It is an equivalent configuration that allows using only one equation for the average degree of consolidation instead of two, since $g(T)$ is no longer needed.

Thus, the average degree of consolidation is:

$$U'(T) = \frac{q(T)}{q_c} - \frac{1}{q_c}\sum_{m=0}^{\infty}\left(\frac{2}{M^4}\right)\sum_{i=1}^{n}\alpha_i \left\{ \begin{array}{l} \left[1 - e^{-M^2(T-T_{2i-2})}\right]\mathcal{H}(T-T_{2i-2}) - \\ \left[1 - e^{-M^2(T-T_{2i-1})}\right]\mathcal{H}(T-T_{2i-1}) \end{array} \right\} \quad (24)$$

For $n = 1$, Equation 24 coincides with Olson (1977) solution during and after construction. In this scenario, $T_1 = T_c$ and $\alpha_i = \frac{q_c}{T_c}$. For $n > 1$, it coincides with Olson (1977) proposition of adding the solutions for each ramp load.
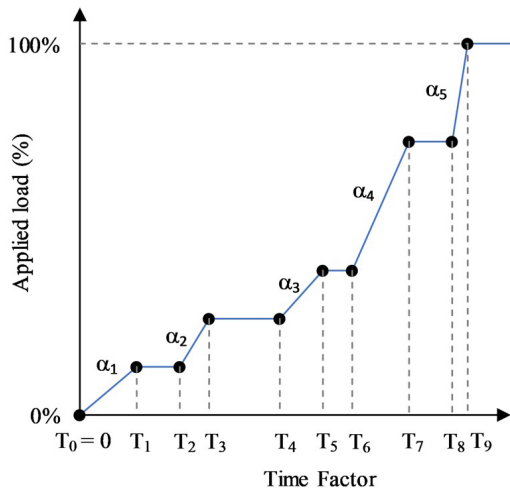
Figure 2. Construction sequence with $n = 5$ ramp loads.

3.3 Other single load functions

In some geotechnical problems, like embankments built at a given rate, loading sequences can be better reproduced by non-linear loads, depending on the speed of construction. Jimenez et al. (2009) studied parabolic loading for vertical and radial consolidation combined. Qin et al. (2010) studied exponential loading for unsaturated soil.

In the case of a quadratic function (parabola), the loading is given by

$$q(T) = \frac{q_c}{T_c^2}T^2 \qquad (25)$$

Now the rate of loading is no longer constant, since $f(T) = \frac{2q_c}{T_c^2}T$, and the shifted function is $f(T) = \frac{2q_c}{T_c^2}(T + T_c)$.

Combining Equation 21 to Equation 25, the average degree of consolidation is expressed by:

$$U'(T \le T_c) = \frac{T^2}{T_c^2} - \frac{1}{T_c^2}\sum_{m=0}^{\infty}\left(\frac{4}{M^6}\right)\left[M^2T - 1 + e^{-M^2T}\right]$$

$$U'(T > T_c) = 1 - \frac{1}{T_c^2}\sum_{m=0}^{\infty}\left(\frac{4}{M^6}\right)\left[\left(M^2T_c - 1\right)e^{-M^2(T-T_c)} + e^{-M^2T}\right] \qquad (26)$$

If the loading is better reproduced in the form of a sinusoidal function until the end of the construction, that load can be represented by:

$$q(T) = q_c \sin\left(\frac{\pi}{2T_c}T\right) \qquad (27)$$

The rate of loading is therefore $f(T) = \frac{\pi}{2T_c}q_c \cos\left(\frac{\pi}{2T_c}T\right)$ and the shifted function is $g(T) = -\frac{\pi}{2T_c}q_c \sin\left(\frac{\pi}{2T_c}T\right)$.

Substituting these equations into Equation 21, the solution for U' is given by:

$$U'(T \le T_c) = \sin\left(\frac{\pi}{2T_c}T\right) - \frac{\pi}{2T_c}\sum_{m=0}^{\infty}\frac{2}{M^4 + \left(\frac{\pi}{2T_c}\right)^2}$$

$$\left[\frac{1}{M^2}\frac{\pi}{2T_c}\sin\left(\frac{\pi}{2T_c}T\right) + \cos\left(\frac{\pi}{2T_c}T\right) - e^{-M^2T}\right] \qquad (28)$$

$$U'(T > T_c) = 1 - \frac{\pi}{2T_c}\sum_{m=0}^{\infty}\frac{2}{M^4 + \left(\frac{\pi}{2T_c}\right)^2}\left[\frac{1}{M^2}\frac{\pi}{2T_c}e^{-M^2(T-T_c)} - e^{-M^2T}\right]$$

In the case of exponential load function, the load expression is:

$$q(T) = \frac{q_c}{1-e^{-\beta T_c}}\left(1-e^{-\beta T}\right) \tag{29}$$

For this loading condition, the average degree of consolidation is expressed by:

$$U'(T \leq T_c) = \left(\frac{1-e^{-\beta T}}{1-e^{-\beta T_c}}\right) - \frac{\beta}{1-e^{-\beta T_c}}\sum_{m=0}^{\infty}\left(\frac{2}{M^2}\right)\left(\frac{1}{M^2-\beta}\right)\left[e^{-\beta T}-e^{-M^2 T}\right]$$

$$U'(T > T_c) = 1 - \frac{\beta}{1-e^{-\beta T_c}}\sum_{m=0}^{\infty}\left(\frac{2}{M^2}\right)\left(\frac{1}{M^2-\beta}\right)\left[e^{-M^2(T-T_c)-\beta T_c}-e^{-M^2 T}\right]$$

$$\tag{30}$$

Equation 29 is able to reproduce other loading conditions. At the upper limit ($\beta \to \infty$), the equation is equivalent to an instantaneous load applied at $T = 0$. On the other hand, if $\beta \to -\infty$ the equivalence occurs as if the instantaneous load was applied at $T = T_c$. If $\beta \to 0$., the equation reproduces a ramp load.

Figure 3 compares the average degree of consolidation versus Time Factor for different loading conditions. The end of construction was set at $T_c = 0.126$ for all non-instantaneous loads. The exponential function was analyzed for $\beta = 40$ and $\beta = -40$ (Equation 29).

In the upper part of Figure 3, the time-dependent loads are shown. Exponential ($\beta = 40$) and sinusoidal loading indicate higher speed at the beginning of construction. Exponential ($\beta = -40$) and parabolic loading indicate higher speed at
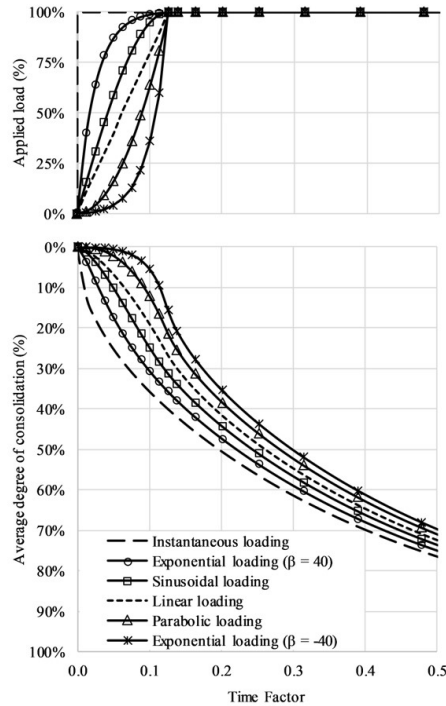
Figure 3. Consolidation curves for parabolic, sinusoidal, exponential, instantaneous and linear loading.

the end of construction. The results showed consistency: the greater the rate of loading the faster the consolidation.

The influence of the construction sequence on the degree of consolidation decreases with time. However, during the construction period, there is a significant difference among the curves. In the comparison shown in Figure 3, the absolute difference between the average degrees of consolidation of both exponential loadings at the end of construction is around 20%.

3.4 Haversine repeated load

Several geotechnical engineering phenomena can produce repeated or cyclic loading, such as vehicular traffic, wind waves, sea waves, etc. (Mitchell, 1993). Huang (1993) studied the influence of the wheel load on highways and airports and proposed the use of a haversine repeated loading given by:

$$q(T) = q_c \sin^2\left(\frac{\pi}{\tau}T\right) \tag{31}$$

Equation 31 assumes that the loading-unloading sequence does not reach an end; that is, the "end of construction" is at infinity. Thus, q_c should now be interpreted as the load amplitude, and the excess pore pressure can only be calculated for $T \leq T_c$. Since the derivative of $q(T)$ is $f(T) = q_c\frac{\pi}{\tau}\sin\left(\frac{2\pi}{\tau}T\right)$, the excess pore pressure (Equation 19) is solved and agrees with Razouki et al. (2013) solution:

$$u'_z(T) = q_c\sum_{m=0}^{\infty}\left[\frac{\left(\frac{2\pi}{\tau}\right)^2}{\left(\frac{2\pi}{\tau}\right)^2 M + M^5}\right]\left(\sin\frac{Mz}{H_d}\right)$$

$$\left[e^{-M^2 T}-\cos\left(\frac{2\pi}{\tau}T\right)+\frac{M^2}{\frac{2\pi}{\tau}}\sin\left(\frac{2\pi}{\tau}T\right)\right] \tag{32}$$

Results for $\tau = 0.15$ are presented in Figure 4. The upper part shows the time-dependent load. The lower part compares the analytical solution, obtained by the present method and by Razouki et al. (2013), with Razouki & Schanz (2011) numerical solution.

3.5 Damped cyclic load

The damped cyclic load may be generated by an instantaneous load that causes a damped oscillation of the applied stress. As shown in Figure 5, the waves have higher amplitude at the beginning, and converge to a residual load after some oscillations.

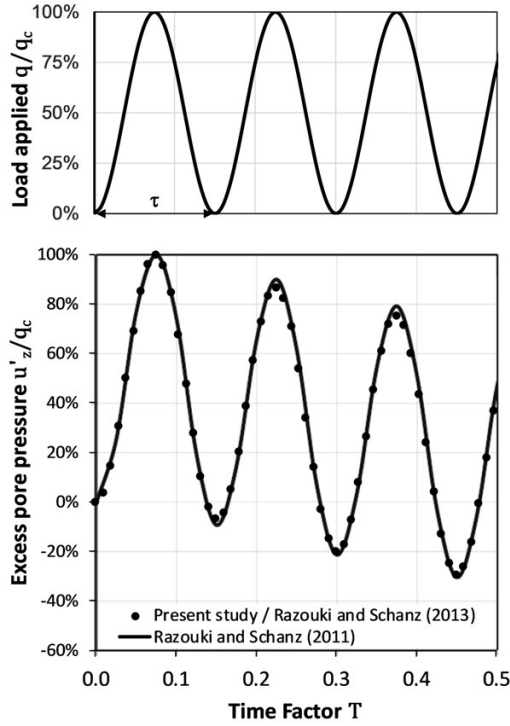This loading condition can be represented by a product of functions, such as:

Figure 4. Normalized excess pore pressure versus time factor for the Haversine repeated load [adapted from Razouki & Schanz (2011)].
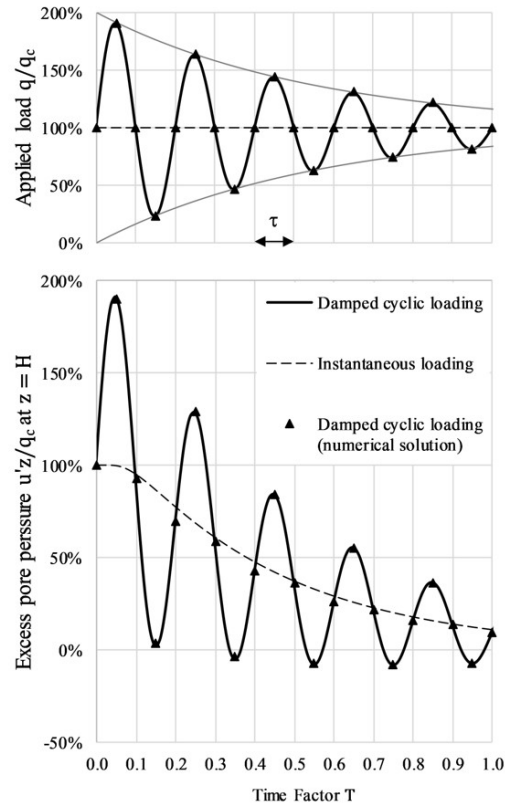

Figure 5. Variation of excess pore pressure due to a damped cyclic loading.

$$q(T) = q_c \left[1 + e^{-\beta T} \sin\left(\frac{\pi}{\tau} T \right) \right] \tag{33}$$

Since there is load being applied instantaneously, it is convenient to separate the function into two parts: i) instantaneous and ii) time-dependent. The instantaneous load is governed by classical theory, while the time-dependent load is obtained by the method herein proposed. In this case, the time-dependent function is given by:

$$q(T) = q_c \left[e^{-\beta T} \sin\left(\frac{\pi}{\tau} \cdot T \right) \right] \tag{34}$$

Similar to the previous example, the solution is only needed for $T \leq T_c$. Combining Equation 34 with Equation 19, the time dependent solution is given by:

$$\frac{u'_z(T)}{q_c} = \sum_{m=0}^{\infty} \frac{2}{M} \left(\sin \frac{Mz}{H_d} \right) \left[Xe^{-\beta T} \cos\left(\frac{\pi}{\tau} T \right) + Ye^{-\beta T} \sin\left(\frac{\pi}{\tau} T \right) - Xe^{-M^2 T} \right] \tag{35}$$

And the final solution, combined with the classical theory (Terzaghi & Fröhlich, 1936) to include the instantaneous load part, is expressed by:

$$\frac{u'_z(T)}{q_c} = \sum_{m=0}^{\infty} \frac{2}{M} \left(\sin \frac{Mz}{H_d} \right) \left[Xe^{-\beta T} \cos\left(\frac{\pi}{\tau} T \right) + Ye^{-\beta T} \sin\left(\frac{\pi}{\tau} T \right) + (1-X) e^{-M^2 T} \right] \tag{36}$$

Where:

$$X = \frac{\left(\frac{\pi}{\tau} \right) M^2}{\beta^2 + \left(\frac{\pi}{\tau} \right)^2 - 2\beta M^2 + M^4}$$

$$\tag{37}$$

$$Y = \frac{\beta^2 + \left(\frac{\pi}{\tau} \right)^2 - \beta M^2}{\beta^2 + \left(\frac{\pi}{\tau} \right)^2 - 2\beta M^2 + M^4}$$

The solution was applied to a hypothetical example, consisting of a damped cyclic load on a single drainage clay deposit. The parameters of this cyclic loading (Equation (34)) are $\beta = 1.8$ and $\tau = 0.1$. Figure 5 shows the normalized excess pore pressure (u'_z/q_c) at the bottom of the clay deposit ($z = H$). As expected, the excess pore pressure tends to hover around Terzaghi & Fröhlich (1936) solution over time (Equation 1).

A numerical finite difference solution was developed to solve the governing differential equation, in order to verify the behavior of the consolidation process. The thickness was divided so that each subdivision measured 0.005. A dimensionless time interval of 0.05 was adopted. It can be seen in Figure 5 that there is a great agreement between analytical (Equation 36) and numerical solution.

It can be noticed that the excess pore pressure eventually becomes negative due to the loading-unloading sequence. Negative excess pore pressure is a common issue in cyclic loading cases (Razouki & Schanz, 2011). That phenomenon is controlled by β, so the smaller the β value, the more negative the excess pore pressure during the unloading phases.

4. Case study

Nascimento (2016) describes a case of an instrumented experimental embankment built on soft soil in Macaé, Rio de Janeiro. The clay layer is 7.85 meters thick, double-drained, and laboratory tests provided a coefficient of consolidation of 10^{-7} m²/s.

The embankment reached a final height of 3.1 m in about 1 month. For the present study, the construction sequence was approximated to an exponential (Equation 29) with β = 80, as shown in the upper part of Figure 6. Nascimento (2016) estimated an immediate settlement of 0.15 m, and a primary settlement of 2.16 m.

The settlement estimate was compared with the readings of settlement plates, in the lower part of Figure 6. Immediate settlement was distributed over the construction period in proportion to the calculated embankment height. The results show a good approximation between settlement estimate and plate readings.
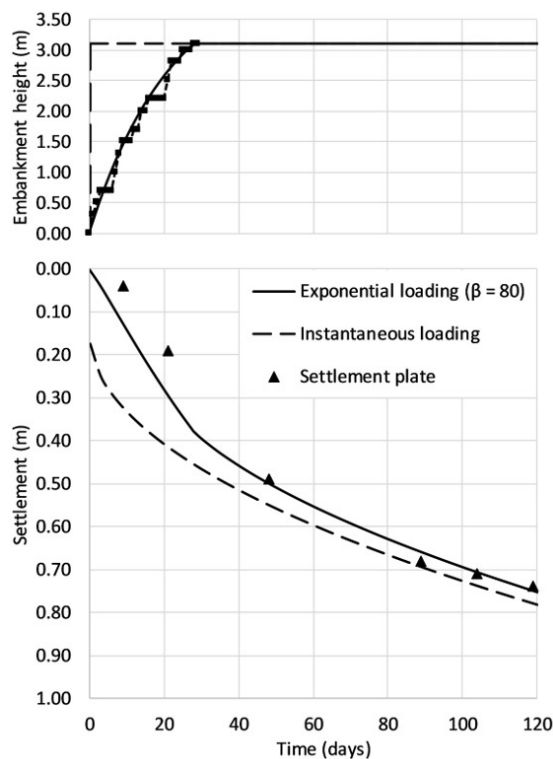
Figure 6. Settlement prediction for Macaé clay (Nascimento, 2016) with a construction sequence approximated to an exponential.

5. Conclusions

This study presented a closed-form consolidation solution for a time-dependent loading function. Two sets of equations were established to determine the excess pore pressure and the average degree of consolidation during construction and after construction.

The method is easy to apply and does not require the development of any differential equation. Solutions for single load functions (linear, parabolic, sinusoidal and exponential) and cyclic loads (haversine and damped) were presented. Results were consistent with the physical consolidation phenomena and agreed with some known analytical solutions and also with a numerical solution.

A case study with an approximately exponential construction sequence was analyzed. A comparison between the settlement plate readings and the solution proposed in the present paper was made, with good results.

Acknowledgements

Declaration of interest

The authors have no conflicts of interest to declare. All co-authors have observed and affirmed the contents of the paper and there is no financial interest to report.

Authors' contributions

Raphael Felipe Carneiro: conceptualization, data curation, formal analysis, investigation, methodology, validation, writing – original draft. Karl Igor Martins Guerra: data curation, formal analysis, investigation, validation. Celso Romanel: supervision, validation, writing – review & editing. Denise Maria Soares Gerscovich: visualization, writing – review & editing. Bernadete Ragoni Danziger: visualization, writing – review & editing.

Data availability

All data produced or examined in the course of the current study are included in this article.

List of symbols

c_v	coefficient of consolidation
f	rate of loading function
g	shifted rate of loading function
i	index
m	count parameter

n	number of ramp loads
q	load function
q_c	total load
s	Laplace parameter
t	time
u_z	excess pore pressure for instantaneous loading
u'_z	excess pore pressure for time-dependent loading
z	depth
F	Laplace transform of f
G	Laplace transform of g
H	total thickness of the clay layer
H_d	maximum length of drainage path
M	count parameter
T	time factor
T_a	time factor before the end of construction
T_b	time factor after the end of construction
T_c	time factor at the end of construction
U	average degree of consolidation for instantaneous loading
U''	average degree of consolidation for a time-dependent loading
U_z	depth-variable degree of consolidation for instantaneous loading
U'_z	depth-variable degree of consolidation for a time-dependent loading
α	inclination of a ramp load
β	fit parameter
$\Delta\sigma$	total vertical stress increase
τ	dimensionless half-period of a sinusoid function

References

Carneiro, R., Gerscovich, D., & Danziger, B. (2021). A simple approach to predict settlement due to constant rate loading in clays. *Soils and Rocks*, *44*(2), 1-8. http://dx.doi.org/10.28927/SR.2021.057120.

Conte, E., & Troncone, A. (2006). One-dimensional consolidation under general time-dependent loading. *Canadian Geotechnical Journal*, *43*(11), 1107-1116. http://dx.doi.org/10.1139/t06-064.

Gerscovich, D., Carneiro, R., & Danziger, B. (2018). Extension of Terzaghi's graphical method to predict settlement due to stepped load. *International Journal of Geomechanics*, *18*(12), 06018033. http://dx.doi.org/10.1061/(ASCE)GM.1943-5622.0001266.

Hanna, D., Sivakugan, N., & Lovisa, J. (2013). Simple approach to consolidation due to constant rate loading in clays. *International Journal of Geomechanics*, *13*(2), 193-196. http://dx.doi.org/10.1061/(ASCE)GM.1943-5622.0000195.

Huang, Y.H. (1993). *Pavement analysis and design*. Prentice-Hall.

Jimenez, R.R., Serrano, G.A., & Olalla, M.C. (2009). Consolidation charts for non-linearly time-increasing loads. *Proceedings of the Institution of Civil Engineers - Ground Improvement*, 162(2), 103-108. http://dx.doi.org/10.1680/grim.2009.162.2.103.

Liu, J., & Ma, Q. (2011). One-dimensional consolidation of soft ground with impeded boundaries under depth-dependent ramp load. In B. Huang, B.F. Bowers, G.-X. Mei, S.-H. Luo & Z. Zhang (Eds.), *Pavement and geotechnical engineering for transportation* (pp. 127-134). American Society of Civil Engineers. https://doi.org/10.1061/9780784412817.015.

Liu, J.C., & Griffiths, D. (2015). A general solution for 1D consolidation induced by depth- and time-dependent changes in stress. *Geotechnique*, *65*(1), 66-72. http://dx.doi.org/10.1680/geot.14.P.077.

Mitchell, J.K. (1993). *Fundamentals of soil behavior*. Wiley.

Nascimento, P.N.C. (2016). *Analysis of an experimental embankment led to failure located in Macaé - RJ* [Master's dissertation]. State University of Northern Rio de Janeiro – UENF. (in Portuguese).

Olson, R. (1977). Consolidation under time dependence loading. *Journal of the Geotechnical Engineering Division*, *103*(1), 55-60. http://dx.doi.org/10.1061/AJGEB6.0000369.

Qin, A.F., Sun, D.A., & Tan, Y.W. (2010). Analytical solution to one-dimensional consolidation in unsaturated soils under loading varying exponentially with time. *Computers and Geotechnics*, *37*(1-2), 233-238. http://dx.doi.org/10.1016/j.compgeo.2009.07.008.

Razouki, S.S., & Schanz, T. (2011). One-dimensional consolidation under haversine repeated loading with rest period. *Acta Geotechnica*, *6*(1), 13-20. http://dx.doi.org/10.1007/s11440-010-0132-1.

Razouki, S.S., Bonnier, P., Datcheva, M., & Schanz, T. (2013). Analytical solution for 1D consolidation under haversine cyclic loading. *International Journal for Numerical and Analytical Methods in Geomechanics*, *37*(14), 2367-2372. http://dx.doi.org/10.1002/nag.2188.

Schiffman, R.L. (January 6-10, 1958). Consolidation of soil under time dependent loading and varying permeability. In H.P. Orland (Ed.), *Proceedings of the Thirty-Seventh Annual Meeting of the Highway Research Board* (pp. 584-615). Washington DC, United States of America: Highway Research Board.

Schiffman, R.L., & Stein, J.R. (1970). One-dimensional consolidation of layered systems. *Journal of the Soil Mechanics and Foundations Division*, *96*(SM4), 1499-1504. http://dx.doi.org/10.1061/JSFEAQ.0001453.

Terzaghi, K. (1943). *Theoretical soil mechanics*. Wiley.

Terzaghi, K.F., & Fröhlich, O.K. (1936). *Theorie der setzung von tonschichten*. Franz Deuticke. In German.

Terzaghi, K.F., & Fröhlich, O.K. (1939). *Théorie du tassement des couches argileuses: introduction à la mécanique analytique des argiles*. Dunod. In French.

Verruijt, A. (2014). *Theory and problems of poroelasticity*. Delft University of Technology.

Zhu, G., & Yin, J. (1998). Consolidation of soil under depth-dependent ramp load. *Canadian Geotechnical Journal*, *35*(2), 344-350. http://dx.doi.org/10.1139/t97-092.

Appendix 1. Laplace Transform calculations.

The following equations were used during the development of the solutions presented in this study. The terms $\dfrac{F(s)}{s+M^2}$ and $\dfrac{G(s)}{s+M^2}$ are already rewritten as a sum of fractions.

▪ Ramp load

$$f(T)=g(T)=\frac{q_c}{T_c}$$

$$F(s)=G(s)=\frac{q_c}{T_c}\frac{1}{s}$$

$$\frac{F(s)}{s+M^2}=\frac{G(s)}{s+M^2}=\frac{q_c}{T_c}\frac{1}{M^2}\left(\frac{1}{s}-\frac{1}{s+M^2}\right)$$

$$\mathcal{L}^{-1}\left\{\frac{F(s)}{s+M^2}\right\}=\mathcal{L}^{-1}\left\{\frac{G(s)}{s+M^2}\right\}=\frac{q_c}{T_c}\frac{1}{M^2}\left(1-e^{-M^2T}\right)$$

(38)

▪ Multiple ramp loads

$$f(T)=\sum_{i=1}^{n}\alpha_i\mathcal{H}(T-T_{2i-2})-\alpha_i\mathcal{H}(T-T_{2i-1})$$

$$F(s)=\sum_{i=1}^{n}\alpha_i\frac{\exp(-sT_{2i-2})}{s}-\alpha_i\frac{\exp(-sT_{2i-1})}{s}$$

(39)

$$\frac{F(s)}{s+M^2}=\sum_{i=1}^{n}\frac{\alpha_i}{M^2}\left[\exp(-sT_{2i-2})\left(\frac{1}{s}-\frac{1}{s+M^2}\right)-\exp(-sT_{2i-1})\left(\frac{1}{s}-\frac{1}{s+M^2}\right)\right]$$

$$\mathcal{L}^{-1}\left\{\frac{F(s)}{s+M^2}\right\}=\sum_{i=1}^{n}\frac{\alpha_i}{M^2}\left\{\left\{1-\exp\left[-M^2(T-T_{2i-2})\right]\right\}\mathcal{H}(T-T_{2i-2})-\left\{1-\exp\left[-M^2(T-T_{2i-1})\right]\right\}\mathcal{H}(T-T_{2i-1})\right\}$$

▪ Parabolic load

$$f(T)=2\frac{q_c}{T_c^2}T$$

$$F(s)=2\frac{q_c}{T_c^2}\frac{1}{s^2}$$

$$\frac{F(s)}{s+M^2}=2\frac{q_c}{T_c^2}\frac{1}{M^4}\left(\frac{1}{s+M^2}-\frac{1}{s}+M^2\frac{1}{s^2}\right)$$

(40)

$$\mathcal{L}^{-1}\left\{\frac{F(s)}{s+M^2}\right\}=2\frac{q_c}{T_c^2}\frac{1}{M^4}\left(e^{-M^2T}-1+M^2T\right)$$

$$G(s)=2\frac{q_c}{T_c^2}\left(\frac{1}{s^2}+T_c\frac{1}{s}\right)$$

$$\frac{G(s)}{s+M^2}=2\frac{q_c}{T_c^2}\left[\frac{1}{M^4}\left(\frac{1}{s+M^2}-\frac{1}{s}+M^2\frac{1}{s^2}\right)+\frac{T_c}{M^2}\left(\frac{1}{s}-\frac{1}{s+M^2}\right)\right]$$

$$\mathcal{L}^{-1}\left\{\frac{G(s)}{s+M^2}\right\}=2\frac{q_c}{T_c^2}\left[\frac{1}{M^4}\left(e^{-M^2T}-1+M^2T\right)+\frac{T_c}{M^2}\left(1-e^{-M^2T}\right)\right]$$

▪ Sinusoidal load

$$f\left(T\right) = \frac{\pi}{2T_c} q_c \cos\left(\frac{\pi}{2T_c}T\right)$$

$$F\left(s\right) = \frac{\pi}{2T_c} q_c \frac{s}{s^2 + \left(\dfrac{\pi}{2T_c}\right)^2}$$

$$\frac{F\left(s\right)}{s+M^2} = \frac{\dfrac{\pi}{2T_c}q_c}{M^4 + \left(\dfrac{\pi}{2T_c}\right)^2}\left(\frac{\pi}{2T_c}\frac{\dfrac{\pi}{2T_c}}{s^2+\left(\dfrac{\pi}{2T_c}\right)^2} + M^2\frac{s}{s^2+\left(\dfrac{\pi}{2T_c}\right)^2} - M^2\frac{1}{s+M^2}\right)$$

$$\mathcal{L}^{-1}\left\{\frac{F\left(s\right)}{s+M^2}\right\} = \frac{\dfrac{\pi}{2T_c}q_c}{M^4 + \left(\dfrac{\pi}{2T_c}\right)^2}\left[\frac{\pi}{2T_c}\sin\left(\frac{\pi}{2T_c}T\right) + M^2\cos\left(\frac{\pi}{2T_c}T\right) - M^2 e^{-M^2 T}\right]$$

$$g\left(T\right) = \frac{\pi}{2T_c} q_c \cos\left[\frac{\pi}{2T_c}\left(T+T_c\right)\right] = -\frac{\pi}{2T_c}q_c\left[\sin\left(\frac{\pi}{2T_c}T\right)\right] \tag{41}$$

$$G\left(s\right) = -\frac{\pi}{2T_c} q_c \frac{\dfrac{\pi}{2T_c}}{s^2 + \left(\dfrac{\pi}{2T_c}\right)^2}$$

$$\frac{G\left(s\right)}{s+M^2} = \frac{-\dfrac{\pi}{2T_c}q_c}{M^4 + \left(\dfrac{\pi}{2T_c}\right)^2}\left[M^2\frac{\dfrac{\pi}{2T_c}}{s^2+\left(\dfrac{\pi}{2T_c}\right)^2} - \frac{\pi}{2T_c}\frac{s}{s^2+\left(\dfrac{\pi}{2T_c}\right)^2} + \frac{\pi}{2T_c}\frac{1}{s+M^2}\right]$$

$$\mathcal{L}^{-1}\left\{\frac{G\left(s\right)}{s+M^2}\right\} = \frac{-\dfrac{\pi}{2T_c}q_c}{M^4 + \left(\dfrac{\pi}{2T_c}\right)^2}\left[M^2\sin\left(\frac{\pi}{2T_c}T\right) - \frac{\pi}{2T_c}\cos\left(\frac{\pi}{2T_c}T\right) + \frac{\pi}{2T_c}e^{-M^2 T}\right]$$

▪ Exponential load

$$f(T) = \frac{q_c}{1 - e^{-\beta T_c}} \beta e^{-\beta T}$$

$$F(s) = \frac{q_c}{1 - e^{-\beta T_c}} \beta \frac{1}{s + \beta}$$

$$\frac{F(s)}{s + M^2} = \frac{q_c}{1 - e^{-\beta T_c}} \left(\frac{\beta}{M^2 - \beta} \right) \left(\frac{1}{s + \beta} - \frac{1}{s + M^2} \right)$$

$$\mathcal{L}^{-1} \left\{ \frac{F(s)}{s + M^2} \right\} = \frac{q_c}{1 - e^{-\beta T_c}} \left(\frac{\beta}{M^2 - \beta} \right) \left(e^{-\beta T} - e^{-M^2 T} \right)$$

$$g(T) = \frac{q_c}{1 - e^{-\beta T_c}} \beta e^{-\beta (T + T_c)} = -\frac{q_c}{1 - e^{-\beta T_c}} \beta e^{-\beta T_c} e^{-\beta T}$$

$$G(s) = \frac{q_c}{1 - e^{-\beta T_c}} \beta e^{-\beta T_c} \frac{1}{s + \beta}$$

$$\frac{G(s)}{s + M^2} = -\frac{q_c}{1 - e^{-\beta T_c}} \left(\frac{\beta e^{-\beta T_c}}{M^2 - \beta} \right) \left(\frac{1}{s + \beta} - \frac{1}{s + M^2} \right)$$

$$\mathcal{L}^{-1} \left\{ \frac{G(s)}{s + M^2} \right\} = -\frac{q_c}{1 - e^{-\beta T_c}} \left(\frac{\beta e^{-\beta T_c}}{M^2 - \beta} \right) \left(e^{-\beta T} - e^{-M^2 T} \right)$$

(42)

▪ Haversine repeated load

$$f(T) = q_c \frac{\pi}{\tau} \sin\left(\frac{2\pi}{\tau} T \right)$$

$$F(s) = q_c \frac{\pi}{\tau} \frac{\frac{2\pi}{\tau}}{s^2 + \left(\frac{2\pi}{\tau} \right)^2} = 2 q_c \left(\frac{\pi}{\tau} \right)^2 \frac{1}{s^2 + \left(\frac{2\pi}{\tau} \right)^2}$$

(43)

$$\frac{F(s)}{s + M^2} = q_c \left[\frac{2 \left(\frac{\pi}{\tau} \right)^2}{\left(\frac{2\pi}{\tau} \right)^2 + M^4} \right] \left[\frac{1}{s + M^2} - \frac{s}{s^2 + \left(\frac{2\pi}{\tau} \right)^2} + \frac{M^2}{\left(\frac{2\pi}{\tau} \right)} \frac{\frac{2\pi}{\tau}}{s^2 + \left(\frac{2\pi}{\tau} \right)^2} \right]$$

$$\mathcal{L}^{-1} \left\{ \frac{F(s)}{s + M^2} \right\} = q_c \left[\frac{2 \left(\frac{\pi}{\tau} \right)^2}{\left(\frac{2\pi}{\tau} \right)^2 + M^4} \right] \left[e^{-M^2 T} - \cos\left(\frac{2\pi}{\tau} T \right) + \frac{M^2}{\left(\frac{2\pi}{\tau} \right)} \sin\left(\frac{2\pi}{\tau} T \right) \right]$$

▪ Dumped cyclic load

$$f(T) = q_c \left[-\beta e^{-\beta T} \sin\left(\frac{\pi}{\tau} \bullet T \right) + \frac{\pi}{\tau} e^{-\beta T} \cos\left(\frac{\pi}{\tau} \bullet T \right) \right]$$

$$F(s) = q_c \left[\frac{-\beta \dfrac{\pi}{\tau}}{(s+\beta)^2 + \left(\dfrac{\pi}{\tau}\right)^2} + \frac{\dfrac{\pi}{\tau}(s+\beta)}{(s+\beta)^2 + \left(\dfrac{\pi}{\tau}\right)^2} \right] = q_c \left[\frac{\dfrac{\pi}{\tau} s}{(s+\beta)^2 + \left(\dfrac{\pi}{\tau}\right)^2} \right]$$

(44)

$$\frac{F(s)}{s+M^2} = \left[\frac{\dfrac{\pi}{\tau}}{\beta^2 + \left(\dfrac{\pi}{\tau}\right)^2 - 2\beta M^2 + M^4} \right] \left\{ M^2 \frac{s+\beta}{(s+\beta)^2 + \left(\dfrac{\pi}{\tau}\right)^2} + \left[\frac{\beta^2 + \left(\dfrac{\pi}{\tau}\right)^2 - M^2\beta}{\dfrac{\pi}{\tau}} \right] \frac{\dfrac{\pi}{\tau}}{(s+\beta)^2 + \left(\dfrac{\pi}{\tau}\right)^2} - M^2 \frac{1}{s+M^2} \right\}$$

$$\mathcal{L}^{-1}\left\{ \frac{F(s)}{s+M^2} \right\} = \left[\frac{\dfrac{\pi}{\tau}}{\beta^2 + \left(\dfrac{\pi}{\tau}\right)^2 - 2\beta M^2 + M^4} \right] \left\{ M^2 e^{-\beta T} \cos\left(\frac{\pi}{\tau} \bullet T \right) + \left[\frac{\beta^2 + \left(\dfrac{\pi}{\tau}\right)^2 - M^2\beta}{\dfrac{\pi}{\tau}} \right] e^{-\beta T} \sin\left(\frac{\pi}{\tau} \bullet T \right) - M^2 e^{-M^2 T} \right\}$$

12

Carneiro et al., Soil. Rocks, São Paulo, 2023 46(1):e2023077721

REVIEW ARTICLES

A systematic review on shallow geothermal energy system: a light into six major barriers

Rajendra Babu Roka[1#] (ID), António José Pereira de Figueiredo[1] (ID),

Ana Maria Carvalho Pinheiro Vieira[2] (ID), José Claudino de Pinho Cardoso[1] (ID)

Review Article

Keywords
Shallow geothermal energy systems
Barriers of geothermal energy
Soil thermal conductivity
Building energy demand

Abstract

Shallow geothermal energy systems (SGES) are being widely recognized throughout the world in the era of renewable energy promotion. The world is aiming to promote and implement the concept of nearly zero energy consumption in the building sector. Shallow geothermal energy systems have huge potential to meet the heating and cooling demand of a building with low carbon emissions. However, the shallow geothermal system exploration rate and its global contribution to renewable energy used in the buildings sector is yet relatively low. Therefore, this study explores specific barriers which hinder the promotion of shallow geothermal energy systems through a systematic review of the literature. The study was carried out by investigating published papers indexed in Scopus and Web of science core collection databases. The selected papers are focused on shallow geothermal energy systems and barriers to their promotion. Only review and research articles types were included in the analysis and constrained to the topic of closed-loop shallow geothermal energy systems. This system's promotion has been influenced by the lack of legislation, little knowledge about the conductivity of soil and by high initial investment cost at its topmost. The least influencing barrier is considered to be the heating and cooling efficiency of shallow geothermal energy systems.

1. Introduction

For efficient cooling and heating of building's indoor environments, SGES offers a clean, lower carbon emission and renewable source of energy. These systems work with ground source heat pumps (GSHP) that are responsible to exchange heat between the ground and the building. The first GSHP was documented in 1945 (Sanner, 2016) and was applied in buildings. Since then, this system typology has been implemented and strongly disseminated in several countries. The evident benefits of direct use of GSHP for space heating and cooling, bathing, fish farms, industry and others are found earlier than 1995 (Freeston, 1996). The exploration of the energy of the surface ground layers has been increasing day by day due to its effectiveness and alternative source of energy for reducing the dependence on fossil energy as well as the building's decarbonization. The use of SGES in urban areas has resulted in an unprecedented boost of 9% market growth during the last decade (García-Gil et al., 2020).

The demand of energy for building heating and cooling has increased expeditiously and is expected to share the global energy consumption by 40% and about 30% of the share of total global carbon emission (Hughes et al., 2011; Yang et al., 2014). By the end of 2020, EU was motivated to achieve 20% of the final energy consumption from renewable sources for the building sector (Witte et al., 2002). Most of the European Union (EU) partners have achieved the target. By the end of 2030, the EU countries have agreed to the aim of attaining at least a 32% share of renewable energy in total energy consumption (EGEC, 2022).

Figure 1 illustrates the publication trend on SGES for heating and cooling purposes of the buildings per year published in the platform *ScienceDirect*. This shows that the published research papers on SGES started in 1995, began to grow visibly only after 2008 and experienced exponential growth after 2010 and nowadays the same tendency still flows.

Figure 2 shows the research on SGES by ten different countries published in *ScienceDirect*. These countries are among the top ten most involved in research on SGES according to their publications on the *ScienceDirect* platform. China is in the lead of the race for the research on SGES as well as the United States, followed by some European countries, that have also shown promising developments, namely the United Kingdom (Figueiredo et al., 2019). Until 2030 the EU has

Roka et al., Soil. Rocks, São Paulo, 2023 46(1):e2023007622
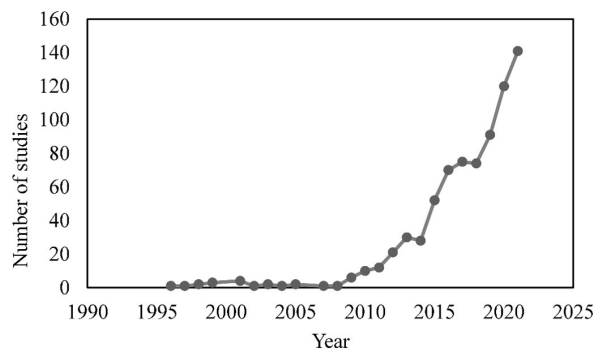
1

Figure 1. The number of research on the trend of using SGES for heating or cooling purposes on buildings published per year in ScienceDirect.
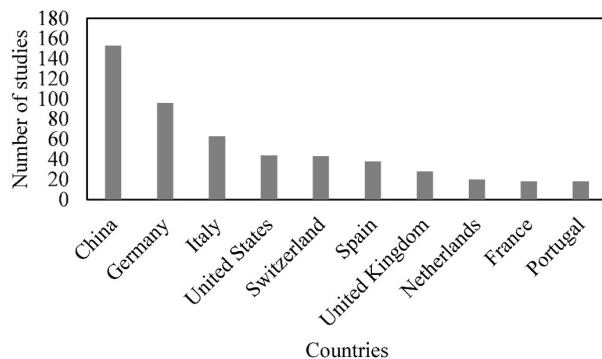

Figure 2. illustrates the research on SGES by ten different countries published in ScienceDirect.

set targets that newly built buildings should use very little conventional energy supply and that the building should be 'nearly Zero-Energy Building' or 'nZEB' (Florence et al., 2013). SGES may be one of the useful energy sources for reaching this target by fulfilling the heating and cooling energy demand of buildings on an urban scale (EGEC, 2022). However, some issues need to be overcome to speed up the development of SGES. Therefore, this paper intends to explore some barriers which might delay the promotion of shallow geothermal systems, to overcome these barriers and encourage the use of SGES which can play an important role to decarbonize carbon emissions from heating and cooling, currently using fossil fuels. Despite being a clean and mature technology that could be installed anywhere in the world, geothermal energy only covers around 2% of total renewable heating (EGEC, 2022). For example, in the case of China which has a huge potential for SGES (Zeng et al., 2021), only about 2.3% of the total potential has been explored to date (Wang et al., 2017).

The potential of using GSHP in Portugal is also significant, though the development of GSHP has not been found to a sufficient extent. Some pilot projects are started to install SGES like in Aveiro University where five buildings are currently equipped with GSHP. The implementation of GSHP in the district heating and cooling context is non-existent in Portugal. However, new studies regarding the SGES applications are essential to explore and extend its application to the district level to cope with the increasing energy demand for heating and cooling of buildings in the country (Nunes et al., 2019).

Table 1 illustrates recent European shallow geothermal energy projects aiming to promote SGES. There are several projects actively involved on the promotion of SGES namely geo trainet, geo power group and ground med etc. Energy use in heating and cooling until 2020 covered by the renewable energy sector in the EU countries has reached about 23.1%, compared to 11.7% in 2004 (European Commission, 2022). Compared to other renewable energy sources, SGES is barely visible in the market despite being sustainable, reliable, stable with no dependence on weather conditions, available near buildings and a renewable source with several advantageous features in comparison to other renewable energy sources (IRENA, 2017). The CO_2 emission from any system is a primary concern of the world now to reduce the consequences of global warming. By the use of SGES, there is evidence of a 33% to 88% of reduction of CO_2 emissions in comparison to the acclimatization of buildings by conventional heating systems (Saner et al., 2010). In this sense, there is a need to eradicate these barriers and make this technology gain competitiveness. This review will help to contribute to identify barriers that affect the acceleration of the promotion of SGES and will try to analyse the issues mentioned by other authors.

2. Materials and methods

2.1 Research methodology

This systematic search followed a strategy to identify relevant papers on the subject under study. The goal of this review is to explore and enlighten the major obstacles related to SGES indicated by several authors. The search of the literature was focused on the major issues with SGES rather than the general issues. On February 2022, the search strategy was implemented considering two databases; Scopus and Web of Science (WoS) core collection. The search was based on the *keywords* ("Shallow Geothermal Energy" OR "Shallow Geothermal System" OR "Shallow Geothermal Energy System") in all fields. The same searches were performed with Scopus and Web of science core collection databases in the Title, Abstract and Keyword fields. The result obtained were 542 and 191 respectively. The search was narrowed down by adding AND (barriers* OR issues* OR limitations* OR hurdles* OR challenges* OR constraints*) in the Title, Abstract and Keyword field in Scopus and Web of science core collection database. The (*) symbol is a wildcard which helps to increase the flexibility in the searches. This substitutes all possible characters searching

Table 1. Recent European shallow geothermal energy projects aiming to promote SGES.

Citation	Project	Aim	Project activities
Geo Power Group (2022)	Geo.Power	The project aimed to expand the knowledge and skills of SGES from the experienced market to the new market.	Replicating the knowledge and skills through training
GeoTrainet (2022)	Geotrainet	Not sufficiently available appropriately skilled personnel (designers and installers) is one of the barriers to SGES promotion. The project started with a qualified training course for SGES designers and developers, with the objective of capacity building for skilled personnel and the development of a common certification scheme.	-European Geothermal Workshop, France/ The geothermal congress DGK, Germany/Geo Power Global Congress, Turkey-2015. -Know RES geothermal career day, Germany/ Geo THERM, Germany/ International short course on step forward in SGES technology, France/-2016. - Shallow Geothermal Energy Days, Belgium-2019. -Test, Romania-2021
Ground Med (2022)	Ground-med	This project aims to develop cost-effective and attainable for both heating and cooling. Already has been installed series of heat pumps in southern Europe.	- Different field tests of contemporary GSHP were carried out by Fraunhofer ISE. -TERRA THERMA; To manage the residential temperature and terrestrial energy recovery using advanced Stirling heat pumps. -Thermo Map; project helps to develop the map potential of very shallow geothermal energy in Europe. -ASTECH; Provides upgraded Sustainable Technologies for Heating and Cooling Applications.
EGEC (2022)	Re-Geo Cities	The project developed the campaign called "Heat Under Your Feet" for the information and promotion of ground source heat pumps. The aim is to increase awareness in European cities about SGES among policymakers and decision-makers. This has proposed a set of simplified administrative procedures and an intelligence regulatory framework.	- With the motivation of promulgating information about GSHPs in EU, "The heat under your feet" is an ambition launched within the framework of the Re- Geo Cities project to promote their use-2015.

for one or more entries. After constraints 66 and 26 papers were found respectively. Moreover, the search was limited to English language final versions, published in ISI journal, final version only, review articles and research articles excluding conference articles or proceedings. The subject areas of mathematics, economics, agriculture, physics and material science were excluded. This gave the result of 29 in Scopus and 14 in the Web of science core collection. To maintain the quality of the review, all duplications were checked thoroughly using the excel command and 12 duplications found were not considered.

2.2 Screening and inclusiveness

The carried-out review was focused on shallow geothermal energy systems and barriers to their promotion. Therefore, the screening of the paper was performed by checking the abstract of the articles thoroughly for the analysis and refining of the articles which helps to ensure the quality and relevance of academic literature. Only papers dealing with vertical and horizontal closed- loop shallow geothermal energy systems were selected excluding open-loop SGES and deep geothermal systems. In addition, papers trying to explore the various barriers of SGES on promotion were selected. Papers focused on the mechanism of heat pumps, thermal imbalance of soil, groundwater pumps, open well systems, groundwater temperature, climate change impact, design of energy piles and design of heat pumps, were also excluded. The framework for the identification, screening and excluding process is shown in Figure 3.

The papers included in the detailed review were 24 from Scopus and Web of Science core collection. By assessing each article on the aforementioned inclusion and exclusion criteria, 7 papers were excluded. Hence, the review was completely confined to issues with SGES exploration for heating and cooling purposes. Particularly, while reviewing the papers, the focus was given to the identification of the barriers to SGES from a global to a regional perspective.
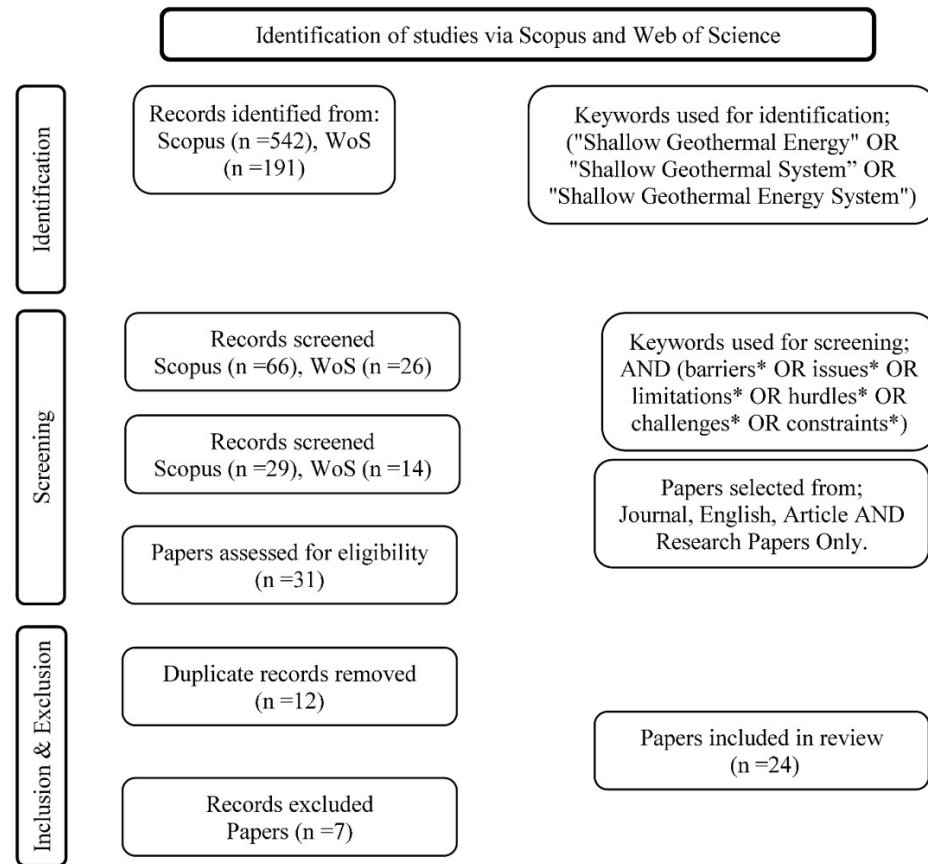
Figure 3. Flow diagram for literature search and filtering research process.

3. Results and discussion

3.1 Definition of barriers in SGES

The term barrier refers to an obstacle or hindrance to progress. SGES are widely considered a highly potential renewable source of energy to cope with future heating and cooling demands which utilize and help to store heat beneath the ground and helps to reduce greenhouse gas emission in the building sector (Cherati & Ghasemi-Fare, 2021). As mentioned before, the progress on the rate of growth in the exploration of this useful energy source is not happening as expected (Tsagarakis, 2020). Any type of hurdles that arose for the progress of propagation of SGES are barriers that should be overcome. Technical, economical, legislative or public awareness are barriers all considered for the analysis, while the mechanical design and operation hurdles in its features are not.

3.2 Identified barriers in SGES

An in-depth review of the papers was performed, specifically focusing on the barriers of SGES. In this sense, six main barriers to the promotion of SGES were identified
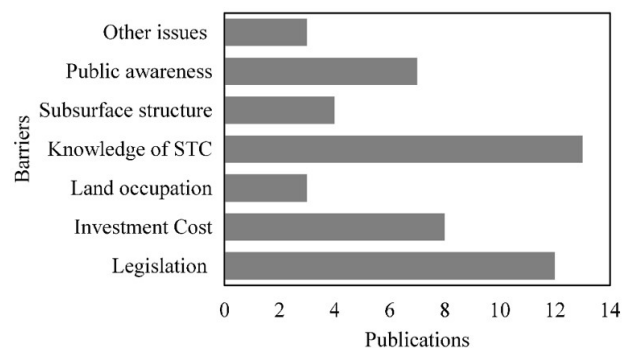
Figure 4. Comparison of the publication numbers with identified barriers on consulted papers.

and are illustrated in Figure 4. A total of 13 papers dealing with the issue of less knowledge on soil thermal conductivity (STC) were found. While the second most discussed issue in literature was related to legislation with 12 papers dealing with this topic. The third main issue detected in the review was that of the initial investment cost, 8 papers dealt with it. Predominantly the papers were indicating the costly nature of system installation. Since SGES is a newer technology that evolved from other existing renewable energy in the

4

Roka et al., Soil. Rocks, São Paulo, 2023 46(1):e2023007622

market, public awareness was also found to be an issue of discussion. For instance, the technology is not familiar among energy consumers and even among technicians. The issue regarding public awareness raised by the authors was found in 7 papers. Papers dealing with an issue regarding subsurface structure were 4 and 3 papers dealt with land occupation. Whereas 3 papers were dealing with heating and cooling efficiency issues and the complex nature of the SGES issues. In summarizing, the majority of papers were raising the issue of little knowledge on the conductivity of underground materials, legislation and initial investment costs. In contrast, the least discussed issue was focused on the topic of land occupation and other issues.

3.2.1 Little knowledge on the thermal conductivity of underground materials

Issues related to little knowledge of STC where SGES are embedded are the most discussed by the authors in this review. A total of 26% of the reviewed papers highlighted the mentioned issue. Revision of the selected papers was done and extracted information on the main view of the authors about STC is presented in Table 2, which eases to compare the views of authors in mentioned issue. The ground thermal conductivity is an important site parameter (Cecinato & Salciarini, 2022) and one of the most influential factors for SGES design (Hoekstra et al., 2020b; Li et al., 2019; Ondreka et al., 2007). This physical property can be measured either by laboratory or in-situ tests (Witte et al., 2002). The high-energy performance of SGES is directly related to the ground thermal conductivity among other site-dependent

factors (Cecinato & Salciarini, 2022; Cherati & Ghasemi-Fare, 2021; Ondreka et al., 2007). According to Fourier's law, thermal conductivity is the coefficient of proportionality between temperature gradient and the corresponding heat flux. It can be affected by factors like soil water content, density, composition and mineral properties (Nowamooz et al., 2016). Hence, to determine the potential of the SGES, the ground thermal conductivity must be explored and carefully measured to assess its suitability of SGES (Cecinato & Salciarini, 2022; Cherati & Ghasemi-Fare, 2021; Tinti et al., 2016). Quartz and Dolomite materials present a high thermal conductivity (Cetin et al., 2020; Tinti et al., 2016). This means that soils or rocks with a high percentage of those minerals have greater potential for higher heat extraction rates, which results in better thermal efficiency of SGES. On the other hand, marlstone and siltstones have relatively low thermal conductivity (Cetin et al., 2020; Tinti et al., 2016) hence, low potential for SGES. The thermal conductivity of rocks and soils also shows spatial variability (Janža et al., 2017).

Rocks classification beneath the ground (Tinti et al., 2016) and the degree of saturation of soil (Vieira et al., 2019) determine the potential for heat extraction for SGES. Therefore, rock classification and degree of saturation might be different according to location and that would be the deciding factor for the design and implementation of SGES (Schelenz et al., 2017). Stegnar et. al. (2019) studied the thermal conductivity of different rocks and soils by measuring average values collected from different boreholes.

Summing up, the difficulties in the characterization of the STC with different degrees of soil saturation and porosities create a barrier to the design and implementation of SGES

Table 2. Main views expressed by authors on the issue with knowledge of STC.

Reference	Views of authors on the issue with little knowledge on the conductivity of soil
Cecinato & Salciarini (2022)	Soil conductivity is of predominant importance in SGES installation efficiency.
Hoekstra et al. (2020a)	STC has huge influence in SGES potential.
Assouline et al. (2019)	Measurement of soil thermal property should be determined before extracting heat from the ground.
Zeng et al. (2021)	The heat transfer rate of SGES is unsatisfactory until the STC is determined properly.
Cherati & Ghasemi-Fare (2021)	To get energy from the earth for the long term, soil thermal properties are the most important parameter for determining the potential of shallow geothermal.
Stegnar et al. (2019)	Among the several parameters, the main parameter governing SGES potential is the STC of the ground.
Li et al. (2019)	Almost accurate measurement and estimation of STC are necessary for SGES design and implementation.
Tinti et al. (2018)	There is a spatial and temporal variation in the ground temperature at shallow depths of the earth due to the different properties of the rocks and soils.
Janža et al. (2017)	Efficient and sustainable extraction of ground heat requires proper knowledge of rock and soil types and their thermal characteristics.
Somogyi et al. (2017a)	The SGES system must be designed by considering the properties of soil and its stratification beneath the surface.
Tinti et al. (2016)	A regional variation in STC is mostly in wide intervals.
Ondreka et al. (2007)	The potential of SGES is related to the rock's classification beneath the ground and heat extraction mainly relies on underground STC.
Cetin et al. (2020)	STC is a key parameter for the quantification of the energy efficiency of SGES.

(Zhang et al., 2021). Aljundi et al. (2020) performed a series of thermal conductivity tests in a laboratory using a thermal needle probe under dry and saturation conditions. The result shows that the thermal conductivity was significantly higher in a fully saturated condition than in a dry condition. In the study developed by Aljundi et al. (2020), the field where the borehole heat exchanger installation takes place is composed of soil with variability in-depth, as well as water content and groundwater velocity. This variability cannot exactly be reproduced along the boreholes deep, and thus, leads to a high level of uncertainty on a small-scale. This is a barrier to the design of the SGES as well as a limitation of knowledge in the design phase. A proper evaluation of STC before the design of SGES is thus essential for a proper heat transfer analysis (Aljundi et al., 2020). Consequently, the lack of knowledge on the ground thermal properties where SGES will be embedded could be a barrier to the SGES implementation. To implement the SGES installation and its promotion, a thorough analysis of the ground thermal properties of the soil layers is necessary. The thermal properties of the soil depend on the different factors that made characterizing and mapping the GSHP potential all over the country a challenging task (Assouline et al., 2019).

3.2.2 Legislation

Figure 5 illustrates that the legislation was the second most discussed issue, among the most highlighted issues by the authors during the review. In this case, 24% of the total reviewed papers discussed the legislation issue in SGES. SGES has been studied and applied worldwide over the past 20 years (Zeng et al., 2021), however, it is observed that the legislation issues were highlighted by papers published only after 2015 (see Figure 6). Zeng et. al. (2021) considered that beyond 2015 was a prosperous stage for the execution of SGES. From the literature, it was observed that 8% of the paper published in 2015, 2017 and 2018 discussed legislation barriers to SGES. Furthermore, the majority of papers published in 2019, 42% of them, mention this issue.
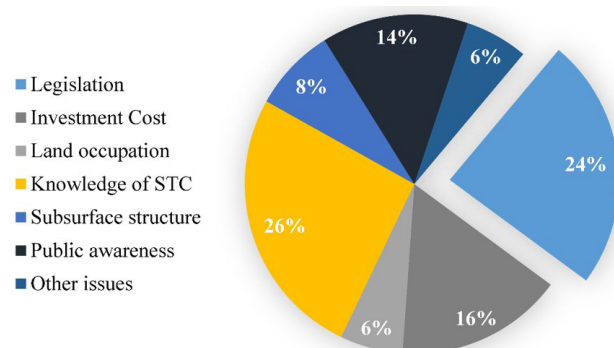
Table 3 shows that there is high diversity in the legislation governing the use of SGES. Haehnlein et. al. (2010) summarized several country's laws concerning the use of SGES, which also shows the huge diversity of the laws among the nations. However, more recently the EU published seven directives regarding SGES to simplify and standardize the procedure among its members. Still, the issue persists because the national regulations are diversified. The issue of legislation persists as in many countries the administrative process for obtaining a license or permit to implement the SGES, should go through the approval of more than one department (Zeng et al., 2021). For instance, the complicated system of administration involved as the process goes through the department of land and resources, environmental protection, construction, municipal administration and power in China, resulting in a long time for the approval process.

On the other side, SGES are relatively new and evolving technology, thus, several countries are trying to improve their legislation procedures to ease the installation of SGES. Whereas some countries legislation makes no mention of SGES development (non-existence) (Tsagarakis et al., 2020; Zeng et al., 2021).

According to Tsagarakis et. al. (2020) failure to establish good guidelines, bringing homogeneity and simplification in the legislation for permitting SGES design and implementation are the key drivers that hinder the promotion of SGES. Changes in the legislation to licensing procedure eventually make the licensing process more complicated (Somogyi et al., 2017a).

Table 4 shows that most of the authors are highlighting that there are issues in legislation, legal framework, laws and regulations. The main views about legislation issues in several countries detected by the authors are highlighted.

There are uncertainties, versatilities, imperfections and the diverse nature of legislation, which hinders the propagation of SGES to meet expectations. Only one article was found that mentioned there are few constraints relating to the ground and subsurface laws and policies (Assouline et al., 2019). However, the study shows that many countries are evolving towards the
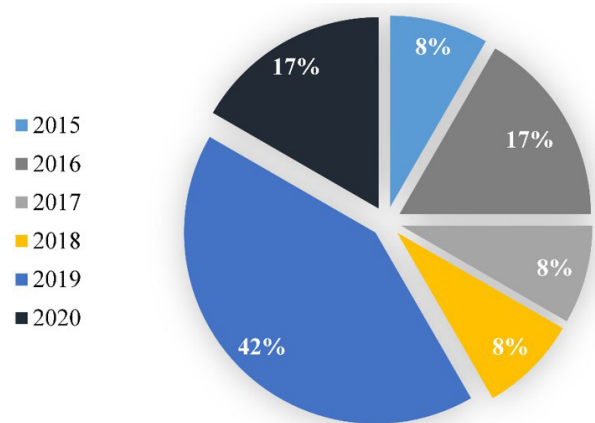

Figure 5. Relative distribution of legislation issue on SGES in percentage.

Figure 6. Temporal relative distribution of legislation issue on SGES.

6

Roka et al., Soil. Rocks, São Paulo, 2023 46(1):e2023007622

Table 3. Identification of legislation concerning the use of SGES among several countries.

Reference	Country	Laws concerning the use of SGES
Somogyi et al. (2017a)	UK	Groundwater investigation consent- Environmental Agency
Zeng et al. (2021)	China	National Energy Administration (NEA), Ministry of Finance (MOF), Ministry of Land and Resources (MLR) and Ministry of Housing and Urban-Rural Development (MOHURD)
Cetin et al. (2020)	Turkey	The national expert group on SGES, Annex-27, and Heat production from renewable energy has not been regulated.
Somogyi et al. (2017a)	France	Mining Authority, GWHP, Water authority, Environmental agency
Zeng et al. (2021) Somogyi et al. (2017a)	Sweden	Normbrunn Guidelines, Geological Survey of Sweden (SGU) and Research Institute of Sweden (RISE), GWHP- Water operation permit, Local council
Zeng et al. (2021) Somogyi et al. (2017a)	Germany	Geological Survey of the respective state, VDI 4640 guideline series, Water authority
Somogyi et al., 2017a)	Italy	According to provincial provision, (UNI 11466-68:2012) guidelines series
(Somogyi et al. (2017a)	Spain	Mining Authorities, Water Authorities
Ryżyński & Bogusz (2016)	Poland	Geological and mining law, Construction law, Theoretically the existing law doesn't prevent the use of SGES
Somogyi et al. (2017a), Tinti et al. (2016)	EU	Directive 2009/28/EC (7 directives)
Tinti et al. (2016)	Adriatic Area	Do not fall within the laws directing SGES in most Adriatic countries

Table 4. Main views by authors on issues regarding legislation.

Reference	Main views of authors on Issues with Legislation
Zeng et al. (2021)	Incompetent laws and regulations (SGES without scientific planning and legal permits)
Somogyi et al. (2017a)	Wavering nature of licensing procedure
Assouline et al. (2019)	Coercion relating to the ground and subsurface laws and policies
Tinti et al. (2016)	Uncertainties regarding the legal framework regulating
Ryżyński & Bogusz (2016)	Lack of proper regulations isa major inhibiting factor for the use of this technology
Christodoulides et al. (2020)	Lack of systematic design guidelines of SGES.
Cetin et al., 2020)	Heat production from renewable energy has not been regulated.
García-Gil et al. (2015)	The diverse international legal status for the use of SGES created an uncertain situation.
Cherati & Ghasemi-Fare (2021)	Lack of detailed regulations on the exploration of SGES.

modifications of the legislative procedures to some extent for the promotion of SGES (Zeng et al., 2021). Moreover, some countries do not have regulations regarding SGES.

Legislation is a vital factor for the development of SGES, as it regulates, guides, promotes or hinders the total process from beginning to end. In most countries, the involvement of various authorities in the authorization process of SGES, for instance, geological and mining law, water authority, environmental agency, construction law, etc. makes the process very complicated, which might be a discouraging factor for the investor, designer and contractor. The lack of recommendations/technical standards for thermoactive geostructures in most countries is also a barrier to the use of SGES. A common regulatory framework among the countries and simple authorization procedures will surely help to overcome this barrier to the promotion of SGES.
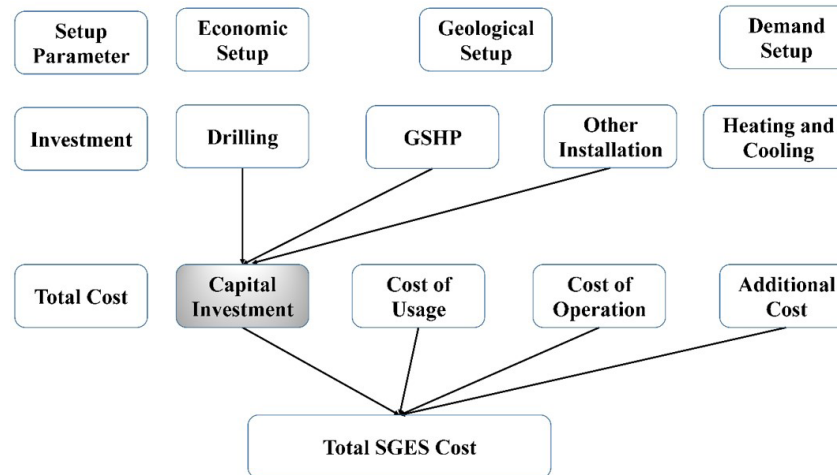
3.2.3 Initial investment cost

Table 5 refers to the highlighted views of the authors from selected papers concerning the initial investment cost

of SGES. Issues related to the initial investment cost were discussed in 16% of the selected papers. Cherati & Ghasemi-Fare (2021) indicated in their paper that the price of fossil fuels in middle-east countries like Iran is very low as they have reservoirs of fossil fuels and therefore, they have very easy access to non-renewable energy.

The cost associated with the design and installation for the exploration of SGES is quite high compared to conventional energy in middle east countries. That leads to less concern for the government in its promotion and less public interest in it (Cherati & Ghasemi-Fare, 2021). Additionally, the issuance of SGES permits is expensive in some countries which made the initial investment cost of SGES higher than other energy sources (Hoekstra et al., 2020a). Another aspect is related to the viability of drilling the boreholes for heat exchangers which depends on the hardness of the subsurface geological formations. This site-specific nature of the SGES brings uncertainties to the cost of the installation (Schelenz et al., 2017). Hence this may cause a proportionally high construction cost during implementation (Tsagarakis, 2020).

Table 5. Main views of authors regarding the initial investment cost of SGES.

Reference	Main views of authors about the initial investment issue
Baralis & Barla (2021)	The high initial investment cost is generally showing the shortcoming of the SGSES.
Zeng et al. (2021)	The most notable difficulty in SGES promotion is the high initial investment cost with an average payback period of approximately 4.31 years (Cui et al., 2018) and capital price should be regulated lower to promote SGES.
Cherati & Ghasemi-Fare (2021)	SGES system remains with high initial investment costs for example, drilling and installation costs. Which restricts the popularity of propagation of SGES.
Hoekstra et al. (2020a)	Commencing costs emerge much higher in SGES in comparison to other renewable energy systems. For instance, the installation cost on average for hydropower is USD 1870/Kw, Bio-energy is USD 2543/Kw and Geothermal is USD 4486/Kw in 2020 (IRENA, 2020).
Tsagarakis (2020)	The soaring construction and operational cost of SGES during the enactment stage is due to its site-specific characteristics.
Assouline et al. (2019)	On the contrary, the installation costs will be low with easy operation and maintenance costs that made SGES a manageable resource. Having soil on the shallow depth mostly at depths of 1–2 m with a high value of thermal conductivity, SGES installed in the uppermost 10 m of the ground, the cost will be low.
Stegnar et al. (2019)	The cost of drilling for the vertical borehole and GSHP is quite high which hinders the propagation of SGES in the proper amounts.
Tinti et al. (2016)	Hybrid solutions and buffer tanks of SGES can help to receive ideal economic issues. More than one building may be connected to the same geothermal system, thereby increasing buffer tank cost-effectiveness and lowering the installation cost.

Figure 7. The cost structure of geothermal heat generation, adapted from the source (NEA, 2015) National Energy Authority, amended 2014.

As shown in Figure 7, the investment cost (capital investment) belongs to the cost of drilling, GSHP and other installations. Since the drilling cost of SGES is more than other associated costs for operation and management, the initial investment cost comes high (NEA, 2015; Ramos-Escudero et al., 2021). In the drilling process, is included cost of tubing as well as grouting and piping. In this sense, the cost can cover up to 60% of the total price of the system upfront (Gemelli et al., 2011). The reason behind the low impact of SGES in the renewable energy market is its relatively high initial investment cost (installation cost) which is the obstacle to SGES promotion (Müller et al., 2018).

Despite having low carbon emission and sustainable nature, exploration and utilisation of SGES are not enough as it has to be in several countries because of its high cost of installation and cost of a heat pump. Hence, this results in a non-substantial contribution to the reduction of greenhouse gas (Stegnar et al., 2019). A single SGES could be applied to double or multiple buildings, improving the energy efficiency of the group with lower installation costs associated (Tinti et al., 2016). On contrary, Assouline et al. (2019) mentioned that the SGES system has a low cost of installation and easy maintenance.

The cost will be low where the highest value of thermal conductivity is found and very shallow geothermal installed in up to 10 m of the depth, and generally at depths of 1–2 m. Even though SGES has huge potential to meet the future demand for heating and cooling of buildings, it might not be affordable to every individual who wants to install SGES due to its high installation cost. The focus of future studies should take into account the need to reduce the initial investment cost and increase energy efficiency. The SGES should be designed in such a way by reducing as much as possible the initial investment cost and lowering the payback period to encourage investors and end users to its promotion.

Governmental subsidy policies for the installation of SGES may help to raise the willingness of individuals towards using SGES. The value added tax (VAT) and other associated tax reductions in the equipment purchase and fee reduction on the license would be a good option for the promotion of SGES (Tinti et al., 2016). The investment cost is one of the crucial parameters along with other environmental parameters to the investors, government and individuals for the decision-making process of SGES. Further research regarding the use of SGES in hybrid systems, in combination with other renewable energy sources like solar energy and bioenergy may improve the efficiency and sustainability of the systems. Additionally, the use of SGES through structural elements in contact with the ground, such as retaining walls, pile foundations and tunnel linings (thermoactive geostructures) can be used as heat exchangers (Cherati & Ghasemi-Fare, 2021). When this combination is observed (SGES integrated in the structural elements), the extra costs observed in boreholes for example, were minimized, helping not to burden extra costs for the construction of infrastructures related to these systems. Furthermore, Sterpi et al. (2020) referred that there are improvements in the heat exchange rate due to the introduction of thermoactive geostructures, turning the system more efficient by reducing both costs of installation and exploration. SGES have the potential to reduce 65-85% of CO_2 emissions when compared to other fossil fuel systems (Ahmed et al., 2022). The cost associated with the reduction of CO_2 emissions by the use of SGES should be taken into account, that is a real concern of the world today (Hakkaki-Fard et al., 2015). The cost of CO_2 emission is more than just a monetary value and should be taken into consideration for the sustainable design of SGES.

3.2.4 Public awareness

Public awareness was also identified in the selected papers as one of the major obstacles to the promotion of SGES. The retrieved information is in a table format highlighting the main view of the authors about the issues related to awareness (see Table 6).

Issues related to public awareness were raised in 15% of the reviewed papers. Although SGES is recognized as an emerging technology for building heating and cooling to reduce carbon emissions, the concept of SGES was introduced only in 1969 and propagated around Europe after the 1980s (Zeng et al., 2021). However, technology has begun to spread around the world at the beginning of the 21st century (Eugster & Rybach, 2000).

As the SGES system is new compared to other clean energy sources, the degree of acceptability by society is relatively low (European Commission, 2014). The majority of the population is still dependent on fossil fuels and the projected scarcity of this non-renewable energy is not realized by the people that create the detrimental effects of using conventional energy (Cherati & Ghasemi-Fare, 2021). Additionally, most governments also did not put much effort into publicity, to achieve public acceptance of SGES (Zeng et al., 2021). The social factors and stakeholders' perceptions of SGES may affect the penetration of SGES widely (Tsagarakis, 2020). A small step towards legislation and procedural framework has been taken by some countries like Finland, Sweden and Germany (Tsagarakis et al., 2020). Besides that, the dissemination of information about SGES, its benefits and steps taken by governments for the promotion of SGES is essential for the fast development of SGES (Tsagarakis et al., 2020). According to Tinti et al. (2016),

Table 6. presentation of main views of authors about the awareness issue.

Reference	Main views of authors about awareness issue
Zeng et al. (2021)	The degree of societal approval is low.
Cherati & Ghasemi-Fare, 2021)	Society has not recognised the benefits of SGES due to a lack of awareness.
Hoekstra et al. (2020a)	Still short of expertise to design, construct and maintain the system. Also having inadequate analytical tools and cost data to assess the techno-economic potential of SGES.
Tsagarakis (2020)	Stakeholders' awareness and societal rejection issues may affect the propagation of the sustainable energy sector.
Tsagarakis et al. (2020)	To move forward on the effective development of SGES, an increase in awareness among the public and stakeholders is required.
Somogyi et al. (2017b)	The definition of SGES is different according to country. An information-sharing network among the countries to establish a common legal framework is required.
Tinti et al. (2016)	Training and up-skilling of technicians, contractors and engineers are necessary. The lack of specific knowledge and information about SGES is one of the hindrances to public acceptance.

not only the local authorities but also the technicians and engineers who recommend the SGES to their clients should be trained and upskilled. The lack of specific information and knowledge on what SGES can offer is a major drawback for the exploration of SGES.

It is interesting to know that in some countries like in the middle-east ones, where the price of the fossil fuel is low enough and freely available, the main obstacle to SGES is the social rejection of the new technology (Cherati & Ghasemi-Fare, 2021). Thus, the government could not create a sufficient environment to understand the benefits of clean energy like SGES to the public.

Moreover, the lack of locally available expertise to design, install and maintain SGES might hinder the installation plan. A lack of local expertise creates an environment that should rely on external experts and designers (Tinti et al., 2016). This may also create mistrust in the system when the system is not managed accurately. Pająk et al. (2016), also mentioned in their study that information campaigns are essential to increase awareness about the feasibility of SGES.

Though SGES is continuously available 24 hours per day, having enormous potential to provide reliable and sustainable energy for heating and cooling, this energy is not recognised by the public easily. For the geothermal sector, public perception and awareness about SGES is always a crucial element that the public is not as informed of what SGES has to contribute, compared to other renewable energy sources. Communication between the contractor, engineer, government, investor and public is paramount to obtain a good relationship among them to speed up the promotion of SGES. The governments should take the initiative to make people aware of the contribution of SGES to a sustainable environment. Awareness of the political decision-makers of this novel technology is also required (Goetzl et al., 2020).

3.2.5 Land availability

Only 6% of the reviewed papers addressed the land availability topic. However, land availability is a fundamental parameter that should be considered during SGES planning. In large and dense cities, where the value of land has rocketed high and limited free space is available, SGES with horizontal loop systems is undesirable (Tsagarakis, 2020), as they take significantly more space than SGES mainly composed of vertical borehole heat exchangers (Somogyi et al., 2017a).

The scarcity of land in the cities for the installation of SGES is a challenging task (Baralis & Barla, 2021) and must be taken into consideration. The land required for SGES installation varies according to the country's legislation (Tsagarakis et al., 2020). The drilling and trenches excavation for SGES may have some limitations to the legislation provisions (Stegnar et al., 2019). For instance, Greek law states that the excavation of trenches should be 2m away from the neighbouring property line, 10m away from gas distribution pipelines and 5m away from water and sewerage

lines (Tsagarakis et al., 2020). In turn, the Swiss standard recommends a minimum distance of 5m between energy piles to reduce the thermal interference among the energy piles and in consequence a variation of performance in terms of energy (Miglani et al., 2018). These types of provisions in the legislation demand a larger space requirement than the exact trench size.

Povilanskas et. al. (2013) mentioned that the landowner not only owns the land but also the space above and below the land in the city area that made the land expensive (Tsagarakis et al., 2020), which hinders the installation planning of SGES (Povilanskas et al., 2013). In horizontal loop systems, the pipes are laid horizontally at very shallow depths (1.5 to 2 m) because of the horizontal nature the space required is more than in other systems (Sarbu & Sebarchievici, 2014). Zhong et. al (2022) examined the thermal interference between piles, in fact, the larger the spacing of the piles the more reduced the thermal interference, which results in better heat performance (Zhong et al., 2022). This means, the installation of vertical borehole energy piles also demands space for installation. In a highly dense city area where the space availability is very low, installation of vertical boreholes is also difficult.

For vertical borehole systems, the minimum land requirement is 20 m^2 and for horizontal loop systems is 150 m^2 (FROnT, 2019). The land requirement might be affected by different factors like the geology of the land, demand for heat, the efficiency of heat pumps, etc. The extra land requirement for the installation can be reduced by installing a vertical borehole system within the foundation of the building during the construction of the building foundation. Accordingly, to overcome this barrier, combining energy piles with the structural elements of the infrastructures which are in connection with the ground like diaphragm walls, pile foundations and tunnel linings as a thermoactive geostructure help to reduce the extra land required for the construction of infrastructures related with SGES (Haehnlein et al., 2010).

3.2.6 Subsurface structures

One common barrier to the development of SGES is related to the unfamiliarity with the subsurface conditions (Hoekstra et al., 2020a). Issues related to subsurface structures were discussed in 6% of the reviewed papers. It is not easy to predict the situations beneath the ground (Pellegrini et al., 2019) since the cities have developed various networks of services beneath the ground over the years. Subsurface structures create significant barriers to the planning of SGES which has a negative impact on the licensing or authorization phase (Pellegrini et al., 2019). This barrier persists during the design phase and monitoring period also (Tsagarakis et al., 2020). The presence of a drinking water pipe network, sewer pipe network, and high voltage transmission system under the ground could be an important barrier to the drilling and installation of SGES. The different countries have their own

rule regarding the drilling distance from other structures or infrastructure (Somogyi et al., 2017a). Underground car parks, city metro lines and tunnel localization in the city area may affect the installation of vertical loop SGES (Ryżyński & Bogusz, 2016).

The presence of infrastructure networks and other structures present beneath the ground makes drilling difficult (Bertermann et al., 2018), which raises the cost of installation (Iba et al., 2018; Somogyi et al., 2017b). This affects the selection of SGES in that area. The process of subsurface data obtaining is often a difficult task that may create uncertainties about the exact subsurface geological conditions (Makasis et al., 2021).

3.2.7 Other barriers

The review identified that 4% of papers raised other issues which could potentially hinder the implementation of SGES like the complexity in application of the SGES (Tinti et al., 2016; Zeng et al., 2021) and 2% of papers mentioned the heating cooling efficiency of the systems (Zeng et al., 2021). According to Tinti et al. (2016) when the building needs energy application is different between thermal zones (not in the whole building or floor), this will bring complexity as the SGES system should be connected to the centralised heating system. This could also be a hindrance factor to the propagation of SGES to a massive extent. Zeng et al. (2021) mentioned the issue of low heat transfer rate (low heating and cooling efficiency). The heating and cooling rates are sometimes unsatisfactory and should be optimised by combining with additional types of renewable energy systems.

In addition, the lack of knowledge on the long-term performance of SGES makes the investors and end users rethink the decision to invest. Continuous extraction of heat from the ground may cause the cooling of the ground and unexpected disturbances on the system with a negative effect on the sustainability of SGES (Miglani et al., 2018). As a consequence, the balance between the heating and the cooling building demands will be affected (Cunha & Bourne-Webb, 2022).

In the case of buildings or spaces with an unbalanced demand, the thermal behaviour of the ground affects more significantly the evolution in time of the whole building's energy performance. This represents another key decision factor actuating as a barrier to the installation of SGES. Consequently, another hybrid system should be adopted to meet the unbalanced demand and influence the overall interest in using SGES due to the increased costs of having a hybrid system.

4. Conclusions

This paper presents the main barriers to the implementation of shallow geothermal energy systems (SGES) identified through a systematic review of scientific papers published in Scopus and Web of Science (WoS) core collection. The review of the literature concerns rigorous information regarding the barriers to shallow geothermal energy systems implementation. There are six main and some other general decelerating factors for the promotion of SGES identified. Almost all studies show that there is still a low rate of contribution of SGES in the renewable energy sector. However, it is recognized that there is a huge potential to extract heat from the ground to meet the growing demand for heating and cooling sustainably. In addition, the majority of the papers raised issues of the legislation as a barrier that needs to be solved. Standardization of the framework governing the SGES exploration is a common issue among nations. In the same way, the majority of papers mentioned the high initial investment cost for the installation of SGES, which is also an aspect of public concern. Moreover, issues with little knowledge of the thermal conductivity of underground materials, availability of land, subsurface structure and awareness of the public are the main hindrance factors to the promotion of SGES discussed in the papers. The focus on the identification of the barriers permits establishing and planning decisive action measures to overcome these hurdles and move forward and support the exploration of shallow geothermal energy systems.

Acknowledgements

Declaration of interest

The authors have no conflicts of interest to declare. All co-authors have observed and affirmed the contents of the paper and there is no financial interest to report.

Authors' contributions

Rajendra Babu Roka: conceptualisation, methodology, visualization, writing – original draft. António José Pereira de Figueiredo: conceptualisation, methodology, writing – review & editing, supervision. Ana Maria Carvalho Pinheiro Vieira: writing – review & editing, supervision. José Claudino de Pinho Cardoso: writing – review & editing, supervision.

Data availability

The authors declare that all data generated or analysed during this study appear in the published article.

References

Ahmed, A.A., Assadi, M., Kalantar, A., Sliwa, T., & Sapińska-śliwa, A. (2022). A critical review on the use of shallow geothermal energy systems for heating and

cooling purposes. *Energies*, 15(12), 4281. http://dx.doi.org/10.3390/en15124281.

Aljundi, K., Vieira, A., Maranha, J., Lapa, J., & Cardoso, R. (2020). Effects of temperature, test duration and heat flux in thermal conductivity measurements under transient conditions in dry and fully saturated states. E3S Web of Conferences, 195, 04007. http://dx.doi.org/10.1051/e3sconf/202019504007.

Assouline, D., Mohajeri, N., Gudmundsson, A., & Scartezzini, J.-L. (2019). A machine learning approach for mapping the very shallow theoretical geothermal potential. *Geothermal Energy*, 7(1), 19. http://dx.doi.org/10.1186/s40517-019-0135-6.

Baralis, M., & Barla, M. (2021). Development and testing of a novel geothermal wall system. *International Journal of Energy and Environmental Engineering*, 12(4), 689-704. http://dx.doi.org/10.1007/s40095-021-00407-y.

Bertermann, D., Bernardi, A., Pockelé, L., Galgaro, A., Cultrera, M., de Carli, M., & Müller, J. (2018). European project "Cheap-GSHPs": installation and monitoring of newly designed helicoidal ground source heat exchanger on the German test site. *Environmental Earth Sciences*, 77(5), 180. http://dx.doi.org/10.1007/s12665-018-7343-4.

Cecinato, F., & Salciarini, D. (2022). Energy performance assessment of thermo-active micro-piles via numerical modeling and statistical analysis. *Geomechanics for Energy and the Environment*, 29, 100268. http://dx.doi.org/10.1016/j.gete.2021.100268.

Cetin, A., Kadioglu, Y.K., & Paksoy, H. (2020). Underground thermal heat storage and ground source heat pump activities in Turkey. *Solar Energy*, 200, 22-28. http://dx.doi.org/10.1016/j.solener.2018.12.055.

Cherati, D.Y., & Ghasemi-Fare, O. (2021). Practical approaches for implementation of energy piles in Iran based on the lessons learned from the developed countries experiences. *Renewable & Sustainable Energy Reviews*, 140, 110748. http://dx.doi.org/10.1016/j.rser.2021.110748.

Christodoulides, P., Vieira, A., Lenart, S., Maranha, J., Vidmar, G., Popov, R., Georgiev, A., Aresti, L., & Florides, G. (2020). Reviewing the modeling aspects and practices of shallow geothermal energy systems. *Energies*, 13(16), 4273.

Cui, Y., Zhu, J., & Meng, F. (2018). Techno-economic evaluation of multiple energy piles for a ground-coupled heat pump system. *Energy Conversion and Management*, 178, 200-216. http://dx.doi.org/10.1016/j.enconman.2018.10.042.

Cunha, R.P., & Bourne-Webb, P.J. (2022). A critical review on the current knowledge of geothermal energy piles to sustainably climatize buildings. *Renewable & Sustainable Energy Reviews*, 158, 112072. http://dx.doi.org/10.1016/j.rser.2022.112072.

Eugster, W., & Rybach, L. (2000). Sustainable production from borehole heat exchanger systems. In *Proceedings World Geothermal Congress 2000* (pp. 825-830), Tohoku, Japan. Retrieved in February 3, 2022, from http://www.geothermal-energy.org/pdf/IGAstandard/WGC/2000/R0103.PDF

European Commission (2014). *Guide to cost-benefit analysis of investment projects: economic appraisal tool for cohesion policy 2014-2020.* Luxembourg: Office of the European Union.

European Commission. Eurostat. Statistics Explained. (2022). *Renewable energy statistics.* Retrieved in June 8, 2022, from https://ec.europa.eu/eurostat/statistics-explained/index.php?title=Renewable_energy_statistics#Over_one_fifth_of_energy_used_for_heating_and_cooling_from_renewable_sources

European Geothermal Energy Council – EGEC. (2022). *Regeocities.* Retrieved in February 3, 2022, from https://www.egec.org/research-projects/regeocities/

Figueiredo, A., Lapa, J., Cardoso, C., Macedo, J., Rodrigues, F., Vieira, A., Pinto, A., & Maranha, J.R. (2019). Shallow geothermal systems for Aveiro University departments: a survey through the energy efficiency and thermal comfort. In H. Sigursteinsson, S. Erlingsson & B. Bessason (Eds.), *17th European Conference on Soil Mechanics and Geotechnical Engineering* (pp. 1-8). Reykjavík, Iceland: The Icelandic Geotechnical Society. https://doi.org/10.32075/17ECSMGE-2019-0583.

Florence, J., Angelino, L., Annunziata, E., van Beek, D., Benson, J., Bezelgues, S., Croufer, M., Cucueteanu, D., Cuevas, J., Frey, M., Godschalk, B., Goumas, A., Jardeby, Å., Nielsen, A.M., Pasquali, R., Poux, A., Räftegård, O., Rizzi, F., & Sanner, B. (2013). *Overview of shallow geothermal legislation in Europe. D2.2 General report of the current situation of the regulative framework for the SGE systems.* Retrieved in October 22, 2022, from http://regeocities.eu/wp-content/uploads/2012/12/D2.2.pdf

Freeston, D.H. (1996). Direct uses of geothermal energy 1995. *Geothermics*, 25(2), 189-214. http://dx.doi.org/10.1016/0375-6505(95)00051-8.

FROnT. (2019). *Geothermal heat pumps: the heat under your feet* (pp. 1-2). European Union.

García-Gil, A., Goetzl, G., Kłonowski, M.R., Borovic, S., Boon, D.P., Abesser, C., Janza, M., Herms, I., Petitclerc, E., Erlström, M., Holecek, J., Hunter, T., Vandeweijer, V.P., Cernak, R., Mejías Moreno, M., & Epting, J. (2020). Governance of shallow geothermal energy resources. *Energy Policy*, 138, 111283. http://dx.doi.org/10.1016/j.enpol.2020.111283.

García-Gil, A., Vázquez-Suñe, E., Schneider, E.G., Sánchez-Navarro, J.Á., & Mateo-Lázaro, J. (2015). Relaxation factor for geothermal use development: criteria for a more fair and sustainable geothermal use of shallow energy resources. *Geothermics*, 56, 128-137. http://dx.doi.org/10.1016/j.geothermics.2015.04.003.

Gemelli, A., Mancini, A., & Longhi, S. (2011). GIS-based energy-economic model of low temperature geothermal resources: a case study in the Italian Marche region. *Renewable Energy*, 36(9), 2474-2483. http://dx.doi.org/10.1016/j.renene.2011.02.014.

Geo Power Group. (2022). *About us.* Retrieved in February 3, 2022, from https://www.geopowergroup.com/about-us/

GeoTrainet. (2022). *About GeoTrainet.* Retrieved in February 3, 2022, from https://geotrainet.eu/about-geotrainet/

12

Roka et al., Soil. Rocks, São Paulo, 2023 46(1):e2023007622

Goetzl, G., Dilger, G., Grimm, R., Hofmann, K., Holecek, J., Cernak, R., Janza, M., Kozdrój, W., Kłonowski, M., Hajto, M., Gabriel, P., & Gregorin, S. (2020). Strategies for fostering the use of shallow geothermal energy for heating and cooling in Central Europe: results from the Interreg Central Europe Project GeoPLASMA-CE. In *Proceedings World Geothermal Congress 2020*, Reykjavik, Iceland. http://dx.doi.org/10.6084/m9.figshare.13256465.

Ground Med. (2022). *Project summary.* Retrieved in February 3, 2022, from http://groundmed.eu/about_ground_med/

Haehnlein, S., Bayer, P., & Blum, P. (2010). International legal status of the use of shallow geothermal energy. *Renewable & Sustainable Energy Reviews*, 14(9), 2611-2625.

Hakkaki-Fard, A., Eslami-Nejad, P., Aidoun, Z., & Ouzzane, M. (2015). A techno-economic comparison of a direct expansion ground-source and an air-source heat pump system in Canadian cold climates. *Energy*, 87, 49-59. http://dx.doi.org/10.1016/j.energy.2015.04.093.

Hoekstra, N., Pellegrini, M., Bloemendal, M., Spaak, G., Andreu Gallego, A., Rodriguez Comins, J., Grotenhuis, T., Picone, S., Murrell, A.J., Steeman, H.J., Verrone, A., Doornenbal, P., Christophersen, M., Bennedsen, L., Henssen, M., Moinier, S., & Saccani, C. (2020a). Increasing market opportunities for renewable energy technologies with innovations in aquifer thermal energy storage. *The Science of the Total Environment*, 709, 136142. http://dx.doi.org/10.1016/j.scitotenv.2019.136142.

Hoekstra, N., Pellegrini, M., Bloemendal, M., Spaak, G., Andreu Gallego, A., Rodriguez Comins, J., Grotenhuis, T., Picone, S., Murrell, A.J., Steeman, H.J., Verrone, A., Doornenbal, P., Christophersen, M., Bennedsen, L., Henssen, M., Moinier, S., & Saccani, C. (2020b). Increasing market opportunities for renewable energy technologies with innovations in aquifer thermal energy storage. *The Science of the Total Environment*, 709, 136142. http://dx.doi.org/10.1016/j.scitotenv.2019.136142.

Hughes, B.R., Chaudhry, H.N., & Ghani, S.A. (2011). A review of sustainable cooling technologies in buildings. *Renewable & Sustainable Energy Reviews*, 15(6), 3112-3120. http://dx.doi.org/10.1016/j.rser.2011.03.032.

Iba, C., Takano, S., & Hokoi, S. (2018). An experiment on heat recovery performance improvements in well-water heat-pump systems for a traditional Japanese house. *Energies*, 11(5), 1023. http://dx.doi.org/10.3390/en11051023.

International Renewable Energy Agency – IRENA. (2017). *Renewable energy in district heating and cooling: a sector roadmap for REmap*. Abu Dhabi: IRENA.

International Renewable Energy Agency – IRENA. (2020). *Renewable power generation costs in 2020.* Retrieved in February 3, 2022, from https://www.irena.org/-/media/Files/IRENA/Agency/Publication/2018/Jan/IRENA_2017_Power_Costs_2018.pdf

Janža, M., Lapanje, A., Šram, D., Rajver, D., & Novak, M. (2017). Research of the geological and geothermal conditions for the assessment of the shallow geothermal potential in the area of Ljubljana, Slovenia. *Geologija*, 60(2), 309-327. http://dx.doi.org/10.5474/geologija.2017.022.

Li, M., Zhang, L., & Liu, G. (2019). Estimation of thermal properties of soil and backfilling material from thermal response tests (TRTs) for exploiting shallow geothermal energy: sensitivity, identifiability, and uncertainty. *Renewable Energy*, 132, 1263-1270. http://dx.doi.org/10.1016/j.renene.2018.09.022.

Makasis, N., Kreitmair, M.J., Bidarmaghz, A., Farr, G.J., Scheidegger, J.M., & Choudhary, R. (2021). Impact of simplifications on numerical modelling of the shallow subsurface at city-scale and implications for shallow geothermal potential. *The Science of the Total Environment*, 791, 148236. http://dx.doi.org/10.1016/j.scitotenv.2021.148236.

Miglani, S., Orehounig, K., & Carmeliet, J. (2018). A methodology to calculate long-term shallow geothermal energy potential for an urban neighbourhood. *Energy and Building*, 159, 462-473. http://dx.doi.org/10.1016/j.enbuild.2017.10.100.

Müller, J., Galgaro, A., Dalla Santa, G., Cultrera, M., Karytsas, C., Mendrinos, D., Pera, S., Perego, R., O'Neill, N., Pasquali, R., Vercruysse, J., Rossi, L., Bernardi, A., & Bertermann, D. (2018). Generalized pan-european geological database for shallow geothermal installations. *Geosciences*, 8(1), 32. http://dx.doi.org/10.3390/geosciences8010032.

National Energy Authority – NEA. (2015). *Geothermal policy options and instruments for the Andean region: based on Icelandic and International Geothermal Experience.* Iceland.

Nowamooz, H., Nikoosokhan, S., & Chazallon, C. (2016). Seasonal thermal energy storage in shallow geothermal systems: thermal equilibrium stage. *E3S Web of Conferences*, 9, 07003. https://doi.org/10.1051/E3SCONF/20160907003.

Nunes, J.C., Coelho, L., Carvalho, J.M., Do, M., Carvalho, R., & Garcia, J. (2019). Geothermal Energy Use, Country Update for Portugal. In *European Geothermal Congress 2019* (pp. 11-14), Den Haag, The Netherlands.

Ondreka, J., Rüsgen, M.I., Stober, I., & Czurda, K. (2007). GIS-supported mapping of shallow geothermal potential of representative areas in south-western Germany-Possibilities and limitations. *Renewable Energy*, 32(13), 2186-2200. http://dx.doi.org/10.1016/j.renene.2006.11.009.

Pająk, L., Kępińska, B., Kasztelewicz, A., Bujakowski, W., Tomaszewska, B., & Grażyna, H. (2016). Some factors detrmining the geothermal energy uses' development in the Central and Eastern European countries in coming years. *Zeszyty Naukowe*, 92, 337-358. Retrieved in October 22, 2022, from https://meeri.eu/Wydawnictwa/ZN92/pajak-i-inni.pdf

Pellegrini, M., Bianchini, A., Guzzini, A., & Saccani, C. (2019). Classification through analytic hierarchy process of the barriers in the revamping of traditional district heating networks into low temperature district heating: an Italian case study. *International Journal of Sustainable Energy Planning and Management*, 20, 51-66. http://dx.doi.org/10.5278/ijsepm.2019.20.5.

Povilanskas, R., Satkūnas, J., & Jurkus, E. (2013). Conditions for deep geothermal energy utilisation in southwest Latvia:

nīca case study. *Baltica*, 26(2), 193-200. http://dx.doi.org/10.5200/baltica.2013.26.20.

Ramos-Escudero, A., García-Cascales, M.S., & Urchueguía, J.F. (2021). Evaluation of the shallow geothermal potential for heating and cooling and its integration in the socioeconomic environment: a case study in the region of murcia, spain. *Energies*, 14(18), 5740. http://dx.doi.org/10.3390/en14185740.

Ryżyński, G., & Bogusz, W. (2016). City-scale perspective for thermoactive structures in Warsaw. *Environmental Geotechnics*, 3(4), 280-290. http://dx.doi.org/10.1680/jenge.15.00031.

Saner, D., Juraske, R., Kübert, M., Blum, P., Hellweg, S., & Bayer, P. (2010). Is it only CO2 that matters? A life cycle perspective on shallow geothermal systems. *Renewable & Sustainable Energy Reviews*, 14(7), 1798-1813. http://dx.doi.org/10.1016/j.rser.2010.04.002.

Sanner, B. (2016). Shallow geothermal energy-history, development, current status, and future prospects. In *European Geothermal Congress* (pp. 19-24), Strasbourg, France.

Sarbu, I., & Sebarchievici, C. (2014). General review of ground-source heat pump systems for heating and cooling of buildings. *Energy and Building*, 70, 441-454. http://dx.doi.org/10.1016/j.enbuild.2013.11.068.

Schelenz, S., Vienken, T., Shao, H., Firmbach, L., & Dietrich, P. (2017). On the importance of a coordinated site characterization for the sustainable intensive thermal use of the shallow subsurface in urban areas: a case study. *Environmental Earth Sciences*, 76(2), 73.

Somogyi, V., Sebestyén, V., & Nagy, G. (2017a). Scientific achievements and regulation of shallow geothermal systems in six European countries: a review. *Renewable & Sustainable Energy Reviews*, 68, 934-952. http://dx.doi.org/10.1016/j.rser.2016.02.014.

Somogyi, V., Sebestyén, V., & Nagy, G. (2017b). Scientific achievements and regulation of shallow geothermal systems in six European countries: a review. *Renewable & Sustainable Energy Reviews*, 68, 934-952. http://dx.doi.org/10.1016/j.rser.2016.02.014.

Stegnar, G., Staničić, D., Česen, M., Čižman, J., Pestotnik, S., Prestor, J., Urbančič, A., & Merše, S. (2019). A framework for assessing the technical and economic potential of shallow geothermal energy in individual and district heating systems: a case study of Slovenia. *Energy*, 180, 405-420. http://dx.doi.org/10.1016/j.energy.2019.05.121.

Sterpi, D., Tomaselli, G., & Angelotti, A. (2020). Energy performance of ground heat exchangers embedded in diaphragm walls: field observations and optimization by numerical modelling. *Renewable Energy*, 147, 2748-2760. https://doi.org/10.1016/J.RENENE.2018.11.102.

Tinti, F., Carri, A., Kasmaee, S., Valletta, A., Segalini, A., Bonduà, S., & Bortolotti, V. (2018). Ground temperature monitoring for a coaxial geothermal heat exchangers field: practical aspects and main issues from the first year of measurements. *Rudarsko-Geološko-Naftni Zbornik*, 33(5), 47-57. http://dx.doi.org/10.17794/rgn.2018.5.5.

Tinti, F., Pangallo, A., Berneschi, M., Tosoni, D., Rajver, D., Pestotnik, S., Jovanović, D., Rudinica, T., Jelisić, S., Zlokapa, B., Raimondi, A., Tollari, F., Zamagni, A., Chiavetta, C., Collins, J., Chieco, M., Mercurio, A., Marcellini, F., Mrvaljević, D., & Meggiolaro, M. (2016). How to boost shallow geothermal energy exploitation in the adriatic area: the LEGEND project experience. *Energy Policy*, 92, 190-204. http://dx.doi.org/10.1016/j.enpol.2016.01.041.

Tsagarakis, K.P. (2020). Shallow geothermal energy under the microscope: Social, economic, and institutional aspects. *Renewable Energy*, 147, 2801-2808. http://dx.doi.org/10.1016/j.renene.2019.01.004.

Tsagarakis, K.P., Efthymiou, L., Michopoulos, A., Mavragani, A., Anđelković, A.S., Antolini, F., Bacic, M., Bajare, D., Baralis, M., Bogusz, W., Burlon, S., Figueira, J., Genç, M.S., Javed, S., Jurelionis, A., Koca, K., Ryżyński, G., Urchueguia, J.F., & Žlender, B. (2020). A review of the legal framework in shallow geothermal energy in selected European countries: need for guidelines. *Renewable Energy*, 147, 2556-2571. http://dx.doi.org/10.1016/j.renene.2018.10.007.

Vieira, A., Maranha, J.R., Lapa, J., & Figueiredo, A. (2019). Some aspects of measurement of sand thermal conductivity from laboratory tests. In *Proceedings of the XVII ECSMGE-2019*, Reykjavík, Iceland. http://dx.doi.org/10.32075/17ECSMGE-2019-0541.

Wang, G.L., Zhang, W., Liang, J.Y., Lin, W.J., Liu, Z.M., & Wang, W.L. (2017). Evaluation of geothermal resources potential in China. *Acta Geoscientica Sinica*, 38(4), 449-459. http://dx.doi.org/10.3975/CAGSB.2017.04.02.

Witte, H.J.L., Van Gelder, G.J., & Spitler, J.D. (2002). In situ measurement of ground thermal conductivity: a dutch perspective. *ASHRAE Transactions*, 108(Pt 1), 263-272.

Yang, L., Yan, H., & Lam, J.C. (2014). Thermal comfort and building energy consumption implications: a review. *Applied Energy*, 115, 164-173. http://dx.doi.org/10.1016/j.apenergy.2013.10.062.

Zeng, S., Yan, Z., & Yang, J. (2021). Review and forecast of ground heat exchangers development: a bibliometric analysis from 2001 to 2020. *Sustainable Energy Technologies and Assessments*, 47, 101547. http://dx.doi.org/10.1016/j.seta.2021.101547.

Zhang, W., Bai, R., Xu, X., & Liu, W. (2021). An evaluation of soil thermal conductivity models based on the porosity and degree of saturation and a proposal of a new improved model. *International Communications in Heat and Mass Transfer*, 129, 105738. http://dx.doi.org/10.1016/j.icheatmasstransfer.2021.105738.

Zhong, Y., Narsilio, G.A., Makasis, N., & Scott, C. (2022). Experimental and numerical studies on an energy piled wall: the effect of thermally activated pile spacing. *Geomechanics for Energy and the Environment*, 29, 100276. http://dx.doi.org/10.1016/j.gete.2021.100276.

Ground improvement techniques applied to very soft clays: state of knowledge and recent advances

Marcio de Souza Soares de Almeida[1] (ID), Maria Esther Soares Marques[2] (ID), Mario Riccio[3#] (ID),
Diego de Freitas Fagundes[4] (ID), Bruno Teixeira Lima[5,6] (ID), Uberescilas Fernandes Polido[7] (ID),
Alessandro Cirone[8] (ID), Iman Hosseinpour[9] (ID)

Review Article

Abstract

Soft ground improvement techniques have evolved substantially in Brazil in recent years. However, their application in soft and very soft clays requires a good understanding of the fundamentals of ground improvement techniques suited to the problem as well as the actual field behavior when implemented on a real scale. This paper describes some of the most widely used ground improvement techniques in the context of very soft clays in Brazil. The techniques described in the paper use prefabricated vertical drains (PVD) such as vacuum preloading; or combine PVD and rigid inclusion, such as CPR grouting; or are purely column-like elements such as piled embankments (including those executed with the deep mixing technique, *DSM*); or combine column-like elements with the drainage function, such as stone columns and geosynthetic encased columns; or use cementitious binders such as shallow soil mixing. The paper reference condition is a soft clay foundation in which no strengthening is implemented, such as, an embankment with basal reinforcement or soft clay with vertical prefabricated drains, or the use of vacuum preloading to speed up the consolidation rate. The applications of the ground improvement techniques are illustrated by case histories, numerical analyses, or physical models. Different types of measurements are used to evaluate the performance of each technique, including settlements, horizontal displacements, excess pore pressures, embankment applied stresses, stress concentration factors, and clay strength following the ground treatment. The settlement improvement factor β, the ratio between the settlements for untreated and treated conditions, is shown to be a suitable parameter to assess the degree of improvement imposed in the soft foundation by ranking the various methods in increased order of strengthening effect.

1. Introduction

Soft soils may require the construction of an embankment in stages, which may lengthen the overall construction time excessively even when prefabricated vertical drains (*PVD*) are used to accelerate settlements (Almeida et al., 2008). In the case of very soft soils, basal geosynthetic reinforcement and lateral berms may also be necessary in order to maintain stability.

A possible design constraint is that post-construction residual (secondary) settlements must be negligible. However,

achieving this goal requires a greater embankment thickness so that secondary settlements occur in the form of primary settlements during construction.

Large fill volumes can make the technique of staged construction with *PVDs* and reinforcement unfeasible, especially in the case of very thick compressible layers. In order to overcome these issues, the embankment may be supported by column-like elements (Almeida & Marques, 2013) or the soft ground may be improved by cementitious binders (e.g., Lemos et al., 2020). The present article discusses these ground improvement techniques as carried out in Brazil over

#Corresponding author. E-mail address: mvrf1000@gmail.com
[1]Universidade Federal do Rio de Janeiro, Civil Engineering Program, Rio de Janeiro, RJ, Brasil.
[2]Instituto Militar de Engenharia, Fortification and Construction Department, Rio de Janeiro, RJ, Brasil.
[3]Universidade Federal de Juiz de Fora, Graduate School of Civil Engineering, Juiz de Fora, MG, Brasil.
[4]Universidade Federal do Rio Grande, School of Engineering, Rio Grande, RS, Brasil.
[5]Universidade do Estado do Rio de Janeiro, RJ, Brasil.
[6]Universidade Federal Fluminense, Niteroi, RJ, Brasil.
[7]GEOCONSULT, Vitória, ES, Brasil.
[8]Pontifícia Universidade Católica do Rio de Janeiro, Department of Civil and Environmental Engineering, Rio de Janeiro, RJ, Brasil.
[9]University of Guilan, Faculty of Engineering, Civil Engineering Department, Rasht, Guilan, Iran.

the last decade by presenting representative field case studies, complemented by physical and numerical modeling studies. The topics covered by this paper reflect basically the work of researchers at *COPPE-UFRJ*, including collaborations with authors from other institutions. The article is an updated written version of the Keynote Lecture presented at the *XVI PCSMGE 2019* (Almeida, 2019) which in turn was based on the 2015 Coulomb Lecture (Almeida, 2015).

2. Background

Very soft clay soils may be characterized by the number of blow counts, measured by the standard penetration test, N_{SPT} lower than 2, undrained strength S_u lower than 20 kPa, and point resistance q_c lower than 1 MPa. These soils are found in many parts of the world as well as along the Brazilian coast where the case histories presented in this paper are located.

Data from sites located to the west of the city of Rio de Janeiro (Baroni & Almeida, 2017, 2022) is presented in the plasticity chart in Figure 1. This chart shows that the range of liquid limit w_L and plasticity index *PI* values for these sites is far greater than those found in classic text books.

Figure 2 presents data from a stage-constructed embankment with *PVDs*, reinforcement and berms built on an extremely soft clay deposit located west of Rio de Janeiro City. The "as built" line shows that the embankment reached a total height of about 6 m with settlements of around 2.5 m over a period of 20 months. Therefore, the net embankment height is just over 3 m, even though 6 m of fill have been applied. As such large volumes of fill and long construction times are not always feasible in practice, other soft ground improvement techniques have been developed to overcome these issues

Figure 3 compares the normalized embankment stress q versus normalized δ settlement curves for the ground improvement techniques discussed in this paper, where S_u is the average undrained clay strength, *H* is the embankment height, and 5 and 3 shown in the horizontal axis indicate limit state and serviceability state conditions respectively for the unreinforced embankment.

The curves presented in Figure 3 show that the efficiency of the ground treatment method increases (greater loads with less settlement) as its foundation is reinforced or becomes stiffer, either by column-like elements or by adding cementitious binders to the soft soil. As shown in Figure 3, the basal geosynthetic reinforcement procedure is often included in all column-like techniques as it allows better load transfer to the column, in addition to improving stability. The basal reinforcement is indicated by dashed lines under the embankments.

In the following sections of the paper the ground improvement techniques presented in Figure 3 are analyzed. First, the unreinforced embankment (*UE*) built on soft soil, associated with the use of vacuum preloading (vacuum consolidation) to accelerate settlements, is presented as the
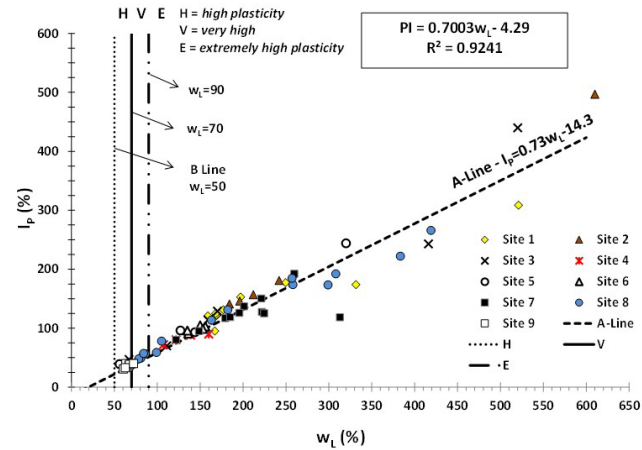
Figure 1. Plasticity chart data for 9 sites west of the city of Rio de Janeiro (Baroni &Almeida, 2017).
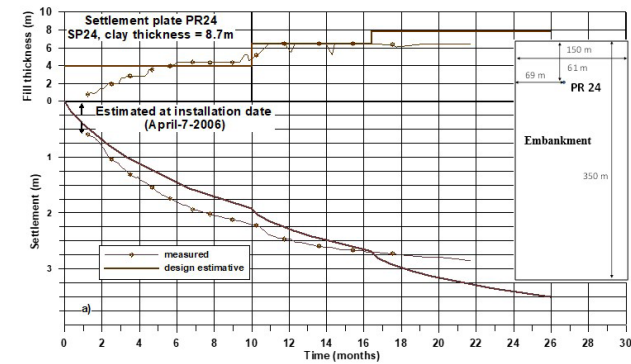
Figure 2. Stage-constructed embankment with *PVDs*, reinforcement and berms on an extremely soft soil (Almeida et al., 2008).
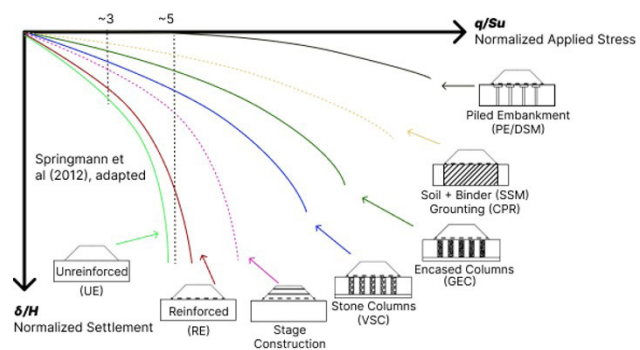

Figure 3. Normalized embankment stresses versus normalized settlements for different ground improvement techniques (adapted from Springman et al., 2012).

reference technique. Then, two techniques using granular columns are discussed: the stone column with vibro replacement (*VSC*), and the geosynthetic encased granular column (*GEC*), which includes a comparison between the GEC with a reinforced embankment (*RE*). The next section

describes the more efficient piled embankment method (*PE*), a column-like alternative in which piles may be driven or executed in situ by means of the deep soil mixing technique (*DSM*), which is also briefly explained. The last three sections of the paper elaborate on three ground improvement techniques that incorporate a cementitious binder, including shallow soil mixing (*SSM*), *CPR* grouting, and the aforementioned *DSM* technique.

An important parameter used in the paper is the settlement improvement factor β proposed by Priebe (1995) for the design of granular stone columns executed by vibro substitution. The parameter β is defined by the ratio between the unimproved soil settlement Δh and the settlements of the soil-column system Δh_c.

$$\beta = \frac{\Delta h}{\Delta h_c} \qquad (1)$$

The concept of settlement improvement factor, is expanded here to be applied to other ground improvement techniques as well and results will be summarized in a final section.

3. Vacuum preloading

The vacuum consolidation technique for soft soil improvement, although idealized by Kjellman (1952) in the 1950s, was used more broadly worldwide only in the 1980s to enable preloading in compressible soils. The method involves applying a vacuum to a clay deposit by means of a pumping system in association with grids of drains. Its application reduces pore pressure related to the atmospheric pressure (≈100 kPa), promoting radial flow, increasing effective stress and accelerating settlement over time.

3.1 Membrane and drain-to-drain techniques

The vacuum consolidation technique was first designed with an airtight membrane and later without the membrane, in a system called drain-to-drain method (Figure 4).

In the vacuum system with membrane, water and air are pumped inside a pump container where pressure is close to -1 atm (Figure 4a). The vacuum pressure is applied to the horizontal drains and the sand layer (encapsulated by an impervious membrane) and thus at the top of vertical drains (*PVDs*). The membrane is stretched until it reaches the water table inside the peripheral trench, thus confining the vacuum inside the soil mass (Marques & Leroueil, 2015). The vacuum is usually measured under the membrane and during vacuum preloading, a conventional embankment can be built to accelerate settlements after the air-tightness of the membrane has been confirmed.

Drain-to-drain vacuum preloading consists of applying suction inside the soft soil layer by *PVDs* linked to a pump system by airtight collector tubes (Figure 4b) (Freitas, 2021;

Cardoso, 2021). In this case, the collectors are installed in lieu of the membrane and horizontal drains, and the *PVDs* are connected to the collectors as shown in detail in Figure 4c. A conventional fill can be carefully constructed above the connectors and collector tubes after the air-tightness of the system has been checked.

Both methods have advantages and disadvantages: the main disadvantage of vacuum system with membrane is in case of sandy layer inside the soft soil deposit, which would lower the efficiency, and for the drain-to-drain is the low efficiency usually observed in field.

The number of pumps used for vacuum preloading depends on the area size and site conditions, and drain spacing is designed to consolidate the clay deposit within a four- to six-month period. Once the proposed degree of consolidation has been achieved, the pumping is stopped and the fill height can be increased to final grade, without pos-construction settlements.

The efficiency of the vacuum system with membrane is determined by the pressure applied to the deposit related to the atmospheric pressure of about 100 kPa. Thus, considering a system efficiency of 70 to 75%, the load applied by vacuum corresponds to a stress increase of about 70 - 75 kPa, approximately the load of a 4 m high embankment applied in a single step.

In the drain-to-drain system, when there is loss of suction, it is faster to repair a vacuum line due to damage, since the vertical drains are connected in lines independent of each other and the rest of the system continues to run without interruption. However, the main disadvantage of the drain-to-drain system is the connections, where leakage can occur. Also, during the consolidation process, excessive deformations can occur, so the horizontal pipes can suffer damage and interrupt the vacuum supply to the *PVDs*. Therefore, it is necessary to leave a slack in the length of the pipes.
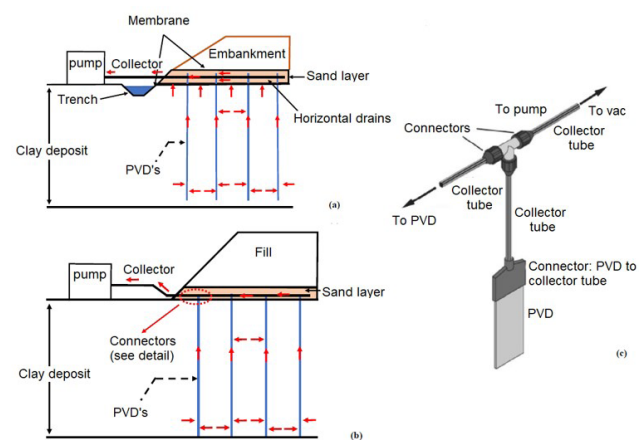

Figure 4. Vacuum consolidation technique: (a) with membrane (b) drain-to-drain (membraneless) (c) detail of connectors in the drain to drain configuration (adapted from Freitas, 2021).

While efficiency of a membrane system can be 70-75% (Marques & Leroueil, 2015), the efficiency of the drain-to-drain method is lower. López-Acosta et al. (2019), when using pressure gauges at the end of the drain-to-drain line at a site in Mexico, reported a loss of vacuum along the horizontal pipes in the order of 30%, which is equivalent to 40 to 50 kPa of pressure. The leakage associated with the drain-to-drain method is a well-known disadvantage.

New forms of vacuum application, such as the dehydration of fluid materials, have also been used in hydraulic landfills and/or soft soils on the seabed in offshore conditions (Harvey, 1997).

3.2 Vacuum preloading test and horizontal displacements

A full-scale vacuum preloading test was performed for an embankment construction on a Canadian structured clay deposit at Saint-Roch-de-l'Achingan (Marques & Leroueil,

2015) presented in Figure 5a. A plane strain finite element analysis was carried out (Almeida et al. 2021) in which the structured soft clay behavior was simulated with the *S-CLAY1S* constitutive model, but also with the Modified Cam-clay model. It is worth presenting in particular the numerical and measured results of horizontal displacements (see Figure 5b) for points *B* and *C* at inclinometer *IA1*. The numerical values ranged from 0.01 m to -0.04 m and field measurements indicated zero horizontal displacements. Therefore, numerical calculations and observed values of horizontal displacements are quite small and overall, in good agreement. The applied load was about 60% vacuum and 40% embankment loading which, according to the literature (Indraratna, 2010), results in negligible horizontal displacements, consistent with the present observed values. Settlements at the axis of the embankments were about 0.26 m stabilized around 5 months were in good agreement with numerical calculations using the *S-CLAY1S* model but were overpredicted by the Modified Cam-clay model.

Figure 5. (a) Saint-Roch-de-l'Achigan embankment test cross section and instrumentation. (Marques & Leroueil, 2015); (b) Variation over time for vacuum pressure, embankment thickness and horizontal displacements U_x (field and numerical values) at points *B* and *C* at inclinometer *IA1* (Almeida et al. 2021).

Legend: SP = settlement plates; SG = tassometer; IA = inclinometer; UA = piezometer.

3.3 Advantages and disadvantages of the vacuum preloading

The vacuum preloading technique is widely used worldwide and has shown excellent results when applied to the improvement of soft soils, in order to reach a shorter deadline, lower fill volumes, and smaller horizontal displacements (Choa, 1989; Qian et al., 1992; Jacob et al., 1994; Rujikiatkamjorn et al., 2007; Marques & Leroueil, 2015; Zheng et al., 2017; Chai et al., 2013; Almeida et al., 2021). This section presents advantages and disadvantages of the vacuum preloading method applied to both membrane and drain-to-drain techniques.

The advantages of vacuum preloading when compared with a conventional embankment over soft soils are (Marques & Leroueil, 2015; López-Acosta et al., 2019):

- The applied vacuum load is unaffected by submersion, although the conventional fill associated with the vacuum system can be submerged, depending on settlement values;
- Earthwork volumes are lower: no berm or backfill material is required to provide preloading;
- Horizontal displacements are much smaller than those of a conventional fill, as exemplified in Figure 5b;
- Unlike traditional embankment loading, vacuum application does not cause rupture even when combined with embankment loading, although stability analysis should be carried out. Stress paths analyzed next complement this statement.

Effective stress paths (*ESP*) below conventional embankments are directly related to the location of the points in the clay foundation. For points under the embankment slope the *ESP* moves almost vertically towards the failure line as

loading progresses (Marques & Leroueil, 2015). However, as the points approach the embankment centerline the *ESP* moves away from the failure line approaching the K_0 line.

Stress paths at mid depth in the clay foundation are now assessed for the test embankment mentioned in Figure 5, a combination of vacuum and embankment loading, 60% and 40% of the total applied load respectively, as mentioned previously. Figure 6 shows the *ESP* in red lines (the numbers indicated refer to the loading stages) numerically calculated at two points located at mid depth in the clay foundation, point A located at the embankment centerline, and point B located under the embankment slope (Figure 6a). The *p'-q* plot in Figure 6b shows the yield curve for each point together with the critical state line and K_0 line. The stress paths of both points, *A* and *B*, presented show that the two stress paths remained fairly close to the K_0 line. Therefore, unlike traditional embankment loading, the *ESPs* when vacuum preloading is used are close to or below the K_0 line, even for points away from the embankment centerline.

The disadvantages of vacuum preloading are:

- Vacuum requires pump maintenance and there is a high energy expenditure during the pumping period, thus is not suitable for small areas;
- Higher clogging of *PVD* with vacuum;
- Vacuum loss along the length of the drain, thus a lower consolidation with depth which can lead to high post-construction settlements;
- In cold regions pumping systems cannot be used under extremely low temperatures, unless the hydraulic system is protected against freezing;
- The membrane must be airtight and vacuum efficiency decreases in clay deposits with granular layers. In
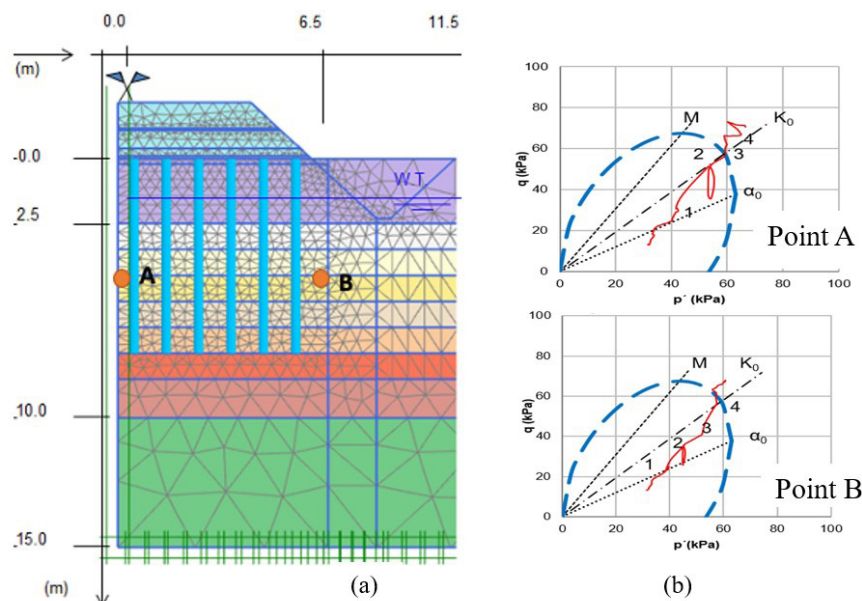
Figure 6. Numerical analysis: (a) FE mesh and points analyzed; (b) Stress paths at points A and B.

addition, in the case of a high permeable layer at the surface, the membrane must reach greater depths;

- Vacuum pumping, when using a membrane system, increases the reference water level from the natural water table level to the level of the horizontal drains where the vacuum is applied. The case history shown in Figure 6 had a lower water table, and even though the pressure measured with the vacuum meter inside the sand layer was 80 kPa, the actual vacuum pressure installed in the clay layer was lower than the 80 kPa measured by the piezometer, as pore pressure measurements showed (Marques & Leroueil, 2015).

3.4 Vacuum preloading in the city of Rio de Janeiro

The drain-to-drain vacuum preloading technique in conjunction with a physical embankment load was used for the first time in Rio de Janeiro city for a residential project on very soft soil (Freitas, 2021; Cardoso, 2021). The vacuum preloading system consisted of 24 pumps (VP-1 to 24), working nonstop for periods between 7.5 and 9.0 months,

as shown in Figure 7. PVDs were installed in a triangular mesh pattern with 1.3 m spacing (Figure 8a) connected to pumps by a collector system (Figure 8b). The embankment thickness was in the range of 3.9 and 6.3 m, including the working platform (Figure 8c).

The site was composed of very soft organic dark gray clay, 8 to 15 m thick, with the occasional occurrence of shell fragments. The bulk weight of the clay (γ) varied between 11.5 and 12.5 kN/m^3 and the natural water content from 191 to 242%. The soil grain size fraction was: 46% clay, 48% silt and 6% of fine sand and medium sand, resulting in a mean activity value of 2.89. The plasticity index was between 103 and 174%, thus highly compressible organic silty clay.

Eighteen settlement plates were distributed across the 5 areas and yielded settlements between 1.0 and 2.5 m. Figure 9 shows settlements measured by settlement plate SP-03 compared with settlements curves calculated for 30 kPa and 70 kPa vacuum load. Although the vacuum pressure measured at the pumps was around 80 kPa, the measured settlements indicated that the actual applied vacuum pressure was closer to 30 kPa (Freitas, 2021; Cardoso, 2021).
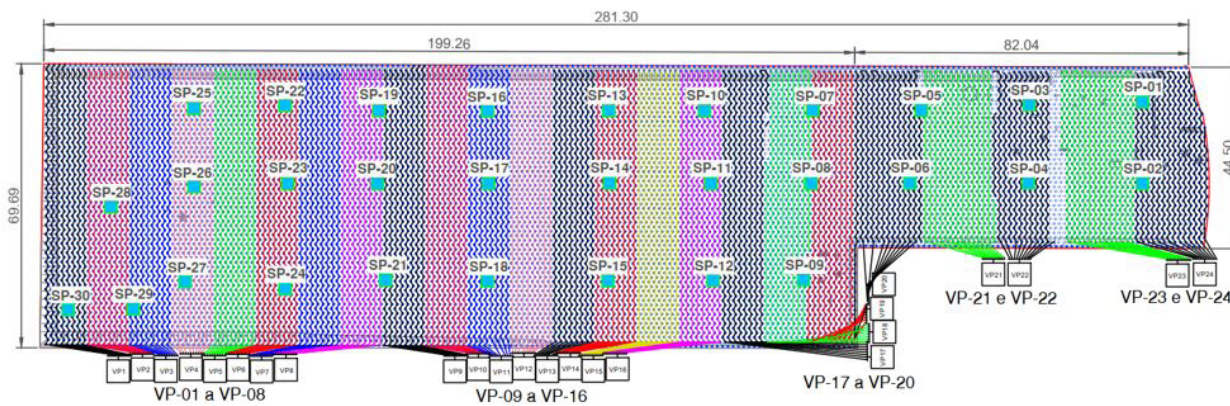
Figure 7. Vacuum application layout and settlement plates location (Freitas, 2021).
Legend: VP = vacuum pumps; SP = settlement plates.
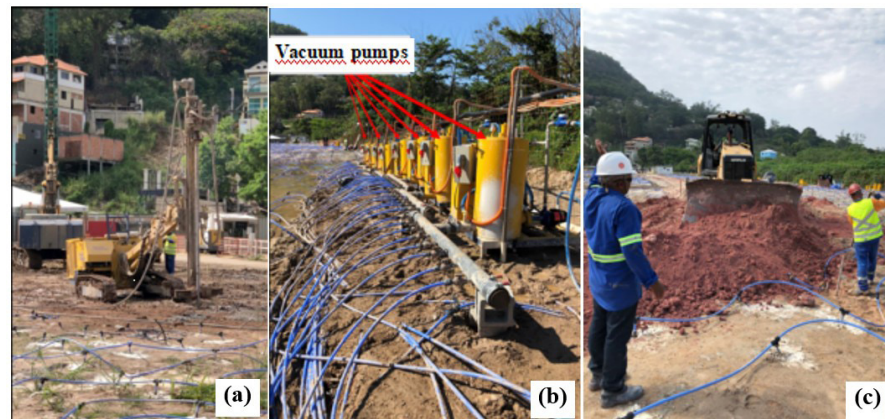
Figure 8. Drain-to-drain vacuum consolidation: (a) vertical drains and installation of collectors (b) pumps and collector tubes (c) detail of embankment construction over collectors and connections (Freitas, 2021).

Data collected from electric piezometers did not exhibit the expected decrease with time in pore pressure due to application of the vacuum, to a maximum expected value of -70kPa. However, the increase of pore pressure was evident at each stage of embankment heightening, thus the piezometer was responding to changes in stress due to heightening.

The increase in effective stress calculated due to the increase in embankment height was around 90 kPa. However, piezocone tests carried out after the vacuum was turned off showed an increase of only 5 kPa of undrained strength in 3 *CPTus*. This increase may be related to an increase in the effective stress of approximately 20 kPa, and more consistent with an applied vacuum pressure of close to 30 kPa.

Results from settlement plates, piezometers and *CPTus* showed that the effective stress increase due to vacuum was lower than 30kPa, thus a low efficiency at this site. The connections with the PVD's and the horizontal pipes are the weak points in the vacuum system, where leakage can occur, thus it is imperative vacuum pressure monitoring in horizontal drain lines, at the end of the horizontal tubes, farthest from the vacuum pump. With this procedure, it is possible to make corrections to ensure maximum pressure, check the efficiency of the system and identify possible damage that could generate the loss of pressure along the line. Further field research to monitor pressures along the drain is needed to obtain the actual efficiency.

3.5 Final remarks

The main lessons learned about vacuum preloading were:
- The thickness of the working platform can be a decisive factor in terms of the embankment stability due to the low initial value of S_u;
- The connections between the PVDs and the horizontal pipes can be the weak points in the drain-to-drain vacuum system, where leakage can occur, thus it is essential to monitor vacuum pressure in the horizontal drain lines at the end of the horizontal tubes, farthest from the vacuum pump.

4. Vibro substitution with stone columns (*VSC*)

Stone columns are used to increase bearing capacity, reduce settlements and increase the consolidation rate. Ground improvement with granular columns involves the replacement of 10% – 50% of compressible soil, by area, with a granular material such as gravel (crushed rock), or sand (FHWA, 1983).

4.1 Design methods

Due to its simplicity, Priebe's (1995) method for stone column design is widely used to obtain the settlement improvement factor β (named n_o by Priebe, 1995). McCabe et al. (2009) reported good agreement between measured and computed values of β given by Priebe's method, as illustrated in Figure 10. Studies carried out in Brazil are also included in Figure 10 (Lima, 2012; Sandroni, 2014; Saboya et. al, 2021; Riccio Filho et al.,2022), showing that, overall, the values are relatively close to the range of values obtained for other studies.

Another important parameter in ground improvement in general is the area replacement ratio (α) defined as the ratio between the area of a column A_c and its area of influence A:

$$\alpha = \frac{A_c}{A} \tag{2}$$

where $A_c = \pi \cdot d_c^2/4$ is the cross-section area of a column; d_c is the column diameter; $A = s^2$ (for square mesh); s is the column spacing, or more generally, $A = \pi \cdot d_e^2/4$; d_e is the diameter of the unit cell; $d_e = 1.13.s$ (square mesh); or $d_e = 1.05.s$ (triangular mesh, less often adopted). The column diameter d_c is a direct function of the average value of the undrained strength of the soft clay (Besançon et al., 1984). The soft clay sites studied here have a typical value of undrained strength S_u around 10 kPa, for which the column diameter d_c is in the range of 0.90 m to 1.0 m.

Figure 9. Settlement values measured at *SP03* and settlement predictions for vacuum of 30 kPa or 70 kPa.
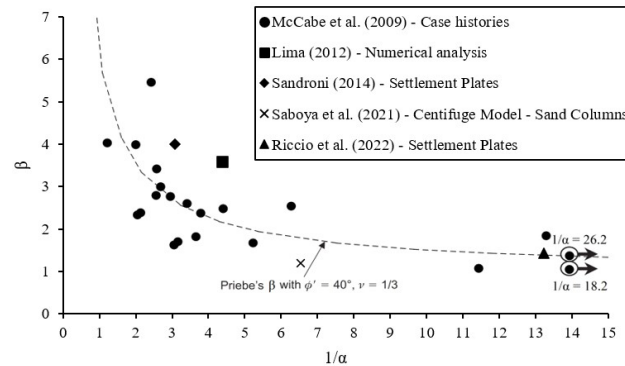
Figure 10. Settlement reduction factor versus inverse of area replacement ratio (see McCabe et al., 2009 for the other case histories).

$$d_c\,(cm)=120-1.4S_u\,(kPa) \qquad (3)$$

The stability analysis of embankments built on vibro stone columns (*VSC*) is usually performed using composite ground parameters (Priebe, 1995), which include the strength and specific weight parameters of the soft clay and the granular column. Stability analysis of a test area with *VSC* are illustrated by Riccio Filho et al. (2022), and a summary of their results are presented below.

Among the several methodologies proposed to predict the settlement rate of an embankment on *VSC*, the approach presented by Han & Ye (2002) is the most widely used. However, consistent analysis may be also obtained using the simple Barron (1948) theory (Riccio Filho et al., 2022).

4.2 Brazilian studies on stone columns applications

The vibro-replacement technique was implemented in Brazil in the mid-2000s, with several additional projects carried out since then, some highlighted next.

4.2.1 Stockyard test area

The first study reported here is related to a test area executed at the TERNIUM stockyard located in Itaguaí, State of Rio de Janeiro (Almeida et al., 2014). The test area was configured in an 8 x 8 square mesh/grid, with 1.85 m spacing. The stone column diameter was 1.0 m (replacement ratio $a_c = 23\%$) and the length was 11.25 m, as shown in Figure 11.

The geotechnical profile is composed by a soft soil layer, about 6.0 m thick, a 2.6 m thick sand layer below, and another soft clays layer, about 3 m thick. The remaining soil profile consisted mainly of sand layers, quite often without continuity. Table 1 summarizes the parameters obtained from samples taken in the three clay layers.

Table 1. Soil parameter values for clay layers 1 to 3 (Almeida et al., 2014).

Parameters	Layer 1	Layer 2*	Layer 3*
C_c	1.59	1.07	1.00
C_s	0.27	0.13	0.12
e_0	3.11	1.91	1.90
c_v [m²/s]×10⁻⁸	2.50	4.45	4.45
OCR	2.7	1.2	1.2
γ [kN/m³]	13.3	15.5	15.5
φ' [degrees]	25.0	25.0	25.0

*Data from Marques et al. (2008). C_c = compression index; C_s = swelling index; e_0 = initial void ratio; c_v = coefficient of consolidation; OCR = overconsolidation ratio, γ = soil init weight; φ' = friction angle
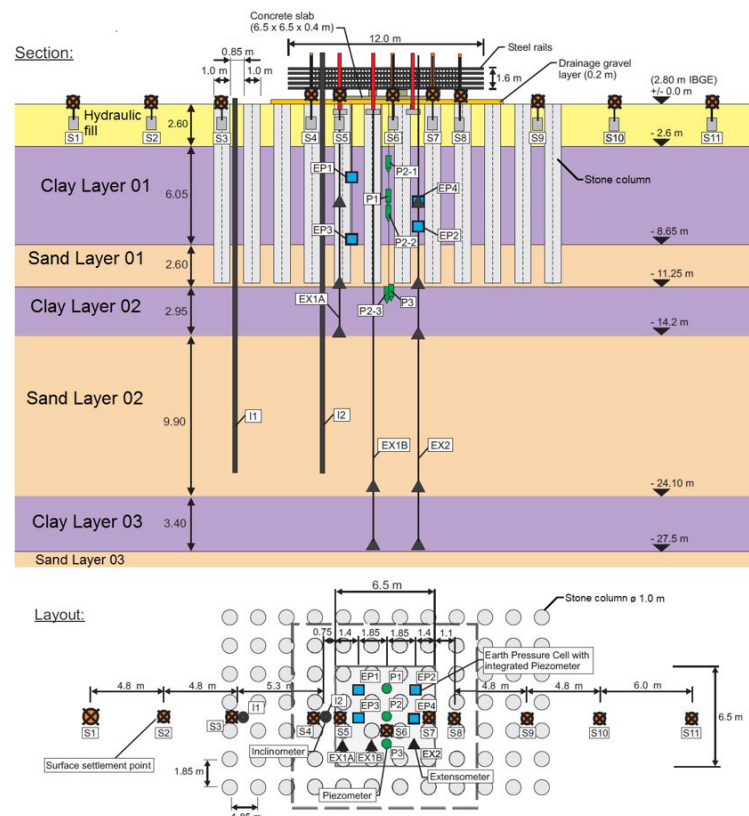
Figure 11. Layout of the test area and instrumentation (Almeida et al., 2014).

Legend: S = Surface settlement point; EP = Earth pressure cell with integrated piezometer; EX = Extensometer; I = Inclinometer; P = Piezometer.

8

Almeida et al., Soil. Rocks, São Paulo, 2023 46(1):e2023008222

The field instrumentation (Figure 11) included eleven settlement plates (*S*), two inclinometers (*IN*), nine vibrating wire piezometers (*PZ*) and four horizontal stress cells (*EP*).

Two- and three-dimensional finite element analyses were carried out (Roza, 2012; Almeida et al., 2014), in which the soft soil layers were simulated with a Cam-Clay type model, and the Mohr Coulomb model was used for the other layers. A study was performed to assess the earth pressure coefficient after stone column installation, *K**, and the best fit between numerical results and field measurements. was provided using *K** = 1.25, which is close to the values presented in the literature (Almeida et al., 2014).

The results of the 2D analysis (FEM 2D) presented for comparison with field measurements are the vertical displacements (inside and outside the loaded area) and horizontal displacements, at Inclinometer *I2*, (Figure 12), excess pore-pressure (Figure 13) and horizontal stresses (Figure 14). Differences between numerical predictions and measurements of the vertical and horizontal displacements increased after the 22ⁿᵈ day, when the limit state condition

was observed, close to failure, which was not adequately modelled in the numerical analyses (Almeida et al. 2014).

4.2.2 Ore piles in the stockyard area

Based on the good results of the test area, further numerical analyses were performed for the ore piles in the stockyard in which the area replacement ratio was 16% (Lima et al., 2019). Figure 15 presents the instrumentation installed at the section of study in the Stockyard, with two horizontal profilometer gauges (HPG), eight settlement sensors (SS) and piezometers (PZ), and the geotechnical profile.

Figure 16 shows the settlements measured by the *SS-N3* (northern part) and the northern *HPG*, together with results of 2D finite element analysis (FE). The average vertical stresses applied by the northern stack of pellets of ore are also plotted. The results show that the numerical analysis provided a good prediction of the settlement measured by settlement sensors and the profilometer. The same constitutive models and soil parameters from the test area were used in the stockyard.
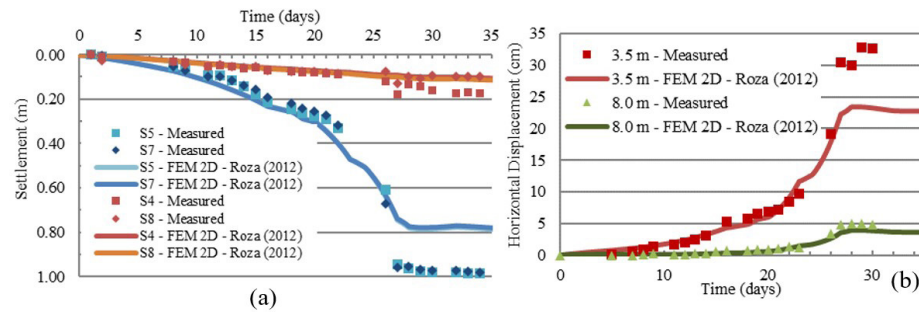
Figure 12. Vertical (a) and horizontal – Inclinometer I2 (b) displacements at instrumentation (Almeida et al., 2014).
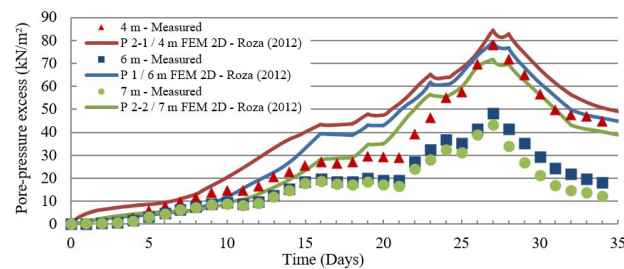
Figure 13. Excess pore-pressure (Almeida et al., 2014).
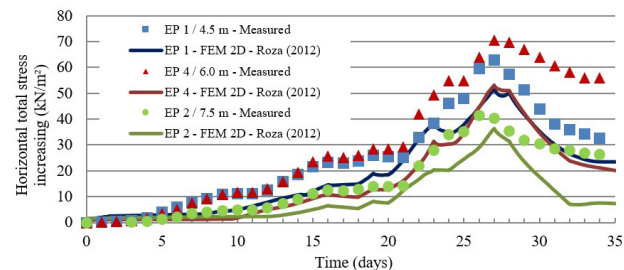
Figure 14. Horizontal stress (Almeida et al., 2014).
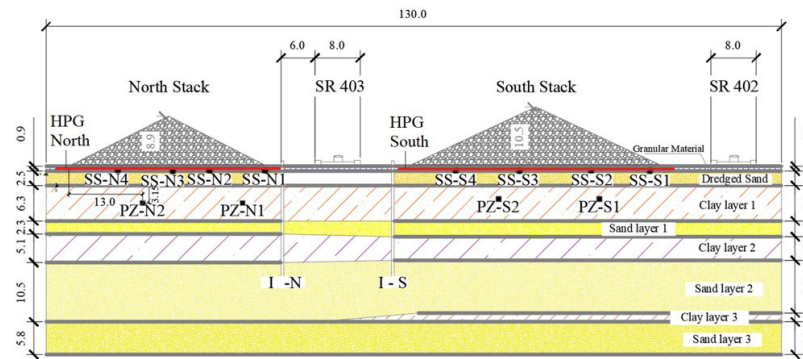
Figure 15. Instrumentation positions in the studied section (dimensions in meter) (Lima et al., 2019).
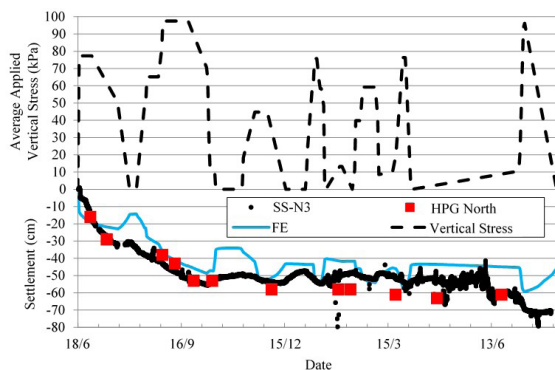
Figure 16. Measured and predicted settlements versus time at northern stack (Lima et al., 2019).
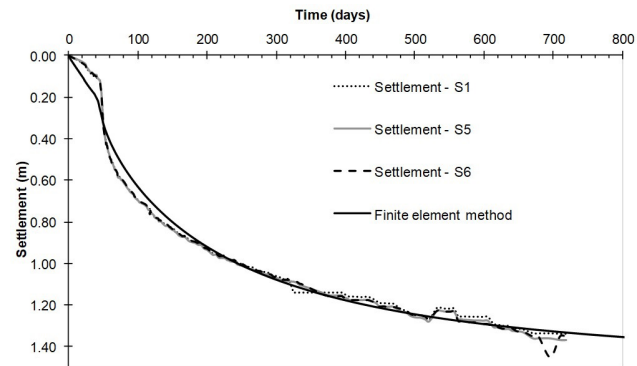
Figure 17. Comparison between measured settlements and predictions from finite element analysis (Riccio Filho et al., 2022).

4.2.3 Sewage plant test embankment

An embankment at a sewage treatment plant, located in the city of São Gonçalo, state of Rio de Janeiro, was supported by *VSC*s with a low area replacement ratio, equal to 7.5% (d_c = 0.90 m s = 2.90 m). Riccio Filho et al. (2022) presented results of monitoring and numerical studies of a 5.35 m high test embankment built on a mesh of ten-by-ten stone columns (*VSC*) built at the site. Analytical and axisymmetric unit cell finite element analyses were compared to the instrumentation data. The measured settlement-time curves were compatible with finite element analysis and favorable regarding settlement values and improvement factors, using the Priebe (1995) method. The low area replacement ratio used was quite effective in reducing the time for settlement stabilization and in providing adequate short-term stability against failure. The improvement factor (β) was equal to 1.43, when comparing the calculated settlement without treatment (2.05 m) to long term settlements after treatment with *VSC*s (1.43 m). Comparison of measured settlements and predictions from finite element analysis is shown in Figure 17. The settlements were measured with three settlement plates (*S1*, *S5* and *S6*) placed over the top of the columns.

Limit equilibrium stability analyses for the end of construction condition were performed for the conditions of treated and untreated clay foundations. The hypotheses regarding the foundation strength and the computed values of the factors of safety (Morgenstern-Price method) are presented in Table 2. The results show that the *VSC* treatment was quite effective in satisfying the ultimate limit state condition for which the standard requirement is a factor of safety greater than 1.5.

4.3 Final remarks

Vibro-Replacement with Stone Columns are commonly recommended for soft clay deposits with undrained strength values greater than 15 kPa. However, the soft clays sites studied here, with a typical value of undrained strength *Su* around 10 kPa, showed quite good performance overall. Considering the limited number of studies of the application of VSC in soft soils with undrained strength values around 10 kPa, these studies showed that finite element calculations may be a satisfactory design tool to complement analytical methods.

5. Granular encased columns (*GEC*)

Granular columns have been one of the most effective methods to improve load-bearing capacity, reduce deformations,

and hasten consolidation of soft soil supporting embankments. When extremely soft soil exists, the lateral stress provided by the soft soil is not sufficient enough to prevent excessive bulging that may cause the granular columns tend to fail even under low embankment loading (Almeida et al., 2018b).

In such cases, using geosynthetic encasement could provide additional hoop stress to the granular columns, magnifying the load-capacity and reducing total deformations of the subsoil. In addition, the encasement acts as a barrier which prevents the aggregates clogging thus maintaining the radial drainage capacity of the granular columns. Raithel & Kempfert (2000) developed a widely used design method to calculate embankments on geosynthetic-encased column (GEC).

5.1 Test embankment

Despite of the available investigations on the performance of the GEC, there are limited studies where the field behavior

of GEC-supporting embankment was reported. This section aims to provide further explorations on the behavior of embankment over GECs using measurements provided by instrumentations.

The test embankment was performed in the stockyard of Ternium Company located at Itaguaí, State of Rio de Janeiro. An extensive site investigation was carried out aiming to define the geotechnical properties of the layered subsoil, as shown in Figure 18. Accordingly, the soil profile was characterized by 10 m-thick soft clay improved by 36 GECs installed in a square pattern. The GECs were 11 m in length, 0.8 m in diameter, and installed in center-to-center spacing of 2.0 m producing an area replacement ratio a_c equal to 12.5%. The encasement material was woven geotextile with a tensile stiffness and allowable tensile strength of 1750 kN/m and 95 kN/m, respectively.

Figure 19 illustrates the embankment center line section with the position of the instrumentation as follows:

Table 2. Limit equilibrium stability analyses for the end of construction condition (Riccio Filho et al., 2022, adapted).

Condition	Hypothesis regarding the foundation strength	Factor of safety
untreated clay foundation	corrected Su (Bjerrum, 1973)	0.90
treated clay	column-clay composite foundation concept (Priebe, 1995)	2.27
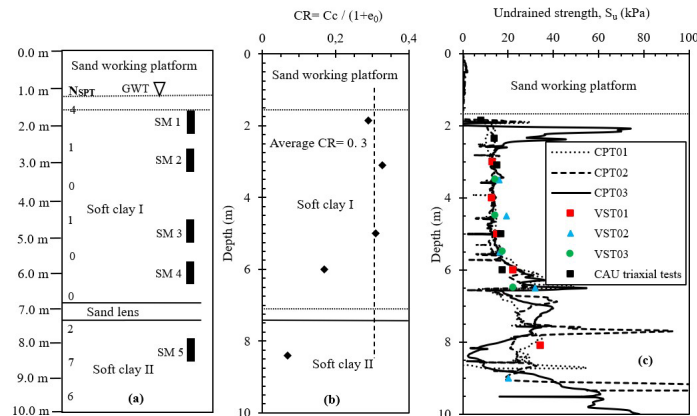
Figure 18. Geotechnical properties of soft clay layers: (a) typical soil profile, (b) compressibility ratio (CR), (c) profile of undrained shear strength (Almeida et al., 2015).
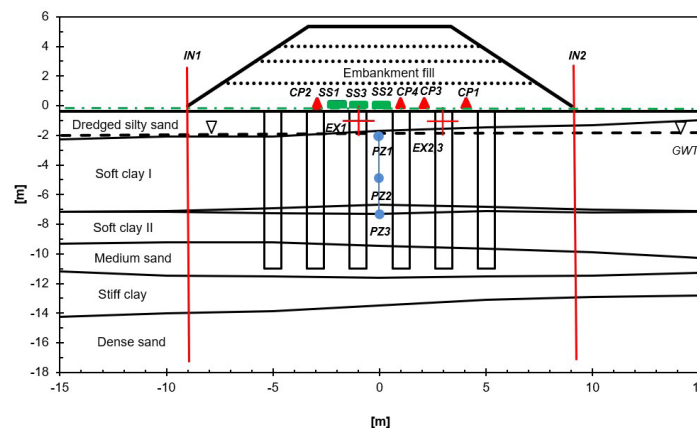
Figure 19. Embankment side view and position of instruments (Almeida et al., 2015).

- Three vibrating wire settlement sensors to measure settlement on top of the soft soil (*SS1*; *SS2*) and on top of the *GEC* (*SS3*);
- Three vibrating wire piezometers installed in soft soil at the depths of: 3 m (*PZ1*), 6 m (*PZ2*) and 8 m (*PZ3*), placed in the embankment centerline;
- Four total stress cells to measure the vertical stresses on the soft soil (*CP1*; *CP3*) and on the *GEC* (*CP2*; *CP4*);
- Three extensometers (*EX*) attached to the geotextile encasement to measure the geotextile hoop strain;
- Two inclinometers (*IN*) to measure distribution of lateral deformation of the soil beneath the embankment toe.

The fill was constructed using sinter feed materials placed in four layers including the consolidation intervals with the total height of 5.35 m. The fill materials had a total unit weight of about 28 kN/m^3 thus equivalent to 150 kPa total vertical stress. The embankment was then left in place for 180 days while the measurements were continuously recorded.

5.2 Settlements and improvement factor

Figure 20 shows central plates settlements data on *GEC* and surrounding soil. Measurements are also compared with those predicted by finite element analyses using the axisymmetric unit cell approach. The soft soil and granular materials were modeled by Cam-clay and Mohr-Coulomb criteria, respectively. A good agreement is seen between measurement and numerical analysis which is also obtained for pore pressures in the clay and vertical stresses on the *GEC* and in between columns as presented by Hosseinpour et al. (2015).

The settlement improvement factor (β), defined by the ratio of the settlement for un-improved to that for the *GEC*s-improved ground, is compared with that available from the literature, as shown in Figure 21. The largest measured settlement shown in Figure 20 was used to compute the settlement reduction factor β = 2.8 for the present field study (a_c = 12.5% and J = 1750 kN/m), which, as seen in Figure 21 (open red circle), suitably falls within the range reported by the literature. The reference settlement in soil was 490mm for calculation of β. Figure 21 also shows the data of other two Brazilian test sites (Riccio Filho et al, 2022; Sandroni, 2014) on stone column without encasing (J = 0) mentioned in section 4. It is observed that these two case histories (blue and green circles) are within the overall range of *VSC* data (J = 0).

5.3 Stress concentration factor

Figure 22a shows vertical stress measured over the *GEC* and in between aligned columns. The stress concentration factor (*n*), defined as total vertical stress supported by *GEC* to that measured on surrounding soil, was also assessed.
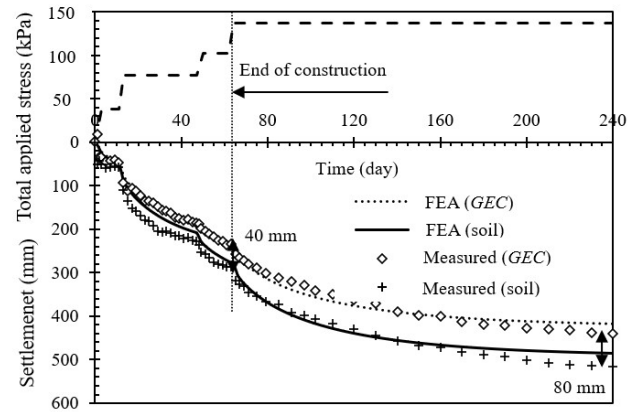
Figure 20. Variation of settlement over the encased column and soft soil (Hosseinpour et al., 2015).
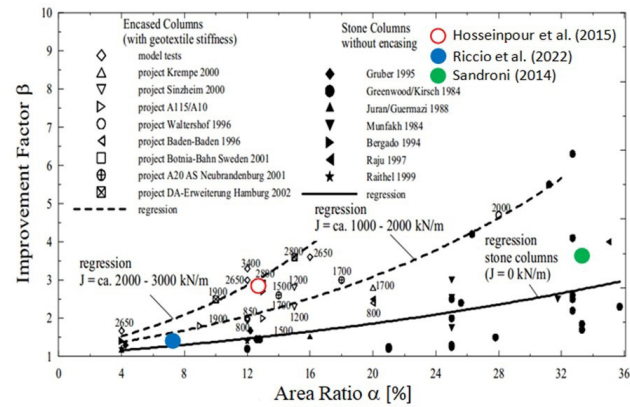
Figure 21. Settlement improvement factor for present test embankment compared with previous case histories (adapted from Almeida et al., 2018b).

Almeida et al. (2013) showed that the stress concentration ranges between 2 and 3 for un-encased columns, but in cases without a working platform "*n*" can be as high as 10 for *GEC*. The low measured value of *n* = 2.3 might be attributed to the existence of a thick sand platform which may modify the stress distribution. The evolution of stress concentration factor shows that there is a reduction in the stress on soil due increase of stiffness in the soil. This increase is due the consolidation along time.

5.4 Effectiveness of *GECs*

In order to verify the effectiveness of *GEC*s, the maximum settlement under the present test embankment (*GEC1*) is compared with that measured for a reinforced test embankment (*RE1*) on a soft clay with quite similar geometrical and geotechnical properties (Magnani et al., 2010).

5.4.1 Settlements

Figure 23 represents embankment settlement against corresponding total applied load for both *GEC1* and *RE1*.
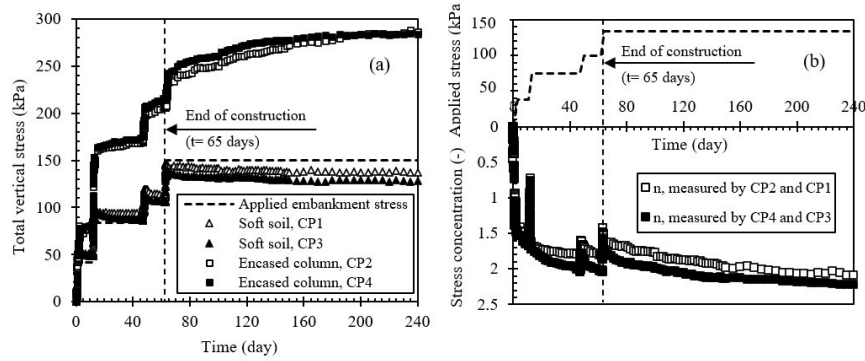
Figure 22. Measurements by stress cells: (a) total vertical stress, (b) stress concentration factor (Hosseinpour et al., 2015).
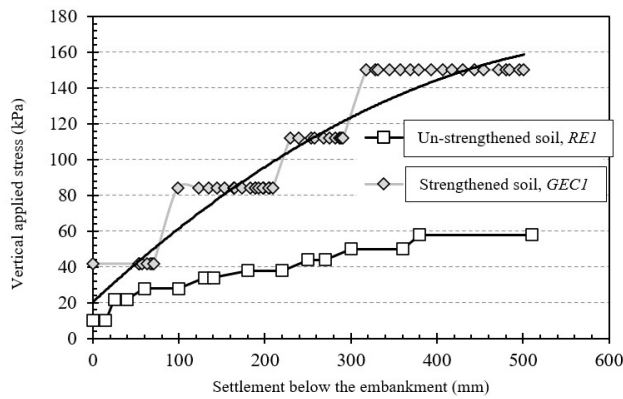
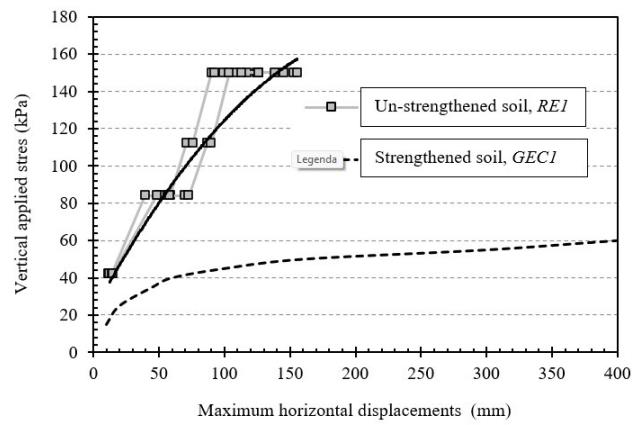**Figure 23.** Maximum settlement vs. vertical applied stress for reinforced embankment (*RE1,* Magnani et al., 2010) and improved (*GEC1,* Hosseinpour et al., 2016) foundations.

It is observed that the *GEC*s cause a substantial reduction on the settlement. For instance, for a vertical applied stress of 60 kPa the settlement under *RE1* is 500 mm; however, this value reduces to about 100 mm for the *GEC1*. In addition, when settlement is 300 mm, the *RE1* foundation supports a vertical stress of 50 kPa, but *GEC1*, instead, supports about 120 kPa.

5.4.2 Horizontal displacements

The effectiveness of *GECs* on soil horizontal displacements is assessed in Figure 24. It is observed that, using *GECs* remarkably reduces the maximum horizontal deformation of the soft foundation. For example, when the total load is 60 kPa, the maximum magnitude for un-improved case (i.e. *RE1*) is about 400 mm, over 10 times greater than that measured for *GEC1*. Also, *RE1* showed a global failure at the vertical load of 60 kPa with a computed safety factor of 1.098. However, the *GEC1* did not show any increase in horizontal deformation, while the total applied load was 2.5 times greater than *RE1,* with a computed factor of safety of 1.80.

The maximum horizontal deformation can be correlated with the maximum settlement under the embankment (Tavenas et al., 1979). As presented in Figure 25, for the

Figure 24. Maximum horizontal displacements vs. vertical applied stress for reinforced embankment (*RTE,* Magnani et al., 2010) and improved (*PTE,* Hosseinpour et al., 2016) foundations.
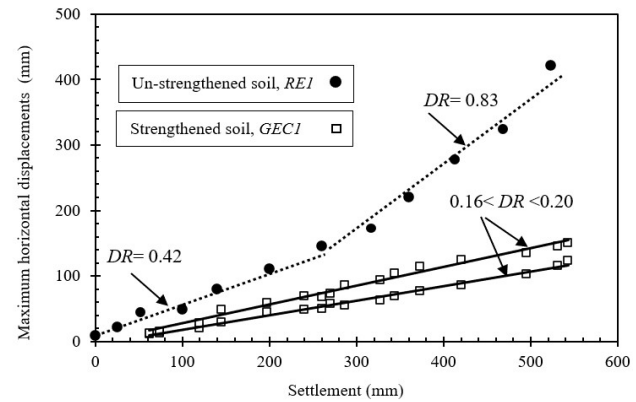
Figure 25. Embankment settlement vs. horizontal displacements for reinforced embankment (RE1, Magnani et al., 2010) and improved (GEC1, Hosseinpour et al., 2016) foundations.

GEC1 the horizontal deformation increased linearly with settlement resulting in a slope (*DR*) ranging from 0.16 to 0.20, much smaller than *DR* = 0.42 for *RE1*. Based on measurements, unlike conventional embankments, the use of *GECs* resulted in quite lower values of *DR*, and in the present case, roughly constant during consolidation period.

5.4.3 Excess pore pressure

Figure 26 shows the variation of the excess pore pressure together with the total vertical load for *GEC1* and *RE1*. For both test embankments the excess pore pressures increased sharply following load application and then dissipated gradually during post-construction. Unlike the *RE1*, the maximum excess pore pressure is reduced significantly at *GEC1*, while the vertical applied stress was 2.5 times greater than that for *RE1*. In fact, the high degree of stress concentration on the top of the *GECs* leads to a reduced vertical stress on the clay. It can also be observed that the radial drainage offered by *GEC* resulted to a faster consolidation for *GEC1* and then to a significant improvement in embankment stability during construction.

5.5 Final remarks

From the measurements provided by instrumentation the following outcome can be drawn from the field load test on geosynthetic enclosed columns:

- Measured settlement for the *GEC* and soft soil showed a rapid increase during the 65- day construction period, followed by a more gradual increase during the 6-month consolidation which indicated settlements almost stabilized.
- Compared to a conventional embankment, the embankment on *GEC*s with 2.5 times greater vertical stresses showed significantly lower soil vertical and horizontal displacements, and yielded a much larger factor of safety against failure.
- For the *GEC* supported embankment, the ratio of maximum horizontal displacement to maximum settlement varied linearly in the range of 0.16 to 0.2, which was relatively constant throughout the loading and consolidation stages.

6. Piled embankments (*PE*)

Geosynthetic-reinforced piles are commonly used for building structures on soft soils, as this method does not require waiting for the consolidation of the compressible layer. Furthermore, this technique uses lower volume of material than other solutions, resulting in a smaller environmental impact and, in general, fewer maintenance requirements.
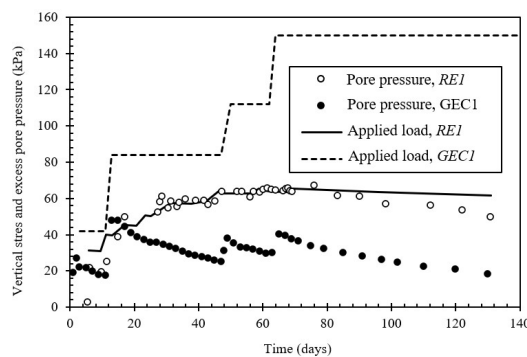
This section summarizes the study of a physical centrifuge model, focusing on the geometric parameters covering the typical values used in Brazilian practice (Fagundes et al. 2015, 2017; Almeida, 2019). It is worth mentioning that other preliminary studies, such as Blanc et al. (2013, 2014, 2018), Hartmann et al. (2014), Pinto et al. (2014), Girout et al. (2016) and Almeida et al. (2018a), were very important to the development and conclusions about the behavior of centrifuge models of piled embankments. The centrifuge tests measured the force transferred to the piles, the embankment surface settlements and the maximum geosynthetic reinforcement deflections below the embankment.

6.1 Reinforced piled embankments

The load transfer mechanisms in reinforced piled embankments are shown in Figure 27a. The arching effect (part A) is defined as the load directly transferred to the piles. The remaining total load not transferred by the arching effect is the vertical stress applied to the subsoil and the basal geosynthetic reinforcement (part B + C) (Figure 27b). The geosynthetic reinforcement (*GR*) in tension allows the transference of the remainder of the load back to the piles. This mechanism is called the membrane effect (part B) and its magnitude depends on both the support provided by the soil reaction (part C) and on the *GR* stiffness.

All of these mechanisms are strictly dependent on the area ratio values $\alpha = \pi . d^2/4s^2$, where d is the pile diameter, or the cap diameter if there is one, and s is the pile spacing (Figure 27c). The efficiency E is the ability of the embankment to transfer the load F to the piles, as defined by:

$$E = \frac{F}{(\gamma H + q)s^2} \tag{4}$$

The studies presented here focused on a wide range of embankment heights H (1.0 m - 7.2 m), area ratios α in the range of 5% - 20%, two pile diameters, three pile spacing, and two values of tensile stiffness (*J1* = 3.86 MN/m and *J2* = 16.8 MN/m), as listed in Table 3.

6.2 Improvement of the load efficiency by reinforcing with geosynthetics

Figure 28 evaluates the influences of the geosynthetic and the *GR* stiffness on load efficiency. Figure 28a shows

Figure 26. Excess pore pressure and total load vs. time for reinforced embankment (*RE1,* Magnani et al., 2010) and improved (*GEC1,* Hosseinpour et al., 2016) foundations.

Table 3. Centrifuge tests configurations.

Configuration	s (m)	d (m)	α (%)
CF1	2.0	0.5	4.9
CF2	4.0	1.0	4.9
CF3	2.8	1.0	9.8
CF4	2.0	1.0	19.6

14

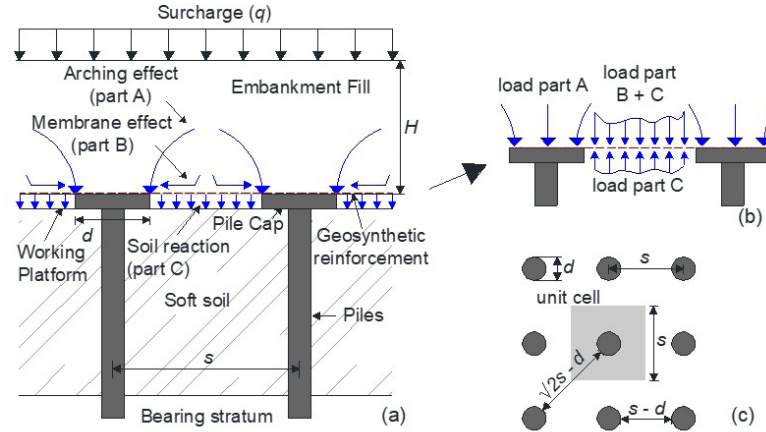Almeida et al., Soil. Rocks, São Paulo, 2023 46(1):e2023008222

Figure 27. Piled embankments: (a) schematic representation of load transfer mechanisms, (b) distribution of the load parts B and C in the geosynthetic reinforcement, (c) definition of geometric configuration and unit cell (adapted from Fagundes et al., 2017).
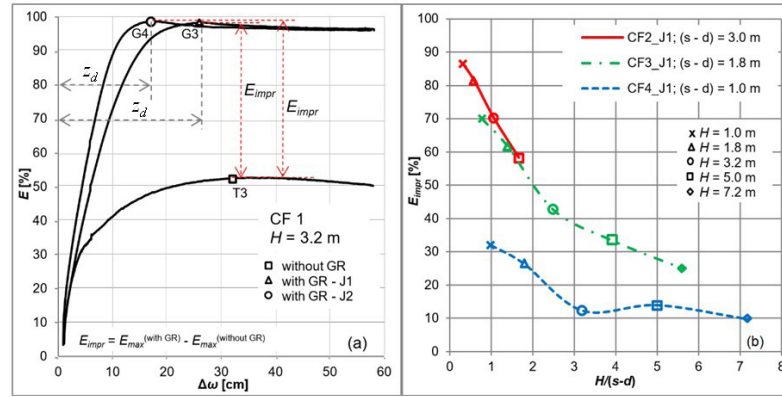

Figure 28. Influence of the geosynthetic in the load efficiency: (a) differences in the load efficiency between tests conducted with and without geosynthetic, (b) efficiency improvement to different test configurations (adapted from Fagundes et al., 2017).

the results of the centrifuge tests with configuration 1 and $H = 3.2$ m, where T3 was performed without GR, and the tests G3 and G4 used the GR $J1$ and $J2$, respectively. Figure 28b presents the differences in load efficiency for tests with and without geosynthetic, $E_{impr} = E_{max}^{(with\ GR)} - E_{max}^{(without\ GR)}$. In Figure 28b the E_{impr} is plotted against the embankment height normalized by $(s - d)$ for the configurations with the same diameter d and geosynthetic $J1$.

In Figure 28a, the value of the load efficiency E increased, reached a peak value, and then reached at a constant value, while the basal embankment settlement $\Delta\omega$ increased continuously. For tests performed with GR, the E_{max} is approximately 100% and the $\Delta\omega$, at which E_{max} was reached, is the main difference between the tests. As E_{max} is reached, the vertical stress applied to the subsoil decreased to zero, i.e., no stress is applied to the soft soil. In other words, the geosynthetic is no longer in contact with the tray and the GR maximum deflection (z_d) has been found, as indicated in Figure 28a. Values of z_d increased with the increasing clear span between the piles $(s - d)$ and the decrease of the GR tensile stiffness. The z_d also increases slightly as H increases.

Results from Fagundes et al. (2015, 2017) are summarized in Figure 28b and show that the geosynthetic reinforcement always improves efficiency. The efficiency improvement E_{impr} is evidently influenced by the clear span $(s - d)$ and the embankment height H (Figure 28b). This improvement in efficiency increases for a larger clear span and a lower embankment height, i.e., when the arching mechanism is less effective: $H < H_{crit}$. For the tests performed with the same configuration, it was observed that the influence of the GR stiffness on the E_{impr} was negligible. However, as mentioned before, E_{max} was reached at lower basal settlements for tests with $J2$ (Figure 28a).

6.3 Analytical versus experimental results: geosynthetic deflection

The maximum deflection of the geosynthetic (z_d) occurs when the loss of contact between the geosynthetic and the soil below takes place (part C is not present) and this value is achieved with the determination of E_{max}. This loss of contact occurs at the mid-point of the diagonal distance between two

piles z_d (mid center between four piles). However, analytical methods calculate the deflection z longitudinally between piles. Fagundes et al. (2017) and Almeida et al. (2020) suggest adopting $z_d/z = \sqrt{2}$, based on experimental and numerical models. Therefore, the procedure adopted in this study was to first obtain z_d experimentally at E_{max}, thus $z = z_d/\sqrt{2}$, which was then compared with values of z calculated analytically.

Figure 29 presents the comparative values of z, inferred experimentally, with analytical predictions of z using the two analytical methods: BS 8006 (BS, 2012) – Figure 29a and EBGEO (2011) – Figure 29b. A hashed trend line is included in Figure 29 and the agreement between the analytical methods and experimental values are quite good for BS 8006 (BS, 2012) and EBGEO (2011), but less satisfactory for CUR (2016). The BS 8006 (BS, 2012) guideline (Figure 29a) provides the best agreement with an under-prediction of around 1%, while EBGEO (2011) over-predicts experimental values by about 7%, on average (Figure 29b).

6.4 Experimental versus numerical results: differential settlement

The settlements at the embankment base and embankment surface are key factors in understanding the behavior of piled embankments. Figure 30 presents photographs of the embankment surface at the end of the tests without differential settlement (Figure 30a) and for a test of a low embankment where differential settlements were observed (Figure 30b). Figure 30c shows the differential settlement normalized by the basal embankment settlement ($\Delta u/\Delta\omega$) versus the normalized height of embankment by the clear span $H/(s-d)$ for all pile configurations evaluated. The trend lines passing through the data points intercept the line of ($\Delta u/\Delta\omega$) = 0, which indicates the values of $H/(s-d)$ (Figure 30c) corresponding to the critical height for each geometric configuration evaluated.

The commonly required serviceability state condition is zero differential surface settlement. It is important to point out that, in practice, the major problems related to the differential settlements are in the post-construction phase, however, part of the differential settlements also occur during the construction phase. Based on the results of this paper, to ensure that no differential settlement occurs on the embankment surface, a value of $H/(s-d)$ greater than 2.1 is necessary, but this value depends on α (Figure 30c).

3D numerical modelling results (Almeida, 2019) were compared with experimental data (Fagundes et al., 2017), in order to validate the numerical model (Figure 31a). The vertical displacements in the numerical models with
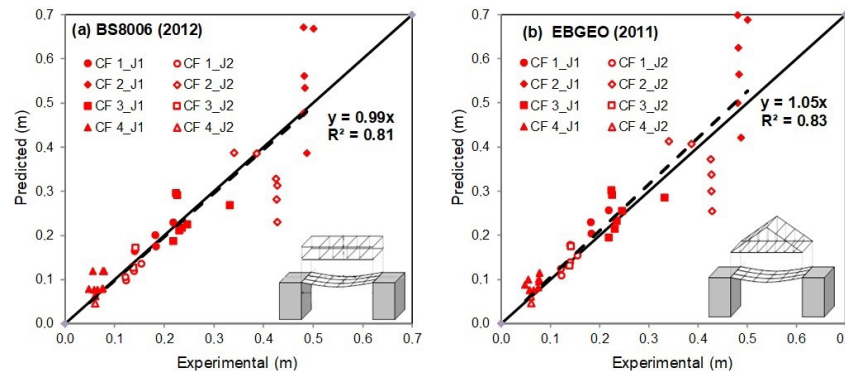
Figure 29. Comparison between the maximum deflection z_d observed experimentally (from Emax) and predicted by analytical methods: (a) BS006 (2012) and (b) EBGEO (2011) (adapted from Almeida, 2019).
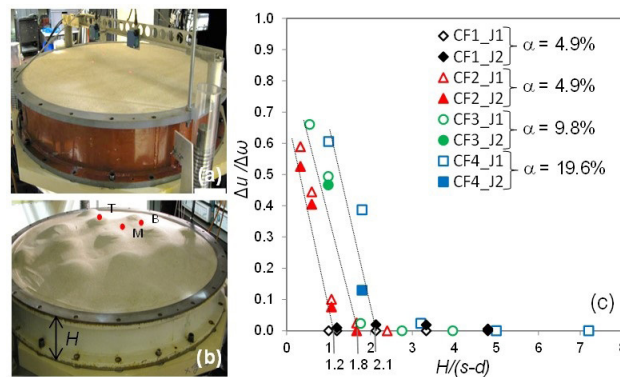
Figure 30. (a) and (b) Surface view of the embankment and (c) the ($\Delta u/\Delta\omega$) vs $H/(s-d)$ for all configurations (adapted from Fagundes et al., 2015, 2017).

a CF3 configuration and different embankment heights are shown in Figure 31b, c and d.

The results obtained through numerical analyses and experimental results indicate that the differential settlement at the top of the embankment increases to a maximum point, followed by a constant value. The computed values of the differential settlements remain constant because the geosynthetic, after reaching its maximum deflection, sustains the entire embankment load, but the mobile plateau continues to move. A good agreement is generally seen between the experimental and numerical results.

The numerical and experimental results indicated that surface differential settlement decreased with an increase in embankment height and an increase in area ratio (or decrease in pile spacing). Thicker embankments showed negligible surface differential settlement Δu. The surface differential settlements were more dependent on the relationship between the clear span and the embankment height than on the presence of the GR. The stiffness of the reinforcement reduced the magnitude of Δu but did not affect the critical height (H_{crit}). The stiffer reinforcement $J2$ leads to a greater reduction in Δu than in $J1$.

6.5 Analytical versus numerical results: tensile forces

3D numerical modeling (Almeida, 2019) was performed to compute the geosynthetic tensile forces not measured in the physical models, compared with values predicted by the European design guidelines. Figure 32 compares the maximum tension of the geosynthetic reinforcement obtained from both numerical and analytical methods. The geosynthetic was simulated with a linear elastic constitutive model. The anisotropic behavior of the $J1$ geosynthetic was modeled using the values of $Jx = 4760$ kN/m (Figure 32a) and $Jy = 2960$ kN/m (Figure 32a) for the secant stiffness for directions x and y, respectively.

Figure 32 shows both the numerical and analytical values, indicating that, as expected, the maximum tensile forces T_{max} increase with increasing embankment height and decrease with the reduction in the clear span between piles. Analysis of the results of T_{max} for the three analytical methods shows that the BS 8006 (BS, 2012) values of T_{max} are higher than those obtained with EBGEO (2011); both of these yielded higher values than those obtained for both load hypotheses assumed in CUR 226 (CUR, 2016).

Comparison between numerical and analytical calculations show that for CF3 (Figure 32a and b), the values of T_{max} computed with EBGEO (2011) and BS 8006 (BS, 2012) are fairly close to the numerical results, although the EBGEO (2011) values are in better agreement. For the CF3 configuration, the CUR226 (2016)-uniform provides reasonable agreement where $H = 1.0$ and 5.0 m, but only for Jy (Figure 32b).
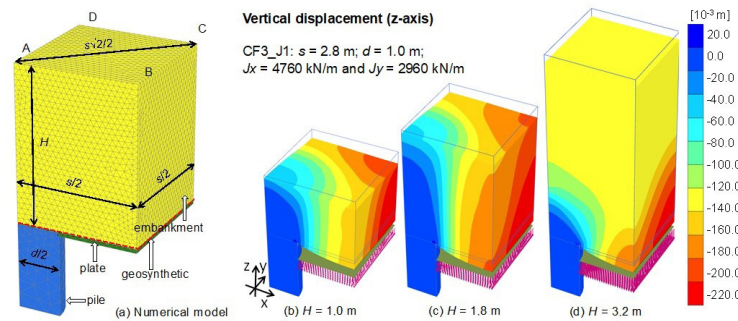
Figure 31. 3D View of the numerical model; vertical displacements to a CF3_J1 and different embankment heights.
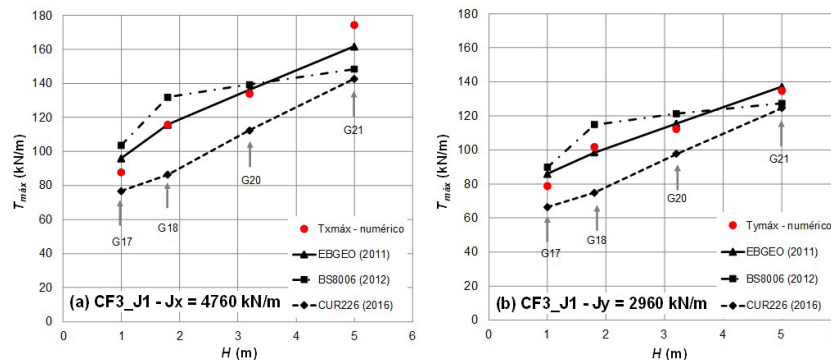
Figure 32. Maximum tensile force of the geosynthetic as a function of the embankment height obtained with the numerical models and the analytical method: a) $Jx = 4760$ kN/m; b) $Jy = 2960$ kN/m (adapted from Almeida, 2019).

6.6 Final remarks

The studies on piled embankments (*PE*) showed that the membrane effect, combined with soil arching, provides values of efficiency (regarding load transfer to the piles) close to 100% for most tests. The efficiency is influenced more by the height and clear span between piles than by the stiffness of *GR*. To ensure that no differential settlement occurs on the embankment surface, a value of *H*/(*s-d*) greater than 2.1 is recommended.

The EBGEO (2011) and BS (2012) guidelines for *PE* yielded good results in the assessment of measured versus computed geosynthetic deflections in the centrifuge tests. Numerical results showed that the maximum tensile forces, with arching and membrane effects in full operation, occur at the pile edge and increase with embankment height, surface surcharge and geosynthetic stiffness.

7. Deep soil mixing (*DSM*)

7.1 Principles and applications

The Deep Soil Mixing (*DSM*) technique was developed in the United States in 1954, but the methodologies most often used today are based on techniques used in Japan and Scandinavian countries (FHWA, 2013). According to Topolnicki (2016), the first application of the *DSM* technique in Scandinavia occurred in the 1960s using quicklime as binder. The effectiveness of using lime was confirmed in the studies performed in the '70s and in more recent studies conducted in Japan. The cast-in-place columns are built by mixing the soft soil with a binder. According to Kitazume & Terashi (2013), soil mixing can be done by adding lime, cement or a combination of these two binders with other special ones. *DSM* application and the related dosage of soil-binder mixtures are guided by EN 14679-2005 (EN, 2005).

DSM uses cast-in-place columns with diameters typically varying from 0.40 m to 2.40 m for a single column, according to Topolnicki (2012, 2016). The piled embankment technique described in section 6 uses piles which are generally driven. The Deep Soil Mixing (*DSM*) technique, shown in Figure 33 for piled embankment, uses cast-in-place piles.

The vertical axial stress (σ_v) acting on the top of the column can be calculated by the piled embankment methods presented in CUR226 (2016), EBGEO (2011) and BS 8006 (BS, 2017). While the German recommendation (EBGEO, 2011) is based on Kempfert et al. (2004), the Dutch standard (CUR226, 2016) is based on van Eekelen et al. (2013). However, in general, a system efficiency of 100% is usually assumed for a robust design of piled embankments.

Once the σ_v is determined, the binder content needs to be calculated in order to achieve the required unconfined compressive strength (q_u) to support the σ_v. According to Topolnicki (2016), the secant elastic modulus ($E_{50\%}$) can be
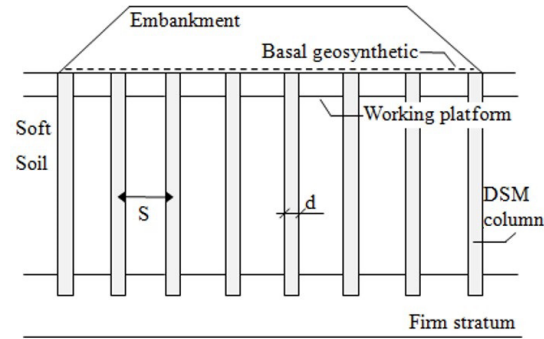
Figure 33. Typical use of *DSM* columns with diameter d for piled embankment on soft soils, piles spaced s center to center.

estimated, as a first approach, from Equation 5 based on the value of q_u. The value of $E_{50\%}$ enables the evaluation of the elastic settlement of the embankment.

$$E_{50\%} = 380 \cdot q_u \tag{5}$$

The q_u value is obtained from the statistical analysis of a series of unconfined compressive strength laboratory tests performed 7, 14, 28 and 56 days after installation of the *DSM* column.

The design parameter $f_{ck,28}$ is related to the 90% confidence interval of 90% for all values of q_u. According to the Topolnicki (2016) the *COV* value must be equal to or less than 0.38 for *DSM* applications in cohesive soils and the S_d (standard deviation) must be determined.

One of the most important factors in the design of an embankment supported by *DSM* columns is the analysis of the critical height (H_{crit}). If the height of the embankment is not greater than this value, the spacing between columns must be reduced. The H_{crit} is defined by McGuire et al. (2012) according to Equation 6.

$$H_{crit} = 1.15s' + 1.44d \tag{6}$$

where: s' is a geometric parameter, S is the space between axes and d is the diameter of the column. For a square mesh pattern, the most common one, Equation 7 should be used.

$$s' = \frac{\sqrt{2 \cdot S^2}}{2} - \frac{d}{2} \tag{7}$$

Alternatively, the H_{crit} can be calculated according to EBGEO (2011), which also accounts for live loads. Another very important parameter is the replacement ratio (α), which provides the ratio between the area of a column and its area of influence given by Equation 2 in section 4. Typically, α ranges from 0.10 to 0.20 for *DSM* applications in piled embankments.

In the next section two case studies using *DSM* applications are presented. Both cases are located at the

Salgado Filho International Airport, Porto Alegre, Brazil. The first case is the cargo terminal and the second is the extension of the takeoff and landing runway.

7.2 *DSM* at airport cargo terminal

The aircargo terminal, in Salgado Filho international Airport and was built in 2014. The soil profile in the region of the cargo terminal, in general, is composed of three main soil layers: a pre-existing upper embankment (0.0m to -2.0m), a soft clay soil layer (-2.0m to -10.0m) and below it, residual soil.

Table 4 shows the main characteristics of the soft clay used in the design of the *DSM* columns. Note that the organic matter content (*OMC*) is less than the maximum acceptable value of 15% and the *pH* of 5.5 indicates low aggressiveness of the soil.

Unconfined compressive strength tests were performed to obtain the optimum content of binder (cement CPII-Z-32, lime, cement and lime, etc) in the mixture. The tests were carried out with seven soil-cement mixtures, which results are shown in Figure 34.

Figure 34 shows that the greatest increase in q_u occurs between 7 and 28 days, for soil-cement and soil-cement-lime, after which the increase is less pronounced. However, the sand mixture exhibited a linear increase in q_u. A comparison of mixture 4 with mixture 5 and mixture 4 with mixture 6 confirms that the addition of lime produces a decrease in q_u. A comparison of mixture 4 with mixture 7 shows that the addition of sand produces an increase in q_u. The behavior observed for mixture 4 was different, with no increase in q_u from 28 to 56 days. In this study, mixture 3 was chosen, presenting unconfined compressive strength at 28 days equal to 1.35MPa based on 130 laboratory tests. In the field, the average q_u value reached a value of 1.78 MPa (greater than 1.35 MPa required in the design) with a confidence interval of 90% and a *COV* equal to 0.31 (within the interval expected for *DSM* for cohesive soils, Topolnicki, 2016).

The *DSM* columns used in the project had a diameter of 0.80m, a distance of 2.25m between column axes configured

in a square mesh pattern (area ratio α = 9.90%), an average length equal to 6.50 m with a 1.00 m penetration in the residual soil layer below. Figure 35 compares field measurements, taken at Test Area 2, located adjacent to the Cargo Terminal, with axisymmetric finite element predictions using PLAXIS 2D software. In Figure 35, "field measurement" represents the average measured settlement from three settlement plates (*PR01*, *PR03* and *PR11*). The beginning of embankment construction has occurred after 28 days and the reduction of settlements was pronounced.

7.3 *DSM* at extension of the takeoff and landing airport runway

The study reported in this section is related to the extension of the takeoff and landing runway (approx. 1.00 km) was built in 2019 at the Salgado Filho International Airport that. The *DSM* technique was applied in the soft clay ground at the site to support the embankment and pavement. The embankment has a maximum height of 5.50 m reaching 6.50 m with applied surcharge. A square mesh pattern was
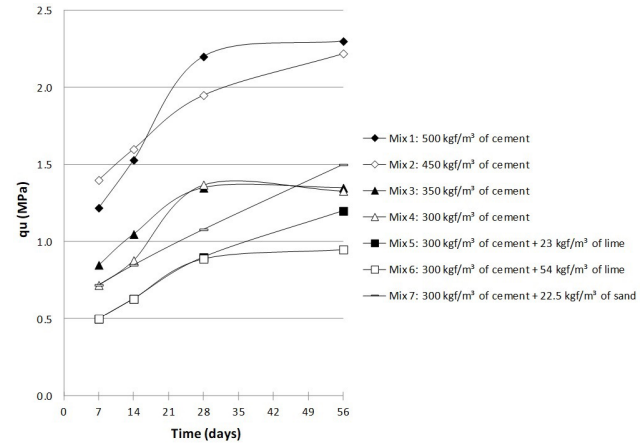
Figure 34. Increase in the q_u with time (days) for mixtures 1-7, adapted from Machado (2016).

Table 4. Characteristics of the soft soil in the Salgado Filho airport (Machado, 2016).

Parameter	Parameter
w	94%
w_p	34%
w_L	69%
PI	35%
γ_S (gf/cm³)	2.58
γ (gf/cm³)	14.8
OMC	8.80
pH	5.50

Note: w = soil natural moisture; w_p = plasticity limit; w_L = liquid limit; PI = plasticity index; γ_s = unit weight of solids; γ = unit weight; OMC = Organic matter content; pH = potential of hydrogen.
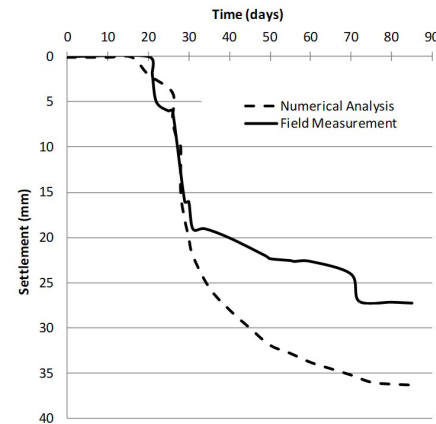
Figure 35. Comparison between numerical predictions and settlements measured in the field (Test Area 2), adapted from Assis (2016).

used, with a 0.80 m column diameter and a 1.80m distance between column axes (area ratio α = 15.4%). The column length was 9.00m on average and a basal geogrid layer was installed on the top of columns.

Figure 36 presents the evolution of q_u with time. The data in the graph is the average q_u at 7, 14, 28 and 56 days obtained from laboratory tests with samples taken directly form the columns using the wet grab method. In total, specimens taken from 450 *DSM* columns were tested. The embankment construction starts after 28 days after installation of columns.

According to Figure 36, the q_u required by the project was reached at approximately 10 days. The mixture was prepared with 350 kgf/m³ of cement. Statistical control yielded an S_d value of 0.55 MPa and a *COV* of 0.33, within the interval expected for the use of *DSM* for cohesive soils (Topolnicki, 2016).

Displacements were monitored by means of settlement plates, showing good performance in terms of embankment stabilization. Figure 37 shows that the settlements were minimum, reaching a maximum value of 17 mm for the embankment (plus surcharge) height of 6.50 m. In Figure 38, *SPOG1* and *SPOG2* are the settlement plates over the geogrid and between columns and *SPOC* is the settlement plate over the geogrid and column top.

The vertical stresses at the top of the column (σ_{vc}) and in between columns (on top of the soil, σ_{vs}) were measured by means of total cells. These measurements enable determination of the stress concentration factor $n = (\sigma_{vc}/\sigma_{vs})$ shown in Figure 27. The value of n over time computed from two sets of total stress cells (A and B) is shown in Figure 38, and as the embankment is heightened, a load transfer from the soil to the column takes place. This load transfer occurs even after the 45-day period of construction of the embankment. It appears that clay consolidation due to work platform loading below the geogrid enhances this load transfer. The built of embankment starts after 28 days of columns installation.

7.4 Final remarks

For the two case histories reported here (Airport Cargo Terminal and Runway), the *DSM* application showed very small settlements, of the order of a few centimeters, and overall good performance. The resulting stress concentration factor (*n*) indicated that part of vertical stresses imposed by the embankment transferred to the columns, significantly reducing the settlements, which were minimum. Therefore, the use of *DSM* columns permitted rapid construction of the embankments, meeting the requirements of the construction schedule.

The practice experience in Brazil with soft soil improvement using *SSM* with Portland cement permitted the following conclusions:

- The technique is efficient for very soft soils ($N_{SPT} < 2$), with high moisture content;
- Significant settlement occurs within a short period after each load step, and a large portion of the total settlement occurs within the preloading period;
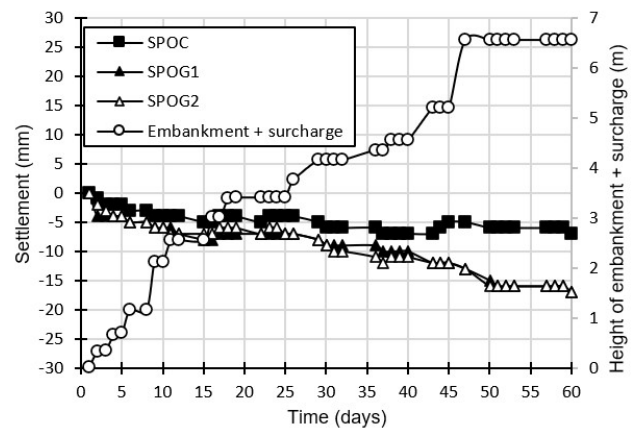
Figure 37. Evolution of the settlements, column top (*SPOC*) and between columns (*SPOG1* and *SPOG1*) over the time, adapted from Ávila (2021).

Figure 36. Evolution of q_u with time, field tests (Ávila, 2021).
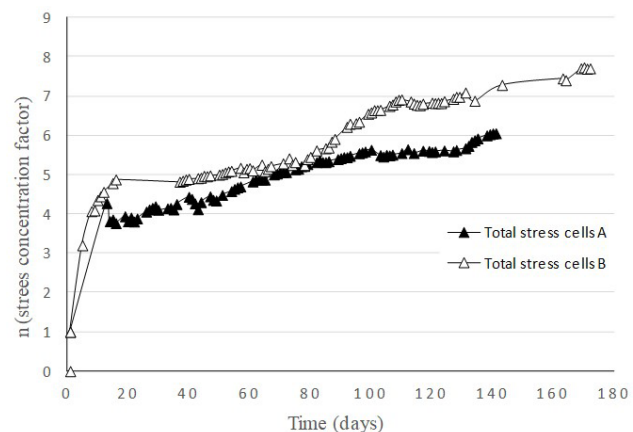
Figure 38. Evolution of the *n* over time (Ávila, 2021).

- Significantly reduced values of field strength and stiffness compared to the laboratory tests was possibly caused by the difficulty of field homogenization;
- The stabilized soil is shown to be a heterogeneous soil mass, with variable characteristics, mainly influenced by difficult field mixing and variable cement content in different portions in the mass.

8. Shallow soil mixing (*SSM*)

Shallow soil mixing (*SSM*) emerged in the 1990s, as a suitable and economically viable method for the stabilization of soft soils (Massarsch & Topolnicki, 2005). In Brazil, the technique has been used for about 15 years, with the commercial name of STABTEC® (Andrade et al., 2010). The technique consists of mechanically mixing a powder binder into soft submerged soils. The equipment available in Brazil has a maximum depth limitation of 6.0 m, but there are reports of equipment reaching up to 8.0 m (Forsman et al., 2015). The technique has the advantage of minimal waste generation, reducing material transport and disposal costs.

8.1 Execution process and main factors involved

The equipment used is an excavator with a hydraulic arm coupled to a mixing tool, connected to feeder tanks. The pressure feeder injects the dry binder powder into the soil directly with the mixing tool, and at the same time, the binder is mixed into the soil. The mixing speed is adjustable and the pressure and dosage of the binder to be injected can be controlled. The area to be treated is divided into cells, with dimensions based on the equipment capacity and the volume of treated soil estimated for the project. Immediately after the mixing, a geotextile is positioned over the stabilized cell and a preloading fill of 1.0 to 1.50 m is applied. The typical equipment and process is illustrated in Figure 39. The purpose of the preloading is to compress the newly stabilized soil mass, forcing the air bubbles formed during mixing to escape, causing immediate settlements, and increasing the strength of the treated mass. The next stage advances over the treated cell on the following day. The main factors involved are the following:
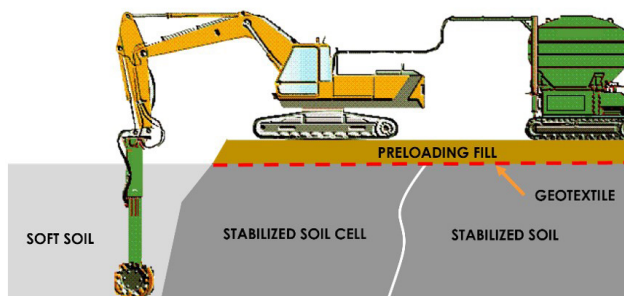
Figure 39. *SSM* technology (Adapted from Andrade at al., 2010).

- Soil characteristics: In general, *SSM* is described as applicable to soft surface soil. Brazilian experience has shown that the technique is efficient for very soft soils, with high moisture content and *SPT* blow count (N_{spt}) less than 2. Generally, for soft soils with higher resistance, the mixing usually becomes inefficient, and homogenization is impaired. Practice experience has also shown that soft soil with sand lens layers, mixed prior to injection of the binder, tend to yield a proportionally higher final strength, due to the increase of sand content in the mass;
- Binders: The most commonly used binders are cement and lime. Binders from industrial processes such as slag, flue gas desulphurization, fly ash and ground glass have also been used, generally combined with cement or lime. In Brazil, high early strength cement is preferred, as it reduces the waiting time to advance to the next step;
- Homogenization: an initial mixing of the soil mass is recommended to obtain a good homogenization for *SSM*. Thereafter, the homogenized soil is mixed with the binder. The operator must develop continuous and repetitive vertical and lateral movements of the mixing tool, as uniformly as possible. A homogeneous mixture is essential to optimize binder dosage and to obtain the design strength;
- Curing time: the curing time varies with the binder and soil type to be mixed. When using only cement, the stabilization reactions are completed in about a month. When binders such as lime, slag and fly ash are used, the stabilization process can continue for several months (EuroSoilStab, 2002).

8.2 Investigation, design and control

Initially, an analysis of the applicability of *SSM* should be carried out, considering the site, predicted use, soils characteristics, time available and surrounding conditions. The design comprises the following steps: a) complementary investigations; b) parameter determinations; and c) ultimate limit state (*ULS*) and serviceability limit state (*SLS*) verifications, as reported by Almeida & Marques (2013). and EuroSoilStab (2002). In order to define the binder and the dosage, laboratory tests should be carried out on the soil. Soil samples must be collected and mixed in the laboratory with different binders and curing conditions. The bulk unit weight, unconfined compression strength (q_u) and deformation modulus must be determined. The chemical properties of the soil such as pH, chlorides, humic acids, organic matter, ion-exchange capacity, sulfide capacity and total sulphur are important to the strength and durability of the stabilized soil mass and can interfere with the amount and type of binder to be used. If chlorides or organic matter are suspected of contributing to poor stabilization, the pore water should be

extracted from the soil for chemical analysis, as reported by EuroSoilStab (2002).

Laboratory samples have higher strength than the corresponding field stabilized material. The ratio between field and laboratory unconfined compressive strength (q_{uF}/q_{uL}) varies between 0.25 and 0.50 (EuroSoilStab, 2002; Nascimento, 2016). The disparity is attributed to several factors, most notably the homogeneity of the laboratory mixture.

Stability analyses should be carried out, considering the loads and the safety factor, according to the current standards. The settlements during and after the stabilization must be estimated considering the curing time. A temporary surcharge may be considered in order to minimize the residual settlements. The stabilization efficiency can be verified by unconfined compression test (*UCT*) performed in undisturbed samples. Alternatively, Standard Penetration Tests (*SPT*), Cone Penetration Test (*CPT*) and Vane Test could be performed. Embankment settlements and any overloads can be monitored using settlement plates.

8.3 Cases histories

This section presents two studies of the application of *SSM*, related to the execution of embankments for the urbanization of a shopping center area (Centro Metropolitano), in 2015, and a real estate development (Pontal Oceânico), in 2020, both in the city of Rio de Janeiro, Brazil. A summary of the properties of the unstabilized soil from the two sites is presented in Table 5.

Centro Metropolitano: An embankment of 3.0 m was constructed over the soft soil deposit improved with *SSM*. The technique was used due the vicinity of neighboring foundation structures and construction deadline constraints. *SPT* performed locally, Figure 40, indicated the existence of a superficial fill layer of roughly 1.0 m thick over a very soft organic clay with a thickness of 6.50 m, followed by a layer of fine clayey sand. The water level was 0.50 m below the surface.

The specimens were prepared in the laboratory using high early strength cement content relative to the wet mass

of the soil of 100, 150 and 200 kg/m³. As the Service Limit State (*SLS*) was the most relevant factor in this case, the dosage of 150 kg/m³ was chosen (Lemos et al., 2020) based on secant modulus (E_{50}). The *SSM* in the field was carried out to a depth of 6.0 m. Immediately after the mixing process, a geotextile was positioned over the stabilized cell, and 1.0 m of preloading fill applied. Figure 40 compares site investigation performed before and after ground treatment (curing of 50 days). The *SPT* after *SSM*, showed that the average N_{spt} increased from close to zero for the intact soil to a range of between 2 and 18 for the stabilized soil. The variability of Nspt after *SSM* is probably due to the heterogeneity of the
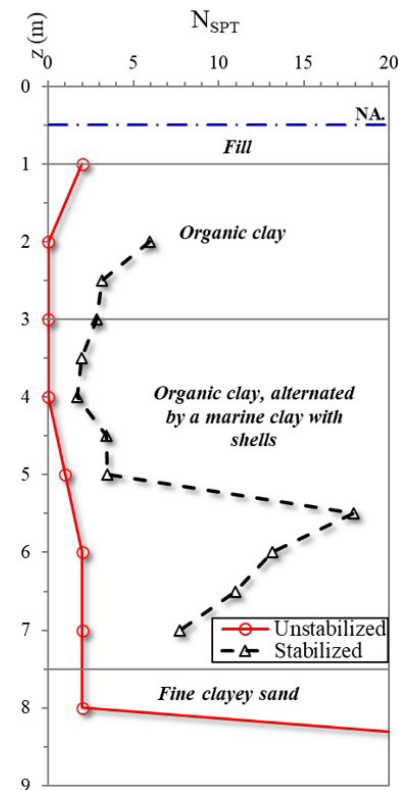
Figure 40. Geotechnical profile of the soft soil deposit: *SPT* for unstabilized and stabilized test results (Adapted from Lemos et al., 2020).

Table 5. Soft soil properties

Properties	Centro Metropolitano	Pontal Oceânico	
	Peat Organic clay	Peat organic clay	Sandy clay
Natural moisture content – w (%)	500-600	525-597	74-87
Liquid limit – w_L (%)	536-540	560-598	53-65
Plastic limit – w_P (%)	200-240	228-246	22-26
Organic matter content – OM (%)	50	65	5-10
pH	3.4	-	-
Specific gravity of soil particles – G_s	1.89	-	-
Bulk unit weight – γ_{nat} (kN/m³)	10.80	-	-
Clay ≤ 0.002mm (%)	49	10-20	40-60
Silt > 0.002mm - 0.063mm (%)	28	-	-
Sand > 0.063mm - 2.0mm (%)	23	-	-

soil layer, as well as the difficulty of mixing in the field, which resulted in variable cement content in the soil mass. Even so, the settlement control data indicated that the *SSM* results were satisfactory.

Undisturbed samples were collected after 30 days of field curing in order to perform *UCT* to determine the effectiveness of the stabilization. As shown in Figure, the results still exhibited significant dispersion, confirming that the stabilized soil presented variable characteristics, influenced mainly by the cement content of different proportions within the mass. Figure 41 shows that q_{uF}/q_{uL} varied between 0.25 and 0.50. The q_u for the unstabilized soil was 12 kPa average, which is about four times lower than results of the field stabilized soil. Whereas the E_{50} values of laboratory tests were two to three times higher than field values. As pointed out before (EuroSoilStab, 2002; Nascimento, 2016), this commonly observed disparity is associated to the fact that laboratory prepared specimens are more homogeneous than field specimens.

Settlement control was carried out after *SSM* and each embankment step, including a temporary surcharge of 1.50 m height, then maintained for 6 months with negligible settlement values. The total settlement measured in the *SSM* was 0.15-0.30 m significantly lower than the estimate without the *SSM,* of about 1.5 m. The settlement improvement ratio β defined by the value of the final settlement of the soft soil without treatment to the value of the final settlement after treatment, often used in granular columns applications, may be also applied to the present case, was 5 to 10 (França et al., 2016).

Pontal Oceânico: The urbanization of 9,000 m², with a 3.0 m embankment, would cause excessive settlements. The geotechnical investigation included *SPT*, *CPTu* (Figure 42) and unconfined compression laboratory tests. The site presented

a superficial soft soil, 3.0 to 6.0 m thick, composed of peat varying to organic clay, eventually to sandy clay in the lower layer. A second soft sandy clay layer, 2.0 to 4.0 m thick, was also identified an underlying sand layer of 1.0 to 3.0 m thick. The *SSM* with cement binder and temporary surcharge was adopted for the site stabilization and in the specific region with significant thickness of the second soft soil layer, *SSM* was combined with vertical drains.

The unconfined compression tests (*UCTs*) indicated undrained strength less than 10 kPa for the soft soil, with the characteristics summarized in Table 5. For *SSM* validation, *UCTs* were carried out on laboratory mixed samples, utilizing the soft soil with cement content of 120 kg/m³. The tests were divided into mixtures using only peat and using a percentage of peat and sandy clay, non-preloaded or preloaded with an equivalent embankment of 1.0 m height (18 kPa). Different curing procedures were used with no significant differences observed.

Field stabilized undisturbed samples were also collected for *UCT*. The results are presented in Figure 43. The most significant q_u increase occurred with the preloaded samples over the curing period, ranging between 90 kPa in 3 days to 230 kPa in 28 days, on average. No significant q_u increase was observed on the non-preloaded samples for both mixtures. In all cases, including the tests carried out on the field stabilized soil, the strength results were significantly higher than unstabilized soil. The field stabilized soil data shown by red squares in Figure 43 is the relevant data for field conditions.

Field tests and settlement monitoring indicated the importance of applied preloading. The significant initial settlement measured (PR11 and PR202 plates, Figure 44), implies a reduction in the void index in the treated soil,
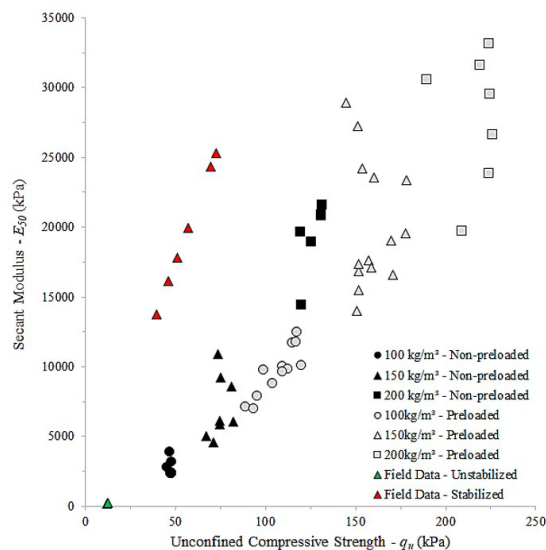
Figure 41. Unconfined compressive strength (q_u) relative to secant modulus (E_{50}) for 18 kPa preloaded and non-preloaded laboratory and field specimens (Adapted from Lemos et al., 2020).
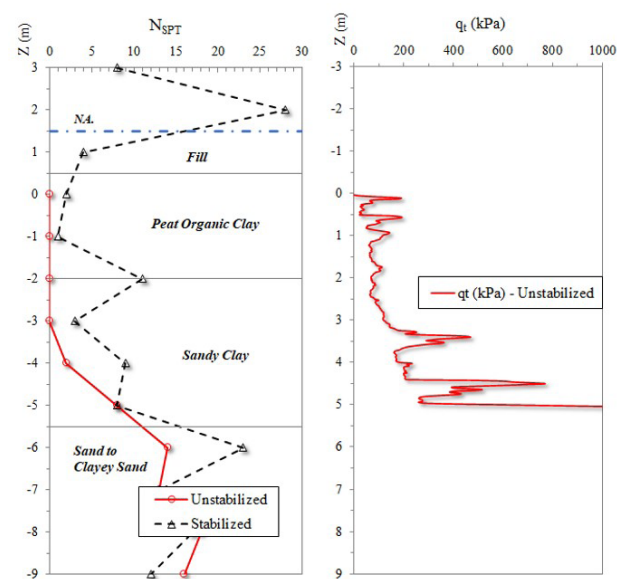
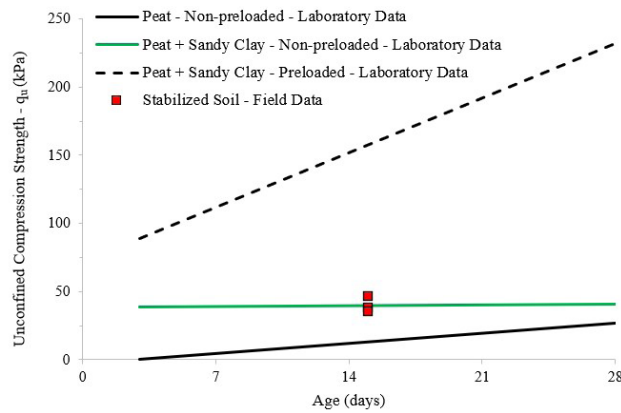**Figure 42.** Geotechnical profile of the soft soil deposit, *SPT* and *CPTu* test results.

Figure 43. Average results for the unconfined compression strength; non-preloaded and preloaded tests with 18 kPa.
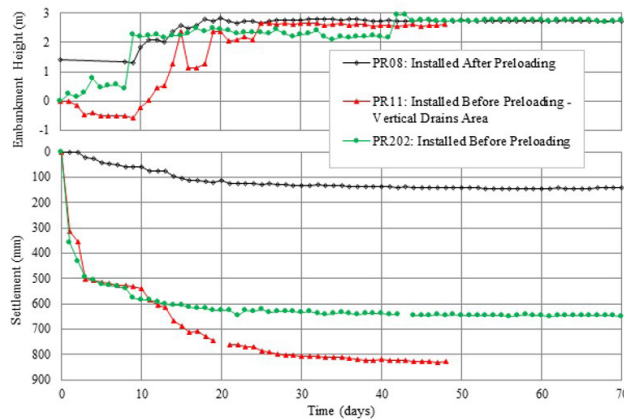

Figure 44. Embankment settlement monitoring.

contributing to a related strength increase. The preloading in lab tests resulted in a significant increase in q_u (Figure 43). On PR08 plate (Figure 44), installed after the preloading period, the resulting deformation was less than 150 mm. On PR202 installed before preloading 80% of the total settlement was measured in the first week, with preloading fill less than 1.5 m high. The same behavior was observed on PR11 installed in a vertical drain area, in which approximately 60% of the total settlement was measured during the preloading period. The total settlement without the *SSM* was estimated in 2.0 m.

8.4 Final remarks

The practice experience in Brazil with soft soil improvement using *SSM* with Portland cement permitted the following conclusions:

(a) The technique is efficient for very soft soils ($N_{spt} < 2$), with high moisture content;
(b) Significant settlement occurs within a short period after each load step, and a large portion of the total settlement occurs within the preloading period;

(c) Significantly reduced values of field strength and stiffness compared to the laboratory tests was possibly caused by the difficulty of field homogenization;
(d) The stabilized soil is shown to be a heterogeneous soil mass, with variable characteristics, mainly influenced by difficult field mixing and variable cement content in different portions in the mass.

9. CPR grouting

9.1 Introduction

CPR grouting is a technique to improve the strength and deformation characteristics of soft clay soils. It was introduced in Brazil as a variation of compaction grouting in the 2000s. Since then, it has become a time tested and proven technique for soft clay improvement, particularly in remedial situations. *CPR* is the Portuguese acronym 'Deep Radial Consolidation'.

CPR grouting involves the injection of a low-slump mortar grout into a pre-installed array of prefabricated vertical drains (*PVDs*). This technique appears to have been first proposed by Wu (2005). The philosophy behind the use of artificial drains is to ensure good drainage of fine-graded soils, allowing faster dissipation of the excess pore pressures induced by grouting.

For *CPR* grouting to be effective, the grout should not travel far from its injection point, nor fracture the soil. It must form an "expanding bulb" to displace and radially compress the soil without claquage. Fracturing can occur in clays in undrained conditions if the grout is too liquid. For this reason, a high viscosity grout with high solid content is essential to prevent undesired fracturing (Au et al., 2003).

9.2 Design aspects

The design of *CPR* grouting is based on the modeling framework developed by Cirone (2016). In general, a grouting project includes:
- Installation of vertical drains;
- Grout hole locations, geometry, spacing, maximum depth and inclination;
- Grout mix and properties;
- Refusal criteria;
- The program of work in stages, the drilling technique and the grout stages (top-down or bottom-up);
- Geotechnical testing program for verification of grouting effectiveness (acceptance criteria).

The stages of *CPR* grouting are summarized here. Drains are installed in a triangular or square pattern, with spacing that varies from 1.0 m to 2.5 m. Next, grout holes are intercalated between the drains. A low-slump (max. 10 cm) soil-cement harsh mortar is injected at low pressures of 5-15 kg/cm² through a four-inch open-ended pipe. Grouting

can proceed according to top-down or bottom-up procedures, depending on specific project needs. The grout is injected holding the pipe in place. On reaching either of the refusal criteria, the pipe is raised (or driven) to the next stage, and the process repeated. Common refusal criteria are:

- • A maximum grout take (target volume) is attained, as predetermined by the volume replacement ratio.
- • Pressure, as measured at the header, reaches a preset maximum operating value.
- • Undesired ground or structural movements are detected.

After completion of primary points, secondary and tertiary points are grouted in sequence.

Typical arrangements are shown in Figure 45. For each layout, the unit cell can be defined as the influence zone of each grout hole. The unit cell can be idealized as a cylinder with a cross sectional area equal to the area enclosed by the *PVDs* in the neighborhood.

The degree of improvement is generally calculated on the assumption that the expansion of the bulbs produces a volume change in the ground due to soil consolidation. It can be estimated according the observations reported by Komiya et al. (2001), Au et al. (2007) and Andrade et al. (2022). Bearing capacity and final settlement of the treated soil are calculated with the equivalent homogeneous medium method. This approach adopts equivalent post-treatment strength and stiffness parameters that are estimated from homogenization theories, assuming the bulbs as rigid inclusions.

One of the most important design parameters is the volume replacement ratio. It represents the volumetric incidence of the ground treatment. It can be defined as:

$$R_s = \frac{G_T}{A} \tag{8}$$

where G_T is the grout take, i.e. the volume of grout injected per unit depth, and A is the area of the unit cell. The volume replacement ratio, R_s, can be conveniently expressed as a percentage or in l/m^3. For example, considering a square grid with hole spacing of 3.0 x 3.0 m and a grout take of 800 l/m, the volume replacement ratio is $R_s = 89$ $l/m^3 = 8.9\%$. Modeling the grout bulb as an equivalent cylinder, its diameter is $d_g = \sqrt{4G_T / \pi} = 101$ cm. As a rule of thumb, the grid spacing can be approximated to two- or three-times the grout bulb diameter.

A combination of in situ tests is strongly recommended to assess the degree of ground improvement. *SPT*, *CPT*, and pressuremeter tests must be used with caution because their results are highly dependent on test location, but can be checked by measuring the shear wave velocity. Seismic testing can provide a macro-scale assessment of grouting effectiveness by analyzing wave propagation characteristics pre- and post-treatment. Successful examples using seismic surface wave analysis to assess the efficiency of *CPR* grouting are reported in Cirone et al. (2017) and Park et al. (2018).

Two cases of special interest will be summarized in the next section, both in the city of Rio de Janeiro.

9.3 Athletes Park

CPR Grouting was used in the construction of Athletes Park located in the Barra da Tijuca district (Riccio Filho et al., 2013). Soil conditions at the site consisted of large deposits of very soft organic clay, up to 10 m thick, underlain by dense sands. Two different engineering solutions were chosen: soft soil of up to a depth of 3 m was replaced; *CPR* grouting was applied in the remaining areas (approximately 16,000 m^2 treated in less than two months) where the soft soil was in the range 4 – 10m thick. Field tests, comprising *CPTu* and vane shear tests, showed extremely low values of undrained strength, as low as 3 kPa up to 6 m depth. Shelby samples tested in the laboratory exhibited very high compressibility, so the expected total settlement was 1.2 m for a 2.2 m high earth fill embankment with no ground treatment.

CPR grouting began with the installation of vertical drains in a square grid pattern, with spacing of 1.5 m. Next, grout was injected into holes in a 3.0 x 3.0 m square grid. The bottom-up method was adopted. The following criteria were established: 800-1000 l/m for the grout take and 1000 kPa for the pressure. Figure 46 shows the grout injection being executed over the pre-installed grid of vertical drains.

To assess the performance of the ground treatment, several pressuremeter tests were conducted, comparing the pre-treatment and post-treatment results. A total of 15 settlement plates were installed and monitored during a period of 3.5 months. Most of the plate readings showed rapid settlement stabilization after the embankment had reached its final height of 2.2 m, with settlements less than 120 mm. The overall project performance was considered quite satisfactory, although the observational time was limited.

9.4 Recreio dos Bandeirantes.

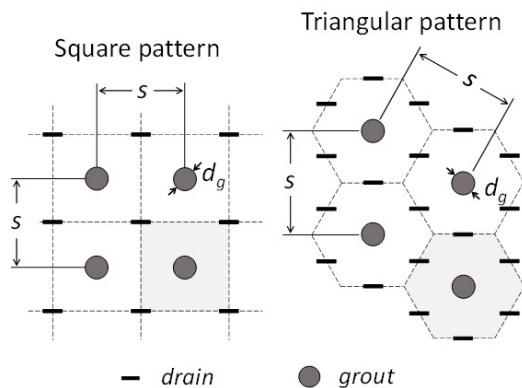The ground treatment at the Recreio dos Bandeirantes is an interesting one because it applied the homogeneous

Figure 45. Typical *CPR* grouting layout plans. The area of the unit cell is shaded.

Figure 46. Ground improvement at the Athletes Park by means of *CPR* grouting. Courtesy of Engegraut ltda.

medium method to a real case consisting of an embankment on soft soil treated with *CPR* grouting. The study is described in detail by Riccio Filho et al. (2020) and a short summary is presented here.

The Recreio dos Bandeirantes district, in the western side of Rio de Janeiro, is a region well known for the presence of soft soil deposits. At the site, *CPR* grouting was carried out in an 8.0m-thick soft soil layer, to reduce settlement and consolidation time due to the loading imposed by a 2.0 m high embankment. Drains were installed in a triangular grid pattern with 1.5 m spacing, and grout injection points were spaced 3.0 m apart. The grout take was 1100 l/m.

An estimate of the improvement factor could be made on the basis of the settlement curves presented in Figure 47. The final settlement for the condition without *CPR* grouting (s = 1.06 m) was calculated using the oedometric method and the data from the site investigations. Settlement with PVDs was predicted considering a triangular pattern with a spacing equal to 1.5 m. The final settlement of the *CPR* grouting improved soil (s = 0.167 m) was obtained by extrapolating the settlement plate readings with Asaoka's method. Comparing the curves revealed that *CPR* grouting was capable of accelerating the time for settlement stabilization (90% degree of consolidation was achieved in 175 days) and providing an improvement factor of about 1.06/0.167 = 6.3.

9.5 Final remarks

The practice experience in Brazil with soft soil improvement using *CPR Grouting* permitted the following conclusions:

CPR grouting is an effective technique for ground improvement of soft clays. Recent research improved the theoretical understanding of the technique, however there is still no acceptance of its effectiveness among many geotechnical engineers. The development of a systematic approach for design, execution, monitoring and control will mark the acceptance of *CPR* grouting as a technique for treatment of soft clays.
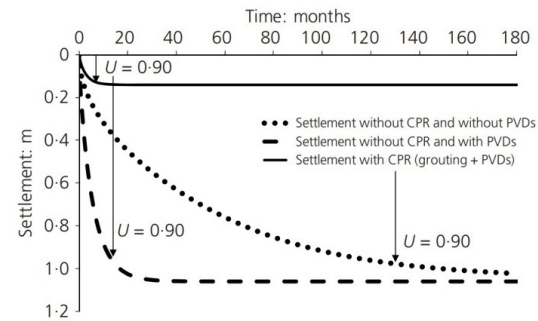
Figure 47. Comparison of settlement vs time curves at Recreio dos Bandeirantes (Riccio Filho et al., 2020).

Table 6. Typical range of β values as a function of soft soil improvement techniques.

Soft soil improvement technique	Typical range of β values
With or without drains or basal reinforcement (*UE/RE*)	1.0
Granular stone columns (*VSC*)	1.5 to 3.0
Geosynthetic encased granular columns (*GEC*)	2 to 4
Shallow soil mixing (*SSM*) and *CPR* grouting	5 to 10 (*)
Piled embankments (*PE* or *DSM*)	(**)

(*) range based on limited literature information. (**) β very high, not adopted.

10. Soft soil improvement techniques: settlement behavior

Based on the literature and the results presented in this paper, ranges of settlement improvement factor values, β, were obtained for the soft soil improvement techniques discussed here, as shown in Table 6. It is observed that as the degree of ground improvement increases the soft foundation gets stiffer and the parameter better increases proportionally. Piled embankments (*PE* or *DSM*) present settlements at least an order of magnitude smaller than other soft soil improvement techniques. Therefore, in this case it is not common to use the β variable to quantify the improvement of settlements, but then the load transfer Efficiency (BS, 2012) is the key design parameter. The consequence of lower settlements, or an increase in the value of β, is a lower required volume of fill and the related environmental benefits.

11. Conclusions

This paper has summarized recent studies related to the application of different soft ground improvement techniques mainly in the context of Brazilian soft clays.

Vacuum consolidation, the first technique discussed, is a highly efficient technique used worldwide for the improvement of soft soils. Even though the study at the Rio de Janeiro site described here presented low efficiency, the technique can and should be used with Brazilian soft clays, however with

better technological control and closer monitoring in order to achieve the necessary efficiency results.

This paper presented and discussed in sequence the different techniques for soft clay improvement that promote the strengthening of the soil, either by means of column-like elements (*VSC*, *GEC*, *PE*/*DSM*) or by incorporating cement (*SSM*) or mortar (*CPR*) mixtures into the soft soil.

Common to all techniques is that settlements decrease with increasing strengthening of the soft soil. The settlement improvement factor β, that relates the settlements with and without treatment of the soft soil, is a good way to rank the various improvement techniques discussed here.

The comparison of the reinforced embankment *RE* (*TE1*) with the embankment built on geosynthetic encased columns *GEC* (*TE2*) presented in section 5 showed that for the same settlement value in both cases, the *GEC* permitted an applied vertical stress 2.5 times greater than the reinforced embankment. The *GEC* technique has proven to be even more efficient when the comparison is made for horizontal displacements.

The results presented throughout the paper showed that the improvement of soft soils generally results in a decrease in construction time. Granular columns (*VSC* or *GEC*) act as large drains and generally accelerate settlements substantially compared to using prefabricated vertical drains. In the other techniques presented here (*CPR*, *SSM*, *PE*/*DSM*) the construction times are dictated primarily by the execution time of the technique itself, since the stabilization of settlements after the execution of the landfill is relatively fast, in general a matter of days or a few months. In any soft soil improvement technique, temporary surcharge is used to reduce post-construction settlements.

The literature shows that soft ground treatment using column-like elements or soil-binder mixtures is usually governed by service limit state conditions rather than by ultimate limit state conditions. In line with this, this paper has given more emphasis to settlement control rather than to stability control, although the latter must also be carefully assessed in design. The clear differences in safety factor values from stability analyses of embankments with and without soft soil improvement, presented in sections 4 and 5 respectively for the *VSC* and *GEC* techniques, confirm this.

Other important factors to be verified in design are, for example, negative friction and lateral embankment load in column-like elements of piled embankments (*PE* or *DSM*), which were outside the scope of this paper.

Acknowledgements

Declaration of interest

The authors have no conflicts of interest to declare. All co-authors have observed and affirmed the contents of the paper and there is no financial interest to report.

Authors' contributions

Marcio de Souza Soares de Almeida: overall conceptualization, planning and organization, writing – abstract, intro and conclusion, plus coordination and critical review of sections written by collaborators. Maria Esther Soares Marques: writing of one section, critical analysis and review entire paper. Diego de Freitas Fagundes, Mário Riccio and Uberescilas Fernandes Polido: section writing and review of sections written by the others. Alessandro Cirone, Bruno Teixeira Lima and Iman Hosseinpour: writing of sections. All authors provided comments to the final version of the paper.

Data availability

The data used for the production of this paper can be found in the following references that are listed in the references section of this paper: Marques & Leroueil (2015), Freitas (2021), Almeida et al. (2013, 2014, 2018b), Almeida (2019), Hosseinpour et al. (2015, 2016), Machado (2016), Assis (2016), Ávila (2021), Nascimento (2016), França et al. (2016), Cirone (2016), Cirone et al. (2017), and Riccio Filho et al. (2020, 2022).

List of acronyms

CAU	Anisotropic triaxial test
COPPE-UFRJ	Instituto Alberto Luiz Coimbra de Pós-Graduação e Pesquisa em Engenharia of the Federal University of Rio de Janeiro
COV	Covariance
CP	Cell pressure
CPR	Deep radial consolidation (Consolidação Profunda Radial)
CPT	Cone penetration test
CPTu	Piezocone Test
CR	Compression ratio
DSM	Deep Soil Mixing
ESP	Effective Stress Path
EX	Extensometer
FEM	Finite element method.
GEC	Geosynthetic encased column

GEC1	Test embankment	*J1x*	Secant stiffness of the GR PP25 in x direction
GR	Geosynthetic reinforcement	*J1y*	Secant stiffness of the GR PP25 in y direction
GWT	Ground water table	*J2*	Secant stiffness of the GR PP60
HPG	Horizontal profilometer gauges	K_{onc}	Coefficient of earth pressure at rest of a normally consolidated clay
IN, I	Inclinometer		
OCR	Overconsolidation ratio	$K*$	Coefficient of earth pressure after stone column installation.
OMC	Organic matter content		
PVD	Prefabricated Vertical Drain	*n*	Stress concentration factor
PZ	Piezometer	N_{spt}	SPT blow count
RE	Reinforced embankment	p'	Mean effective stress
RE1	Reinforced test embankment	P	Piezometer
SLS	Serviceability Limit State	*PI*	Plasticity index
SP, S, PR	Settlement plate	*pH*	Potential of hydrogen
SPT	Standard Penetration Test	*q*	Deviator Stress
SS	Settlement sensor	*q*	Vertical stress (surcharge) applied to the embankment surface
SSM	Shallow soil mixing		
UCT	Unconfined compression test	q_c	Tip resistance from CPT
UE	Unreinforced embankment	q_t	Corrected tip resistance from CPT
ULS	Ultimate Limit State	q_u	Unconfined compressive strength
VP	Vacuum pump	q_{uF}	Unconfined compressive strength of field samples
VSC	Vibro replacement		
VST	Vane shear test	q_{uL}	Unconfined compressive strength of laboratory samples

List of symbols

A	Influence area of column	*RS*	Replacement Ratio
A_c	Cross sectional area of a column	*s*	Centre to centre pile spacing
a_c	Area replacement ratio	*S*	Surface settlement point
B	Membrane effect	S_u	Undrained shear strength
C	Soil reaction	S_d	Standard deviation
C_c	Compression index	s'	Geometric parameter
C_s	Swelling index	*t*	Time
c_v	Vertical consolidation coefficient	*T*	Tensile force
d	Pile diameter, pile size or pile cap size	T_{max}	Maximum tensile force
d_c	Column diameter	T_u	Geosynthetic ultimate tensile strength
d_e	Diameter of influence	*w*	Natural water content
dg	Equivalent diameter of grout bulb	w_p	Plastic limit
DR	Ratio between maximum horizontal δh and maximum vertical displacements Δh ($DR=\delta h/\Delta h$)	w_l	Liquid limit
		z	Orthogonal maximum deflection of the geosynthetic
E	Efficiency of the load transfer mechanism	z_d	Diagonal maximum deflection of the geosynthetic
E_{impr}	Efficiency improvement	α	Area replacement ratio
E_{max}	Maximum load efficiency	β	Settlement improvement factor ($\beta=\Delta h/\Delta h_c$)
EP	Earth pressure cell with integrated piezometer	γ	Unit weight of the embankment fill material
e_0	Initial void ratio	γ_s	Unit weight of solids
E_{50}	Secant modulus at 50% strength	Δh	settlement or maximum settlement without columns
F	Vertical pile load	Δh_c	settlement with columns
$f_{ck,28}$	Characteristic unconfined compressive strength at 28 days	Δu	Differential settlement at the top of embankment
		Δω	Simulated settlement of the subsoil using the mobile tray
G_T	Grout take, liters/m		
GR	geosynthetic reinforcement	μ	Bjerrum (1973) correction factor
H	Embankment height	σ_v	Vertical stress
H_{crit}	Critical height	σ_{vc}	Vertical stress on the top of column
I	Inclinometer	σ_{vs}	Vertical Stress on the top of soil
J	Geosynthetic secant stiffness modulus	φ'	Effective soil friction angle

References

Almeida, M.S.S., Lima, B.T., Riccio, M.V.F., Jud, H., Almeida, M.C.F., & Roza, F. (2014). Stone columns field test: monitoring data and numerical analyses. *Geotechnical Engineering Journal of the SEAGS and AGSSEA*, 45(1), 103-112.

Almeida, M.S.S., & Marques, M.E.S. (2013). *Design and performance of embankments on very soft soils*. London: CRC Press.

Almeida, M.S.S., Marques, M.E.S., Lima, B.T., & Alvez, F. (2008). Failure of a reinforced embankment an extremely soft peat clay layer. In *Eurogeo4* (Vol. 1, pp. 1-8), Scotland.

Almeida, M.S.S. (2015). Amélioration des sols compressibles: études en vraie grandeur, modèles physiques et numériques. In *Conférence Coulomb*, Paris. Retrieved in July 26, 2022, from https://www.cfms-sols.org/manifestations/conference-coulomb

Almeida, M.S.S. (2019). Soft ground improvement: field and numerical studies. In *XVI Pan-American Conference on Soil Mechanics and Geotechnical Engineering* (Keynote Lecture of Technical Session, No. 5, "Soft soils"), Cancun, Mexico.

Almeida, M.S.S., Fagundes, D.F., Almeida, M.C.F., Hartmann, D.A., Giroult, R., Thorell, L., & Blanc, M. (2018a). Load transfer mechanism of reiforced piled embankments. In *Physical Modelling in Geotechnics - ICPMG18* (Vol. 2, pp. 1031-1036). London: CRC Press.

Almeida, M.S.S., Riccio Filho, M., Hosseinpour, I., & Alexiew, D. (2018b). *Geosynthetic encased columns for soft soil improvement*. London: CRC Press. http://dx.doi.org/10.1201/9781315177144.

Almeida, M.S.S., Fagundes, D.F., Thorel, L., & Blanc, M. (2020). Geosynthetic-reinforced pile-embankments: numerical, analytical and centrifuge modelling. *Geosynthetics International*, 27(3), 301-314. http://dx.doi.org/10.1680/jgein.19.00011.

Almeida, M.S.S., Hosseinpour, I., & Riccio, M. (2013). Performance of a geosynthetic-encased column (GEC) in soft ground: numerical and analytical studies. *Geosynthetics International*, 20(4), 252-262. http://dx.doi.org/10.1680/gein.13.00015.

Almeida, M.S.S., Hosseinpour, I., Riccio, M., & Alexiew, D. (2015). Behavior of geotextile-encased granular columns supporting test embankment on soft deposit. *Journal of Geotechnical and Geoenvironmental Engineering*, 141(3), 04014116. http://dx.doi.org/10.1061/(ASCE)GT.1943-5606.0001256.

Almeida, M.S.S., Deotti, L., Almeida, M.C.F., Marques, M.E.S., & Cardoso, I.M. (2021). Vacuum preloading on structured clay: field, laboratory and numerical studies. *International Journal of Geomechanics*, 1(10), 21. http://dx.doi.org/10.1061/(ASCE)GM.1943-5622.0002170.

Andrade, G.F.S.M., Lima, B.T., & Sieira, A.C.C.F. (2022). Laboratory investigation of geogrout inclusion: the influence of the substitution ratio. *Proceedings of the Institution of Civil Engineers - Ground Improvement*. In press. http://dx.doi.org/10.1680/jgrim.21.00009.

Andrade, G.G., Lopes, A.N., Antunes, R.P., & Dias, D.R. (2010). Experiências Brasileiras com estabilização de solos moles saturados através de sistema Dry-Mix – STABTEC. In *Anais do XV Congresso Brasileiro de Mecânica dos Solos e Engenharia Geotécnica* (pp. 1-6), Gramado. ABMS, CBMR, ISRM and SPG (in Portuguese).

Assis, V.C. (2016). *Structured embankment on soft soil over DSM columns* [Master's dissertation]. Federal University of Rio de Janeiro' repository (in Portuguese). Retrieved in July 26, 2022, from http://www.coc.ufrj.br/pt/dissertacoes-de-mestrado/389-msc-pt-2016/4696-vinicius-cardoso-de-assis

Au, S.K.A., Yeung, A.T., Soga, K., & Cheng, Y.M. (2007). Effects of subsurface cavity expansion in clays. *Geotechnique*, 57(10), 821-830. http://dx.doi.org/10.1680/geot.2007.57.10.821.

Au, S.K.A., Soga, K., Jafari, M.R., Bolton, M.D., & Komiya, K. (2003). Factors affecting long-term efficiency of compensation grouting in clays. *Journal of Geotechnical and Geoenvironmental Engineering*, 129(3), 254-262. http://dx.doi.org/10.1061/(ASCE)1090-0241(2003)129:3(254).

Ávila, C.T.B. (2021). *Structured embankment over columns with soil cement mixture* [Master's dissertation]. Federal University of Juiz de Fora' repository (in Portuguese). Retrieved in July 26, 2022, from https://www2.ufjf.br/pec/wp-content/uploads/sites/115/2022/02/Disserta%C3%A7%C3%A3o-102470031.pdf

Baroni, M., & Almeida, M.S.S. (2022). Undrained shear strength correlation analysis based on vane tests in the Jacarepaguá Lowlands, Brazil. *Soils and Rocks*, 45(2), e2022072721. http://dx.doi.org/10.28927/SR.2022.072721.

Baroni, M., & Almeida, M. (2017). Compressibility and stress history of very soft organic clays. *Geotechnical Engineering*, 170(2), 148-160. http://dx.doi.org/10.1680/jgeen.16.00146.

Barron, R.A. (1948). Consolidation of fine-grained soils by drain wells. *Transactions of the American Society of Civil Engineers*, 113(1), 718-724.

Besançon, G., Iorio, J.P., & Soyezet, B. (1984). Analyse des paramètres de calcul intervenant dans le dimensionnement des colonnes ballastées. In *Renforcement en Place des Sols et des Roches: Comptes Rendus du Colloque International* (pp. 119-126), Paris.

Bjerrum, L. (1973). Problems of soil mechanics and construction on soft clays and structurally instable soils. In *Proceedings of the 8th International Conference on Soil Mechanics and Foundation Engineering* (Vol. 3, pp. 111-159), Moscow.

Blanc, M., Rault, G., Thorel, L., & Almeida, M.S.S. (2013). Centrifuge investigation of load transfer mechanisms in a granular mattress above a rigid inclusions network.

Geotextiles and Geomembranes, 36, 92-105. http://dx.doi. org/10.1016/j.geotexmem.2012.12.001.

Blanc, M., Thorel, L., Girout, R., & Almeida, M.S.S. (2014). Geosynthetic reinforcement of a granular load transfer platform above rigid inclusions: comparison between centrifuge testing and analytical modelling. *Geosynthetics International*, 21(1), 37-52. http://dx.doi.org/10.1680/ gein.13.00033.

Blanc, M., Thorel, L., Girout, R., Almeida, M.S.S., & Fagundes, D.F. (2018). Load transfer mechanism of piled embankments: centrifuge tests versus analytical models. In *Proceedings of the 9th International Conference on Physical Modelling in Geotechnics* (Vol. 1, pp. 1043-1048). London: CRC Press.

BS 8006. (2012). *Code of practice for strengthened/reinforced soils and other fills, incorporating Corrigendum 1.* British Standards Institution, London.

BS 8006-1. (2017). *Code of practice for strengthened/ reinforced soils and others fills.* British Standards Institution, London.

Cardoso, I.M. (2021). *Vacuum Preloading as a solution for construction on soft soils* [Master's dissertation]. Federal University of Rio de Janeiro' repository (in Portuguese). Retrieved in July 26, 2022, from http://www.coc.ufrj. br/pt/dissertacoes-de-mestrado/635-2021/9865-igor-medeiros-cardoso

Cirone, A. (2016). *Geotechnical modeling of CPR grouting* [Master's dissertation]. Politecnico di Milano' repository. Retrieved in July 26, 2022, from https://www.politesi. polimi.it/handle/10589/120023

Cirone, A., Rodrigues, R., & Park, C. (2017). MASW control of grouting. In *SEG Technical Program Expanded Abstracts 2017* (pp. 5228-5232). Houston: Society of Exploration Geophysicists. http://dx.doi.org/10.1190/ segam2017-17740142.1.

Chai, J.C., Ong, C.Y., Carter, J.P., & Bergado, D.T. (2013). Lateral displacement under combined vacuum pressure and embankment loading. *Geotechnique*, 63(10), 842-856. http://dx.doi.org/10.1680/geot.12.P.060.

Choa, V. (1989). Drains and vacuum preloading pilot test. In *Proceedings of the 12th International Conference on Soil Mechanics and Foundation Engineering* (pp. 1347-1350), Rio de Janeiro.

CUR 226 (2016). Ontwerprichtlijn paalmatrassystemen [Design guideline piled embankments]. Stichting CUR, Gouda, Netherlands (in Dutch).

EBGEO. (2011). *Recommendations for design and analysis of earth structures using geosynthetic reinforcements.* Deutsche Gesellschaft für Geotechnik e.V. (DGGT), Berlin.

EN 14679. (2005). *Execution of special geotechnical works: deep mixing.* European Standard, London.

EuroSoilStab. (2002). *CT97-0351: development of design and construction methods to stabilize soft organic soils: design guide for soft soil stabilization.* European Commission, Industrial and Materials Technologies Program, Watford, UK.

Fagundes, D.F., Almeida, M.S.S., Girout, R., Blanc, M., & Thorel, L. (2015). Behaviour of piled embankment without reinforcement. *Geotechnical Engineering*, 168(6), 514-525. http://dx.doi.org/10.1680/jgeen.14.00155.

Fagundes, D.F., Almeida, M.S.S., Thorel, L., & Blanc, M. (2017). Load transfer mechanism and deformation of reinforced piled embankments. *Geotextiles and Geomembranes*, 45(2), 1-10. http://dx.doi.org/10.1016/j. geotexmem.2016.11.002.

FHWA. (1983). *Design and construction of stone columns* (Report, No. FHWA/RD-83/027, Vol. 1). FHWA, Washington.

FHWA-HRT-13-046. (2013). Deep mixing for embankment and foundation support (Federal Highway Administration Design Manual, No. FHWA-HRT-13-046). FHWA, Washington.

Forsman, J., Jyrävä, H., Lahtinen, P., Niemelin, T., & Hyvönen, I. (2015). *Mass stabilization manual.* Retrieved in July 23, 2022, from https://nzstirrers.com/wp-content/ uploads/2014/02/ALLU-Ramboll-Mass-Stabilisation-Ma-1.pdf

França, H.F., Polido, U.F., Nascimento, T.Z., & Lemos, S.G.F.P. (2016). Estabilização de solo mole por mistura de cimento em área da Barra da Tijuca, RJ: estudo de caso. In *Anais do 17º Congresso Brasileiro de Mecânica dos Solos e Engenharia Geotécnica*, Belo Horizonte. ABMS, CBMR, ISRM and SPG (in Portuguese). http:// dx.doi.org/10.20906/CPS/CB-03-0021.

Freitas, M.D.S. (2021). *Técnica de vácuo em solos moles aplicada a infraestrutura de transportes* [Master's dissertation]. Military Institute of Engineering (in Portuguese). Retrieved in July 23, 2022, from https:// sucupira.capes.gov.br/sucupira/public/consultas/ coleta/trabalhoConclusao/viewTrabalhoConclusao. jsf?popup=true&id_trabalho=11152264

Girout, R., Blanc, M., Thorel, L., Fagundes, D.F., & Almeida, M.S.S. (2016). Arching and deformation in a piled embankment: centrifuge tests compared to analytical calculations. *Journal of Geotechnical and Geoenvironmental Engineering*, 142(12), 04016069. http://dx.doi.org/10.1061/(ASCE)GT.1943-5606.0001557.

Han, J., & Ye, S.L. (2002). A theoretical solution for consolidation rates of stone column reinforced foundations accounting for smear and well resistance effects. *International Journal of Geomechanics*, 2(2), 135-151. http://dx.doi. org/10.1061/(ASCE)1532-3641(2002)2:2(135).

Hartmann, D.A., Almeida, M.C.F., Almeida, M.S.S., Blanc, M., & Thorel, L. (2014). On the influence of pretension and number of geosynthetic layers on piled embankment performance. In *Proceedings of the 10th International Conference on Geosynthetics - ICG 2014*, Berlin, Germany.

30

Almeida et al., Soil. Rocks, São Paulo, 2023 46(1):e2023008222

Harvey, J.A.F. (1997). Vacuum drainage to accelerate submarine consolidation at Chek Lap Kok, Hongkong. *Ground Engineering*, 1997(30), 34-36.

Hosseinpour, I., Almeida, M.S.S., & Riccio, M. (2015). Full-scale load test and finite-element analysis of soft ground improved by geotextile-encased granular columns. *Geosynthetics International*, 22(6), 428-438. http://dx.doi.org/10.1680/jgein.15.00023.

Hosseinpour, I., Almeida, M.S.S., Riccio, M.V.F. (2016). Ground improvement of soft soil by geotextile-encased columns. *Proceedings of the ICE - Ground Improvement,* 169, 297-305.

Indraratna, B. (2010). Recent advances in the application of vertical drains and vacuum preloading in soft soil stabilisation. *Australian Geomechanics Journal*, 45(2), 1-43.

Jacob, A., Thevanayagam, S., & Kavazanjian, E. (1994) Vacuum-assisted consolidation of a hydraulic landfill. In Proceedings of the Conference on Vertical and Horizontal Deformations of Foundations and Embankments (Geotechnical Special Publication, No. 40, pp. 1249-1261). ASCE.

Kempfert, H.-G., Gobel, C., Alexiew, D., & Heitz, C. (2004). German recommendations for reinforced embankments on pile-similar elements. In *Proceedings of the 3rd European Geosynthetics Conference* (pp. 279-284), Munique.

Kitazume, M., & Terashi, M. (2013). *The deep mixing method*. Boca Raton: CRC Press. http://dx.doi.org/10.1201/b13873.

Kjellman, W. (1952). Consolidation of clay soil by means of atmospheric pressure. In *Proceedings of the Conference on Soil Stabilization* (pp. 258-263). Cambridge: MIT.

Komiya, K., Soga, K., Akagi, H., Jafari, M.R., & Bolton, M.D. (2001). Soil consolidation associated with grouting during shield tunneling in soft clayey ground. *Geotechnique*, 51(10), 835-846. http://dx.doi.org/10.1680/geot.2001.51.10.835.

Lemos, S.G.F.P., Almeida, M.S.S., Consoli, N.C., Nascimento, T.Z., & Polido, U.F. (2020). Field and laboratory investigation of highly organic clay stabilized with Portland cement. *Journal of Materials in Civil Engineering*, 32(4), 04020063. http://dx.doi.org/10.1061/(ASCE)MT.1943-5533.0003111.

Lima, B.T. (2012). *Study of the use of stone columns on very soft clayey soils* [Doctoral thesis]. Federal University of Rio de Janeiro' repository (in Portuguese). Retrieved in July 23, 2022, from http://www.coc.ufrj.br/pt/teses-de-doutorado/156-2012/4103-bruno-teixeira-lima

Lima, B.T., Almeida, M.S.S., & Hosseinpour, I. (2019). Field measured and simulated performance of a stone columns-strengthened soft clay deposit. *International Journal of Geotechnical Engineering*, 16(6), 776-785. http://dx.doi.org/10.1080/19386362.2019.1653506.

López-Acosta, N.P., Espinosa-Santiago, A.L., Pineda-Núñez, V.M., Ossa, A., Mendoza, M.J., Ovando-Shelley, E., & Botero, E. (2019). Performance of a test embankment on very soft clayey soil improved with drain-to-drain vacuum preloading technology. *Geotextiles and Geomembranes*, 47(5), 618-631. http://dx.doi.org/10.1016/j.geotexmem.2019.103459.

Machado, M.C.B. (2016). *Treatment of clayey soft soils by cement mixtures in deep* [Master's dissertation]. Federal University of Rio de Janeiro' repository (in Portuguese). Retrieved in July 23, 2022, from http://www.coc.ufrj.br/pt/dissertacoes-de-mestrado/389-msc-pt-2016/4683-michelle-christini-de-brito-machado

Magnani, H.O., Ehrlich, M., & Almeida, M.S.S. (2010). Embankments over soft clay deposits: contribution of basal reinforcement and surface sand layer to stability. *Journal of Geotechnical and Geoenvironmental Engineering*, 136(1), 260-264. http://dx.doi.org/10.1061/(ASCE)GT.1943-5606.0000200.

Marques, M.E.S., & Leroueil, S. (2015). Vacuum consolidation and vacuum consolidation with heating. In B. Indraratna, J. Chu & C. Rujikiatkamjorn (Eds.), *Ground improvement series: chemical, electrokinetic, thermal and bioengineering* (Vol. 3, pp. 537-554). Amsterdam: Elsevier. http://dx.doi.org/10.1016/B978-0-08-100191-2.00017-4.

Marques, M.E.S., Lima, B.T., Oliveira, J.R.M., Antoniutti Neto, L., & Almeida, M.S.S. (2008). Geotechnical characterization of a compressible soil of Itaguaí, Rio de Janeiro. In *IV Proceedings of the Luso Brazilian Geotechnical Congress*, Coimbra. CD-ROM (in Portuguese).

Massarsch, K.R., & Topolnicki, M. (2005). Regional report: European practice of soil mixing technology. In *Proceedings of the International Conference on Deep Mixing – Best Practice and Recent Advances*, Stockholm.

McCabe, B.A., Nimmons, G.J., & Egan, D. (2009). A review of field performance of stone columns in soft soils. *Geotechnical Engineering*, 162(6), 323-334. http://dx.doi.org/10.1680/geng.2009.162.6.323.

McGuire, M., Sloan, J., Collin, J., Filz, G., 2012, Critical Height of Column-Supported embankments from Bench-Scale and Field-Scale Tests. In *ISSMGE - TC 211 International Symposium on Ground Improvement IS-GI* Brussels.

Nascimento, T.Z. (2016). *Laboratory and field behavior of a cement stabilized very soft clay* [Master's dissertation]. Federal University of Rio de Janeiro's repositor (in Portuguese). Retrieved in July 23, 2022, from http://www.coc.ufrj.br/pt/dissertacoes-de-mestrado/389-msc-pt-2016/4695-tayro-zonta-nascimento

Park, C., Richter, J., Rodrigues, R., & Cirone, A. (2018). MASW applications for road construction and maintenance. *The Leading Edge*, 37(10), 724-730. http://dx.doi.org/10.1190/tle37100724.1.

Pinto, C.S., Almeida, M.S.S., Almeida, M.C.F., Jenck, O., Briacom, L., Houda, M., & Emeriault, F. (2014). Physical model studies on piled embankments with and without geosynthetics. In *Proceedings of the 10 th International Conference on Geosynthetics - ICG 2014*, Berlin.

Priebe, H.J. (1995). *The design of vibro replacement* (pp. 31-37). London: Ground Engineering. Retrieved in July 23, 2022, from https://www.geplus.co.uk/technical-paper/technical-paper-the-design-of-vibro-replacement-01-12-1995/

Qian, J.H., Zhao, W.B., Cheung, Y.K., & Lee, P.K.K. (1992). The theory and practice of vacuum preloading. *Computers and Geotechnics*, 13(2), 103-118. http://dx.doi.org/10.1016/0266-352X(92)90027-Q.

Raithel, M., & Kempfert, H.G. (2000). Calculation models for dam foundations with geotextile coated sand column. In *Proceedings of the ISRM International Symposium* (pp. 347-352), Melbourne, Australia.

Riccio Filho, M.V., Baroni, M., & Almeida, M.S.S. (2013). Ground improvement in soft soils in Rio de Janeiro: the case of Athletics Park. *Proceedings of the Institution of Civil Engineers. Civil Engineering*, 166(6), 36-43. http://dx.doi.org/10.1680/cien.13.00008.

Riccio Filho, M.V., Cirone, A., Almeida, M.S.S., Rodriguez, T.T., & Faria, D.A. (2020). Site investigation and performance of radial deep consolidation grouting in soft soil. *Proceedings of the Institution of Civil Engineers –. Ground Improvement*, 173(1), 28-39. http://dx.doi.org/10.1680/jgrim.18.00036.

Riccio Filho, M.V., Almeida, M.S.S., Vasconcelos, S.M., Pires, L.G.S., & Nicodemos, L.F. (2022). Embankment supported by low area replacement ratio stone columns, monitoring and numerical studies. *KSCE Journal of Civil Engineering*, 26(2), 619-629. http://dx.doi.org/10.1007/s12205-021-0540-9.

Roza, F.C. (2012). *Behavior of works on soft soils with stone columns* [Master's dissertation]. Federal University of Rio de Janeiro' repository (in Portuguese). Retrieved in July 26, 2022, from http://www.coc.ufrj.br/pt/dissertacoes-de-mestrado/112-msc-pt-2012/4130-felipe-costa-roza

Rujikiatkamjorn, C., Indraratna, B., & Chu, J. (2007). Numerical modelling of soft soil stabilized by vertical drains, combining surcharge and vacuum preloading for a storage yard. *Canadian Geotechnical Journal*, 44(3), 326-342. http://dx.doi.org/10.1139/t06-124.

Saboya, F., Tibana, S., Reis, R.M., Fonte-Boa, T., Almeida, M.S.S., & Marques, M.E.S. (2021). Centrifuge modeling of soft soil reinforced with granular columns. *Geotechnical and Geological Engineering*, 39(4), 2955-2967. http://dx.doi.org/10.1007/s10706-020-01671-1.

Sandroni, S.S. (2014), Deslocamentos observados por longo período em aterro sobre solo mole reforçado com colunas de brita. In *Anais do 17° Congresso Brasileiro de Mecânica dos Solos e Engenharia Geotécnica*, Goiânia, Brasil (in Portuguese).

Springman, S.M., Laue, J., Askarinejad, A., & Gautray, J.N.F. (2012). On the design of ground improvement for embankements on soft ground. In *Proceedings of the International Conference on Ground Improvement and Ground Control: Transport Infrastructure Development and Natural Hazards Mitigation* (Vol. 1, pp. 67-83), Wollongong, Australia. http://dx.doi.org/10.3850/978-981-07-3559-3_101-0006.

Tavenas, F., Mieussens, C., & Bourges, F. (1979). Lateral displacement in clay foundations under embankments. *Canadian Geotechnical Journal*, 16(3), 532-550. http://dx.doi.org/10.1139/t79-059.

Topolnicki, M. (2012). Design and execution practice of wet Soil Mixing in Poland. In *Proceedings of the International Symposium on Deep Mixing and Admixture Stabilization* (pp. 195-202), Okinawa.

Topolnicki, M. (2016). General overview and advances in Deep Soil Mixing. In *Proceedings of the XXIV Geotechnical Conference of Torino Design, Construction and Controls of Soil Improvement Systems* (pp. 25-26), Torino.

van Eekelen, S.J.M., Bezuijen, A., & van Tol, A.F. (2013). An analytical model for arching in piled embankments. *Geotextiles and Geomembranes*, 39, 78-102. http://dx.doi.org/10.1016/j.geotexmem.2013.07.005.

Wu, J.Y. (2005). Numerical study of radial ground improvement technology in soft clay. In *Proceedings of Computing in Civil Engineering* (pp. 1-10), Cancun, Mexico. ASCE.

Zheng, G., Liu, J., Lei, H., Rahman, M.S., & Tan, Z. (2017). Improvement of very soft ground by a high-efficiency vacuum preloading method: a case study. *Marine Georesources and Geotechnology*, 35(5), 631-642. http://dx.doi.org/10.1080/1064119X.2016.1215363.

32

Almeida et al., Soil. Rocks, São Paulo, 2023 46(1):e2023008222
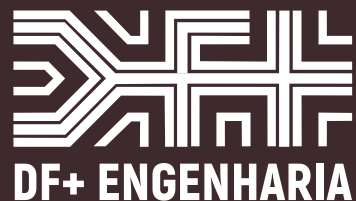
**GABIÃO BELGO.
UMA ESCOLHA PARA
ELEVAR A QUALIDADE
DA SUA OBRA.**

A linha **Belgo GeoTech** traz ao mercado soluções em aço para aplicações geotécnicas. Entre os nossos produtos, disponibilizamos **gabiões**, **malhas talude**, **fibras de aço Dramix®**, **telas de fortificação**, **cordoalhas** e **barras helicoidais**. Mas também oferecemos suporte técnico qualificado para atender a todas as necessidades do seu projeto. **Aqui se faz geotecnia com a força do aço.**

Saiba mais em: belgogeotech.com.br

BELGO GeoTech

Belgo Bekaert Arames

ArcelorMittal

BEKAERT
better together

Maccaferri Rockfall barrier installed alongside mesh systems

Combining different systems to provide the most effective solution for rock faces and soil slopes.

Maccaferri RB Series of rockfall barriers is specifically designed to retain impacts of falling boulders, protecting people and infrastructure. Maccaferri rockfall barriers are available with energy absorption capacity starting from 35 kJ and up to 9,000 kJ, which is equivalent to the kinetic energy generated by a block of 29 tons falling at 90 km/h.

Maccaferri additionally developed numerous rockfall mitigation and erosion protection system to be implemented directly within the detachment zone. Among those, soil nailing is a technique that combines the use of steel anchors and facing systems to provide global and surficial stability to soil and weathered rocks.

The facing system plays a key role since it restrains the superficial portion of the slope which can mobilise between the anchors, potentially destabilizing the overall slope. Therefore, Maccaferri developed MacMat®, an innovative reinforced 3D geomat that provide surficial stabilization while promoting the revegetation of the slope.

Very often the use of combined solutions such as the two mentioned above leads to the best results. It also provides the most cost-effective balance between technical performance, risk, client value, ease/safety of installation and environmental benefits.

/maccaferri /maccaferrimatriz @Maccaferri_BR /MaccaferriWorld /maccaferriworld

MACCAFERRI

> **Prospecção Geotécnica**
> *Site Investigation*
> **Consultoria Geotécnica**
> *Geotechnical Consultancy*
> **Obras Geotécnicas**
> *Ground Treatment-Construction Services*
> **Controlo e Observação**
> *Field Instrumentation Services and Monitoring Services*
> **Laboratório de Mecânica de Solos**
> *Soil and Rock Mechanics Laboratory*

Certificada ISO 9001 por

BVQi

Parque Oriente, Bloco 4, EN10
2699-501 Bobadela LRS
Tel. 21 995 80 00
Fax. 21 995 80 01
e.mail: mail@geocontrole.pt
www.geocontrole.pt

Geocontrole
Geotecnia e Estruturas de Fundação SA

tPF

TPF - CONSULTORES DE ENGENHARIA E ARQUITETURA, S.A.

BUILDING THE WORLD, BETTER
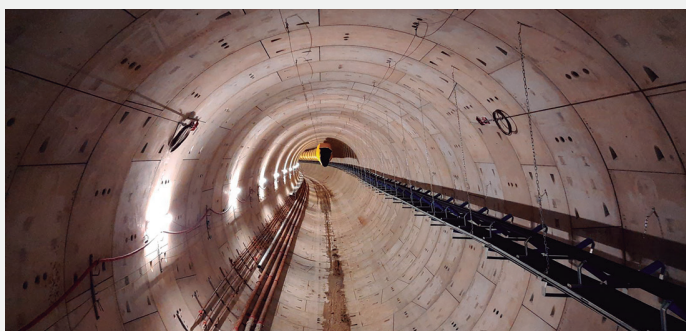
ENGINEERING AND ARCHITECTURAL CONSULTANCY

> GEOLOGY, GEOTECHNICS, SUPERVISION OF GEOTECHNICAL WORKS

> EMBANKMENT DAMS, UNDERGROUND WORKS, RETAINING STRUCTURES

> SPECIAL FOUNDATIONS, SOIL IMPROVEMENT, GEOMATERIALS

www.tpf.pt

Guide for Authors

Soils and Rocks is an international scientific journal published by the Brazilian Association for Soil Mechanics and Geotechnical Engineering (ABMS) and by the Portuguese Geotechnical Society (SPG). The aim of the journal is to publish original papers on all branches of Geotechnical Engineering. Each manuscript is subjected to a single-blind peer-review process. The journal's policy of screening for plagiarism includes the use of a plagiarism checker on all submitted manuscripts.

Soils and Rocks embraces the international Open Science program and is striving to meet all the recommendations. However, at this moment, the journal is not yet accepting preprints and open data, and has not adopted open peer reviews.

Soils and Rocks provides a manuscript template available at the journal's website.

1. Category of papers

Submissions are classified into one of the following categories:

Article – an extensive and conclusive dissertation about a geotechnical topic, presenting original findings.

Technical Note – presents a study of smaller scope or results of ongoing studies, comprising partial results and/or particular aspects of the investigation.

Case Study – report innovative ways to solve problems associated with design and construction of geotechnical projects. It also presents studies of the performance of existing structures.

Review Article – a summary of the State-of-the-Art or State-of-the-Practice on a particular subject or issue and represents an overview of recent developments.

Discussion – specific discussions about published papers.

Authors are responsible for selecting the correct category when submitting their manuscript. However, the manuscript category may be altered based on the recommendation of the Editorial Board. Authors are also requested to state the category of paper in their Cover Letter.

When submitting a manuscript for review, the authors should indicate the category of the manuscript, and is also understood that they:

a) assume full responsibility for the contents and accuracy of the information in the paper;
b) assure that the paper has not been previously published, and is not being submitted to any other journal for publication.

2. Paper length

Full-length manuscripts (Article, Case Study) should be between 4,000 and 8,000 words. Review articles should have up to 10,000 words. Technical Notes have a word count limit of 3,500 words. Discussions have a word count limit of 1,000 words. These word count limits exclude the title page, notation list (e.g., symbols, abbreviations), captions of tables and figures, acknowledgments and references. Each single column and double column figure or table is considered as equivalent to 150 and 300 words, respectively.

3. Scientific style

The manuscripts should be written in UK or US English, in the third person and all spelling should be checked in accordance with a major English Dictionary. The manuscript should be able to be readily understood by a Civil Engineer and avoid colloquialisms. Unless essential to the comprehension of the manuscript, direct reference to the names of persons, organizations, products or services is not allowed. Flattery or derogatory remarks about any person or organization should not be included.

The author(s) of Discussion Papers should refer to himself (herself/themselves) as the reader(s) and to the author(s) of the paper as the author(s).

The International System (SI) units must be used. The symbols are recommended to be in accordance with Lexicon in 14 Languages, ISSMFE (2013) and the ISRM List of Symbols. Use italics for single letters that denote mathematical constants, variables, and unknown quantities, either in tables or in the text.

4. Submission requirements and contents

A submission implies that the following conditions are met:

- the authors assume full responsibility for the contents and accuracy of the information presented in the paper;
- the manuscript contents have not been published previously, except as a lecture or academic thesis;
- the manuscript is not under consideration for publication elsewhere;
- the manuscript is approved by all authors;
- the manuscript is approved by the necessary authorities, when applicable, such as ethics committees and institutions that may hold intellectual property on contents presented in the manuscript;
- the authors have obtained authorization from the copyright holder for any reproduced material;
- the authors are aware that the manuscript will be subjected to plagiarism check.

The author(s) must upload two digital files of the manuscript to the Soils and Rocks submission system. The size limit for each submission file is 20 MB. The manuscript should be submitted in docx format (Word 2007 or higher) or doc format (for older Word versions). An additional PDF format file of the manuscript is also required upon submission. Currently, the journal is not accepting manuscripts prepared using LaTeX.

The following documents are required as minimum for submission:

- cover letter;
- manuscript with figures and tables embedded in the text (doc or docx format);

manuscript with figures and tables embedded in the text for revision (PDF format);
- permission for re-use of previously published material when applicable, unless the author/owner has made explicit that the image is freely available.

4.1 Cover letter

The cover letter should include: manuscript title, submission type, authorship information, statement of key findings and work novelty, and related previous publications if applicable.

4.2 Title page

The title page is the first page of the manuscript and must include:

- A concise and informative title of the paper. Avoid abbreviations, acronyms or formulae. Discussion Papers should contain the title of the paper under discussion. Only the first letter of the first word should be capitalized.
- Full name(s) of the author(s). The first name(s) should not be abbreviated. The authors are allowed to abbreviate middle name(s).
- The corresponding author should be identified by a pound sign # beside his/her and in a footnote.
- The affiliation(s) of the author(s), should follow the format: Institution, (Department), City, (State), Country.
- Affiliation address and e-mail must appear below each author's name.
- The 16-digit ORCID of the author(s) – mandatory
- Main text word count (excluding abstract and references) and the number of figures and tables

4.3 Permissions

Figures, tables or text passages previously published elsewhere may be reproduced under permission from the copyright owner(s) for both the print and online format. The authors are required to provide evidence that such permission has been granted at the moment of paper submission.

4.4 Declaration of interest

Authors are required to disclose conflicting interests that could inappropriately bias their work. For that end, a section entitled "Declaration of interest" should be included following any acknowledgments and prior to the "Authors' contributions" section. In case of the absence of conflicting interests, the authors should still include a declaration of interest.

4.5 Authors' contributions

Authors are required to include an author statement outlining their individual contributions to the paper according to the CASRAI CRediT roles (as per https://casrai.org/credit). The minimum requirements of contribution to the work for recognition of authorship are: a) Participate actively in the discussion of results; b) Review and approval of the final version of the manuscript. A section entitled "Authors' contributions" should be included after the declaration of interest section, and should be formatted with author's name and CRediT role(s), according to the example:

Samuel Zheng: conceptualization, methodology, validation. Olivia Prakash: data curation, writing - original draft preparation. Fatima Wang: investigation, validation. Kwame Bankole: supervision. Sun Qi: writing - reviewing and editing.

Do not include credit items that do not follow the Taxonomy established by CASRAI CRediT roles.

The authors' contributions section should be omitted in manuscripts that have a single author.

5. Plagiarism checking

Submitted papers are expected to contain at least 50 % new content and the remaining 50 % should not be verbatim to previously published work.

All manuscripts are screened for similarities. Currently, the Editorial Board uses the plagiarism checker Plagius (www. plagius.com) to compare submitted papers to already published works. Manuscripts will be rejected if more than 20 % of content matches previously published work, including self-plagiarism. The decision to reject will be under the Editors' discretion if the percentage is between 10 % and 20 %.

IMPORTANT OBSERVATION: Mendeley software plug-in (suggested in this guide) for MS-Word can be used to include the references in the manuscript. This plug-in uses a field code that sometimes includes automatically both title and abstract of the reference. Unfortunately, the similarity software adopted by the Journal (Plagius) recognizes the title and abstract as an actual written text by the field code of the reference and consequently increases considerably the percentage of similarity. Please do make sure to remove the abstract (if existing) inside Mendeley section where the adopted reference is included. This issue has mistakenly caused biased results in the past. The Editorial Board of the journal is now aware of this tendentious feature.

6. Formatting instructions

The text must be presented in a single column, using ISO A4 page size, left, right, top, and bottom margins of 25 mm, Times New Roman 12 font, and line spacing of 1.5. All lines and pages should be numbered.

The text should avoid unnecessary italic and bold words and letters, as well as too many acronyms. Authors should avoid to capitalize words and whenever possible to use tables with distinct font size and style of the regular text.

Figures, tables and equations should be numbered in the sequence that they are mentioned in the text.

Abstract

Please provide an abstract between 150 and 250 words in length. Abbreviations or acronyms should be avoided. The abstract should state briefly the purpose of the work, the main results and major conclusions or key findings.

Keywords

A minimum of three and a maximum of six keywords must be included after the abstract. The keywords must represent the

content of the paper. Keywords offer an opportunity to include synonyms for terms that are frequently referred to in the literature using more than one term. Adequate keywords maximize the visibility of your published paper.

Examples:

Poor keywords – piles; dams; numerical modeling; laboratory testing

Better keywords – friction piles; concrete-faced rockfill dams; material point method; bender element test

List of symbols

A list of symbols and definitions used in the text must be included before the References section. Any mathematical constant, variable or unknown quantity should appear in italics.

6.1 Citations

References to other published sources must be made in the text by the last name(s) of the author(s), followed by the year of publication. Examples:

- Narrative citation: […] while Silva & Pereira (1987) observed that resistance depended on soil density
- Parenthetical citation: It was observed that resistance depended on soil density (Silva & Pereira, 1987).

In the case of three or more authors, the reduced format must be used, e.g.: Silva et al. (1982) or (Silva et al., 1982). Do not italicize "et al."

Two or more citations belonging to the same author(s) and published in the same year are to be distinguished with small letters, e.g.: (Silva, 1975a, b, c.).

Standards must be cited in the text by the initials of the entity and the year of publication, e.g.: ABNT (1996), ASTM (2003).

6.2 References

A customized style for the Mendeley software is available and may be downloaded from this link.

Full references must be listed alphabetically at the end of the text by the first author's last name. Several references belonging to the same author must be cited chronologically.

Some formatting examples are presented here:

Journal Article

Bishop, A.W., & Blight, G.E. (1963). Some aspects of effective stress in saturated and partly saturated soils. *Géotechnique*, 13(2), 177-197. https://doi.org/10.1680/geot.1963.13.3.177

Castellanza, R., & Nova, R. (2004). Oedometric tests on artificially weathered carbonatic soft rocks. *Journal of Geotechnical and Geoenvironmental Engineering*, 130(7), 728-739. https://doi.org/10.1061/(ASCE)1090-0241(2004)130:7(728)

Fletcher, G. (1965). Standard penetration test: its uses and abuses. Journal of the Soil Mechanics Foundation Division, 91, 67-75.

Indraratna, B., Kumara, C., Zhu S-P., Sloan, S. (2015). Mathematical modeling and experimental verification of fluid flow through deformable rough rock joints. *International Journal of Geomechanics*, 15(4): 04014065-1-04014065-11. https://doi.org/10.1061/(ASCE)GM.1943-5622.0000413

Garnier, J., Gaudin, C., Springman, S.M., Culligan, P.J., Goodings, D., Konig, D., ... & Thorel, L. (2007). Catalogue of scaling laws and similitude questions in geotechnical centrifuge modelling. *International Journal of Physical Modelling in Geotechnics*, 7(3), 01-23. https://doi.org/10.1680/ijpmg.2007.070301

Bicalho, K.V., Gramelich, J.C., & Santos, C.L.C. (2014). Comparação entre os valores de limite de liquidez obtidos pelo método de Casagrande e cone para solos argilosos brasileiros. *Comunicações Geológicas*, 101(3), 1097-1099 (in Portuguese).

Book

Lambe, T.W., & Whitman, R.V. (1979). *Soil Mechanics, SI version*. John Wiley & Sons.

Das, B.M. (2012). *Fundamentos de Engenharia Geotécnica*. Cengage Learning (in Portuguese).

Head, K.H. (2006). *Manual of Soil Laboratory Testing - Volume 1*: Soil Classification and Compaction Tests. Whittles Publishing.

Bhering, S.B., Santos, H.G., Manzatto, C.V., Bognola, I., Fasolo, P.J., Carvalho, A.P., ... & Curcio, G.R. (2007). *Mapa de solos do estado do Paraná*. Embrapa (in Portuguese).

Book Section

Yerro, A., & Rohe, A. (2019). Fundamentals of the Material Point Method. In *The Material Point Method for Geotechnical Engineering* (pp. 23-55). CRC Press. https://doi.org/10.1201/9780429028090

Sharma, H.D., Dukes, M.T., & Olsen, D.M. (1990). Field measurements of dynamic moduli and Poisson´s ratios of refuse and underlying soils at a landfill site. In *Geotechnics of Waste Fills - Theory and Practice* (pp. 57-70). ASTM International. https://doi.org/10.1520/STP1070-EB

Cavalcante, A.L.B., Borges, L.P.F., & Camapum de Carvalho, J. (2015). Tomografias computadorizadas e análises numéricas aplicadas à caracterização da estrutura porosa de solos não saturados. In *Solos Não Saturados no Contexto Geotécnico* (pp. 531-553). ABMS (in Portuguese).

Proceedings

Jamiolkowski, M.; Ladd, C.C.; Germaine, J.T., & Lancellotta, R. (1985). New developments in field and laboratory testing of soils. *Proc. 11th International Conference on Soil Mechanics and Foundation Engineering,* San Francisco, August 1985. Vol. 1, Balkema, 57-153.

Massey, J.B., Irfan, T.Y. & Cipullo, A. (1989). The characterization of granitic saprolitic soils. *Proc. 12th International Conference on Soil Mechanics and Foundation Engineering*, Rio de Janeiro. Vol. 6, Publications Committee of XII ICSMFE, 533-542.

Indraratna, B., Oliveira D.A.F., & Jayanathan, M. (2008b). Revised shear strength model for infilled rock joints considering overconsolidation effect. *Proc. 1st Southern Hemisphere International Rock Mechanics Symposium*, Perth. ACG, 16-19.

Barreto, T.M., Repsold, L.L., & Casagrande, M.D.T. (2018). Melhoramento de solos arenosos com polímeros. *Proc. 19° Congresso Brasileiro de Mecânica dos Solos e Engenharia Geotécnica*, Salvador. Vol. 2, ABMS, CBMR, ISRM & SPG, 1-11 (in Portuguese).

Thesis

Lee, K.L. (1965). *Triaxial compressive strength of saturated sands under seismic loading conditions* [Unpublished doctoral dissertation]. University of California at Berkeley.

Chow, F.C. (1997). *Investigations into the behaviour of displacement pile for offshore foundations* [Doctoral thesis, Imperial College London]. Imperial College London's repository. https://spiral.imperial.ac.uk/handle/10044/1/7894

Araki, M.S. (1997). *Aspectos relativos às propriedades dos solos porosos colapsíveis do Distrito Federal* [Unpublished master's dissertation]. University of Brasília (in Portuguese).

Sotomayor, J.M.G. (2018). *Evaluation of drained and non-drained mechanical behavior of iron and gold mine tailings reinforced with polypropylene fibers* [Doctoral thesis, Pontifical Catholic University of Rio de Janeiro]. Pontifical Catholic University of Rio de Janeiro's repository (in Portuguese). https://doi.org/10.17771/PUCRio.acad.36102*

* *official title in English should be used when available in the document.*

Report

ASTM D7928-17. (2017). Standard Test Method for Particle-Size Distribution (Gradation) of Fine-Grained Soils Using the Sedimentation (Hydrometer) Analysis. *ASTM International, West Conshohocken, PA.* https://doi.org/10.1520/D7928-17

ABNT NBR 10005. (2004). Procedure for obtention leaching extract of solid wastes. *ABNT - Associação Brasileira de Normas Técnicas*, Rio de Janeiro, RJ (in Portuguese).

DNIT. (2010). Pavimentação - Base de solo-cimento - Especificação de serviço DNIT 143. *DNIT -Departamento Nacional de Infraestrutura de Transportes*, Rio de Janeiro, RJ (in Portuguese).

USACE (1970). Engineering and Design: Stability of Earth and Rock-Fill Dams, Engineering Manual 1110-2-1902. Corps of Engineers, Washington, D.C.

Web Page

Soils and Rocks. (2020). *Guide for Authors*. Soils and Rocks. Retrieved in September 16, 2020, from http://www.soilsandrocks.com/

6.3 Artworks and illustrations

Each figure should be submitted as a high-resolution image, according to the following mandatory requirements:

- Figures must be created as a TIFF file format using LZW compression with minimum resolution of 500 dpi.
- Size the figures according to their final intended size. Single-column figures should have a width of up to 82 mm. Double-column figures should have a maximum width of 170 mm.
- Use Times New Roman for figure lettering. Use lettering sized 8-10 pt. for the final figure size.
- Lines should have 0.5 pt. minimum width in drawings.
- Titles or captions should not be included inside the figure itself.

Figures must be embedded in the text near the position where they are first cited. Cite figures in the manuscript in consecutive numerical order. Denote figure parts by lowercase letters (a, b, c, etc.). Please include a reference citation at the end of the figure caption for previously published material. Authorization from the copyright holder must be provided upon submission for any reproduced material.

Figure captions must be placed below the figure and start with the term "Figure" followed by the figure number and a period. Example:

Figure 1. Shear strength envelope.

Do not abbreviate "Figure" when making cross-references to figures.

All figures are published in color for the electronic version of the journal; however, the print version uses grayscale. Please format figures so that they are adequate even when printed in grayscale.

Accessibility: Please make sure that all figures have descriptive captions (text-to-speech software or a text-to-Braille hardware could be used by blind users). Prefer using patterns (e.g., different symbols for dispersion plot) rather than (or in addition to) colors for conveying information (then the visual elements can be distinguished by colorblind users). Any figure lettering should have a contrast ratio of at least 4.5:1

Improving the color accessibility for the printed version and for colorblind readers: Authors are encouraged to use color figures because they will be published in their original form in the online version. However, authors must consider the need to make their color figures accessible for reviewers and readers that are colorblind. As a general rule of thumb, authors should avoid using red and green simultaneously. Red should be replaced by magenta, vermillion, or orange. Green should be replaced by an off-green color, such as blue-green. Authors should prioritize the use of black, gray, and varying tones of blue and yellow.

These rules of thumb serve as general orientations, but authors must consider that there are multiple types of color blindness, affecting the perception of different colors. Ideally, authors should make use of the following resources: 1) for more information on how to prepare color figures, visit https://jfly.uni-koeln.de/; 2) a freeware software available at http://www.vischeck.com/ is offered by Vischeck, to show how your figures would be perceived by the colorblind.

6.4 Tables

Tables should be presented as a MS Word table with data inserted consistently in separate cells. Place tables in the text near the position where they are first cited. Tables should be numbered consecutively using Arabic numerals and have a caption consisting of the table number and a brief title. Tables should always be cited in the text. Any previously published material should be identified by giving the original source as a reference at the end of the table caption. Additional comments can be placed as footnotes, indicated by superscript lower-case letters.

When applicable, the units should come right below the corresponding column heading. Horizontal lines should be used at the top and bottom of the table and to separate the headings row. Vertical lines should not be used.

Table captions must be placed above the table and start with the term "Table" followed by the table number and a period. Example:

Table 1. Soil properties.

Do not abbreviate "Table" when making cross-references to tables. Sample:

Table 1. Soil properties

Parameter	Symbol	Value
Specific gravity of the sand particles	G_s	2.64
Maximum dry density (Mg/m^3)	$\rho_{d(max)}$	1.554
Minimum dry density (Mg/m^3)	$\rho_{d(min)}$	1.186
Average grain-size (mm)	d_{50}	0.17
Coefficient of uniformity	C_u	1.97

6.5 Mathematical equations

Equations must be submitted as editable text, created using MathType or the built-in equation editor in MS Word. All variables must be presented in italics.

Equations must appear isolated in a single line of the text. Numbers identifying equations must be flushed with the right margin. International System (SI) units must be used. The definitions of the symbols used in the equations must appear in the List of Symbols.

Do not abbreviate "Equation" when making cross-references to an equation.